Improved Voltage Clamp Fluorometry to Investigate the Molecular Function of the P2X7 Receptor C-Terminus and Characterization of Novel P2X7 Receptor Ligands

Anna Durner

München 2023

Aus dem Walther-Straub-Institut für Pharmakologie und
Toxikologie der Ludwig-Maximilians-Universität München

Vorstand: Prof. Dr. med. Thomas Gudermann

Improved Voltage Clamp Fluorometry to Investigate the Molecular Function of the P2X7 Receptor C-Terminus and Characterization of Novel P2X7 Receptor Ligands

Dissertation

zum Erwerb des Doktorgrades der Naturwissenschaften
an der Medizinischen Fakultät
der Ludwig-Maximilians-Universität München

vorgelegt von

Anna Durner

aus Heidelberg

2023

Mit Genehmigung der Medizinischen Fakultät
der Universität München

Betreuerin:	Prof. Dr. phil. nat. Annette Nicke
Zweitgutachter:	Prof. Dr. rer. nat. Alexander Faußner
Dekan:	Prof. Dr. med. Thomas Gudermann

Tag der mündlichen Prüfung: 30. August 2023

Abstract

The ATP-gated, purinergic P2X7 receptor (P2X7R) is a trimeric, non-selective cation channel with key functions in inflammation and immunity. It mediates a multitude of cellular events that are normally not associated with ion channel functions (e.g. modification of the plasma membrane, cytokine release, and cell death). Compared to the other homologous P2X receptor subunits (P2X1-P2X6), the P2X7 subunit contains an unusually long intracellular C-terminus, which is thought to be essential for most of these cellular responses **[4.1]**. However, the underlying molecular mechanisms and signaling pathways are incompletely understood. The role of the P2X7R in immune signaling and especially its involvement in diverse pathophysiological processes such as inflammation, epilepsy, Alzheimer's disease, and cancer makes it an interesting drug target. To validate the P2X7R as a drug target, detailed understanding of its molecular and physiological functions, cell-type specific expression, and selective ligands are required. A major aim of this work was the investigation of the molecular consequences of P2X7R activation and the identification of potent antagonists. In addition, I investigated the localization of the P2X7R and thereby contributed to the characterization of a novel P2X7 mouse model.

To investigate conformational changes in the molecular structure of the P2X7R that are associated with its activation, I applied voltage clamp fluorometry (VCF) (**[4.2]**). To this end, I refined a method for the incorporation of the environment-sensitive fluorescent unnatural amino acid (fUAA) ANAP into *Xenopus laevis* oocyte-expressed receptors. Furthermore, I constructed a VCF setup optimized for the detection of ANAP-specific fluorescence changes. VCF measurements from ANAP-containing P2X7R-expressing oocytes provided evidence that the ATP-induced conformational changes in extracellular and transmembrane domains are not translated to the intracellular C-terminus and that the P2X7-characteristic current facilitation is an intrinsic receptor property and likely associated with change in its gating (**[3.1]**).

To determine and compare the potency of novel small-molecule P2X7R antagonists, I performed two-electrode voltage clamp (TEVC) analysis on P2X7R-expressing *X. laevis* oocytes (**[3.2]**, **[4.3]**). These data revealed a compound with nanomolar potency, for which I further analyzed association and dissociation kinetics and confirmed its binding to the P2X7R allosteric binding pocket by site-directed mutagenesis.

Finally, I contributed to the validation of a novel BAC transgenic reporter mouse model and the determination of the controversially discussed P2X7 expression pattern (**[4.4]** and **[3.3]**) by performing immunohistochemical tissue stainings to compare endogenous and transgenic P2X7R expression patterns.

Together, these studies advanced our knowledge about molecular principles underlying P2X7 signal transduction, identified a new potent drug lead, and helped to provide a novel mouse model to investigate P2X7R localization and physiological functions.

In an unrelated publication (**[3.4]**), I helped to characterize nicotinic acetylcholine receptor ligands by TEVC.

Affidavit

Durner, Anna Katharina

Surname, first name

I hereby declare, that the submitted thesis entitled

Improved Voltage Clamp Fluorometry to Investigate the Molecular Function of the P2X7 Receptor C-Terminus and Characterization of Novel P2X7 Receptor Ligands

is my own work. I have only used the sources indicated and have not made unauthorised use of services of a third party. Where the work of others has been quoted or reproduced, the source is always given.

I further declare that the dissertation presented here has not been submitted in the same or similar form to any other institution for the purpose of obtaining an academic degree.

Munich, 05.10.2023

Place, Date

Anna Katharina Durner

Signature doctoral candidate

Confirmation of congruency between printed and electronic version of the doctoral thesis

Doctoral candidate: Frau Anna Katharina Durner

I hereby declare that the electronic version of the submitted thesis, entitled

Improved Voltage Clamp Fluorometry to Investigate the Molecular Function of the P2X7 Receptor C-Terminus and Characterization of Novel P2X7 Receptor Ligands

is congruent with the printed version both in content and format.

München, 05.10.2023
Place, Date

Anna Katharina Durner
Signature doctoral candidate

Contents

List of Abbreviations

aa	amino acid/-s
ABC method	Avidin-Biotin Complex method
ACh	Acetylcholine
ADP	adenosine 5′-diphosphate
AFM	atomic force microscopy
AMP	adenosine 5′-monophosphate
ANAP	L-3-(6-acetylnaphthalen-2-ylamino)-2-aminopropanoic acid
BAC	bacterial artificial chromosome
ATP	adenosine 5′-triphosphate
BN-PAGE	blue native polyacrylamide gel electrophoresis
cDNA	complementary deoxyribonucleic acid
cRNA	complementary ribonucleic acid
Cryo-EM	cryo-electron microscopy
DAB	3, 3′-Diaminobenzidine
DMPK	dtrug metabolism and pharmacokinetics
DRC	dose-response curve
EGFP	enhanced green fluorescent protein
FACS	fluorescence-activated cell sorting
FRET	fluorescence resonance energy transfer
fUAA	fluorescent unnatural amino acid
GECO	genetically encoded Ca^{2+}-indicator for optical imaging
GPCR	G-protein coupled receptor
IC_{50}	half maximal inhibitory concentration
LGIC	ligand-gated ion channel
MD simulations	molecular dynamics simulations
MPPC	multi-pixel photon counter
NA	numerical aperture
nAChR	nicotinic acetylcholine receptor
NAM	negative allosteric modulator
Ni-NTA	nickel-nitrilotriacetic acid
NLRP	NOD-like receptor pyrin domain-containing
NOD	nucleotide-binding oligomerization domain
P2XR	P2X receptor
PS-flip	phosphatidylserine flip
SCAM	substituted-cysteine accessibility method
SDS-PAGE	sodium dodecyl sulfate-polyacrylamide gel electrophoresis
sEGFP	soluble enhanced green fluorescent protein
SNP	single nucleotide polymorphism
TEVC	two-electrode voltage clamp
TM2	second transmembrane domain
TMRM	tetramethyl-rhodamine-maleimide
UAA	unnatural amino acid
VCF	voltage clamp fluorometry
wt	wild type
X. laveis	*Xenopus laevis*

List of Publications

0.1 Thesis-relevant Publications (Results)

[1] **Anna Durner**, Ellis Durner, Annette Nicke, "Improved ANAP incorporation and VCF analysis reveal details of P2X7 current facilitation and a limited conformational interplay between ATP binding and the intracellular ballast domain", eLife, 2023, DOI: 10.7554/eLife.82479

[2] Dimitra T. Pournara, **Anna Durner**, Eftichia Kritsi, Alexios Papakostas, Panagiotis Zoumpoulakis, Annette Nicke, and Maria Koufaki, "Design, Synthesis, and in vitro Evaluation of P2X7 Antagonists", ChemMedChem, 2020, DOI: 10.1002/cmdc.202000303

[3] Antonio Ramírez-Fernández, Lidia Urbina-Treviño, Giorgia Conte, Mariana Alves, Björn Rissiek, **Anna Durner**, Nicolas Scalbert, Jiong Zhang, Tim Magnus, Friedrich Koch-Nolte, Nikolaus Plesnila, Jan M. Deussing, Tobias Engel, Robin Kopp, and Annette Nicke, "Deviant reporter expression and P2X4 passenger gene overexpression in the soluble EGFP BAC transgenic P2X7 reporter mouse model", Scientific Reports, 2020, DOI: 10.1038/s41598-020-76428-0

[4] Julien Giribaldi*, Yves Haufe*, Edward R. J. Evans, Muriel Amar, **Anna Durner**, Casey Schmidt, Adèle Faucherre, Hamid Moha Ou Maati, Christine Enjalbal, Jordi Molgó, Denis Servent, David T. Wilson, Norelle L. Daly, Annette Nicke, and Sébastien Dutertre, "Backbone Cyclization Turns a Venom Peptide into a Stable and Equipotent Ligand at Both Muscle and Neuronal Nicotinic Receptors", Journal of Medicinal Chemistry, 2020, DOI: 10.1021/acs.jmedchem.0c00957

0.2 Additional Publications (Appendix)

[1] **Anna Durner**, Annette Nicke, "A Simplified Protocol to Incorporate the Fluorescent Unnatural Amino Acid ANAP into Xenopus laevis Oocyte-Expressed P2X7 Receptors", Methods in Molecular Biology (Clifton, N.J.), 2022, DOI: 10.1007/978-1-0716-2384-8_10

[2] Robin Kopp*, **Anna Krautloher***, Antonio Ramírez-Fernández, and Annette Nicke, "P2X7 Interactions and Signaling – Making Head or Tail of It", Frontiers in Molecular Neuroscience, 2019, DOI: 10.3389/fnmol.2019.00183

[3] Karina Kaczmarek-Hajek*, Jiong Zhang*, Robin Kopp*, Antje Grosche, Björn Rissiek, Anika Saul, Santina Bruzzone, Tobias Engel, Tina Jooss, **Anna Krautloher**, Stefanie Schuster, Tim Magnus, Christine Stadelmann, Swetlana Sirko, Friedrich Koch-Nolte, Volker Eulenburg, and Annette Nicke, "Re-evaluation of neuronal P2X7 expression using novel mouse models and a P2X7-specific nanobody", eLife, 2018, DOI: 10.7554/eLife.36217

For readability, publications are presented in a different order in the following thesis.

* These authors contributed equally to this work

Part I

Introduction

1
Scientific Context

1.1 Purinergic Signaling

The ubiquitous molecule adenosine 5′-triphosphate (ATP) provides energy in intracellular metabolic processes, is crucial for DNA/RNA synthesis, and additionally functions as an extracellular messenger: Thus, it can act as autocrine and paracrine signaling molecule, as neurotransmitter, e.g. in sensory or autonomous neurotransmission, and additionally as a pro-inflammatory danger signal [1–3]. Extracellular ATP activates P2Y and P2X receptors, two classes of the purinergic plasma membrane receptor family. Purinoceptors are distributed throughout mammalian tissues [4] and comprise three classes (see Fig. 1.1) [2]: The adenosine-sensitive P1 receptors and the purine- and pyrimidine-sensitive P2Y receptors are metabotropic G-protein coupled receptors (GPCRs). The ATP-gated P2X receptors (P2XRs) are ionotropic receptors or ligand-gated ion channels (LGICs). Generally, the binding of specific agonists to (an) orthosteric binding site(s) of a LGIC induces a conformational change of the protein, leading to the opening of a transmembrane pore and facilitating the conduction of ions along the electrochemical gradient. These gating events happen within milliseconds and can be regulated by effector molecules binding to allosteric sites of the receptor (allosteric modulators) [5, 6].

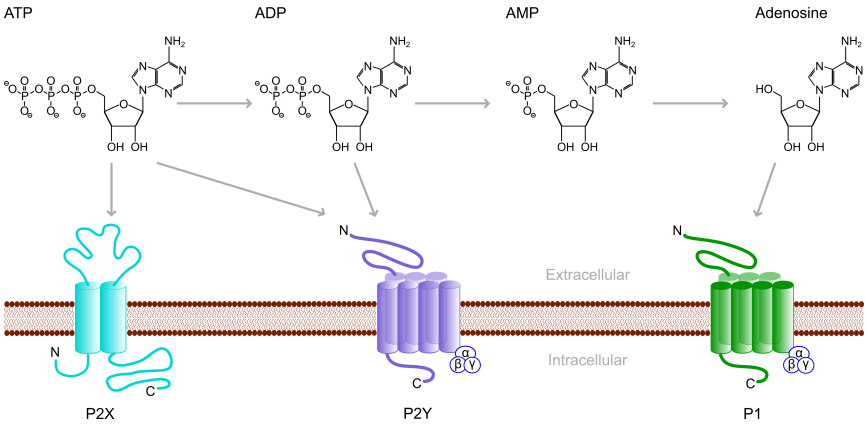

Figure 1.1. Purinergic Signaling and Classification of Purinoceptors: Hydrolysis of extracellular ATP results in breakdown products that target different classes of purinoceptors [7]: P1 receptors are metabotropic adenosine receptors; P2 receptors are activated by ATP and can be further devided into P2X and P2Y receptors. While P2X receptors are ionotropic and ATP is their only known physiological ligand, P2Y receptors are metabotropic and can also be activated by adenosine 5′-diphosphate (ADP) and additionally by uridine nucleotides.

1.2 P2X Receptors

P2XRs represent non-selective cation channels and are involved in numerous physiological processes, such as taste and hearing, synaptic transmission, pain sensation, smooth muscle contraction, and inflammatory processes [8].
Seven mammalian subunits (P2X1-P2X7) are known, and they all have a common topology with intracellular N- and C-termini, two transmembrane domains (TM1 and TM2), and an extracellular domain [9, 10]. The overall shape of a subunit resembles the form of a dolphin and domains are referred to accordingly: TM1 and TM2 are the designated "flukes", the extracellular domain is defined as the "body", and extracellular loops are named left and right "flippers", "dorsal fin", and "head" domain (see Fig. 1.2). The subunits can form functional homotrimeric (except for P2X6) or heterotrimeric membrane receptors with three inter-subunit orthosteric binding sites [11, 12]. Their trimeric structure was originally shown by BN-PAGE analysis, chemical cross-linking, electrophysiological analysis of binding site mutants, and atomic force microscopy (AFM) experiments [13–17] and subsequently confirmed by X-ray crystallization of the *Danio rerio* P2X4 receptor in the closed apo [9] and the ATP-bound open state [18]. Crystal structures of invertebrate (*Amblyomma maculatum* P2XR [19]) and vertebrate P2XRs (e.g. chicken P2X7R (*Gallus gallus*) [20], giant panda P2X7R (*Ailuropoda melanoleuca)* [21], and human P2X3R [22]) and more recently also cryo-electron microscopy (cryo-EM) structures (rat P2X7R (*Rattus norvegicus*)) have since been determined, further extending our understanding of their molecular organization and gating mechanism and revealing fundamental insights into subunit differences as well as ligand interactions (summarized in [23]).

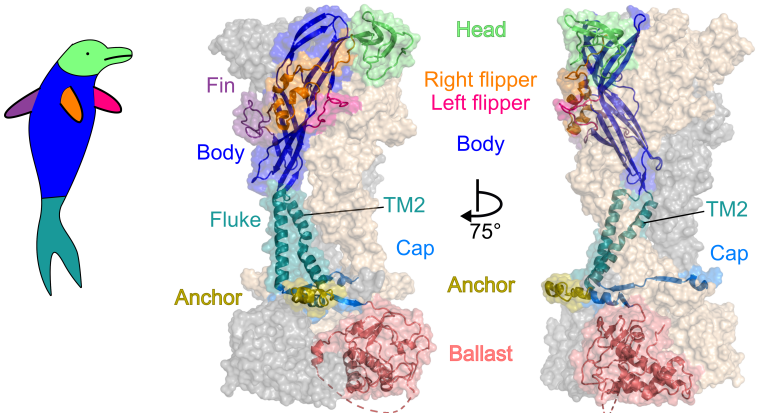

Figure 1.2. Overall architecture of the P2X7 receptor: Surface representation of the rat P2X7 cryo-EM structure in the open state (PDB ID: 6u9w). Two subunits are shown in gray and wheat, while the third subunit is domain-specifically colored and additionally overlayed by its ribbon representation. (Figure taken from Publication [3.1].)

1.3 The P2X7 Receptor

1.3.1 Structure and Functional Properties

The P2X7 receptor (P2X7R) is exceptional for several reasons. Structurally, P2X7 differs from the other subunits by its unusually long intracellular C-terminus: With a length of 240 amino acids (aa) it constitutes 40% of the total P2X7 protein. As revealed by the cryo-EM structure of the full-length rat P2X7R in the open and closed state [24], it contains an open-state stabilizing "cap" domain, a palmitoylated cysteine-rich "anchor" domain, and a globular "ballast" domain (see Fig. 1.2). A stretch of 29 aa (S443-R471) was not resolved. Hence, it is possible, that each cytoplasmic ballast domain is either formed by a single subunit, or alternatively by neighboring subunits as a result of domain swapping. Additionally, within the cytoplasmic ballast, a novel GTP/GDP binding pocket as well as a dinuclear Zn^{2+} binding site were identified, both with yet unknown functions.
Besides these structural differences, the P2X7R also differs functionally from the other subtypes. Thus, it has an at least 10-fold lower sensitivity towards the ubiquitous ligand ATP [8, 25], and it shows a total lack of receptor desensitization as well as increased current responses upon prolonged or repeated receptor activation (current facilitation) [26–28]. In addition, activation of the P2X7R initiates various short and long-term cellular events, such as modification of the plasma membrane (blebbing, PS-flip, permeabilization), activation of transcription factors and kinases, T-cell activation and differentiation, cytokine release, and cell death [29] (see also 1.3.2). The P2X7R C-terminus is thought to be essential for many of these responses that are rather unusual for ion channels. However, the underlying molecular mechanisms and signaling pathways are incompletely understood.

1.3.2 Localization and Patho-/ Physiological Functions

The P2X7R has been reported to be highly expressed in cells of hematopoietic origin [30], in epithelial [31], in endothelial and in smooth muscle cells [10, 32, 33], as well as in different types of cells present in the central and the peripheral nervous systems [34, 35]. However, its neuronal expression has been controversially debated [36–38]. The P2X7R can act as a danger signal detector [39]: Due to its low sensitivity towards ATP, the P2X7R is thought to be inactive under normal physiological conditions. ATP is considered a damage-associated molecular pattern (DAMP) and under pathophysiological conditions (e.g. tissue damage) extracellular ATP concentrations can increase from low nanomolar to high micromolar levels, that are high enough to activate P2X7Rs [40]. This has been implicated in the stimulation of immune responses and the regulation of inflammation [8, 34, 41, 42]. The best-described immune response associated with P2X7R activation is the assembly and activation of the NLRP3 inflammasome and release of the pro-inflammatory cytokine IL-1β in macrophages and microglia [43]. Other known P2X7-mediated immune responses are the secretion of additional cytokines or chemokines, formation of reactive oxygen species (ROS), T cell activation and differentiation via ATP-induced Ca^{2+}-influx, stimulation or inhibition of phagocytosis, and initiation of apoptosis (reviewed in [29, 39, 42, 44, 45]). Considering these P2X7-mediated immune responses and that many diseases are

associated with inflammation, the role of the P2X7R in pathophysiological processes is of great interest. The receptor has been shown to be involved in, cardiovascular, autoimmune, neurodegenerative, and neurological diseases as well as mood disorders and cancer [38, 44, 46–52].

1.3.3 The P2X7 Receptor as a Drug Target and P2X7 Antagonists

The involvement of the P2X7R in inflammation and immunity and especially its role in diverse pathophysiological processes makes this receptor an interesting drug target. However, the receptor exhibits a dual nature as its activation was shown to have protective as well as deleterious effects in immune responses [44] and both pro- and antitumor effects [52, 53] depending on numerous factors, e.g. cell type and level of stimulation. For targeted manipulation of P2X7 signaling, cell-specific localization of the P2X7R and a detailed understanding of its molecular and physiological functions are necessary. To that end, potent and subtype-specific ligands and modulators can be employed as pharmacological tools and for target validation.
Considerable effort is put into finding or developing P2X7-specific antagonists, as inhibition of P2X7R signaling was shown to ameliorate disease symptoms [8, 54, 55]. Additionally, the receptor's low sensitivity towards ATP compared to other P2XR subtypes suggests that inhibition of the receptor has minimal side effects under physiological conditions. P2X7R-specific antagonists have been described, some of which have been investigated in clinical trials [7, 56]. The majority of potent P2X7R antagonists act as negative allosteric modulators (NAMs) and do not bind to the orthosteric binding site. Many NAMs are adamantane based compounds, but alternative polycyclic scaffolds are explored [57]. Crystal structures of the giant panda P2X7R (*Ailuropoda melanoleuca)* with structurally distinct P2X7 antagonists (amongst them the adamantyl derivative AZ10606120) [21] as well as additional structural and functional studies with chemically diverse P2X7 antagonists [58–61] revealed a common inter-subunit allosteric binding pocket near the orthosteric ATP-binding site. Occupation of this allosteric binding site is thought to hinder ATP-induced conformational changes and thereby receptor activation. Specific residues that mediate interactions with antagonists have been identified [21]. Antagonist-binding is suggested to be mainly mediated by hydrophobic interactions and differences in antagonist-interacting residues affect antagonist sensitivity. It is worth pointing out that the site of action for several P2X7R antagonists remains to be established and other allosteric binding sites cannot be excluded.
Notably, a novel orthosteric human P2X7R antagonist has recently been discovered in a structure-based study, which displays low micromolar potency at human P2X7 (IC_{50} 8.7 μM) and is inactive at human P2X4.
Many of the so far available P2X7R antagonists have failed clinical trials or lack druglikeness, leaving room for the development of novel P2X7R tool compounds with improved properties and therapeutic potential [56, 62].

1.3.4 Methodological Aspects

A powerful method to analyze conformational changes associated with receptor functions such as activation or desensitization is the **voltage clamp fluorometry** (VCF) method. It combines electrophysiology and fluorescence microscopy and allows simultaneous recording of ligand-induced current responses and associated molecular movements that are reported by a site-specifically attached and environment-sensitive fluorophore (see Fig. 1.4). This technique has been widely applied to analyze *X. laevis* oocyte expressed voltage-gated ion channels (VGIC) as well as LGICS [63–65]. Analysis of LGICS however is particularly challenging since the speed of ligand application can limit kinetic analyses and solution change can cause artifacts that may interfere with the usually faint fluorescence signals. Commonly, site-specific cysteine-substitution and subsequent labeling of the receptor with a thiol-reactive fluorophore is performed [66, 67]. This approach, however, only allows for fluorescent labeling of solvent-accessible, extracellular domains. This limitation can be overcome by incorporating an environment-sensitive fluorescent unnatural amino acid (fUAA) directly into the protein backbone.
In general, the site-specific incorporation of an unnatural amino acid (UAA) can be achieved via the **stop-codon suppression** approach, which makes use of a model organism's ribosomal translational machinery: Usually, an *amber* stop codon (TAG) is introduced at the site-of interest into the protein-coding gene and a corresponding *amber* suppressor tRNA (CUA anticodon) is employed to suppress the stop codon and incorporate the UAA into the nascent polypeptide chain during translation [67–69]. The *amber* suppressor tRNA already carrying the UAA can be chemically synthesized and introduced into cells together with the target gene carrying the *amber* stop codon [70]. Alternatively, the suppressor tRNA can be loaded with the UAA inside the cell by an aminoacyl-tRNA synthetase. To that end, a bio-orthogonal and UAA-specific *amber* suppressor tRNA/tRNA synthetase pair is transfected into the expression system together with the UAA and the modified target gene carrying the stop codon (see Fig. 1.3) [71]. In previous studies, the expression of UAA-containing receptors in prokaryotic and eukaryotic cells was achieved with plasmids encoding such specialized co-evolved tRNA/tRNA-synthetase pairs [72–76]. For the expression of fUAA-containing receptors specifically in *X. laevis* oocytes, a protocol has been established by Kalstrup and Blunck [77–79] using the plasmid pANAP[1] [75] and successfully applied to label Shaker voltage-gated potassium channels (Kv) with the environment-sensitive fUAA L-3-(6-acetylnaphthalen-2-ylamino)-2-aminopropanoic acid (ANAP) for VCF experiments. ANAP is a prodan derivative with absorption and emission maxima at 360 nm and 490 nm, respectively (in water) [73, 75]. *X. laevis* oocytes emit considerable background fluorescence upon illumination in the ANAP excitation spectrum. Hence, for the detection of ANAP-specific fluorescence signals in VCF experiments, an optimized recording system must feature a high dynamic range while maintaining good sensitivity as well as pulsed illumination to reduce photobleaching (see Fig. 1.4).

[1] Addgene plasmid # 48696 ; http://n2t.net/addgene:48696 ; RRID:Addgene_48696

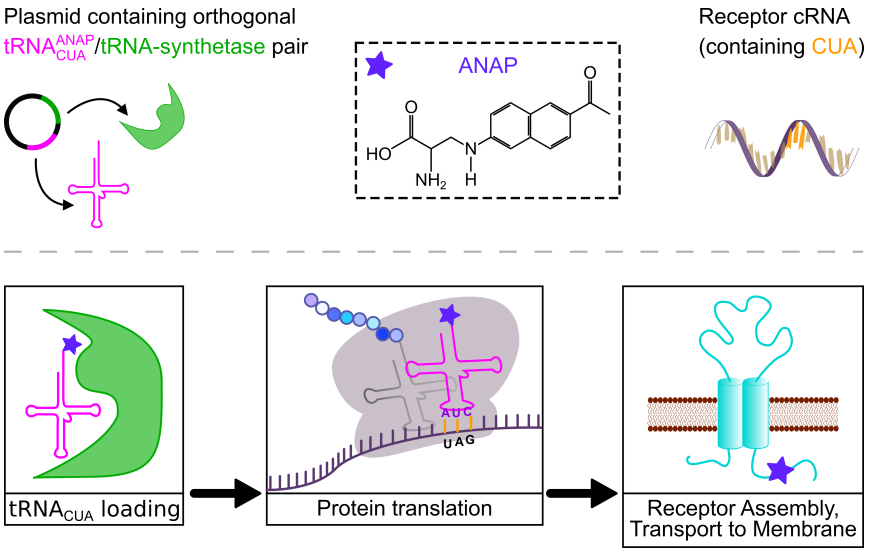

Figure 1.3. Stop-codon suppression: *Upper panel:* Components required for site-specific ANAP-incorporation into receptor proteins using the *amber* stop codon and a plasmid containing a co-evolved, ANAP-specific tRNA$_{CUA}$/tRNA-synthetase. *Lower panel:* Schematic representation of *amber* stop-codon suppression. ANAP is coupled to the suppressor tRNA (CUA anticodon) by its cognate tRNA-synthetase (*left*) and during translation incorporated into the nascent polypeptide in response to a suppressed *amber* stop codon (*center*), resulting in plasma membrane surface expression of an ANAP-containing receptor (*right*).

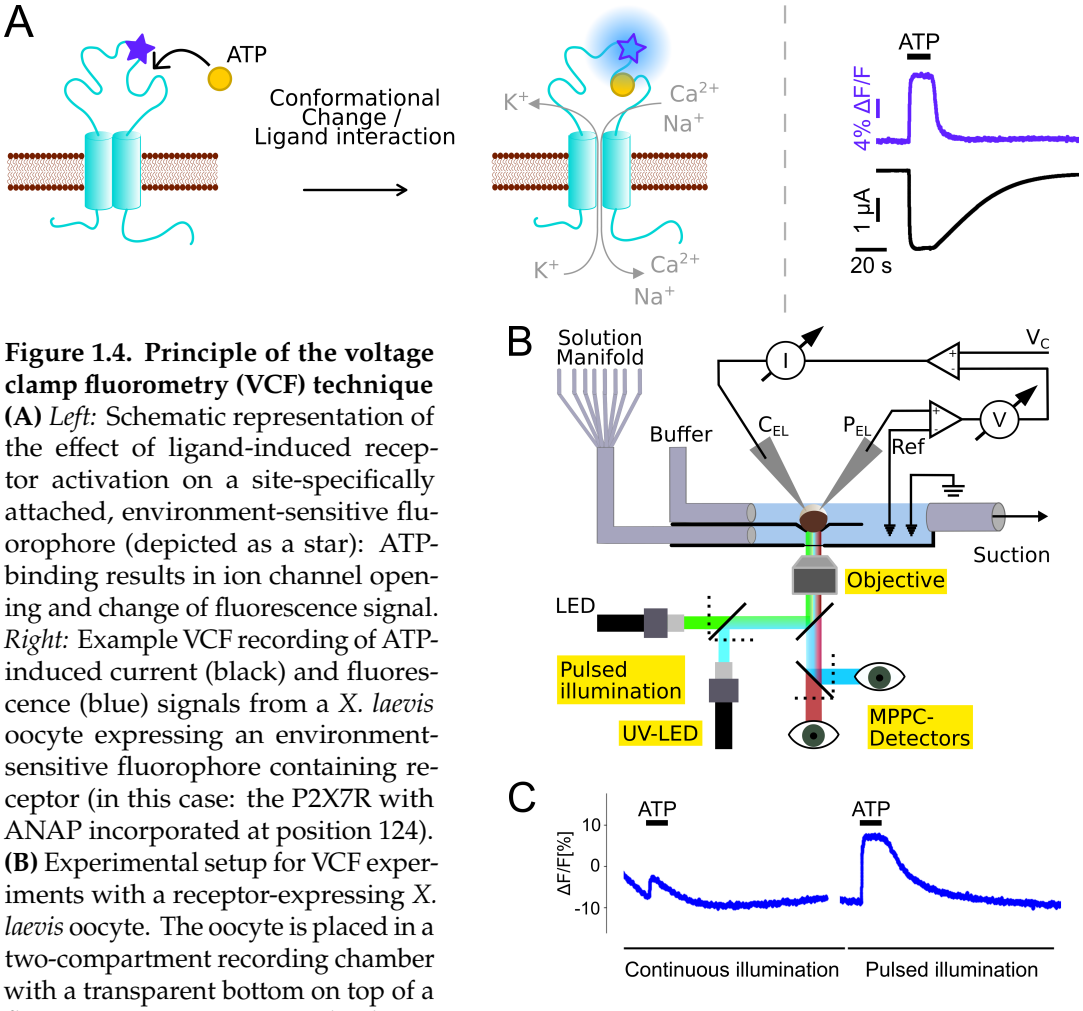

Figure 1.4. Principle of the voltage clamp fluorometry (VCF) technique
(A) *Left:* Schematic representation of the effect of ligand-induced receptor activation on a site-specifically attached, environment-sensitive fluorophore (depicted as a star): ATP-binding results in ion channel opening and change of fluorescence signal. *Right:* Example VCF recording of ATP-induced current (black) and fluorescence (blue) signals from a *X. laevis* oocyte expressing an environment-sensitive fluorophore containing receptor (in this case: the P2X7R with ANAP incorporated at position 124).
(B) Experimental setup for VCF experiments with a receptor-expressing *X. laevis* oocyte. The oocyte is placed in a two-compartment recording chamber with a transparent bottom on top of a fluorescence microscope and voltage-clamped with two electrodes (for more information, see [4.2]). Requirements for the detection of ANAP-specific signal changes are highlighted: a UV-LED, a high-NA water immersion objective, pulsed illumination for reduced photobleaching, and two cooled, high-sensitivity MPPC-detectors for simultaneous fluorescence detection at two different spectral segments. These detectors feature a wide dynamic range, while maintaining a sufficiently high sensitivity in order to record small fluorescence changes in spite of relatively high background fluorescence levels caused by UV-excitation of oocytes. By equipping the microscope with two LEDs and two detectors, the setup can also be used for parallel excitation of two different fluorophores within the same protein. Excitation and emission filters as well as dichroic mirrors are chosen depending on the used fluorophores.
(C) Illustration of the effect of pulsed versus continuous illumination with example recordings of ATP-induced fluorescence signals from a *X. laevis* oocyte expressing an ANAP-containing receptor (in this case: the P2X7R with the fluorophore ANAP incorporated in TM2 at position 340. For more information, see [3.1]).

1.4 Aim of this Work

The primary aim of this work was the investigation of the molecular function of the P2X7R, in particular of its large intracellular domain, by VCF. This included optimization of a method to incorporate the fUAA ANAP [73] into *Xenopus laevis* oocyte expressed receptors and extensive rebuilding and validation of a recording system, that is sensitive enough to detect faint ANAP fluorescence signals **[Appendix 4.2]**.
Positions for ANAP incorporation into the P2X7R protein were selected based on previous structure-function studies [65, 80]., as well as X-ray structures and cryo-EM structures [9, 22, 24, 81]. More than 60 mutants were generated and biochemically and functionally analyzed **[Results 3.1]**.
In additional projects, the potency, binding kinetics, and binding sites of novel anatagonists of the human P2X7R were determined using two-electrode voltage clamp (TEVC) analysis and mutagenesis. The small-molecule compounds were based on previously described adamantyl derivatives (AstraZeneca derivative AZ1 [82] and AZ10606120 [83]) and either still contained an adamantane scaffold **[Results 3.2]** or instead other polycyclic hydrocarbons **[Appendix 4.3]**.
Finally, to investigate a possible P2X7R localization in neurons, I contributed with immunohistochemistry stainings to two studies, in which two transgenic P2X7 reporter mouse models were characterized and compared **[Appendix 4.4** and **Results 3.3]**. Signals from immunofluorescence stainings were rather weak and colorimetric stainings that yielded more intense signals were performed for confirmation.

2
Summary

2.1 Summary

In this thesis, the molecular function and localization of the trimeric P2X7R as well as the potency of novel P2X7 antagonists were investigated, combining molecular biology, protein biochemistry, electrophysiology, and fluorescence microscopy, as well as immunohistochemistry on tissues from (transgenic) mice.
The P2X7R is an ATP-gated non-selective cation channel, that is involved in inflammation and immune signaling [42]. Its activation triggers various cellular events, such as plasma membrane permeabilization, interleukin secretion, and cell death. The underlying processes and molecular mechanisms are incompletely understood. A long intracellular C-terminus, that distinguishes the P2X7R from the other six homologous P2XR subunits (P2X1-P2X6), is supposed to be involved in the initiation of these pathways, as they are often disrupted by modifications of this region. In a detailed **Review [Appendix 4.1]**, I summarized the effects of mutations, truncations, or full deletion of the P2X7R C-terminus and reviewed proposed interaction domains and motifs within this region.
Although the protein structures of the P2X7R in the open and closed state were resolved by McCarthy et al. in 2019 and revealed for the first time the structure of the P2X7 C-terminus [24], it still represents only a static image of the receptor and does not provide information about its dynamics in a native membrane environment and the sequence of events during receptor activation.
Therefore, the main aim of this work was the investigation of localized structural rearrangements, in particular within the C-terminus, that are associated with P2X7 activation by voltage clamp fluorometry (VCF). To that end, the genetically encoded and environment-sensitive fluorescent unnatural amino acid ANAP was introduced in 61 different positions within the receptor. The targeted introduction of an UAA into proteins can be achieved by hijacking a model organism's translation machinery through repurposing the *amber* stop codon and introducing a suppressor tRNA charged with the UAA. In **Publication [Appendix 4.2]**, I presented two methods for fUAA-incorporation into *Xenopus laevis* oocyte-expressed receptors with detailed step-by-step instructions: The first one follows a previously published protocol [78], which involves sequential nuclear and cytoplasmic injections into oocytes. In addition, I developed a faster and simplified protocol, that involves only one cytoplasmic injection, is less harmful for the oocytes, and yields more reproducible results.
In **Publication [Results 3.1]**, I further refined this method by adding a mutated form of the eukaryotic release factor 1 (eRF1 (E55D)), to reduce premature translational termination events. In addition, I rebuilt and optimized the VCF instrumentation (see Fig. 1.4), to enable the simultaneous recording of ligand-induced current re-

sponses and associated structural rearrangements reported by ANAP from oocytes that express functional P2X7R constructs in the plasma membrane. Thus, in **Publication [Results 3.1]**, I could confirm conformational changes in the extracellular loop projecting over the inter-subunit ATP-binding site (head domain) and within the second transmembrane domain (TM2) predicted by crystal and cryo-EM structures. Notably, VCF recordings suggested limited translation of these ligand-induced movements to the cytosolic, globularly folded C-terminus (ballast domain). This region seems to function rather independently from the extracellular ligand-binding domain and might require intracellular interactors to mediate downstream signaling events. For future analysis of such P2X7-mediated signaling pathways and possible interactions with yet unknown ligands or proteins, I presented double-labeled P2X7Rs as novel tools together with protocols for parallel recording of ANAP with either another environment-sensitive dye (tetramethyl-rhodamine-maleimide, TMRM), a Ca^{2+}-sensor (R-GECO1.2), or mNeonGreen as a FRET partner.
Further, the data provided insight into the P2X7R-characteristic process known as current facilitation, which describes a faster onset and/or an increase in amplitude of current responses upon prolonged or repeated receptor activation. VCF recordings indicate this process to be an intrinsic feature of the P2X7R, that involves a change in channel gating rather than in ligand-binding.
A second goal of this work was the generation of dose-response curves (DRCs) to determine and compare the potency of novel P2X7R antagonists. In **Publication [Results 3.2]**, I characterized 24 analogues of the adamantane-based antagonist AZ1 (AstraZeneca, [82]) that were synthesized by collaboration partners (Dr. Maria Koufaki and colleagues, Institute of Chemical Biology, National Hellenic Research Foundation). Their potency was determined by two-electrode voltage clamp (TEVC) analysis using human P2X7R-expressing *X. laevis* oocytes.
In another project as part of a multidisciplinary collaboration on P2X7R inhibitors (in preparation), I compared the potencies of four compounds (provided by Prof. Dr. Santiago Vázquez and colleagues, Medicinal Chemistry & Pharmacology, University of Barcelona), that instead of an adamantane scaffold contain alternative polycyclic hydrocarbons. Here, I additionally established protocols to analyze association and dissociation kinetics of the most potent compound and generated two P2X7 mutants to confirm its binding to the allosteric binding site (described in **Report [Appendix 4.3]**).
In addition to these studies on *X. laevis* oocyte-expressed P2X7Rs, I contributed to two studies **[Appendix 4.4** and **Results 3.3]** that describe the validation of a bacterial artificial chromosome (BAC) transgenic P2X7-EGFP reporter mouse model generated in our laboratory [35], and its comparison with a P2X7 reporter mouse model in which a soluble EGFP (sEGFP) is expressed under the control of a BAC-derived mouse P2X7 gene (*P2rx7*) promoter (generated in the framework of the GENSAT Project [84]). In these studies, I performed 3, 3'-Diaminobenzidine (DAB) immunohistochemistry stainings in order to compare the localization of the endogenous P2X7R with the P2X7-EGFP fusion protein and to confirm results from immunofluorescence stainings, that produced weak signals compared to the colorimetric stainings.
In **Publication [Appendix 4.4]**, in-depth analysis of the BAC-transgenic P2X7-EGFP mouse together with the use of a novel P2X7-specific nanobody revealed a dominant expression of the P2X7R in microglia and oligodendrocytes, but no detectable expres-

sion in neurons. This is in contrast to the expression pattern described in the mouse model, in which sEGFP is expected to be expressed under the control of a BAC-derived *P2rx7* promoter and neuronal sEGFP expression was observed. As described above (see 1.3.2), the existence of neuronal P2X7R was a matter of debate until recently. In **Publication [Results 3.3]** the two BAC-transgenic reporter models were therefore evaluated in more detail by carefully comparing transcript and protein expression. The sEGFP-overexpressing mouse model shows an aberrant EGFP reporter pattern, unexpected increased P2X7 expression, and overexpression of a *P2rx4* passenger gene. Using sequence analysis, I could show that these effects may be explained at least partly by the genetic engineering approach that was used for the generation of the transgenic construct and its insertion into the genome.
Finally, I contributed methodologically to a project on *X. laevis* oocyte expressed nicotinic acetylcholine receptors (nAChR). In **Publication [Results 3.4]**, the inhibitory potencies of synthesized cyclic analogues of the α-conotoxin CIA on various nAChR subtypes were analyzed using TEVC. Such analogues are interesting because they show superior stability compared to the α-conotoxin CIA peptide.

2.2 Zusammenfassung

In der vorliegenden Arbeit wurden die molekularen Funktionen und die Lokalisation des P2X7 Rezeptors untersucht. Darüber hinaus wurden eine Reihe neuartiger P2X7-Antagonisten charakterisiert. Bei dem P2X7 Rezeptor handelt es sich um einen homotrimeren, unspezifischen Kationenkanal, der durch ATP aktiviert wird. Er stellt eine wichtige Zielstruktur für die Arzneimittelentwicklung dar, da er eine wesentliche Rolle bei Entzündungsreaktionen und der Funktion von Immunzellen spielt [42]. So wird er u.a. in myeloiden und lymphoiden Immunzellen und Mastzellen exprimiert und seine Stimulation trägt u.a. zur Bildung und Aktivierung des NLRP3 Inflammasoms bei, was anschließend zur Freisetzung von Zytokinen führt [8]. In zahlreichen Studien mit Krankheitsmodellen wurde diesem Rezeptor außerdem eine pathophysiologische Funktion zugeordnet, vor allem in neurodegenerativen Erkrankungen wie Morbus Alzheimer und Epilepsie, wobei seine Expression in Neuronen zu Beginn dieser Arbeit noch kontrovers diskutiert wurde [36–38].
Der P2X7 Rezeptor wird mit zahlreichen zellulären Prozessen und biologischen Funktionen in Verbindung gebracht, die für einen Ionenkanal eher untypisch sind. Für viele dieser Signalwege scheint der lange intrazelluläre C-Terminus des P2X7 Rezeptors eine Rolle zu spielen. In einem **Übersichtsartikel [Appendix 4.1]**, in welchem die bisher bekannten Signalwege und möglichen Interaktionspartner des P2X7 Rezeptors beschrieben wurden, fasste ich bisher publizierte Motive und Interaktionsdomänen in der P2X7-Struktur zusammen, wobei der Fokus auf dem ungewöhnlich langen intrazellulären C-Terminus lag. Trotz einer Vielzahl postulierter Interaktionen sind nur wenige gut belegt und die zugrundeliegenden molekularen Mechanismen der P2X7-Funktionsweise und Signaltransduktion sind unvollständig verstanden. Die im Verlauf dieser Arbeit von McCarthy et al., 2019 [24] per Kryoelektronenmikroskopie fast vollständig aufgelöste Struktur des offenen und des geschlossenen P2X7 Rezeptors lässt zwar Rückschlüsse auf seine Funktionsweise zu, kann aber keine Informationen über seine Dynamik und Funktion in natürlichen Membranen liefern [78]. So geht aus den Strukturen beispielsweise nicht hervor, wie sich die Rezeptoraktivierung auf mögliche Interaktionspartner und weitere Signalwege auswirkt, oder in welcher Reihenfolge Konformationsänderungen in verschiedenen Domänen des Rezeptors beim Übergang von geschlossenem zu offenem Zustand stattfinden.
Hauptziel dieser Arbeit war daher die Etablierung und Optimierung von Methoden zur Untersuchung lokalisierter räumlicher Änderungen in der molekularen Struktur des P2X7 Rezeptors und der damit verbundenen Rezeptorfunktionen. Die dazu von mir etablierten Protokolle und Techniken wurden mit einer Schritt-für-Schritt-Anleitung als **Methodenarbeit [Appendix 4.2]** veröffentlicht. Zusammengefasst habe ich eine Technik zum Einbau der fluoreszierenden unnatürlichen Aminosäure ANAP in *Xenopus laevis* Oozyten-exprimierte Rezeptorproteine verbessert und eine Messapparatur umgebaut, um die Identifizierung von durch Konformationsänderungen hervorgerufenen Fluoreszenzänderungen mittels "voltage clamp fluorometry" (VCF) zu ermöglichen. Die fluoreszierende, umgebungssensitive Aminosäure ANAP kann auch in nicht für Farbstoffe zugängliche Regionen von Membranproteinen (wie intrazelluläre und transmembrane Domänen) eingebracht werden und dort als molekularer Sensor dienen [73]. VCF erlaubt die zeitgleiche elektrophysiologische (mittels der Zwei-Elektroden-Spannungsklemmtechnik) und optische Analyse von

Konformationsänderungen des Rezeptors (z.B. strukturelle Änderungen oder Interaktionen mit anderen Molekülen).
In meiner **Hauptarbeit [Results 3.1]** verfeinerte ich zunächst die Methode und wandte sie zur Bestätigung von vorausgesagten Konformationsänderungen der Ligandenbindungsdomäne und Transmembrandomänen während der P2X7-Aktivierung an [24]. Weiter untersuchte ich die dem P2X7 Rezeptor typische Eigenschaft der "current facilitation", einer Sensibilisierung des Rezeptors nach andauernder und/oder mehrfacher Aktivierung, sowie eine mögliche Aktivierung des C-Terminus durch ATP-Bindung. Dazu generierte ich insgesamt 61 ANAP-markierte Mutanten und untersuchte biochemisch deren Expression in der Zellmembran von *X. laevis* Oozyten sowie elektrophysiologisch deren Funktionalität mittels VCF. Meine Ergebnisse liefern Evidenz dafür, dass die "current facilitation" eine intrinsische Rezeptoreigenschaft ist, die auf erleichterte Rezeptoröffnung zurückzuführen ist, und weiter, dass der ungewöhnlich lange C-Terminus funktional unabhängig von der extrazellulären ATP-Aktivierung ist. Darüber hinaus beschreibt **Publikation [Results 3.1]** die Analyse zweifach fluoreszenzmarkierter Rezeptoren, die zur weiteren Aufklärung der Signaltransduktion des P2X7-Rezeptors geeignet sind.
Neben diesen funktionellen Messungen habe ich zusätzlich die Wirkung von neuartigen Antagonisten des humanen P2X7 Rezeptors untersucht. In **Publikation [Results 3.2]** wurde in den Laboren von Dr. Maria Koufaki (Institut für Chemische Biologie, National Hellenic Research Foundation) 24 niedermolekulare Adamantan-basierte Verbindungen hergestellt, für die ich anschließend mittels der Zwei-Elektroden-Spannungsklemmtechnik Dosis-Wirkungskurven erstellte. In der noch nicht publizierten **Arbeit [Appendix 4.3]** etablierte ich zur Evaluierung von Antagonisten aus der Gruppe von Prof. Dr. Santiago Vázquez (Medicinal Chemistry & Pharmacology, University of Barcelona) zusätzlich Protokolle für die Untersuchung von Bindungskinetiken und bestätigte durch Mutagenese ihre allosterische Bindungsstelle.
Neben diesen Arbeiten an Oozyten-exprimierten P2X7 Rezeptoren trug ich mit immunhistochemischen Gewebeschnittfärbungen und Sequenzanalysen zu zwei Studien mit transgenen P2X7-Reportermäusen bei, um die Lokalisation des P2X7 Rezeptors zu untersuchen. **Publikation [Appendix 4.4]** beschreibt die Generierung und Charakterisierung eines BAC-transgenen Mausmodells. Hierbei konnte ich durch DAB-Färbungen histologischer Hirnschnitte zeigen, dass das Expressionsmuster des P2X7-EGFP-Fusionsproteins dem des endogenen P2X7-Rezeptors entspricht. In einer weiteren **Publikation [Results 3.3]** wurde die P2X7-EGFP-Reportermaus mit einer anderen BAC-transgenen Reportermaus, die lösliches EGFP exprimiert, vergleichen. Hier konnte ich mittels Gensequenzierung nachweisen, dass ein abweichendes Expressionsmuster des Reporters vom endogenen P2X7 Rezeptor zumindest teilweise auf eine nicht optimale Rekombinationsstrategie zurückgeführt werden kann. Die Daten beider Arbeiten deuten darauf hin, dass der P2X7 Rezeptor nicht in Neuronen exprimiert wird (**[Appendix 4.4]** und **[Results 3.3]**).
Schließlich konnte ich zu einer Arbeit beitragen, bei der die Wirksamkeit neuer Peptidanaloge an Oozyten-exprimierten nikotinischen Acetylcholinrezeptoren elektrophysiologisch untersucht wurden (**Publikation [Results 3.4]**).

Part II

Results

3
Publications with Summary and Contributions

3.1 Improved ANAP incorporation and VCF analysis reveal details of P2X7 current facilitation and a limited conformational interplay between ATP binding and the intracellular ballast domain

In this publication, we investigated how the P2X7R functions on a molecular basis. In particular, we tried to understand the mechanism of current facilitation and to identify structural changes in its large intracellular domain. Therefore, we applied VCF with the genetically encoded and environment-sensitive fUAA ANAP.
For the site-specific UAA-incorporation into *X. laevis* oocyte expressed receptor, a plasmid encoding the suppressor tRNA and a corresponding suppressor tRNA synthetase for specific UAA-aminoacylation is usually injected into the nucleus of the oocyte, followed by cytoplasmic injection of receptor cRNA containing an *amber* stop codon substitution together with ANAP. By circumventing nuclear injection (as described in **[Appendix 4.2]**) and additionally utilizing a mutated form of the eukaryotic release factor 1 (eRF1(E55D)), which favors UAA incorporation over premature translational termination, I established and validated a simplified and improved procedure yielding more reproducible expression levels of ANAP-containing full-length receptors. Using this procedure, I generated a total of 61 P2X7 mutants, each with one *amber* stop codon substitution either within the extracellular head domain, in the second transmembrane domain, or in intracellular receptor regions and assessed their membrane surface expression and functionality by VCF. The VCF recordings confirmed predicted conformational changes within the extracellular head domain that projects over the ATP-binding site, and the second transmembrane domain (TM2) near the identified channel gate and selectivity filter. In addition, our data show that current facilitation was paralleled by fluorescence changes for the majority of the P2X7R constructs. Only one of the constructs containing ANAP near the ATP-binding site displayed faster fluorescence signals, most likely because of a movement or interaction related to ligand binding that precedes channel opening. Based on these data we concluded, that current facilitation is an intrinsic P2X7R property and involves a change in receptor gating rather than ligand binding.
A major aim of this work was the identification of domains within the long intracellular C-terminus involved in P2X7-mediated secondary downstream processes. However, clear fluorescence signals were only detected for seven out of 48 P2X7R mutants with *amber* stop codon substitutions in intracellular regions, with five of them containing ANAP either in the N-terminus or directly beneath TM2. Only two mutants with ANAP in the more C-terminal globular ballast domain displayed small ligand-induced fluorescence changes. Thus, structural rearrangements within the intracellular domains appear to be restricted to juxtamembrane regions. For the majority of ANAP-substituted positions within the C-terminus, the fluorophore did not report any localized environment changes upon ligand-application, despite promising surface expression and functionality of the respective mutants. Therefore, we concluded that ligand-induced movements resulting in receptor activation and channel opening do not translate to this region and that intracellular interaction partners or ligands are required for its activation.
For future investigation of such interactions, we advanced the ANAP-based method for detection of localized structural rearrangements by combining it with other fluorophores. Using dual wavelength VCF, we developed specific protocols to simul-

taneously record fluorescence changes from i) ANAP and the fluorescent dye TMRM coupled to introduced cysteine residues, ii) ANAP and the Ca^{2+}-sensor R-GECO1.2, and iii) FRET signals between ANAP and mNeonGreen.
All experiments in this study were performed by myself. In addition, I contributed to the design of the study, and was largely responsible for the assembly and optimization of the dual wavelength VCF setup (see also **[Appendix 4.2]**), data analysis, and interpretation of the results. I also prepared the first draft of the manuscript and all figures and tables presented in this publication. Note, that supporting data is published as 12 additional figure supplements[1] and is included as supporting information following the main article.

[1] `https://elifesciences.org/articles/82479/figures#content` accessed on Feb. 6th, 2023

Improved ANAP incorporation and VCF analysis reveal details of P2X7 current facilitation and a limited conformational interplay between ATP binding and the intracellular ballast domain

Anna Durner, Ellis Durner, Annette Nicke

published in

eLife 2023, 12:e82479

eLife

RESEARCH ARTICLE

Improved ANAP incorporation and VCF analysis reveal details of P2X7 current facilitation and a limited conformational interplay between ATP binding and the intracellular ballast domain

Anna Durner[1], Ellis Durner[2], Annette Nicke[1]*

[1]Walther Straub Institute of Pharmacology and Toxicology, Faculty of Medicine, LMU Munich, Munich, Germany; [2]Lehrstuhl für Angewandte Physik and Center for Nanoscience, LMU Munich, Munich, Germany

Abstract The large intracellular C-terminus of the pro-inflammatory P2X7 ion channel receptor (P2X7R) is associated with diverse P2X7R-specific functions. Cryo-EM structures of the closed and ATP-bound open full-length P2X7R recently identified a membrane-associated anchoring domain, an open-state stabilizing "cap" domain, and a globular "ballast domain" containing GTP/GDP and dinuclear Zn^{2+}-binding sites with unknown functions. To investigate protein dynamics during channel activation, we improved incorporation of the environment-sensitive fluorescent unnatural amino acid L-3-(6-acetylnaphthalen-2-ylamino)–2-aminopropanoic acid (ANAP) into *Xenopus laevis* oocyte-expressed P2X7Rs and performed voltage clamp fluorometry. While we confirmed predicted conformational changes within the extracellular and the transmembrane domains, only 3 out of 41 mutants containing ANAP in the C-terminal domain resulted in ATP-induced fluorescence changes. We conclude that the ballast domain functions rather independently from the extracellular ATP binding domain and might require activation by additional ligands and/or protein interactions. Novel tools to study these are presented.

***For correspondence:** annette.nicke@lrz.uni-muenchen.de

Competing interest: The authors declare that no competing interests exist.

Funding: See page 25

Preprinted: 01 September 2022
Received: 05 August 2022
Accepted: 03 January 2023
Published: 04 January 2023

Reviewing Editor: Stephan A Pless, University of Copenhagen, Denmark

Editor's evaluation

This manuscript constitutes a valuable foray into the conformational rearrangements throughout various domains of the notoriously difficult-to-study P2X7 receptor, with a focus on the enigmatic intracellular 'ballast' domain. The molecular origin of the facilitation process and effects by intracellular factors will require future study, but the authors provide convincing evidence that the ballast domain is unlikely to undergo major conformational changes upon ATP-induced gating. The work is of interest to those interested in the role of enzymatically active intracellular domains of membrane proteins.

Introduction

P2X receptors (P2XR) are trimeric non-selective cation channels that are activated by extracellular adenosine triphosphate (ATP). The structure of a single P2X subunit has been compared to a dolphin, with two transmembrane domains (TM1 and TM2) that form the 'fluke', and a large extracellular domain, comprising the 'body', left and right 'flippers', and a 'head' domain that reaches over one of three inter-subunit ATP binding sites (***Kawate et al., 2009***). The intracellular N- and C-termini are

short in most P2X subtypes and have only been resolved in the open state of the P2X3R and, more recently, in the open and closed states of the P2X7R (**Mansoor et al., 2016**; **McCarthy et al., 2019**). The pro-inflammatory P2X7 subtype is expressed in immune cells and considered an important drug target. In contrast to the other P2XR family members, it has a low ATP sensitivity, shows complete lack of desensitization, and contains a large intracellular C-terminus (240 amino acids [aa]), which mediates diverse downstream effects such as interleukin secretion, plasma membrane permeabilization, blebbing, phosphatidylserine flip, and cell death (**Kopp et al., 2019**). The recently determined cryo-EM structures of the full-length rat P2X7R in the apo/closed and ATP-bound open states (**McCarthy et al., 2019**) did not only elucidate details of P2X desensitization, but finally unveiled the structure of the large P2X7 C-terminus. Accordingly, intertwined β-strands from all three subunits form an open state-stabilizing 'cap domain', that was also found in the P2X3R (**Mansoor et al., 2016**). In the P2X7R, however, this 'cap' is stabilized by a highly palmitoylated membrane-associated 'Cys-anchor' domain, which prevents desensitization. The remaining residues 393–595 fold into a dense globular structure (the so-called 'ballast domain'), which contains a novel guanosine nucleotide binding motif and a dinuclear zinc binding site. A stretch of 27–29 aa (S443-R471) was not resolved, and it is unclear if each ballast domain is formed by a single subunit or if a domain swap occurs between subunits (**McCarthy et al., 2019**). While these structures represent a milestone in P2X7 research, the transition dynamics between receptor states in a cellular environment as well as the molecular function of the ballast domain and how it is affected by ATP binding remain unclear. Likewise, the molecular mechanism of current facilitation, a P2X7-characteristic process that describes faster and/or increased current responses upon repeated ATP application, is not understood. In this study, we set out to determine conformational changes associated with P2X7-specific functions by voltage clamp fluorometry (VCF). This method allows simultaneous recording of current responses and associated molecular movements that are reported by an environment-sensitive fluorophore. We have previously used site-specific cysteine-substitution and the thiol-reactive fluorophore tetramethyl-rhodamine-maleimide (TMRM) to show a closing movement of the head domain during activation of the oocyte-expressed P2X1R (**Lörinczi et al., 2012**). However, this procedure is limited to extracellularly accessible residues. To investigate intracellular rearrangements, we therefore employed the fluorescent unnatural amino acid (fUAA) L-3-(6-acetylnaphthalen-2-ylamino)–2-aminopropanoic acid (ANAP) (**Lee et al., 2009**). This can be site-specifically incorporated into a protein by repurposing the *amber* stop codon (TAG) and introducing a corresponding suppressor tRNA (CUA anticodon) loaded with ANAP. A plasmid encoding an ANAP-specific bio-orthogonal suppressor tRNA/aminoacyl-tRNA synthetase pair (**Chatterjee et al., 2013**) has been obtained by co-evolution and selection (**Lee et al., 2009**) and was successfully used to study voltage-gated and ligand-gated ion channels (**Andriani and Kubo, 2021**; **Kalstrup and Blunck, 2018**; **Kalstrup and Blunck, 2013**; **Soh et al., 2017**; **Wulf and Pless, 2018**). This stop-codon suppression can, however, lead to premature translational termination or aberrant stop-codon substitution (read-through) (**Braun et al., 2020**; **Kalstrup and Blunck, 2017**; **Klippenstein et al., 2018**; **Pless et al., 2015**; **Poulsen et al., 2019**).

Here, we provide an improved method for fUAA incorporation into *Xenopus laevis* oocyte-expressed proteins and analyzed membrane surface expression and functionality for a total of 61 P2X7R mutants with ANAP substitutions in the extracellular head domain, the second transmembrane domain (TM2), and the intracellular N- and C-termini. Using VCF, we identified 19 positions in which ANAP reported ATP-induced localized rearrangements. To further expand the VCF toolbox, we demonstrate simultaneous recordings of fluorescence changes from ANAP in combination with other fluorophores. We conclude from our data that (i) current facilitation is intrinsic to the P2X7 protein and likely caused by a change in gating and (ii) the cytoplasmic ballast functions rather independently from the extracellular ligand binding domain and might require activation by additional ligands or protein interactions.

Results

Improved ANAP incorporation by cytosolic co-injection of mutated *X. laevis* eRF1 cRNA

To implement and optimize a protocol for incorporation of ANAP into *Xenopus* oocyte-expressed protein, we initially used the P2X1R as it was already intensively studied in our lab (**Lörinczi et al., 2012**) and has functional similarity with the P2X3R, which at the beginning of this study, represented

the only P2XR for which the intracellular termini were resolved (***Mansoor et al., 2016***). Using the original 2-step-injection protocol (***Kalstrup and Blunck, 2017***; ***Kalstrup and Blunck, 2013***) and a simplified procedure where all components required for the expression of UAA-containing receptors are injected simultaneously (***Figure 1A and C***), we introduced ANAP into non-conserved positions within the N-terminally His-tagged P2X1R N- and C-termini (position 10 and 388, respectively, ANAP substitutions indicated by *) and compared the formation of full-length and truncated receptors in the plasma membrane by SDS-PAGE. As seen in ***Figure 1B***, ANAP-containing P2X1Rs were efficiently expressed and virtually no read-through product was detected in the absence of ANAP. The new protocol resulted in less variable protein expression but also a reduced ratio of full-length and truncated His-P2X1 EGFP protein (***Figure 1D***). The relative amount of full-length protein was neither increased by different forms of ANAP application nor by variation of injection protocols (***Figure 1—figure supplement 1A and B***). Therefore, we tested if a mutated eukaryotic release factor (eRF1(E55D)), which was previously shown to favor UAA-incorporation over translational termination in HEK293T cells (***Gordon et al., 2018***; ***Schmied et al., 2014***) could also be used in the *Xenopus* oocyte expression system. Indeed, co-injection of either purified *X. laevis* eRF1(E55D) protein (***Figure 1—figure supplement 1B***) or the respective *in vitro* synthesized cRNA (***Figure 1C and D***) resulted in a more than threefold higher ratio of full-length and truncated receptor constructs compared to the 1-step injection method without eRF1(E55D) and a smaller standard deviation compared to the 2-step injection method (1-step+eRF1(E55D): 1.469±0.229; 1-step: 0.418±0.082; 2-step: 1.603±0.933; mean ± S.D.). The applicability of this approach was confirmed for the hα1 glycine receptor (GlyR) A52* mutant (***Figure 1—figure supplement 1C***; ***Soh et al., 2017***). In conclusion, this optimized protocol led to more reproducible expression and increased formation of full-length ANAP-labeled receptors and was used in all following experiments.

Evaluation of plasma membrane expression of full-length ANAP-containing P2X7Rs

Next, we incorporated ANAP into the P2X7R in sites chosen based on previous structure-function studies and the cryo-EM structures (***McCarthy et al., 2019***). As a positive control, we first introduced ANAP into the head domain (***Figure 2A and B***), which is known to undergo substantial movements and/or ligand interactions with clear changes of TMRM fluorescence in the P2X1R (***Lörinczi et al., 2012***) and P2X7R (***Figure 2—figure supplement 1A***). Next, based on the comparison of the P2X4 and P2X3 crystal structures in the open and closed states (***Hattori and Gouaux, 2012***; ***Kawate et al., 2009***; ***Mansoor et al., 2016***), and the identification of the human P2X7 channel gate and selectivity filter around residue S342 (***Pippel et al., 2017***), we selected positions in the second transmembrane helix. Finally, we introduced ANAP throughout the intracellular region in positions that we suspected to undergo conformational changes upon channel activation, as well as in six positions in the unresolved 29 aa stretch. As shown in ***Figure 2C***, all constructs with ANAP substitutions in the N-terminus and the head domain as well as three out of four constructs with substitutions in TM2 were formed in full length, indicating that receptors that are truncated before or within TM2 are retained in the endoplasmic reticulum and likely undergo degradation. Interestingly, ANAP incorporation into G338 completely prevented membrane incorporation while cysteine substitution in the equivalent position of human P2X7R led previously to surface-expressed, but non-functional receptors (***Pippel et al., 2017***).

Starting from T357 in the C-terminus, introduction of the *amber* stop codon resulted in variable ratios of truncated and full-length receptors. Surface expression of full-length receptors was particularly low for constructs containing ANAP in the C-terminal cap (K387*, C388*) and ballast (I577*) domains, while it was most efficient for ANAP-substitutions in positions 517–537 (in particular L527* and E537*) and in the very C-terminus (Y595* and 596*).

In summary, most substitutions within the C-terminus led to a dominant formation of truncated P2X7 protein besides full-length receptors. Nevertheless, the majority of these constructs showed clear current responses (***Figure 2C***, ***Table 1***). Since the truncated forms were not expected to interfere with the fluorescence signal, functional constructs that were expressed at least partly in full length were further analyzed by VCF.

eLife Research article Biochemistry and Chemical Biology | Structural Biology and Molecular Biophysics

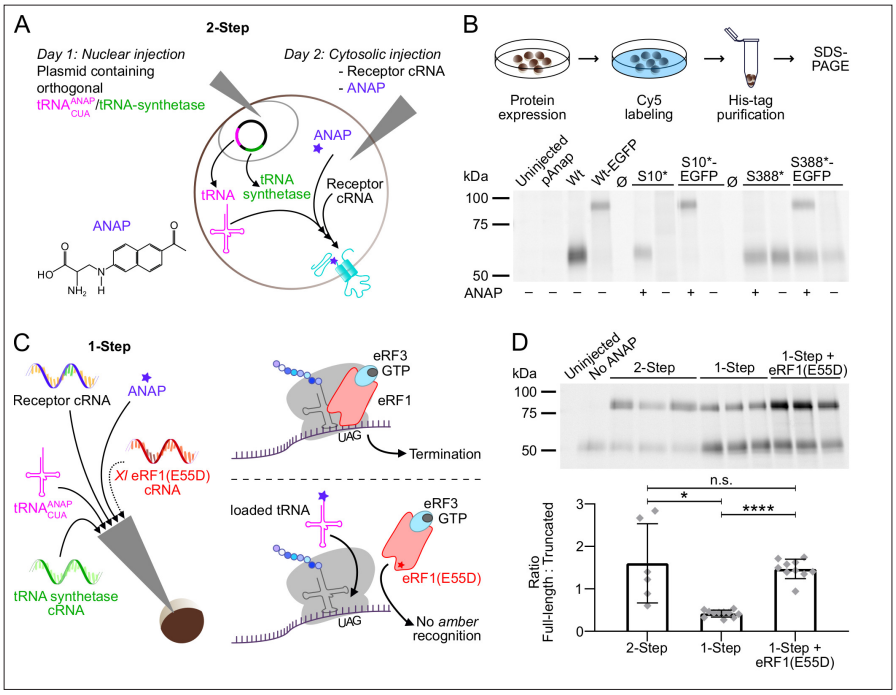

Figure 1. Optimization of fluorescent unnatural amino acid (fUAA) incorporation into *Xenopus laevis* oocyte-expressed P2X1 receptor. (**A**) Molecular structure of L-3-(6-acetylnaphthalen-2-ylamino)–2-aminopropanoic acid (ANAP) and schematic representation of the 2-step injection method for site-specific ANAP incorporation using the *amber* stop-codon (UAG) and a plasmid containing the orthogonal tRNA/tRNA-synthetase pair. (**B**) Representative SDS-PAGE analysis of plasma membrane-expressed ANAP-labeled (S10* or S388*) rat P2X1Rs (46 kDa without glycosylation). A C-terminal EGFP-tag (27 kDa) was added as indicated to enable detection of premature termination at position 388. Oocytes were injected as shown in A and labeled with membrane impermeable Cy5-NHS ester. His-tagged P2X1Rs were extracted in 0.5% *n*-dodecyl-β-D-maltoside, purified via Ni^{2+}-NTA agarose, and separated by SDS-PAGE (8%). Noninjected oocytes and oocytes injected only with the plasmid pANAP, P2X1 cRNA without the *amber* stop codon (Wt), or without ANAP (as indicated) served as controls. Note, that twice the amount of protein was loaded for P2X1(S10*). Ø indicates empty lanes. Two to three independent experiments were performed. (**C**) Representation of the 1-step injection method and all components required for UAA-labeling plus optional *X. laevis* eRF1(E55D) cRNA (left) and (right) scheme of protein translation termination by eRF1 (upper panel) and how overexpression of the mutated form of eRF1 favors *amber*-encoded fUAA incorporation by outcompeting endogenous eRF1 (lower panel). (**D**) Comparison of Cy5-labeled membrane-expressed full-length and truncated His-rP2X1-EGFP(388*) ratios upon expression by the 2-step and 1-step injection method with or without eRF1(E55D) co-expression. A representative SDS-PAGE gel (prepared as in B) and statistical analysis of data from 6 to 11 experiments including oocytes from 4 to 6 different *X. laevis* frogs per group are shown. Data are represented as mean ± S.D., and significance was determined by a two-tailed unpaired Welch's *t*-test and is indicated as *p<0.05 and ****p<0.0001.

The online version of this article includes the following source data and figure supplement(s) for figure 1:

Source data 1. Original gel, ***Figure 1B***.

Source data 2. Original gel, ***Figure 1D***.

Source data 3. Original gels for bar graph in ***Figure 1D***: Gel2, Gel3, Gel4, and Gel5.

Source data 4. Original gels for bar graph in ***Figure 1D***: GelA, GelB, and GelC.

Figure supplement 1. Variation of experimental conditions to optimize L-3-(6-acetylnaphthalen-2-ylamino)–2-aminopropanoic acid (ANAP) incorporation into oocyte-expressed ion channels.

Figure 1 continued on next page

Figure 1 continued

Figure supplement 1—source data 1. Original gel, ***Figure 1—figure supplement 1A***.

Figure supplement 1—source data 2. Original gel, ***Figure 1—figure supplement 1B***.

Figure supplement 1—source data 3. Original gel, ***Figure 1—figure supplement 1C***.

Recording of ANAP fluorescence in the head domain reveals mainly gating-associated movements

Next, we recorded ANAP fluorescence changes upon application of 0.3 mM ATP. Control oocytes expressing wt P2X7R showed a gradual fluorescence decrease during ATP application, even when no ANAP was injected (***Figure 3—figure supplement 1***). A similar fluorescence drift was observed with the P2X2R, but not with the hα1 GlyR or the fast-desensitizing P2X1R. The reason for this drift is unclear but needs to be considered when evaluating mutants with small negative fluorescence changes. Specificity of tRNA loading and ANAP-incorporation was evaluated in further control experiments (***Figure 3—figure supplement 2***). Only recordings that met specific inclusion criteria (see Methods) were considered for analysis.

As a prodan derivative, ANAP is highly sensitive to the polarity of its environment and shows a redshift in emission with increasing polarity (***Lee et al., 2009***; ***Weber and Farris, 1979***). Consequently, alterations in ANAP fluorescence can be attributed to (i) quenching by ligands, small molecules, or (aromatic) aa, (ii) spectral shift due to changes in the polarity of the environment, or (iii) a combination of these two effects, e.g., in case of ligand interaction.

To allow differentiation between presumably wavelength-independent (de-)quenching of ANAP fluorescence by other molecules or spectral shifts due to changes in the polarity, we simultaneously recorded fluorescence in distinct spectral segments, i.e., (i) 430–470 nm and 470–500 nm with filter set 1 and (ii) 430–490 nm and >500 nm with filter set 2 (***Figure 3A***). This also enabled us to identify mutants that only showed fluorescence changes at certain wavelengths and would have escaped detection, otherwise.

We first recorded ATP-induced fluorescence changes from P2X7Rs containing ANAP in the head domain, which projects over the ATP-binding site (P120-Q128, ***Figure 3B***). In agreement with the pronounced conformational changes and ligand interactions of this domain during receptor activation (***Lörinczi et al., 2012***; ***McCarthy et al., 2019***), all mutants except E121* and Q128* showed clear fluorescence signals in all spectral segments (***Figure 3C and D***, ***Table 1*** and ***Figure 2—figure supplement 1B***). For E121* and Q128* fluorescence changes were only detected with filter set 2, albeit with minimal changes for E121*. Analysis of mutants P120*, E121*, and P123* with filter set 1 was only preliminary (***Figure 2—figure supplement 1B***) but showed the same trends as signals recorded with filter set 2 (***Figure 3C and D***). Independently of the wavelength, fluorescence changes were always positive for P120* and G126* and negative for Y122*, P123*, and K127*. These consistent changes over the entire ANAP emission spectrum indicate de-/quenching of ANAP either by the ligand ATP and/or other aa residues (see insert table in ***Figure 3E***). In contrast, S124* (***Figure 3E***), R125*, and Q128* (***Figure 3C and D*** and ***Figure 2—figure supplement 1B***) showed positive fluorescence changes in most spectral segments but negative changes for wavelengths >500 nm. The opposite directions imply that these changes result, at least partly, from an ANAP emission shift toward shorter wavelengths and suggest that ANAP enters a less polar environment during receptor activation (***Figure 3E***).

In all head-domain constructs that showed clear kinetics, with the exception of K127*, fluorescence and current changes started simultaneously and showed shorter rising times upon repeated ATP applications, thus recapitulating the characteristic 'current facilitation' of the P2X7R (***Allsopp and Evans, 2015***; ***Janks et al., 2019***; ***Roger et al., 2008***). To confirm that these fluorescence signals indeed tracked current facilitation, we analyzed the effects of three additional mutants that were expected to affect facilitation: (i) a single point mutation in the juxtamembrane region (S23N) that in human P2X7 was shown to eliminate current facilitation (***Allsopp and Evans, 2015***), (ii) a Cys-Ala mutant (replacement of residues identified to be palmitoylated [***McCarthy et al., 2019***] in the cysteine-rich region by alanine residues [Ser360, Cys362, Cys371, Cys373, Cys374, and Cys377]), and (iii) a ΔCys-mutant (deletion of the cysteine-rich intracellular region, S360-C377 [***McCarthy et al., 2019***; ***Roger et al., 2010***]). Contrary to findings in human P2X7 (***Allsopp and Evans, 2015***), the S23N mutation did not eliminate current facilitation in rat P2X7 (***Figure 3—figure supplement 3***). As expected (***Roger et al.,***

eLife Research article Biochemistry and Chemical Biology | Structural Biology and Molecular Biophysics

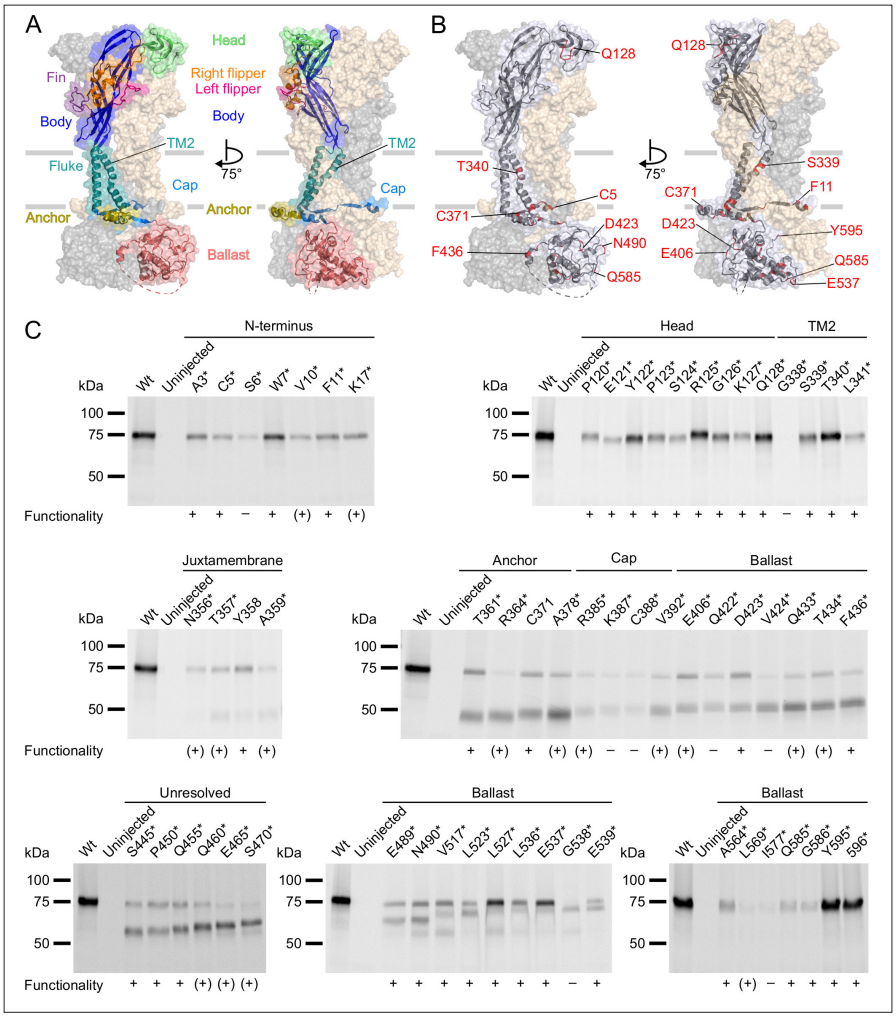

Figure 2. P2X7Rs containing L-3-(6-acetylnaphthalen-2-ylamino)–2-aminopropanoic acid (ANAP) at various positions within the extracellular, transmembrane, and cytoplasmic regions are expressed in the plasma membrane and functional. (**A, B**) Surface representations of the rat P2X7 Cryo-EM structure in the open state (PDB ID: 6u9w). The different domains (**A**) and selected sites of ANAP substitutions (**B**) are indicated in one subunit while the two other subunits are shown in gray and wheat, respectively. (**C**) Evaluation of surface expression and functionality of P2X7Rs generated from constructs containing an *amber* stop codon in the indicated positions. *X. laevis* oocytes expressing the constructs were labeled with membrane-impermeant Cy5-NHS ester. His-tagged P2X7Rs were extracted in 0.5% *n*-dodecyl-β-D-maltoside, purified via Ni^{2+} NTA agarose, and analyzed by SDS-PAGE (8%).

Figure 2 continued on next page

Figure 2 continued

Symbols indicate current responses to 0.3 mM ATP as determined by two-electrode voltage clamp recordings in the voltage clamp fluorometry setup: +, functional and currents comparable to wt P2X7 after 2–4 days of expression; (+), functional and currents comparable to wt P2X7 after 5–7 days of expression; –, not functional or currents ≤0.5 µA and not reproducible after 4 days. Representative data from two to five independent biochemical experiments are shown.

The online version of this article includes the following source data and figure supplement(s) for figure 2:

Source data 1. Original gel (1), ***Figure 2C*** (N-terminus).

Source data 2. Original gel (2), ***Figure 2C*** (head domain and TM2).

Source data 3. Original gel (3), ***Figure 2C*** (juxtamembrane).

Source data 4. Original gel (4), ***Figure 2C*** (anchor, cap, and ballast domain).

Source data 5. Original gel (5), ***Figure 2C*** (unresolved).

Source data 6. Original gel (6), ***Figure 2C*** (ballast domain, part a).

Source data 7. Original gel (7), ***Figure 2C*** (ballast domain, part b).

Figure supplement 1. Comparative analysis of tetramethyl-rhodamine-maleimide (TMRM)-labeled and L-3-(6-acetylnaphthalen-2-ylamino)–2-aminopropanoic acid (ANAP)-labeled P2X7 head domain mutants.

Figure supplement 1—source data 1. Original gel, ***Figure 2—figure supplement 1A***.

Figure supplement 1—source data 2. Summarized data for box plot in ***Figure 2—figure supplement 1A***.

Figure supplement 1—source data 3. Original recordings for box plot in ***Figure 2—figure supplement 1A*** and for representative VCF recordings in ***Figure 2—figure supplement 1A and B***.

2010) and in contrast to the wt and most of the analyzed ANAP-containing mutants, current rise times of the ΔCys mutant were not significantly altered between first and second ATP applications, demonstrating that we can indeed identify current facilitation in our setup (***Figure 3—figure supplement 3***). However, the strongly reduced functional expression of the Cys-Ala or ΔCys mutant with additional ANAP-incorporation sites prevented reliable analysis of current and fluorescence kinetics.

Remarkably, the K127* mutant showed a fluorescence change that was faster than the current increase already upon the first receptor activation (***Figure 3F***, ***Figure 3—figure supplement 3***). EC_{50} values for ATP were similar at wt, S124* and K127* mutants (***Table 2***). We conclude from this, that ANAP in position 127 reports a process that precedes channel opening and is most likely related to ligand binding, whereas ANAP reports gating-associated conformational changes in the other positions.

Detection of TM2 movements in response to receptor activation

The following VCF recordings were performed mainly with filter set 2 (430–490 nm and >500 nm), since this revealed more pronounced signals for most mutants.

To exclude fluorescence changes induced by a direct interaction with ATP and to further investigate P2X7 gating, we next investigated positions 339–341 (***Figure 4A***), just preceding S342, the major determinant of the channel gate (***Pippel et al., 2017***). Cysteine substitutions in these positions have previously been shown to be accessible to thiol-reactive dyes only in the open state of the receptor (***Pippel et al., 2017***). In agreement with a critical role in gating, current recordings from mutants S339*, T340*, and L341* were compromised by 10–20-fold higher leak currents compared to wt receptors or other mutants (see also ***Figure 4—figure supplement 1***). Nevertheless, they showed clear fluorescence changes during receptor activation (***Figure 4B***), although with higher variability in amplitude and shape between oocytes. While P2X7R mutants S339* and L341* showed positive signals in all spectral ranges, fluorescence changes in T340* were inconsistent at shorter emission wavelengths, but mostly negative below 470 nm, and positive above 470 nm, indicating again that a spectral shift contributed to these signals (***Figure 4B and C***).

Notably, fluorescence signals from P2X7 T340* were also significantly larger during the first ATP application compared to the second (***Figure 4B and C***), suggesting that the environment of this position changed between both ATP applications. An intriguing explanation could be an involvement of this region in the facilitation process. However, as the T340* mutant displayed no change in fluorescence or current kinetics between ATP applications (***Figure 4D*** and ***Figure 4—figure supplement 1***) the facilitation-associated gating mechanism is likely disturbed by this mutation.

Table 1. Summary of surface expression, current responses (ΔI), and L-3-(6-acetylnaphthalen-2-ylamino)–2-aminopropanoic acid fluorescence changes (%ΔF/F) of the investigated P2X7 mutants.

		Surface expression			%ΔF/F Filter set 1		%ΔF/F Filter set 2	
	Position	Full-length	Truncated	ΔI	430–470 nm	470–500 nm	430–490 nm	>500 nm
N-terminus	A3	+	–	+	↑	↑	↑	↑
	C5	+	–	+	(–)	(–)	↑	↑
	S6	+	–	–	(–)	(–)	(–)	(–)
	W7	+	–	+	(↑)	(↑)	↑	↑
	V10	+	–	(+)	(–)	(–)	(↑)	(↑)
	F11	+	–	+	(–)	(–)	↑	↑
	K17	+	–	(+)	(–)	(–)	(–)	(–)
Head domain	P120	+	–	+	(↑)	(↑)	↑	↑
	E121	+	–	+	(–)	(–)	↑	↑
	Y122	+	–	+	↓	↓	↓	↓
	P123	+	–	+	n.d.	n.d.	↓	↓
	S124	+	–	+	↑	↑	↑	↓
	R125	+	–	+	↑	↑	↑	↓
	G126	+	–	+	↑	↑	↑	↑
	K127	+	–	+	↓	↓	↓	↓
	Q128	+	–	+	–	–	↑	↓
TM2	G338	–	–	–	n.d.	n.d.	(–)	(–)
	S339	+	–	+	↑	↑	↑	↑
	T340	+	–	+	– / ↓	↑	↑	↑
	L341	+	–	+	(↑)	(↑)	↑	↑

Table 1 continued on next page

Table 1 continued

		Surface expression			%ΔF/F Filter set 1		%ΔF/F Filter set 2	
	Position	Full-length	Truncated	ΔI	430–470 nm	470–500 nm	430–490 nm	>500 nm
	N356	+	–	(+)	(–)	(–)	(–)	(–)
	T357	+	+	(+)	(–)	(–)	(–)	(–)
	Y358	+	+	+	(–)	(–)	–	–
	A359	+	+	(+)	(–)	(–)	(–)	(–)
	T361	+	+	+	(–)	(↓)	–	↓
	R364	+	+	(+)	n.d.	n.d.	(–)	(–)
	C371	+	+	+	–	–	(–)	(–)
	A378	+	+	(+)	(–)	(–)	n.d.	n.d.
	R385	+	+	(+)	n.d.	n.d.	(–)	(–)
C-terminus	K387	+	+	–	n.d.	n.d.	(–)	(–)
	C388	+	+	–	n.d.	n.d.	(–)	(–)
	V392	+	+	(+)	(–)	(–)	(–)	(–)
	E406	+	+	(+)	(–)	(–)	(–)	(–)
	Q422	+	+	–	n.d.	n.d.	(–)	(–)
	D423	+	+	+	(–)	(–)	↑	↑
	V424	+	+	–	n.d.	n.d.	(–)	(–)
	Q433	+	+	(+)	(–)	(–)	n.d.	n.d.
	T434	+	+	(+)	(–)	(–)	n.d.	n.d.
	F436	+	+	+	n.d.	n.d.	(–)	(–)
Unresolved	S445	+	+	+	(–)	(–)	–	(–)
	P450	+	+	+	–	–	–	–
	Q455	+	+	+	–	–	–	–
	Q460	+	+	(+)	(–)	(–)	(–)	(–)
	E465	+	+	(+)	(–)	(–)	n.d.	n.d.
	S470	+	+	(+)	(–)	(–)	n.d.	n.d.

Table 1 continued on next page

Table 1 continued

		Surface expression			%ΔF/F Filter set 1		%ΔF/F Filter set 2	
	Position	Full-length	Truncated	ΔI	430–470 nm	470–500 nm	430–490 nm	>500 nm
C-terminus	E489	+	+	+	(–)	(–)	–	–
	N490	+	+	+	(–)	(–)	–	–
	V517	+	+	+	n.d.	n.d.	–	–
	L523	+	+	+	n.d.	n.d.	–	–
	L527	+	+	+	n.d.	n.d.	–	–
	L536	+	+	+	(–)	(–)	–	–
	E537	+	+	+	–	–	–	–
	G538	–	+	–	(–)	(–)	(–)	(–)
	E539	+	+	+	(–)	(–)	–	–
	A564	+	?	+	n.d.	n.d.	↑	↑
	L569	+	?	(+)	n.d.	n.d.	(–)	(–)
	I577	+	?	–	n.d.	n.d.	(–)	(–)
	Q585	+	?	+	(–)	(–)	–	–
	G586	+	?	+	(–)	(–)	–	–
	Y595	+	?	+	–	–	–	–
	596	+	?	+	–	–	–	–

+ and – indicate presence and absence of protein or signals, respectively. In case of current responses, + means response comparable to wt receptors and (+) means reduced responses. ↑ and ↓ indicate positive and negative fluorescence signals, respectively. 3–50 oocytes were measured per construct and filter set. In case of fluorescence responses, symbols in brackets indicate where less than three recordings met the criteria defined in the methods (mostly because of impaired fucntionality) and represent tendencies only. ?, not distinguishable (because of similar length of full-length and truncated constructs); n.d., not determined.

The online version of this article includes the following source data for table 1:

Source data 1. Summarized data for ***Table 1*** with assignment to the original VCF recordings; also including data from ***Figure 2—figure supplement 1B*** (box plot); ***Figure 3C, D, E, F***; ***Figure 3—figure supplement 3C***; ***Figure 4B, C, D***; ***Figure 4—figure supplement 1B***; and ***Figure 5B, C, D***. The respective original recordings are deposited with Dryad.

Scanning of the P2X7 intracellular domains for ATP-induced conformational changes

The large intracellular P2X7 C-terminus mediates many of the P2X7R downstream effects (***Kopp et al., 2019***). While the P2X7 cryo-EM structures revealed the role of the juxtamembrane N- and C-terminal domains in receptor desensitization, their role in downstream signaling and in particular the molecular function of the ballast domain remain completely unclear. Analysis of ANAP fluorescence changes within the cytoplasmic domain was therefore a primary aim of this study. We first introduced ANAP into juxtamembrane regions within the N- and C-termini (***Figure 5A***) that form the cytoplasmic cap and anchor domains excluding palmitoylated residues (C4, S360, C362, C363, C374, and C377) (***McCarthy et al., 2019***). Although all receptors with N-terminal ANAP substitutions were formed in full length (***Figure 2C***), current and fluorescence responses for S6*, V10*, and K17* substitutions remained small and inconsistent even after 6 days of expression. A3*, C5*, W7*, and F11* mutants showed positive fluorescence signals of variable sizes (***Figure 5B***), and the kinetics of F11* fluorescence correlated with current facilitation (***Figure 5C***, ***Figure 3—figure supplement 3***). ANAP fluorescence in F11* was not quenched by the nearby Trp (W7), as its removal had no apparent effect (***Figure 5—figure supplement 1***). Within the juxtamembrane C-terminal regions,

eLife Research article Biochemistry and Chemical Biology | Structural Biology and Molecular Biophysics

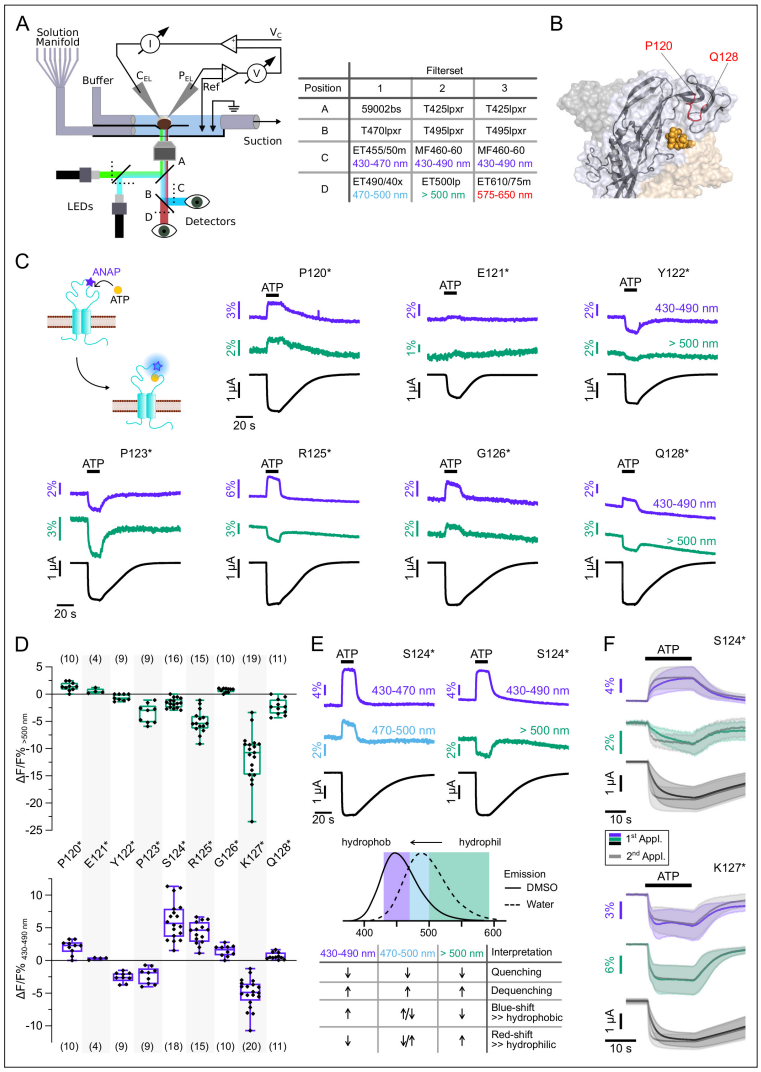

Figure 3. Characterization of ATP-induced fluorescence changes in the P2X7 head domain recorded at different wavelengths. (**A**) Schematic of the voltage clamp fluorometry (VCF)-recording system and summary of filter/dichroic mirror configurations used to detect distinct spectral parts of L-3-(6-acetylnaphthalen-2-ylamino)–2-aminopropanoic acid (ANAP)-fluorescence (sets 1 and 2) and ANAP in combination with tetramethyl-rhodamine-maleimide (TMRM) or R-GECO1.2 (set 3). The corresponding positions A, B, C, and D are shown in the schematic. A second LED (green) was used for

Figure 3 continued on next page

Figure 3 continued

additional excitation of TMRM or R-GECO1.2. (**B**) Close-up of the P2X7 head domain in surface representation indicating the ANAP-substituted amino acid residues P120-Q128 (red). The three subunits are colored in gray, wheat, and light blue. (**C**) Principle of VCF and representative VCF recordings in response to 0.3 mM ATP (upon second application). Change of fluorescence intensity of a site-specifically introduced environment-sensitive fluorophore can be induced by ligand binding and/or conformational changes. (**D**) Box plots summarizing results from the indicated ANAP-labeled P2X7Rs at two different emission wavelengths with ΔF/F% representing the maximum fluorescence signal during a 15-s ATP application. Numbers of recordings are given in brackets. (**E**) Representative VCF recordings in response to 0.3 mM ATP of P2X7(S124*) at three different emission wavelengths and summary of most likely interpretations. Note that fluorescence changes are most likely resulting from multiple effects, and only the dominant effect is stated. Arrows indicate direction of fluorescent changes. (**F**) Overlay of VCF recordings upon first (colored) and second (gray) ATP applications (0.3 mM) at two different emission wavelengths for P2X7(S124*) (14 oocytes) and P2X7(K127*) (17 oocytes), respectively. Averaged VCF recordings are shown as lines, and standard deviations are plotted as envelopes. Baseline currents (15 s before ATP application) were adjusted for clarity. All recordings were performed in divalent-free buffer, and oocytes were clamped at –30 mV. Original recordings have also been deposited with Dryad and summarized and assigned in ***Table 1—source data 1***.

The online version of this article includes the following source data and figure supplement(s) for figure 3:

Source data 1. Original recordings, ***Figure 3C, E and F***.

Figure supplement 1. Control voltage clamp fluorometry (VCF) recordings from oocytes expressing different non-mutated ion channels.

Figure supplement 1—source data 1. Original recordings, ***Figure 3—figure supplement 1***.

Figure supplement 2. Control experiments to test the specificity of tRNA-loading and L-3-(6-acetylnaphthalen-2-ylamino)–2-aminopropanoic acid (ANAP) incorporation into P2X7.

Figure supplement 2—source data 1. Original recordings, ***Figure 3—figure supplement 2A***.

Figure supplement 2—source data 2. Original gel, ***Figure 3—figure supplement 2B***.

Figure supplement 3. Deletion of the cysteine-rich region eliminates current facilitation, and F11* and S124* mutants track current facilitation.

Figure supplement 3—source data 1. Summarized data, ***Figure 3—figure supplement 3A and B***.

Figure supplement 3—source data 2. Original recordings, ***Figure 3—figure supplement 3A and B***.

Figure supplement 3—source data 3. Original recordings, ***Figure 3—figure supplement 3C***.

ANAP was introduced between TM2 and the anchor domain (N356*, T357*, Y358*, A359*), upstream of β_{15}, which is part of the cytoplasmic cap structure (T361*, R364*, C371*, A378*, R385*, K387*), and upstream of the cytosolic ballast domain (C388* and V392*). Surface expression of functional full-length receptors was observed for all constructs except for K387* and C388*. In contrast to the juxtamembrane N-terminal residues, however, only one of these C-terminal mutants, T361*, showed a fluorescence change, albeit in only ~50% of the recordings (***Figure 5D***). Interestingly, both F11 and T361 lie within two of at least four possible cholesterol recognition amino acid consensus (CRAC)

Table 2. EC_{50} values for ATP and Hill coefficients (n_H) at wt and L-3-(6-acetylnaphthalen-2-ylamino)–2-aminopropanoic acid-containing P2X7 receptor constructs.

Mutant	EC_{50} (M)	n_H
Wt	4.202e-005 (3.211e-005–5.704e-005)	1.049 (0.7962–1.380)
F11*	7.802e-005 (6.268e-005–9.893e-005)	1.148 (0.9345–1.410)
S124*	8.316e-005 (6.068e-005–0.0001236)	1.122 (0.8271–1.519)
F11*, S124C	0.0001003 (8.439e-005–0.0001216)	1.290 (1.069–1.571)
K127*	6.511e-005 (4.281e-005–0.0001339)	0.6601 (0.4779–0.8662)
D423*	6.513e-005 (4.729e-005–0.0001057)	1.240 (0.8087–1.821)
A564*	5.159e-005 (3.491e-005–9.976e-005)	0.7810 (0.5364–1.087)

Number in brackets are 95% confidence intervals, n=3–11.

The online version of this article includes the following source data for table 2:

Source data 1. Original recordings for ***Table 2***; ***Figure 3—figure supplement 3D***; and ***Figure 5—figure supplement 2A***.

Source data 2. Summarized data for ***Table 2***; ***Figure 3—figure supplement 3D***; and ***Figure 5—figure supplement 2A***.

eLife Research article Biochemistry and Chemical Biology | Structural Biology and Molecular Biophysics

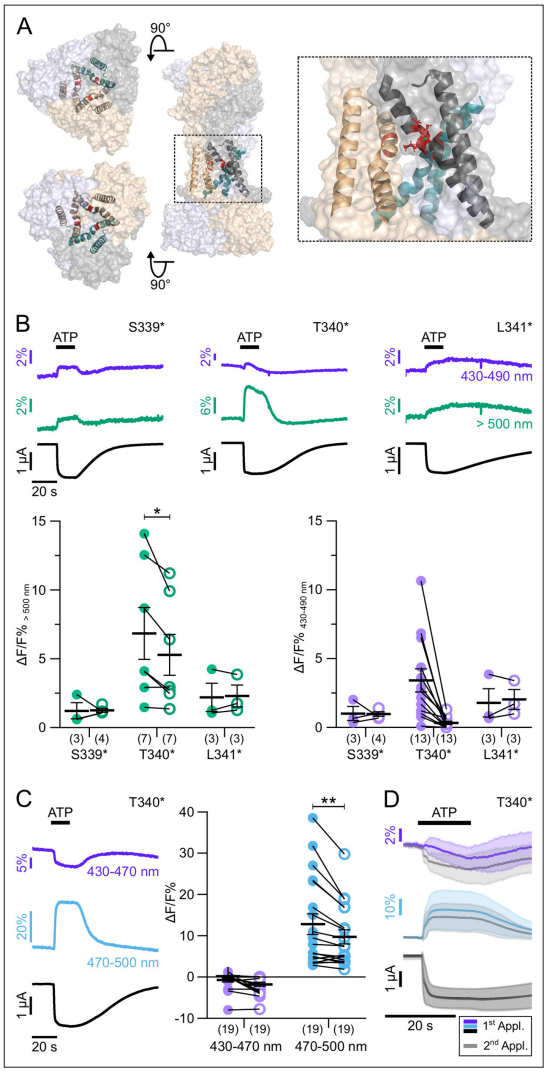

Figure 4. ATP-induced L-3-(6-acetylnaphthalen-2-ylamino)–2-aminopropanoic acid (ANAP) fluorescence changes in the P2X7 TM2 domain. (**A**) Overview and close-up of the three P2X7 subunits (in wheat, gray, and purple) with the TM helices as cartoon representations (in wheat, gray, and green) and the ANAP-substituted residues S339, T340, and L341 (in red). (**B**) Representative voltage clamp fluorometry (VCF) recordings from the indicated

Figure 4 continued on next page

Figure 4 continued

mutants in response to 0.3 mM ATP (upon second application) and summary of results at two different emission wavelengths. Note that recordings from all constructs were compromised by high leak currents. Graphs compare maximal fluorescence signals during first (closed circles) and second (open circles) ATP applications (interval 195 s). Data are represented as mean ± S.E.M. Significance was determined using the two-tailed paired Student's *t*-test (*, p<0.05; **, p<0.005). (**C**) Representative recordings and summary (performed as in B) from P2X7(T340*) with filter set 2. (**D**) Overlay of VCF recordings from P2X7(T340*) upon first (colored) and second (gray) ATP applications (0.3 mM) at two different emission wavelengths. Averaged VCF recordings from 11 oocytes are shown as lines, and standard deviations are plotted as envelopes. Baseline currents (15 s before ATP application) were adjusted for clarity. All recordings were performed in divalent-free buffer, and oocytes were clamped at –30 mV. Wavelengths passed by the used filter sets are indicated. Original recordings have also been deposited with Dryad and summarized and assigned in ***Table 1—source data 1***.

The online version of this article includes the following source data and figure supplement(s) for figure 4:

Source data 1. Original recordings, ***Figure 4B, C, and D***.

Figure supplement 1. L-3-(6-acetylnaphthalen-2-ylamino)–2-aminopropanoic acid (ANAP) in TM2 causes leakiness and affects current facilitation.

Figure supplement 1—source data 1. Original recordings, ***Figure 4—figure supplement 1A***.

motifs that have been proposed to be involved in the cholesterol sensitivity of P2X7 channel gating (***Robinson et al., 2014***).

ANAP introduction in most of the 29 ballast domain positions led to a dominant formation of truncated protein, indicating that this domain does not tolerate substitutions very well and/or that the truncated constructs form stable proteins. Four of these mutants (Q422*, V424*, G538*, I577*) did not form functional receptors at all. For most of the remaining constructs, no specific fluorescence changes could be detected, despite promising surface transport and current responses comparable to wt receptors for at least 12 of them (see ***Table 1***, ***Figure 2C***).

Only in two mutants, A564* and D423*, fluorescence changes could be recorded: A564* showed clearly positive signals, while D423* showed positive signals in only ~40% of the recordings (***Figure 5D***). Both mutants showed EC_{50} values similar to wt P2X7 and were not functional in control oocytes injected without ANAP (***Figure 5—figure supplement 2***), suggesting that the respective truncated proteins (compare ***Figure 2C***) do either not contribute to current responses or only in complex with full-length (ANAP-containing) P2X7 subunits. D423 is located within a loop connecting the β_{17} and β_{18} strands and situated on the outer surface of the cytoplasmic ballast, facing away from both the central axis of the receptor and the neighboring subunits (***Figure 5F***). Notably, mutation of the neighboring positions (Q422*, V424*) resulted in non-functional receptors. A564 is located in the α_{15} helix at the very end of a cavity formed by the α_{13}, α_{14}, and α_{16} helices and a short α_9 helix of the neighboring subunit (***Figure 5E***). This cavity harbors the guanosine nucleotide binding site identified by cryo-EM and liquid chromatography-tandem mass spectrometry analysis, and GDP was found to interact with residues A567 and L569 (***McCarthy et al., 2019***), both in close proximity to A564. α_{16}, is also part of a proposed lipid interaction or lipopolysaccharide (LPS) binding motif (***Denlinger et al., 2001***) and α_{14} at the bottom of the cavity is part of a proposed calcium-dependent calmodulin binding motif (residues I541-S560) (***Roger et al., 2010***; ***Roger et al., 2008***). To identify possible palmitoylation or CaM-dependent movements of the ballast domain or effects on receptor function, we analyzed the influence of the non-palmitoylated ΔCys- and Cys-Ala mutants (***Figure 3—figure supplement 3***) as well as a ΔCaM mutant, in which a proposed calmodulin binding site was deleted (***Roger et al., 2010***) on ANAP fluorescence. While the poor expression of the ΔCys and Cys-Ala mutants in combination with ANAP prevented VCF analysis, combination of the ΔCaM mutation with ANAP (in intracellular positions F11*, D423*, or A564* or in the head domain S124*, K127*) yielded good expression and similar current kinetics and fluorescence changes, as observed before for the single mutants (***Figure 5—figure supplement 3***). This argues against a major functional effect of the CaM binding site mutation on the current facilitation or on molecular movements, at least in the oocyte-expressed receptor.

Taken together, only two positions, D423 and A564, could be identified within the ballast domain, where ANAP reported environmental changes, suggesting only limited ATP-induced movements in

eLife Research article Biochemistry and Chemical Biology | Structural Biology and Molecular Biophysics

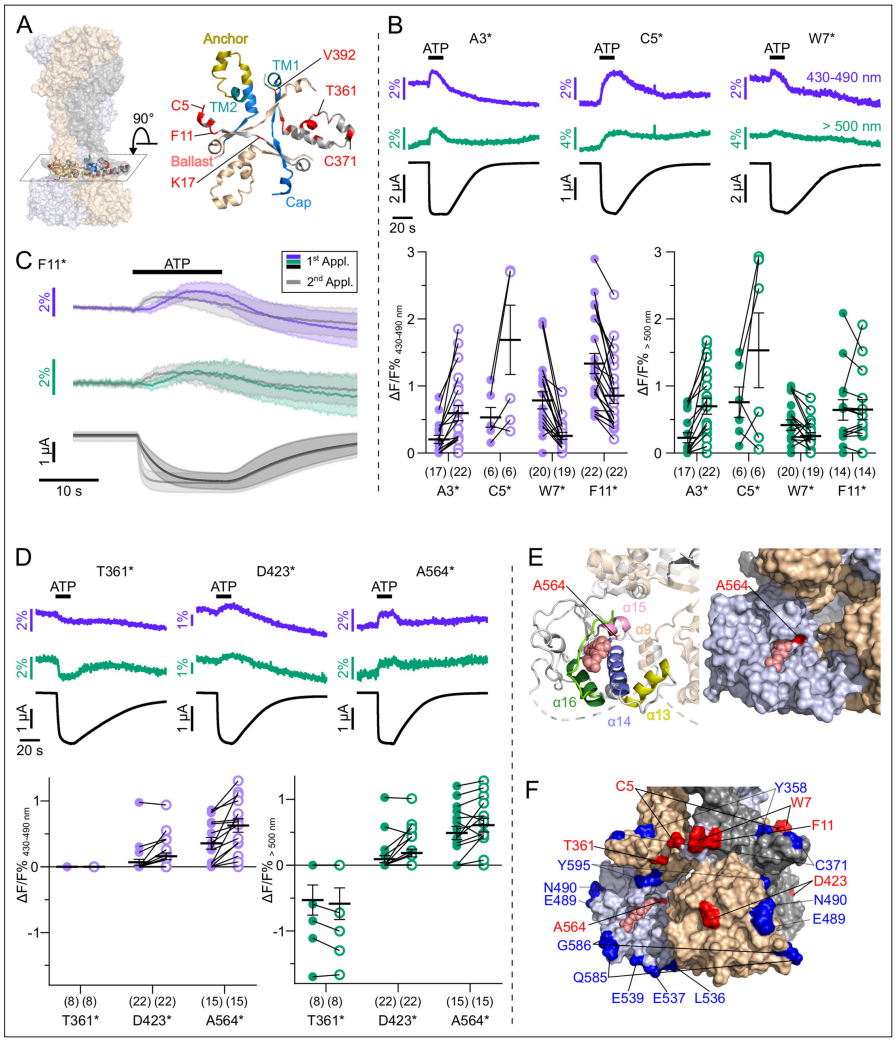

Figure 5. L-3-(6-acetylnaphthalen-2-ylamino)–2-aminopropanoic acid (ANAP) incorporation into 41 positions of the cytosolic P2X7 domain identified seven positions that report ATP-induced fluorescence changes. (**A**) Surface representation of all three P2X7 subunits (in wheat, gray, and purple) showing location of the juxtamembrane regions and close up (top view) detailing the anchor and cap domains (in yellow and blue, respectively) and ANAP-substituted positions (in red) within a single P2X7 subunit. (**B**) Representative voltage clamp fluorometry (VCF) recordings and data summary from P2X7R mutants containing ANAP at different positions within the N-terminus. Responses to 0.3 mM ATP were recorded at two different emission

Figure 5 continued on next page

Figure 5 continued

wavelengths. Graphs compare maximal fluorescence signals during first (closed circles) and second (open circles) ATP applications (interval 195 s). Data are represented as mean ± S.E.M. (**C**) Overlay of VCF recordings from P2X7(F11*) upon first (colored) and second (gray) ATP application (0.3 mM) at two different emission wavelengths. Lines represent averaged VCF recordings from 13 oocytes. Standard deviations are plotted as envelopes. Baseline currents (15 s before ATP application) were adjusted for clarity. (**D**) Representative VCF recordings from the indicated mutants in response to a second application of 0.3 mM ATP and summary of results at the indicated emission wavelengths (performed as in B). Graphs compare maximal fluorescence signals during first (closed circles) and second (open circles) ATP applications (interval 195 s). Data are represented as mean ± S.E.M. All recordings were performed in divalent-free buffer, and oocytes were clamped at –30 mV. (**E**) Close-up of the cytoplasmic ballast domain from one P2X7 subunit in cartoon and surface representation highlighting a bound GDP (salmon), surrounding α-helices, and residue A564 (red). (**F**) Surface representation of the cytoplasmic domains of all three P2X7 subunits (in gray, light blue, and wheat) with bound GDP (salmon). Positions in which ATP-induced ANAP fluorescence changes were identified are shown in red. ANAP-substituted positions in which no fluorescence changes were seen (despite surface expression and current responses) are shown in blue. Original recordings have also been deposited with Dryad and summarized and assigned in ***Table 1—source data 1***.

The online version of this article includes the following source data and figure supplement(s) for figure 5:

Source data 1. Original recordings, ***Figure 5B and D***.

Figure supplement 1. The fluorescence change in P2X7(F11*) is not caused by a dequenching effect of the nearby Trp residue.

Figure supplement 1—source data 1. Summarized data for bar graph in ***Figure 5—figure supplement 1B***.

Figure supplement 1—source data 2. Original recordings, ***Figure 5—figure supplement 1A and B***.

Figure supplement 1—source data 3. Original gel, ***Figure 5—figure supplement 1C***.

Figure supplement 2. Dose-response analysis for intracellular P2X7 mutants F11*, D423*, and A564* and contribution of D423 and A564 deletion mutants to current responses.

Figure supplement 2—source data 1. Original recordings, ***Figure 5—figure supplement 2B***.

Figure supplement 2—source data 2. Summarized data, ***Figure 5—figure supplement 2B***.

Figure supplement 3. Elimination of a CaM-binding motif has no apparent effect on current kinetics or fluorescence responses.

Figure supplement 3—source data 1. Summarized data for box plot in ***Figure 5—figure supplement 3A*** and representative VCF recordings in ***Figure 5—figure supplement 3B***.

Figure supplement 3—source data 2. Original recordings, ***Figure 5—figure supplement 3A and B***.

this domain. However, mutant A564* has great potential as a reporter for yet undefined processes that affect GDP binding and/or metabolism.

Parallel recording of ANAP fluorescence with other fluorophores

Based on the above findings, we propose that yet unknown intracellular ligands or protein interactors are required to mediate downstream signaling via the ballast domain. As potential tools to further investigate such molecules and the dynamics of their molecular interplay with the P2X7R, we combined ANAP with other fluorophores and equipped the VCF setup with a second LED for parallel excitation of two different fluorophores within the same protein.

First, we generated a double mutant (F11*/ S124C) suited to investigate the dynamics of P2X7 activation in different parts of the receptor by parallel labeling with the thiol-reactive fluorophore TMRM in the extracellular head domain and with ANAP in the cytoplasmic N-terminus. As seen in ***Figure 6A***, and similar to ANAP in K127*, TMRM in the head-domain showed an instant fluorescent change already upon a first ATP application, whereas the ANAP fluorescence change in F11* was clearly slower. However, both signals coincided upon a second ATP application, further supporting our hypothesis that the so-called current facilitation in P2X7 is due to a change in receptor gating rather than ligand binding. EC_{50} values for ATP at these mutants and at wt P2X7 were comparable (***Figure 3—figure supplement 3*** and ***Table 2***).

Since P2X7 is known to permeate Ca^{2+}, an important mediator of intracellular signaling, we also established a protocol to combine VCF recording of ANAP-fluorescence with imaging of P2X7-mediated Ca^{2+} influx by fusing the genetically encoded Ca^{2+}-sensor R-GECO1.2 (***Wu et al., 2013***) C-terminally to the receptor. Combination of P2X7 R-GECO1.2 with the K127* mutant, in which ANAP most likely reports a ligand binding-associated process, showed a clearly delayed onset of the Ca^{2+}-dependent R-GECO fluorescence signal, as expected (***Figure 6B***). A limitation of this protocol was, however, that Ca^{2+} promoted P2X7 desensitization and affected baseline fluorescence, specifically

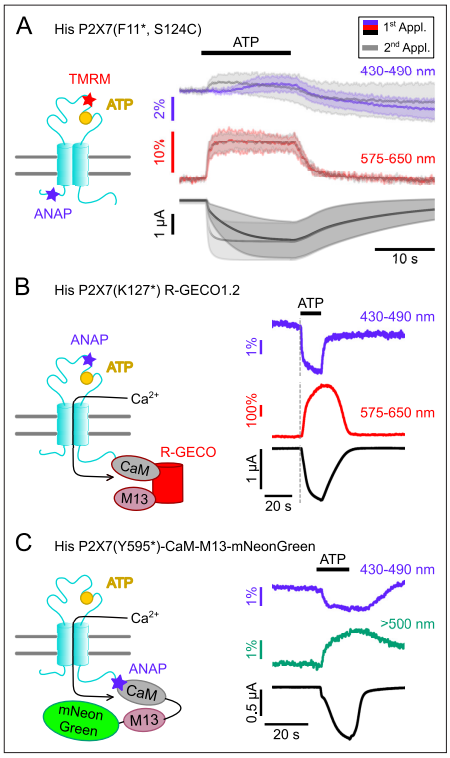

Figure 6. Double-labeled P2X7Rs as potential tools to analyze intracellular domain movements, downstream signaling events, and protein interactions. (**A**) Scheme of a P2X7 subunit double-labeled with L-3-(6-acetylnaphthalen-2-ylamino)–2-aminopropanoic acid (ANAP) and tetramethyl-rhodamine-maleimide (TMRM) (F11*, S124C) and overlay of fluorescence and current responses to first (colored) and second (gray) ATP applications (0.3 mM) at the indicated emission wavelengths. Lines represent averaged voltage clamp fluorometry (VCF) recordings from five different oocytes and standard deviations are plotted as envelopes. Baseline currents (15 s before ATP application) were adjusted for clarity. (**B**) Scheme of P2X7(K127*) subunit C-terminally fused to R-GECO1.2 and representative VCF recording in response to 0.3 mM ATP. Recordings were performed in buffer containing 0.5 mM Ca^{2+}. (**C**) Scheme showing the P2X7(Y595*)-CaM-M13-mNeonGreen construct that served as positive control for recordings of FRET between ANAP and mNeonGreen. Ca^{2+} entry through the P2X7R is supposed to induce conformational changes in the CaM-M13-mNeonGreen reporter, which are detected as a FRET signal. A representative VCF recording in response to 0.3 mM ATP is shown. In all recordings, oocytes were clamped at –30 mV.

The online version of this article includes the following source data and figure supplement(s) for figure 6:

Source data 1. Original recordings, ***Figure 6A, B, and C***.

Figure supplement 1. Ca^{2+}-containing buffers cause large fluorescence changes, even in the absence of L-3-(6-acetylnaphthalen-2-ylamino)–2-aminopropanoic acid (ANAP).

Figure supplement 1—source data 1. Original recordings, ***Figure 6—figure supplement 1A, B, C***.

Figure supplement 1—source data 2. Original and summarized photometric data for ***Figure 6—figure***

Figure 6 continued on next page

Figure 6 continued

supplement 1E.

Figure supplement 2. Control constructs and corresponding voltage clamp fluorometry recordings to confirm the specificity of the FRET signals.

Figure supplement 2—source data 1. Summarized data for bar graph in ***Figure 6—figure supplement 2***.

Figure supplement 2—source data 2. Original recordings for bar graph in ***Figure 6—figure supplement 2***.

Figure supplement 3. Experiments with L-3-(6-acetylnaphthalen-2-ylamino)–2-aminopropanoic acid (ANAP)-containing P2X7 constructs and soluble mNeonGreen-tagged CaM reveal unspecific fluorescence signals.

Figure supplement 3—source data 1. Summarized data for bar graph in ***Figure 6—figure supplement 3***.

Figure supplement 3—source data 2. Original recordings for bar graph in ***Figure 6—figure supplement 3***.

in the ANAP emission spectrum (***Figure 6—figure supplement 1***). Use of an alternative fluorescent unnatural amino acid (fUAA) would therefore be advantageous.

ANAP has been successfully used as a FRET partner in combination with acceptor transition metals (***Gordon et al., 2018***), with EGFP (***Mitchell et al., 2017***), and with YFP to study the apoptosis-regulating Bax-Hsp70 interaction in HeLa cells (***Park et al., 2019***) and the interaction between BACE1 and KCNQ2/3 in tsA-201 cells (***Dai, 2022***). Thus, we finally tested whether we could detect FRET signals between ANAP and potential interactors carrying a mNeonGreen-tag. As a proof of concept and based on a CaM-M13-EGFP fusion protein (***Mitchell et al., 2017***), we generated a positive control (P2X7(Y595*)CaM-M13-mNeonGreen), in which ANAP was introduced into the very C-terminus of a P2X7R that was C-terminally fused to a construct consisting of calmodulin (CaM), CaM-binding myosin light chain kinase (M13), and mNeonGreen (***Shaner et al., 2013***). Upon Ca^{2+}-binding, this construct should move the acceptor protein mNeonGreen in closer proximity to ANAP, which acts as FRET donor.

As expected, ATP-induced Ca^{2+}-influx reduced ANAP fluorescence and increased mNeonGreen fluorescence (***Figure 6C***). The specificity of the signals was confirmed in control experiments (***Figure 6—figure supplement 2***).

Driven by these results we sought to investigate a potential interaction between the rat P2X7 receptor and CaM (***Roger et al., 2010***; ***Roger et al., 2008***) and performed experiments with ANAP-labeled P2X7 receptors and mNeonGreen-tagged CaM. However, these recordings revealed no differences to the negative controls, as the CaM-mNeonGreen construct yielded unspecific fluorescence signals (***Figure 6—figure supplement 3***), possibly due to interaction of soluble mNeonGreen-tagged CaM with the co-injected ANAP.

Since the small FRET signals additionally complicated these analyses, the use of another fUAA with superior photophysical properties such as Acd (***Zagotta et al., 2021***) might provide a better alternative.

In summary, we identified kinetically different fluorescence changes in the head domain that are most likely associated with ligand binding and gating, respectively, and suggest an involvement of the region around T340 in P2X7 current facilitation. We find, however, only limited ATP-induced movements in the intracellular domains and hypothesize that additional interactions might be required to 'activate' the ballast domain. Protocols for parallel recordings of ANAP with TMRM, mNeonGreen, and R-Geco1.2 were established to further analyze such interactions.

Discussion

Optimization of UAA incorporation into P2X7

Site-specific UAA-incorporation represents a powerful method for protein structure-function analysis, and protocols exist for several model systems (***Braun et al., 2020***; ***Klippenstein et al., 2018***; ***Leisle et al., 2015***; ***Pless et al., 2015***). In *X. laevis* oocytes, stop codon suppression either by *in vitro* synthesized UAA-aminoacylated tRNAs or by expression of co-evolved tRNA/aminoacyl-tRNA synthetase pairs has been established. Recently, the semisynthetic ligation of peptide fragments containing the modification using split intervening proteins (inteins) (***Sarkar et al., 2021***) has also been described (***Galleano et al., 2021***; ***Khoo et al., 2020***). While chemically aminoacylated tRNA cannot be reloaded after deacylation without a tRNA synthetase (***Klippenstein et al., 2018***), expression of co-evolved

orthogonal tRNA/aminoacyl-tRNA synthetase pairs requires an additional nuclear injection (***Kalstrup and Blunck, 2013***; ***Ye et al., 2013***). Here, we combined both methods by simultaneously injecting a synthesized suppressor tRNA, cRNA encoding the tRNA synthetase, ANAP, and cRNA encoding the target protein into the cytoplasm. We further enhanced ANAP incorporation by co-injection of cRNA encoding mutated *X. laevis* eRF1, disfavoring premature translation termination. While mutated eRF1 could potentially interfere with correct translation of endogenous *amber*-terminated oocyte proteins, we observed no apparent impact on oocyte properties. The presented procedure also improved oocyte quality, expression efficiency, and reproducibility and facilitated optimization of injection ratios. While it does not require equipment for synthesis and purification of UAA-labeled tRNA and is easily applicable in a molecular biology lab, it still depends on a co-evolved tRNA/aminoacyl-tRNA synthetase pair. In combination with UAAs suitable for click chemistry, its flexibility and the choice of fluorophores or functional groups could be greatly expanded (***Braun et al., 2020***). Here, we could successfully employ the optimized ANAP labeling strategy to explore conformational changes associated with P2X7R activation.

Is P2X7 current facilitation an intrinsic receptor property?

Based on crystal and cryo-EM structures, a molecular mechanism of P2XR gating has been established: ATP-binding to its extracellular inter-subunit binding sites leads to a jaw-like tightening of the head and dorsal fin domains of neighboring subunits around the ATP molecule. This induces an upward movement of β strands in the lower part of the extracellular domain and associated pore opening. Upon prolonged and/or repeated activation, the P2X7R shows a characteristic increase in current amplitude and speed of channel opening, which is generally associated with a shift toward higher ATP sensitivity. Several mechanisms have been proposed to contribute to this so-called current facilitation: modulation of receptor activity by cholesterol (via direct binding to TM domains or cholesterol recognition amino acid consensus [CRAC] motifs) (***Karasawa et al., 2017***; ***Murrell-Lagnado, 2017***; ***Robinson et al., 2014***), palmitoylation (***Di Virgilio et al., 2018***; ***Gonnord et al., 2009***; ***Karasawa et al., 2017***), cooperative interactions between intracellular N- and C-termini (***Allsopp and Evans, 2015***), and calcium-dependent calmodulin binding (***Roger et al., 2008***). The latter, however, appeared to be specific for rat P2X7 and was not found in the human isoform (***Roger et al., 2010***). In monocyte-derived human macrophages, current facilitation as well as inflammasome activation, IL-1β release, blebbing, PS flip, and membrane permeabilization were inhibited by phospholipase A2 (PLA2) and Cl^- channel antagonists (***Janks et al., 2019***), and it was suggested that facilitation represents a downstream effect of P2X7-mediated PLA2 and Cl^- channel activation. Single channel recordings of HEK293 cell-expressed rat P2X7Rs recently revealed an increased open probability as a result of ATP-evoked current facilitation (***Dunning et al., 2021***). Here, we also observed a faster onset of current signal upon the second ATP application while changes in the amplitude were less obvious. Importantly, for most ANAP-containing P2X7R constructs studied here, fluorescence changes mirrored this behavior, strongly suggesting that it is a receptor-intrinsic property and does not involve currents from downstream-activated channels, such as Ca^{2+}-activated Cl^- channels or pannexins (***Dunning et al., 2021***; ***Ousingsawat et al., 2015***; ***Pelegrin and Surprenant, 2006***; ***Riedel et al., 2007***). Interestingly, the K127* head domain mutant showed faster fluorescence than current changes even upon the first ATP application. Thus, ANAP in this position reports a movement or interaction that precedes channel opening and is most likely related to ligand binding. A similar result was observed for the TMRM-labeled F11*/S124C double mutant, where the onset of TMRM signal upon the first ATP application was faster than the current and ANAP fluorescence change (but coincided upon the second application). In contrast to TMRM, ANAP in position 124 showed fluorescence signals that paralleled current responses, suggesting that different fluorophores can report different processes, possibly due to differences in size and/or sensitivity to the environment. Supporting the idea that these fast fluorescence changes are related to ligand binding, they were only observed in mutants containing fluorophores near the ATP binding site. Fast ligand-induced fluorescence changes already in the non-facilitated P2X7 state imply that ligand binding is unaltered between the first and second activation and consequently, changes in channel gating account for the observed current facilitation.

Fluorescence signals recorded from ANAP in positions near the channel gate (***Pippel et al., 2017***) could result from different simultaneously occurring effects during channel opening and evidence for both, a shift in ANAP emission toward longer wavelengths (position 340) and dequenching (positions

339 and 341) were observed. Interestingly, ANAP in position 340 revealed significant differences in the fluorescence amplitudes between the first and second ATP application. An intriguing explanation would be that it detects a slowly or non-reversible conformational change after the first ATP application, which could facilitate subsequent gating movements and thereby account for current facilitation. However, T340* was the only construct that did not show a faster current onset upon the second ATP application, possibly because ANAP substitution in this critical position already strongly facilitated gating, as indicated by the large 'leak' currents, likely reflecting partial constitutive ligand-independent opening.

Based on the above observations, we propose that the faster activation upon the second ATP application is an intrinsic property of the P2X7R. This conclusion is also in good agreement with the fact that the current facilitation but not downstream signaling events is seen in truncated P2X7 constructs (***Kopp et al., 2019***; ***McCarthy et al., 2019***). One possibility for a molecular mechanism would be a pre-tensioning of TM2-helices during the first receptor activation that eases channel opening upon a second activation. It is not known, but likely that the cryo-EM structure of the ATP-bound open P2X7R represents the facilitated state. If so, the open-state stabilizing cap domain might not be locked in place in the naïve state but could be formed during the first receptor activation and then stabilized via the cysteine-rich anchor domain. The cap domain may then support the upward transition of TM2 and thereby accelerate current responses. Dynamic cysteine palmitoylation and cholesterol interactions might modulate this process as suggested before (***Di Virgilio et al., 2018***; ***Dunning et al., 2021***; ***Karasawa et al., 2017***; ***Robinson et al., 2014***). Alternatively, initial receptor activation may change accessibility and/or affinity for a yet unknown allosteric ligand and thereby modulate P2X7 activation. All these suggested mechanisms are not mutually exclusive.

Is the ballast domain affected by ATP-binding/channel opening?

While the functionality of P2X7 as a cation channel is not impaired by lack of the intracellular C-terminus (***Becker et al., 2008***; ***Klapperstück et al., 2001***; ***McCarthy et al., 2019***), its deletion disrupts a number of P2X7-mediated effects (***Kopp et al., 2019***), which most likely depend on downstream signaling pathways. A major aim of this study was the identification of C-terminal domains involved in such signaling. Most of the intracellular positions in which ANAP reported relative protein rearrangements were, however, located upstream of the cap domain either within the N-terminus (A3, C5, W7, F11) or right after TM2 (T361). Despite clear surface expression and current responses of at least 12 constructs with ANAP in the cytoplasmic ballast domain, only two of these mutants (D423* and A564*) revealed detectable but small fluorescence changes upon ligand application, suggesting that ATP binding induces only limited structural rearrangement in this domain, and that it is largely uncoupled from the extracellularly initiated conformational changes. Interestingly D423*, which showed only sporadic changes, lies in a short sequence with homology to an α-actinin 2 binding sequence (***Kim et al., 2001***). Since P2X7 activation induces plasma membrane morphology changes, and interactions with cytoskeletal proteins have been proposed (***Gu et al., 2009***; ***Kim et al., 2001***; ***Kopp et al., 2019***), an intriguing possibility would be that ANAP in position 423 reports interactions with cytoskeletal components. In A564*, ANAP is located near the GTP/GDP-binding site but showed much smaller signals than in positions near the ATP binding site, arguing against GTP/GDP (un-)binding, in agreement with the cryo-EM structures (***McCarthy et al., 2019***). However, A564 is also surrounded by other proposed interaction sites, including an LPS binding sequence and a calcium-dependent CaM binding motif (***Denlinger et al., 2001***; ***Roger et al., 2010***; ***Roger et al., 2008***), which might account for the observed signals.

In summary, we improved ANAP incorporation into *Xenopus* oocyte-expressed protein and performed an extensive VCF analysis of P2X7R mutants carrying ANAP in 61 positions throughout the receptor. We conclude from our data, that current facilitation is, at least partly, an intrinsic property of the P2X7R and involves an accelerated channel gating rather than ligand binding. In addition, we propose that ligand-induced extracellular and TM domain movements are not significantly translated to the cytosolic ballast domain and that intracellular ligands or interactors are required to 'activate' this domain. Protocols for simultaneous recording of ANAP with TMRM, Ca^{2+}-dependent R-GECO1.2, or mNeonGreen-labeled FRET partners are presented that might help to validate P2X7 downstream signaling events and analyze their molecular mechanisms and dynamics, once such interactors have been reliably determined.

Materials and methods

Xenopus laevis oocytes

X. laevis females were obtained from NASCO (Fort Atkinson, WI) and kept at the Core Facility Animal Models (CAM) of the Biomedical Center (BMC) of LMU Munich, Germany (Az:4.3.2–5682/LMU/BMC/CAM) in accordance with the EU Animal Welfare Act. To obtain oocytes, frogs were deeply anesthetized in MS222 and killed by decapitation. Surgically extracted ovary lobes were divided into smaller lobes and dissociated by ~2.5 hr incubation (16°C) with gentle shaking in ND96 solution (96 mM NaCl, 2 mM KCl, 1 mM $CaCl_2$, 1 mM $MgCl_2$, 5 mM HEPES, pH 7.4) containing 2 mg/ml collagenase (Nordmark, Uetersen, Germany) and subsequently defolliculated by washing (15 min) with Ca^{2+}-free oocyte Ringer solution (90 mM NaCl, 1 mM KCl, 2 mM $MgCl_2$, 5 mM HEPES). Stage V-VI oocytes were selected and kept in ND96 containing 5 µg/ml gentamicin until further use. In some cases, oocytes were commercially obtained (Ecocyte Bioscience, Dortmund, Germany), or ovaries were provided by Prof. Dr. Luis Pardo (Max Planck Institute for Experimental Medicine, Göttingen, Germany).

cDNA and cloning

N-terminally His-tagged rat P2X1 cDNA in pNKS2 has been described (***Lörinczi et al., 2012***). An EGFP-tag was C-terminally added via a GSAGSA-linker sequence by Gibson assembly (***Gibson et al., 2009***) according to the protocol of the manufacturer (New England Biolabs GmbH, Frankfurt am Main, Germany).

cDNA encoding an N-terminally His-tagged rat P2X7R was subcloned into a pUC19 vector modified for cRNA expression in oocytes (termed pUC19o). pUC19o was generated by insertion (from 5` to 3`) of a synthesized T7 promoter sequence, a *Xenopus* globin 5′-UTR, and a Kozak sequence (***Kozak, 1987***) (GeneArt String DNA fragment, Life Technologies / Thermo Fisher Scientific Inc, Regensburg, Germany) and a 27 bp 3′-UTR (***Tanguay and Gallie, 1996***) followed by a poly A tail (51 adenines) obtained from the pNKS2 vector (***Gloor et al., 1995***) (for details of the UTRs see Key resource table).

The cDNA sequence of the aminoacyl-tRNA synthetase was obtained from the plasmid pANAP (Addgene #48696) (***Chatterjee et al., 2013***) and subcloned via Gibson assembly into pUC19o.

The coding sequence of *X. laevis* eRF1 (NCBI Reference Sequence: NM_001090894.1) with an E55D mutation (GeneArt String DNA fragment, Life Technologies/Thermo Fisher Scientific Inc, Regensburg, Germany) was cloned into pNKS2 via Gibson assembly. For recombinant expression in *E. coli*, the coding sequence of His-eRF1(E55D) was cloned into a modified pET28a vector via Gibson assembly.

Site-specific mutagenesis was performed with the Q5 Site-Directed Mutagenesis Kit (based on PCR-amplification) according to the manufacturer's protocol (New England Biolabs GmbH, Frankfurt am Main, Germany). Oligonucleotides were ordered from metabion GmbH (Planegg/Steinkirchen, Germany).

All constructs contained either an *ochre* (TAA) or *opal* (TGA) stop codon for normal translational termination to avoid C-terminal ANAP incorporation and read-through and were confirmed by sequencing (Eurofins Genomics, Ebersberg, Germany).

eRF1 protein preparation

NiCo(DE3) bacteria were transformed with His-eRF1(E55D) in pET28a. 5 ml of a LB-Kanamicin preculture (~12 hr) was added to 300 ml ZY-5052 autoinduction media (***Studier, 2005***) supplemented with 100 µg/ml Kanamycin and grown for 6 hr at 37°C. The temperature was then reduced to 25°C, and bacteria were grown for another 18 hr. After pelleting by centrifugation (6500 g, 20 min) cells were resuspended in 40 ml lysis buffer (50 mM TRIS (tris(hydroxymethyl)aminomethane)-HCl, pH 8.0, 50 mM NaCl, 5 mM $MgCl_2$, 10% (v/v) glycerol, 0.1% (v/v) Triton X-100, 10 µg/ml DNase I, 100 µg/ml lysozyme), and sonicated (Bandelin Sono plus, TT13 cap, 50% duty cycle, 50% power) for 5 min in an ice bath. The lysate was pelleted at 40,000 × g (1 hr at 4°C). The supernatant was filtered (0.2 µm) and applied onto a Ni-NTA column (HisTrap FF, 5 ml, GE Healthcare Europe GmbH, Freiburg, Germany). Bound protein was washed with 10 column volumes of washing buffer (25 mM TRIS-HCl, pH 7.8, 500 mM NaCl, 20 mM imidazole, 0.25% [v/v] Tween 20, 10% [v/v] glycerol) and eluted with 6 column volumes of elution buffer (25 mM TRIS-HCl, pH 7.8, 500 mM NaCl, 300 mM imidazole, 0.25% [v/v] Tween 20 [v/v], 10% [v/v] glycerol). The eluate was concentrated (Amicon Ultra-15, 10 kDa MWCO, Millipore/Merck KgaA, Darmstadt, Germany), and buffer was exchanged by low-salt buffer (20 mM TRIS, 100 mM NaCl, pH 7.5) for subsequent anion exchange chromatography on a 5 ml Mono-Q

column (GE Healthcare Europe GmbH, Freiburg, Germany). Following an elution gradient with high-salt buffer (20 mM TRIS, 1 M NaCl, pH 7.5), protein-containing fractions were pooled, concentrated, and buffer was exchanged (1× PBS with 500 mM NaCl) for size exclusion chromatography on a Superdex 75 Increase (10/300). Purified His-eRF1(E55D) was shock-frozen in 10 µl aliquots and stored at –80°C.

cRNA synthesis and tRNA

To prepare templates for cRNA synthesis, plasmids were linearized with EcoRI-HF (pNKS2) or NotI-HF (pUC19o) from New England Biolabs GmbH (Frankfurt am Main, Germany) and purified via MinElute Reaction Cleanup columns (Qiagen, Hilden, Germany) according to the manufacturer's protocol. Alternatively, templates (including the 5'-terminal RNA polymerase promoter site (T7 or SP6) and the 3'-terminal poly A) were amplified by PCR and purified using the NucleoSpin Gel and PCR Clean-up Kit (Macherey-Nagel, Düren, Germany) according to the manufacturer's protocol.

Capped cRNA was synthesized using the mMESSAGE mMACHINE SP6 or T7 Transcription Kits (Invitrogen/Thermo Fisher Scientific Inc, Schwerte, Germany), precipitated with LiCl, and dissolved in nuclease-free water (1 µg/µl if not stated otherwise).

The *amber* suppressor tRNA sequence was translated from the plasmid pANAP (Addgene #48696) (***Chatterjee et al., 2013***), provided with an universal 3'-terminal CCA-sequence (important for tRNA aminoacylation and translation), and chemically synthesized and purified via PAGE and HPLC (biomers.net GmbH, Ulm, Germany).

Oocyte injection and ANAP incorporation

A Nanoject II injector (Science Products GmbH/Drummond, Hofheim, Germany) was used for nuclear and cytoplasmic injections.

cRNAs encoding cysteine-substituted receptors for TMRM labeling were injected as described (***Lörinczi et al., 2012***). Two different procedures were used for incorporation of ANAP:

The 2-step injection method was performed according to ***Kalstrup and Blunck, 2017*** using the plasmid pANAP that encodes the co-evolved, orthogonal, and ANAP-specific *amber* suppressor tRNA/tRNA synthetase pair (Addgene #48696 ***Chatterjee et al., 2013***). 9.2 nl of pANAP (0.1 µg/µl) per oocyte were injected into the nucleus. 1–2 days later, 46 nl of an injection mix containing 0.20–0.25 µg/µl receptor-encoding cRNA (with or without an UAG codon at the site of interest) and 0.2–1.0 mM ANAP (L-ANAP trifluoroacetic salt or L-ANAP methyl ester, both AsisChem Inc, Waltham, MA) were injected into the cytoplasm.

The 1-step injection method was performed as described before (***Durner and Nicke, 2022***) with addition of mutated *X. laevis* eRF1 as indicated. An injection master mix comprising 0.25 mM ANAP TFA, 0.25 µg/µl cRNA encoding *X. laevis* eRF1 E55D, 0.2 µg/µl cRNA encoding the tRNA synthetase, and 0.4 µg/µl tRNA was freshly prepared. Three parts of the injection master mix were added to one part of 1 µg/µl receptor-encoding cRNA (with or without an UAG codon). 50.6 nl per oocyte were injected into the cytoplasm. Uninjected oocytes and oocytes injected with wt receptor cRNA served as negative and positive controls, respectively. Nuclease free water served as a substitute for individual components in control groups.

To optimize fUAA incorporation into *X. laevis* oocyte-expressed receptors, different procedures, concentrations of substances, and injection time points were compared (***Figure 1—figure supplement 1***). To optimize the concentrations of an individual component, the ratios and concentrations of the other components, as well as the expression times and receptor cRNA concentrations were kept constant in individual experiments. In cases where oocytes were incubated in membrane-permeable L-ANAP methyl ester, a 2 µM concentration in ND96 buffer (see below) was used.

Injected oocytes were kept in ND96 (96 mM NaCl, 2 mM KCl, 1 mM $MgCl_2$, 1 mM $CaCl_2$, 5 mM HEPES, pH 7.4–7.5) supplemented with gentamicin (50 µg/ml) at 16°C for at least 2 days.

Receptor purification and SDS-PAGE

To evaluate plasma membrane expression of truncated and full-length His-tagged P2X7R mutants, surface-expressed receptors were fluorescently labeled, purified, and analyzed by SDS-PAGE. Three days after injection, 10 oocytes per group were labeled for 30–60 min (in the dark under rotation) in 200 µl 0.003% (m/V) aminoreactive, membrane-impermeant Cy5 Mono NHS Ester (Merck /

Sigma-Aldrich, Taufkirchen, Germany, diluted from a 1% [m/V] stock in DMSO) in ND96 (pH 8.5, 4°C) and then washed in ND96. Bright blue-stained damaged oocytes were then discarded, and intact oocytes were homogenized with a 200 µl pipet tip in 10 µl homogenization buffer per oocyte (0.1 M sodium phosphate buffer, pH 8.0, containing 0.4 mM Pefabloc SC and 0.5% *n*-dodecyl-β-D-maltoside, [both Merck/Sigma-Aldrich, Taufkirchen, Germany]). Membrane proteins were extracted by 10 min incubation on ice and separated from the debris by two centrifugation steps (10 min at 14,000 × g and 4°C). 100 µl of the protein extract were then supplemented with 400 µl of homogenization buffer containing 10 mM imidazole and added to 50 µl Ni^{2+}-NTA agarose beads (Qiagen GmbH, Hilden, Germany) preconditioned with washing buffer (0.1 M sodium phosphate buffer [pH 8.0] containing 0.08 mM Pefabloc, 0.1% *n*-dodecyl-β-D-maltoside, and 25 mM imidazole). After 1 hr incubation under inversion at 4°C in the dark, beads were washed three to four times with 500 µl washing buffer, and His-tagged protein was eluted (≥10 min at RT with occasional flipping to suspend the beads) with 2×50 µl elution buffer (20 mM Tris-HCl, 300 mM imidazole, 10 mM EDTA, and 0.5% *n*-dodecyl-β-D-maltoside). 32 µl of the eluate were supplemented with 8 µl 5× lithium dodecyl sulfate (LiDS) sample buffer (5% [w/v] LiDS, 0.1% bromphenol blue, 100 mM dithiothreitol, 40% [v/v] glycerol in 0.3 M Tris HCl [pH 6.8]), incubated at 95°C for 10 min, and separated by reducing SDS-PAGE on an 8% gel. Fluorescence-labeled protein was visualized with a Typhoon trio fluorescence scanner (GE Healthcare, Chicago, IL), and relative protein quantities were determined using FIJI (***Schindelin et al., 2012***). Lanes were selected as regions of interest and transformed into 1D profile plots. Band intensities were then quantified by integrating the area of each peak in the profile plot relative to the baseline of each lane. Data was visualized using GraphPad Prism software (Version 9.3.0, San Diego, CA).

VCF recordings

Recordings were performed in a custom-made measuring chamber (***Figure 3***) that is split into an upper and lower compartment, which are individually perfused and connected by a 0.75 mm hole on which the oocyte is placed. The lower compartment has a transparent bottom, and the chamber was mounted on an Axiovert 200 inverted fluorescence microscope (Carl Zeiss Microscopy LLC, Oberkochen, Germany) so that the oocyte was centered above the objective with the animal pole facing down to avoid increased background fluorescence by the lighter vegetal pole. Upper and lower compartments were separately perfused with recording solution and recording or agonist solution, respectively, using a gravity-based perfusion system and a membrane vacuum pump. Solutions in the lower compartment were switched by computer-controlled magnetic valves.

To avoid inhibition by Ca^{2+} or Mg^{2+} and Ca^{2+}-mediated downstream effects and to obtain reproducible current responses, recordings were performed in divalent-free buffer (90 mM NaCl, 1 mM KCl, 5 mM HEPES, pH 7.4–7.5) complemented with flufenamic acid and ethylene glycol tetraacetic acid (EGTA) (both 0.1 mM). For measurements with Ca^{2+}-containing buffers, EGTA was omitted, and Ca^{2+} (0.2–0.5 mM) was added (in case of P2X7-R-GECO constructs, FRET measurements between ANAP and mNeonGreen and control measurements of ANAP-containing constructs to test for Ca^{2+}-specific effects). If not otherwise noted, the agonist solution contained 300 µM ATP and was applied for 15 s in 195 s intervals. Intracellular electrode resistances were below 1.2 MΩ, and recordings were performed at room temperature at a holding potential of –30 mV to keep the current amplitudes reproducible. The solution exchange in the lower chamber is finished in about 1 s (***Lörinczi et al., 2012***).

To exclude mechanically induced fluorescence changes due to solution switching, all recording protocols started with sequential applications of ATP-free recording solutions from different tubes and magnetic valves. If required, solution speed and oocyte position were readjusted to ensure the absence of mechanical artifacts.

For fluorescence recordings, the microscope was equipped with two LEDs as excitation sources (UV-LED M365LP1 with 365 nm, green LED M565L3 with 565 nm, both Thorlabs GmbH, Bergkirchen, Germany). Since UV excitation in oocytes causes relatively high background fluorescence levels, detectors must feature a wide dynamic range, while maintaining a sufficiently high sensitivity in order to record small fluorescence changes. To this end, two cooled, high-sensitivity MPPC detectors (Hamamatsu Photonics K.K., Japan) were used for simultaneous fluorescence detection at two different spectral segments. For optical filters and dichroic mirrors see Key resource table.

Single-channel fully programmable instrumentation amplifiers with Bessel low-pass filter characteristics (Alligator Technologies, Costa Mesa, CA) were used for signal scaling. To minimize

photobleaching, LEDs were pulsed using self-developed high-speed LED drivers with sub-µs rise time. Pulse lengths were set in the ~20 µs range to allow for the fluorescence readout signal chain to settle. Fluorescence signal digitization was synchronized to the excitation pulses using an STM32F407 microcontroller (STMicroelectronics, Geneva, Switzerland). Its timer peripherals were re-triggered by each ADC conversion cycle in order to create an LED illumination pulse that starts shortly before the next ADC conversion cycle. Whenever two excitation wavelengths were used, excitation pulses were staggered in time with the longer wavelength excitation pulse signal being digitized first, preventing bleedthrough of background fluorescence excited by the shorter excitation wavelength to the longer-wavelength detection channel. A water-immersion objective with high numerical aperture and a large working distance (W N-Achroplan 63×/0,9 M27, Carl Zeiss Microscopy LLC, Oberkochen, Germany) was used to maximize the collection of emitted photons and to focus on the oocyte membrane.

Currents were measured with a Turbo Tec-05X amplifier and CellWorks E 5.5.1 software (both npi electronic GmbH, Tamm, Germany) and were used for current and fluorescence recordings and valve control. Current signals were digitized at 400 Hz and downsampled in CellWorks to 200 Hz.

Dose-response analysis

To determine agonist dose-response curves, ATP was applied for 15 s in 195 s intervals. A reference concentration (ATP_{Ref}) of 300 µM was applied until stable responses were obtained and was then alternately applied with ATP concentrations ranging from 10 µM to 3 mM (ATP_{Test}). All responses were normalized to the response of ATP_{Ref}, and EC_{50} values were calculated using the four-parameter Hill equation: *% Response = Bottom + (Top−Bottom)/(1+10^[(LogEC$_{50}$−X)*n$_H$])* with *Bottom* and *Top* constrained to 0%, *and* maximum responses, respectively, *X* corresponding to the log of agonist concentration, and n_H corresponding to the Hill coefficient.

Data analysis

Fluorescence and current signals were analyzed and visualized using a Python-based script (for packages used, see Key resource table): Fluorescence signals were denoised using a fifth-order Bessel filter with a low-pass corner frequency of 4 Hz. Maximum amplitudes of ATP-evoked current and fluorescence responses from different receptor constructs were summarized, compared, and visualized using GraphPad Prism software (Version 9.3.0, San Diego, CA). The following inclusion criteria were applied for recordings:

(i) ATP application must evoke a current response >0.1 µA, (ii) leak currents must be stable for the duration of the recording (at least two ATP applications), (iii) repeated ATP applications must elicit reproducible current responses (>0.8 µA), (iv) fluorescence signals must be without mechanical artifacts and clearly distinguishable from fluorescence changes of wt expressing oocytes (see below). 2–3 days after injection, repeated application of 300 µM ATP to wt-expressing oocytes elicited reproducible currents (i.e. first and second current responses differed less than 10% and reached a plateau, at least during the second application), which were taken as a reference. Longer expression times resulted in irregular and irreproducible current responses and less stable oocytes. In case of mutated receptors, longer expression times were often needed to yield current responses comparable to wt P2X7.

We observed a gradual decrease in fluorescence signal for the duration of ligand application in control oocytes expressing wt receptors even in the absence of ANAP. To distinguish ANAP-specific fluorescence signals from these gradual changes, for signal analysis only fluorescence changes upon ATP application were considered that were either positive, or negative but additionally not linear. If fluorescence signals from mutant expressing oocytes were not distinguishable from fluorescence changes observed for wt expressing oocytes no fluorescence change was assumed (0% ΔF/F). Only signals that were recorded in at least three different oocytes were considered for analysis. Additionally, fluorescence changes that were recorded in less than 40% of analyzed oocytes expressing one specific receptor construct or that had averaged ΔF/F values <0.3% were not considered.

Statistical analysis

Data were either represented as mean ± S.D., as box plots, or as mean ± S.E.M. with the number of recordings given in brackets, and statistical analysis was performed by either two-tailed unpaired Welch's *t*-test or two-tailed paired Student's *t*-test, as indicated. Values of $p<0.05$ were defined as

statistically significant with *, **, ***, and **** denoting values of p<0.05, 0.005, 0.0005, and 0.0001 or 0.00005, respectively.

Data availability

All data generated or analyzed during this study are included in the manuscript and supporting files. Original VCF recordings, extracted VCF data, and scans from SDS-PAGE gels are provided as source data files for ***Figure 1***, ***Figure 1—figure supplement 1***, ***Figure 2***, ***Figure 2—figure supplement 1***, ***Figure 3***, ***Figure 3—figure supplement 1***, ***Figure 3—figure supplement 2***, ***Figure 3—figure supplement 3***, ***Figure 4***, ***Figure 4—figure supplement 1***, ***Figure 5***, ***Figure 5—figure supplement 1***, ***Figure 5—figure supplement 2***, ***Figure 5—figure supplement 3***, ***Figure 6***, ***Figure 6—figure supplement 1***, ***Figure 6—figure supplement 2***, ***Figure 6—figure supplement 3***, ***Table 1***, and ***Table 2***. The source data files of ***Table 1*** include source data of ***Figure 2—figure supplement 1***, ***Figure 3***, ***Figure 4***, and ***Figure 5*** and are assigned accordingly in ***Table 1—source data 1***. The original recordings of ***Table 1*** have been deposited with Dryad (DOI https://doi.org/10.5061/dryad.p8cz8w9tb). The source data files of ***Table 2*** include source data of ***Figure 3—figure supplement 3*** and ***Figure 5—figure supplement 2***.

Note that original current and fluorescence recordings provided as comma separated value files each contain three columns of values (from left to right): (1) current values, (2) fluorescence signals of longer emission wavelengths, and (3) fluorescence signals of shorter emission wavelengths.

Acknowledgements

This work was supported by the Deutsche Forschungsgemeinschaft (DFG, German Research Foundation, Project-ID: 335447717 - SFB 1328, A15). We thank Luis Pardo, Kerstin Dümke, and Monika Haberland for providing *Xenopus laevis* oocytes.

Additional information

Funding

Funder	Grant reference number	Author
Deutsche Forschungsgemeinschaft	335447717 - SFB 1328, Project A15	Annette Nicke

The funders had no role in study design, data collection and interpretation, or the decision to submit the work for publication.

Author contributions

Anna Durner, Conceptualization, Formal analysis, Investigation, Methodology, Writing - original draft, Writing - review and editing; Ellis Durner, Conceptualization, Resources, Formal analysis, Methodology, Writing - original draft, Writing - review and editing; Annette Nicke, Conceptualization, Supervision, Funding acquisition, Writing - original draft, Project administration, Writing - review and editing

Author ORCIDs

Anna Durner http://orcid.org/0000-0002-0993-8869
Ellis Durner http://orcid.org/0000-0002-4461-9257
Annette Nicke http://orcid.org/0000-0001-6798-505X

Decision letter and Author response

Decision letter https://doi.org/10.7554/eLife.82479.sa1
Author response https://doi.org/10.7554/eLife.82479.sa2

Additional files

Supplementary files

- MDAR checklist

Data availability

All data generated or analyzed during this study are included in the manuscript and supporting files. Original recordings or scans from SDS-PAGE gels are provided as source data with the respective figures. Original recordings of Table 1 are deposited with Dryad (for data assignment see Table 1-source data 1). This paper does not report original code.

The following dataset was generated:

Author(s)	Year	Dataset title	Dataset URL	Database and Identifier
Nicke A, Durner A, Durner E	2023	Table 1-source data 1 (original recordings)	http://dx.doi.org/10.5061/dryad.p8cz8w9tb	Dryad Digital Repository, 10.5061/dryad.p8cz8w9tb

References

Allsopp RC, Evans RJ. 2015. Contribution of the juxtatransmembrane intracellular regions to the time course and permeation of ATP-gated P2X7 receptor ion channels. *The Journal of Biological Chemistry* **290**:14556–14566. DOI: https://doi.org/10.1074/jbc.M115.642033, PMID: 25903136

Andriani RT, Kubo Y. 2021. Voltage-clamp fluorometry analysis of structural rearrangements of ATP-gated channel P2X2 upon hyperpolarization. *eLife* **10**:e65822. DOI: https://doi.org/10.7554/eLife.65822, PMID: 34009126

Becker D, Woltersdorf R, Boldt W, Schmitz S, Braam U, Schmalzing G, Markwardt F. 2008. The P2X7 carboxyl tail is a regulatory module of P2X7 receptor channel activity. *The Journal of Biological Chemistry* **283**:25725–25734. DOI: https://doi.org/10.1074/jbc.M803855200, PMID: 18617511

Braun N, Sheikh ZP, Pless SA. 2020. The current chemical biology tool box for studying ion channels. *The Journal of Physiology* **598**:4455–4471. DOI: https://doi.org/10.1113/JP276695, PMID: 32715480

Chatterjee A, Guo J, Lee HS, Schultz PG. 2013. A genetically encoded fluorescent probe in mammalian cells. *Journal of the American Chemical Society* **135**:12540–12543. DOI: https://doi.org/10.1021/ja4059553, PMID: 23924161

Dai G. 2022. Neuronal KCNQ2/3 channels are recruited to lipid raft microdomains by palmitoylation of BACE1. *The Journal of General Physiology* **154**:e202112888. DOI: https://doi.org/10.1085/jgp.202112888, PMID: 35201266

Denlinger LC, Fisette PL, Sommer JA, Watters JJ, Prabhu U, Dubyak GR, Proctor RA, Bertics PJ. 2001. Cutting edge: the nucleotide receptor P2X7 contains multiple protein- and lipid-interaction motifs including a potential binding site for bacterial lipopolysaccharide. *Journal of Immunology* **167**:1871–1876. DOI: https://doi.org/10.4049/jimmunol.167.4.1871, PMID: 11489964

Di Virgilio F, Schmalzing G, Markwardt F. 2018. The elusive P2X7 macropore. *Trends in Cell Biology* **28**:392–404. DOI: https://doi.org/10.1016/j.tcb.2018.01.005, PMID: 29439897

Dunning K, Martz A, Peralta FA, Cevoli F, Boué-Grabot E, Compan V, Gautherat F, Wolf P, Chataigneau T, Grutter T. 2021. P2X7 receptors and TMEM16 channels are functionally coupled with implications for macropore formation and current facilitation. *International Journal of Molecular Sciences* **22**:6542. DOI: https://doi.org/10.3390/ijms22126542, PMID: 34207150

Durner A, Nicke A. 2022. A simplified protocol to incorporate the fluorescent unnatural amino acid ANAP into *Xenopus laevis* oocyte-expressed P2X7 receptors. *Methods in Molecular Biology* **2510**:193–216. DOI: https://doi.org/10.1007/978-1-0716-2384-8_10, PMID: 35776326

Galleano I, Harms H, Choudhury K, Khoo K, Delemotte L, Pless SA. 2021. Functional cross-talk between phosphorylation and disease-causing mutations in the cardiac sodium channel na V 1.5. *PNAS* **118**:e2025320118. DOI: https://doi.org/10.1073/pnas.2025320118, PMID: 34373326

Gibson DG, Young L, Chuang RY, Venter JC, Hutchison CA, Smith HO. 2009. Enzymatic assembly of DNA molecules up to several hundred kilobases. *Nature Methods* **6**:343–345. DOI: https://doi.org/10.1038/nmeth.1318, PMID: 19363495

Gloor S, Pongs O, Schmalzing G. 1995. A vector for the synthesis of crnas encoding myc epitope-tagged proteins in *Xenopus laevis* oocytes. *Gene* **160**:213–217. DOI: https://doi.org/10.1016/0378-1119(95)00226-v, PMID: 7543868

Gonnord P, Delarasse C, Auger R, Benihoud K, Prigent M, Cuif MH, Lamaze C, Kanellopoulos JM. 2009. Palmitoylation of the P2X7 receptor, an ATP-gated channel, controls its expression and association with lipid rafts. *The FASEB Journal* **23**:795–805. DOI: https://doi.org/10.1096/fj.08-114637, PMID: 18971257

Gordon SE, Munari M, Zagotta WN. 2018. Visualizing conformational dynamics of proteins in solution and at the cell membrane. *eLife* **7**:e37248. DOI: https://doi.org/10.7554/eLife.37248, PMID: 29923827

Gu BJ, Rathsam C, Stokes L, McGeachie AB, Wiley JS. 2009. Extracellular ATP dissociates nonmuscle myosin from P2X (7) complex: this dissociation regulates P2X (7) pore formation. *American Journal of Physiology. Cell Physiology* **297**:C430–C439. DOI: https://doi.org/10.1152/ajpcell.00079.2009, PMID: 19494237

Hattori M, Gouaux E. 2012. Molecular mechanism of ATP binding and ion channel activation in P2X receptors. *Nature* **485**:207–212. DOI: https://doi.org/10.1038/nature11010, PMID: 22535247

Janks L, Sprague RS, Egan TM. 2019. Atp-gated P2X7 receptors require chloride channels to promote inflammation in human macrophages. *Journal of Immunology* **202**:883–898. DOI: https://doi.org/10.4049/jimmunol.1801101, PMID: 30598517

Kalstrup T, Blunck R. 2013. Dynamics of internal pore opening in K (V) channels probed by a fluorescent unnatural amino acid. *PNAS* **110**:8272–8277. DOI: https://doi.org/10.1073/pnas.1220398110, PMID: 23630265

Kalstrup T, Blunck R. 2017. Voltage-clamp fluorometry in xxenopus oocytes using fluorescent unnatural amino acids. *Journal of Visualized Experiments* **27**:e55598. DOI: https://doi.org/10.3791/55598, PMID: 28605379

Kalstrup T, Blunck R. 2018. S4-S5 linker movement during activation and inactivation in voltage-gated K+ channels. *PNAS* **115**:E6751–E6759. DOI: https://doi.org/10.1073/pnas.1719105115, PMID: 29959207

Karasawa A, Michalski K, Mikhelzon P, Kawate T. 2017. The P2X7 receptor forms a dye-permeable pore independent of its intracellular domain but dependent on membrane lipid composition. *eLife* **6**:e31186. DOI: https://doi.org/10.7554/eLife.31186, PMID: 28920575

Kawate T, Michel JC, Birdsong WT, Gouaux E. 2009. Crystal structure of the ATP-gated P2X (4) ion channel in the closed state. *Nature* **460**:592–598. DOI: https://doi.org/10.1038/nature08198, PMID: 19641588

Khoo KK, Galleano I, Gasparri F, Wieneke R, Harms H, Poulsen MH, Chua HC, Wulf M, Tampé R, Pless SA. 2020. Chemical modification of proteins by insertion of synthetic peptides using tandem protein trans-splicing. *Nature Communications* **11**:2284. DOI: https://doi.org/10.1038/s41467-020-16208-6, PMID: 32385250

Kim M, Jiang LH, Wilson HL, North RA, Surprenant A. 2001. Proteomic and functional evidence for a P2X7 receptor signalling complex. *The EMBO Journal* **20**:6347–6358. DOI: https://doi.org/10.1093/emboj/20.22.6347, PMID: 11707406

Klapperstück M, Büttner C, Schmalzing G, Markwardt F. 2001. Functional evidence of distinct ATP activation sites at the human P2X (7) receptor. *The Journal of Physiology* **534**:25–35. DOI: https://doi.org/10.1111/j.1469-7793.2001.00025.x, PMID: 11432989

Klippenstein V, Mony L, Paoletti P. 2018. Probing ion channel structure and function using light-sensitive amino acids. *Trends in Biochemical Sciences* **43**:436–451. DOI: https://doi.org/10.1016/j.tibs.2018.02.012, PMID: 29650383

Kopp R, Krautloher A, Ramírez-Fernández A, Nicke A. 2019. P2X7 interactions and signaling-making head or tail of it. *Frontiers in Molecular Neuroscience* **12**:183. DOI: https://doi.org/10.3389/fnmol.2019.00183, PMID: 31440138

Kozak M. 1987. An analysis of 5'-noncoding sequences from 699 vertebrate messenger rnas. *Nucleic Acids Research* **15**:8125–8148. DOI: https://doi.org/10.1093/nar/15.20.8125, PMID: 3313277

Lee HS, Guo J, Lemke EA, Dimla RD, Schultz PG. 2009. Genetic incorporation of a small, environmentally sensitive, fluorescent probe into proteins in *Saccharomyces cerevisiae*. *Journal of the American Chemical Society* **131**:12921–12923. DOI: https://doi.org/10.1021/ja904896s, PMID: 19702307

Leisle L, Valiyaveetil F, Mehl RA, Ahern CA. 2015. Incorporation of non-canonical amino acids. *Advances in Experimental Medicine and Biology* **869**:119–151. DOI: https://doi.org/10.1007/978-1-4939-2845-3_7, PMID: 26381943

Lörinczi É, Bhargava Y, Marino SF, Taly A, Kaczmarek-Hájek K, Barrantes-Freer A, Dutertre S, Grutter T, Rettinger J, Nicke A. 2012. Involvement of the cysteine-rich head domain in activation and desensitization of the P2X1 receptor. *PNAS* **109**:11396–11401. DOI: https://doi.org/10.1073/pnas.1118759109, PMID: 22745172

Mansoor SE, Lü W, Oosterheert W, Shekhar M, Tajkhorshid E, Gouaux E. 2016. X-ray structures define human P2X (3) receptor gating cycle and antagonist action. *Nature* **538**:66–71. DOI: https://doi.org/10.1038/nature19367, PMID: 27626375

McCarthy AE, Yoshioka C, Mansoor SE. 2019. Full-length P2X7 structures reveal how palmitoylation prevents channel desensitization. *Cell* **179**:659–670. DOI: https://doi.org/10.1016/j.cell.2019.09.017, PMID: 31587896

Mitchell AL, Addy PS, Chin MA, Chatterjee A. 2017. A unique genetically encoded FRET pair in mammalian cells. *Chembiochem* **18**:511–514. DOI: https://doi.org/10.1002/cbic.201600668, PMID: 28093840

Murrell-Lagnado RD. 2017. Regulation of P2X purinergic receptor signaling by cholesterol. *Current Topics in Membranes* **80**:211–232. DOI: https://doi.org/10.1016/bs.ctm.2017.05.004, PMID: 28863817

Ousingsawat J, Wanitchakool P, Kmit A, Romao AM, Jantarajit W, Schreiber R, Kunzelmann K. 2015. Anoctamin 6 mediates effects essential for innate immunity downstream of P2X7 receptors in macrophages. *Nature Communications* **6**:6245. DOI: https://doi.org/10.1038/ncomms7245, PMID: 25651887

Park SH, Ko W, Lee HS, Shin I. 2019. Analysis of protein-protein interaction in a single live cell by using a FRET system based on genetic code expansion technology. *Journal of the American Chemical Society* **141**:4273–4281. DOI: https://doi.org/10.1021/jacs.8b10098, PMID: 30707019

Pelegrin P, Surprenant A. 2006. Pannexin-1 mediates large pore formation and interleukin-1beta release by the ATP-gated P2X7 receptor. *The EMBO Journal* **25**:5071–5082. DOI: https://doi.org/10.1038/sj.emboj.7601378, PMID: 17036048

Pippel A, Stolz M, Woltersdorf R, Kless A, Schmalzing G, Markwardt F. 2017. Localization of the gate and selectivity filter of the full-length P2X7 receptor. *PNAS* **114**:E2156–E2165. DOI: https://doi.org/10.1073/pnas.1610414114, PMID: 28235784

Pless SA, Kim RY, Ahern CA, Kurata HT. 2015. Atom-by-atom engineering of voltage-gated ion channels: magnified insights into function and pharmacology. *The Journal of Physiology* **593**:2627–2634. DOI: https://doi.org/10.1113/jphysiol.2014.287714, PMID: 25640301

Poulsen MH, Poshtiban A, Klippenstein V, Ghisi V, Plested AJR. 2019. Gating modules of the AMPA receptor pore domain revealed by unnatural amino acid mutagenesis. *PNAS* **116**:13358–13367. DOI: https://doi.org/10.1073/pnas.1818845116, PMID: 31213549

Riedel T, Schmalzing G, Markwardt F. 2007. Influence of extracellular monovalent cations on pore and gating properties of P2X7 receptor-operated single-channel currents. *Biophysical Journal* **93**:846–858. DOI: https://doi.org/10.1529/biophysj.106.103614, PMID: 17483156

Robinson LE, Shridar M, Smith P, Murrell-Lagnado RD. 2014. Plasma membrane cholesterol as a regulator of human and rodent P2X7 receptor activation and sensitization. *The Journal of Biological Chemistry* **289**:31983–31994. DOI: https://doi.org/10.1074/jbc.M114.574699, PMID: 25281740

Roger S, Pelegrin P, Surprenant A. 2008. Facilitation of P2X7 receptor currents and membrane blebbing via constitutive and dynamic calmodulin binding. *The Journal of Neuroscience* **28**:6393–6401. DOI: https://doi.org/10.1523/JNEUROSCI.0696-08.2008, PMID: 18562610

Roger S, Gillet L, Baroja-Mazo A, Surprenant A, Pelegrin P. 2010. C-terminal calmodulin-binding motif differentially controls human and rat P2X7 receptor current facilitation. *The Journal of Biological Chemistry* **285**:17514–17524. DOI: https://doi.org/10.1074/jbc.M109.053082, PMID: 20378545

Sarkar D, Harms H, Galleano I, Sheikh ZP, Pless SA. 2021. Ion channel engineering using protein trans-splicing. *Methods in Enzymology* **654**:19–48. DOI: https://doi.org/10.1016/bs.mie.2021.01.028, PMID: 34120713

Schindelin J, Arganda-Carreras I, Frise E, Kaynig V, Longair M, Pietzsch T, Preibisch S, Rueden C, Saalfeld S, Schmid B, Tinevez JY, White DJ, Hartenstein V, Eliceiri K, Tomancak P, Cardona A. 2012. Fiji: an open-source platform for biological-image analysis. *Nature Methods* **9**:676–682. DOI: https://doi.org/10.1038/nmeth.2019, PMID: 22743772

Schmied WH, Elsässer SJ, Uttamapinant C, Chin JW. 2014. Efficient multisite unnatural amino acid incorporation in mammalian cells via optimized pyrrolysyl trna synthetase/trna expression and engineered erf1. *Journal of the American Chemical Society* **136**:15577–15583. DOI: https://doi.org/10.1021/ja5069728, PMID: 25350841

Shaner NC, Lambert GG, Chammas A, Ni Y, Cranfill PJ, Baird MA, Sell BR, Allen JR, Day RN, Israelsson M, Davidson MW, Wang J. 2013. A bright monomeric green fluorescent protein derived from branchiostoma lanceolatum. *Nature Methods* **10**:407–409. DOI: https://doi.org/10.1038/nmeth.2413, PMID: 23524392

Soh MS, Estrada-Mondragon A, Durisic N, Keramidas A, Lynch JW. 2017. Probing the structural mechanism of partial agonism in glycine receptors using the fluorescent artificial amino acid, ANAP. *ACS Chemical Biology* **12**:805–813. DOI: https://doi.org/10.1021/acschembio.6b00926, PMID: 28121133

Studier FW. 2005. Protein production by auto-induction in high density shaking cultures. *Protein Expression and Purification* **41**:207–234. DOI: https://doi.org/10.1016/j.pep.2005.01.016, PMID: 15915565

Tanguay RL, Gallie DR. 1996. Translational efficiency is regulated by the length of the 3′ untranslated region. *Molecular and Cellular Biology* **16**:146–156. DOI: https://doi.org/10.1128/MCB.16.1.146, PMID: 8524291

Weber G, Farris FJ. 1979. Synthesis and spectral properties of a hydrophobic fluorescent probe: 6-propionyl-2-(dimethylamino)naphthalene. *Biochemistry* **18**:3075–3078. DOI: https://doi.org/10.1021/bi00581a025, PMID: 465454

Wu J, Liu L, Matsuda T, Zhao Y, Rebane A, Drobizhev M, Chang YF, Araki S, Arai Y, March K, Hughes TE, Sagou K, Miyata T, Nagai T, Li WH, Campbell RE. 2013. ± indicators and photophysical considerations for optogenetic applications. *ACS Chemical Neuroscience* **4**:963–972. DOI: https://doi.org/10.1021/cn400012b, PMID: 23452507

Wulf M, Pless SA. 2018. High-sensitivity fluorometry to resolve ion channel conformational dynamics. *Cell Reports* **22**:1615–1626. DOI: https://doi.org/10.1016/j.celrep.2018.01.029, PMID: 29425514

Yang TT, Cheng L, Kain SR. 1996. Optimized codon usage and chromophore mutations provide enhanced sensitivity with the green fluorescent protein. *Nucleic Acids Research* **24**:4592–4593. DOI: https://doi.org/10.1093/nar/24.22.4592, PMID: 8948654

Ye S, Riou M, Carvalho S, Paoletti P. 2013. Expanding the genetic code in *Xenopus laevis* oocytes. *Chembiochem* **14**:230–235. DOI: https://doi.org/10.1002/cbic.201200515, PMID: 23292655

Zagotta WN, Sim BS, Nhim AK, Raza MM, Evans EGB, Venkatesh Y, Jones CM, Mehl RA, Petersson EJ, Gordon SE. 2021. An improved fluorescent noncanonical amino acid for measuring conformational distributions using time-resolved transition metal ion FRET. *eLife* **10**:e70236. DOI: https://doi.org/10.7554/eLife.70236, PMID: 34623258

Appendix 1

Appendix 1—key resources table

Reagent type (species) or resource	Designation	Source or reference	Identifiers	Additional information
Recombinant DNA reagent	cDNA *Xenopus laevis* eRF1(E55D)	NCBI Reference Sequence: NM_001090894.1, Life Technologies / Thermo Fisher Scientific		GeneArt String DNA fragment (cloned into pET28a and pNKS2)
Recombinant DNA reagent	cDNA *Rattus norvegicus* P2X7			in modified pUC19 (pUC19o)
Recombinant DNA reagent	cDNA *Rattus norvegicus* P2X1	***Lörinczi et al., 2012***		in pNKS2
Recombinant DNA reagent	cDNA *Rattus norvegicus* calmodulin-1	UniProt: PDP29; NCBI Reference Sequence: NM_031969.3		Codon-optimized for *Xenopus laevis* (Invitrogen / Thermo Fisher Scientific), C-terminally linked to *Rattus norvegicus* P2X7 via GS-linker (ggatct)
Recombinant DNA reagent	Plasmid: pNKS2	***Gloor et al., 1995***		
Recombinant DNA reagent	Plasmid: pUC19	New England Biolabs GmbH	CAT# N3041S	
Recombinant DNA reagent	Plasmid: pANAP	***Chatterjee et al., 2013***	CAT#48696	
Recombinant DNA reagent	EGFP	***Yang et al., 1996***		the original enhanced GFP, mammalian codon-optimized, C-terminally linked to *Rattus norvegicus* P2X1 via GSAGSA-linker sequence (ggatctgcaggatctgca)
Recombinant DNA reagent	R-GECO1.2	***Wu et al., 2013***	Addgene #45494	
Recombinant DNA reagent	mNeonGreen	***Shaner et al., 2013***		Codon-optimized for *Xenopus laevis* (Invitrogen / Thermo Fisher Scientific)
Recombinant DNA reagent	M13-like peptide from CaM-dependent kinase	*Rattus norvegicus* myosin light chain kinase, smooth muscle; Uniprot: D3ZFU9		RRKWQKTGNAVRAIGRLSSM; cloned between *Rattus norvegicus* calmodulin-1 and mNeonGreen with N- and C-terminal GS-linkers (ggcagc and ggatct, respectively)
Sequence-based reagent	Oligonucleotides	metabion GmbH		
Sequence-based reagent	*Amber* suppressor tRNA, synthesized oligonucleotide, sequence derived from pANAP, an universal 3'-terminal CCA-sequence was added: 5'-gcc cgg aug gug gaa ucg gua gac aca agg gau ucu aaa ucc cuc ggc guu cgc gcu gug cgg guu caa guc ccg cuc cgg gua cca –3'	biomers.net GmbH; ***Chatterjee et al., 2013***; ***Durner and Nicke, 2022***		
Sequence-based reagent	Sanger sequencing	Eurofins Genomics, https://eurofinsgenomics.eu/		
Sequence-based reagent	5'-UTR, GeneArt String DNA fragment (cloned into pUC19 (small letters) before the start codon (italic letters)), gtacccggggatcctctTAATACGACTCACTATAGGCTTGTCTTTTTTGCAGA AGCTCAGAATAAACGCTCAACTTTGGCTCGAG GCCACCatg	Life Technologies / Thermo Fisher Scientific, ***Kozak, 1987***		
Sequence-based reagent	3'-UTR, (cloned into pUC19 (small letters) after the stop codon (italic letters)), *tga*CCCAAAACAAAAACGGAATATG CAAACAAAAAAAAAAAAAAAAAAAAAAAAA AAAAAAAAAAAAAAAAAAAAAAAAAAAAAA GAATTCTAGAGCGGCCGCagagtcgacctgcagg	pNKS2, ***Gloor et al., 1995***		

Appendix 1 Continued on next page

Appendix 1 Continued

Reagent type (species) or resource	Designation	Source or reference	Identifiers	Additional information
Peptide, recombinant protein	EcoRI-HF	New England Biolabs GmbH	CAT#R3101S	
Peptide, recombinant protein	NotI-HF	New England Biolabs GmbH	CAT#R3189S	
Commercial assay or kit	Gibson Assembly Master Mix	New England Biolabs GmbH	CAT#E2611L	
Commercial assay or kit	Q5 Site-Directed Mutagenesis Kit	New England Biolabs GmbH	CAT#E0552S	
Commercial assay or kit	MinElute Reaction Cleanup Kit	QIAGEN GmbH	CAT#28204	
Commercial assay or kit				
Commercial assay or kit	Macherey-Nagel NucleoSpin Gel and PCR Clean-up Kit	Fisher Scientific / Thermo Fisher Scientific	CAT# 11992242	
Commercial assay or kit	mMESSAGE mMACHINE T7 Transcription Kit	Invitrogen / Thermo Fisher Scientific	CAT# AM1344	
Commercial assay or kit	mMESSAGE mMACHINE SP6 Transkription Kit	Invitrogen / Thermo Fisher Scientific	CAT#AM1340	
Chemical compound, drug	ATP disodium salt hydrate	Sigma-Aldrich	Cat#A3377	
Chemical compound, drug	L-ANAP trifluoroacetic salt	AsisChem Inc.	Cat#ASIS-0014	
Chemical compound, drug	L-ANAP methyl ester	AsisChem Inc.	Cat#ASIS-0146	
Chemical compound, drug	Collagenase NB 4 G proved grade	Nordmark Pharma GmbH	Cat#S1746502	
Chemical compound, drug	Gentamicin sulfate	Roth	CAT#0233.4	
Chemical compound, drug	Cy5 Mono NHS Ester	Merck / Sigma-Aldrich	CAT#GEPA15101	
Chemical compound, drug	Pefabloc SC	Merck / Sigma Aldrich	CAT#76307	
Chemical compound, drug	n-Dodecyl-β-D-Maltoside, ULTROL grade	Merck / Sigma Aldrich	CAT#324355	
Chemical compound, drug	Ni-NTA Agarose	QIAGEN GmbH	CAT#1018244	
Chemical compound, drug	Flufenamic acid	Merck / Sigma Aldrich	CAT#F9005	
Chemical compound, drug	0.5 M EDTA ph 8.0	Thermo Scientific	CAT#R1021	
Chemical compound, drug	TMRM	Biomol	CAT#ABD-419	
Chemical compound, drug	A 438079 hydrochloride	TOCRIS	CAT#2972	

Appendix 1 Continued on next page

Appendix 1 Continued

Reagent type (species) or resource	Designation	Source or reference	Identifiers	Additional information
Software, algorithm	CellWorks E 5.5.1	npi electronic, http://cellworks.de/		
Software, algorithm	PyMOL	http://www.pymol.org/	RRID:SCR_000305	
Software, algorithm	Python Programming Language 3.10.4	http://www.python.org/	RRID:SCR_008394	
Software, algorithm	NumPy 1.22.3	http://www.numpy.org	RRID:SCR_008633	
Software, algorithm	MatPlotLib 3.5.1	http://matplotlib.sourceforge.net	RRID:SCR_008624	
Software, algorithm	SciPy 1.8.0	http://www.scipy.org/	RRID:SCR_008058	
Software, algorithm	GraphPad Prism 9.3.0 and 9.5.0	http://www.graphpad.com/	RRID:SCR_002798	
Software, algorithm	(Fiji Is Just) ImageJ 2.3.0	***Schindelin et al., 2012***, http://fiji.sc	RRID:SCR_002285	
Other	Turbo Tec-05X Amplifier	npi electronic GmbH	CAT#TEC-05X	VCF-Setup components, electronics
Other	PCI-6221, DAQ, Multifunction I/O Device, 16-Bit	National Instruments	CAT# 779066–01	VCF-Setup components, electronics
Other	Single-channel fully programmable Instrumentation Amplifier Low Pass Filter, USBPGF-S1/L with 8th pole Bessel filter characteristics	Alligator Technologies	CAT#USBPGF-S1/L	VCF-Setup components, electronics
Other	2 x MPPC modules	Hamamatsu Photonics K.K.	CAT#C13366-3050GA	VCF-Setup components, electronics
Other	Power adapter/linear regulator	KNIEL System-Electronic GmbH	Custom-made	VCF-Setup components, electronics
Other	Axiovert 200 inverted fluorescence microscope	Carl Zeiss Microscopy LLC		VCF-Setup components, optics
Other	Objektiv W N-Achroplan 63 x/0,9 M27	Carl Zeiss Microscopy LLC	CAT#420987-9900-000	VCF-Setup components, optics
Other	M565L3, mounted LED at 565 nm	Thorlabs GmbH	CAT#M565L3	VCF-Setup components, optics
Other	M365LP1, Mid Power Mounted LED at 365 nm	Thorlabs GmbH	CAT#M365LP1	VCF-Setup components, optics
Other	2× lenses for LED collimation	Thorlabs GmbH	CAT#ACL2520U-A	VCF-Setup components, optics
Other	ET555/20×, 25 mm Dia Mounted, Single Bandpass Filter (for excitation)	Chroma Technology GmbH	CAT# IN026697	VCF-Setup components, optics
Other	ET365/20×, 25 mm Dia Mounted, Single Bandpass Filter (for excitation)	Chroma Technology GmbH	CAT# IN053211	VCF-Setup components, optics
Other	T387lp, 25.5×36×1 mm, Longpass Dichroic Beamsplitter	Chroma Technology GmbH	CAT# IN040921	VCF-Setup components, optics
Other	79003bs, Multi Dichroic Beamsplitter	Chroma Technology GmbH	CAT# CS294227	VCF-Setup components, optics
Other	59002bs, Multi Dichroic Beamsplitter	Chroma Technology GmbH	CAT# IN040206	VCF-Setup components, optics
Other	T425lpxr,25.5×36×1 mm, Longpass Dichroic Beamsplitter	Chroma Technology GmbH	CAT# IN025246	VCF-Setup components, optics
Other	Relay lense	Thorlabs GmbH	CAT#AC254-060-A	VCF-Setup components, optics
Other	DMLP550R, Longpass Dichroic Beamsplitter	Thorlabs GmbH	CAT#DMLP550R	VCF-Setup components, optics
Other	T470lpxr, Longpass Dichroic Beamsplitter	Chroma Technology GmbH	CAT# IN030502	VCF-Setup components, optics

Appendix 1 Continued on next page

Appendix 1 Continued

Reagent type (species) or resource	Designation	Source or reference	Identifiers	Additional information
Other	T495lpxr, 25.5×36×1 mm, Longpass Dichroic Beamsplitter	Chroma Technology GmbH	CAT# IN005752	VCF-Setup components, optics
Other	ET490/40×, 25 mm Dia Mounted (for emission)	Chroma Technology GmbH	CAT# IN039532	VCF-Setup components, optics
Other	ET610/75 m, 25 mm Dia Mounted (for emission)	Chroma Technology GmbH	CAT# IN036520	VCF-Setup components, optics
Other	ET455/50 m (for emission)	Chroma Technology GmbH	CAT# IN067607	VCF-Setup components, optics
Other	ET500lp, 25 mm Dia Mounted (for emission)	Chroma Technology GmbH	CAT# IN006640	VCF-Setup components, optics
Other	MF460-60 (for emission)	Thorlabs GmbH	CAT#MF460-60	VCF-Setup components, optics
Other	2× lenses for focusing on MPPC	Thorlabs GmbH	CAT#LB1761-A	VCF-Setup components, optics

Supporting Information – Figure Supplements

Improved ANAP incorporation and VCF analysis reveal details of P2X7 current facilitation and a limited conformational interplay between ATP binding and the intracellular ballast domain

Anna Durner, Ellis Durner, Annette Nicke

published in

eLife 2023, 12:e82479

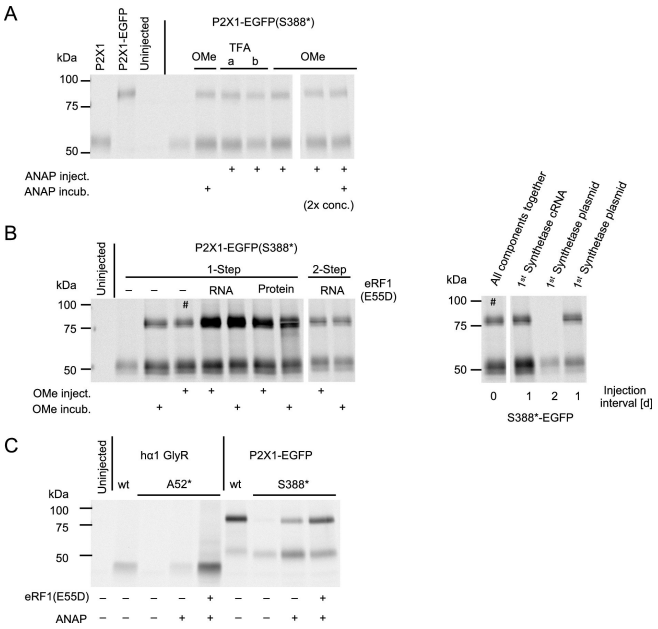

Figure 1 – figure supplement 1 **Variation of experimental conditions to optimize L-3-(6-acetylnaphthalen-2-ylamino)–2-aminopropanoic acid (ANAP) incorporation into oocyte-expressed ion channels.**
(A) Comparison of ANAP-trifluoroacetic salt (TFA, a and b indicate two different batches) and membrane-permeable ANAP methyl ester (OMe) and application forms (injection and/or incubation in 2 mM solution). In the last two lanes, a twofold higher concentration (500 mM) was used for injection. Lanes shown in the same figure are from the same gel but rearranged for clarity. **(B)** Left: Comparison of ANAP-OMe application forms (injection and incubation as above) and effect of co-injected *X. laevis* eRF1(E55D) (as purified protein or as cRNA, as indicated) for the 1-step and the 2-step injection method. Right: Effect of different injection intervals. tRNA synthetase was expressed first, either from the pANAP plasmid (injected into the nucleus) or from the *in vitro* synthesized cRNA (injected into the cytoplasm) as indicated. All other components were then injected into the cytoplasm after the shown intervals. Note that the gel was rearranged for clearer presentation and that lanes marked with a hashtag are shown twice. **(C)** The optimized 1-step injection protocol with and without co-injection of eRF1(E55D) applied to hα1 GlyR(A52*) and P2X1(S388*)-EGFP.

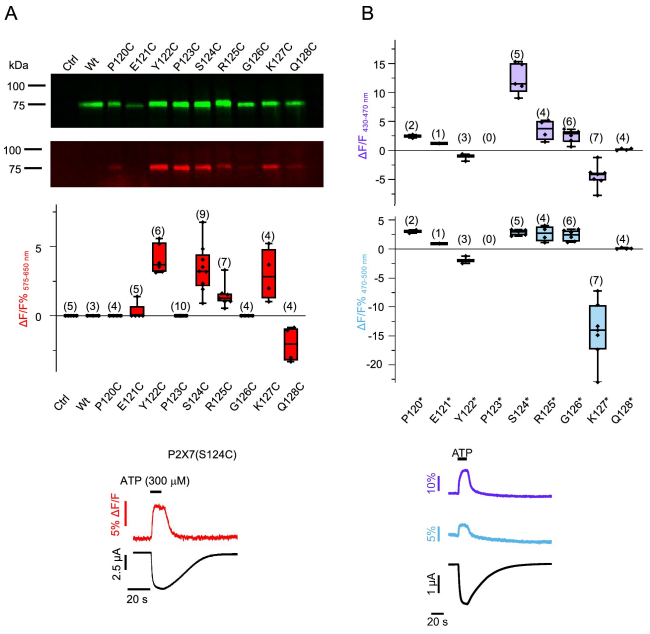

Figure 2 – figure supplement 1 **Comparative analysis of tetramethylrhodamine-maleimide (TMRM)-labeled and L-3-(6-acetylnaphthalen-2-ylamino)–2-aminopropanoic acid (ANAP)-labeled P2X7 head domain mutants.**
(A) To estimate plasma membrane expression (upper gel) and accessibility of introduced cysteine residues (lower gel), intact oocytes expressing the indicated cysteine-substituted P2X7R mutants were either labeled with the membrane-impermeant amino-reactive Cy5-NHS ester or with TMRM. Purified His-tagged protein was visualized by fluorescence scanning. Below: Box plot summarizing results from TMRM-labeled oocytes expressing indicated P2X7R mutants with $\Delta F/F\%$ representing the maximum fluorescence signal during a 15-s ATP application (300 μM). Numbers of recordings are given in brackets and a representative voltage clamp fluorometry (VCF)-recording (-60 mV) of a TMRM-labeled oocyte expressing P2X7(S124C) is shown. **(B)** Summary of fluorescence (violet and blue) changes of oocytes expressing P2X7Rs containing ANAP in the indicated positions within the head domain and a representative VCF-recording (at –30 mV) from an oocyte expressing P2X7 with ANAP in position 124 (P2X7(S124*)). Note that in case of mutants P120*, E121*, and P123* less than three recordings fulfilled the inclusion criteria described in Material and methods. Original recordings have also been deposited with Dryad and summarized and assigned in Table 1—source data 1.

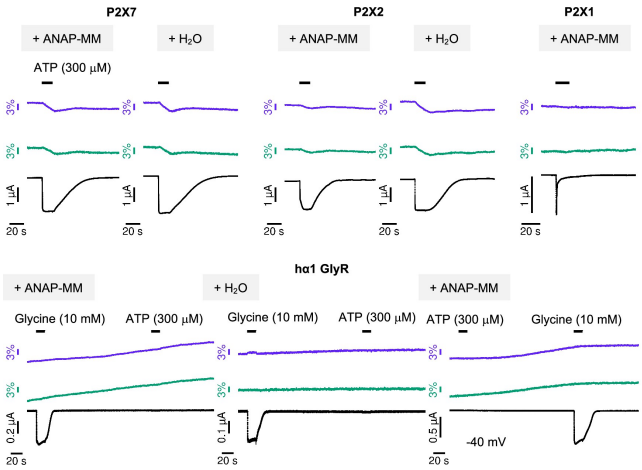

Figure 3 – figure supplement 1 **Control voltage clamp fluorometry (VCF) recordings from oocytes expressing different non-mutated ion channels.** Representative VCF-recordings of oocytes injected with cRNA encoding the indicated receptors plus either water (negative control) or L-3-(6-acetylnaphthalen-2-ylamino)–2-aminopropanoic acid (ANAP)-Master Mix (ANAP-MM, containing ANAP, tRNA, cRNA ecoding tRNA-syntethase, and cRNA encoding eRF1(E55D)). The holding potential was –30 mV, if not otherwise indicated.

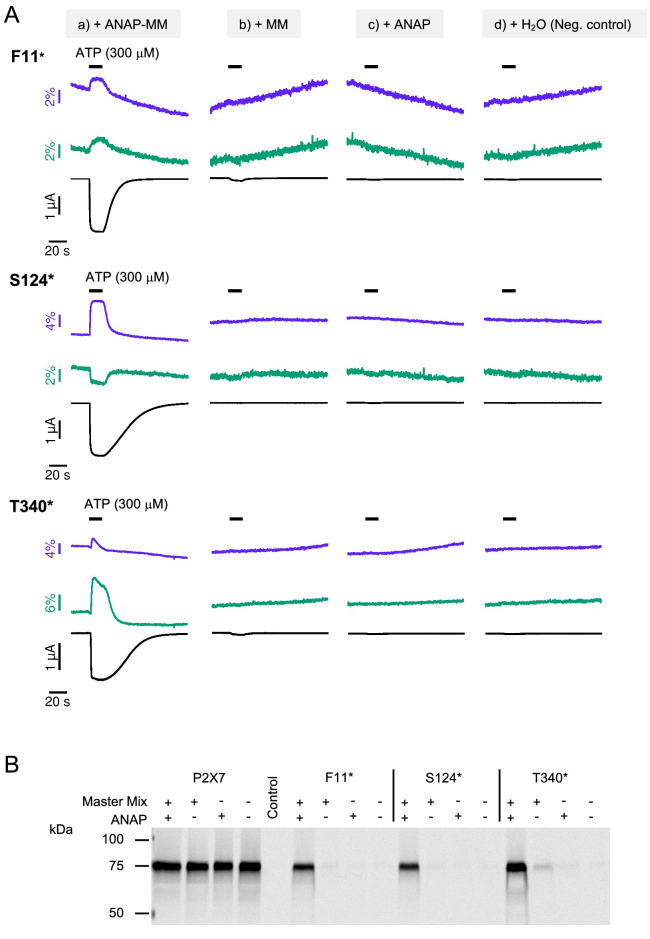

Figure 3 – figure supplement 2

Figure 3 – figure supplement 2 **Control experiments to test the specificity of tRNA-loading and L-3-(6-acetylnaphthalen-2-ylamino)–2-aminopropanoic acid (ANAP) incorporation into P2X7.**
(A,B) Representative voltage clamp fluorometry (VCF) recordings **(A)** and analysis of membrane expression **(B)** from oocytes that were injected with cRNA encoding non-mutated P2X7 or P2X7 containing an *amber* stop codon at the indicated positions together with (a) both, ANAP and a master mix containing tRNA-synthetase cRNA, tRNA, and eRF1(E55D) cRNA (positive control), (b) with the master mix only, (c) with ANAP only, or (d) with water as a negative control. ANAP emission was recorded at two different wavelengths (purple: 430–490 nm, green: >500 nm). VCF recordings showed clear ATP-evoked signals only for the oocytes injected with all essential components necessary for ANAP-incorporation and were in agreement with surface-expression analysis experiments. Although faint surface expression of full-length receptors was seen in the absence of ANAP (indicating limited read through), ATP-evoked fluorescence and current responses were negligible (no fluorescence change and current responses less than 10% of those from positive controls).

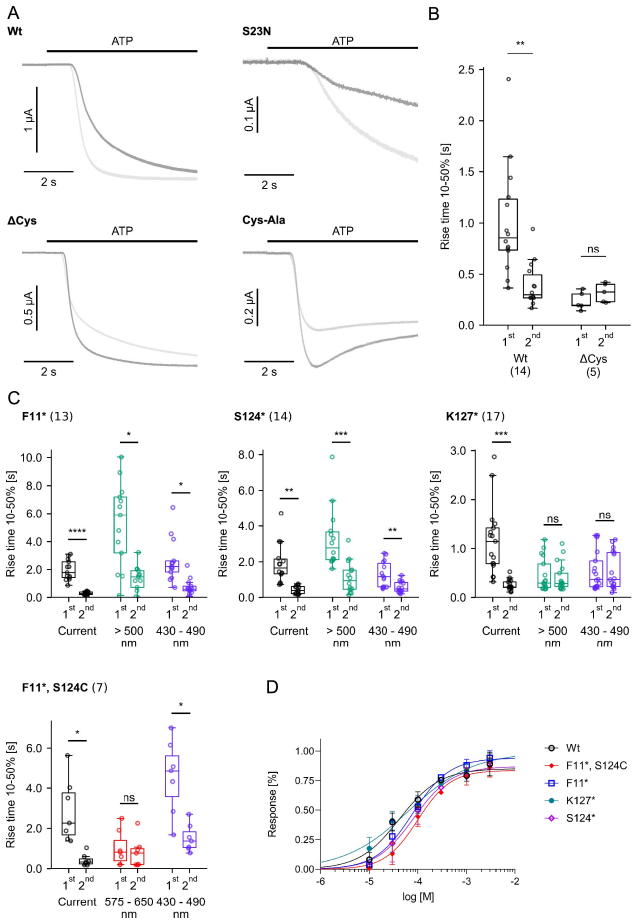

Figure 3 – figure supplement 3

Figure 3 – figure supplement 3 **Deletion of the cysteine-rich region eliminates current facilitation, and F11* and S124* mutants track current facilitation.** **(A)** Overlay of representative current traces upon first (black) and second (gray) ATP applications (0.3 mM in 195 s interval) for wt P2X7, and the indicated mutations that were expected to prevent facilitation. Baseline currents (15 s before ATP application) were adjusted for clarity. **(B)** Box plot summarizing 10–50% rise times of the first and second current responses to ATP for wt and ΔCys P2X7. Note that the low expression of the S23N and Cys-Ala mutants prevented further analysis. **(C)** Box plots summarizing 10–50% rise times of the first and second current (black) and fluorescence (colored) responses at the indicated emission wavelengths for F11*, S124*, K127*, and the tetramethyl-rhodamine-maleimide-labeled double mutant (F11*, S124C). Significance was determined using the two-tailed paired Student's t-test (*, $p<0.05$; **, $p<0.005$; ***, $p<0.0005$; ****, $p<0.00005$; ns, not significant). **(D)** Normalized dose-response curves for ATP at wt P2X7 and the indicated L-3-(6-acetylnaphthalen-2-ylamino)–2-aminopropanoic acid-containing receptors. Lines represent nonlinear curve fits of the Hill equation to the data. For EC_{50} values see Table 2. Error bars represent S.D. of 3–11 experiments. All recordings were performed in divalent-free buffer, and oocytes were clamped at –30 mV. Original recordings have also been deposited with Dryad and summarized and assigned in Table 1—source data 1.

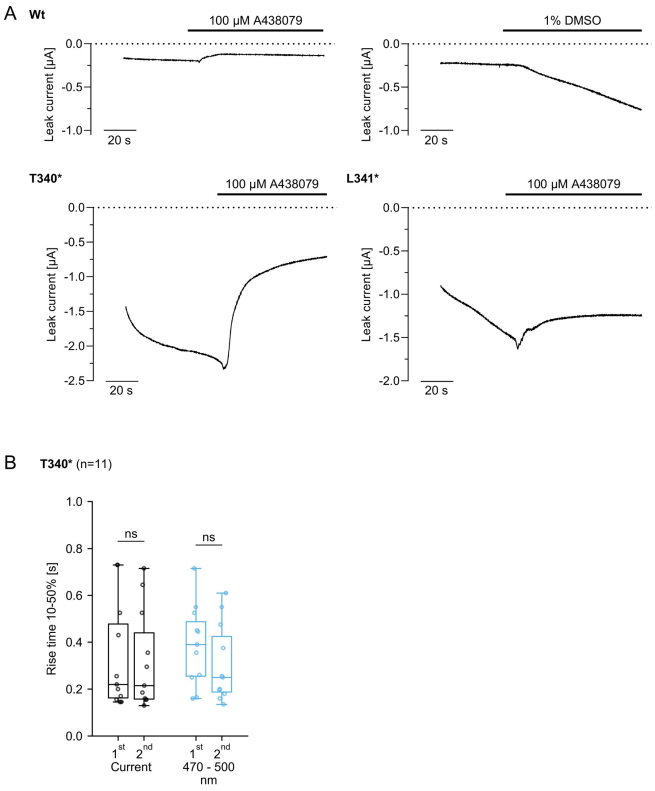

Figure 4 – figure supplement 1 **L-3-(6-acetylnaphthalen-2-ylamino)–2-aminopropanoic acid (ANAP) in TM2 causes leakiness and affects current facilitation.**
(A) Representative current traces showing the effect of the P2X7 antagonist A438079 (100 μM) on baseline currents of mutants containing ANAP within TM2 (T340*, L341*) and on wt P2X7. A438079 was diluted from a 10 mM stock in Dimethyl sulfoxide (DMSO) using divalent-free buffer and applied into the static bath. Control experiments were conducted with 1% DMSO. Oocytes were clamped at –30 mV. **(B)** Box plot showing 10–50% rise times (in seconds) of the first and second current (black) and fluorescence (blue) responses to 0.3 mM ATP (interval 195 s) for P2X7(T340*). Significance was determined using the two-tailed paired Student's t-test (*, $p<0.05$; ns, not significant). Original recordings have also been deposited with Dryad and summarized and assigned in Table 1—source data 1.

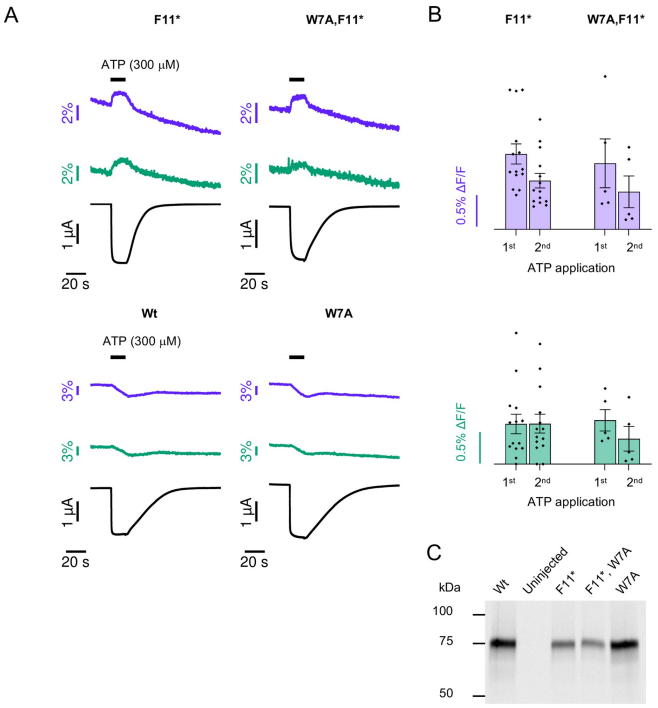

Figure 5 – figure supplement 1 **The fluorescence change in P2X7(F11*) is not caused by a dequenching effect of the nearby Trp residue.**
(A, B) Comparison of voltage clamp fluorometry recordings from oocytes expressing P2X7(F11*) with or without Trp in position 7 (W7A, F11*). Oocytes expressing either non-mutated P2X7R or P2X7(W7A) served as controls. Recordings from P2X7(F11*) and P2X7 (W7A, F11*) are not significantly different, indicating that L-3-(6-acetylnaphthalen-2-ylamino)–2-aminopropanoic acid in position 11 is not quenched by Trp7. Data are represented as mean ± S.E.M. **(C)** Surface expression of P2X7(F11*), P2X7(F11*, W7A), and P2X7(W7A), with unmutated P2X7 and uninjected oocytes as positive and negative controls, respectively.

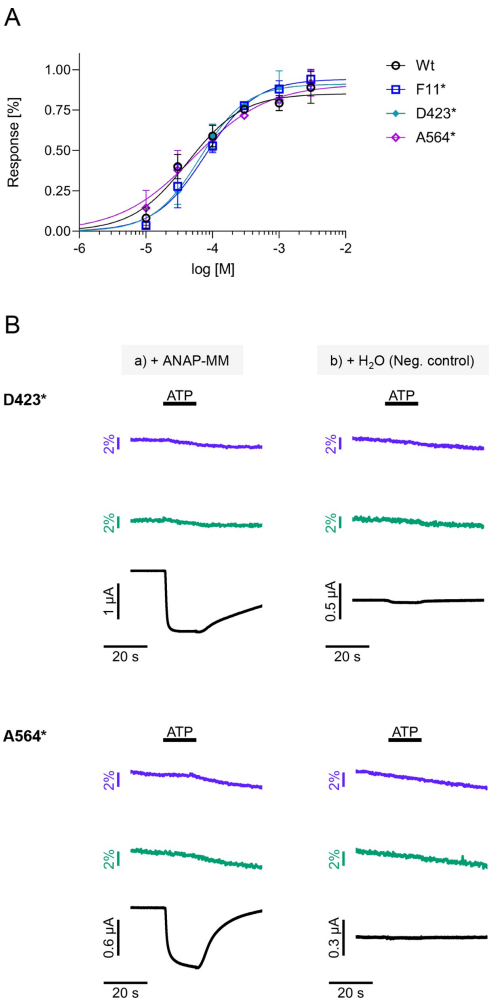

Figure 5 – figure supplement 2

Figure 5 – figure supplement 2 **Dose-response analysis for intracellular P2X7 mutants F11*, D423*, and A564* and contribution of D423 and A564 deletion mutants to current responses.**
(A) Normalized dose-response curves for ATP at wt P2X7 and the indicated L-3-(6-acetylnaphthalen-2-ylamino)–2-aminopropanoic acid (ANAP)-containing receptors. For EC_{50} values see Table 2. Error bars represent S.D. of three to eight experiments. **(B)** Representative voltage clamp fluorometry (VCF) recordings from oocytes that were injected with cRNA encoding P2X7 containing an *amber* stop codon at D423 or A564 with either ANAP and a master mix containing tRNA-synthetase cRNA, tRNA, and eRF1(E55D) cRNA, or with water to produce P2X7 protein truncated at these positions. ANAP emission was recorded at two different wavelengths (purple: 430–490 nm, green: >500 nm). VCF recordings showed clear ATP-evoked signals only for the oocytes injected with all essential components necessary for ANAP incorporation. Current responses of truncated P2X7Rs were less than 5% of those from positive controls. All recordings were performed in divalent-free buffer, and oocytes were clamped at –30 mV.

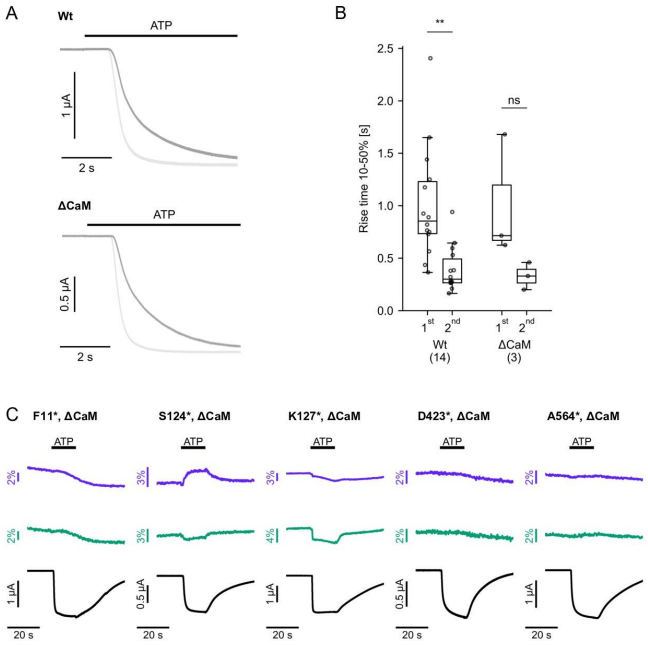

Figure 5 – figure supplement 3 **Elimination of a CaM-binding motif has no apparent effect on current kinetics or fluorescence responses.**
(A) ΔCaM-P2X7 contained the single point mutations I541T, S552C, and V559G (Roger et al., 2010). Overlay of representative current traces during first (dark gray) and second (light gray) ATP applications (0.3 mM, applied in 195 s interval). Baseline currents (15 s before ATP application) were adjusted for clarity. **(B)** Box plot showing 10–50% rise times (in seconds) of the first and second current responses for wt P2X7 and ΔCaM P2X7. Significance was determined using the two-tailed paired Student's t-test (**, $p<0.005$; ns, not significant). All recordings were performed in divalent-free buffer, and oocytes were clamped at –30 mV. **(B)** Representative voltage clamp fluorometry (VCF) recordings in response to the second ATP application of the indicated mutants ΔCaM F11*, n=2 (3); ΔCaM, S124*, n=1 (3); ΔCaM, K127*, n=3 (8); ΔCaM, D423*, n=4 (9); ΔCaM, A564*, n=3 (15) with n and numbers in brackets indicating the number of successful and total VCF recordings, respectively. All recordings were performed in divalent-free buffer, and oocytes were clamped at –30 mV.

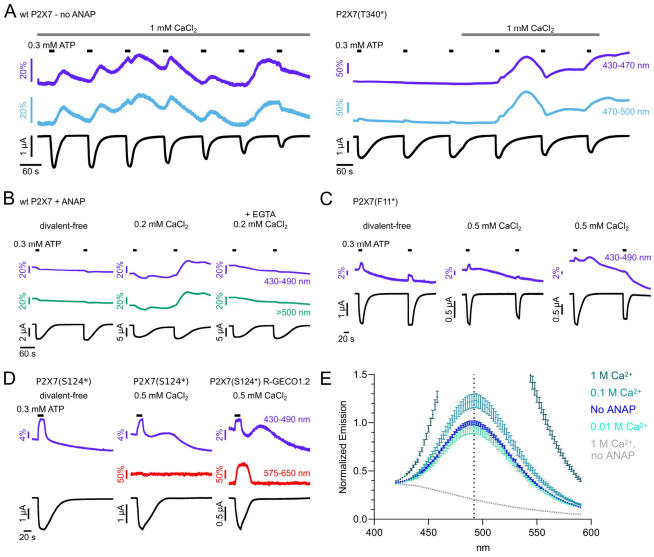

Figure 6 – figure supplement 1 **Ca^{2+}-containing buffers cause large fluorescence changes, even in the absence of L-3-(6-acetylnaphthalen-2-ylamino)–2-aminopropanoic acid (ANAP).**
(A) In Ca^{2+}-containing buffers, voltage clamp fluorometry (VCF) recordings from unmutated wt P2X7R (left) showed large irregular fluorescence changes in the ANAP emission range, even in the absence of ANAP. These masked ATP-evoked and ANAP-specific fluorescence signals from ANAP-substituted P2X7(T340*) (right). **(B)** The irregular fluorescence changes in Ca^{2+}-containing buffers could be prevented by injection of EGTA (1 mM) 3–4 hr before the measurement. **(C)** VCF recordings of oocytes expressing P2X7(F11*) in divalent-free buffer supplemented with EGTA and flufenamic acid (left) and in buffer containing 0.5 mM Ca^{2+} (center and right). **(D)** VCF recordings of oocytes expressing P2X7(S124*) and P2X7(S124*)-R-GECO1.2. The Ca^{2+}-dependent fluorescence changes are only detected in the ANAP emission spectrum. If not otherwise indicated, recordings were performed at –30 mV in divalent-free buffer supplemented with EGTA and flufenamic acid. **(E)** ANAP (1 μM) and the indicated $CaCl_2$ concentrations were dissolved in otherwise divalent-free recording solution. Fluorescence emission spectra were measured using a Tecan Reader Infinite M200 Pro (excitation 360 nm) and normalized to the averaged fluorescence emission at the maximum emission (492 nm, dotted line) of buffer containing only ANAP. Note that values for the (1 M Ca^{2+} + ANAP)–solution were out of measurement range.

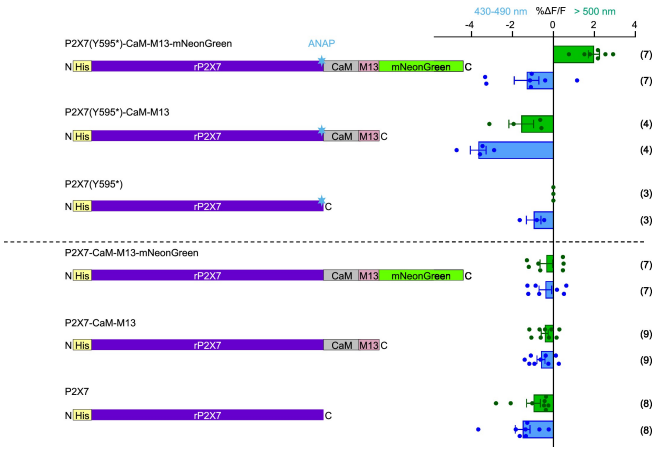

Figure 6 – figure supplement 2 **Control constructs and corresponding voltage clamp fluorometry recordings to confirm the specificity of the FRET signals.** Scheme representing the constructs tested (left) with fluorescence signals at two different emission wavelengths (for L-3-(6-acetylnaphthalen-2-ylamino)–2-aminopropanoic acid [ANAP; blue] and mNeonGreen [green], respectively) summarized as horizontal bar diagrams (right). The positive control P2X7(Y595*)-CaM-M13-mNeonGreen is the only construct showing negative fluorescence signals for ANAP and positive signals for mNeonGreen, consistent with FRET. The control constructs containing only ANAP show either negative or no fluorescence signal for mNeonGreen. Constructs without sites for ANAP incorporation but co-injected ANAP (as master mix with tRNA and cRNAs) served as a control for background fluorescence. Error bars represent S.E.M. Numbers of experiments are given in brackets.

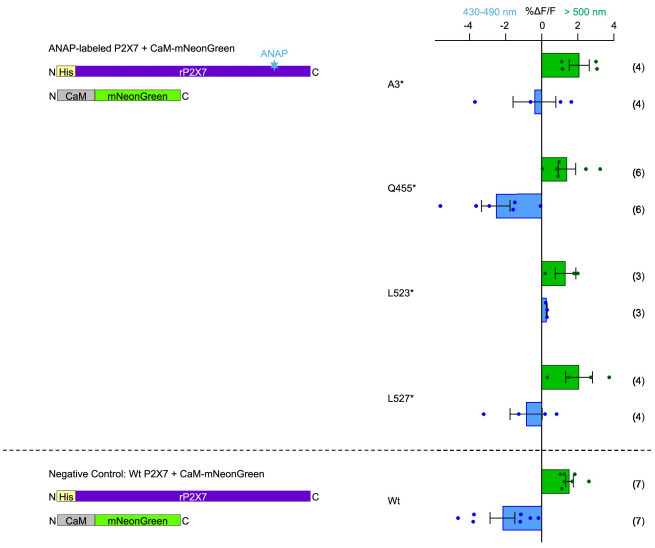

Figure 6 – figure supplement 3 **Experiments with L-3-(6-acetylnaphthalen-2-ylamino)–2-aminopropanoic acid (ANAP)-containing P2X7 constructs and soluble mNeonGreen-tagged CaM reveal unspecific fluorescence signals.**
The indicated ANAP-containing P2X7 constructs were co-injected with soluble mNeonGreen-tagged CaM and ANAP-Master Mix containing ANAP, tRNA, cRNA encoding tRNA-syntethase, and cRNA encoding eRF1(E55D). Corresponding fluorescence signals at two different emission wavelengths are summarized for ANAP (blue) and mNeonGreen (green). Note that soluble mNeonGreen-tagged CaM appeared to interact with the co-injected ANAP. Error bars represent S.E.M. Numbers of experiments are given in brackets.

3.2 Design, Synthesis, and *in vitro* Evaluation of P2X7 Antagonists

The aim of this work was to investigate structure-function relations of P2X7 antagonists and to develop potent pharmacological and therapeutic tools. A series of 24 compounds was synthesized and evaluated via *in silico* and *in vitro* studies.
The design of the compounds was based on the chemical scaffold of AZ1 from AstraZeneca, an adamantane analogue and potent inhibitor of human P2X7R activation [82]. AZ1 was also used as a positive control throughout the study. To enhance potential anti-inflammatory effects, the first generation of compounds were adamantane-based analogues bearing groups that are able to release nitric oxide (NO) or hydrogen sulfide (H_2S). Additional compounds were designed by replacing structural features, such as an amide bond or the adamantane ring itself by other moieties.
All 24 derivatives were evaluated by a ligand-based pharmacophore model that was used to predict crucial stereoelectronic features for P2X7R binding and to identify the compounds with the most promising pharmacophore-fit scores. Their inhibitory potencies at human P2X7Rs were then investigated by TEVC analysis of *X. laevis* oocyte-expressed receptors. For 13 compounds, dose-response relationships and IC_{50} values were determined. The two compounds exhibiting the best potencies are an adamantane-based analogue bearing a nitrate ester group able to release NO (IC_{50} = 0.34 μM) and a structurally modified analogue with an aryl-cyclohexyl moiety instead of the adamantane ring (IC_{50} = 0.39 μM).
For this study, I performed all TEVC experiments, analyzed the data and generated DRCs resulting in Fig.4, Fig. 5, Fig. 6, Fig. 7, Table 3, and Table 4. Further, I contributed to the interpretation of the results and editing of the manuscript.

Design, Synthesis, and *in vitro* Evaluation of P2X7 Antagonists

Dimitra T. Pournara, Anna Durner, Eftichia Kritsi, Alexios Papakostas
Panagiotis Zoumpoulakis, Annette Nicke, Maria Koufaki

published in

ChemMedChem 2020, 15, 2530-2543

Reprinted from [86]

ChemMedChem | Full Papers
doi.org/10.1002/cmdc.202000303
Check for updates
Chemistry Europe
European Chemical Societies Publishing

Design, Synthesis, and *in vitro* Evaluation of P2X7 Antagonists

Dimitra T. Pournara,[a] Anna Durner,[b] Eftichia Kritsi,[a] Alexios Papakostas,[a] Panagiotis Zoumpoulakis,[a] Annette Nicke,*[b] and Maria Koufaki*[a]

The P2X7 receptor is a promising target for the treatment of various diseases due to its significant role in inflammation and immune cell signaling. This work describes the design, synthesis, and in vitro evaluation of a series of novel derivatives bearing diverse scaffolds as potent P2X7 antagonists. Our approach was based on structural modifications of reported (adamantan-1-yl)methylbenzamides able to inhibit the receptor activation. The adamantane moieties and the amide bond were replaced, and the replacements were evaluated by a ligand-based pharmacophore model. The antagonistic potency of the synthesized analogues was assessed by two-electrode voltage clamp experiments, using *Xenopus laevis* oocytes that express the human P2X7 receptor. SAR studies suggested that the replacement of the adamantane ring by an aryl-cyclohexyl moiety afforded the most potent antagonists against the activation of the P2X7 cation channel, with analogue 2-chloro-*N*-[1-(3-(nitrooxymethyl)phenyl)cyclohexyl)methyl]benzamide (**56**) exhibiting the best potency with an IC_{50} value of 0.39 μM.

Introduction

P2X receptors are trimeric, ligand-gated, non-selective cation channel receptors with seven clearly established subtypes (P2X1-7) that are involved in diverse physiological functions, including the cardiovascular, neuronal, and immune system.[1] The P2X7 subtype is the largest member of the P2X receptor family, composed of a 595-amino acid polypeptide chain.[2] Its long intracellular C-terminus distinguishes the P2X7 receptor from the other P2X family members and has been reported to be involved in pore formation,[3] protein-protein interactions,[4] as well as activation of downstream signaling pathways[5] such as cytokine release, modulation of cell proliferation and phagocytosis,[6] and cell death. Moreover, P2X7 is present in a wide variety of cells in the human body[7] and has been associated with multiple diseases, including inflammatory[8] and CNS disorders,[9,10] inflammatory pain, rheumatoid arthritis[11] and cardiovascular diseases.[12]

The activation of P2X7 requires high extracellular ATP concentrations (1 mM), in contrast to concentrations <100 μM needed to activate other P2X subtypes, and leads to the formation of a large conductance pore rather than to desensitization.[9] This non-selective macropore facilitates the influx of large ions and hydrophilic solutes (up to 900 Da) that may cause cell death due to apoptosis and necrosis.[13] Specifically, it has been shown that the efflux of K^+ ions through the P2X7 macropore triggers the activation of the most widely characterized inflammasome,[14] Nod-like receptor family pyrin domain containing protein 3 (NLRP3), leading to the ultimate release of pro-inflammatory factors such as active caspase-1 and interleukin-1β (IL-1β).[15]

During the last decade, numerous classes of P2X7 antagonists featuring drug-like properties have been generated.[16] Particularly, three small antagonists have entered clinical trials for the treatment of CNS disorders.[17] However, AZD9056 and CE-224535 were proven inefficient in Phase II clinical studies for rheumatoid arthritis,[18,19] while GSK1482160 was provento be unsafe for neuropathic pain inhibition.[20]

In this study, we report the design, synthesis, and *in vitro* evaluation of novel P2X7 antagonists based on diverse structural motifs and supported by structure–activity relationship (SAR) data. The novel analogues bear substituents that could release nitric oxide (NO) or hydrogen sulfide (H_2S),[21] aiming to enhance their anti-inflammatory effect, as experimental data have shown that both NO and H_2S downregulate the IL-1β secretion and caspase-1 activation.[22–25] A recent study also revealed that P2X7 can be blocked by endogenous H_2S, thus limiting the IL-1β secretion involved in the pathogenesis of secondary brain injury.[26]

Results and Discussion

Experiment design

Our approach towards the development of potent P2X7 antagonists was based mainly on reported adamantane analogues able to inhibit the receptor activation (Figure 1).

[a] Dr. D. T. Pournara, Dr. E. Kritsi, A. Papakostas, Dr. P. Zoumpoulakis, Dr. M. Koufaki
Institute of Chemical Biology
National Hellenic Research Foundation
48 Vassileos Constantinou Ave.
11635 Athens (Greece)
E-mail: mailto:
E-mail: mkoufa@eie.gr
[b] A. Durner, Prof. Dr. A. Nicke
Walther-Straub-Institut für Pharmakologie und Toxikologie
Ludwig-Maximilians-Universität München
Nußbaumstr. 26
80336 München (Germany)
E-mail: annette.nicke@lrz.uni-muenchen.de

Supporting information for this article is available on the WWW under https://doi.org/10.1002/cmdc.202000303

ChemMedChem
Full Papers
doi.org/10.1002/cmdc.202000303
Chemistry Europe
European Chemical Societies Publishing

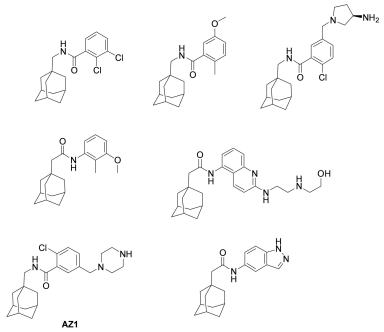

Figure 1. Structures of known adamantane-based P2X7 antagonists.

Specifically, analogue **AZ1**, developed by Furber *et al.* from Astra Zeneca R&D U.K., has shown significant selectivity to human P2X7 (*h*P2X7) compared to related P2X receptors.[27] Moreover, an X-ray structure of **AZ1** revealed that the amide carbonyl is twisted by 44 out of the plane of the phenyl group by the *ortho*-chloro substituent, supporting its P2X7 selectivity. This structural feature has been observed in all the analogues of these series and was also associated with high potency to the P2X7 receptor.[27]

Additional structural features of the reported analogues (Figure 1) were also exploited to design novel adamantane-based antagonists. Particularly, it has been observed that the methylene linker to adamantane is essential for high antagonistic potency,[28,29] which is not affected by reversing the connectivity of the amide.[27] However, chain extension between the amide and the adamantane from methylene to ethylene resulted in a significant decrease in the antagonistic potency.[29] Similarly, *N*-methyl substituted amides were not tolerated, whereas an *ortho*-substitution of the aryl moiety by a chloro or methyl group was proven to be essential for efficient P2X7 inhibition.[30] It should also be noted that the *ortho*-chloro substitution has been related to enhanced activity of other benzamide classes.[31–33]

Therefore, in order to develop novel P2X7 antagonists, the present SAR study involved structural modifications (Figure 2) based on these earlier findings and the main scaffold of **AZ1**. The replacement of the amide bond and the adamantane moieties was also evaluated using a ligand-based pharmacophore model (Supporting Information), utilized as a 3D search query to screen the ZINC chemical database that led to the identification of analogues with the most promising pharmacophore-fit scores (Tables 1 and 2).

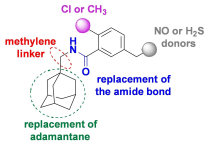

Figure 2. Structural modifications of analogue **AZ1**. The structural features required for high antagonistic potency are indicated in red, purple, and grey. Green and blue colors indicate the structural characteristics that were replaced during the design of the novel analogues.

Table 1. Pharmacophore-fit scores of the synthesized adamantane-based analogues.

Adamantane-based analogues	Pharmacophore-fit score	Adamantane-based analogues	Pharmacophore-fit score
AZ1	36.28	**19a**	45.48
4	44.57	**19b**	37.46
5	46.12	**23b**	44.78
11	37.34	**24a**	25.49
18a	36.03	**24b**	25.39
18b	35.96		

Table 2. Pharmacophore-fit scores of the structurally modified analogues.

Structurally modified analogues	Pharmacophore-fit score	Structurally modified analogues	Pharmacophore-fit score
AZ1	36.28	**60**	43.69
30	35.67	**61**	35.81
35	62.13	**63**	44.27
42a	62.35	**64**	43.32
42b	52.28	**67**	62.39
43	52.77	**68**	46.22
53	53.63	**70**	52.53
56	45.31		

Adamantane-based putative P2X7 antagonists

Initially, three adamantyl amide analogues were synthesized; **AZ1**, which was used as positive control throughout the study, and two additional compounds bearing a group that could release NO (**4**) or H_2S (**5**) at the 5-position of the phenyl ring, respectively. 1-Adamantylmethanamine (**1**) was obtained in quantitative yield from 1-adamantaneacetic acid via a Schmidt reaction. Coupling of **1** with 2-chloro-5-methylbenzoic acid in the presence of 1-ethyl-3-(3-(dimethylamino)propyl) carbodiimide hydrochloride (EDC hydrochloride) and triethylamine (Et_3N) gave amide **2**. Radical bromination of the methyl group with azobisisobutyronitrile (AIBN) as initiator and *N*-bromosuccinimide (NBS) afforded bromide **3**, which then reacted with piperazine,[27] methanesulfonothioate sodium salt, or $AgNO_3$ to afford analogues **AZ1**, **4**, and **5**, respectively (Scheme 1).

ChemMedChem | Full Papers doi.org/10.1002/cmdc.202000303 | Chemistry Europe European Chemical Societies Publishing

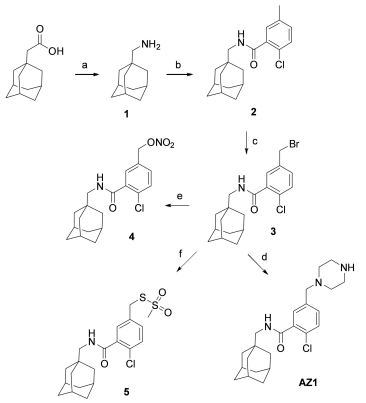

Scheme 1. Reagents and conditions: (a) NaN_3, H_2SO_4, H_2O, $CHCl_3$, 50 C-r.t., 5.5 h, 86%; (b) 2-chloro-5-methylbenzoic acid, EDC hydrochloride, Et_3N, CH_2Cl_2, r.t., 22 h, 63%; (c) NBS, AIBN, $CHCl_3$, reflux, 4 h, obtained as mixture with **2**; (d) piperazine, CH_3OH, 0 C-r.t., 3 h, 29%; (e) $AgNO_3$, CH_3CN, 60 C, 2 h, 50%; (f) sodium methanesulfonothioate; DMF, 60 C, 5 h, 58%.

Replacement of the amide bond by the 1,2,3-triazole ring

Although hundreds of benzamide analogues have been reported as P2X7 antagonists in research papers and patents,[34] and 1,2,4-triazoles have been reported as isosteres of tetrazoles several years ago,[35] information on derivatives in which the amide bond is replaced by the bioisosteric 1,2,3-triazole is scarce.[36] Given also that the use of 1,2,3-triazoles has attracted increasing research interest for the development of new therapeutic agents,[37] we replaced the amide bond of **AZ1** by its bioisostere 1,2,3-triazole ring. The new analogues preserved the necessary structural features, i.e., a relatively bulky *ortho*-substitution (chloro or methyl) and a nitrate ester or a (methylsulfonyl)thio moiety at the *meta*-position of the phenyl ring.

As shown in Scheme 2, adamantyl azide **9** was synthesized using the commercially available 1-adamantanecarboxylic acid. The 1,2,3-triazoles **11**, **18a**–**b**, **19a**–**b**, and **24a**–**b** were then obtained via a copper-catalyzed azide-alkyne cycloaddition (click reaction) between azide **9** and the appropriate aryl alkyne under microwave conditions. Compound **11**, bearing only an *ortho*-chloro-substituted benzene, was synthesized from 1-chloro-2-iodobenzene, which was coupled with ethynyltrimethylsilane via a Sonogashira reaction using Pd(II)/Cu(I) as the catalytic system. Cleavage of the TMS group by tetrabutylammonium fluoride (TBAF) in THF afforded an intermediate alkyne, which was not isolated but used directly for the subsequent cycloaddition due to its low boiling point (Scheme 2).

For the preparation of analogues **18a**–**b** and **19a**–**b**, the methyl esters of 4-methyl-3-iodobenzoic acid or 4-chloro-3-iodobenzoic acid were coupled with ethynyltrimethylsilane in

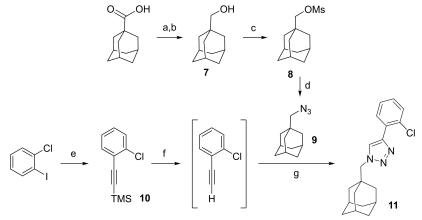

Scheme 2. Reagents and conditions: (a) EtOH, H_2SO_4, 70 C, 18 h, 95%; (b) $LiAlH_4$, THF, 0 C-r.t., 1.5 h, 97%; (c) methanesulfonyl chloride, Et_3N, 0 C-r.t., 21 h, 95%; (d) NaN_3, DMF, mw, 100 Watt, 130 C, 1 h, 84%; (e) ethynyltrimethylsilane, CuI, $Pd(PPh_3)_2Cl_2$, Et_3N/THF, 60 C, 22 h, 64%; (f) TBAF, THF, r.t., 1 h; (g) sodium ascorbate, $CuSO_4 \cdot 5H_2O$, mw, 80 Watt, 90 C, 30 min, 15%.

the presence of $PdCl_2(PPh_3)_2$ and Cu(I) via a Sonogashira cross-coupling reaction to give the intermediates **13a** and **13b**, respectively. After reducing the methyl esters with $LiAlH_4$ in THF, the TMS-protective group was cleaved under basic conditions. The isolated alkynes (**15a**–**b**) afforded triazoles **16a** and **16b** after a click reaction with azide **9**. Bromination of the benzyl alcohols was achieved using PBr_3 in anhydrous CH_2Cl_2. Treatment of analogues **17a** and **17b** with $AgNO_3$ or sodium methanesulfonothioate yielded compounds **18a**/**19a** and **18b**/**19b**, respectively (Scheme 3).

To investigate the effect of bulky substituents at the *meta*-position of the phenyl ring, 3-(hydroxymethyl)-4-phenyl-1,2,5-oxadiazole 2-oxide ring (**20**), a well-known NO donor,[38] was also employed. Compound **20** was synthesized from cinnamyl alcohol after cyclization with $NaNO_2$ and glacial CH_3COOH.[39]

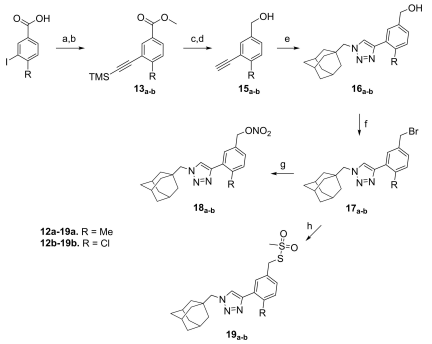

Scheme 3. Reagents and conditions: (a) CH_3OH, H_2SO_4, reflux, 24 h, 98%; (b) ethynyltrimethylsilane, CuI, $Pd(PPh_3)_2Cl_2$, Et_3N/THF, 60 C, 86–95%; (c) $LiAlH_4$, THF, 0 C-r.t., 45 min; (d) KOH (aq.), CH_3OH, r.t., 15 min, 99% over two steps; (e) **9**, sodium ascorbate, $CuSO_4 \cdot 5H_2O$, *t*BuOH/H_2O, mw, 80 Watt, 90 C, 30 min, 79–85%; (f) PBr_3, CH_2Cl_2, 0 C-r.t., 2 h, 84–91%; (g) $AgNO_3$, CH_3CN, 60 C, dark, 2–17 h, 35–71%; (h) sodium methanethionosulfonate, DMF, 70 C, 2–5 h, 23–51%.

ChemMedChem
Full Papers
doi.org/10.1002/cmdc.202000303
Chemistry Europe
European Chemical Societies Publishing

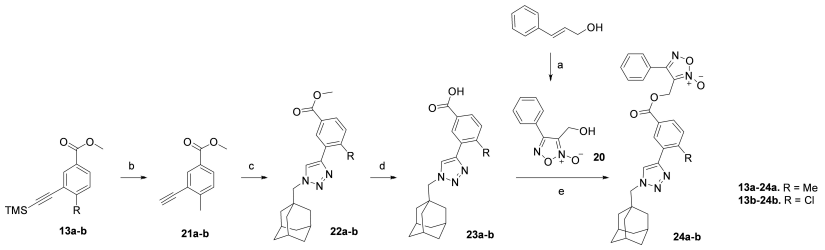

Scheme 4. Reagents and conditions: (a) glacial acetic acid, $NaNO_2$ (aq.), 0 °C-r.t., 24 h, 50 %; (b) KOH (aq.), CH_3OH, r.t., 20–30 min, 70–98 %; (c) **9**, sodium ascorbate, $CuSO_4 \cdot 5H_2O$, *t*BuOH/H_2O, mw, 80 Watt, 90 °C, 30 min, 91–93 %; (d) LiOH (2 N), THF, r.t., 24 h, 87–95 %; (e) DMAP, DCC, CH_2Cl_2, 0 °C-r.t., 2 h, 48–71 %.

Despite the reported tautomerism,[39] only the indicated isomer **20** was obtained under these conditions,[40] which was used for the synthesis of analogues **24a–b** (Scheme 4). Then, the TMS-protected methyl esters **13a–b** yielded alkynes **21a–b** upon treatment with a saturated aqueous KOH solution. A click reaction with **9** followed, and the obtained esters (**22a–b**) were hydrolyzed to the corresponding carboxylic acids with LiOH (2N). The subsequent Steglich esterification of **23a–b** with **20** in the presence of *N,N'*-dicyclohexylcarbodiimide (DCC) and 4-dimethylaminopyridine (DMAP) afforded adamantyl analogues **24a** and **24b**.

Structurally modified putative P2X7 antagonists

The adamantane ring has been earlier replaced by other polycyclic scaffolds[41] or fluorine bioisosteres.[42] In our study, the ZINC chemical database was virtually screened to identify alternative scaffolds of adamantane, indicating the (i) 3-fluoro-4-(trifluoromethyl)phenyl, (ii) aryl-substituted cyclohexyl, and (iii) 1,2,5-oxadiazole-2-oxide (furoxan) moieties as potential units (Figure 3). Especially the heteroaryl-substituted cyclohexyl group has earlier been employed for research on the P2X7 receptor.[43] Examination of their structural and pharmacophore features revealed that all three moieties shared the necessary hydrophobic features, while the fluorine atoms along with the nitrogen and oxygen heteroatoms fulfilled the required hydrogen bond acceptor (HBA) features.

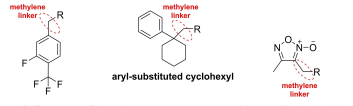

Figure 3. The 3-fluoro-4-(trifluoromethyl)phenyl, aryl-substituted cyclohexyl, and furoxan scaffolds used for the replacement of the adamantane ring.

Thus, a series of novel, structurally modified 1,2,3-triazoles and amides that exhibited the highest pharmacophore-fit scores (Table 2) were synthesized by replacing the adamantane ring with the identified units (Figure S83). In agreement with the above results, the nitrogen atoms of the triazole analogues served as HBAs, while the substituted benzene rings displayed hydrophobic interactions. In addition, the 3-fluoro-4-(trifluoromethyl)phenyl derivatives **30**, **35**, **42a–b**, and **43** displayed three hydrophobic regions and two HBAs. In the aryl-substituted cyclohexyl derivatives **53**, **56**, **67**, **68**, and **70** the cyclohexyl ring did not develop interactions, whereas the carbonyl oxygen atom of the amide served as HBA and the halogen benzene ring constituted a hydrophobic region (Figure S83). The fluorine atoms in **67**, **68**, and **70** also served as HBAs. Additionally, the pharmacophore model of the furoxan analogues (**60**, **61**, **63**, and **64**) suggested that the ring's heteroatoms, the carbonyl oxygen atom, and the triazole ring's nitrogen atom act as HBAs, while the halogen benzene rings developed hydrophobic interactions (Figure S83).

Replacement of adamantane by the 3-fluoro-4-(trifluoromethyl)phenyl moiety

In line with the adamantane-based analogues, both amides and 1,2,3-triazoles were synthesized, while the *ortho*- and *meta*-substitutions on the phenyl ring were maintained. 2-(3-Fluoro-4-(trifluoro-methyl)phenyl)acetic acid yielded amine **25** through an one-step Schmidt reaction. The methyl ester of 2-chloro-5-methylbenzoic acid (**26**) was prepared upon treatment with CH_3OH and H_2SO_4. Bromination of the aryl methyl group followed, using AIBN and NBS in anhydrous $CHCl_3$, giving the intermediate **27**. Hydrolysis of the carboxylic acid group with LiOH (2N) in THF resulted in the concurrent replacement of the bromine atom by a hydroxyl group. The isolated benzoic acid **28** was then successfully coupled with **25** using 1-[bis(dimethylamino)methylene]-1*H*-1,2,3-triazolo[4,5-b] pyridinium 3-oxide hexafluorophosphate (HATU) and *N,N*-diisopropylethylamine (DIPEA) in DMF.[44] The *in situ* formation of the bromide using PPh_3 and NBS in an anhydrous CH_3CN/CH_2Cl_2 mixture and the

ChemMedChem | Full Papers doi.org/10.1002/cmdc.202000303 | Chemistry Europe European Chemical Societies Publishing

subsequent addition of $AgNO_3$ afforded the desired compound **30** (Scheme 5).[45]

To study the influence of the structure of the amide bond on the potency, a reverse amide was also synthesized, using 2-(3-fluoro-4-(trifluoromethyl) phenyl)acetic acid and aniline **33**. The nitro-group of the methyl ester **31** was reduced under mild conditions with Fe(0) and an aqueous solution of NH_4Cl in ethanol, resulting in ester **32**. Reduction of the ester group with $LiAlH_4$ in anhydrous THF afforded aniline **33**. 2-(3-Fluoro-4-(trifluoro-methyl)phenyl) acetic acid was then heated overnight with **33** and HATU/DIPEA in DMF to give **34**. The *in situ* formation of the bromide and the subsequent addition of $AgNO_3$ in a mixture of anhydrous CH_2Cl_2/CH_3CN afforded the nitrate ester **35** (Scheme 6).

In addition, three triazoles were prepared as corresponding analogues of **18a–b** and **19a**. The methyl ester (**36**) of 3-fluoro-4-(trifluoromethyl)benzoic acid was reduced with $LiAlH_4$ in anhydrous THF to give benzyl alcohol **37**. Bromination of **37** with PBr_3 afforded analogue **38**, which was further heated with NaN_3 in DMF to give azide **39**. Microwave irradiation was then applied to obtain the *ortho*-methyl and -chloro 1,2,3-triazoles **40a** and **40b**, respectively. Upon treatment with PBr_3, bromides **41a–b** were obtained and reacted with $AgNO_3$ or sodium methanesulfonothioate to afford analogues **42a–b** and **43**, respectively (Scheme 7).

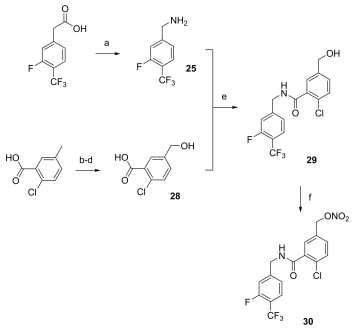

Scheme 5. Reagents and conditions: (a) H_2SO_4, NaN_3, $CHCl_3$, H_2O, 50 C, 5 h, 50%; (b) CH_3OH, H_2SO_4, 70 C, 18 h, 77%; (c) NBS, AIBN, $CHCl_3$, reflux, 2.5 h, 53%; (d) LiOH (2 N), THF, 40 C, 20 h, 92%; (e) HATU, DIPEA, DMF, r.t., 72 h, 41%; (f) PPh_3, NBS, $AgNO_3$, dark, CH_2Cl_2/CH_3CN, 0–50 C, 24 h, 39%.

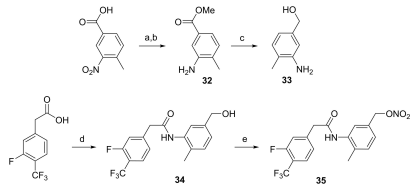

Scheme 6. Reagents and conditions: (a) CH_3OH, H_2SO_4, reflux, 18 h, 94%; (b) Fe(0), NH_4Cl (aq.), EtOH, reflux, 3 h, 86%; (c) $LiAlH_4$, THF, 0 C-r.t., 1.5 h, 100%; (d) **33**, HATU, DIPEA, DMF, 70 C, 15 h, 67%; (e) PPh_3, NBS, $AgNO_3$, CH_2Cl_2/CH_3CN, 0–50 C, dark, 5 h, 29%.

Replacement of adamantane by the aryl-substituted cyclohexyl moiety

5-(4-Hydroxyphenyl)-3*H*-1,2-dithiol-3-thione (ADT-OH),[46] a known H_2S-releasing agent,[47] was used for the synthesis of analogue **49**. Elimination of the α-hydrogen atoms of cyanomethyl propionate by Cs_2CO_3, followed by a double attack from 1,5-dibromopentane, resulted in compound **44**. Reduction of the nitrile with $LiAlH_4$ afforded amine **45**, which was further protected using Boc_2O. A Mitsunobu reaction between the Boc-protected derivative **46** and ADT-OH afforded compound **47**, which was deprotected by trifluoroacetic acid (TFA). Amine **48** was then coupled with 2-chloro-5-methylbenzoic acid using EDC hydrochloride and Et_3N in anhydrous CH_2Cl_2 to afford analogue **49** (Scheme 8).

Analogues **53** and **56** were synthesized bearing the nitrate ester group on opposite phenyl rings (Scheme 9) to examine the effect of the substitution position on the antagonistic potency. NaH was used for the α-deprotonation of (4-methylphenyl)acetonitrile to yield analogue **50**. Reduction of the nitrile was achieved with $BH_3{\cdot}S(CH_3)_2$ in THF. Amine **51** was then coupled with **28** using HATU/DIPEA in anhydrous DMF. *In situ* bromination of the benzylic hydroxyl group with PPh_3 and NBS in an anhydrous CH_2Cl_2/CH_3CN mixture, followed by the formation of the nitrate ester, afforded amide **53**. For the synthesis of compound **56**, amine **51** was coupled with 2-chlorobenzoic acid using EDC hydrochloride and hydroxybenzotriazole (HOBt) as the coupling agent in anhydrous DMF. Radical

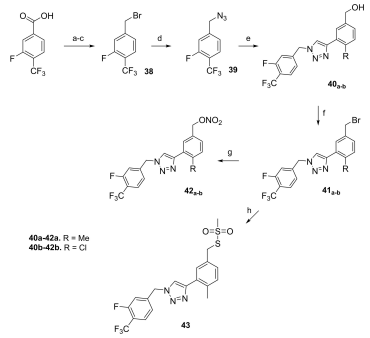

Scheme 7. Reagents and conditions: (a) CH_3OH, H_2SO_4, 60 C, 24 h, 83%; (b) $LiAlH_4$, THF, 0 C-r.t., 1.5 h, 82%; (c) PBr_3, CH_2Cl_2, 0 C-r.t., 2.5 h, 26%; (d) NaN_3, DMF, 40 C, 3 h, 50%; (e) **15a–b**, sodium ascorbate, $CuSO_4{\cdot}5H_2O$, *t*BuOH/H_2O, mw, 80 Watt, 90 C, 30 min, 52–55%; (f) PBr_3, CH_2Cl_2, 0 C-r.t., 2.5 h, 31–50%; (g) $AgNO_3$, CH_3CN, 60 C, dark, 2.5 h, 42–82%; (h) sodium methanesulfonothioate, DMF, 60 C, 2.5 h, 47%.

ChemMedChem
Full Papers
doi.org/10.1002/cmdc.202000303
Chemistry Europe
European Chemical Societies Publishing

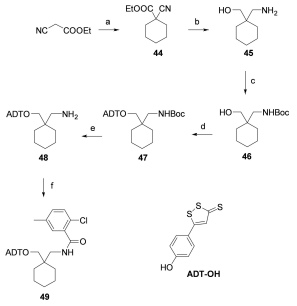

Scheme 8. Reagents and conditions: (a) 1,5-dibromopentane, Cs_2CO_3, DMF, 0 C-r.t., 24 h, 79%; (b) $LiAlH_4$, THF, 0 C-r.t., 29 h, 98%; (c) Boc_2O, THF, r.t., 23 h, 99%; (d) ADT-OH, PPh_3, DIAD, THF, r.t., 72 h, 29%; (e) TFA, CH_2Cl_2, r.t., 1 h, 95%; (f) 2-chloro-5-methylbenzoic acid, EDC hydrochloride, Et_3N, CH_2Cl_2, r.t., 20 h, 28%.

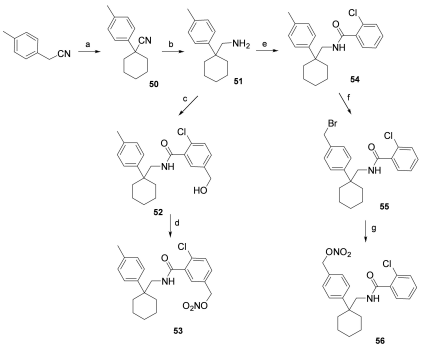

Scheme 9. Reagents and conditions: (a) 1,5-dibromopentane, NaH (60%), DMF, 0 C-r.t., 4 h, 67%; (b) $BH_3{\cdot}S(CH_3)_2$, THF, 0 C-r.t., 3 h, 49%; (c) **28**, HATU, DIPEA, DMF, r.t., 48 h; (d) PPh_3, NBS, $AgNO_3$, CH_2Cl_2/CH_3CN, 0–50 C, dark, 24 h, 21%; (e) 2-chlorobenzoic acid, HOBt, EDC hydrochloride, Et_3N, DMF, r.t., 22 h, 45%; (f) NBS, AIBN, $CHCl_3$, reflux, 90 min, 57%; (g) $AgNO_3$, CH_3CN, 60 C, dark, 1 h, 63%.

bromination of **54** with AIBN and NBS afforded amide **55**, which was subsequently refluxed with $AgNO_3$ to yield analogue **56** (Scheme 9).

Replacement of adamantane by the furoxan ring

Furoxan analogues are interesting pharmacophores endowed with various biological effects such as anticancer[48] and antimicrobial.[49,50] However, P2X7 antagonists bearing this group have not been reported so far. Thus, in this study, adamantane was replaced by the furoxan ring to afford an amide and a 1,2,3-triazole derivative. In particular, bromide **57** reacted with NaN_3 in DMF to afford azide **58**. Amine **59** was obtained via a Staudinger reaction of azide **58** with PPh_3 and H_2O in THF and was subsequently used for the synthesis of analogue **60** (Scheme 10). Microwave irradiation of **58** and the chloro-substituted alkyne (isolated from **10**, as in Scheme 2) in the presence of Cu(II) and sodium ascorbate in a mixture of *t*BuOH/H_2O afforded analogue **61**.

The furoxan ring (**20**) was also used in place of the phenyl ring of the 3-fluoro-4-(trifluoromethyl)phenyl and aryl-substituted cyclohexyl derivatives to further investigate its role on the potency. Thus, the furoxan carboxylic acid (**62**) was quantitatively obtained by the oxidation of **20** with the Jones reagent, which gave analogue **63** using HATU/DIPEA.[51] In the case of **64**, the coupling reaction was performed using EDC/Et_3N in anhydrous CH_2Cl_2 (Scheme 11).

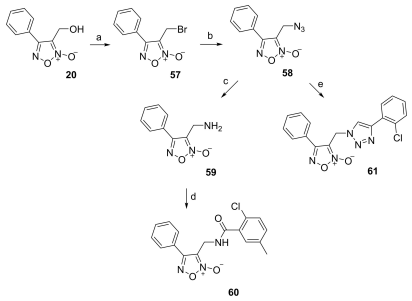

Scheme 10. Reagents and conditions: (a) PBr_3, CH_2Cl_2, 0 C-r.t., 3.5 h, 55%; (b) NaN_3, DMF, 40 C, 4 h, 99%; (c) PPh_3, H_2O, THF, r.t., 22 h, obtained as mixture with PPh_3O; (d) 2-chloro-5-methylbenzoic acid, EDC hydrochloride, Et_3N, CH_2Cl_2, r.t, 24 h, 21% over two steps; (e) 1-chloro-2-ethynylbenzene, sodium ascorbate, $CuSO_4{\cdot}5H_2O$, *t*BuOH/H_2O, mw, 80 Watt, 90 C, 30 min, 45%.

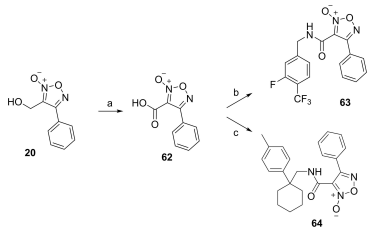

Scheme 11. Reagents and conditions: (a) Jone's reagent, acetone, 0 C-r.t., 3.5 h, 74%; (b) **25**, HATU, DIPEA, DMF, r.t., 22 h, 73%; (c) **51**, HOBt, EDC hydrochloride, Et_3N, DMF, r.t., 20 h, 26%.

ChemMedChem | Full Papers doi.org/10.1002/cmdc.202000303 | Chemistry Europe European Chemical Societies Publishing

Combination of the 3-fluoro-4-(trifluoromethyl)phenyl and aryl-substituted cyclohexyl moieties

Finally, three additional analogues that combined the 3-fluoro-4-(trifluoromethyl)phenyl and aryl-substituted cyclohexyl moieties were synthesized to elucidate the structural features responsible for the interactions with the P2X7 receptor. Thus, the cyclohexyl ring of **65** was prepared using the commercially available 2-(3-fluoro-4-(trifluoromethyl)phenyl)acetonitrile and 1,5-dibromopentane in the presence of NaH in anhydrous DMF. Reduction of the nitrile with $BH_3{\cdot}S(CH_3)_2$ in THF afforded amine **66**, which was then coupled with 2-chlorobenzoic acid or 2-chloro-5-methylbenzoic acid to yield compounds **67** and **68**, respectively. Analogue **68** was further radically brominated with AIBN and NBS in anhydrous CHCl3 to afford compound **69** as a non-separable mixture with the starting material (**68**). Upon treatment with $AgNO_3$ analogue **70** was obtained (Scheme 12).

***In vitro* evaluation of the antagonistic potency: SAR study**

The synthesized analogues were evaluated *in vitro* by two-electrode voltage clamp (TEVC) experiments using *Xenopus laevis* oocytes that express the human P2X7 (*h*P2X7) receptor. The already reported P2X7 antagonist **AZ1** was used as a positive control to allow the comparison of the isolated compounds' antagonistic potencies. In general, the synthesized analogues featured drug-like properties based on predictions of their absorption, distribution, metabolism, and excretion (ADME) properties (Table S1).

The blocking potency was initially estimated by incubating *h*P2X7 expressing oocytes for 3 min with 10 μM of each compound. **AZ1** completely blocked ATP-induced (300 μM) current responses under these conditions, while analogues **4** and **5**, bearing a chloro group at the *ortho*-position of the phenyl ring, were equally potent, irrespective of the benzyl

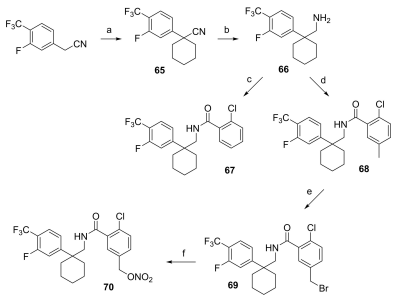

Scheme 12. Reagents and conditions: (a) 1,5-dibromopentane, NaH (60%), DMF, 0 C-r.t., 1 h, 81%; (b) $BH_3{\cdot}S(CH_3)_2$, THF, reflux, 1 h, 81%; (c) 2-chlorobenzoic acid, HOBt, EDC hydrochloride, Et_3N, DMF, r.t., 18 h, 55%; (d) 2-chloro-5-methyl benzoic acid, HOBt, EDC hydrochloride, Et_3N, DMF, r.t., 22 h, 30%; (e) NBS, AIBN, $CHCl_3$, reflux, 2 h, obtained as mixture with **68**; (f) $AgNO_3$, CH_3CN, 50 C, dark, 30 min, 10% over two steps.

meta-substitution (Figure 4). Replacement of the amide bond by its bioisostere 1,2,3-triazole ring in analogues that bear the same *meta*-substitution and an *ortho*-chloro or -methyl substitution (**11**, **18a**–**b**, and **19a**–**b**) impaired the antagonistic effect compared to the control (**AZ1**). According to the data shown in Figure 4, the *ortho*-methyl group in analogues **18a** and **19a** probably favored the interaction with the receptor compared to the chloro group (**18b** and **19b**). However, the presence of the (methylsulfonyl)thio group reduced the antagonistic potency, especially in the case of analogue **19b**.

Additionally, the *in vitro* evaluation of analogues **24a**–**b**, bearing the furoxan ring, confirmed the results of the pharmacophore model that bulky substituents do not improve the compound's activity (Figure 4). However, the congener of **24b**, compound **23b**, displayed potent inhibition of *h*P2X7, suggesting that inactive esters may be hydrolyzed after their insertion into the host and result in a more active form of the initial analogue.

Since seven of these analogues led to a reduction of ATP-induced current responses of at least 50%, their dose–response relationships were determined (Figure 5). The IC_{50} values (Table 3) showedthat analogues **4** and **18a** were the most potent adamantane-based P2X7 antagonists of the current study, with about five- and ten-fold reduced potency compared to **AZ1**, respectively. However, except for analogue **18a**, the replacement of the amide bond by the 1,2,3-triazole ring

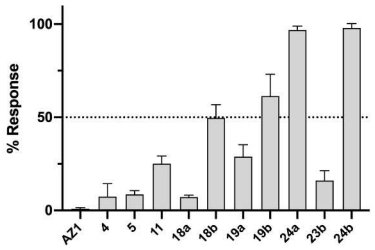

Figure 4. Antagonistic potencies of **AZ1** and the indicated analogues by TEVC. *Xenopus leavis* oocytes expressing the *h*P2X7 receptor were clamped at −70 mV. 10 μM of the indicated compounds were preincubated for 3 min before application of 300 μM ATP. Responses are normalized to ATP-evoked current responses in the absence of antagonist. Error bars represent S.D. **AZ1** (n = 4), **4** (n = 8), **5** (n = 3), **11** (n = 6), **18a** (n = 3), **18b** (n = 3), **19a** (n = 7), **19b** (n = 4), **24a** (n = 4), **23b** (n = 6), and **24b** (n = 3).

Table 3. IC_{50} values with 95% confidence intervals (CI) of the most active adamantane-based analogues.

Compound	IC_{50} [μM]	95% CI [μM]
AZ1	0.065	0.054–0.077
4	0.339	0.253–0.452
5	2.716	1.901–3.799
11	4.355	3.761–5.039
18a	0.735	0.611–0.894
18b	8.004	5.990–10.69
19a	3.859	3.027–4.920
23b	1.712	1.442–2.030

ChemMedChem
Full Papers
doi.org/10.1002/cmdc.202000303
Chemistry Europe
European Chemical Societies Publishing

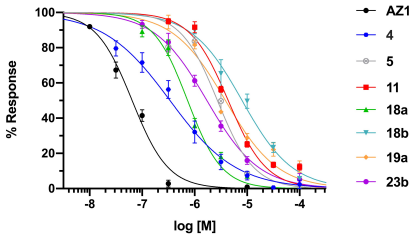

Figure 5. Dose–response curves of compound **AZ1** and the indicated analogues. All compounds were preincubated for 3 min and the current responses of the oocyte-expressed *h*P2X7 receptor to 300 μM ATP were recorded by TEVC at −70 mV. Each point represents the average of at least three measurements and error bars represent S.D.

significantly reduced the potency. Complete absence of the *meta*-substitution (**11**) as well as a bulkier substituent, such as the (methylsulfonyl)thio group (**19a**), also negatively affected the analogues' antagonistic abilities. Moreover, the IC_{50} values of amides **4** (0.34 μM) and **5** (2.72 μM), as well as those of triazoles **18a** (0.74 μM) and **18b** (8.00 μM), were remarkably different, suggesting that the nature of the *ortho*- and *meta*-substitution might affect the interaction with the receptor and thus the antagonistic potency.

Regarding the scaffold exchange strategy of adamantane, its replacement by the (3-fluoro-4-(trifluoromethyl)phenyl moiety in analogues **30**, **35**, **42a–b**, and **43** resulted in very low potencies for both amides and 1,2,3-triazoles compared to the control (**AZ1**) (Figure 6). In contrast, the replacement of adamantane by the aryl-cyclohexyl moiety improved the analogues' potency. Except for analogue **49**, which could not be tested due to its low solubility confirming the ADME predictions (Table S1), the aryl-cyclohexyl amides bearing a nitrate ester group (**53** and **56**) were potent *h*P2X7 antagonists irrespective of the substituents' position on the phenyl ring (Figure 6).

The replacement of adamantane by the furoxan ring led to analogues with no inhibition at 10 μM (**60** and **61**) (Figure 6). No blocking effect was also observed by replacing the phenyl ring of the (3-fluoro-4-(trifluoromethyl)phenyl-based analogues with the furoxan ring (**63**), suggesting that this moiety deteriorates the interactions with the *h*P2X7 receptor. In contrast, a similar replacement in the aryl-cyclohexyl-based compounds afforded analogue **64**, which exhibited significantly increased potency and indicated again the aryl-cyclohexyl moiety as a suitable scaffold to replace adamantane. Surprisingly, the aryl-cyclohexyl analogues bearing the fluoro-substituted aromatic moiety (**67**, **68**, and **70**) exhibited moderate potency, while the lack of the *meta*-substitution (**67** and **70**) seemingly favored the interaction with the receptor compared to analogue **68** (Figure 6).

Dose-response analysis (Figure 7, Table 4) further confirmed that the aryl-cyclohexyl moiety is an ideal substitute of adamantane. Specifically, analogue **56** had the lowest IC_{50} value (0.39 μM), while analogue **53**, bearing the nitrate ester on the non-chloro phenyl ring, had an IC_{50} value of 1.43 μM. Additionally, it was shown that the (3-fluoro-4-(trifluoromethyl)phenyl moiety did not eliminate the potency when used as a substituent, giving compounds with IC_{50} values ranging from 0.69 μM (**67**) to 3.24 μM (**70**) and 4.80 μM (**68**). For all the aryl-

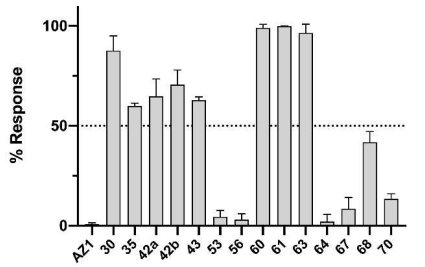

Figure 6. Antagonistic potencies of **AZ1** and the indicated analogues by TEVC. *Xenopus leavis* oocytes expressing the *h*P2X7 receptor were clamped at −70 mV. 10 μM of the indicated compounds were preincubated for 3 min before application of 300 μM ATP. Responses are normalized to ATP-evoked current responses in the absence of antagonist. Error bars represent S.D. **AZ1** (n = 4), **30** (n = 3), **35** (n = 3), **42a** (n = 3), **42b** (n = 3), **43** (n = 3), **53** (n = 4), **56** (n = 3), **60** (n = 4), **61** (n = 4), **63** (n = 4), **64** (n = 3), **67** (n = 3), **68** (n = 3), and **70** (n = 3).

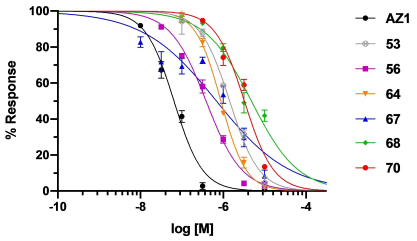

Figure 7. Dose–response curves of compound **AZ1** and the indicated analogues. All compounds were preincubated for 3 min and the current responses of the oocyte-expressed *h*P2X7 receptor to 300 μM ATP were recorded by TEVC at −70 mV. Each point represents the average of at least three measurements and error bars represent S.D.

Table 4. IC_{50} values with 95% confidence intervals (CI) of the most active analogues in μM after the replacement of the adamantane ring.

Compound	IC_{50} [μM]	95% CI [μM]
AZ1	0.065	0.054–0.077
53	1.430	1.240–1.648
56	0.385	0.332–0.443
64	0.878	0.784–0.983
67	0.686	0.399–1.176
68	4.804	3.514–7.012
70	3.243	2.515–4.164

ChemMedChem | Full Papers doi.org/10.1002/cmdc.202000303 | Chemistry Europe European Chemical Societies Publishing

cyclohexyl analogues, it was revealed that the substitution at the 5-position of the phenyl ring results in lower potency (**53**, **68**, and **70**). Furthermore, analogue **64**, bearing the bulkier furoxan moiety in place of the phenyl ring, was effective in inhibiting P2X7 activation with an IC_{50} value of 0.88 μM, which was similar to those of the aryl-cyclohexyl analogues **56** and **67**.

Summarizing, the replacement of the amide bond by its bioisostere 1,2,3-triazole resulted in adamantyl analogues with low antagonistic effect (**11**, **18a–b**, **19a–b**, and **24a–b**). The use of the (3-fluoro-4-(trifluoromethyl)phenyl moiety in place of adamantane afforded novel amides and 1,2,3-triazoles with very low potency (**30**, **35**, **42a–b**, **43**, and **63**). Furthermore, replacement of the adamantane ring by the furoxan moiety did not favor the blocking effect of **60** and **61**. Nevertheless, potent P2X7 antagonists were obtained by replacing adamantane by the aryl-cyclohexyl moiety (**53**, **56**, **64**, **67**, **68**, and **70**). Among them, analogue **56** exhibited the lowest IC_{50} value (0.39 μM), which was equivalent to that of analogue **4** (0.34 μM).

Conclusions

Although P2X7 is an important drug target and various classes of P2X7 antagonists have already been described, successful clinical candidates are missing. Moreover, neither papers nor patents have reported SAR studies on the class of compounds described in this work. Herein, by replacing several structural features of the Astra Zeneca derivative (**AZ1**) with moieties that have not yet been examined to block the activation of the P2X7 channel and based on an *in silico* refined SAR study, a series of hit compounds were developed as novel putative P2X7 antagonists bearing low micromolar to high nanomolar potencies. Our data showed that analogue **4** bearing a nitrate ester group in place of piperazine could effectively inhibit P2X7 activation (IC_{50} = 0.34 μM), while the aryl-cyclohexyl group was proven to be the most promising alternative for adamantane with analogue **56** exhibiting an IC_{50} value of 0.39 μM. Most importantly, this work provides different structural starting points for further hit-to-lead optimization towards the development of derivatives with improved structural features that can effectively block the activation of the P2X7 ion channel with nanomolar potency.

Experimental Section

General chemistry

Commercial reagents and solvents were obtained from *Acros Organics*, *Merck*, *Sigma-Aldrich* or *Fluorochem* in the qualities puriss, p.a. or purum and used without further purification. All non-aqueous reactions were set up under argon atmosphere, utilizing glassware that was flame-dried and cooled under vacuum. Thin layer chromatography (TLC) was performed using precoated SiO_2 aluminum plates (Macherey-Nagel Sil G-25 UV254), while the chromatographic purifications were performed with silica gel (200–400 mesh). The ^1H and ^{13}C spectra were recorded on Varian spectrometers operating at 300 MHz or 600 MHz/75 MHz or 150 MHz, respectively, at 25 C using $CDCl_3$, DMSO-d_6, CD_3OD, acetone-d_6, or CD_2Cl_2. The processing and evaluation of the spectra were performed using the program MestReNova 9.0. The resonance multiplicity is indicated as *s* (singlet), *d* (doublet), *t* (triplet), and *m* (multiplet) or combinations of them, and the coupling constants (*J*) are given in Hz. The mass spectra were obtained on a HPLC-MSn Fleet-Thermo system in the ESI mode. The HRMS spectra were recorded in the ESI mode, on a UPLC-MSn Orbitrap Velos-Thermo instrument. The purity of the tested compounds was determined by HPLC (Thermo Scientific HPLC Spectra System) using a column EC 250/4.6 Nucleosil 100-5C18 HD (particle size 5 μm, Macherey-Nagel) under the following conditions: gradient elution 50/50 H_2O_0.1%TFA/CH_3CN_0.1%TFA to 0/100 H_2O_0.1%TFA/CH_3CN_0.1%TFA over 20 min; flow rate: 1.2 mL/min; detection at 216 nm. All the synthesized analogues exhibited a purity >97%, unless otherwise noted. The microwave-assisted experiments were carried out with a CEM Discover 300 W monomode microwave instrument. The melting points were measured on a Büchi 510 Apparatus and are not corrected.

Synthesis of analogues AZ1, 4, 5, 11, 18a–b, 19a–b, 24a–b

N-[(Adamantan-1-yl)methyl]-2-chloro-5-(piperazin-1-ylmethyl) benzamide (AZ1)

To a stirred solution of piperazine (11 mg, 0.13 mmol) in 2 mL anhydrous CH_3OH, a solution of *N*-[(adamantan-1-yl)methyl]-5-(bromomethyl)-2-chlorobenzamide (**3**) (25 mg, 0.06 mmol) in anhydrous CH_3OH was added at 0 C. The mixture was allowed to warm to room temperature, while stirring for 3 h. The solvent was removed *in vacuo* and **AZ1** was obtained by flash column chromatography (CH_2Cl_2/CH_3OH, 90:10 to 20:80) as white sticky solid (29%) HPLC: t_R: 15.4 min, purity 86%; ^1H NMR (600 MHz, CD_3OD): δ = 7.44–7.40 (*m*, 3H, Ar*H*), 3.62 (*s*, 2H, CH_2NCH_2), 3.23–3.21 (*m*, 4H, CH_2-piperazine), 3.07 (*s*, 2H, CH_2NHCO), 2.70 (*bs*, 4H, CH_2-piperazine), 1.99 (*bs*, 3H, *CH*-adamantane), 1.79–1.63 (*m*, 12H, CH_2-adamantane); ^{13}C NMR (150 MHz, CD_3OD): δ = 170.2 (*C*=O), 138.2, 137.9, 132.5, 131.0, 130.7, 130.4, 62.1 (CH_2N-piperazine), 52.6, 50.7, 45.0 (CH_2NH), 41.5, 38.1, 35.7, 29.8; HRMS (ESI): *m/z* calcd for $C_{23}H_{32}ClN_3O+H^+$: 402.2307 $[M+H]^+$, found: 402.2310. Data are in accordance with the literature.[27]

N-[(Adamantan-1-yl)methyl]-2-chloro-5-(nitrooxymethyl) benzamide (4)

N-[(Adamantan-1-yl)methyl]-5-(bromomethyl)-2-chlorobenzamide (**3**) (41 mg) was dissolved in 4 mL of anhydrous CH_3CN, followed by the addition of $AgNO_3$ (20 mg, 0.12 mmol). The suspension formed was heated in the dark at 60 C for 2 h. Upon completion of the reaction, the solvent was removed under reduced pressure and the crude material was purified by flash column chromatography (*n*-hexane/EtOAc 85:15 to 80:20) as white solid (50%). m.p. 118.0–120.0 C; HPLC: t_R: 10.4 min; ^1H NMR (300 MHz, $CDCl_3$): δ = 7.72 (*s*, 1H, Ar*H*), 7.45–7.37 (*m*, 2H, Ar*H*), 6.31 (*s*, 1H, CH_2NH), 5.40 (*s*, 2H, CH_2ONO_2), 3.16 (*d*, *J* = 6.2 Hz, 2H, CH_2NH), 2.00 (*bs*, 3H, *CH*-adamantane), 1.75–1.58 (*s*, 12H, CH_2-adamantane); ^{13}C NMR (75 MHz, $CDCl_3$): δ = 165.9 (*C*=O), 136.1, 131.8, 131.7, 131.5, 131.1, 130.9, 73.3 (CH_2ONO_2), 51.9 (CH_2NH), 40.4, 37.0, 34.0, 28.3; HRMS (ESI): *m/z* calcd for $C_{19}H_{23}ClN_2O_4+H^+$: 379.1419 $[M+H]^+$; found: 379.1419.

ChemMedChem | Full Papers doi.org/10.1002/cmdc.202000303 | Chemistry Europe European Chemical Societies Publishing

N-[(Adamantan-1-yl)methyl]-2-chloro-5-[(methylsulfonyl)thio] methyl)benzamide (5)

N-[(Adamantan-1-yl)methyl]-5-(bromomethyl)-2-chlorobenzamide (**3**) (15 mg, 0.04 mmol) was dissolved in anhydrous DMF (2 mL) and sodium methanesulfonothioate (8 mg, 0.06 mmol) was added. The mixture was heated at 60 C for 5 h. Afterwards, it was washed several times with H_2O and saturated aqueous NaCl solution, and the aqueous layer was extracted with EtOAc. The combined organic layers were dried over Na_2SO_4, filtered, and concentrated under reduced pressure. Flash column chromatography (*n*-hexane/EtOAc 80:20) afforded **5** in 58% yield (white solid, 10 mg). m.p. 125.0–127.0 C; HPLC: t_R: 9.1 min; ^{1}H NMR (600 MHz, $CDCl_3$): δ = 7.73 (*s*, 1H, Ar*H*), 7.39 (*s*, 2H, Ar*H*), 6.27 (*s*, 1H, CH_2NH), 4.35 (*s*, 2H, CH_2S), 3.16 (*d*, *J* = 6.3 Hz, 2H, CH_2NH), 3.10 (*s*, 3H, $S_2O_2CH_3$), 2.00 (*bs*, 3H, *CH*-adamantane), 1.73–1.57 (*m*, 12H, CH_2-adamantane); ^{13}C NMR (150 MHz, $CDCl_3$): δ = 165.9 (*C*=O), 136.1, 134.9, 131.9, 131.3, 131.1, 130.5, 52.0 (SCH_3), 51.4 (CH_2NH), 40.5, 39.7, 37.0, 34.1, 28.4; HRMS (ESI): *m/z* calcd for $C_{20}H_{26}ClNO_3S_2 + H^+$: 428.1115 $[M+H]^+$; found: 428.1116.

1-(Adamantan-1-yl)methyl)-4-(2-chlorophenyl)-1H-1,2,3-triazole (11)

To a stirred solution of [(2-chlorophenyl)ethynyl]trimethylsilane (**10**) (50 mg, 0.24 mmol) in 1.5 mL anhydrous THF, TBAF (0.17 mL, 0.60 mmol) was added. After stirring at room temperature for 1 h, the crude intermediate solution was transferred in a microwave tube. 1-Adamantantylmethyl azide (**9**) (46 mg, 0.24 mmol), sodium ascorbate (29 mg, 0.15 mmol), and $CuSO_4 \cdot 5H_2O$ (18 mg, 0.07 mmol) were added and the mixture was irradiated at 90 C (80 Watt) for 30 min. Purification by flash column chromatography (*n*-hexane/EtOAc 95:5 to 85:15) yielded compound **11** as white sticky solid (12 mg, 15%). HPLC: t_R: 15.1 min; ^{1}H NMR (300 MHz, $CDCl_3$): δ = 8.28 (*dd*, *J* = 7.8, 1.7 Hz, 1H, Ar*H*), 8.10 (*s*, 1H, *CH*-triazole), 7.45 (*dd*, 1H, Ar*H*), 7.37 (*m*, 1H, Ar*H*), 7.26 (*m*, 1H, Ar*H*), 4.09 (*s*, 2H, CH_2NCH), 2.01 (*bs*, 3H, *CH*-adamantane), 1.73–1.56 (*m*, 12H, CH_2-adamantane); ^{13}C NMR (75 MHz, $CDCl_3$): δ = 143.4 (*C*-N), 131.3, 130.3, 129.9, 129.6, 129.0, 127.3, 124.8, 62.5 (CH_2N), 40.4, 36.7, 34.4, 28.2; HRMS (ESI): *m/z* calcd for $C_{19}H_{22}ClN_3 + H^+$: 328.1575 $[M+H]^+$; found: 328.1573.

1-(Adamantan-1-yl) methyl)-4-[2-methylphenyl-5-(nitrooxymethyl)]-1H-1,2,3-triazole (18a)

To a stirred solution of 1-(adamantan-1-yl)methyl)-4-[5-(bromomethyl)-2-methylphenyl]-1*H*-1,2,3-triazole (**17a**) (44 mg, 0.11 mmol) in anhydrous CH_3CN (5 mL), $AgNO_3$ (20 mg, 0.13 mmol) was added and the reaction mixture was heated at 60 C in the dark for 17 h. The resulting mixture was filtered through celite and washed with EtOAc, and the obtained filtrate was extracted with EtOAc. The combined organic layers were then washed with saturated aqueous NaCl solution, dried over Na_2SO_4, filtered, and concentrated *in vacuo* to afford the nitrate ester derivative **18a** as yellow solid (31 mg, 71%). m.p. 115.0–118.0 C; HPLC: t_R: 12.9 min, purity 90%; ^{1}H NMR (300 MHz, $CDCl_3$): δ = 7.88 (*s*, 1H, Ar*H*), 7.59 (*s*, 1H, *CH*-triazole), 7.29 (*s*, 2H, Ar*H*), 5.44 (*s*, 2H, CH_2ONO_2), 4.08 (*s*, 2H, CH_2NCH), 2.48 (*s*, 3H, ArCH_3), 2.01 (*bs*, 3H, *CH*-adamantane), 1.74–1.56 (*m*, 12H, CH_2-adamantane); ^{13}C NMR (75 MHz, $CDCl_3$): δ = 145.6 (*C*-N), 137.0, 131.6, 130.8, 130.1, 129.8, 128.7, 123.5, 74.8 (CH_2ONO_2), 62.4 (CH_2N), 40.4, 36.7, 34.4, 28.2, 21.5; HRMS (ESI): *m/z* calcd for $C_{21}H_{26}N_4O_3 + H^+$: 383.2078 $[M+H]^+$; found: 383.2080.

1-(Adamantan-1-yl) methyl)-4-[2-chlorophenyl-5-(nitrooxymethyl)]-1H-1,2,3-triazole (18b)

Analogue **18b** was prepared following the synthetic procedure for analogue **18a** and was obtained as pale yellow solid without any further purification (24 mg, 35%). m.p. 142.0–144.0 C; HPLC: t_R: 15.3 min; ^{1}H NMR (300 MHz, $CDCl_3$): δ = 8.35–8.34 (*m*, 1H, Ar*H*), 8.12 (*s*, 1H, *CH*-triazole), 7.48 (*d*, *J* = 8.2 Hz, 1H, Ar*H*), 7.30 (*dd*, *J* = 8.2, 2.0 Hz, 1H, Ar*H*), 5.46 (*s*, 2H, CH_2ONO_2), 4.10 (*s*, 2H, CH_2NCH), 2.01 (*bs*, 3H, *CH*-adamantane), 1.74–1.56 (*m*, 12H, CH_2-adamantane); ^{13}C NMR (75 MHz, $CDCl_3$): δ = 142.7 (*C*-N), 132.2, 131.7, 130.8, 130.5, 130.0, 129.1, 124.9, 73.8 (CH_2ONO_2), 62.5 (CH_2N), 40.3, 36.6, 34.4, 28.2; HRMS (ESI): *m/z* calcd for $C_{20}H_{23}ClN_4O_3 + H^+$: 403.1531 $[M+H]^+$; found: 403.1534.

1-(Adamantan-1-yl) methyl)-4-[5-(methylsulfonyl)thio)methyl)-2-methyl-phenyl]-1H-1,2,3-triazole (19a)

To a stirred solution of 1-(adamantan-1-yl)methyl)-4-[5-(bromomethyl)-2-methylphenyl]-1*H*-1,2,3-triazole (**17a**) (64 mg, 0.16 mmol) in 1.2 mL anhydrous DMF, sodium methanesulfonothioate (32 mg, 0.24 mmol) was added and the mixture was heated at 70 C for 5 h. Extraction with EtOAc followed and the combined organic layers were washed with saturated aqueous NaCl solution, dried over Na_2SO_4, filtered, and concentrated under reduced pressure. Flash column chromatography (*n*-hexane/EtOAc 80:20 to 70:30) afforded **19a** as white solid in 51% yield (35 mg). m.p. 124.0–125.0 C; HPLC: t_R: 10.9 min, purity 96%; ^{1}H NMR (300 MHz, $CDCl_3$): δ = 7.86 (*s*, 1H, Ar*H*), 7.58 (*s*, 1H, *CH*-triazole), 7.26–7.25 (*m*, 2H, Ar*H*), 4.38 (*s*, 2H, CH_2S), 4.07 (*s*, 2H, CH_2NCH), 3.02 (*s*, 3H, $S_2O_2CH_3$), 2.45 (*s*, 3H, ArCH_3), 2.00 (*bs*, 3H, *CH*-adamantane), 1.72–1.55 (*m*, 12H, CH_2-adamantane); ^{13}C NMR (75 MHz, $CDCl_3$): δ = 145.5 (*C*-N), 135.5, 132.7, 131.6, 130.9, 129.3, 128.5, 123.4, 62.3 (CH_2N), 51.1 (SCH_3), 40.5, 40.3, 36.5, 34.3, 28.2, 21.3; HRMS (ESI): *m/z* calcd for $C_{22}H_{29}N_3O_2S_2 + H^+$: 432.1774 $[M+H]^+$; found: 432.1774.

1-(Adamantan-1-yl) methyl)-4-[2-chlorophenyl-5-(methylsulfonyl)thio)methyl)]-1H-1,2,3-triazole (19b)

Analogue **19b** was prepared following the synthetic procedure for analogue **19a** and was isolated by flash column chromatography (*n*-hexane/EtOAc 80:20) as white solid (18 mg, 23%). m.p. 139.0–140.0 C; ^{1}H NMR (300 MHz, $CDCl_3$): δ = 8.34–8.33 (*m*, 1H, Ar*H*), 8.12 (*s*, 1H, *CH*-triazole), 7.45 (*d*, *J* = 8.2 Hz, 1H, Ar*H*), 7.31 (*dd*, *J* = 8.2, 2.2 Hz, 1H, Ar*H*), 4.41 (*s*, 2H, CH_2S), 4.09 (*s*, 2H, CH_2NCH), 3.10 (*s*, 3H, $S_2O_2CH_3$), 2.01 (*bs*, 3H, *CH*-adamantane), 1.74–1.56 (*m*, 12H, CH_2-adamantane); ^{13}C NMR (75 MHz, $CDCl_3$): δ = 142.7 (*C*-N), 134.5, 131.1, 131.0, 130.31, 130.27, 129.5, 125.0, 62.5 (CH_2N), 51.4 (SCH_3), 40.4, 40.1, 36.6, 34.4, 28.2; HRMS (ESI): *m/z* calcd for $C_{21}H_{26}ClN_3O_2S_2 + H^+$: 452.1228 $[M+H]^+$; found: 452.1231.

[1-(Adamantan-1-yl) methyl]-3-[[5-[(4-methylbenzoyloxy)-4-phenyl-1,2,5-oxa-diazole-2-oxide]-2-methylphenyl]-1H-1,2,3-triazole (24a)

3-(Hydroxymethyl)-4-phenyl-1,2,5-oxadiazole 2-oxide (**20**) (31 mg, 0.16 mmol) and DMAP (2 mg, 0.008 mmol) were added to a stirred solution of 3-[1-[(adamantan-1-yl)methyl]-1*H*-1,2,3-triazol-4-yl]-4-methylbenzoic acid (**23a**) (28 mg, 0.08 mmol) in anhydrous CH_2Cl_2 (3 mL). DCC (18 mg, 0.09 mmol) was added at 0 C and the reaction mixture was stirred at this temperature for 5 min and then at room temperature for 2 h. Upon completion of the reaction, the mixture

ChemMedChem | Full Papers doi.org/10.1002/cmdc.202000303 | Chemistry Europe European Chemical Societies Publishing

was filtered, and the filtrate was extracted with CH_2Cl_2. The combined organic phases were dried over Na_2SO_4, filtered, and concentrated *in vacuo*. The crude product was purified by flash column chromatography (*n*-hexane/EtOAc 50:50) to afford **24a** (30 mg, 71%) as colorless oil. ^{1}H NMR (300 MHz, $CDCl_3$): δ=8.33 (*s*, 1H, Ar*H*), 7.85 (*d*, *J*=8.0 Hz, 1H, Ar*H*), 7.77–7.74 (*m*, 2H, Ar*H*-furoxan), 7.60 (*s*, 1H, C*H*-triazole), 7.53–7.50 (*m*, 3H, Ar*H*-furoxan), 7.34 (*d*, 1H, Ar*H*), 5.38 (*s*, 2H, OCH_2), 4.09 (*s*, 2H, CH_2NCH), 2.55 (*s*, 3H, ArCH_3), 2.01 (*bs*, 3H, C*H*-adamantane), 1.74–1.55 (*m*, 12H, CH_2-adamantane); ^{13}C NMR (75 MHz, $CDCl_3$): δ=165.6 (*C*=O), 157.0, 145.6, 142.4, 131.5, 130.8, 130.5, 129.6, 129.3, 127.8, 126.7, 126.2, 123.6, 111.5, 62.4 (CH_2O), 54.8 (CH_2N), 40.4, 36.6, 34.4, 28.2; HRMS (ESI): *m/z* calcd for $C_{30}H_{31}N_5O_4+Na^+$: 548.2268 $[M+Na]^+$; found: 548.2270.

1-(Adamantan-1-yl) methyl)-3-[5-[(4-methylbenzoyloxy)-4-phenyl-1,2,5-oxadiazole-2-oxide]-2-chlorophenyl]-1H-1,2,3-triazole (24b)

Analogue **24b** was prepared following the procedure of analogue **24a**. Purification by flash column chromatography (CH_2Cl_2 to CH_2Cl_2/CH_3OH 99:1) afforded **24b** (50 mg, 48%) as white powder. ^{1}H NMR (300 MHz, $CDCl_3$): δ=8.86 (*d*, *J*=2.2 Hz, 1H, Ar*H*), 8.09 (*s*, 1H, C*H*-triazole), 7.85 (*dd*, *J*=8.4, 2.2 Hz, 1H, Ar*H*), 7.76–7.73 (*m*, 2H, Ar*H*-furoxan), 7.53–7.50 (*m*, 4H, Ar*H*, Ar*H*-furoxan), 5.40 (*s*, 2H, OCH_2), 4.09 (*s*, 2H, CH_2NCH), 2.01 (*bs*, 3H, C*H*-adamantane), 1.73–1.55 (*m*, 12H, CH_2-adamantane); ^{13}C NMR (75 MHz, $CDCl_3$): δ=164.8 (*C*=O), 156.9, 142.3, 136.8, 131.5, 131.3, 130.7, 130.2, 129.9, 129.6, 127.9, 127.8, 126.1, 125.0, 111.3, 62.5 (CH_2O), 55.1 (CH_2N), 40.4, 36.6, 34.4, 28.2; HRMS (ESI): *m/z* calcd for $C_{29}H_{28}ClN_5O_4+H^+$: 546.1903 $[M+H]^+$; found: 546.1928.

Synthesis of analogues 30, 35, 42a–b, 43, 49, 53, 56, 60, 61, 63, 64, 67, 68, 70

2-Chloro-N-(3-fluoro-4-(trifluoromethyl) benzyl)-5-(nitrooxymethyl)benzamide (30)

To a stirred solution of 2-chloro-*N*-(3-fluoro-4-(trifluoromethyl) benzyl)-5-(hydroxymethyl) benzamide (**29**) (18 mg, 0.05 mmol) in a mixture of anhydrous CH_2Cl_2/CH_3CN (1:2.5), PPh_3 (13 mg, 0.05 mmol) and NBS (9 mg, 0.05 mmol) were added at 0 C and the mixture was stirred at room temperature for 2 h. $AgNO_3$ (10 mg, 0.06 mmol) was then added and the resulting deep red solution was heated at 50 C in the dark for 24 h. Afterwards, the mixture was filtered through celite and was purified by flash column chromatography (*n*-hexane/EtOAc 70:30) to afford 8 mg (39%) of **30** as white solid. m.p. 114.0–116.0 C; HPLC: t_R: 13.3 min; ^{1}H NMR (600 MHz, $CDCl_3$): δ=7.79 (*s*, 1H, Ar*H*), 7.60 (*t*, *J*=7.6 Hz, 1H, Ar*H*), 7.49–7.43 (*m*, 2H, Ar*H*), 7.27–7.23 (*m*, 2H, Ar*H*), 6.72 (*bs*, 1H, CH_2N*H*CO), 5.42 (*s*, 2H, CH_2ONO_2), 4.72 (*d*, *J*=6.0 Hz, 2H, CH_2NHCO); ^{13}C NMR (75 MHz, $CDCl_3$): δ=165.9 (*C*=O), 144.9, 134.8, 132.2, 132.1, 131.9, 131.2 (*d*, *J*=4.4 Hz), 127.8–127.7 (*m*), 123.2 (*d*, *J*=3.5 Hz), 116.1 (*d*, *J*=21.1 Hz), 73.1 (CH_2ONO_2), 43.5 (CH_2NH); ^{19}F NMR (282 MHz, $CDCl_3$): δ=−61.3 (*d*, *J*=12.4 Hz, *CF*$_3$), −113.5–−113.7 (*m*, *C-F*); HRMS (ESI): *m/z* calcd for $C_{16}H_{11}ClF_4N_2O_4-H^-$: 405.0271 $[M-H]^-$; found: 405.0263.

2-[3-Fluoro-4-(trifluoromethyl) phenyl]-N-[2-methylphenyl-5-(nitrooxymethyl)] acetamide (35)

Analogue **35** was prepared following the synthetic procedure for analogue **30** and was isolated by flash column chromatography (*n*-hexane/EtOAc, 60:40) as white solid (10 mg, 29%). m.p. 162.0–164.0 C; ^{1}H NMR (600 MHz, $CDCl_3$): δ=7.67 (*s*, 1H, Ar*H*), 7.65 (*t*, *J*=7.8 Hz, 1H, Ar*H*), 7.27–7.25 (*m*, 2H, Ar*H*), 7.20 (*d*, *J*=7.7 Hz, 1H, Ar*H*), 7.12 (*d*, *J*=8.1 Hz, 1H, Ar*H*), 6.92 (*bs*, 1H, CH_2CONH), 5.38 (*s*, 2H, CH_2ONO_2), 3.82 (*s*, 2H, CH_2CONH), 2.12 (*s*, 3H, ArCH_3); ^{13}C NMR (75 MHz, CD_3OD): δ=171.2 (*C*=O), 160.9 (*d*, ^1J=256.1 Hz, *C*-F) 144.6, 137.1, 135.6, 132.4, 132.1, 128.3, 127.7, 126.6 (*d*, *J*=3.5 Hz), 118.8 (*d*, *J*=21.2 Hz), 75.6 (CH_2ONO_2), 43.3 (CH_2CO), 17.9; ^{19}F NMR (282 MHz, $CDCl_3$): δ=−61.4 (*t*, *J*=13.1 Hz, *CF*$_3$), −113.0–−113.1 (*m*, *C-F*); HRMS (ESI): *m/z* calcd for $C_{17}H_{14}F_4N_2O_4-H^-$: 385.0817 $[M-H]^-$; found: 385.0806.

1-(3-Fluoro-4-(trifluoromethyl)benzyl)-4-[5-(nitrooxymethyl)-2-methylphenyl)]-1H-1,2,3-triazole (42a)

Analogue **42a** was prepared following the synthetic procedure for analogue **18a** and was obtained by flash column chromatography (*n*-hexane/EtOAc, 95:5 to 70:30) as colorless oil (10 mg, 42%). ^{1}H NMR (300 MHz, $CDCl_3$): δ=7.83 (*s*, 1H, Ar*H*), 7.68–7.61 (*m*, 2H, C*H*-triazole, Ar*H*), 7.30 (*s*, 2H, Ar*H*), 7.19–7.11 (*m*, 2H, Ar*H*), 5.66 (*s*, 2H, CH_2NCH), 5.43 (*s*, 2H, CH_2ONO_2), 2.46 (*s*, 3H, ArCH_3); ^{13}C NMR (75 MHz, $CDCl_3$): δ=160.2 (*d*, ^1J=260.6 Hz, *C*-F), 147.4, 141.6 (*d*, *J*=8.1 Hz), 137.2, 131.7, 130.3 (*d*, *J*=15.5 Hz), 129.8 (*d*, *J*=3.5 Hz), 129.1, 128.32–128.29 (*m*), 122.7 (*dd*, *J*=180.6, 3.9 Hz), 116.4 (*d*, *J*=21.8 Hz), 74.6 (CH_2ONO_2), 53.1 (CH_2N), 21.4; ^{19}F NMR (282 MHz, $CDCl_3$): δ=−61.5 (*d*, *J*=12.5 Hz, *CF*$_3$), −112.31–−112.33 (*m*, C-*F*); HRMS (ESI): *m/z* calcd for $C_{18}H_{14}F_4N_4O_3+H^+$: 411.1075 $[M+H]^+$; found: 411.1072.

1-(3-Fluoro-4-(trifluoromethyl)benzyl)-4-[2-chlorophenyl-5-(nitrooxymethyl)]-1H-1,2,3-triazole (42b)

Analogue **42b** was prepared following the synthetic procedure for analogue **18a** and was obtained by flash column chromatography (*n*-hexane/EtOAc, 80:20) as yellowish solid (14 mg, 82%). m.p. 84.0–85.0 C. ^{1}H NMR (300 MHz, $CDCl_3$): δ=8.34 (*d*, *J*=2.2 Hz, 1H, Ar*H*), 8.23 (*s*, 1H, C*H*-triazole), 7.64 (*t*, *J*=7.6 Hz, 1H, Ar*H*), 7.50–7.47 (*m*, 1H, Ar*H*), 7.33 (*dd*, *J*=8.3, 2.0 Hz, 1H, Ar*H*), 7.18–7.11 (*m*, 2H, Ar*H*), 5.67 (*s*, 2H, CH_2NCH), 5.46 (*s*, 2H, CH_2ONO_2); ^{13}C NMR (75 MHz, $CDCl_3$): δ=160.1 (*d*, ^1J=260.5 Hz, *C*-F), 144.1, 141.3, 132.0 (*d*, *J*=35.9 Hz), 130.8, 130.3, 129.4, 128.3–128.1 (*m*), 123.5, 123.1 (*d*, *J*=3.9 Hz), 116.2 (*dd*, *J*=65.0, 22.4 Hz), 73.6 (CH_2ONO_2), 53.0 (CH_2N); ^{19}F NMR (282 MHz, $CDCl_3$): δ=−61.5 (*d*, *J*=12.5 Hz, *CF*$_3$), −112.3–−112.4 (*m*, C-*F*); HRMS (ESI): *m/z* calcd for $C_{17}H_{11}ClF_4N_4O_3+H^+$: 431.0529 $[M+H]^+$; found: 431.0529.

1-(3-Fluoro-4-(trifluoromethyl)benzyl)-4-[5-(methylsulfonyl)thio) methyl)-2-methylphenyl]-1H-1,2,3-triazole (43)

Analogue **43** was prepared following the synthetic procedure for analogue **19a** and was isolated by flash column chromatography (CH_3OH 0.2% in CH_2Cl_2) as colorless oil (13 mg, 47%). ^{1}H NMR (300 MHz, $CDCl_3$): δ=7.82 (*s*, 1H, Ar*H*), 7.69 (*s*, 1H, C*H*-triazole), 7.64 (*t*, *J*=7.5 Hz, 1H, Ar*H*), 7.31–7.28 (*m*, 2H, Ar*H*), 7.19–7.13 (*m*, 2H, Ar*H*), 5.66 (*s*, 2H, CH_2NCH), 4.39 (*s*, 2H, CH_2S), 3.02 (*s*, 3H, $S_2O_2CH_3$), 2.45 (*s*, 3H, ArCH_3); ^{13}C NMR (150 MHz, $CDCl_3$): δ=160.2 (*d*, ^1J=260.3 Hz, *C*-F), 147.4, 141.6 (*d*, *J*=8.0 Hz), 135.9, 133.0, 131.9, 130.4, 129.6 (*d*, *J*=3.9 Hz), 129.1, 129.0 (*d*, *J*=22.0 Hz), 128.32–128.29 (*m*), 123.4 (*d*, *J*=3.8 Hz), 122.1, 116.4 (*d*, *J*=21.7 Hz), 53.1 (CH_2N), 51.3 (SCH_3), 40.5 (CH_2S), 21.4; ^{19}F NMR (282 MHz, $CDCl_3$): δ=−61.5 (*t*, *J*=10.5 Hz, *CF*$_3$), −112.3–−112.4 (*m*, C-*F*); HRMS (ESI): *m/z* calcd for $C_{19}H_{17}F_4N_3O_2S_2+H^+$: 460.0771 $[M+H]^+$; found: 460.0770.

ChemMedChem | Full Papers doi.org/10.1002/cmdc.202000303 | Chemistry Europe European Chemical Societies Publishing

2-Chloro-5-methyl-N-[1-(4-(3-thioxo-3H-1,2-dithiol-5-yl) phenoxy)methyl)cyclohexyl)methyl]benzamide (49)

A mixture of 5-[4-(1-(aminomethyl)cyclohexyl)methoxy)phenyl]-3*H*-1,2-dithiol-3-thione (**48**) (43 mg, 0.12 mmol), 2-chloro-5-methylbenzoic acid (42 mg, 0.24 mmol), EDC hydrochloride (70 mg, 0.37 mmol), and Et_3N (0.10 mL, 0.73 mmol) in 4 mL of anhydrous CH_2Cl_2 was stirred at room temperature for 20 h. Afterwards, the reaction was washed with H_2O and the aqueous phase was extracted with CH_2Cl_2. The organic layer was washed with saturated aqueous NaCl solution and the combined organic phases were dried over Na_2SO_4, filtered, and concentrated *in vacuo*. The crude material was purified by flash column chromatography (*n*-hexane/EtOAc, 85:15 to 75:25) to afford **49** as orange oil (17 mg, 28%). ^{1}H NMR (600 MHz, $CDCl_3$): δ = 7.59 (*d*, *J* = 8.7 Hz, 2H, Ar*H*), 7.48 (*s*, 1H, Ar*H*), 7.37 (*s*, 1H, *CH*-dithiol-thione), 7.25 (*d*, *J* = 5.6 Hz, 1H, Ar*H*), 7.15 (*d*, *J* = 6.8 Hz, 1H, Ar*H*), 6.97 (*d*, *J* = 8.7 Hz, 2H, Ar*H*), 6.57 (*s*, 1H, CH_2NHCO), 3.92 (*s*, 2H, CH_2O), 3.65 (*d*, *J* = 6.1 Hz, 2H, CH_2NHCO), 2.32 (*s*, 3H, $ArCH_3$), 1.63–1.49 (*m*, 10H, CH_2-cyclohexyl); ^{13}C NMR (150 MHz, $CDCl_3$): δ = 215.3 (*C*=S), 173.0 (*C*-S), 166.8 (*C*=O), 162.4 (*C*-O), 137.4, 134.9, 134.85, 134.79, 132.3, 131.2, 130.1, 128.7, 127.3, 124.6, 115.7, 74.6 (CH_2O), 45.5 (CH_2N), 38.2, 31.2, 26.2, 21.5; HRMS (ESI): *m/z* calcd for $C_{25}H_{26}ClNO_2S_3+H^+$: 504.0887 $[M+H]^+$; found: 504.0890.

2-Chloro-5-(nitrooxymethyl)-N-[1-(4-methylphenyl)cyclohexyl) methyl]benzamide (53)

Analogue **53** was prepared following the synthetic procedure for analogue **30**. Purification by flash column chromatography (*n*-hexane/EtOAc, 70:30) afforded 8 mg of **53** as colorless oil (21%). HPLC: t_R: 11.7 min; ^{1}H NMR (600 MHz, $CDCl_3$): δ = 7.58 (*s*, 1H, Ar*H*), 7.37–7.34 (*m*, 2H, Ar*H*), 7.28 (*d*, *J* = 8.2 Hz, 2H, Ar*H*), 7.17 (*d*, *J* = 7.9 Hz, 2H, Ar*H*), 5.77 (*bs*, 1H, CH_2NHCO), 5.36 (*s*, 2H, CH_2ONO_2), 3.60 (*d*, *J* = 5.9 Hz, 2H, CH_2NHCO), 2.33 (*s*, 3H, $ArCH_3$), 2.13–1.43 (*m*, 10H, CH_2-cyclohexyl); ^{13}C NMR (75 MHz, $CDCl_3$): δ = 165.7 (*C*=O), 141.2, 136.0, 135.9, 131.8, 131.7, 131.4, 130.9, 129.7, 126.9, 73.3 (CH_2ONO_2), 51.2 (CH_2NH), 42.0, 34.2, 26.5, 22.2, 21.0. HRMS (ESI): *m/z* calcd for $C_{22}H_{25}ClN_2O_4+H^+$: 417.1576 $[M+H]^+$; found: 417.1574.

2-Chloro-N-[1-(3-(nitrooxymethyl)phenyl)cyclohexyl)methyl] benzamide (56)

Analogue **56** was prepared following the synthetic procedure for analogue **18a** and was obtained by flash column chromatography (*n*-hexane/EtOAc, 80:20) as white solid (23 mg, 63%). m.p. 76.0–77.0 C; HPLC: t_R: 9.3 min; ^{1}H NMR (600 MHz, $CDCl_3$): δ = 7.53 (*dd*, *J* = 7.6, 1.7 Hz, 1H, Ar*H*), 7.45 (*d*, *J* = 8.3 Hz, 2H, Ar*H*), 7.39 (*d*, *J* = 8.3 Hz, 2H, Ar*H*), 7.33–7.25 (*m*, 3H, Ar*H*), 5.77 (*bs*, 1H, CH_2NHCO), 5.41 (*s*, 2H, CH_2ONO_2), 3.63 (*d*, *J* = 6.3 Hz, 2H, CH_2NHCO), 2.13–1.39 (*m*, 10H, CH_2-cyclohexyl); ^{13}C NMR (150 MHz, $CDCl_3$): δ = 166.4 (*C*=O), 146.1, 135.0, 131.2, 130.4, 130.2, 130.1, 130.0, 129.6, 127.5, 127.0, 74.5 (CH_2ONO_2), 42.5 (CH_2NH), 33.9, 29.7, 26.2, 22.0. HRMS (ESI): *m/z* calcd for $C_{21}H_{23}ClN_2O_4+H^+$: 403.1419 $[M+H]^+$; found: 403.1415.

3-[(2-Chloro-5-methyl)-(4-phenyl-1,2,5-oxadiazole-2-oxide) methyl]benzamide (60)

Analogue **60** was prepared following the synthetic procedure for analogue **49** and was isolated by flash column chromatography (*n*-hexane/EtOAc, 80:20) as white solid (82 mg). m.p. 129.0–130.0 C; HPLC: t_R: 6.97 min; ^{1}H NMR (600 MHz, $CDCl_3$): δ = 7.95–7.94 (*m*, 2H, Ar*H*-furoxan), 7.59–7.57 (*m*, 3H, Ar*H*-furoxan), 7.45 (*s*, 1H, Ar*H*), 7.27 (*d*, *J* = 8.2 Hz, 1H, Ar*H*), 7.18 (*d*, *J* = 7.9 Hz, 1H, Ar*H*), 7.07 (*bs*, 1H, CH_2NHCO), 4.76 (*d*, *J* = 6.1 Hz, 2H, CH_2NHCO), 2.33 (*s*, 3H, $ArCH_3$); ^{13}C NMR (150 MHz, $CDCl_3$): δ = 166.9 (*C*=O), 156.5, 137.4, 133.1, 132.8, 131.4, 130.9, 130.2, 129.5, 128.1, 127.7, 126.1, 113.3, 32.9 (CH_2NH), 20.8; HRMS (ESI): *m/z* calcd for $C_{17}H_{14}ClN_3O_3+H^+$: 344.0796 $[M+H]^+$; found: 344.0794.

4-(2-Chlorophenyl)-1-[(4-phenyl-1,2,5-oxadiazole 2-oxide) methyl]-1H-1,2,3-triazole (61)

Analogue **61** was prepared following the synthetic procedure for analogue **11** using a *t*BuOH/H_2O (1:1) mixture as the reaction solvent. Purification by flash column chromatography (*n*-hexane/EtOAc, 80:20) yielded **61** (37 mg, 45%) as white solid. m.p. 102.0–104.0 C; ^{1}H NMR (600 MHz, $CDCl_3$): δ = 8.48 (*s*, 1H, *CH*-triazole), 8.18 (*d*, *J* = 7.8 Hz, 1H, Ar*H*), 7.92–7.91 (*m*, 2H, Ar*H*-furoxan), 7.60–7.59 (*m*, 3H, Ar*H*-furoxan), 7.45 (*d*, *J* = 8.1 Hz, 1H, Ar*H*), 7.36 (*t*, *J* = 7.5 Hz, 1H, Ar*H*), 7.29 (*t*, *J* = 7.6 Hz, 1H, Ar*H*), 5.64 (*s*, 2H, CH_2N); ^{13}C NMR (150 MHz, $CDCl_3$): δ = 156.7, 145.0, 131.9, 131.6, 130.4, 130.0, 129.8, 129.6, 128.7, 128.3, 127.3, 125.5, 124.5, 111.5, 42.3 (CH_2N); HRMS (ESI): *m/z* calcd for $C_{17}H_{12}ClN_5O_2+H^+$: 354.0752 $[M+H]^+$; found: 354.0752.

N-(3-Fluoro-4-(trifluoromethyl)-3-(4-phenyl-1,2,5-oxadiazole-2-oxide)benzamide (63)

To a stirred solution of 4-carboxy-3-phenyl-1,2,5-oxadiazole 2-oxide (**62**) (10 mg, 0.05 mmol) in 1.5 mL anhydrous DMF, 3-fluoro-4-(trifluoromethyl)phenyl)methanamine (**25**) (19 mg, 0.10 mmol), HATU (37 mg, 0.10 mmol), and anhydrous DIPEA (0.02 mL, 0.10 mmol) were added and the mixture was stirred at room temperature for 22 h. The resulting mixture was washed with H_2O and saturated aqueous NaCl solution, and the aqueous layers were extracted with EtOAc. The combined organic phases were dried over Na_2SO_4, filtered, and concentrated *in vacuo*. The crude material was purified by column chromatography (*n*-hexane/EtOAc, 8:2) to afford **63** (14 mg, 73%) as yellowish solid. m.p. 108.0–110.0 C; ^{1}H NMR (600 MHz, $CDCl_3$): δ = 7.80 (*d*, 2H, Ar*H*-furoxan), 7.57–7.52 (*m*, 2H, Ar*H*, Ar*H*-furoxan), 7.46–7.43 (*m*, 2H, Ar*H*-furoxan), 7.21–7.17 (*m*, 2H, Ar*H*), 6.70 (*bs*, 1H, CH_2NHCO), 4.67 (*d*, *J* = 5.4 Hz, 2H, CH_2NHCO); ^{13}C NMR (150 MHz, $CDCl_3$): δ = 167.8 (*C*=O), 160.1 (*d*, ^1J = 260.1 Hz, *C*-F) 145.7–145.6 (*m*), 133.9, 132.1, 128.9, 127.7–127.6 (*m*), 127.1 (*d*, *J* = 6.3 Hz), 123.1, 120.2, 116.0 (*d*, *J* = 22.2 Hz), 43.2 (CH_2NH); ^{19}F NMR (282 MHz, $CDCl_3$): δ = −61.3 (*t*, *J* = 11.9 Hz, CF_3), −113.7–−113.9 (*m*, C-*F*).

4-Phenyl-(1,2,5-oxadiazole-2-oxide)-3-[N-(1-(4-methylphenyl) cyclohexyl)methyl]benzamide (64)

4-Carboxy-3-phenyl-1,2,5-oxadiazole 2-oxide (**62**) (30 mg, 0.15 mmol) was dissolved in 3 mL anhydrous DMF. HOBt (27 mg, 0.18 mmol) was added and the mixture was stirred at room temperature for 10 min, followed by the addition of EDC hydrochloride (31 mg, 0.16 mmol). After 10 min, amine **51** (30 mg, 0.15 mmol) and Et_3N (0.02 mL, 0.16 mmol) were added and the resulting mixture was stirred at room temperature for 20 h. The mixture was washed several times with saturated aqueous NaCl solution, and the aqueous phase was extracted with EtOAc. The combined organic layers were dried over Na_2SO_4, filtered, and concentrated *in vacuo*. Flash column chromatography (*n*-hexane/EtOAc, 90:10) afforded **64** (15 mg, 26%) as white solid. m.p. 103.0–105.0 C; HPLC: t_R: 10.3 min; ^{1}H NMR (300 MHz, $CDCl_3$): δ = 7.58 (*d*, *J* = 7.4 Hz, 2H, Ar*H*-furoxan), 7.44 (*t*, *J* = 7.4 Hz, 1H, Ar*H*-furoxan), 7.38–7.35 (*m*, 2H, Ar*H*-furoxan), 7.30 (*d*, *J* = 8.1 Hz, 2H, Ar*H*), 7.22 (*d*, *J* = 8.0 Hz, 2H, Ar*H*), 5.68 (*bs*, 1H, CH_2NHCO), 3.55 (*d*, *J* = 6.1 Hz, 2H, CH_2NHCO), 2.36 (*s*, 3H, $ArCH_3$), 2.10–1.38 (*m*, 10H, CH_2-cyclohexyl); ^{13}C NMR (75 MHz, $CDCl_3$): δ = 167.4 (*C*=O), 141.4, 136.0, 134.9,

ChemMedChem | Full Papers doi.org/10.1002/cmdc.202000303 | Chemistry Europe European Chemical Societies Publishing

131.4, 129.7, 128.6, 126.85, 126.82, 50.7 (CH_2NH), 42.4, 34.0, 26.5, 22.2, 21.0.

2-Chloro-N-[1-(3-fluoro-4-(trifluoromethyl)phenyl)cyclohexyl) methyl]benzamide (67)

Analogue **67** was prepared following the synthetic procedure for analogue **64** and was obtained by flash column chromatography (*n*-hexane/EtOAc 80:20) as colorless oil (64 mg, 55%). HPLC: t_R: 11.1 min; ^{1}H NMR (600 MHz, $CDCl_3$): $\delta = 7.60–7.54$ (*m*, 2H, Ar*H*), 7.39–7.24 (*m*, 5H, Ar*H*), 5.83 (*bs*, 1H, CH_2NHCO), 3.63 (*d*, $J = 6.3$ Hz, 2H, CH_2NHCO), 2.12–1.24 (*m*, 10H, CH_2-cyclohexyl); ^{13}C NMR (75 MHz, $CDCl_3$): $\delta = 168.0$ (*C*=O), 141.6, 137.4, 136.5, 134.2, 132.3, 130.9, 130.1, 127.5–127.2 (*m*), 115.8 (*d*, $J = 20.9$ Hz), 50.8 (CH_2NH), 34.0, 26.0, 21.9; HRMS (ESI): *m/z* calcd for $C_{21}H_{20}ClF_4NO + H^+$: 414.1242 $[M+H]^+$; found: 414.1245.

2-Chloro-N-[1-(3-fluoro-4-(trifluoromethyl)phenyl)cyclohexyl) methyl]-5-methylbenzamide (68)

Analogue **68** was prepared following the synthetic procedure for analogue **64** and was obtained by flash column chromatography (*n*-hexane/EtOAc, 90:10 to 80:20) as colorless oil (69 mg, 30%). ^{1}H NMR (600 MHz, $CDCl_3$): $\delta = 7.57$ (*t*, $J = 7.9$ Hz, 1H, Ar*H*), 7.35 (*s*, 1H, Ar*H*), 7.28 (*d*, $J = 8.3$ Hz, 1H, Ar*H*), 7.24–7.19 (*m*, 2H, Ar*H*), 7.12–7.10 (*m*, 1H, Ar*H*), 5.84 (*bs*, 1H, CH_2NHCO), 3.60 (*d*, $J = 6.3$ Hz, 2H, CH_2NHCO), 2.29 (*s*, 3H, $ArCH_3$), 2.11–1.23 (*m*, 10H, CH_2-cyclohexyl); ^{13}C NMR (75 MHz, $CDCl_3$): $\delta = 166.7$ (*C*=O), 141.6, 137.4, 134.4, 132.3, 131.0, 130.1, 127.5–127.2 (*m*), 122.9, 116.0 (*d*, $J = 20.9$ Hz), 50.8 (CH_2N), 43.4, 34.0, 26.2, 22.1, 20.8; HRMS (ESI): *m/z* calcd for $C_{22}H_{22}ClF_4NO + H^+$: 428.1399 $[M+H]^+$; found: 428.1400.

2-Chloro-N-[1-(3-fluoro-4-(trifluoromethyl)phenyl)cyclohexyl) methyl]-5-(nitrooxymethyl)-benzamide (70)

Analogue **70** was prepared following the synthetic procedure for analogue **18a** and was obtained by flash column chromatography (*n*-hexane/EtOAc, 90:10 to 80:20) in 10% yield. HPLC: t_R: 12.1 min, purity 80%; ^{1}H NMR (600 MHz, $CDCl_3$): $\delta = 7.61–7.58$ (*m*, 2H, Ar*H*), 7.39–7.35 (*m*, 2H, Ar*H*), 7.29 (*d*, $J = 8.3$ Hz, 1H, Ar*H*), 7.23 (*s*, 1H, Ar*H*), 5.83 (*bs*, 1H, CH_2NHCO), 5.36 (*s*, 2H, CH_2ONO_2), 3.63 (*d*, $J = 6.3$ Hz, 2H, CH_2NHCO), 2.12–1.25 (*m*, 10H, CH_2-cyclohexyl); ^{13}C NMR (75 MHz, $CDCl_3$): $\delta = 166.9$ (*C*=O), 141.6, 137.4, 134.4, 132.3, 131.0, 130.5, 127.5–127.2 (*m*), 122.9, 116.0 (*d*, $J = 20.9$ Hz), 78.9 (CH_2ONO_2), 50.9 (CH_2NH), 43.2, 33.8, 26.2, 22.9; HRMS (ESI): *m/z* calcd for $C_{22}H_{21}ClF_4N_2O_4 + H^+$: 489.1199 $[M+H]^+$; found: 489.1200.

In silico studies

Ligand-based pharmacophore model generation and validation

The LigandScout 4.0 Advanced software, available from InteLigand, GmbH, Vienna, Austria (http://www.inteligand.com/ligandscout) was used for the generation and validation of the pharmacophore model.[52] A detailed description of the experimental procedure is referred to the section Pharmacophore Model generation and validation in the Supporting Information.

In vitro studies

Two-electrode voltage clamp recordings

cDNA encoding *h*P2X7 was obtained from Life Technologies and cloned into a modified pUC19 vector via Gibson Assembly (New England Biolabs). cRNA was synthesized from linearized plasmids with T7 RNA polymerase using the mMessageMachinekit (Invitrogen/Thermo Fisher). *Xenopus laevis* (NASCO) oocytes were provided by Prof. Dr. Luis Pardo (Max Planck Institute for Experimental Medicine, Göttingen) and injected with 50 nL aliquots of cRNA (0.5 μg/μL). Two-electrode voltage clamp recordings in oocytes were performed 1–10 days after cRNA injection at a holding potential of −70 mV using a Turbo Tec-05X Amplifier (npi electronic, Tamm, Germany). The currents were filtered at 1 kHz and digitized at 200 Hz, using CellWorks E 5.5.1 software. The perfusion medium was automatically switched between ND96 [NaCl (96 mM), KCl (2 mM), $MgCl_2$ (1 mM), $CaCl_2$ (1 mM), HEPES (5 mM)] and ATP (300 μM) containing low divalent buffer in which $MgCl_2$ was omitted and $CaCl_2$ was reduced to 0.5 mM (in order to reduce inhibition of the P2X7 receptor by divalent cations). A fast and reproducible solution exchange (< 300 ms) was achieved using a 50 μL funnel-shaped oocyte chamber combined with a fast solution flow (~150 μL/s) fed through a custom-made manifold mounted immediately above the oocyte. ATP was applied for 2 s in 4 min intervals. After each application, the cell was superfused for 54 s with agonist-free ND96, and the flow was then stopped for 3 min.[53] When the agonist responses were stabilized, the compoundswere mixed from a 10-fold stock into the static bath and preincubated for 3 min. The dose–response curves were fit to the data by the equation $Y = Bottom + (Top-Bottom)/(1 + 10((Log-IC_{50}-X) \times HillSlope))$ using Prism software (GraphPad Software, Inc., Version 8.3.0, San Diego, CA).

Acknowledgments

This work was partly supported by an Alexander S. Onassis Public Benefit Foundation fellowship of D.P. and the Deutsche Forschungsgemeinschaft (DFG, German Research Foundation) – Project-ID: 335447717 – SFB 1328. This work was related to the Ph.D. thesis of D.P. (National Hellenic Research Foundation, Institute of Chemical Biology).

Conflict of Interest

The authors declare no conflict of interest.

Keywords: adamant-1-yl · aryl-cyclohexyl · P2X7 antagonists · structure–activity relationship · two-electrode voltage clamp

[1] R. A. North, *Physiol. Rev.* **2002**, *82*, 1013–1067.
[2] R. Bartlett, L. Stokes, R. Sluyter, *Pharmacol. Rev.* **2014**, *66*, 638–675.
[3] A. Karasawa, K. Michalski, P. Mikhelzon, T. Kawate, *eLife* **2017**, *6*, e31186.
[4] P. Illes, T. M. Khan, P. Rubini, *J. Neurosci.* **2017**, *37*, 7049–7062.
[5] R. Kopp, A. Krautloher, A. Ramírez-Fernández, A. Nicke, *Front. Mol. Neurosci.* **2019**, *12*, 183.
[6] J. S. Wiley, B. J. Gu, *Purinerg. Signal.* **2012**, *8*, 579–586.
[7] G. Burnstock, G. E. Knight, *Int. Rev. Cytol.*, **2004**, pp. 31–304.

ChemMedChem
Full Papers
doi.org/10.1002/cmdc.202000303
Chemistry Europe
European Chemical Societies Publishing

[8] G. Homerin, S. Jawhara, X. Dezitter, D. Baudelet, P. Dufrénoy, B. Rigo, R. Millet, C. Furman, G. Ragé, E. Lipka, et al., *J. Med. Chem.* **2020**, *63*, 2074–2094.
[9] E. M. Jimenez-Mateos, J. Smith, A. Nicke, T. Engel, *Brain Res. Bull.* **2019**, *151*, 153–163.
[10] P. Illes, P. Rubini, L. Huang, Y. Tang, *Expert Opin. Ther. Targets* **2019**, *23*, 165–176.
[11] F. Cao, L. Q. Hu, S. R. Yao, Y. Hu, D. G. Wang, Y. G. Fan, G. X. Pan, S. S. Tao, Q. Zhang, H. F. Pan, et al., *Autoimmun. Rev.* **2019**, *18*, 767–777.
[12] C. Guerra Martinez, *Clin. Exp. Pharmacol. Physiol.* **2019**, *46*, 513–526.
[13] F. Di Virgilio, G. Schmalzing, F. Markwardt, *Trends Cell Biol.* **2018**, *28*, 392–404.
[14] X. Ye, T. Shen, J. Hu, L. Zhang, Y. Zhang, L. Bao, C. Cui, G. Jin, K. Zan, Z. Zhang, et al., *Exp. Neurol.* **2017**, *292*, 46–55.
[15] F. Bauernfeind, A. Ablasser, E. Bartok, S. Kim, J. Schmid-Burgk, T. Cavlar, V. Hornung, *Cell. Mol. Life Sci.* **2011**, *68*, 765–783.
[16] J. Park, Y. Kim, *Expert Opin. Ther. Pat.* **2017**, *27*, 257–267.
[17] J. C. Rech, A. Bhattacharya, M. A. Letavic, B. M. Savall, *Bioorg. Med. Chem. Lett.* **2016**, *26*, 3838–3845.
[18] E. C. Keystone, M. M. Wang, M. Layton, S. Hollis, I. B. McInnes, *Ann. Rheum. Dis.* **2012**, *71*, 1630–1635.
[19] T. C. Stock, B. J. Bloom, N. Wei, S. Ishaq, W. Park, X. Wang, P. Gupta, C. A. Mebus, *J. Rheumatol.* **2012**, *39*, 720–727.
[20] Z. Ali, B. Laurijssens, T. Ostenfeld, S. Mchugh, A. Stylianou, P. Scott-Stevens, L. Hosking, O. Dewit, J. C. Richardson, C. Chen, *Br. J. Clin. Pharmacol.* **2013**, *75*, 197–207.
[21] C. Pereira-Leite, C. Nunes, K. Jamal Sarah, M. Cuccovia Iolanda, S. Reis, *Med. Res. Rev.* **2017**, *37*, 802–859.
[22] B. B. Mishra, V. A. K. Rathinam, G. W. Martens, A. J. Martinot, H. Kornfeld, K. A. Fitzgerald, C. M. Sassetti, *Nat. Immunol.* **2013**, *14*, 52–60.
[23] Z. Lin, N. Altaf, C. Li, M. Chen, L. Pan, D. Wang, L. Xie, Y. Zheng, H. Fu, Y. Han, et al., *BBA-mol. Basis Dis.* **2018**, *1864*, 2890–2900.
[24] M. Castelblanco, J. Lugrin, D. Ehirchiou, S. Nasi, I. Ishii, A. So, F. Martinon, N. Busso, *J. Biol. Chem.* **2018**, *293*, 2546–2557.
[25] E. Hernandez-Cuellar, K. Tsuchiya, H. Hara, R. Fang, S. Sakai, I. Kawamura, S. Akira, M. Mitsuyama, *J. Immunol.* **2012**, *189*, 5113–5117.
[26] H. Zhao, P. Pan, Y. Yang, H. Ge, W. Chen, J. Qu, J. Shi, G. Cui, X. Liu, H. Feng, et al., *J. Neuroinflammation* **2017**, *14*, 163.
[27] M. Furber, L. Alcaraz, J. E. Bent, A. Beyerbach, K. Bowers, M. Braddock, M. V. Caffrey, D. Cladingboel, J. Collington, D. K. Donald, et al., *J. Med. Chem.* **2007**, *50*, 5882–5885.
[28] E. C. N. Wong, T. A. Reekie, E. L. Werry, J. O'Brien-Brown, S. L. Bowyer, M. Kassiou, *Bioorg. Med. Chem. Lett.* **2017**, *27*, 2439–2442.
[29] J. O'Brien-Brown, A. Jackson, T. A. Reekie, M. L. Barron, E. L. Werry, P. Schiavini, M. McDonnell, L. Munoz, S. Wilkinson, B. Noll, et al., *Eur. J. Med. Chem.* **2017**, *130*, 433–439.
[30] N. Mehta, M. Kaur, M. Singh, S. Chand, B. Vyas, P. Silakari, M. S. Bahia, O. Silakari, *Bioorg. Med. Chem.* **2014**, *22*, 54–88.
[31] P. Pevarello, S. Lohmer, C. Llberati, P. Seneci, C. Pesenti, A. Prandi, WO2015118019A1, **2015**.
[32] P. Pevarello, E. Severi, M. Sodano, R. Vitalone, A. Prandi, EP3290417A1, **2016**.
[33] Y. Xiao, S. Karra, A. Goutopoulos, N. T. Morse, S. Zhang, M. Dhanabal, H. Tian, J. Seenisamy, J. Jayadevan, R. Caldwell, et al., *Bioorg. Med. Chem. Lett.* **2019**, *29*, 1660–1664.
[34] C. F. Gelin, A. Bhattacharya, M. A. Letavic, *Prog. Med. Chem.*, Elsevier B. V., **2020**, pp. 63–99.
[35] W. A. Carroll, D. M. Kalvin, A. Perez Medrano, A. S. Florjancic, Y. Wang, D. L. Donnelly-Roberts, M. T. Namovic, G. Grayson, P. Honoré, M. F. Jarvis, *Bioorg. Med. Chem. Lett.* **2007**, *17*, 4044–4048.
[36] D. T. G. Gonzaga, L. B. G. Ferreira, T. E. Moreira Maramaldo Costa, N. L. von Ranke, P. Anastácio Furtado Pacheco, A. P. Sposito Simões, J. C. Arruda, L. P. Dantas, H. R. de Freitas, R. A. de Melo Reis, et al., *Eur. J. Med. Chem.* **2017**, *139*, 698–717.
[37] E. Bonandi, M. S. Christodoulou, G. Fumagalli, D. Perdicchia, G. Rastelli, D. Passarella, *Drug Discovery Today* **2017**, *22*, 1572–1581.
[38] A. Gasco, R. Fruttero, G. Sorba, A. Di Stilo, R. Calvino, *Pure Appl. Chem.* **2004**, *76*, 973–981.
[39] H. Hopf, A. F. E. Mourad, P. G. Jones, *Beilstein J. Org. Chem.* **2010**, *6*, No. 68.
[40] A. Horton, K. Nash, E. Tackie-Yarboi, A. Kostrevski, A. Novak, A. Raghavan, J. Tulsulkar, Q. Alhadidi, N. Wamer, B. Langenderfer, et al., *J. Med. Chem.* **2018**, *61*, 4593–4607.
[41] M. Barniol-Xicota, S. H. Kwak, S. D. Lee, E. Caseley, E. Valverde, L. H. Jiang, Y. C. Kim, S. Vázquez, *Bioorg. Med. Chem. Lett.* **2017**, *27*, 759–763.
[42] S. M. Wilkinson, M. L. Barron, J. O'Brien-Brown, B. Janssen, L. Stokes, E. L. Werry, M. Chishty, K. K. Skarratt, J. A. Ong, D. E. Hibbs, et al., *ACS Chem. Neurosci.* **2017**, *8*, 2374–2380.
[43] H. A. Lundbeck, R. Bakthavatchalam, D. C. Ihle, S. M. Capitosti, D. J. Wustrow, J. Yuan, WO 2009/108551A2, **2009**.
[44] H. Liu, Y. Tian, K. Lee, P. Krishnan, M. K. M. Wang, S. Whelan, E. Mevers, V. Soloveva, B. Dedic, X. Liu, et al., *J. Med. Chem.* **2018**, *61*, 6293–6307.
[45] A. Berkessel, M. Krüger, K. Kreuzer, S. Poll-Wolbeck, WO2015044177A1, **2015**.
[46] D. Pournara, G. A. Heropoulos, M. Koufaki, *Tetrahedron Lett.* **2017**, *58*, 2378–2380.
[47] A. M. Qandil, *Int. J. Mol. Sci.* **2012**, *13*, 17244–17274.
[48] Y. Ling, X. Ye, Z. Zhang, Y. Zhang, Y. Lai, H. Ji, S. Peng, J. Tian, *J. Med. Chem.* **2011**, *54*, 3251–3259.
[49] L. A. Dutra, L. de Almeida, T. G. Passalacqua, J. S. Reis, F. A. E. Torres, I. Martinez, R. G. Peccinini, C. M. Chin, K. Chegaev, S. Guglielmo, et al., *Antimicrob. Agents Chemother.* **2014**, *58*, 4837–4847.
[50] G. F. dos S. Fernandes, P. C. de Souza, L. B. Marino, K. Chegaev, S. Guglielmo, L. Lazzarato, R. Fruttero, M. C. Chung, F. R. Pavan, J. L. dos Santos, *Eur. J. Med. Chem.* **2016**, *123*, 523–531.
[51] A. Nagle, N. S. Gray, Y. Liu, P. Ren, T. Sim, S. You, WO2006124462A2, **2006**.
[52] G. Wolber, T. Langer, *J. Chem. Inf. Model.* **2005**, *45*, 160–169.
[53] S. Dutertre, A. Nicke, R. J. Lewis, *J. Biol. Chem.* **2005**, *280*, 30460–30468.

Manuscript received: May 6, 2020
Revised manuscript received: August 9, 2020
Accepted manuscript online: August 25, 2020
Version of record online: October 16, 2020

ChemMedChem

Supporting Information

Design, Synthesis, and *in vitro* Evaluation of P2X7 Antagonists

Dimitra T. Pournara, Anna Durner, Eftichia Kritsi, Alexios Papakostas, Panagiotis Zoumpoulakis, Annette Nicke,* and Maria Koufaki*

Supporting Information

Experimental procedures

(Adamantan-1-yl)methanamine (1)

To a stirred solution of 1-adamantaneacetic acid (200 mg, 1.03 mmol) in H_2SO_4 (98%) (0.44 mL), $CHCl_3$ (3 mL) and NaN_3 (87 mg, 1.34 mmol) were added. The reaction mixture was heated at 45–50 ºC for 5 h and then, it was allowed to cool to room temperature. Iced water was added and 30 min of stirring followed. CH_2Cl_2 (2 mL) was added and the mixture was basified with NaOH (40%). The mixture was then partitioned between CH_2Cl_2 and H_2O and the organic layer was separated, washed with saturated aqueous NaCl solution, and dried over Na_2SO_4. The organic layer was concentrated under reduced pressure to give (adamantan-1-yl)methanamine (**1**) as colorless oil (146 mg, 86%). ^{1}H NMR (300 MHz, $CDCl_3$): δ = 2.15 (*s*, 2H, C*H*$_2$NH$_2$), 1.82 (*bs*, 3H, C*H*-adamantane), 1.59–1.29 (*m*, 12H, C*H*$_2$-adamantane); ^{13}C NMR (75 MHz, $CDCl_3$): δ = 54.6, 39.7, 36.9, 33.5, 28.1; MS *m/z*: 166.06 (*M*+H$^+$, 100%).

***N*-((Adamantan-1-yl)methyl)-2-chloro-5-methylbenzamide (2)**

To a stirred solution of (adamantan-1-yl)methanamine (**1**) (50 mg, 0.3 mmol) and 2-chloro-5-methylbenzoic acid (103 mg, 0.6 mmol) in anhydrous CH_2Cl_2 (4 mL), EDC hydrochloride (174 mg, 0.9 mmol) and Et_3N (0.25 mL, 1.8 mmol) were added, and the mixture was stirred at ambient temperature for 22 h. H_2O was then added and the mixture was extracted from CH_2Cl_2. The combined organic layers were washed with saturated aqueous NaCl solution, dried over Na_2SO_4, filtered, and concentrated *in vacuo*. The resulting residue was purified by flash column chromatography (CH_2Cl_2 100% to CH_2Cl_2/CH_3OH, 95:5) to afford amide **2** as white solid (60 mg, 63%). ^{1}H NMR (600 MHz, $CDCl_3$): δ = 7.47 (*s*, 1H, Ar*H*), 7.24 (*d*, *J* = 8.2 Hz, 1H, Ar*H*), 7.12 (*d*, *J* = 7.7 Hz, 1H, Ar*H*), 6.31 (*s*, 1H, CH$_2$N*H*), 3.14 (*d*, *J* = 6.3 Hz, 2H, C*H*$_2$NH), 2.32 (*s*, 3H, ArC*H*$_3$), 1.98 (*bs*, 3H, C*H*-adamantane), 1.72–1.56 (*m*, 12H, C*H*$_2$-adamantane); ^{13}C NMR (150 MHz, $CDCl_3$): δ = 166.8, 137.2, 135.0, 132.0, 131.1, 130.0, 127.3, 51.8, 40.4, 37.0, 34.0, 28.3, 20.84, 20.77; MS *m/z*: 657.13/659.02 (2*M*+Na$^+$, 100%).

***N*-[(Adamantan-1-yl)methyl]-5-(bromomethyl)-2-chlorobenzamide (3)**

A stirred solution of amide *N*-((adamantan-1-yl)methyl)-2-chloro-5-methylbenzamide (**2**) (60 mg, 0.19 mmol) in anhydrous $CHCl_3$ (4 mL) was heated at 50 ºC. NBS (35 mg, 0.20 mmol) and AIBN (1 mg, cat.) were added and the mixture was refluxed for 4 h. The solvent was then removed under reduced pressure and the residue was dissolved in Et_2O to remove the NBS excess by filtration. The filtrate was quenched with saturated aqueous NH_4Cl solution and the organic layers were dried over Na_2SO_4, filtered, and concentrated *in vacuo*. The desired compound was obtained by flash column chromatography (*n*-hexane/EtOAc 85:15 to 80:20) as a mixture with the starting material (**2**). ^{1}H NMR (600 MHz, $CDCl_3$): δ = 7.70 (*s*, 1H, Ar*H*), 7.38 (*s*, 2H, Ar*H*), 6.28 (*s*, 1H, CH$_2$N*H*), 4.44 (*s*,

2H, CH_2Br), 3.16 (*s*, 2H, CH_2NH), 2.00 (*bs*, 3H, C*H*-adamantane), 1.74–1.58 (*m*, 12H, CH_2-adamantane); MS *m/z*: 417.14/419.01/421.13 (*M*+Na^+, 15%).

1-Adamantantylmethanol (7)

To a stirred solution of 1-adamantanecarboxylic acid (1.0 g, 5.55 mmol) in EtOH (3.2 mL, 55.5 mmol), H_2SO_4 (98%) (15 drops) was added and the mixture was heated at 70 ºC for 18 h. Upon completion of the reaction, the remaining solvent was concentrated *in vacuo*, and the mixture was partitioned between H_2O and EtOAc. The organic layer was separated, washed with saturated aqueous NaCl solution, and dried over Na_2SO_4. The obtained organic layers were concentrated under reduced pressure to give a residue, which was purified by flash column chromatography (Pet. Ether/EtOAc 90:10) to yield ethyl-adamantane-1-carboxylate (**6**) as colorless oil (1.098 g, 95%). To a stirred suspension of $LiAlH_4$ (342 mg, 9 mmol) in anhydrous THF (20 mL), a solution of ethyl ester **6** (1.041 g, 5 mmol) in 15 mL anhydrous THF was added dropwise at 0 ºC. The mixture was allowed to warm at room temperature and was stirred for 1.5 h. Afterwards, a 1:1 mixture of H_2O/THF was added slowly to neutralize the $LiAlH_4$ excess. The suspension was further diluted with EtOAc and Na_2SO_4 was added. After stirring for 20 min, the mixture was filtered through celite. The concentrated filtrate afforded 1-adamantantylmethanol (**7**) as white solid (810 mg, 97%). ^{1}H NMR (300 MHz, $CDCl_3$): δ = 3.19 (*s*, 2H, CH_2OH), 1.99 (*bs*, 3H, C*H*-adamantane), 1.75–1.50 (*m*, 12H, CH_2-adamantane); ^{13}C NMR (75 MHz, $CDCl_3$): δ = 73.9, 39.0, 37.2, 34.5, 28.2; MS *m/z*: 189.10 (*M*+Na^+, 25%). Data are in accordance with the literature.[1]

1-Adamantantylmethyl methanesulfonate (8)

1-Adamantantylmethanol (**7**) (810 mg, 4.87 mmol) was dissolved in 20 mL CH_2Cl_2. Methanesulfonyl chloride (0.45 mL, 5.85 mmol) was then added at 0 ºC, followed by the dropwise addition of Et_3N (1.02 mL, 7.31 mmol) at the same temperature. After stirring at 0 ºC for 30 min, the mixture was allowed to warm at room temperature and stirring was continued for 21 h. H_2O was then added, and the aqueous layer was extracted with CH_2Cl_2. The organic layers were washed with saturated aqueous NaCl solution and dried over Na_2SO_4. The concentrated residue was used without further purification (1.13 g, 95%). ^{1}H NMR (300 MHz, $CDCl_3$): δ = 3.76 (*s*, 2H, CH_2S), 2.97 (*s*, 3H, SO_3CH_3), 2.00 (*bs*, 3H, C*H*-adamantane), 1.75–1.56 (*m*, 12H, CH_2-adamantane); ^{13}C NMR (75 MHz, $CDCl_3$): δ = 79.3, 38.7, 37.0, 36.7, 33.4, 27.8.; MS *m/z*: 510.54 (2*M*+Na^+, 100%).

1-Adamantantylmethyl azide (9)

1-Adamantantylmethyl methanesulfonate (**8**) (150 mg, 0.61 mmol), NaN_3 (120 mg, 1.84 mmol), and DMF (3 mL) were added in a microwave tube. The applied reaction conditions were: Power: 100 Watt; Reaction time: 1 h; Temperature: 130 ºC. Upon completion of the reaction, the mixture was washed with H_2O and saturated aqueous NaCl solution, and the aqueous layer was extracted with EtOAc. The organic layers were dried over Na_2SO_4, filtered, and concentrated *in vacuo*. The desired azide **9** was isolated without further purification as yellowish oil (84%). ^{1}H NMR (300 MHz,

$CDCl_3$): δ = 2.94 (*bs*, 2H, CH_2N_3), 1.98 (*bs*, 3H, C*H*-adamantane), 1.73–1.62 (*m*, 12H, CH_2-adamantane); ^{13}C NMR (75 MHz, $CDCl_3$): δ = 64.3, 40.0, 36.8, 34.7, 28.2. Data are in accordance with the literature.[2]

[(2-Chlorophenyl)ethynyl]trimethylsilane (10)

A solution of 1-chloro-2-iodobenzene (0.13 mL, 1.05 mmol), CuI (8 mg, 0.04 mmol), and $Pd(PPh_3)_2Cl_2$ (15 mg, 0.02 mmol) was prepared in a mixture of 4 mL Et_3N/anhydrous THF (1:3). Ethynyltrimethylsilane (0.15 mL, 1.05 mmol) was then added and the reaction mixture was heated at 60 ºC for 22 h. Afterwards, it was washed with a saturated aqueous NH_4Cl solution and the aqueous phase was extracted with EtOAc. The combined organic phases were washed with saturated aqueous NaCl solution, dried over Na_2SO_4, filtered, and concentrated *in vacuo*. The crude material was purified by flash column chromatography (Pet. Ether) to afford **10** (140 mg, 64%) as colorless oil. ^{1}H NMR (300 MHz, $CDCl_3$): δ = 7.25 (*dd*, *J* = 7.3, 1.9 Hz, 1H, Ar*H*), 7.14 (*dd*, *J* = 7.7, 1.3 Hz, 1H, Ar*H*), 7.01–6.91 (*m*, 2H, Ar*H*), 0.05 (*s*, 9H, Si(CH_3)$_3$); ^{13}C NMR (300 MHz, $CDCl_3$): δ = 136.3, 133.7, 129.5, 129.3, 126.4, 123.2, 101.4, 100.3, 0.0; MS *m/z*: 207.99 (*M*, 100%).

Methyl 4-methyl-3-[(trimethylsilyl)ethynyl]benzoate (13a)

3-Iodo-4-methylbenzoic acid (500 mg, 1.91 mmol) was dissolved in 2.5 mL CH_3OH and 1.5 mL H_2SO_4 (98%) was added. The mixture was heated under reflux for 24 h. After cooling to room temperature, H_2O was added, and the aqueous phase was extracted with EtOAc. The combined organic phases were dried over Na_2SO_4, filtered, and concentrated *in vacuo*. Methyl 3-iodo-4-methylbenzoate (**12a**) was isolated by flash column chromatography (Pet. Ether/EtOAc 95:5) as colorless oil (518 mg, 98%). Compound **12a** (300 mg, 1.09 mmol), CuI (8 mg, 0.04 mmol), and $Pd(PPh_3)_2Cl_2$ (15 mg, 0.02 mmol) were dissolved in a mixture of Et_3N/anhydrous THF (1:3, 6 mL). Ethynyltrimethylsilane (0.15 mL, 1.09 mmol) was then added. After heating at 60 ºC for 22 h, the reaction mixture was quenched with a saturated aqueous NH_4Cl solution and the aqueous phase was extracted with EtOAc. The combined organic phases were washed with saturated aqueous NaCl solution, dried (Na_2SO_4), filtered, and concentrated *in vacuo*. Flash column chromatography (Pet. Ether/EtOAc 98:2) afforded **13a** (256 mg) in 95% yield as yellowish oil. ^{1}H NMR (600 MHz, $CDCl_3$): δ = 7.83 (*s*, 1H, Ar*H*), 7.59 (*dd*, *J* = 8.0, 1.7 Hz, 1H, Ar*H*), 6.99 (*d*, *J* = 8.1 Hz, 1H, Ar*H*), 3.63 (*s*, 3H, OCH_3), 2.21 (*s*, 3H, ArCH_3), 0.00 (*s*, 9H, Si(CH_3)$_3$); ^{13}C NMR (75 MHz, $CDCl_3$): δ = 166.6, 145.9, 133.5, 129.5, 127.8, 123.5, 118.0, 103.0, 99.4, 52.2, 21.0, 0.1; HRMS (ESI): *m/z* calcd for $C_{14}H_{18}O_2Si$+H^+: 247.1147 [*M*+H]$^+$; found: 247.1148.

Methyl 4-chloro-3-((trimethylsilyl)ethynyl)benzoate (13b)

Compound **13b** (86%, yellowish oil) was prepared following the synthetic procedure for compound **13a**. ^{1}H NMR (300 MHz, $CDCl_3$): δ = 7.85 (*d*, *J* = 2.1 Hz, 1H, Ar*H*), 7.57 (*dd*, *J* = 8.4, 2.1 Hz, 1H, Ar*H*), 7.14 (*d*, *J* = 8.4 Hz, 1H, Ar*H*), 3.61 (*s*, 3H, OCH_3), 0.00 (*s*, 9H, Si(CH_3)$_3$); ^{13}C NMR (75 MHz,

$CDCl_3$): δ = 165.7, 141.1, 134.9, 130.3, 129.6, 128.8, 123.6, 101.6, 100.5, 52.5, 0.0; MS *m/z*: 289.34/292.34 (*M*+Na^+, 25%).

(3-Ethynyl-4-methylphenyl)methanol (15a)

A solution of methyl 4-methyl-3-[(trimethylsilyl)ethynyl]benzoate (**13a**) (100 mg, 0.41 mmol) in anhydrous THF was prepared and added dropwise to a stirred suspension of $LiAlH_4$ (31 mg, 0.81 mmol) in anhydrous THF at 0 ºC. The reaction mixture was allowed to warm at room temperature and stirred for 1 h. The $LiAlH_4$ excess was quenched with a 1:1 mixture of H_2O/THF (2 mL). The reaction mixture was then diluted with 10 mL EtOAc and dried over Na_2SO_4 (stirring for 20 min). Filtration through celite followed to afford, after evaporation, a mixture of 4-methyl-3-[(trimethylsilyl)ethynyl)phenyl]methanol (**14a**) and (3-ethynyl-4-methylphenyl)methanol (**15a**) (70 mg), which was subsequently dissolved in 3 mL CH_3OH. An aqueous solution of 1.0 eq. KOH (15 mg) was added and the mixture was stirred for 15 min. The solvent was evaporated and the residue was extracted with EtOAc. The combined organic phases were washed with saturated aqueous NaCl solution, dried over Na_2SO_4, filtered, and concentrated *in vacuo* to afford pure **15a** as yellowish oil in quantitative yield (64 mg). ^{1}H NMR (300 MHz, $CDCl_3$): δ = 7.43 (*s*, 1H, Ar*H*), 7.22–7.15 (*m*, 2H, Ar*H*), 4.56 (*s*, 2H, CH_2OH), 3.27 (*s*, 1H, C*H*-aryl alkyne), 2.43 (*s*, 3H, ArCH_3); ^{13}C NMR (75 MHz, $CDCl_3$): δ = 140.1, 138.4, 131.1, 129.7, 127.6, 122.1, 82.5, 81.1, 64.5, 20.4; HRMS (ESI): *m/z* calcd for $C_{10}H_{10}$−OH^-: 129.0699 [*M*−OH]$^-$; found: 129.0695.

(4-Chloro-3-ethynylphenyl)methanol (15b)

Compound **15b** was prepared employing methyl 4-chloro-3-((trimethylsilyl)ethynyl)benzoate (**13b**) and following the reduction procedure for compound **15a** with $LiAlH_4$. The product was used without further purification. ^{1}H NMR (300 MHz, $CDCl_3$): δ = 7.22 (*d*, *J* = 2.1 Hz, 1H, Ar*H*), 7.10 (*d*, *J* = 8.3 Hz, 1H, Ar*H*), 6.97 (*dd*, *J* = 8.3, 2.2 Hz, 1H, Ar*H*), 4.32 (*s*, 2H, CH_2OH), 3.13 (*s*, 1H, C*H*-aryl alkyne); ^{13}C NMR (75 MHz, $CDCl_3$): δ = 139.6, 135.2, 132.2, 129.4, 128.4, 122.0, 82.6, 80.3, 63.8; MS *m/z*: 333.32/334.32 (2*M*+H^+, 100%).

1-(Adamantan-1-yl)methyl]-4-[5-(hydroxymethyl)-2-methylphenyl)-1*H*-1,2,3-triazole (16a)

A solution of (3-ethynyl-4-methylphenyl)methanol (**15a**) (64 mg, 0.44 mmol), azide **9** (84 mg, 0.44 mmol), sodium ascorbate (52 mg, 0.26 mmol), and $CuSO_4 \cdot 5H_2O$ (33 mg, 0.13 mmol) in 2 mL of *t*BuOH/H_2O (1:1) was irradiated under the following microwave conditions: Power: 80 Watt; Temperature: 90 ºC; Reaction time: 30 min. A saturated aqueous solution of NH_4Cl was then added and the mixture was extracted with EtOAc. The combined organic layers were washed with saturated aqueous NaCl solution, dried over Na_2SO_4, filtered, and concentrated *in vacuo*. The product was used without further purification (white solid,127 mg, 85%). ^{1}H NMR (600 MHz, $CDCl_3$): δ = 7.73 (*s*, 1H, Ar*H*), 7.56 (*s*, 1H, C*H*-triazole), 7.23–7.19 (*m*, 2H, Ar*H*), 4.65 (*s*, 2H, CH_2OH), 4.03 (*s*, 2H, CH_2NCH), 2.43 (*s*, 3H, ArCH_3), 1.98 (*bs*, 3H, C*H*-adamantane), 1.70–1.52 (*m*, 12H, CH_2-adamantane); ^{13}C NMR (75 MHz, $CDCl_3$): δ = 146.3, 139.1, 134.5, 131.1, 130.4, 130.0, 127.5,

126.7, 123.4, 64.7, 62.3, 40.3, 36.6, 34.3, 28.1, 21.2; HRMS (ESI): *m/z* calcd for $C_{21}H_{27}N_3O+H^+$: 338.2227 $[M+H]^+$; found: 338.2221.

1-(Adamantan-1-yl)methyl)-4-[2-chlorophenyl-5-(hydroxymethyl)]-1*H*-1,2,3-triazole (16b)

Compound **16b** (79%, white solid) was obtained following the synthetic procedure for compound **16a**. ^{1}H NMR (600 MHz, $CDCl_3$): δ = 7.80 (*s*, 1H, Ar*H*), 7.70 (*s*, 1H, C*H*-triazole), 7.02–6.90 (*m*, 2H, Ar*H*), 4.35 (*s*, 2H, CH_2OH), 3.70 (*s*, 2H, CH_2NCH), 3.26 (*bs*, 1H, CH$_2$O*H*), 1.63 (*bs*, 3H, C*H*-adamantane), 1.34–1.15 (*m*, 12H, CH_2-adamantane); ^{13}C NMR (150 MHz, $CDCl_3$): δ = 145.9, 143.2, 132.8, 132.5, 131.6, 130.7, 130.1, 127.4, 66.7, 64.9, 42.8, 39.1, 36.9, 30.7; MS *m/z*: 737.10/739.04 (2*M*+Na^+, 100%).

1-(Adamantan-1-yl)methyl)-4-[5-(bromomethyl)-2-methylphenyl]-1*H*-1,2,3-triazole (17a)

PBr_3 (0.015 mL, 0.17 mmol) was added dropwise at 0 ºC to a stirred solution of compound **16a** (0.17 mmol) in 3 mL anhydrous CH_2Cl_2. The mixture was stirred at 0 ºC for 1 h and at room temperature for 2 h. Upon completion of the reaction, the mixture was poured into ice and extracted with CH_2Cl_2. The combined organic layers were washed with saturated aqueous NaCl solution, dried over Na_2SO_4, filtered, and concentrated *in vacuo*. The isolated white solid product (57 mg, 84%) was used without further purification. ^{1}H NMR (600 MHz, $CDCl_3$): δ = 7.80 (*s*, 1H, Ar*H*), 7.52 (*s*, 1H, C*H*-triazole), 7.22 (*dd*, *J* = 7.9, 2.0 Hz, 1H, Ar*H*), 7.18 (*t*, *J* = 7.4 Hz, 1H, Ar*H*), 4.46 (*s*, 2H, CH_2Br), 4.01 (*s*, 2H, CH_2NCH), 2.39 (*s*, 3H, ArCH_3), 1.94 (*bs*, 3H, C*H*-adamantane), 1.65–1.48 (*m*, 12H, CH_2-adamantane); ^{13}C NMR (150 MHz, $CDCl_3$): δ = 145.7, 135.8, 135.8, 131.6, 130.5, 129.5, 128.8, 123.5, 62.4, 40.4, 36.7, 34.4, 33.5, 28.2, 21.4; HRMS (ESI): *m/z* calcd. for $C_{21}H_{26}BrN_3+H^+$: 400.3027 $[M+H]^+$, found: 400.3025.

1-(Adamantan-1-yl)methyl)-4-[5-(bromomethyl)-2-chlorophenyl]-1*H*-1,2,3-triazole (17b)

Compound **17b** (91%, white solid) was prepared following the synthetic procedure for compound **17a**. ^{1}HNMR (600 MHz, $CDCl_3$): δ = 8.24 (*s*, 1H, Ar*H*), 8.11 (*s*, 1H, C*H*-triazole), 7.17–7.13 (*m*, 2H, Ar*H*), 4.26 (*s*, 2H, CH_2Br), 4.00 (*s*, 2H, CH_2NCH), 1.74 (*bs*, 3H, C*H*-adamantane), 1.44–1.28 (*m*, 12H, CH_2-adamantane); ^{13}C NMR (150 MHz, $CDCl_3$): δ = 140.4, 137.8, 131.5, 131.34, 131.32, 131.1, 126.9, 125.4, 63.9, 40.1, 36.4, 34.5, 31.8, 28.0; MS *m/z*: 420.18/422.23 (*M*+H^+, 5%).

3-(Hydroxymethyl)-4-phenyl-1,2,5-oxadiazole 2-oxide (20)

Cinnamyl alcohol (0.45 g, 3.35 mmol) was mixed with glacial CH_3COOH (2 mL). A saturated aqueous solution of $NaNO_2$ (694 mg, 10.0 mmol) was added dropwise at 0 ºC, so that the temperature does not exceed 70 ºC. The reaction mixture was stirred at room temperature for 24 h. H_2O was added, and the organic layer was extracted with Et_2O. The combined organic layers were washed with saturated aqueous NaCl solution, dried (Na_2SO_4), and concentrated *in vacuo*. Flash column chromatography (Pet. Ether/EtOAc 90:10) afforded **20** (325 mg, 50%) as yellow oil. ^{1}H NMR (300 MHz, $CDCl_3$): δ = 7.83–7.80 (*m*, 2H, Ar*H*), 7.58–7.53 (*m*, 3H, Ar*H*), 4.76 (*s*, 2H, CH_2OH);

^{13}C NMR (75 MHz, $CDCl_3$): δ = 157.2, 131.3, 129.3, 127.6, 126.3, 115.1, 52.1. Data are in accordance with literature data.[3]

Methyl 3-ethynyl-4-methylbenzoate (21a)

Methyl 4-methyl-3-[(trimethylsilyl)ethynyl]benzoate (**13a**) (93 mg, 0.38 mmol) was dissolved in 3 mL CH_3OH. An aqueous solution of KOH (21 mg in 1 mL H_2O) was added and the reaction mixture was stirred at room temperature for 30 min. CH_3OH was evaporated, H_2O was added, and the aqueous phase was extracted with EtOAc. The combined organic phases were washed with saturated aqueous NaCl solution, dried (Na_2SO_4), filtered, and concentrated *in vacuo*. Compound **21a** was obtained as orange solid in 98% yield (63 mg). ^{1}H NMR (300 MHz, $CDCl_3$): δ = 8.13 (*s*, 1H, Ar*H*), 7.89 (*d*, *J* = 7.9 Hz, 1H, Ar*H*), 7.27 (*d*, *J* = 7.9 Hz, 1H, Ar*H*), 3.90 (*s*, 3H, OCH_3), 3.31 (*s*, 1H, C*H*-aryl alkyne), 2.49 (*s*, 3H, ArCH_3); ^{13}C NMR (75 MHz, $CDCl_3$): δ = 166.5, 146.1, 133.8, 129.8, 129.7, 128.0, 122.5, 82.0, 81.6, 52.2, 21.0; MS *m/z*: 349.37 (2*M*+H^+, 10%).

Methyl 4-chloro-3-ethynylbenzoate (21b)

Compound **21b** was obtained as white solid in 70% yield, following the synthetic procedure for compound **21a**. ^{1}H NMR (300 MHz, $CDCl_3$): δ = 8.17 (*d*, *J* = 1.9 Hz 1H, Ar*H*), 7.91 (*dd*, *J* = 8.4, 2.0 Hz, 1H, Ar*H*), 7.46 (*d*, *J* = 8.4 Hz, 1H, Ar*H*), 3.90 (*s*, 3H, OCH_3), 3.42 (*s*, 1H, C*H*-aryl alkyne); ^{13}C NMR (75 MHz, $CDCl_3$): δ = 165.6, 141.1, 135.2, 130.7, 129.6, 128.9, 122.6, 83.5, 79.4, 52.6; MS *m/z*: 392.75/393.73 (2*M*+Na^+, 100%).

Methyl 3-(1-(-adamantan-1-yl)methyl)-1*H*-1,2,3-triazol-4-yl)-4-methylbenzoate (22a)

A solution of methyl 3-ethynyl-4-methylbenzoate (**21a**) (64 mg, 0.36 mmol), azide **9** (69 mg, 0.36 mmol), sodium ascorbate (43 mg, 0.22 mmol), and $CuSO_4 \cdot 5H_2O$ (27 mg, 0.11 mmol) was irradiated in a 2 mL mixture of *t*BuOH/H_2O (1:1) under microwave conditions (Power: 80 Watt; Temperature: 90 ºC; Reaction time: 30 min). A saturated aqueous solution of NH_4Cl was then added and the mixture was extracted with EtOAc. The combined organic layers were washed with saturated aqueous NaCl solution, dried over Na_2SO_4, filtered, and concentrated *in vacuo*. The product, a yellowish oil (120 mg, 91%), was used without further purification. ^{1}H NMR (300 MHz, $CDCl_3$): δ = 8.37 (*s*, 1H, Ar*H*), 7.88 (*dd*, *J* = 8.0, 1.6 Hz, 1H, Ar*H*), 7.62 (*s*, 1H, C*H*-triazole), 7.30 (*d*, *J* = 8.0 Hz, 1H, Ar*H*), 4.05 (*s*, 2H, CH_2NCH), 3.87 (*s*, 3H, OCH_3), 2.51 (*s*, 3H, ArCH_3), 1.97 (*bs*, 3H, C*H*-adamantane), 1.70–1.52 (*m*, 12H, CH_2-adamantane); ^{13}C NMR (75 MHz, $CDCl_3$): δ = 167.0, 145.8, 141.2, 131.2, 130.4, 130.2, 129.0, 128.2, 123.5, 64.4, 52.1, 40.4, 36.6, 34.3, 28.2, 21.8; HRMS (ESI): *m/z* calcd for $C_{22}H_{27}N_3O_2$+H^+: 366.2176 [*M*+H]$^+$; found: 366.2170.

Methyl 3-(1-(adamantan-1-yl)methyl)-1*H*-1,2,3-triazol-4-yl)-4-chlorobenzoate (22b)

Compound **22b** was obtained as brown solid (151 mg, 93%), following the synthetic procedure for compound **22a**. ^{1}H NMR (300 MHz, $CDCl_3$): δ = 8.81 (*d*, *J* = 2.2 Hz, 1H, Ar*H*), 8.03 (*s*, 1H, C*H*-triazole), 7.82 (*dd*, *J* = 8.4, 2.2 Hz, 1H, Ar*H*), 7.42 (*d*, *J* = 8.4 Hz, 1H, Ar*H*), 4.02 (*s*, 2H, CH_2NCH),

3.83 (*s*, 3H, OCH_3), 1.90 (*bs*, 3H, C*H*-adamantane), 1.70–1.52 (*m*, 12H, CH_2-adamantane); ^{13}C NMR (75 MHz, $CDCl_3$): δ = 166.0, 142.5, 135.8, 131.0, 130.4, 129.7, 129.6, 129.3, 124.9, 62.3, 52.2, 40.2, 36.5, 34.3, 28.1; MS *m/z*: 770.15/772.83 ($2M^+$, 100%).

3-[1-[(Adamantan-1-yl)methyl]-1*H*-1,2,3-triazol-4-yl]-4-methylbenzoic acid (23a)

To a stirred solution of compound **22a** (56 mg, 0.15 mmol) in THF (3 mL), an aqueous solution of LiOH (2 N) (0.05 mL, 0.61 mmol) was added and the mixture was stirred at room temperature for 24 h. The solvent was then evaporated and the pH was adjusted to 3.0 with HCl (10%). The aqueous layer was extracted with EtOAc, dried over Na_2SO_4, and concentrated *in vacuo*. A yellowish solid was isolated in 87% yield (46 mg). ^{1}H NMR (600 MHz, acetone-d_6): δ = 8.52 (*s*, 1H, Ar*H*), 8.21 (*s*, 1H, C*H*-triazole), 7.91 (*dd*, *J* = 7.9, 1.4 Hz, 1H, Ar*H*), 7.43 (*d*, *J* = 7.9 Hz, 1H, Ar*H*), 4.18 (*s*, 2H, CH_2NCH), 2.58 (*s*, 3H, ArCH_3), 1.99 (*bs*, 3H, C*H*-adamantane), 1.74–1.62 (*m*, 12H, CH_2-adamantane); ^{13}C NMR (150 MHz, acetone-d_6): δ = 167.5, 145.7, 141.6, 132.0, 131.9, 130.6, 129.5, 129.4, 125.3, 62.3, 40.9, 37.3, 34.9, 29.1, 21.9; MS *m/z*: 350.30 ($M-H^-$, 100%).

3-(1-(Adamantan-1-yl)methyl)-1*H*-1,2,3-triazol-4-yl)-4-chlorobenzoic acid (23b)

Compound **23b** (yellowish solid, 95%) was prepared following the synthetic procedure for compound **23a**. m.p. 227.0–230.0 ºC; ^{1}H NMR (300 MHz, acetone-d_6): δ = 8.92 (*s*, 1H, Ar*H*), 8.52 (*s*, 1H, C*H*-triazole), 7.98 (*dd*, *J* = 8.4, 2.1 Hz, 1H, Ar*H*), 7.67 (*d*, *J* = 8.3 Hz, 1H, Ar*H*), 4.22 (*s*, 2H, CH_2NCH), 1.98–1.61 (*m*, 15H, C*H*- and CH_2-adamantane); ^{13}C NMR (75 MHz, acetone-d_6): δ = 166.8, 142.8, 136.2, 132.8, 131.8, 131.6, 131.3, 130.6, 129.5, 126.5, 62.4, 40.9, 37.4, 35.0, 29.2; HRMS (ESI): *m/z* calcd for $C_{20}H_{21}ClN_3O_2+H^+$: 372.1473 [*M*+H]$^+$, found: 372.1472.

(3-Fluoro-4-(trifluoromethyl)phenyl)methanamine (25)

To a stirred solution of 2-(3-fluoro-4-(trifluoromethyl)phenyl)acetic acid (100 mg, 0.45 mmol) in H_2SO_4 (0.19 mL), $CHCl_3$ (3 mL) and NaN_3 (38 mg, 1.3 mmol) were added and the mixture was heated at 50 ºC for 5 h. After cooling to room temperature, iced H_2O (1 mL) was added and the mixture was stirred for 30 min. The pH was adjusted to basic with an aqueous NaOH solution (40%) and the aqueous layer was extracted with CH_2Cl_2. The obtained organic phases were dried over Na_2SO_4, filtered, and concentrated *in vacuo* to afford **25** as colorless oil (50 mg, 50%), which was used without further purification. ^{1}H NMR (600 MHz, $CDCl_3$): δ = 7.55 (*t*, *J* = 7.7 Hz, 1H, Ar*H*), 7.21–7.18 (*m*, 2H, Ar*H*), 3.94 (*s*, 2H, CH_2NH_2), 1.78 (*bs*, 2H, CH_2NH_2); ^{13}C NMR (75 MHz, $CDCl_3$): δ = 160.1 (*d*, ^1J = 256.5 Hz, *C*–F), 150.5 (*d*, *J* = 9.1 Hz), 127.3–127.2 (*m*), 123.3 (*d*, *J* = 3.7 Hz), 122.5 (*d*, *J* = 3.8 Hz), 117.1–116.5 (*m*), 115.3 (*d*, *J* = 20.8 Hz), 45.6; MS *m/z*: 193.96 (*M*+H$^+$, 69%).

Methyl 5-(bromomethyl)-2-chlorobenzoate (27)

To a stirred solution of 2-chloro-5-methylbenzoic acid (400 mg, 2.3 mmol) in CH_3OH (1 mL, 23 mmol), H_2SO_4 (98%) (20 drops) was added and the mixture was heated at 70 ºC for 18 h. H_2O was then added and the aqueous layer was extracted with EtOAc. The collected organic layers were

washed with saturated aqueous NaCl solution, dried (Na_2SO_4), filtered, and concentrated *in vacuo*. Flash column chromatography (*n*-hexane/EtOAc, 95:5) afforded methyl 2-chloro-5-methylbenzoate (**26**) as colorless fluid (324 mg, 77%). Compound **27** (colorless oil, 53%) was synthesized following the synthetic procedure for analogue **3**. ^{1}H NMR (300 MHz, $CDCl_3$): δ = 7.84 (*s*, 1H, Ar*H*), 7.41 (*s*, 2H, Ar*H*), 4.44 (*s*, 2H, CH_2Br), 3.92 (*s*, 3H, OCH_3); ^{13}C NMR (75 MHz, $CDCl_3$): δ = 165.5, 136.7, 133.8, 133.1, 131.9, 131.6, 130.3, 52.7, 31.5; MS *m/z*: 284.79/286.88 (*M*+Na^+, 100%).

2-Chloro-5-(hydroxymethyl)benzoic acid (28)

To a stirred solution of methyl 5-(bromomethyl)-2-chlorobenzoate (**27**) (215 mg, 0.82 mmol) in THF (2 mL), a 2 N solution of LiOH (0.82 mL, 1.63 mmol) was added and the mixture was heated at 40 ºC for 20 h. The solvent was then evaporated, and the residue was acidified with HCl (10%) (pH ~2–3). The subsequent extraction with EtOAc and evaporation of the solvent afforded **28** as white solid (151 mg, 92%). ^{1}H NMR (300 MHz, CD_3OD): δ = 7.83 (*s*, 1H, Ar*H*), 7.48–7.45 (*m*, 2H, Ar*H*), 4.89 (*bs*, 1H, COO*H*), 4.61 (*s*, 2H, CH_2OH); ^{13}C NMR (75 MHz, CD_3OD): δ = 168.9, 138.7, 132.8, 132.0, 131.8, 131.4, 130.5, 63.9; MS *m/z*: 184.89 (*M*−H^-, 68%).

2-Chloro-*N*-(3-fluoro-4-(trifluoromethyl)benzyl)-5-(hydroxymethyl)benzamide (29)

A solution of (3-fluoro-4-(trifluoromethyl)phenyl)methanamine (**25**) (32 mg, 0.17 mmol) and 2-chloro-5-(hydroxymethyl)benzoic acid (**28**) (22 mg, 0.12 mmol) was prepared in 3 mL of anhydrous DMF, followed by the addition of HATU (67 mg, 0.18 mmol) and 0.13 mL anhydrous DIPEA (0.77 mmol). The resulting solution was stirred at ambient temperature for 72 h. H_2O was then added and the organic layer was extracted with EtOAc. The combined organic layers were washed several times with saturated aqueous NaCl solution, dried (Na_2SO_4), filtered, and concentrated *in vacuo*. Flash column chromatography (*n*-hexane/EtOAc, 60:40) yielded 18 mg of a colorless oil (41%). ^{1}H NMR (600 MHz, $CDCl_3$): δ = 7.67 (*t*, *J* = 7.7 Hz, 1H, Ar*H*), 7.39–7.37 (*m*, 2H, Ar*H*), 7.30 (*s*, 1H, Ar*H*), 7.21 (*d*, *J* = 8.0 Hz, 1H, Ar*H*), 7.14 (*d*, *J* = 7.8 Hz, 1H, Ar*H*), 4.55 (*s*, 2H, CH_2OH), 3.84 (*s*, 2H, CH_2NHCO); HRMS (ESI): *m/z* calcd for $C_{16}H_{12}ClF_4NO_2$+H^+: 362.0550 [*M*+H]$^+$; found: 362.0548.

Methyl 3-amino-4-methylbenzoate (32)

To a stirred solution of 4-methyl-3-nitrobenzoic acid (1.0 g, 5.5 mmol) in 3 mL CH_3OH, H_2SO_4 (1.5 mL) was added and the reaction mixture was refluxed for 18 h. The mixture was then partitioned between H_2O and EtOAc and the combined organic layers were washed with saturated aqueous NaCl solution, dried over Na_2SO_4, filtered, and concentrated *in vacuo*. The obtained methyl 4-methyl-3-nitrobenzoate (**31**) (200 mg, 1.02 mmol) (white solid, 94%), which was not further purified, was then dissolved in 5 mL EtOH. Fe(0) (electrolytic powder) (229 mg, 4.10 mmol) was added and the suspension was refluxed. At this temperature, a saturated aqueous NH_4Cl (548 mg, 10.2 mmol) solution was added dropwise. The color of the solution turned to deep red and the reflux continued for 3 h. Upon completion of the reaction, the mixture was filtered through celite. The concentrated filtrate was extracted with EtOAc and H_2O and the organic layer was washed with saturated aqueous

NaCl solution, dried (Na_2SO_4), and concentrated *in vacuo*. The mixture was purified by flash column chromatography (*n*-hexane/EtOAc, 85:15) to afford **32** (145 mg, 86%) as a white solid. ^{1}H NMR (600 MHz, $CDCl_3$): δ = 7.37–7.33 (*m*, 2H, Ar*H*), 7.08 (*d*, *J* = 7.7 Hz, 1H, Ar*H*), 3.86 (*s*, 3H, OCH_3), 3.70 (*bs*, 2H, ArNH_2), 2.18 (*s*, 3H, ArCH_3); ^{13}C NMR (150 MHz, $CDCl_3$): δ = 167.4, 144.7, 130.4, 128.9, 127.7, 119.8, 115.6, 51.9, 17.6; MS *m/z*: 166.06 (*M*+H$^+$, 100%).

(3-Amino-4-methylphenyl)methanol (33)

Methyl 3-amino-4-methylbenzoate (**32**) (145 mg, 0.88 mmol) was dissolved in 5 mL anhydrous THF and was added dropwise to a stirred suspension of $LiAlH_4$ (67 mg, 1.76 mmol) in anhydrous THF (5 mL) at 0 ºC. The mixture was allowed to warm to room temperature and stirred for 1.5 h. The $LiAlH_4$ excess was neutralized with THF/H_2O (1:1) and the mixture was diluted with EtOAc. Na_2SO_4 was added and after stirring for 30 min, the mixture was filtered through celite. Evaporation of the solvent afforded compound **33** (white solid, 100%), which was used in the next step without further purification. ^{1}H NMR (600 MHz, $CDCl_3$): δ = 7.03 (*d*, *J* = 7.8 Hz, 1H, Ar*H*), 6.69–6.68 (*m*, 2H, Ar*H*), 4.57 (*s*, 2H, CH_2OH), 2.96 (*bs*, 1H, CH_2O*H*), 2.16 (*s*, 3H, ArCH_3); ^{13}C NMR (150 MHz, $CDCl_3$): δ = 144.8, 140.0, 130.7, 121.9, 117.4, 113.7, 65.5, 17.2; MS *m/z*: 138.02 (2*M*+H$^+$, 100%).

2-(3-Fluoro-4-(trifluoromethyl)phenyl)-*N*-(5-(hydroxymethyl)-2-methylphenyl)acetamide (34)

Compound **34** was obtained as white solid in 67% yield, following the synthetic procedure for analogue **29**, while heating at 70 ºC for 15 h. m.p. 188.0–189.0 ºC; ^{1}H NMR (600 MHz, CD_3OD): δ = 7.67 (*t*, *J* = 7.7 Hz, 1H, Ar*H*), 7.39–7.37 (*m*, 2H, Ar*H*), 7.30 (*s*, 1H, Ar*H*), 7.21 (*d*, *J* = 8.0 Hz, 1H, Ar*H*), 7.14 (*d*, *J* = 7.8 Hz, 1H, Ar*H*), 4.55 (*s*, 2H, CH_2OH), 3.84 (*s*, 2H, CH_2CONH), 2.19 (*s*, 3H, ArCH_3); ^{13}C NMR (75 MHz, DMSO-d_6): δ = 167.9 (*C*=O), 158.7 (*d*, ^{1}*J* = 250.3 Hz, *C*–F), 144.6–144.5 (*d*, *J* = 8.1 Hz), 140.5, 135.8, 130.2, 130.1, 127.2 (*d*, *J* = 5.4 Hz), 126.0 (*d*, *J* = 3.2 Hz), 123.6 (*d*, *J* = 21.4 Hz), 117.8 (*d*, *J* = 20.4 Hz), 114.6, 62.6, 42.1, 17.6; ^{19}F NMR (282 MHz, CD_3OD): δ = −62.7 (*d*, *J* = 12.7 Hz, CF_3), −117.1–−117.2 (*m*, C–*F*); HRMS (ESI): *m/z* calcd for $C_{17}H_{15}F_4NO_2$+H$^+$: 342.1112 [*M*+H]$^+$; found: 342.1103.

(3-Fluoro-4-(trifluoromethyl)phenyl)methanol (37)

To a stirred solution of 3-fluoro-4-(trifluoromethyl)benzoic acid (0.5 g, 2.4 mmol) in 1 mL CH_3OH, H_2SO_4 (98%) (15 drops) was added and the mixture was heated at 60 ºC for 24 h. Upon completion of the reaction, H_2O was added, and the aqueous phase was extracted with EtOAc. The combined organic layers were washed with saturated aqueous NaCl solution, dried over Na_2SO_4, filtered, and concentrated *in vacuo* to afford **36** (440 mg, 83%) as colorless oil without further purification. A solution of methyl 3-fluoro-4-(trifluoromethyl)benzoate (**36**) (440 mg, 1.98 mmol) in anhydrous THF (5 mL) was added dropwise at 0 ºC to a suspension of $LiAlH_4$ (150 mg, 3.96 mmol) in anhydrous THF (5 mL). The reaction mixture was stirred at 0 ºC for 30 min and at ambient temperature for 1 h. The $LiAlH_4$ excess was neutralized with a mixture of H_2O in THF (1:1). The mixture was then diluted with EtOAc, dried over Na_2SO_4, and filtered through celite. Compound **37** was obtained after solvent

evaporation as colorless oil (315 mg, 82%) and was used without further purification. ^{1}H NMR (300 MHz, $CDCl_3$): δ = 7.58 (*t*, *J* = 7.7 Hz, 1H, Ar*H*), 7.24–7.20 (*m*, 2H, Ar*H*), 4.76 (*s*, 2H, CH_2OH); ^{13}C NMR (75 MHz, $CDCl_3$): δ = 160.0 (*d*, ^1J = 252.4 Hz, *C*–F), 148.3 (*d*, *J* = 7.3 Hz), 127.3–127.1 (*m*), 122.7 (*dd*, *J* = 65.0, 3.4 Hz), 121.6, 117.4–115.8 (*m*), 114.6 (*d*, *J* = 21.1 Hz), 63.5.

4-(Bromomethyl)-2-fluoro-1-(trifluoromethyl)benzene (38)

Compound **38** (colorless liquid, 26%) was synthesized following the synthetic procedure for compound **17a**. ^{1}H NMR (300 MHz, $CDCl_3$): δ = 7.58 (*t*, *J* = 7.7 Hz, 1H, Ar*H*), 7.27–7.23 (*m*, 2H, Ar*H*), 4.45 (*s*, 2H, CH_2Br); ^{13}C NMR (75 MHz, $CDCl_3$): δ = 160.0 (*d*, ^1J = 257.1 Hz, *C*–F), 144.5 (*d*, *J* = 8.1 Hz), 131.9–131.7 (*m*), 127.8–127.6 (*m*), 124.6 (*d*, *J* = 3.7 Hz), 117.5 (*d*, *J* = 21.4 Hz), 116.7–115.6 (*m*), 30.8; MS *m/z*: 255.96/256.96 (M^+, 25%).

4-(Azidomethyl)-2-fluoro-1-(trifluoromethyl)benzene (39)

To a stirred solution of 4-(bromomethyl)-2-fluoro-1-(trifluoromethyl)benzene (**38**) (118 mg, 0.46 mmol) in anhydrous DMF (3 mL), NaN_3 (298 mg, 4.6 mmol) was added and the reaction mixture was heated at 40 ºC for 3 h. H_2O was then added and the mixture was extracted with EtOAc. The combined organic layers were washed with saturated aqueous NaCl solution, dried over Na_2SO_4, filtered, and concentrated *in vacuo* to afford **39** (123 mg, 50%) as colorless oil without further purification. ^{1}H NMR (600 MHz, $CDCl_3$): δ = 7.62 (*t*, *J* = 7.7 Hz, 1H, Ar*H*), 7.21–7.18 (*m*, 2H, Ar*H*), 4.44 (*s*, 2H, CH_2N_3); ^{13}C NMR (75 MHz, $CDCl_3$): δ = 160.0 (*d*, ^1J = 255.0 Hz, *C*–F), 143.0 (*d*, *J* = 7.5 Hz), 131.8–130.7 (*m*), 127.6–127.4 (*m*), 124.2–123.9 (*m*), 123.2 (*d*, *J* = 3.7 Hz), 116.1 (*d*, *J* = 21.3 Hz), 53.3.

1-(3-Fluoro-4-(trifluoromethyl)benzyl)-4-[5-(hydroxymethyl)-2-methylphenyl]-1*H*-1,2,3-triazole (40a)

Compound **40a** was obtained in 52% yield (colorless oil) following the microwave assisted synthetic procedure for analogue **16a**. ^{1}H NMR (300 MHz, $CDCl_3$): δ = 7.69–7.58 (*m*, 3H, C*H*-triazole, Ar*H*), 7.24–7.06 (*m*, 4H, Ar*H*), 5.61 (*s*, 2H, CH_2OH), 4.63 (*s*, 2H, CH_2NCH), 2.78 (*bs*, 1H, CH$_2$O*H*), 2.38 (*s*, 3H, ArCH_3); ^{13}C NMR (75 MHz, $CDCl_3$): δ = 160.0 (*d*, ^1J = 260.4 Hz, *C*–F), 147.9, 141.8 (*d*, *J* = 7.5 Hz), 139.1, 134.7, 132.2, 131.2, 129.4, 128.2–128.0 (*m*), 127.5, 127.1, 127.0 (*d*, *J* = 9.2 Hz), 123.3 (*d*, *J* = 3.8 Hz), 122.0 (*d*, *J* = 17.9 Hz), 116.4–114.5 (*m*), 64.7, 52.9, 21.1; HRMS (ESI): *m/z* calcd for $C_{18}H_{15}F_4N_3O+H^+$: 366.1224 [*M*+H]$^+$; found: 366.1218.

1-(3-Fluoro-4-(trifluoromethyl)benzyl)-4-[5-(hydroxymethyl)-2-chlorophenyl]-1*H*-1,2,3-triazole (40b)

Compound **40b** was obtained in 55% yield (colorless oil), following the microwave assisted synthetic procedure for analogue **16a**. ^{1}H NMR (600 MHz, $CDCl_3$): δ = 8.18 (*s*, 1H, C*H*-triazole), 7.77 (*s*, 1H, Ar*H*), 7.61–7.58 (*m*, 1H, Ar*H*), 7.36–7.26 (*m*, 2H, Ar*H*), 7.14–7.07 (*m*, 2H, Ar*H*), 5.64 (*s*, 2H, CH_2OH), 4.69 (*s*, 2H, CH_2NCH), 2.97 (*bs*, 1H, CH$_2$O*H*); ^{13}C NMR (150 MHz, $CDCl_3$): δ = 160.8 (*d*,

^{1}J = 254.6 Hz, *C*–F), 148.6, 144.8, 141.9, 140.6, 130.4, 129.1, 128.0 (*d*, *J* = 26.7 Hz), 127.1, 124.9, 124.3, 123.6, 123.3 (*dd*, *J* = 19.5, 3.5 Hz), 120.1, 116.4–116.2 (*m*), 64.2, 53.1; HRMS (ESI): *m/z* calcd for $C_{17}H_{12}ClF_4N_3O+H^+$: 386.0671 $[M+H]^+$; found: 386.0668.

4-[5-(Bromomethyl)-2-methylphenyl]-1-(3-fluoro-4-(trifluoromethyl)benzyl)-1*H*-1,2,3-triazole (41a)

Compound **41a** (white solid, 50%) was synthesized according to the procedure for compound **17a**. ^{1}H NMR (300 MHz, $CDCl_3$): δ = 7.82 (*s*, 1H, Ar*H*), 7.67–7.61 (*m*, 2H, C*H*-triazole, Ar*H*), 7.30–7.11 (*m*, 4H, Ar*H*), 5.66 (*s*, 2H, CH_2NCH), 4.52 (*s*, 2H, CH_2Br), 2.44 (*s*, 3H, ArCH_3); ^{13}C NMR (75 MHz, $CDCl_3$): δ = 160.0 (*d*, ^{1}J = 254.8 Hz, *C*–F), 144.3, 141.8 (*d*, *J* = 7.5 Hz), 138.7, 137.3, 130.9, 130.3, 130.0, 129.5–129.2 (*m*), 126.5, 125.9, 127.0 (*d*, *J* = 9.5 Hz), 123.3 (*d*, *J* = 3.8 Hz), 123.2 (*d*, *J* = 17.9 Hz), 118.4–116.3 (*m*), 53.1, 32.6, 21.8; MS *m/z*: 873.05/874.91 (2*M*+Na^+, 100%).

4-[5-(Bromomethyl)-2-chlorophenyl]-1-(3-fluoro-4-(trifluoromethyl)benzyl)-1*H*-1,2,3-triazole (41b)

Compound **41b** (white solid, 31%) was synthesized following the synthetic procedure for analogue **17a**. ^{1}H NMR (300 MHz, $CDCl_3$): δ = 8.32 (*s*, 1H, C*H*-triazole), 8.22 (*s*, 1H, Ar*H*), 7.63 (*t*, *J* = 7.6 Hz, 1H, Ar*H*), 7.44–7.11 (*m*, 4H, Ar*H*), 5.67 (*s*, 2H, CH_2NCH), 4.51 (*s*, 2H, CH_2Br); ^{13}C NMR (150 MHz, $CDCl_3$): δ = 160.1 (*d*, ^{1}J = 257.6 Hz, *C*–F), 144.3, 138.7, 137.3, 131.2 (*d*, *J* = 11.5 Hz), 130.9, 130.3, 129.5, 129.2, 128.31–128.27 (*m*), 126.5, 125.9, 123.4–123.2 (*m*), 116.5–116.2 (*m*), 77.4, 65.8, 53.1; HRMS (ESI): *m/z* calcd for $C_{17}H_{11}BrClF_4N_3+H^+$: 447.9834 $[M+H]^+$; found: 447.9832.

Ethyl 1-cyanocyclohexane-1-carboxylate (44)

To a stirred solution of ethyl 2-cyanoacetate (1.0 g, 8.84 mmol) in 5 mL anhydrous DMF, Cs_2CO_3 (7.2 g, 22.1 mmol) was added in portions at 0 ºC and the mixture was stirred at that temperature for 15 min. 1,5-Dibromopentane (3.6 mL, 26.5 mmol) was then added at 0 ºC and stirring followed at the same temperature for 30 min and at ambient temperature for 24 h. The reaction mixture was washed several times with saturated aqueous NaCl solution, and the aqueous phase was extracted with EtOAc. Purification by flash column chromatography (*n*-hexane/EtOAc, 97:3) afforded compound **44** in 79% yield as colorless oil (1.27 g). ^{1}H NMR (600 MHz, $CDCl_3$): δ = 4.16 (*q*, *J* = 7.1 Hz, 2H, CH_2CH$_3$), 3.31 (*t*, *J* = 7.1 Hz, 3H, CH$_2$CH_3), 1.99–1.47 (*m*, 10H, CH_2-cyclohexyl); ^{13}C NMR (75 MHz, $CDCl_3$): δ = 168.1, 118.4, 61.5, 47.9, 35.6, 35.4, 25.9, 22.3, 22.2, 14.1; MS *m/z*: 384.68 (2*M*+Na^+, 100%). Data are in accordance with literature data.[4]

(1-(Aminomethyl)cyclohexyl)methanol (45)

To a suspension of $LiAlH_4$ (1.063 g, 28 mmol) in anhydrous THF (5 mL), a solution of ethyl 1-cyanocyclohexane-1-carboxylate (**44**) in 5 mL of anhydrous THF was added dropwise at 0 ºC. The resulting mixture was stirred at room temperature for 29 h. The reaction mixture was then quenched with THF/H_2O 1:1 and subsequently diluted with EtOAc. Na_2SO_4 was added and after 30 min the

mixture was filtered through celite. The evaporation of the solvent resulted in compound **45** (colorless oil, 983 mg, 98%), which was used without further purification. ^{1}H NMR (600 MHz, $CDCl_3$): δ = 3.60 (*s*, 2H, C*H*$_2$OH), 2.76 (*s*, 2H, C*H*$_2$NH$_2$), 1.42–1.20 (*m*, 10H, C*H*$_2$-cyclohexyl); ^{13}C NMR (75 MHz, $CDCl_3$): δ = 66.6, 51.9, 42.4, 35.4, 35.2, 25.9, 22.2, 21.9; MS *m/z*: 144.08 (*M*+H$^+$, 41%).

***tert*-Butyl-[(1-(hydroxymethyl)cyclohexyl)methyl]carbamate (46)**

Boc-anhydride (1.68 g, 8.0 mmol) was added to a solution of **45** (1.0 g, 7.0 mmol) in anhydrous THF (6 mL) and the mixture was stirred at room temperature for 23 h. $NaHCO_3$ (sat.) was then added and the aqueous layer was extracted with CH_2Cl_2, washed with saturated aqueous NaCl solution, dried, filtered, and concentrated *in vacuo*. The Boc-protected derivative **46** (quantitative yield) was used without further purification. ^{1}H NMR (600 MHz, $CDCl_3$): δ = 4.82 (*bs*, 1H, CH$_2$N*H*CO), 3.31 (*s*, 2H, C*H*$_2$OH), 3.05 (*d*, *J* = 6.9 Hz, 2H, C*H*$_2$NHCO), 1.44 (*s*, 9H, C*H*$_3$-*t*-butyl), 1.38–1.20 (*m*, 10H, C*H*$_2$-cyclohexyl); ^{13}C NMR (75 MHz, $CDCl_3$): δ = 156.1, 80.5, 66.6, 55.1, 42.4, 35.4, 35.2, 28.2, 28.1, 27.8, 25.9, 22.2, 22.1; MS *m/z*: 508.94 (2*M*+Na$^+$, 100%).

***tert*-Butyl-[1-(4-(3-thioxo-3*H*-1,2-dithiol-5-yl)phenoxy)methyl)cyclohexyl)methyl]carbamate (47)**

To a stirred solution of PPh_3 (323 mg, 1.23 mmol) in 8 mL of anhydrous THF, DIAD (249 mg, 1.23 mmol) was added at 0 °C and the mixture was stirred for 15 min. Compound **46** (200 mg, 0.82 mmol) was then added at the same temperature, followed by the addition of ADT-OH (186 mg, 0.82 mmol). The resulting mixture was stirred at room temperature for 72 h and the solvent was removed *in vacuo*. Compound **47** was isolated by flash column chromatography (*n*-hexane/EtOAc, 95:5 to 90:10) as bright orange solid (108 mg, 29%). ^{1}H NMR (600 MHz, $CDCl_3$): δ = 7.60 (*d*, *J* = 8.7 Hz, 2H, Ar*H*), 7.38 (*s*, 1H, C*H*-dithiol-thione), 6.98 (*d*, *J* = 8.5 Hz, 2H, Ar*H*), 4.73 (*bs*, 1H, CH$_2$N*H*CO), 3.81 (*s*, 2H, C*H*$_2$O), 3.04 (*d*, *J* = 6.9 Hz, 2H, C*H*$_2$NHCO), 1.49–1.21 (*m*, 19H, C*H*$_2$-cyclohexyl, C*H*$_3$-*t*-butyl); ^{13}C NMR (75 MHz, $CDCl_3$): δ = 215.0, 173.0, 162.4, 156.2, 134.6, 128.5, 124.2, 115.5, 79.2, 73.4, 45.6, 37.9, 30.7, 28.4, 26.0, 21.3; HRMS (ESI): *m/z* calcd for $C_{22}H_{29}NO_3S_3$+H$^+$: 452.1382 [*M*+H]$^+$; found: 452.1379.

5-[4-(1-(Aminomethyl)cyclohexyl)methoxy)phenyl]-3*H*-1,2-dithiol-3-thione (48)

To a solution of compound **47** (68 mg, 0.15 mmol) in 2 mL CH_2Cl_2, TFA (0.35 mL, 4.5 mmol) was added and the mixture was stirred at ambient temperature for 1 h. The solvent was evaporated, H_2O was added, and the pH was adjusted at 8.0 with an aqueous NaOH solution (40%). After extraction with CH_2Cl_2, the combined organic layers were dried over Na_2SO_4, filtered, and concentrated *in vacuo* to afford 50 mg (95%) of **48** an orange solid. ^{1}H NMR (300 MHz, $CDCl_3$): δ = 7.60 (*d*, *J* = 8.8 Hz, 2H, Ar*H*), 7.38 (*s*, 1H, C*H*-dithiol-thione), 7.03 (*d*, *J* = 8.8 Hz, 2H, Ar*H*), 3.93 (*s*, 2H, C*H*$_2$O), 3.49 (*s*, 2H, C*H*$_2$NH$_2$), 2.85 (*bs*, 2H, CH$_2$N*H*$_2$), 1.61–1.15 (*m*, 10H, C*H*$_2$-cyclohexyl); ^{13}C NMR (75 MHz, $CDCl_3$): δ = 215.1, 173.0, 162.6, 134.6, 128.5, 124.2, 115.6, 72.4, 46.7, 37.6, 30.7, 26.1, 21.4; HRMS (ESI): *m/z* calcd for $C_{17}H_{21}NOS_3$+H$^+$: 352.0858 [*M*+H]$^+$; found: 352.0857.

1-(4-Methylbenzyl)cyclohexane-1-carbonitrile (50)

To a solution of 4-methylbenzyl cyanide (0.5 mL, 3.8 mmol) in 5 mL anhydrous DMF, 1,5-dibromopentane (0.57 mL, 4.19 mmol) was added at 0 ºC, followed by the portionwise addition of NaH (60%) (329 mg, 8.23 mmol) at the same temperature. The resulting orange mixture was stirred at room temperature for 4 h. Afterwards it was poured into ice and the aqueous phase was extracted with EtOAc. The combined organic layers were washed with saturated aqueous NaCl solution, dried over Na_2SO_4, filtered, and concentrated *in vacuo*. Flash column chromatography (*n*-hexane/EtOAc, 95:5) afforded **50** as colorless oil in 67% yield (508 mg). ^{1}H NMR (300 MHz, $CDCl_3$): δ = 7.40 (*d*, *J* = 8.3 Hz, 2H, Ar*H*), 7.21 (*d*, *J* = 8.4 Hz, 2H, Ar*H*), 2.37 (*s*, 3H, ArCH_3), 1.33–1.26 (*m*, 10H, CH_2-cyclohexyl); ^{13}C NMR (75 MHz, $CDCl_3$): δ = 138.6, 137.5, 129.5, 125.4, 122.8, 44.0, 37.4, 25.0, 23.6, 20.9; MS *m/z*: 420.86 (2*M*+H$^+$, 100%). Data are in accordance with literature data.[5]

(1-(4-Methylbenzyl)cyclohexyl)methanamine (51)

1-(4-Methylbenzyl)cyclohexane-1-carbonitrile (**50**) (400 mg, 2.0 mmol) was dissolved in anhydrous THF (8 mL) and $BH_3{\cdot}S(CH_3)_2$ (0.25 mL, 2.6 mmol) was added. The mixture was refluxed for 90 min. Upon completion of the reaction, CH_3OH (3 mL) was added at room temperature and the mixture was stirred for 30 min. The solvents were then evaporated and amine **51** (203 mg, 49%, white solid) was isolated by flash column chromatography (CH_2Cl_2/CH_3OH, 9:1). ^{1}H NMR (300 MHz, $CDCl_3$): δ = 7.38 (*d*, *J* = 8.6 Hz, 2H, Ar*H*), 7.21 (*d*, *J* = 8.4 Hz, 2H, Ar*H*), 2.62 (*s*, 2H, CH_2NH$_2$), 2.33 (*s*, 3H, ArCH_3), 1.77–1.35 (*m*, 10H, CH_2-cyclohexyl); ^{13}C NMR (75 MHz, $CDCl_3$): δ = 129.2, 128.8, 127.1, 124.5, 43.1, 38.9, 33.7, 26.7, 22.2, 20.8; MS *m/z*: 203.96 (*M*+H$^+$, 100%).

2-Chloro-5-(hydroxymethyl)-*N*-[(1-(4-methylbenzyl)cyclohexyl)methyl]benzamide (52)

Compound **52** was prepared following the synthetic procedure for compound **29**. ^{1}H NMR (600 MHz, $CDCl_3$): δ = 7.47 (*s*, 1H, Ar*H*), 7.28–7.25 (*m*, 4H, Ar*H*), 7.14 (*d*, *J* = 8.0 Hz, 2H, Ar*H*), 5.76 (*bs*, 1H, CH$_2$N*H*CO), 4.60 (*s*, 2H, CH_2OH), 3.57 (*d*, *J* = 6.0 Hz, 2H, CH_2NHCO), 2.30 (*s*, 3H, ArCH_3), 2.11–1.24 (*m*, 10H, CH_2-cyclohexyl); HRMS (ESI): *m/z* calcd for $C_{22}H_{26}ClNO_2$+H$^+$: 372.1725 [*M*+H]$^+$; found: 372.1715.

2-Chloro-*N*-[1-(4-methylbenzyl)cyclohexyl)methyl]benzamide (54)

To a stirred solution of 2-chlorobenzoic acid (77 mg, 0.49 mmol) in 3 mL anhydrous DMF, HOBt (90 mg, 0.59 mmol), EDC hydrochloride (104 mg, 0.54 mmol), amine **51** (100 mg, 0.49 mmol), and Et_3N (0.07 mL, 0.53 mmol) were added. After each addition, 10 min stirring followed and the resulting mixture was stirred at ambient temperature for 22 h. The reaction was then washed with saturated aqueous NaCl solution and the aqueous phase was extracted with EtOAc. The combined organic layers were dried over Na_2SO_4, filtered, and concentrated *in vacuo*. The resulting residue was purified by flash column chromatography (*n*-hexane/EtOAc, 90:10) to yield **54** (75 mg, 45%) as colorless oil. ^{1}H NMR (600 MHz, $CDCl_3$): δ = 7.53 (*dd*, 1H, *J* = 7.5, 1.7 Hz, Ar*H*), 7.31–7.23 (*m*, 5H, Ar*H*), 7.15 (*d*, *J* = 8.0 Hz, 2H, Ar*H*), 5.74 (*bs*, 1H, CH$_2$N*H*CO), 3.59 (*d*, *J* = 6.0 Hz, 2H, CH_2NHCO),

2.31 (*s*, 3H, ArCH_3), 2.11–1.41 (*m*, 10H, CH_2-cyclohexyl); ^{13}C NMR (150 MHz, $CDCl_3$): δ = 166.6, 135.9, 135.4, 131.4, 131.0, 130.5, 130.1, 129.8, 129.3, 127.3, 127.1, 126.9, 126.7, 42.0, 34.3, 34.2, 34.1, 26.5, 22.2; MS *m/z*: 704.99 (2*M*+Na^+, 100%).

***N*-[1-(3-(Bromomethyl)phenyl)cyclohexyl)methyl]-2-chlorobenzamide (55)**

Compound **55** was obtained as colorless oil in 57% yield following the synthetic procedure for compound **3**. ^{1}H NMR (600 MHz, $CDCl_3$): δ = 7.55–7.52 (*m*, 1H, Ar*H*), 7.40–7.37 (*m*, 4H, Ar*H*), 7.32–7.24 (*m*, 3H, Ar*H*), 5.77 (*bs*, 1H, CH_2NHCO), 4.47 (*s*, 2H, CH_2Br), 3.61 (*d*, *J* = 6.1 Hz, 2H, CH_2NHCO), 2.11–1.41 (*m*, 10H, CH_2-cyclohexyl); ^{13}C NMR (150 MHz, $CDCl_3$): δ = 166.4, 135.7, 135.0, 131.1, 130.4, 130.2, 130.1, 129.4, 127.4, 127.0, 126.8, 42.3, 34.0, 33.2, 26.2, 22.0; MS *m/z*: 860.66/862.59/864.55 (2*M*+Na^+, 100%).

3-(Bromomethyl)-4-phenyl-1,2,5-oxadiazole 2-oxide (57)

Compound **57** was obtained as yellowish oil in 55% yield following the synthetic procedure for compound **17a**. ^{1}H NMR (300 MHz, $CDCl_3$): δ = 7.81–7.78 (*m*, 2H, Ar*H*), 7.62–7.56 (*m*, 3H, Ar*H*), 4.40 (*s*, 2H, CH_2Br); ^{13}C NMR (75 MHz, $CDCl_3$): δ = 155.7, 131.6, 129.6, 127.6, 125.9, 113.4, 17.5; MS *m/z*: 277.18/279.19 (*M*+Na^+, 30%).

3-(Azidomethyl)-4-phenyl-1,2,5-oxadiazole 2-oxide (58)

Compound **58** was prepared in quantitative yield following the synthetic procedure for compound **39**. ^{1}H NMR (600 MHz, $CDCl_3$): δ = 7.62 (*d*, *J* = 7.1 Hz, 2H, Ar*H*), 7.50–7.45 (*m*, 3H, Ar*H*), 4.39 (*s*, 2H, CH_2N_3); ^{13}C NMR (75 MHz, $CDCl_3$): δ = 154.3, 131.6, 129.6, 127.5, 125.2, 113.4, 42.5; MS *m/z*: 432.95 (2M^+, 21%).

3-(Aminomethyl)-4-phenyl-1,2,5-oxadiazole 2-oxide (59)

To a stirred solution of 3-(azidomethyl)-4-phenyl-1,2,5-oxadiazole 2-oxide (**58**) (242 mg, 1.11 mmol) in THF (5 mL), PPh_3 (351 mg, 1.34 mmol) and H_2O (0.07 mL, 4.01 mmol) were added. The mixture was stirred at room temperature for 22 h. H_2O was then added, and the aqueous layer was extracted with EtOAc. The combined organic layers were washed with saturated aqueous NaCl solution, dried over Na_2SO_4, filtered, and concentrated *in vacuo*. Flash column chromatography (*n*-hexane/EtOAc 90:10 to EtOAc 100%) afforded amine **59** (yellowish oil) as a mixture with triphenylphosphine oxide (180 mg), which was not further purified. ^{1}H NMR (600 MHz, $CDCl_3$): δ = 7.60 (*d*, *J* = 7.1 Hz, 2H, Ar*H*), 7.53–7.48 (*m*, 3H, Ar*H*), 3.86 (*s*, 2H, CH_2NH_2); MS *m/z*: 191.91 (*M*+H^+, 14%).

3-Carboxy-4-phenyl-1,2,5-oxadiazole 2-oxide (62)

For the preparation of the Jone's reagent, CrO_3 (0.8 g, 8.0 mmol) was mixed with H_2SO_4 (0.85 mL, 16.0 mmol) at 0 ºC, H_2O (2.5 mL) was carefully added, and the mixture was stirred for 15 min. 3-(Hydroxymethyl)-4-phenyl-1,2,5-oxadiazole 2-oxide (**20**) (0.25 g, 1.3 mmol) was dissolved in 4 mL anhydrous acetone and the Jone's reagent was added at 0 ºC until the color remained red. After stirring for 3.5 h, isopropanol was added, and the reaction color turned from green to blue. H_2O was

added and the aqueous phase was extracted with EtOAc, washed with saturated NaCl, and the combined organic phases were dried (Na_2SO_4) and evaporated. The desired product was obtained as yellow solid and was used without further purification (197 mg, 74%). ^{1}H NMR (600 MHz, $CDCl_3$): δ = 10.14 (*s*, 1H, COO*H*), 8.11 (*s*, 2H, Ar*H*), 7.61–7.47 (*m*, 3H, Ar*H*); ^{13}C NMR (150 MHz, $CDCl_3$): δ = 172.4, 134.0, 130.4, 129.3, 128.6; MS *m/z*: 230.16 (*M*+Na^+, 25%).

1-(3-Fluoro-4-(trifluoromethyl)phenyl)cyclohexane-1-carbonitrile (65)

Compound **65** was obtained as colorless oil in 81% yield following the synthetic procedure for compound **50**. ^{1}H NMR (600 MHz, $CDCl_3$): δ = 7.62 (*t*, *J* = 7.8 Hz, 1H, Ar*H*), 7.40 (*d*, *J* = 8.2 Hz, 1H, Ar*H*), 7.33 (*dd*, *J* = 11.6, 1.8 Hz, 1H, Ar*H*), 2.15–1.72 (*m*, 10H, CH_2-cyclohexyl); ^{13}C NMR (150 MHz, $CDCl_3$): δ = 160.1 (*d*, ^{1}*J* = 256.4 Hz, *C*–F), 148.7 (*d*, *J* = 7.6 Hz), 128.0 (*d*, *J* = 42.9 Hz), 123.5, 122.1 (*t*, *J* = 3.9 Hz), 121.7, 121.41–121.38 (*m*), 118.1 (*dd*, *J* = 33.4, 12.5 Hz), 115.3–114.6 (*m*), 114.4 (*d*, *J* = 24.1 Hz), 44.8, 37.4, 24.9, 23.6; MS *m/z*: 294.03 (*M*+Na^+, 100%).

(1-(3-Fluoro-4-(trifluoromethyl)phenyl)cyclohexyl)methanamine (66)

Analogue **65** (640 mg, 2.4 mmol) was dissolved in anhydrous THF (12 mL) and $BH_3{\cdot}S(CH_3)_2$ (0.29 mL, 3.08 mmol) was added. The mixture was refluxed for 1 h. Upon completion of the reaction, CH_3OH (3 mL) was added at room temperature and the mixture was stirred for 40 min. The solvents were then evaporated and amine **66** (536 mg, 81%, white solid) was isolated and used without further purification. ^{1}H NMR (600 MHz, $CDCl_3$): δ = 7.46 (*t*, *J* = 7.9 Hz, 1H, Ar*H*), 6.91 (*d*, *J* = 8.3 Hz, 1H, Ar*H*), 6.86–6.83 (*m*, 1H, Ar*H*), 3.01 (*s*, 2H, CH_2NH_2), 2.12–1.70 (*m*, 10H, CH_2-cyclohexyl); ^{13}C NMR (75 MHz, $CDCl_3$): δ = 160.1 (*d*, ^{1}*J* = 256.4 Hz, *C*–F), 148.5 (*d*, *J* = 7.6 Hz), 128.0 (*d*, *J* = 42.9 Hz), 122.3 (*t*, *J* = 3.9 Hz), 122.0, 121.41–121.37 (*m*), 117.9 (*dd*, *J* = 33.4, 12.5 Hz), 115.3–114.6 (*m*), 114.4 (*d*, *J* = 24.1 Hz), 53.0, 44.6, 37.4, 24.8, 23.2; MS *m/z*: 276.06 (*M*+H^+, 100%).

5-(Bromomethyl)-2-chloro-*N*-[(1-(3-fluoro-4-(trifluoromethyl)phenyl)cyclohexyl)methyl] benzamide (69)

To a solution of amide **68** (31 mg, 0.07 mmol) in anhydrous $CHCl_3$ (2 mL), AIBN (1 mg, cat.) and NBS (13 mg, 0.07 mmol) were added and the mixture was refluxed for 2 h. The reaction was not allowed to be completed in order to avoid the dibromo derivative. The solvent was evaporated, and the residue was dissolved in Et_2O and filtered. The filtrate was purified by flash column chromatography (*n*-hexane/EtOAc, 85:15) to afford 16 mg of a **68**/**69** mixture, which was used in the next step. ^{1}H NMR (600 MHz, $CDCl_3$): δ = 7.58 (*s*, 2H, Ar*H*), 7.36–7.11 (*m*, 4H, Ar*H*), 5.84 (*bs*, 1H, CH_2N*H*CO), 4.41 (*s*, 2H, CH_2Br), 3.62 (*d*, *J* = 6.3 Hz, 2H, CH_2NHCO), 2.13–1.26 (*m*, 10H, CH_2-cyclohexyl); MS *m/z*: 506.08/508.11 (*M*+H^+, 26%).

^{1}H/^{13}C/^{19}F NMR and HRMS spectroscopic data

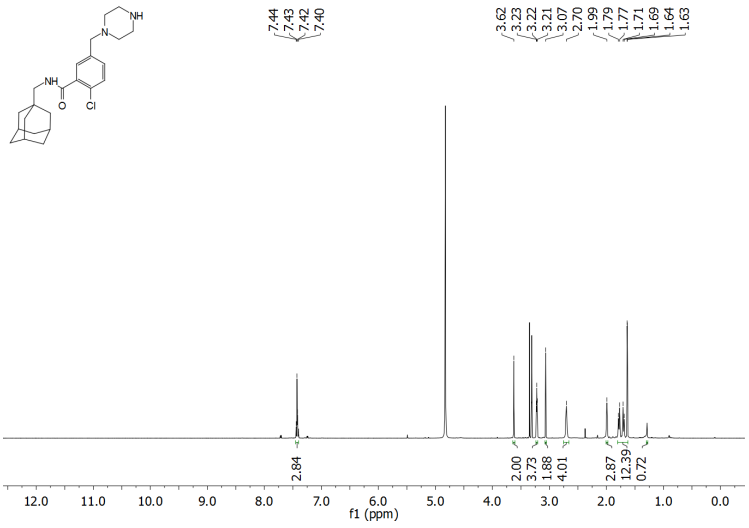

Figure S1. ^{1}H NMR spectrum of **AZ1** (CD_3OD, 600 MHz).

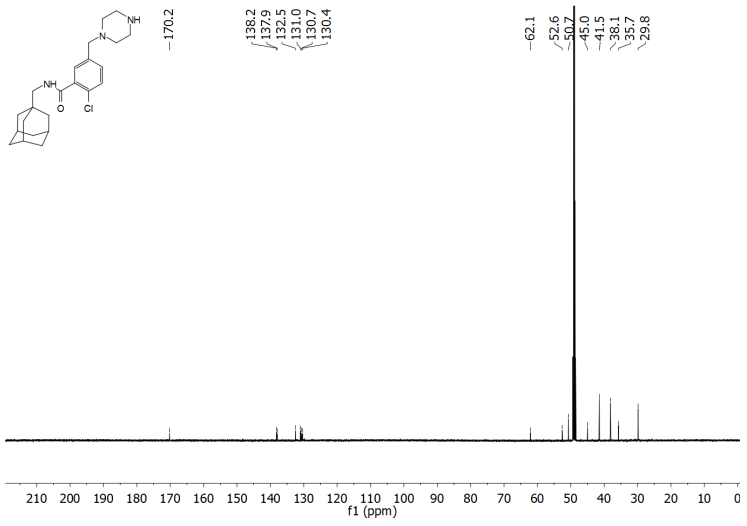

Figure S2. ^{13}C NMR spectrum of **AZ1** (CD_3OD, 150 MHz).

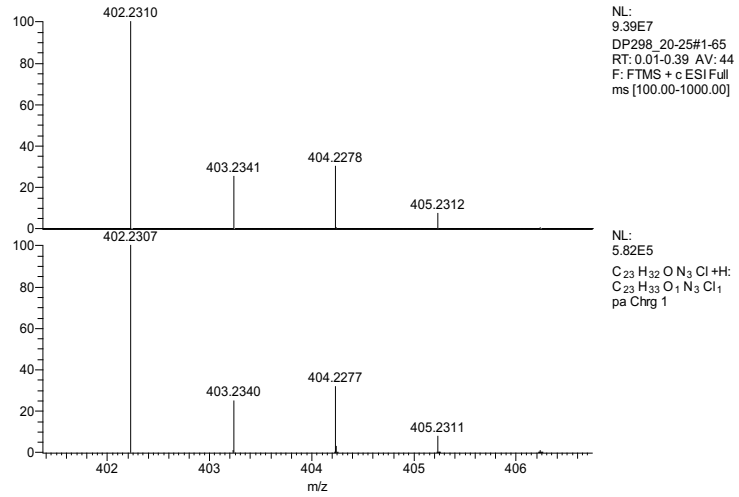

Figure S3. Experimental (upper) and simulated (lower) HRMS spectrum of **AZ1**.

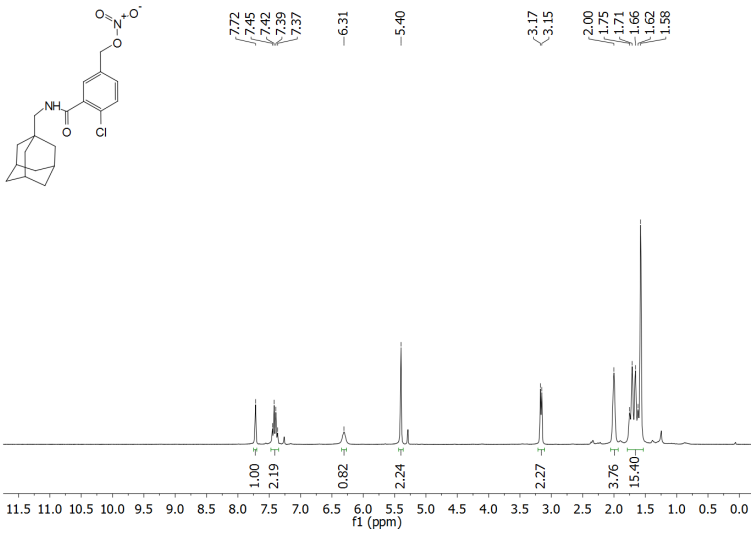

Figure S4. ^{1}H NMR spectrum of **4** ($CDCl_3$, 300 MHz).

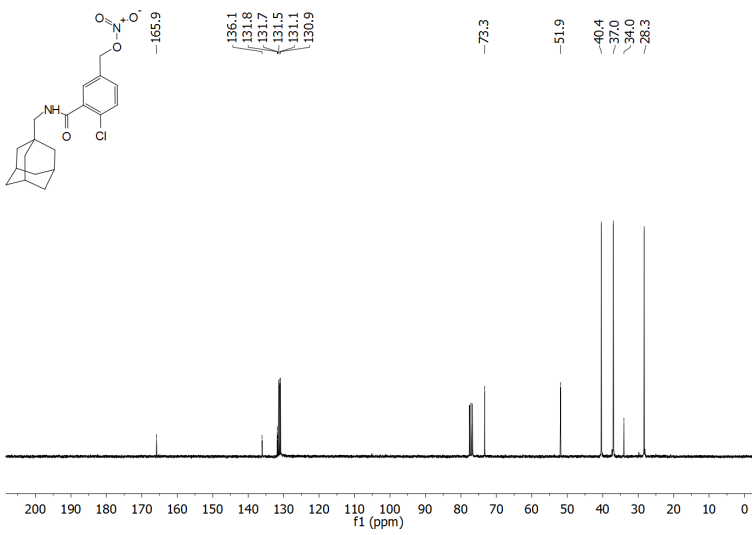

Figure S5. ^{13}C NMR spectrum of **4** ($CDCl_3$, 75 MHz).

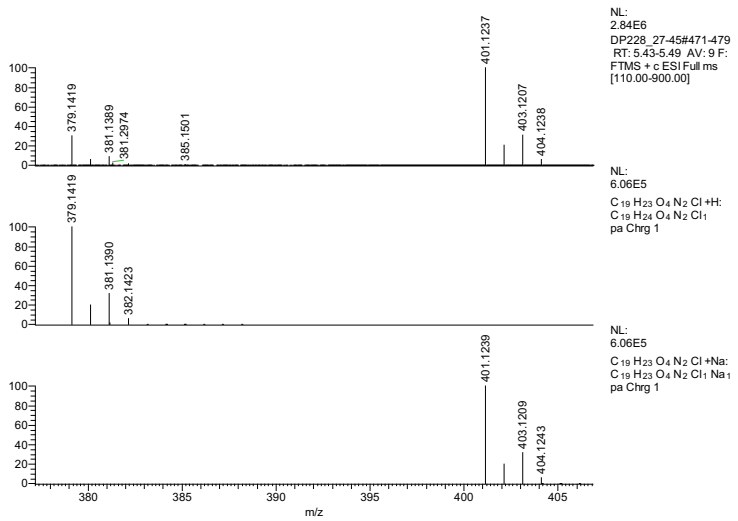

Figure S6. Experimental (upper) and simulated (lower) HRMS spectrum of **4**.

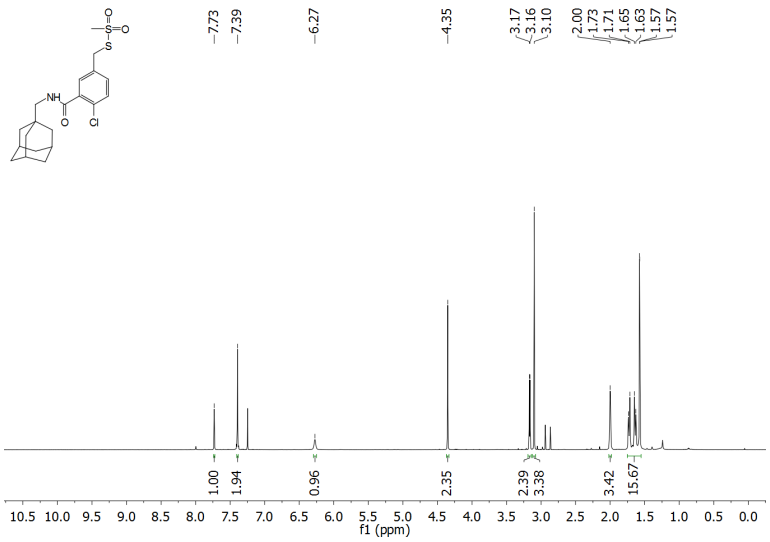

Figure S7. ^{1}H NMR spectrum of **5** ($CDCl_3$, 600 MHz).

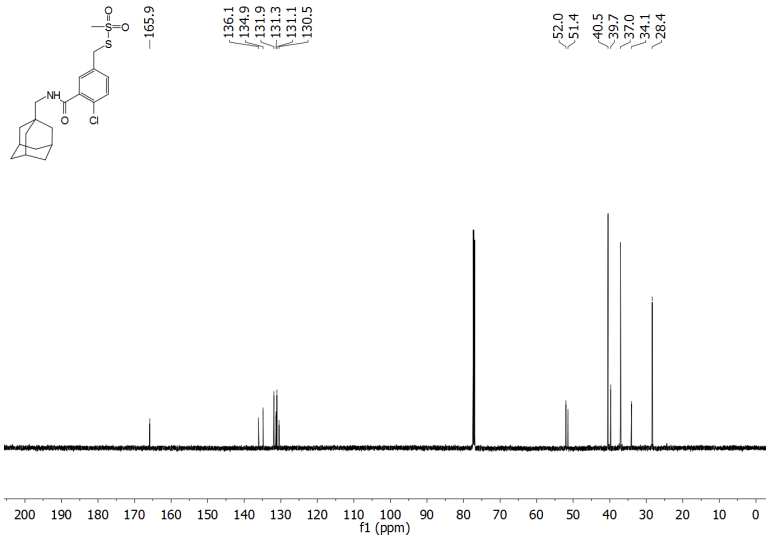

Figure S8. ^{13}C NMR spectrum of **5** ($CDCl_3$, 150 MHz).

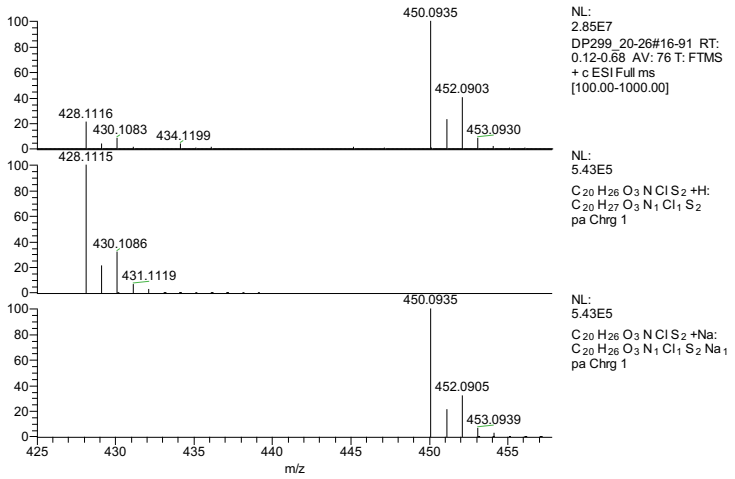

Figure S9. Experimental (upper) and simulated (lower) HRMS spectrum of **5**.

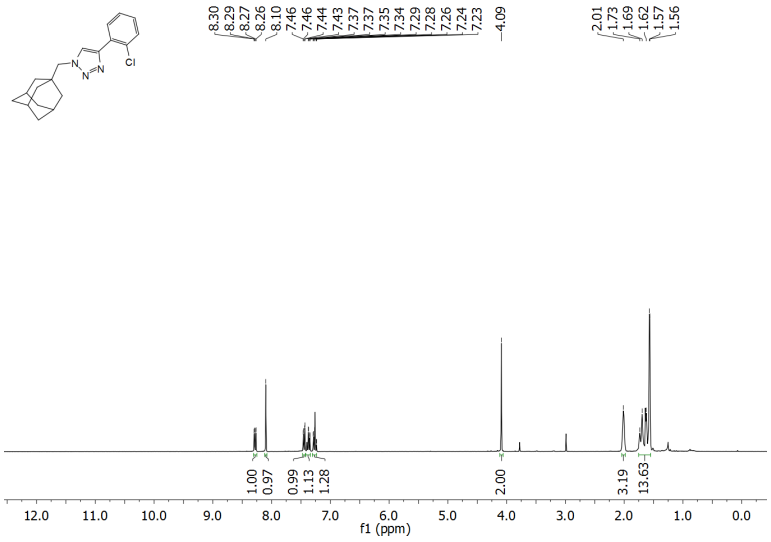

Figure S10. ^{1}H NMR spectrum of **11** ($CDCl_3$, 300 MHz).

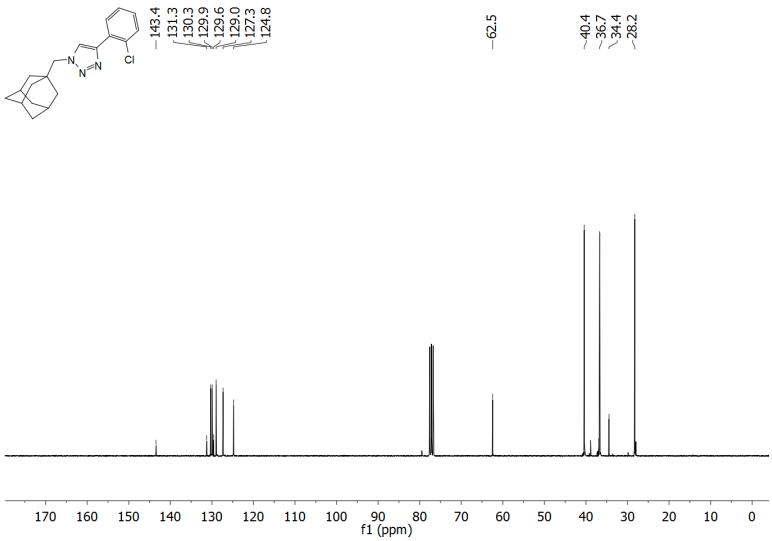

Figure S11. ^{13}C NMR spectrum of **11** ($CDCl_3$, 75 MHz).

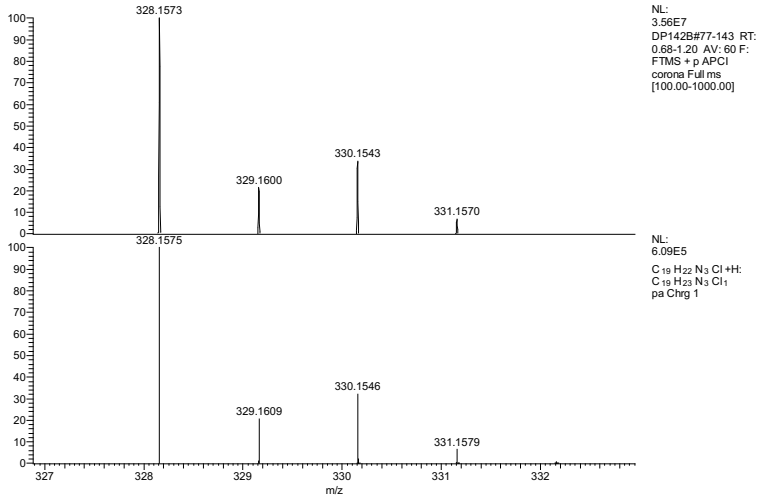

Figure S12. Experimental (upper) and simulated (lower) HRMS spectrum of **11**.

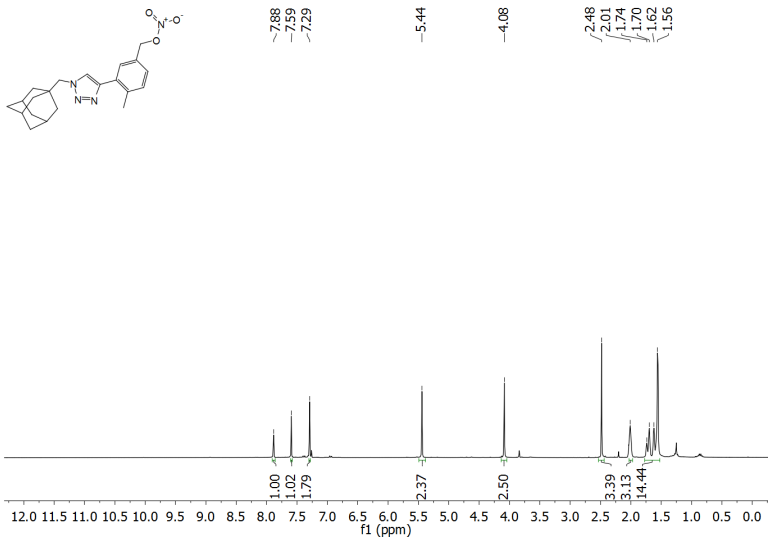

Figure S13. ^{1}H NMR spectrum of **18a** ($CDCl_3$, 300 MHz).

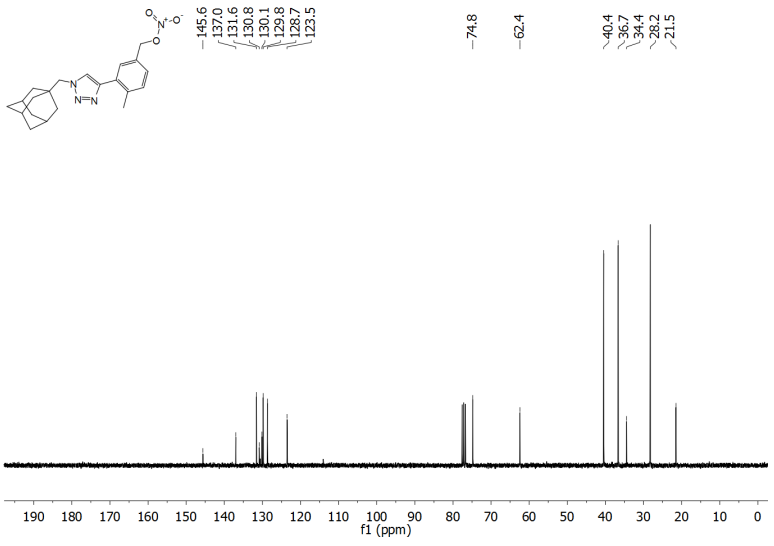

Figure S14. ^{13}C NMR spectrum of **18a** ($CDCl_3$, 75 MHz).

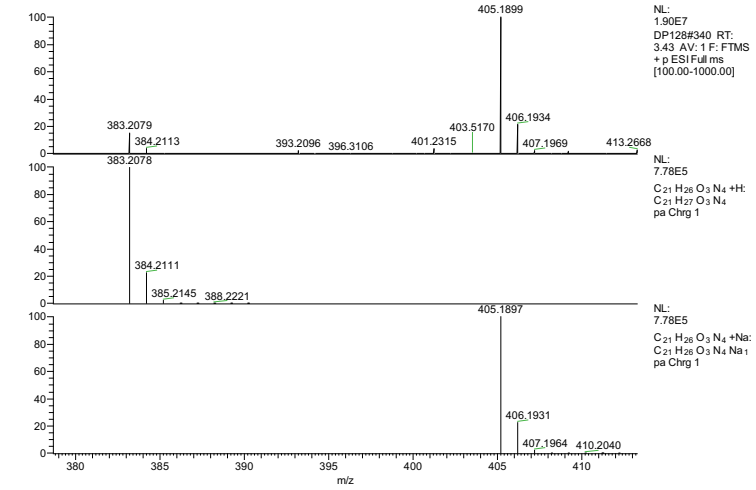

Figure S15. Experimental (upper) and simulated (lower) HRMS spectrum of **18a**.

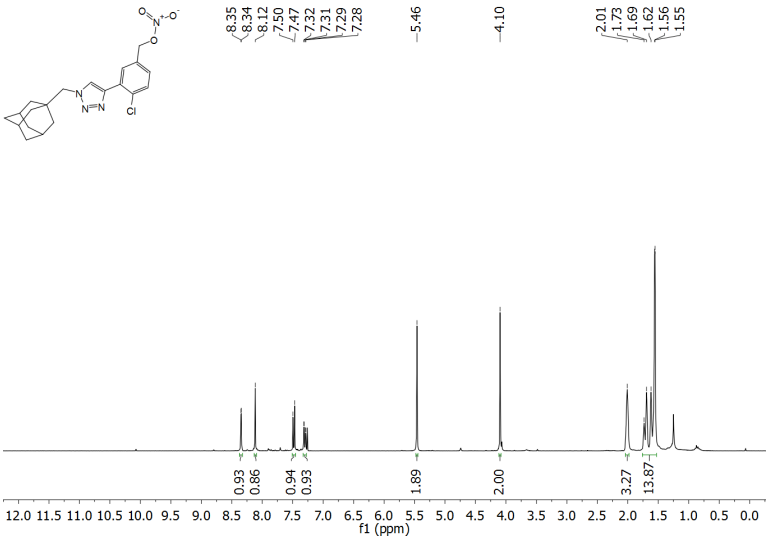

Figure S16. ^{1}H NMR spectrum of **18b** ($CDCl_3$, 300 MHz).

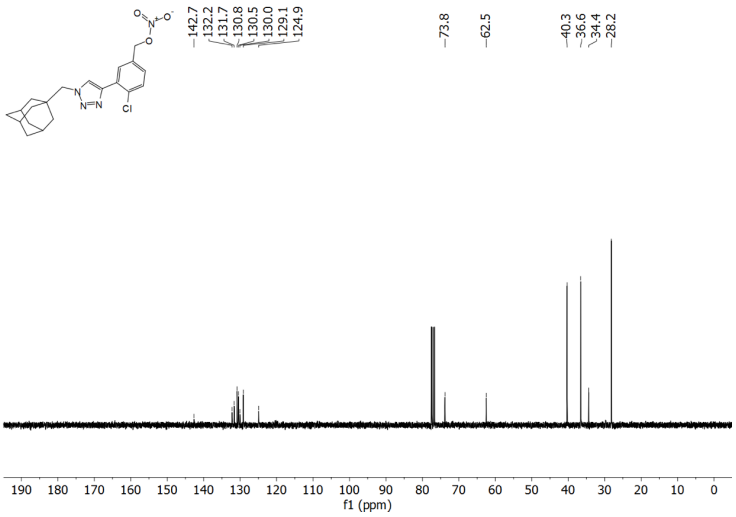

Figure S17. ^{13}C NMR spectrum of **18b** ($CDCl_3$, 75 MHz).

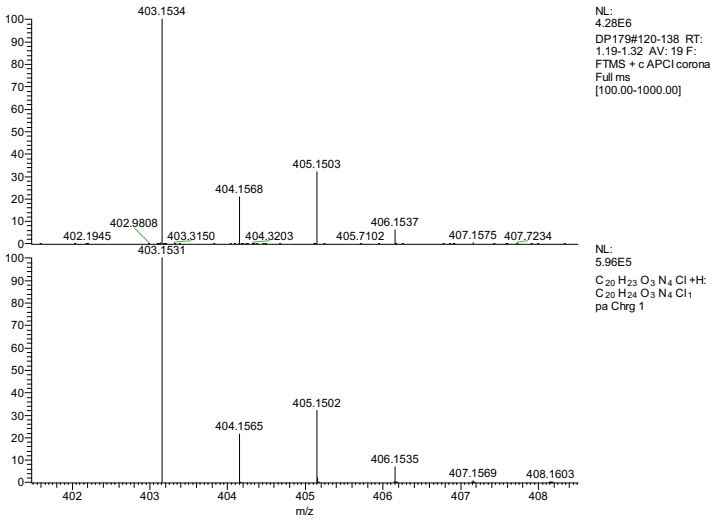

Figure S18. Experimental (upper) and simulated (lower) HRMS spectrum of **18b**.

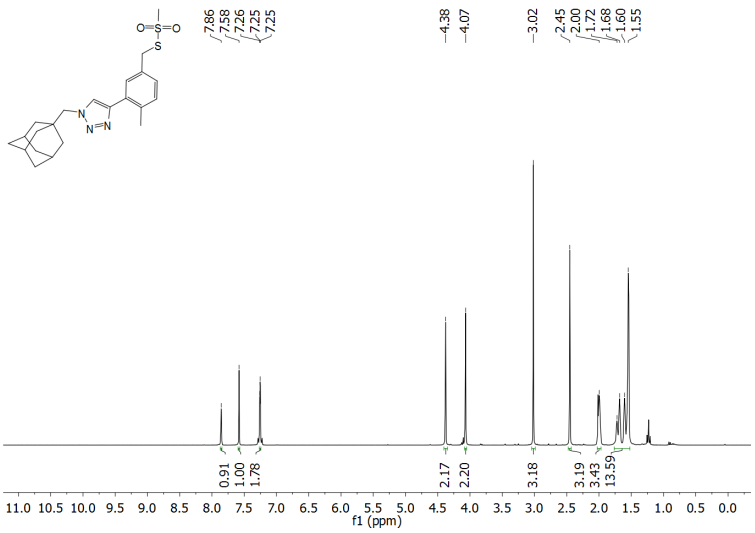

Figure S19. ^{1}H NMR spectrum of **19a** ($CDCl_3$, 300 MHz).

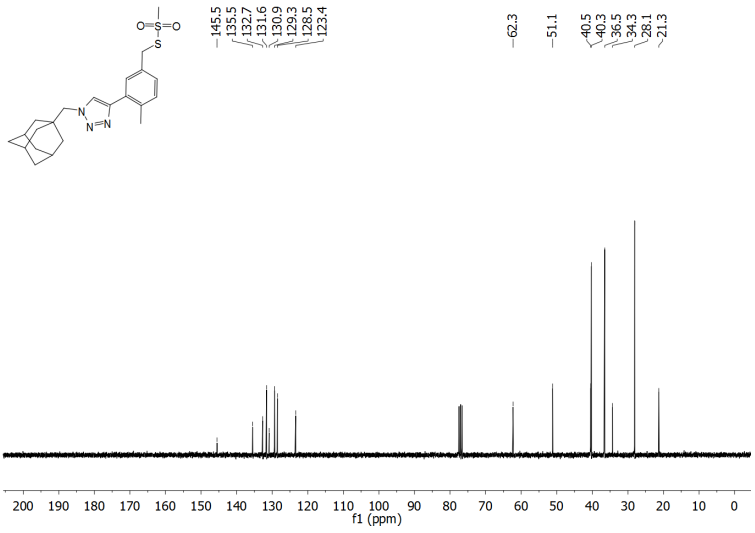

Figure S20. ^{13}C NMR spectrum of **19a** ($CDCl_3$, 75 MHz).

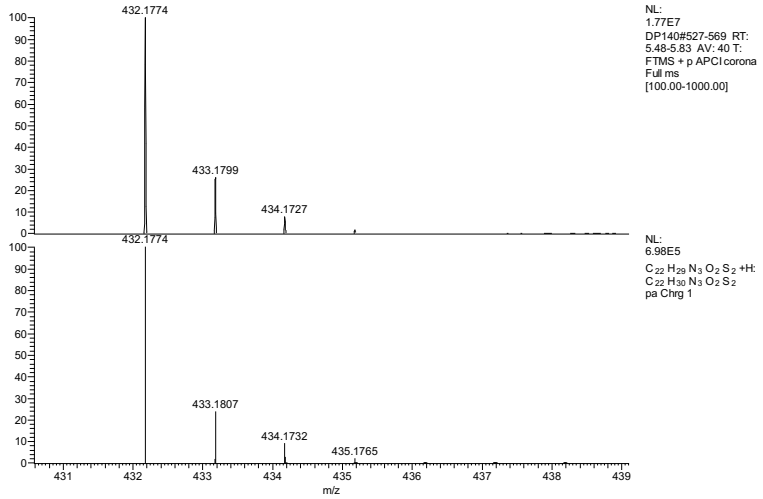

Figure S21. Experimental (upper) and simulated (lower) HRMS spectrum of **19a**.

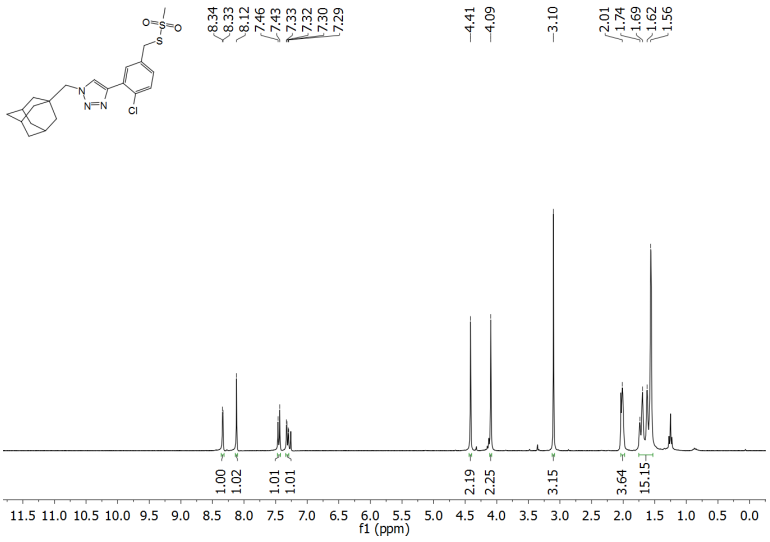

Figure S22. ^{1}H NMR spectrum of **19b** ($CDCl_3$, 300 MHz).

26

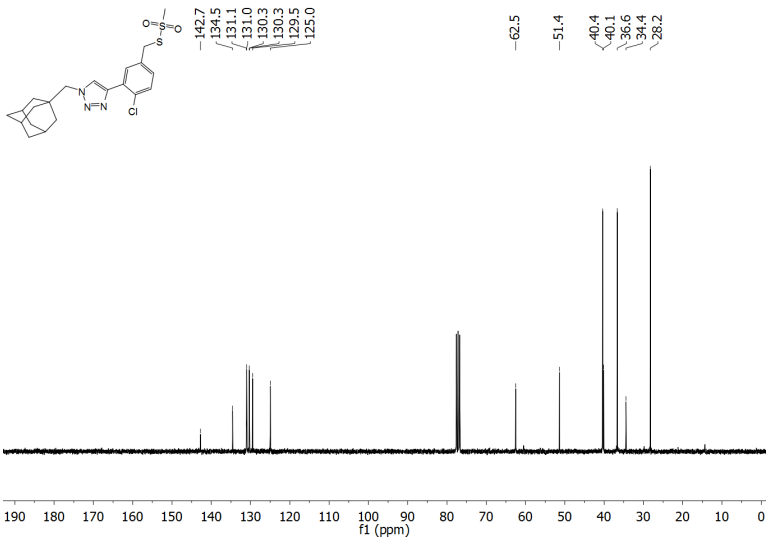

Figure S23. ^{13}C NMR spectrum of **19b** ($CDCl_3$, 75 MHz).

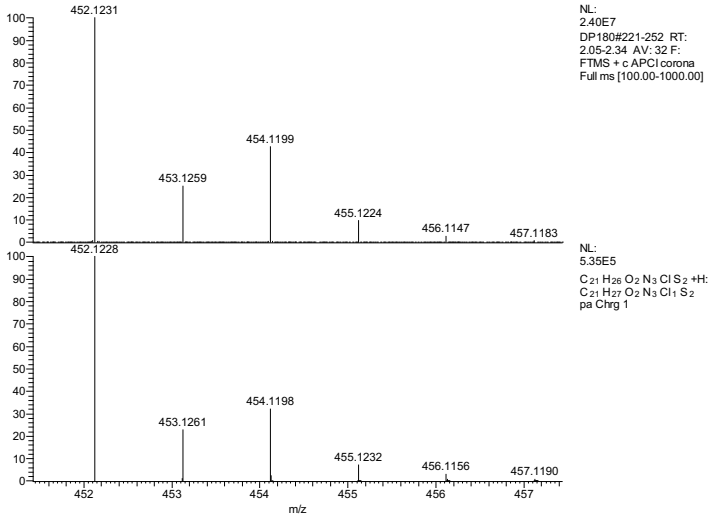

Figure S24. Experimental (upper) and simulated (lower) HRMS spectrum of **19b**.

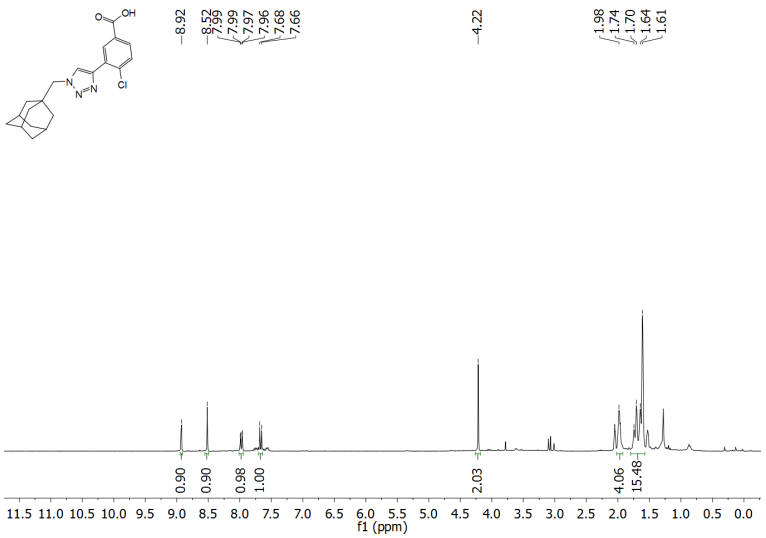

Figure S25. ^{1}H NMR spectrum of **23b** (acetone-d_6, 300 MHz).

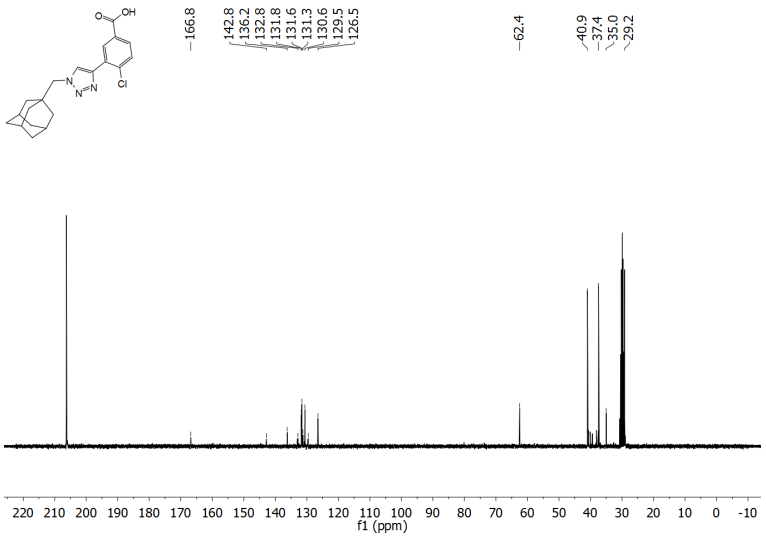

Figure S26. ^{13}C NMR spectrum of **23b** (acetone-d_6, 75 MHz).

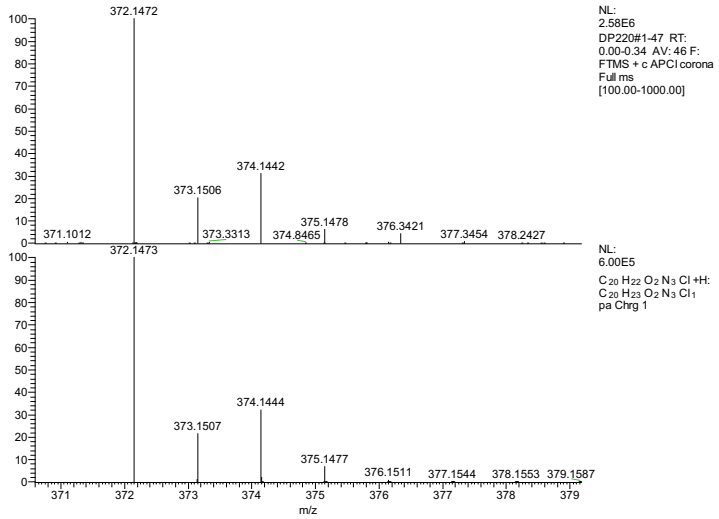

Figure S27. Experimental (upper) and simulated (lower) HRMS spectrum of **23b**.

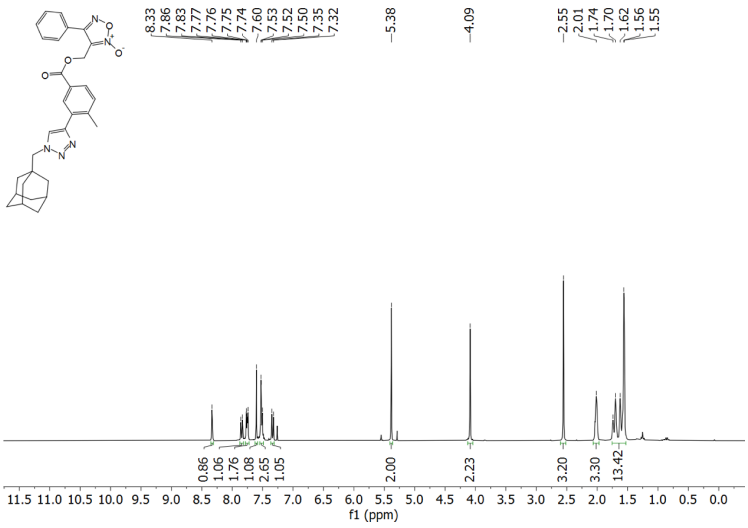

Figure S28. ^{1}H NMR spectrum of **24a** ($CDCl_3$, 300 MHz).

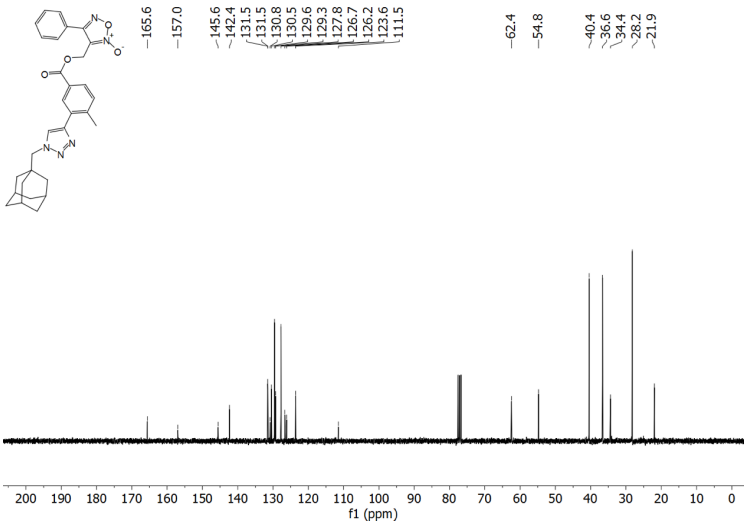

Figure S29. ^{13}C NMR spectrum of **24a** ($CDCl_3$, 75 MHz).

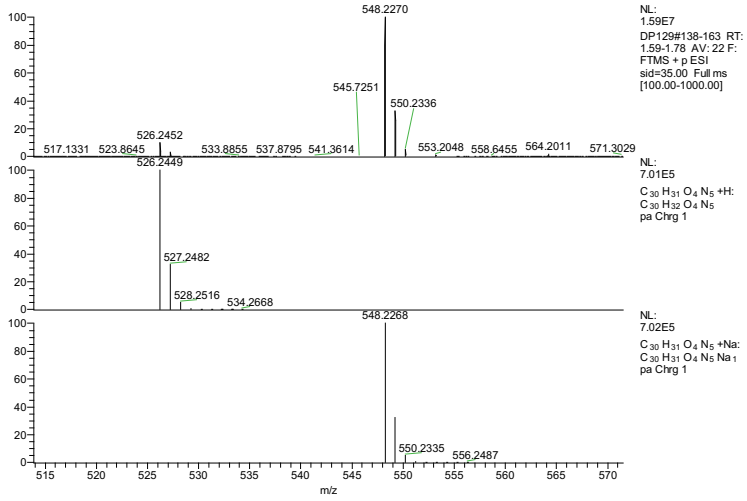

Figure S30. Experimental (upper) and simulated (lower) HRMS spectrum of **24a**.

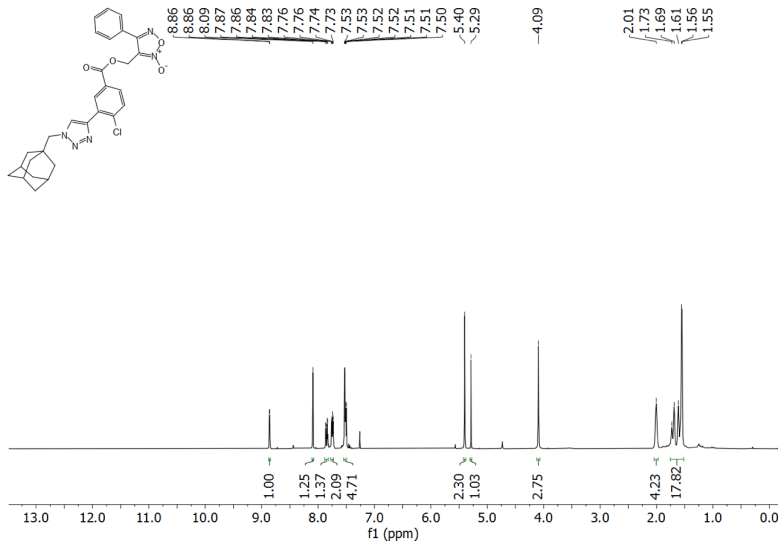

Figure S31. ^{1}H NMR spectrum of **24b** ($CDCl_3$, 300 MHz).

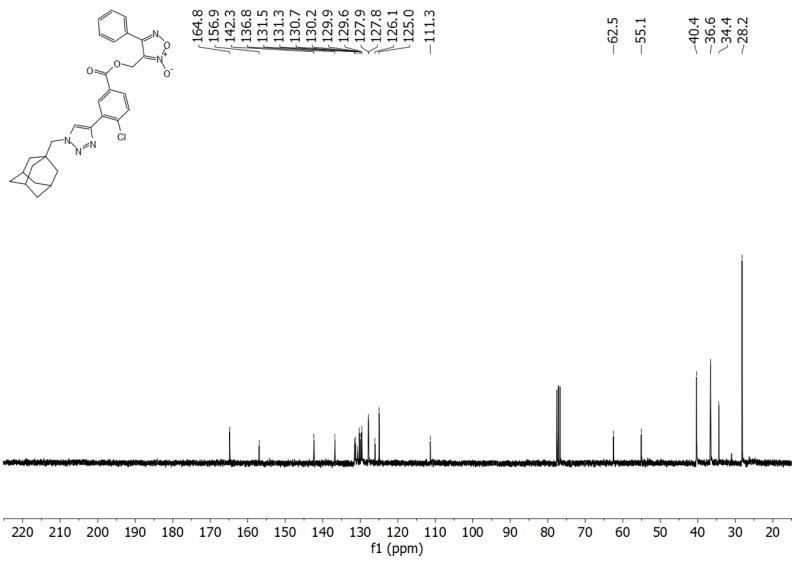

Figure S32. ^{13}C NMR spectrum of **24b** ($CDCl_3$, 75 MHz).

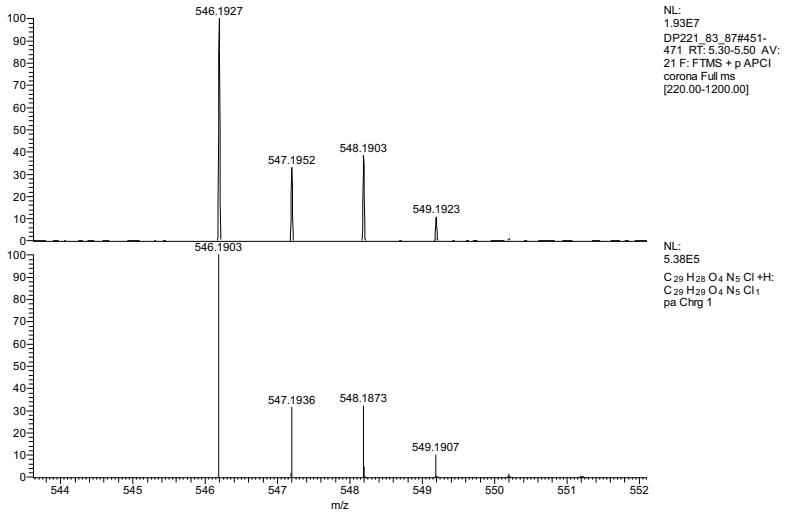

Figure S33. Experimental (upper) and simulated (lower) HRMS spectrum of **24b**.

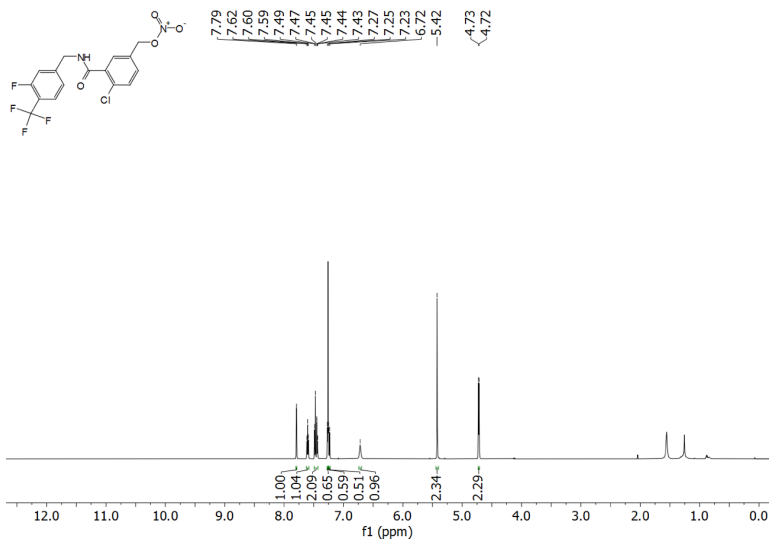

Figure S34. ^{1}H NMR spectrum of **30** ($CDCl_3$, 600 MHz).

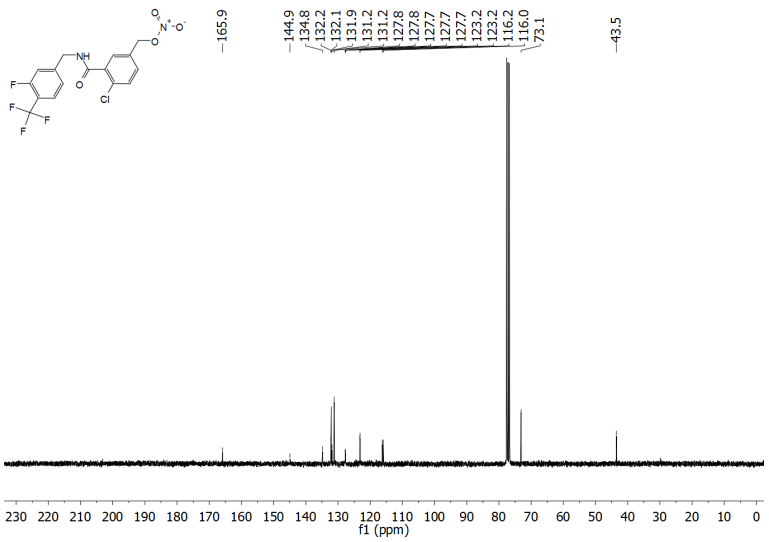

Figure S35. ^{13}C NMR spectrum of **30** ($CDCl_3$, 75 MHz).

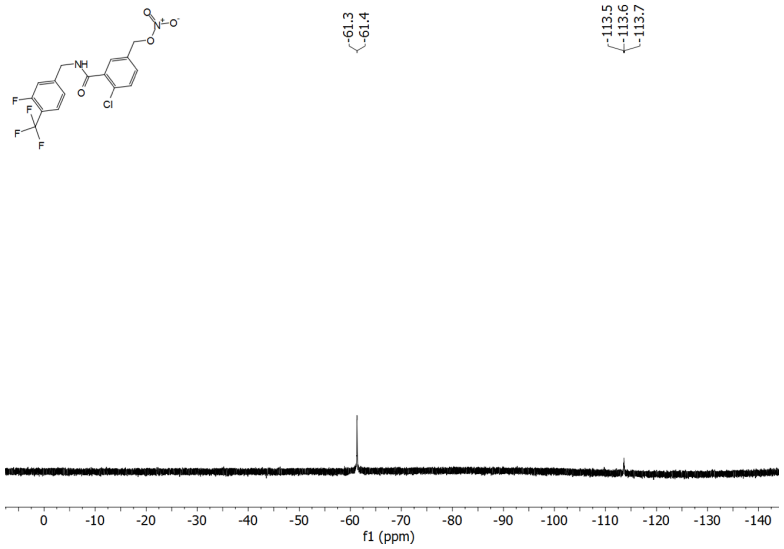

Figure S36. ^{19}F NMR spectrum of **30** ($CDCl_3$, 282 MHz).

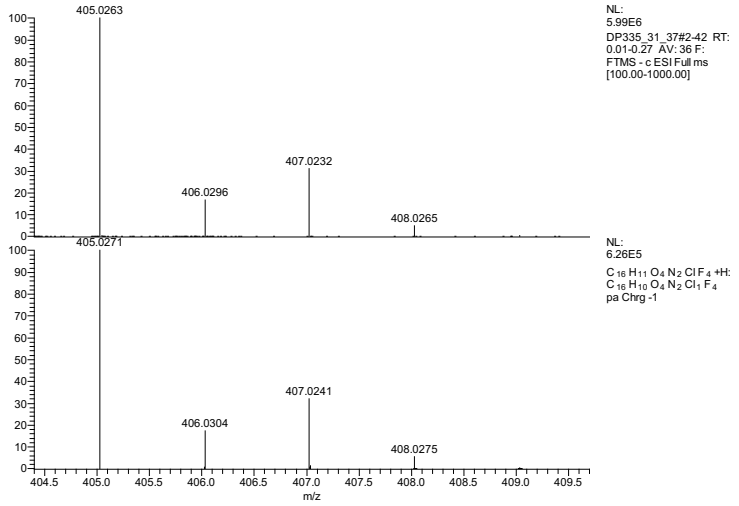

Figure S37. Experimental (upper) and simulated (lower) HRMS spectrum of **30**.

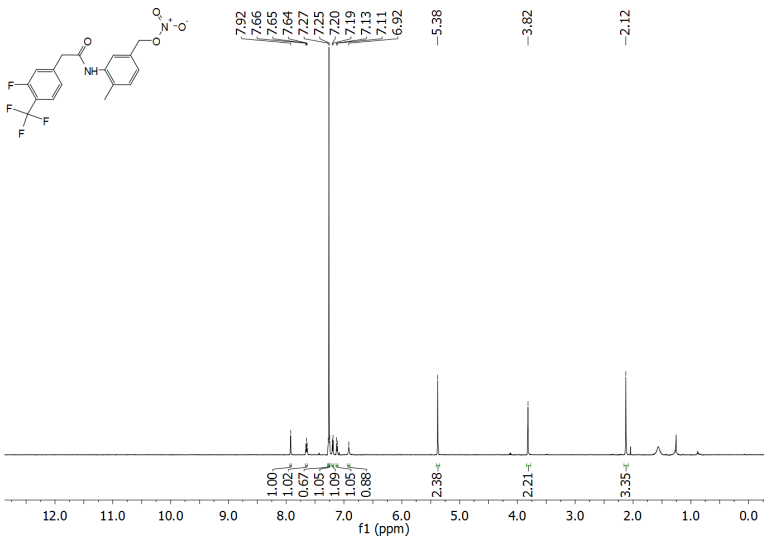

Figure S38. ^{1}H NMR spectrum of **35** ($CDCl_3$, 600 MHz).

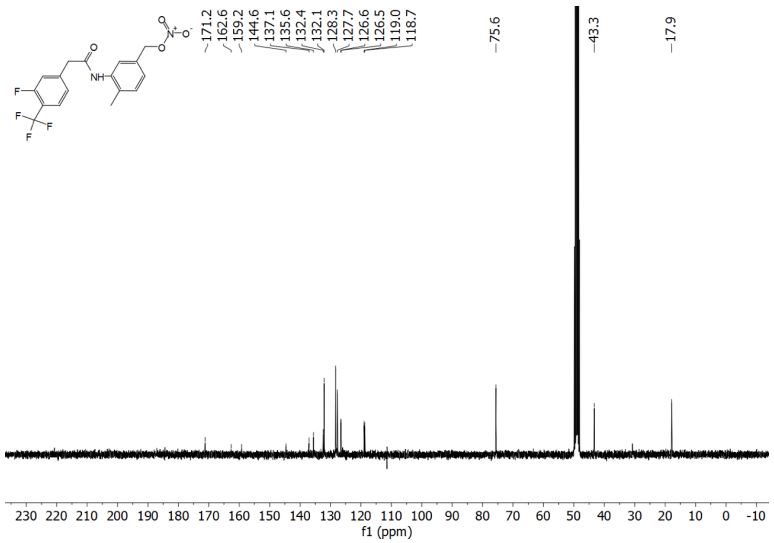

Figure S39. ^{13}C NMR spectrum of **35** (CD_3OD, 75 MHz).

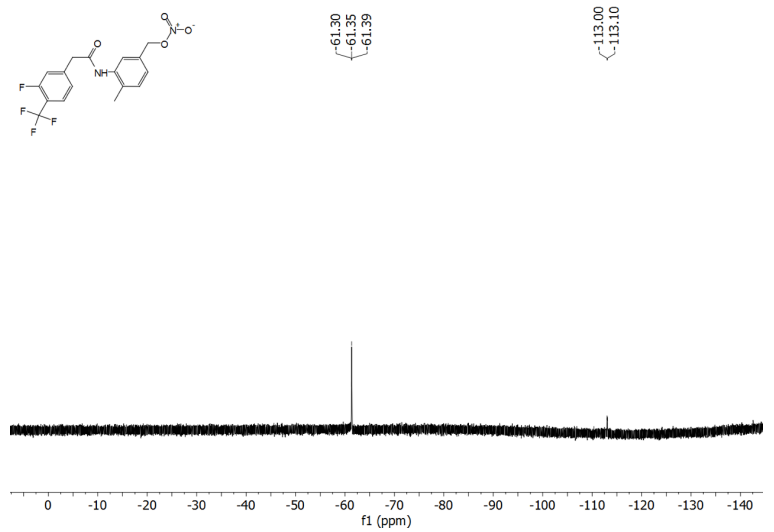

Figure S40. ^{19}F NMR spectrum of **35** ($CDCl_3$, 282 MHz).

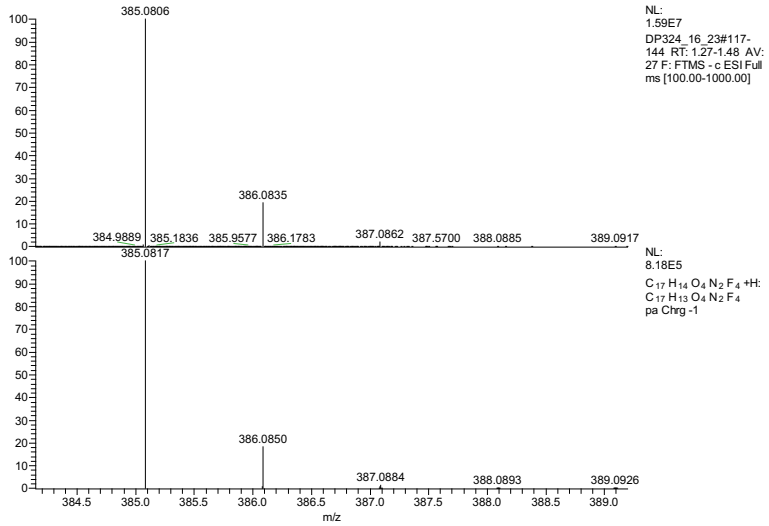

Figure S41. Experimental (upper) and simulated (lower) HRMS spectrum of **35**.

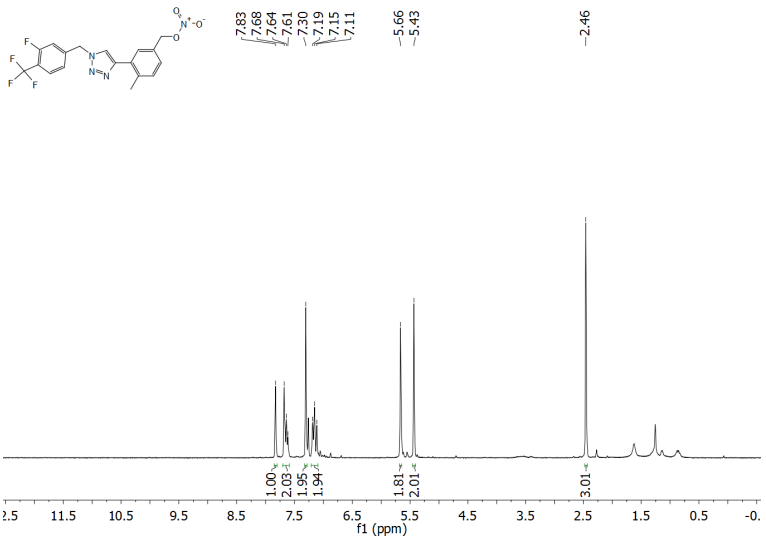

Figure S42. ^{1}H NMR spectrum of **42a** ($CDCl_3$, 300 MHz).

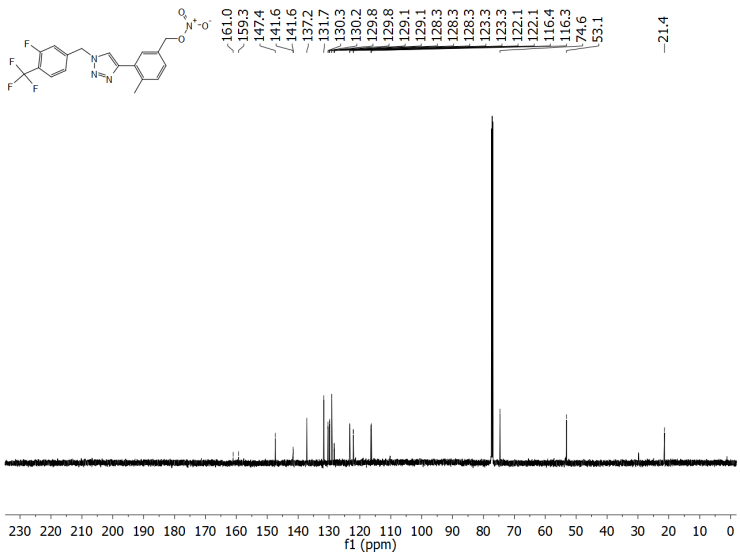

Figure S43. ^{13}C NMR spectrum of **42a** ($CDCl_3$, 75 MHz).

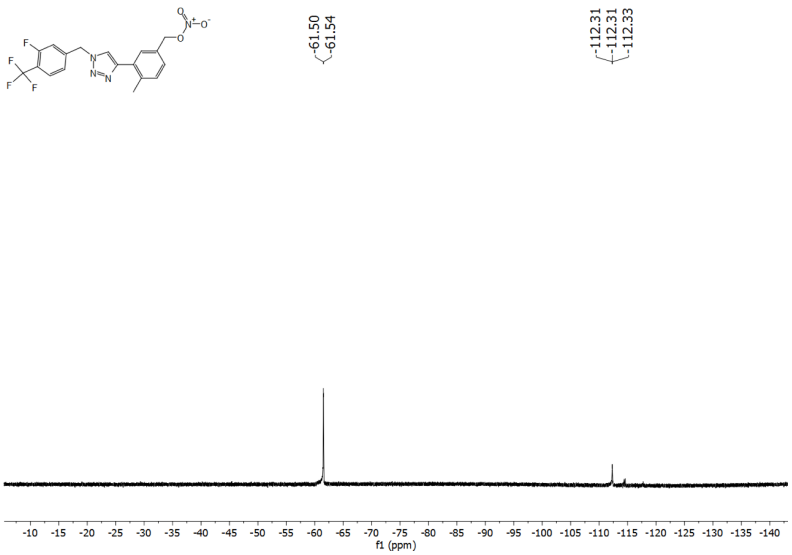

Figure S44. ^{19}F NMR spectrum of **42a** ($CDCl_3$, 282 MHz).

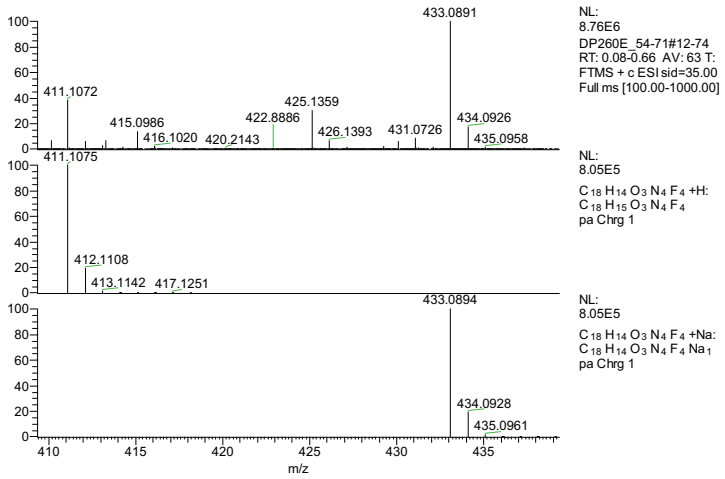

Figure S45. Experimental (upper) and simulated (lower) HRMS spectrum of **42a**.

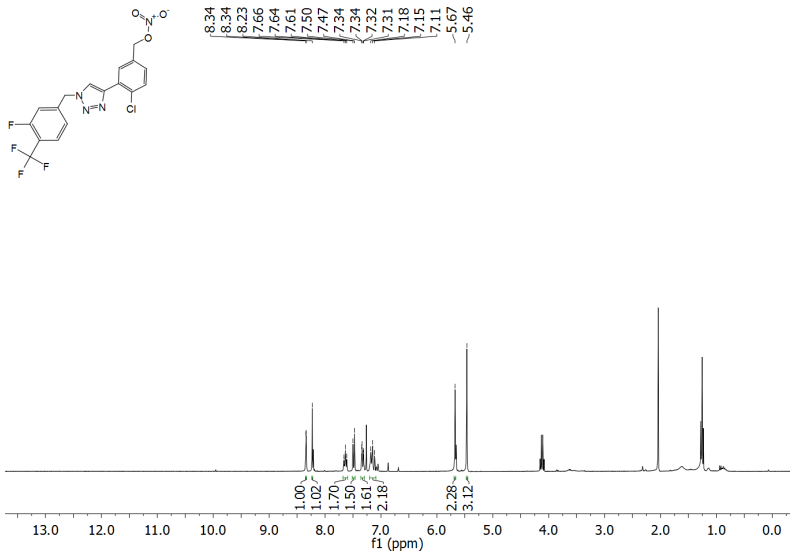

Figure S46. ^{1}H NMR spectrum of **42b** ($CDCl_3$, 300 MHz).

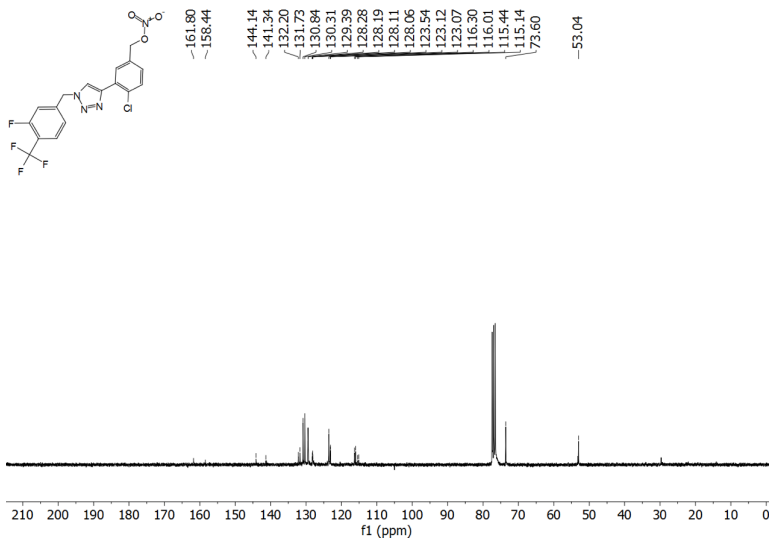

Figure S47. ^{13}C NMR spectrum of **42b** ($CDCl_3$, 75 MHz).

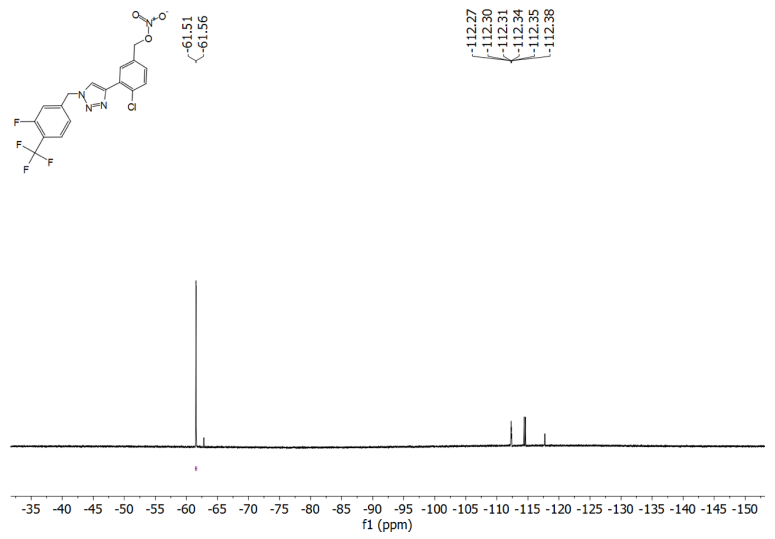

Figure S48. ^{19}F NMR spectrum of **42b** ($CDCl_3$, 282 MHz).

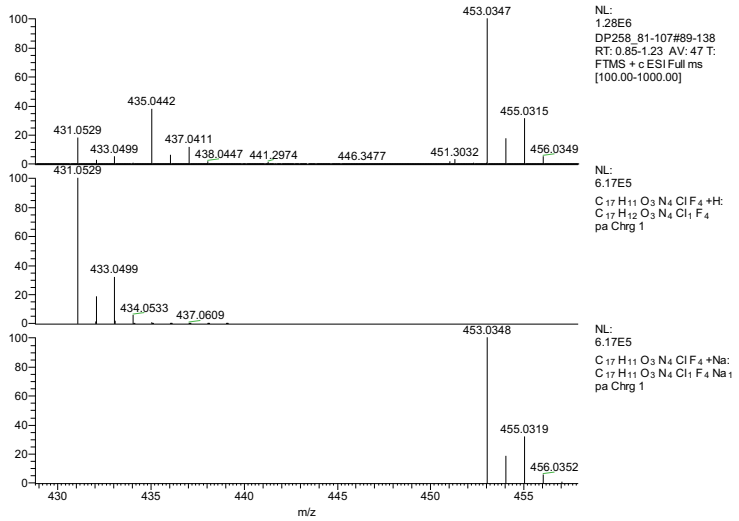

Figure S49. Experimental (upper) and simulated (lower) HRMS spectrum of **42b**.

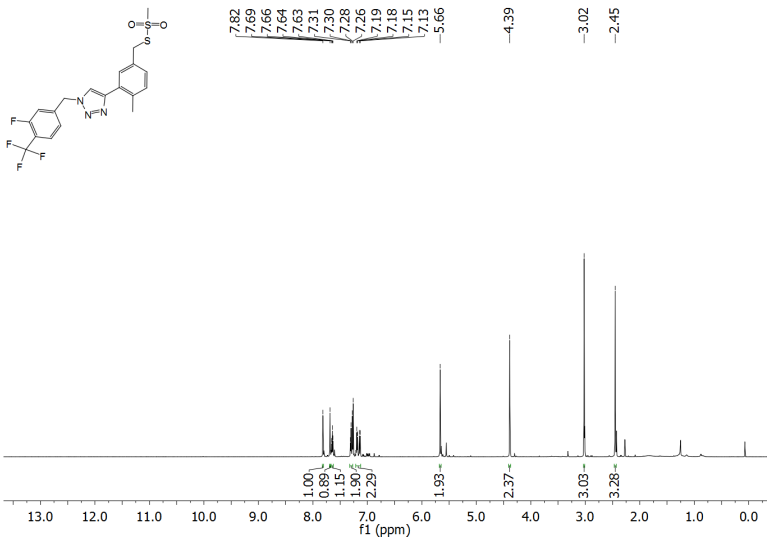

Figure S50. ^{1}H NMR spectrum of **43** ($CDCl_3$, 300 MHz).

40

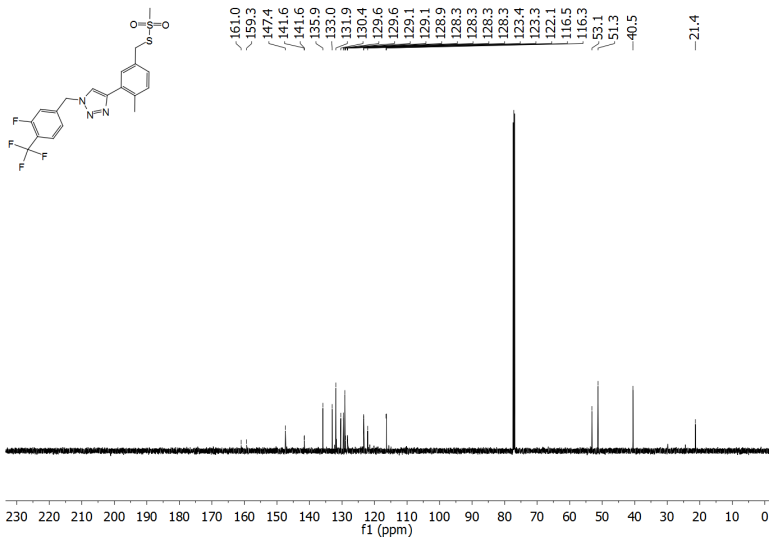

Figure S51. ^{13}C NMR spectrum of **43** ($CDCl_3$, 150 MHz).

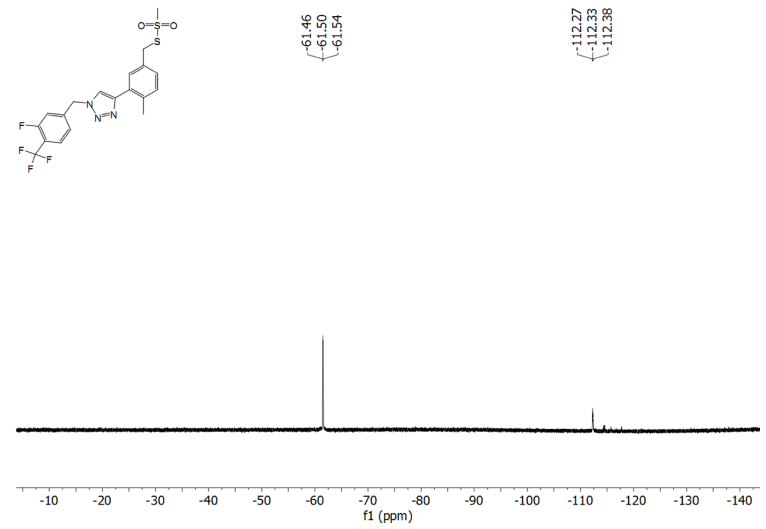

Figure S52. ^{19}F NMR spectrum of **43** ($CDCl_3$, 282 MHz).

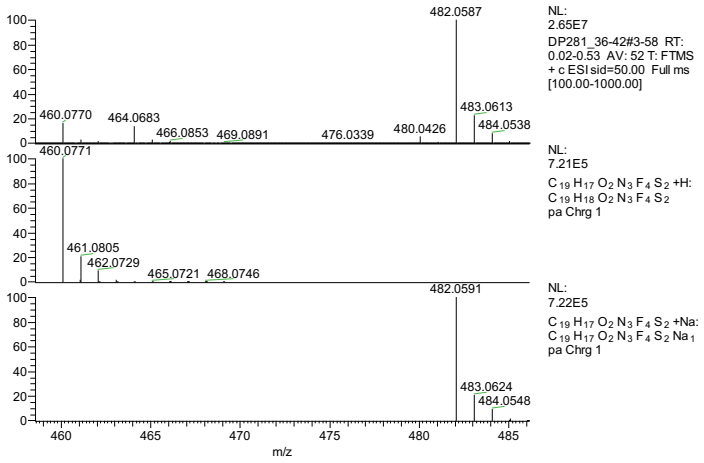

Figure S53. Experimental (upper) and simulated (lower) HRMS spectrum of **43**.

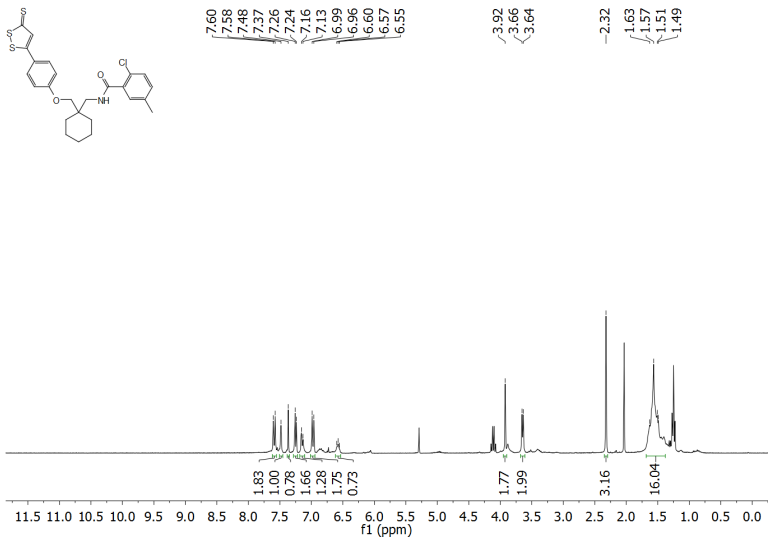

Figure S54. ^{1}H NMR spectrum of **49** ($CDCl_3$, 600 MHz).

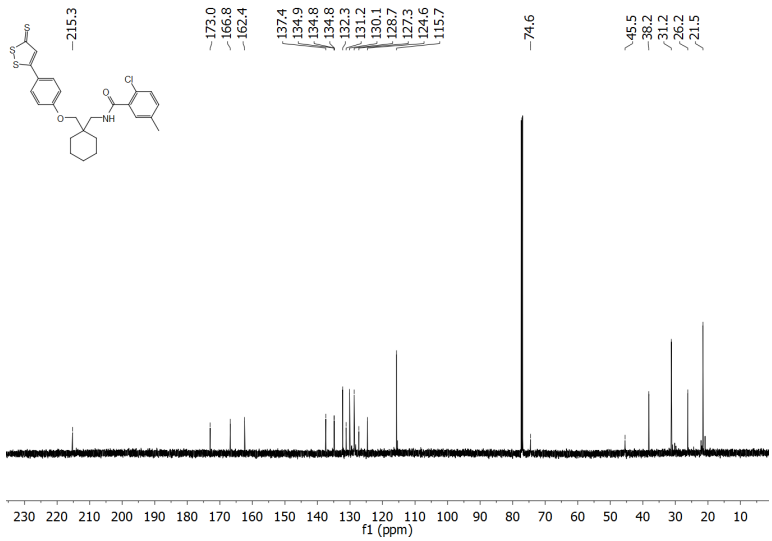

Figure S55. ^{13}C NMR spectrum of **49** ($CDCl_3$, 150 MHz).

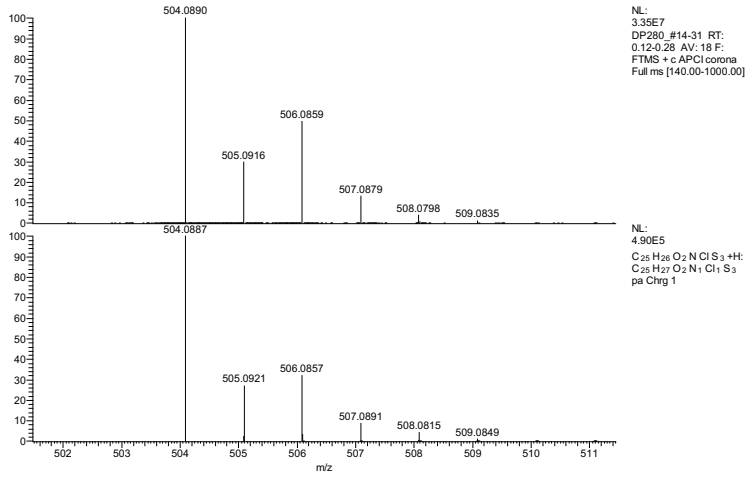

Figure S56. Experimental (upper) and simulated (lower) HRMS spectrum of **49**.

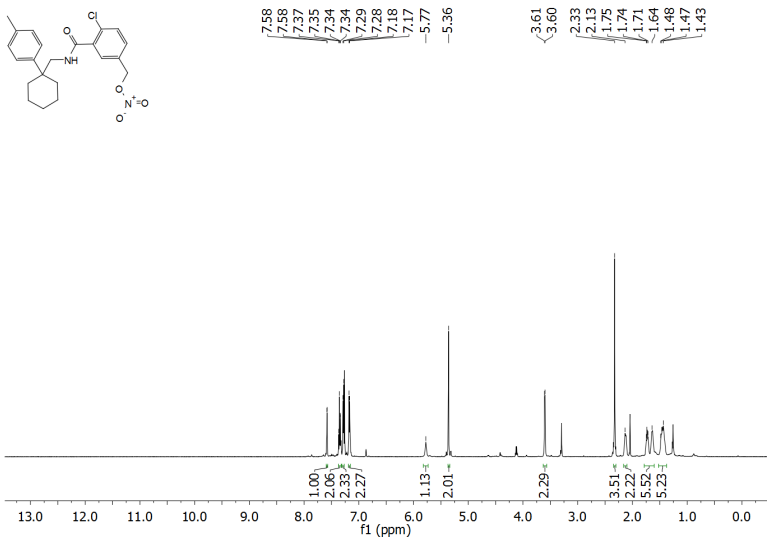

Figure S57. ^{1}H NMR spectrum of **53** ($CDCl_3$, 600 MHz).

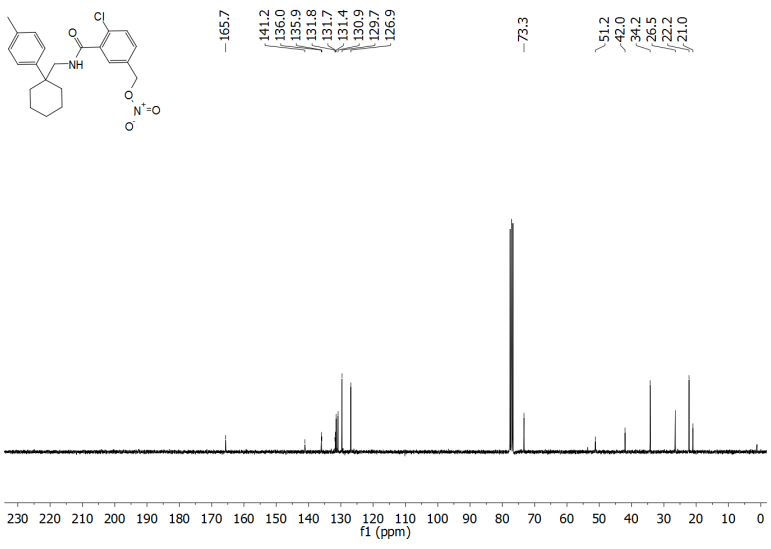

Figure S58. ^{13}C NMR spectrum of **53** ($CDCl_3$, 75 MHz).

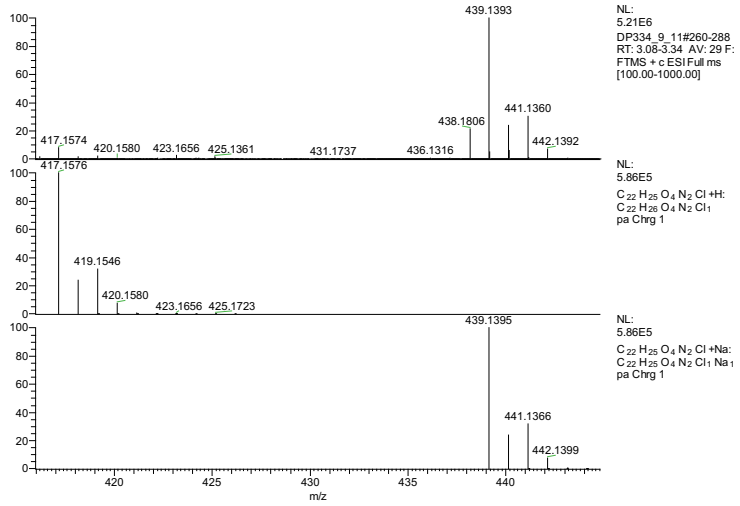

Figure S59. Experimental (upper) and simulated (lower) HRMS spectrum of **53**.

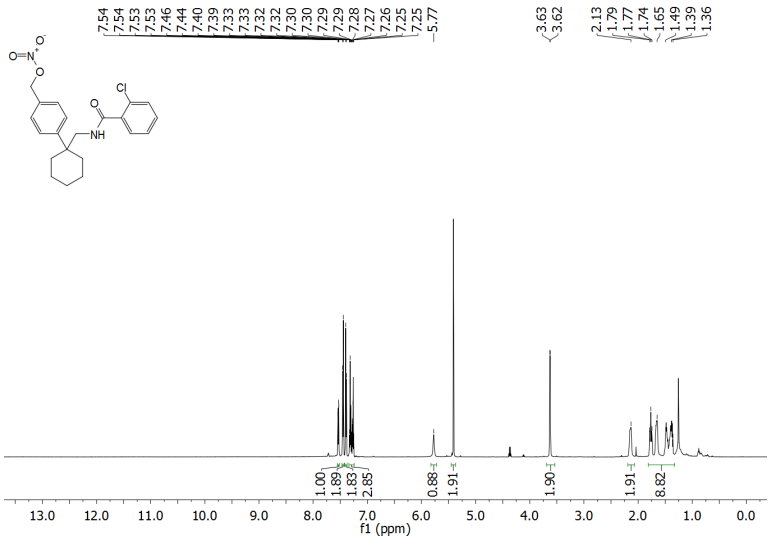

Figure S60. ^{1}H NMR spectrum of **56** ($CDCl_3$, 600 MHz).

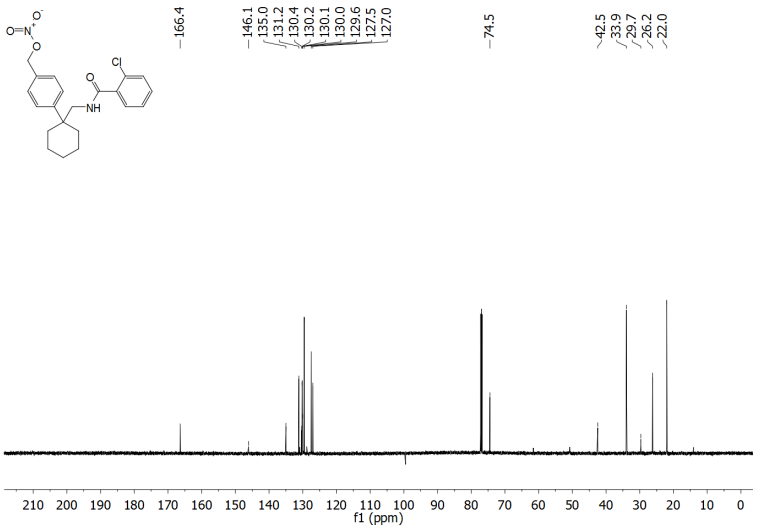

Figure S61. ^{13}C NMR spectrum of **56** ($CDCl_3$, 150 MHz).

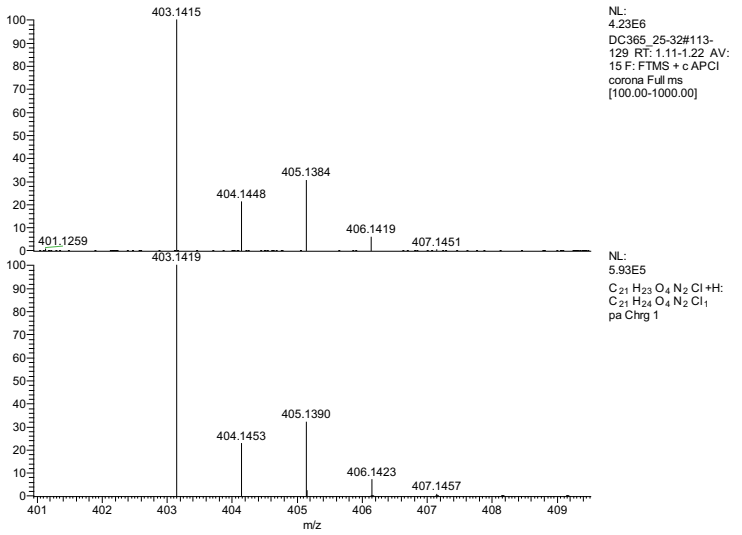

Figure S62. Experimental (upper) and simulated (lower) HRMS spectrum of **56**.

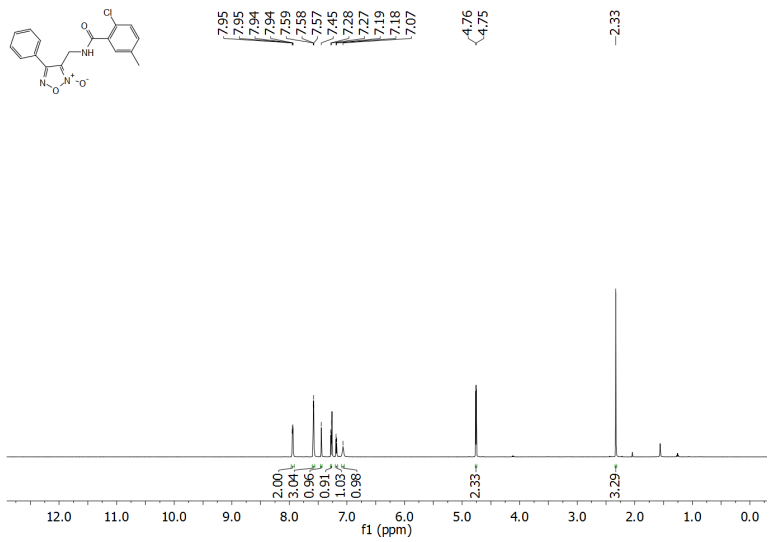

Figure S63. ^{1}H NMR spectrum of **60** ($CDCl_3$, 600 MHz).

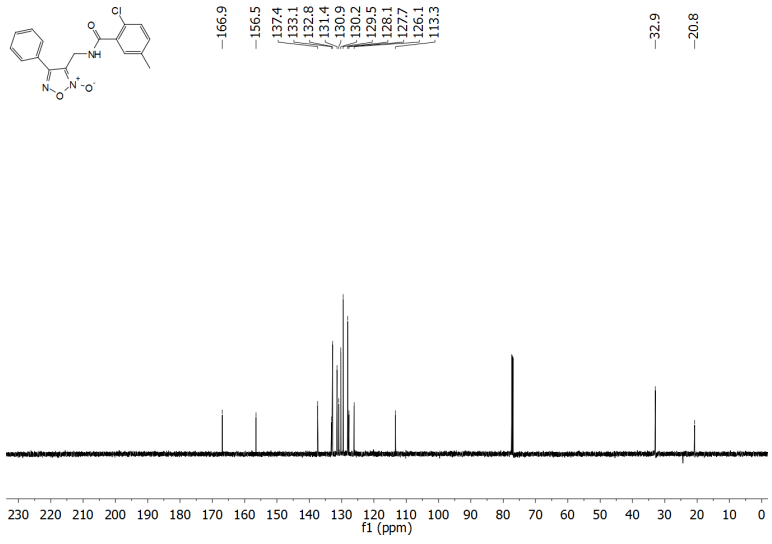

Figure S64. ^{13}C NMR spectrum of **60** ($CDCl_3$, 150 MHz).

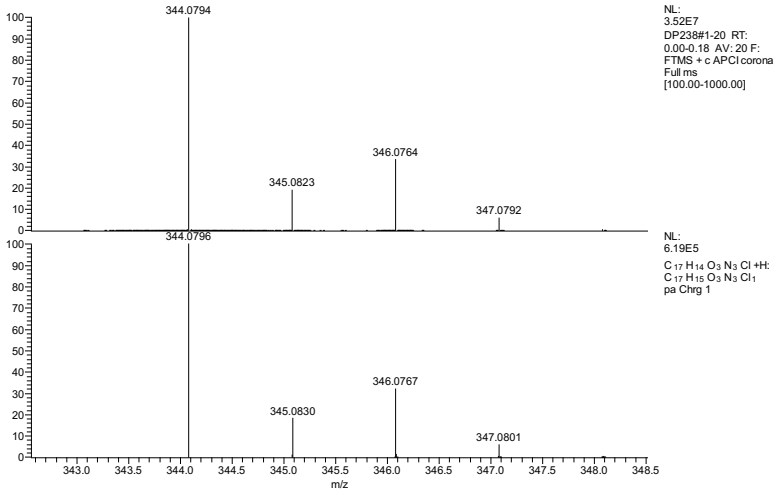

Figure S65. Experimental (upper) and simulated (lower) HRMS spectrum of **60**.

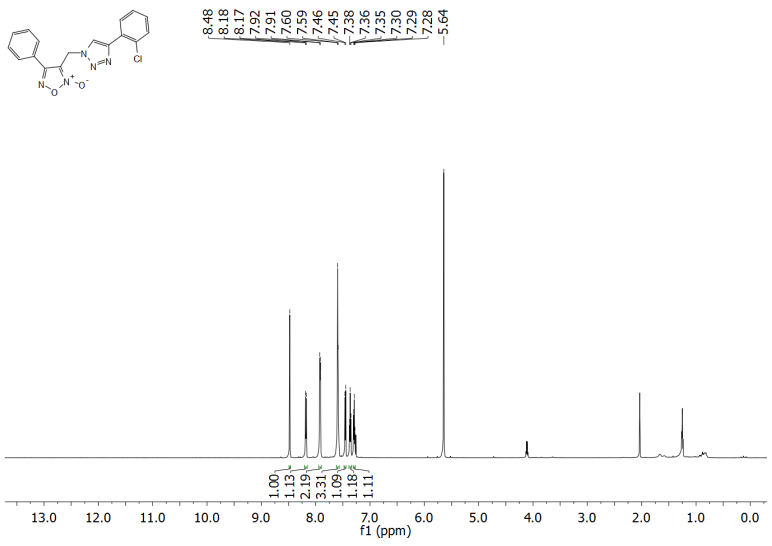

Figure S66. ^{1}H NMR spectrum of **61** ($CDCl_3$, 600 MHz).

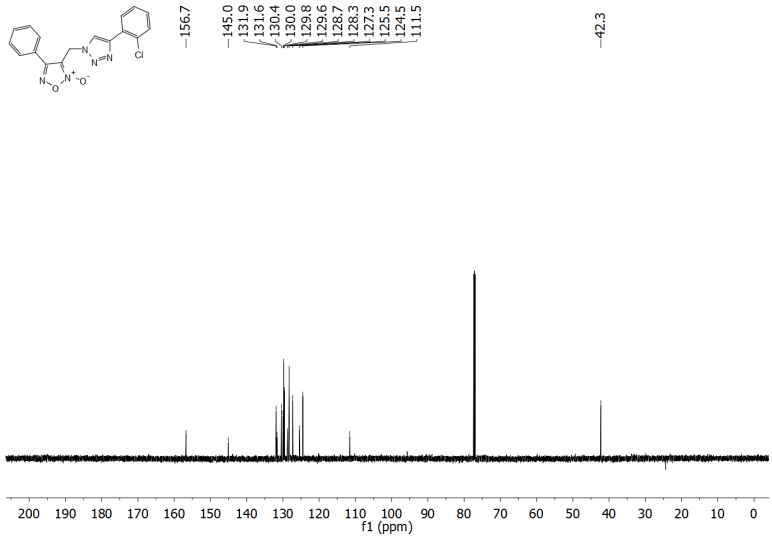

Figure S67. ^{13}C NMR spectrum of **61** ($CDCl_3$, 150 MHz).

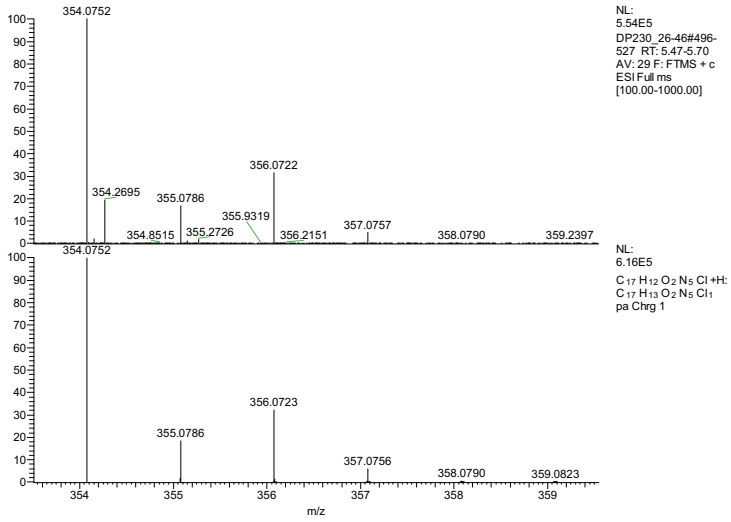

Figure S68. Experimental (upper) and simulated (lower) HRMS spectrum of **61**.

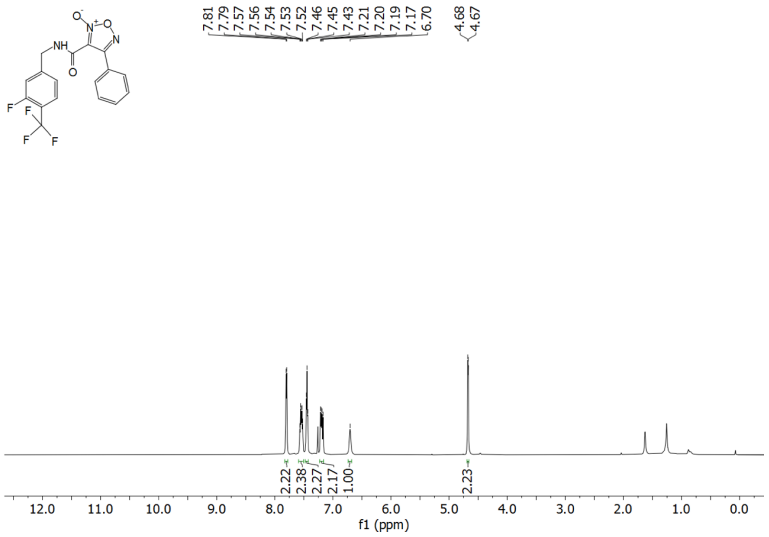

Figure S69. ^{1}H NMR spectrum of **63** ($CDCl_3$, 600 MHz).

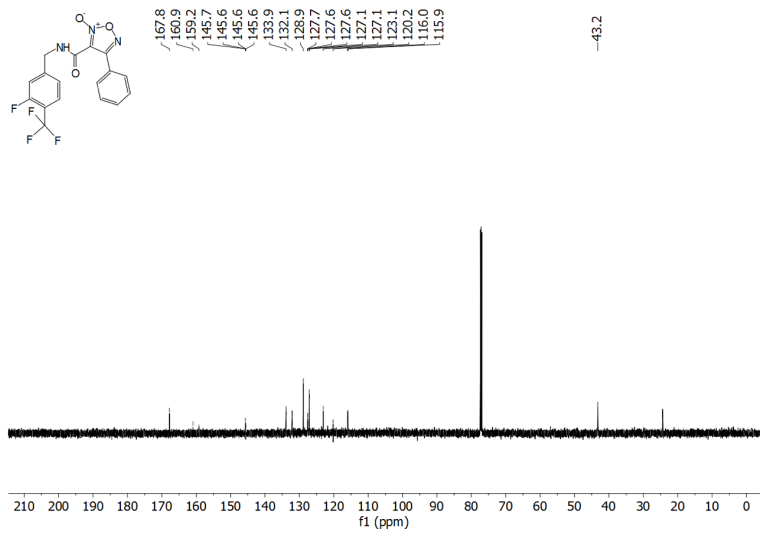

Figure S70. ^{13}C NMR spectrum of **63** ($CDCl_3$, 150 MHz).

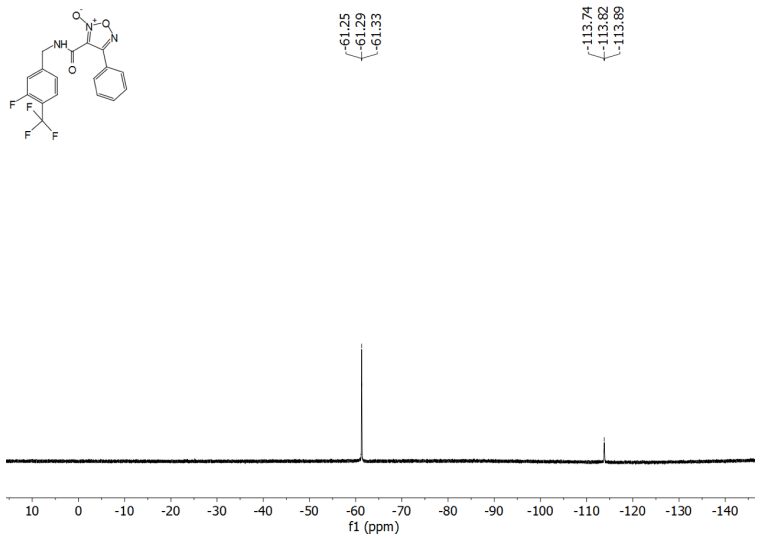

Figure S71. ^{19}F NMR spectrum of **63** ($CDCl_3$, 282 MHz).

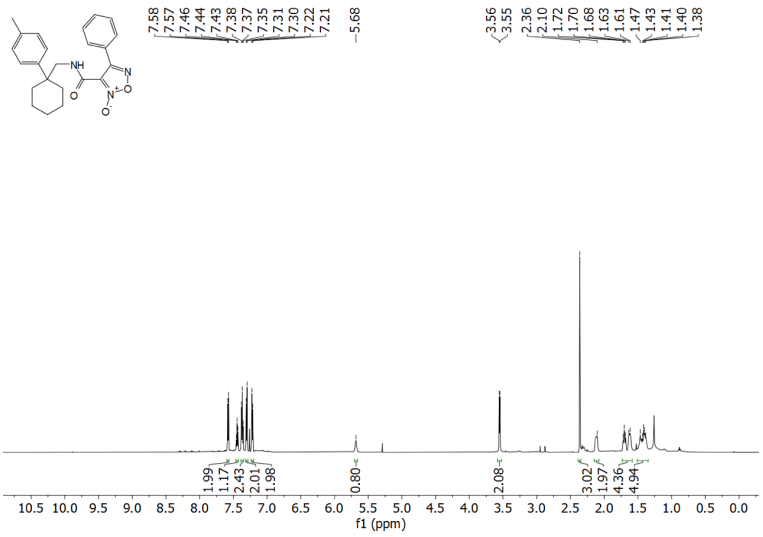

Figure S72. ^{1}H NMR spectrum of **64** ($CDCl_3$, 300 MHz).

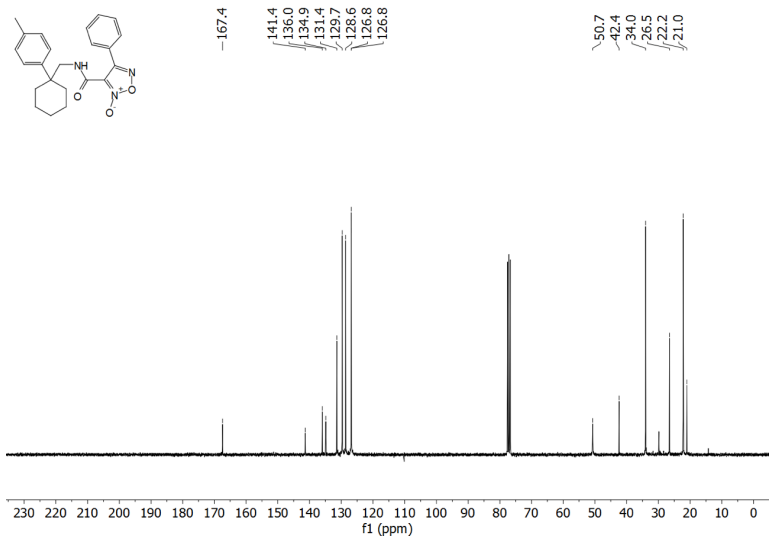

Figure S73. ^{13}C NMR spectrum of **64** ($CDCl_3$, 75 MHz).

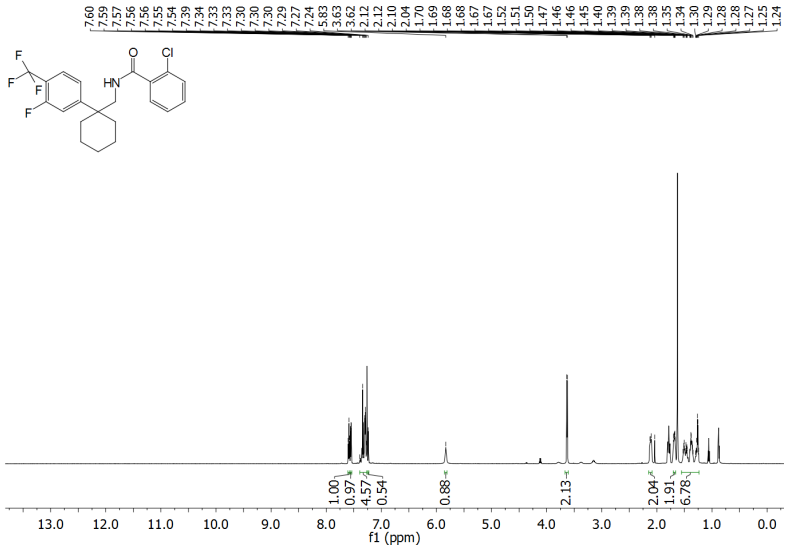

Figure S74. ^{1}H NMR spectrum of **67** ($CDCl_3$, 600 MHz).

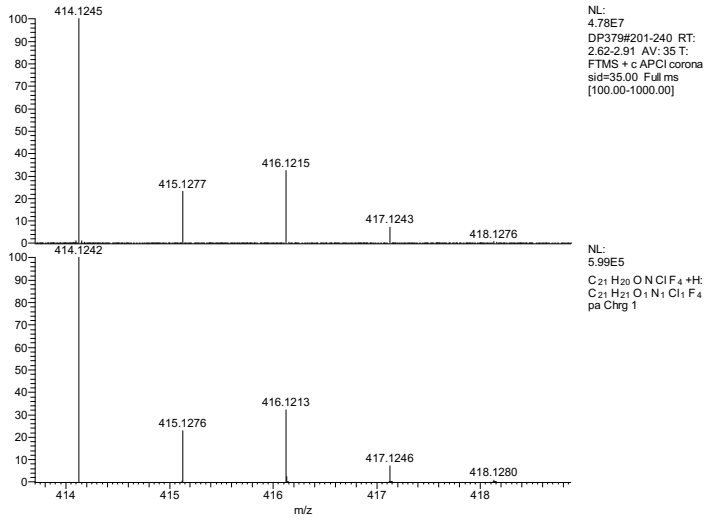

Figure S75. Experimental (upper) and simulated (lower) HRMS spectrum of **67**.

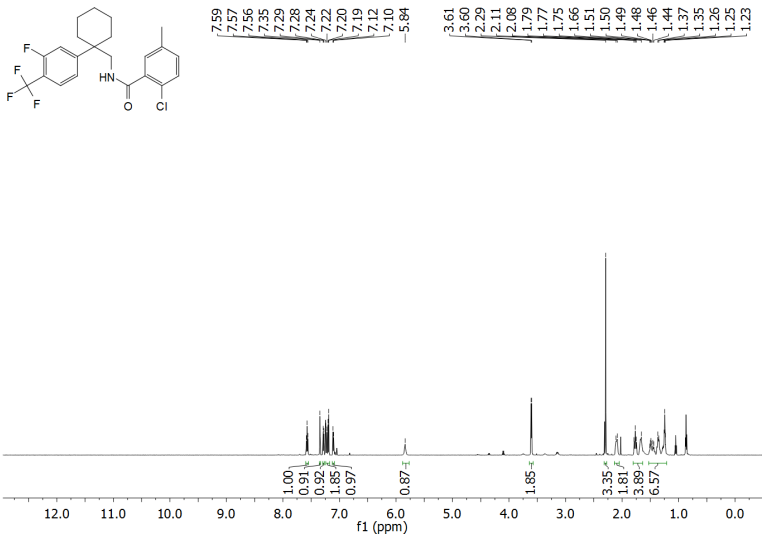

Figure S76. ^{1}H NMR spectrum of **68** ($CDCl_3$, 600 MHz).

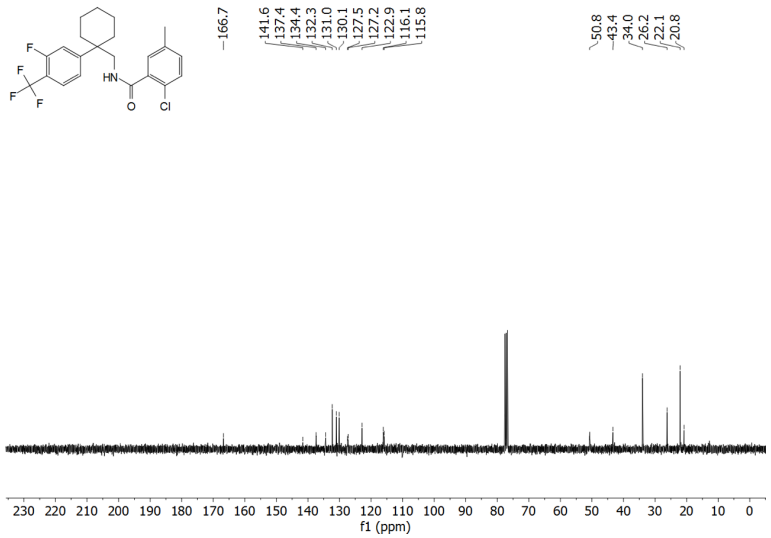

Figure S77. ^{13}C NMR spectrum of **68** ($CDCl_3$, 75 MHz).

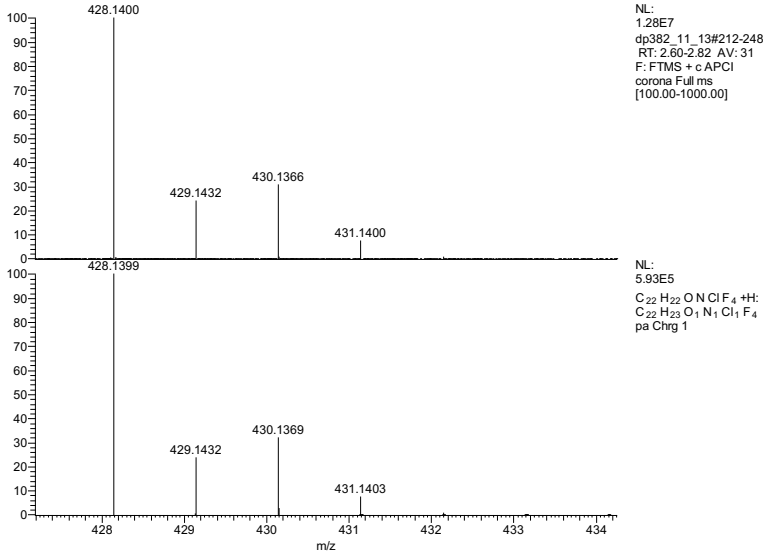

Figure S78. Experimental (upper) and simulated (lower) HRMS spectrum of **68**.

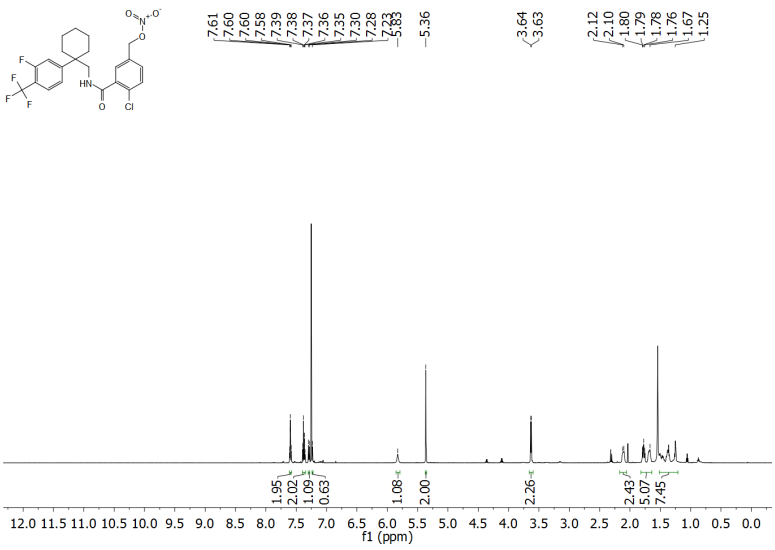

Figure S79. ^{1}H NMR spectrum of **70** ($CDCl_3$, 600 MHz).

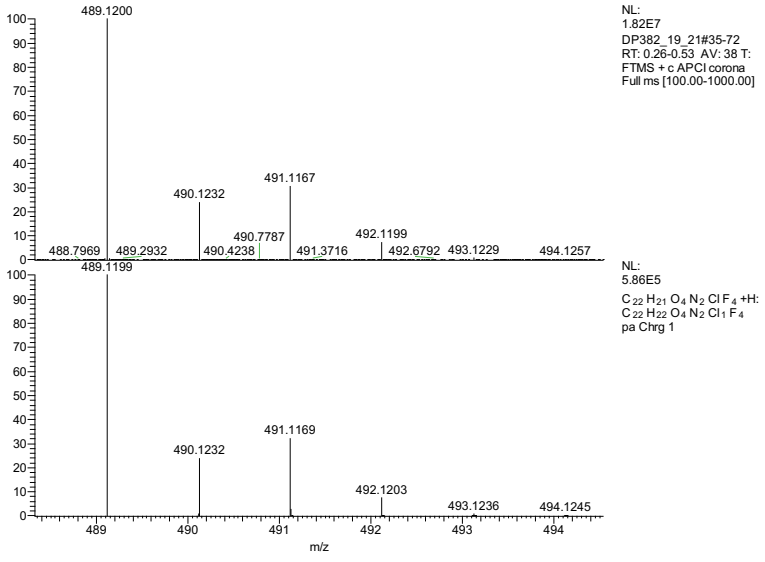

Figure S80. Experimental (upper) and simulated (lower) HRMS spectrum of **70**.

ADME properties

The ADME (absorption, distribution, metabolism, excretion) properties were also calculated (Table S1). In general, all the synthesized analogues possess drug-like properties. Compounds with high clogP values, which are representative for the solubility and lipophilicity of the compounds, were in fact insoluble in water, indicating that the preliminary prediction of the ADME properties may allow the rejection of otherwise promising designed molecules.

Table S1. ADME properties of the synthesized P2X7 inhibitors.

	#rotor	mol MW	donorHB	accptHB	QPlogPo/w	QPlogHERG	PSA	clogP
RANGE	**0–15**	**130–725**	**0–6**	**2–20**	**−2–6.5**	**>−5**	**7–200**	**<5**
AZ1	5	401.978	2	6	3.467	−6.267	53.628	4.996
4	6	378.855	1	5	3.429	−4.25	92.948	2.304
5	6	428.003	1	6.5	3.57	−4.169	75.723	5.241
11	2	327.856	0	2.5	5.002	−4.735	29.825	6.386
18a	5	382.461	0	5	3.746	−4.997	89.844	3.126
18b	5	402.88	0	5	3.924	−5.134	89.095	3.427
19a	5	431.61	0	6.5	4.603	−5.828	70.557	6.063
19b	5	452.028	0	6.5	4.336	−5.33	69.524	6.364
23b	3	371.866	1	4.5	4.311	−3.016	77.988	6.244
24a	5	525.606	0	7.5	5.134	−6.818	120.738	7.216
24b	5	546.024	0	7.5	5.398	−7.007	120.215	7.485
30	6	406.721	1	5	4.008	−5.572	92.83	0.980
35	6	386.302	1	5	4.002	−5.647	91.994	0.615
42a	5	410.327	0	5	4.268	−6.065	90.162	1.602
42b	5	430.746	0	5	4.397	−6.086	90.652	1.903
43	5	459.476	0	6.5	4.724	−6.246	70.186	4.539
49	6	504.119	1	5.25	6.994	−6.057	52.907	7.495
53	6	416.903	1	5	4.262	−4.643	90.574	2.693
56	6	402.877	1	5	4.347	−5.686	90.33	2.194
60	3	343.769	1	5.5	2.841	−5.059	88.601	2.679
61	2	353.767	0	5.5	2.762	−5.26	87.25	3.103
63	3	381.286	1	5.5	3.587	−5.951	88.952	2.962
64	3	391.469	1	5.5	4.396	−5.878	87.439	4.675
67	3	413.842	1	2.5	6.384	−5.334	32.754	6.179
68	3	427.869	1	2.5	6.624	−5.038	31.857	6.678
70	6	488.866	1	5	5.467	−5.544	90.001	3.220

Pharmacophore model generation and validation

The pharmacophore model was generated and validated using LigandScout 4.1 Advanced software available from InteLigand, GmbH, Vienna, Austria.[6,7] Due to the absence of the *h*P2X7R crystal structure, a ligand-based pharmacophore model was created. The model was based on the common features of compounds with proved activity on *h*P2X7 receptor. In order to establish the features of the pharmacophore model, two different sets of known active *h*P2X7R antagonists were prepared; the training and the test set, including 21 and 24 compounds, respectively. The training set provided the required chemical characteristics of the pharmacophore, while the test set was used to check the selectivity of the generated pharmacophore model. ChEMBL[8] and Binding DB[9] databases were used to create these sets, while the IC_{50} values of the distinguished ligands ranged between 0.01 nM and 1.00 nM.

Then, a series of ten pharmacophore hypotheses were initially generated and evaluated according to the pharmacophore-fit score. For the best pharmacophore hypothesis, all the examined compounds comprised of four common pharmacophore features (Figure S81A). This initial model was assessed as non-selective and subjected to further feature modifications. Specifically, two hydrophobic regions (one optimal) and one optimal hydrogen bond acceptor were added. Finally, the pharmacophore model was optimized by increasing the number of the exclusion volumes (from 11 to 263). The features of the optimum pharmacophore model are presented in Figure S81B.

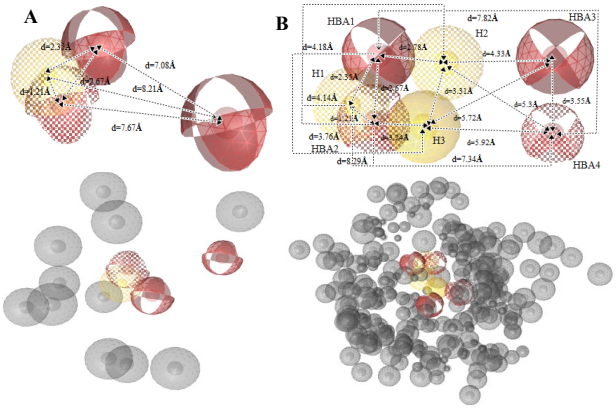

Figure S81. Representation of (A) the initial and (B) the optimum pharmacophore model features. The features are colored as follows: hydrogen bond acceptors (HBA) as red spheres, hydrophobic regions (H) as yellow spheres, and exclusion volumes (Ex. Vol.) as grey spheres. The distances (Å) between the chemical features are illustrated as black lines.

The reliability of the pharmacophore model was examined using two different sets of compounds,[10] retrieved from ChEMBL[8] and BindingDB[9] databases. The first set, consisting of 833 compounds with known activity against *h*P2X7R ($1 < IC_{50} < 80$ nM), formed the group of actives, and the second

with 85 compounds (IC_{50} >> 80 μM) constituted the group of inactive analogues. The validity of the model was examined using Receiver Operating Characteristic (ROC) curve analysis (Figure S82) and statistically significant variables (Table S2). The reliability of the examined model was also confirmed by the fact that it retrieves almost 86% of the active compounds (Table S2). According to these results the derived model was validated, constituting a reliable filter for further virtual screening.

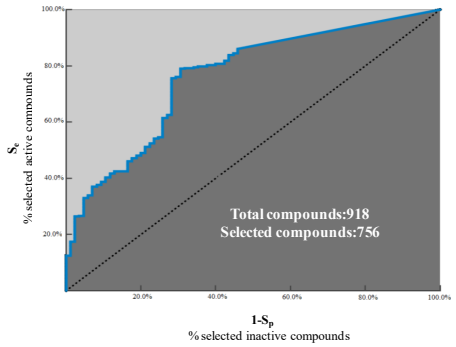

Figure S82. ROC curve of the examined pharmacophore model.

Table S2. Quantitative key parameters derived from the ROC curve analysis.

Key Parameters	Value
Sensitivity (Se)	0.86
False Positive Rate (1-Sp)	0.46
Enrichment Factor (EF)	1.10
Area under the curve (AUC)	0.75
Total number of Actives in the database	833
Total number of Inactives in the database	85
Total number of compounds in the database	918
Number of hits retrieved (Hit list)	756
Number of Actives in the Hit list	717
Number of Inactives in the Hit list	39

Pharmacophore-based virtual screening

Pharmacophore-based virtual screening was implemented to the ZINC database (http://zinc.docking.org/), containing ~13 million compounds, to identify scaffolds that could replace the adamantane ring. The idbgen tool of LigandScout[6,7] was used to convert the examined pool of compounds to an appropriate database. The hits with the top-ranked pharmacophore-fit score were further filtered according to the physicochemical properties predicted by the Qikprop[11] module of MAESTRO.[12] The filtering criteria were based on the Lipinski parameters values of the training set (Table S3).

Table S3. Range of values of the Lipinski parameters of the training set.

Criteria	Range of values
Hydrogen Bond Acceptor (HBA)	2–4
Hydrogen Bond Donor (HBD)	0–3
Lipophilicity (AlogP)	2.35–5.44
Rotatable Bonds (RB)	1–8
Polar Surface Area (PSA) [Å^2]	41.99–94.19

The screening results pointed out compounds bearing i) 3-fluoro-4-(trifluoromethyl)phenyl, ii) aryl-substituted cyclohexyl and iii) 1,2,5-oxadiazole-2-oxide (furoxan) moieties, which would be favorable materials for the replacement of the adamantane ring (Figure S83).

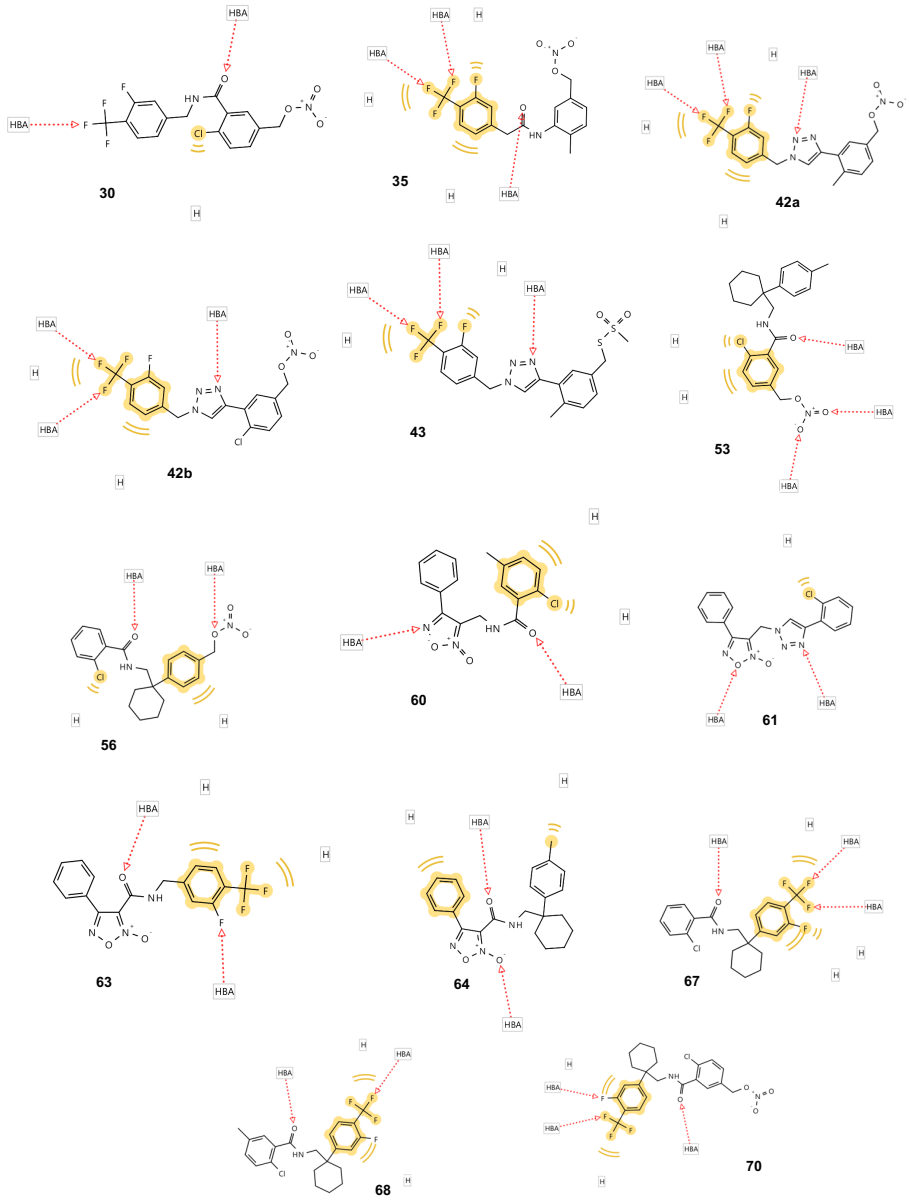

Figure S83. Fitness of the designed and synthesized structurally modified analogues on the pharmacophore model features. The hydrogen bond acceptors (HBA) are depicted with red arrows and the hydrophobic regions (H) with yellow color.

61

References

[1] A. S. K. Hashmi, R. Salathé, W. Frey, *Chem-Eur. J.* **2006**, *12*, 6991–6996.

[2] T. Sasaki, S. Eguchi, T. Katada, O. Hiroaki, *J. Org. Chem.* **1977**, *42*, 3741–3743.

[3] R. Matsubara, A. Ando, Y. Saeki, K. Eda, N. Asada, T. Tsutsumi, Y.S. Shin, M. Hayashi, *J. Heterocyclic Chem.* **2016**, *53*, 1094–1105.

[4] C. J. Sutton, M. Wiesmann, W. Wang, M. Lindvall, J. Lan, S. Ramurthy, A. Sharma, E. Mieuli, L. M. Klivanski, W. Lenahan, et al., US2008045528A1, **2008**.

[5] A. Yanagisawa, T. Nezu, S.I. Mohri, *Org. Lett.* **2009**, *11*, 5286–5289.

[6] G. Wolber, T. Langer, *J. Chem. Inf. Model.* **2005**, *45*, 160–169.

[7] http://www.inteligand.com/ligandscout/ (11.03.20)

[8] https://www.ebi.ac.uk/chembl (11.03.20)

[9] https://www.bindingdb.org/bind/index.jsp (11.03.20)

[10] T. Langer, G. Wolber, *Drug Discov. Today: Technol.* **2004**, *1*, 203–207.

[11] QikProp, Schrödinger, LLC, New York, NY, **2020**.

[12] Maestro, Schrödinger, LLC, New York, NY, **2020**.

3.3 Deviant Reporter Expression and P2X4 Passenger Gene Overexpression in the Soluble EGFP BAC Transgenic P2X7 Reporter Mouse Model

In this publication, two BAC transgenic P2X7 reporter mouse models are compared by analysis of their P2X7 expression patterns and levels. In addition, the functional phenotype of the reporter mice was assessed. The Tg(RP24-114E20P2X7451P-StrepHis-EGFP)Ani reporter model overexpresses a P2X7-EGFP fusion protein under the control of a BAC-derived mouse P2X7 gene (*P2rx7*) promoter and was generated and characterized in our group [Appendix 4.4]. Here, Strep-His-EGFP sequence was integrated in frame into exon 13 of (*P2rx7*) to preserve the exon-intron structure of the gene. The Tg(P2rx7-EGFP)FY174Gsat mouse model was generated in the framework of the GENSAT project [84] and expresses a soluble EGFP (sEGFP) under the control of a BAC-derived *P2rx7* promoter. Here, a targeting vector was used to integrate the sEGFP sequence followed by a poly(A) signal into the *start* ATG in exon 1 of the *P2rx7* gene, which should prevent its expression. Comparison of both BAC constructs showed that the BAC clone used for this sEGFP model encoded not only the *P2rx7* gene with 5′ and 3′ non-translated regions, but also a neighboring *P2rx4* passenger gene. Accordingly, we found RNA and protein levels of P2X4 to be increased in the sEGFP mouse model. Surprisingly, this was also true for P2X7 levels. Comparative analysis of EGFP, *P2rx7*, and *P2rx4* transcripts revealed correlating expression patterns for wt and P2X7-EGFP overexpressing mice, but striking differences for the sEGFP mouse line. While we observed a relatively even distribution of *P2rx4* and *P2rx7* transcripts in different brain regions for the P2X7-EGFP mouse, the levels varied considerably for the sEGFP mouse. DAB stainings using a P2X7-specific nanobody revealed that the P2X7 expression pattern in both reporter mouse models mirror the endogenous P2X7 distribution in wt mice, as expected. However, analysis of EGFP reporter expression patterns analyzed by DAB and immunofluorescence stainings revealed striking differences between the two mouse models, similar to the RNA transcript expression patterns. Additionally, for the sEGFP mouse, we also observed dissimilarities in EGFP and P2X7 expression patterns. FACS analysis and co-immunostainings of EGFP and cell type-specific markers in brain slices from BAC-transgenic mice confirmed the expression of the P2X7-EGFP fusion protein in microglia, oligodendrocytes, macrophages, and $CD4^+$ T cells, but not in neurons [Appendix 4.4], whereas sEGFP was absent in microglia and $CD4^+$ T cells, showed highly variable expression in macrophages and mast cells and most importantly, at least partial neuronal expression. Preliminary studies in a *status epilepticus* model suggest functional consequences of the P2X4 and/ or P2X7 overexpression.

In summary, although in both reporter models the EGFP constructs are expected to be expressed under the control of the *P2rx7* promoter, the EGFP reporter expression pattern of the sEGFP model differs greatly from the one of the P2X7-EGFP model and does not correlate well with endogenous P2X7R distribution in wt mice. By sequencing the integration sites of the EGFP cDNA, we found that the P2X7 *start* ATG at the 3′ integration site, which should have been interrupted by the integration of the sEGFP and poly(A) sequences, was complemented due to the used recombination strategy and is in fact intact. This would explain the increased P2X7 expression levels. A possible explanation for the deviant reporter expression in the sEGFP mouse model could be the modification or deletion of regulatory sequences, since the sEGFP is

translated from a truncated mRNA sequence and possibly lacks such regulatory elements. Additionally, the 5′ non-translated region of *P2rx7* is altered with potential impact on post-transcriptional and translational regulatory mechanisms.
We conclude from this, that although BAC transgenic reporter mouse models have greatly advanced the field, limitations that are inherent to this approach need to be considered and caveats of BAC-transgenic approaches are discussed.
I contributed to this publication by performing DNA sequence analysis and interpretation, resulting in Supplementary Fig. 4. In addition, I performed DAB stainings shown in Supplementary Fig. 5 and assisted with staining protocols, and text editing.

Deviant Reporter Expression and P2X4 Passenger Gene Overexpression in the Soluble EGFP BAC Transgenic P2X7 Reporter Mouse Model

Antonio Ramírez-Fernández, Lidia Urbina-Treviño, Giorgia Conte, Mariana Alves, Björn Rissiek, Anna Durner, Nicolas Scalbert, Jiong Zhang, Tim Magnus, Friedrich Koch-Nolte, Nikolaus Plesnila, Jan M. Deussing, Tobias Engel, Robin Kopp and Annette Nicke

published in

Scientific Reports 2020, 10: 19876

www.nature.com/scientificreports

scientific reports

Check for updates

OPEN

Deviant reporter expression and P2X4 passenger gene overexpression in the soluble EGFP BAC transgenic P2X7 reporter mouse model

Antonio Ramírez-Fernández[1], Lidia Urbina-Treviño[2], Giorgia Conte[3], Mariana Alves[3], Björn Rissiek[4], Anna Durner[1], Nicolas Scalbert[1], Jiong Zhang[1], Tim Magnus[4], Friedrich Koch-Nolte[5], Nikolaus Plesnila[6,8], Jan M. Deussing[2], Tobias Engel[3,7], Robin Kopp[1] & Annette Nicke[1]✉

The ATP-gated P2X7 receptor is highly expressed in microglia and has been involved in diverse brain diseases. P2X7 effects were also described in neurons and astrocytes but its localisation and function in these cell types has been challenging to demonstrate in situ. BAC transgenic mouse lines have greatly advanced neuroscience research and two BAC-transgenic P2X7 reporter mouse models exist in which either a soluble EGFP (sEGFP) or an EGFP-tagged P2X7 receptor (P2X7-EGFP) is expressed under the control of a BAC-derived *P2rx7* promoter. Here we evaluate both mouse models and find striking differences in both P2X expression levels and EGFP reporter expression patterns. Most remarkably, the sEGFP model overexpresses a P2X4 passenger gene and sEGFP shows clear neuronal localisation but appears to be absent in microglia. Preliminary functional analysis in a *status epilepticus* model suggests functional consequences of the observed P2X receptor overexpression. In summary, an aberrant EGFP reporter pattern and possible effects of P2X4 and/or P2X7 protein overexpression need to be considered when working with this model. We further discuss reasons for the observed differences and possible caveats in BAC transgenic approaches.

The P2X7 receptor plays a key role in inflammation[1,2] and is considered a therapeutic target for a variety of diseases including depression, Alzheimer's disease, and epilepsy[2–7]. While there exists a general consent regarding its presence and proinflammatory functions in macrophages and microglia, its pathophysiological roles in neurons and astrocytes are less clear. Although P2X7-mediated effects on neurotransmitter release, neuronal excitability, and neuronal cell death have been shown[8–10], its expression and function in neurons have been particularly challenging to demonstrate[11,12]. This is partly due to its complex pharmacology and a lack of specific antibodies. To allow cell type-specific visualization and analysis of protein expression in complex tissues, the generation of bacterial artificial chromosome (BAC) transgenic reporter mice has proven to represent an invaluable method that greatly advanced neuroscience research[13–15]. In this approach, reporter proteins, such as enhanced green fluorescent protein (EGFP), are either directly expressed under the control of BAC-derived regulatory sequences of the gene of interest or a BAC-controlled Cre recombinase is used to cell-specifically drive fluorescent protein expression in floxed reporter mouse lines. Although numerous studies proved that this approach is able to reliably reproduce the expression pattern of the respective gene[16–18], several caveats need to be considered: (i) the

[1]Walther Straub Institute of Pharmacology and Toxicology, Faculty of Medicine, LMU Munich, Munich, Germany. [2]Max Planck Institute of Psychiatry, Molecular Neurogenetics, Munich, Germany. [3]Department of Physiology and Medical Physics, Royal College of Surgeons in Ireland, Dublin D02 YN77, Ireland. [4]Department of Neurology, University Medical Center Hamburg-Eppendorf, Hamburg, Germany. [5]Institute of Immunology, University Medical Center Hamburg-Eppendorf, Hamburg, Germany. [6]Institute for Stroke and Dementia Research, Munich University Hospital, LMU Munich, Germany. [7]FutureNeuro, Science Foundation Ireland Research Centre for Chronic and Rare Neurological Diseases, Royal College of Surgeons in Ireland, Dublin D02 YN77, Ireland. [8]Munich Cluster of Systems Neurology (Synergy), Munich, Germany. ✉email: annette.nicke@lrz.uni-muenchen.de

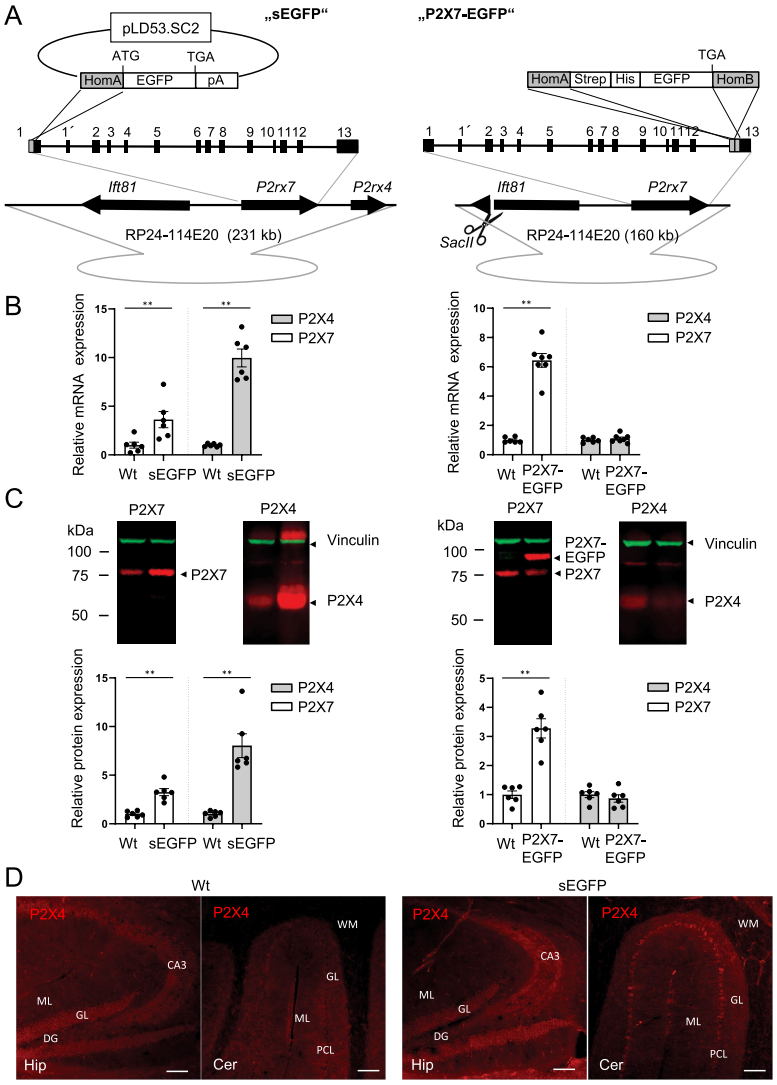
A
„sEGFP“
„P2X7-EGFP“
pLD53.SC2
ATG
TGA
HomA
EGFP
pA
Strep
His
HomB
Ift81
P2rx7
P2rx4
RP24-114E20 (231 kb)
SacII
RP24-114E20 (160 kb)
B
Relative mRNA expression
P2X4
P2X7
Wt
sEGFP
P2X7-EGFP
C
kDa
100
75
50
Vinculin
Relative protein expression
D
Wt
sEGFP
Hip
Cer
CA3
ML
GL
DG
WM
PCL

Figure 1. Comparison of BAC transgenic P2X7 reporter mice and *P2rx4* and *P2rx7* expression in these mice. (**A**) The sEGFP sequence followed by a poly(A) signal was inserted in the start ATG in exon 1 of the *P2rx7* gene. The recombination strategy resulted in co-integration of the pLD53.SC2 vector downstream of the poly(A) signal. In case of the P2X7-EGFP fusion construct, a Strep-His-linker followed by the EGFP sequence was inserted in front of the Stop TGA in exon 13 of *P2rx7*. Use of two homology arms prevented vector integration. Intraflagellar transport protein *Ift81* and, in case of the sEGFP model, *P2rx4* are introduced as passenger genes together *with P2rx7*. In the P2X7-EGFP model, *Ift81* is destroyed by *Sac II* linearization. HomA/B: gene-specific homology arms; opened grey circle: vector backbone of the BAC. For further details see Table 1. (**B**) Quantitative RT-PCR analysis of hippocampal *P2rx4* and *P2rx7 expression* in both mouse models compared to wt mice. Data were normalized to expression of β-actin and the respective levels in wt controls. Bars represent mean ± SEM from 2 independent experiments and 6–7 mice (both sexes, around eight weeks of age). Significance was analysed using the Mann–Whitney test. $^{**}p < 0.01$. (**C**) Representative Western blot analysis of P2X4 and P2X7 protein expression. 50 µg of total lung protein (extracted in 1% NP-40) were loaded per lane. Proteins were immunoblotted and quantified by infrared imaging with fluorescent secondary antibodies. Bars represent mean ± SEM from two independent experiments and 6 mice (both sexes, 10–35 weeks of age). Significance was analysed using the Mann–Whitney test. $^{**}p < 0.01$. Note that the overexpression of P2X4 leads to aggregation and multimer formation in the sEGFP sample. The full gels are shown in Supplementary Fig. 6. (**D**) Immunofluorescence staining with a P2X4 antibody to demonstrate increased P2X4 expression level in the sEGFP reporter mouse. Three different animals were analysed per group, and representative images of cerebellum and hippocampus are shown. GL, granular cell layer; ML, molecular cell layer; DG, dentate gyrus; PCL, Purkinje cell layer; WM, white matter; CA3, cornu amonis region 3; Scale bars 100 µm.

stability and regulation of the resulting reporter mRNA and protein might differ from that of the gene of interest, (ii) critical regulatory elements (which are generally not known) may be absent in the chosen BAC, (iii) possible position effects caused by the random integration of the modified BAC in the genome should be excluded by comparison of several transgenic mouse lines, and (iv) integration of multiple fluorescent reporter gene copies is usually required to allow efficient visualization.

In the case of P2X7, two BAC-transgenic reporter mouse models have been generated (Fig. 1A). In the Tg(P2rx7-EGFP)FY174Gsat mouse (https://www.gensat.org/), a sequence encoding a soluble EGFP (sEGFP) followed by a polyadenylation signal (pA) was inserted into Exon 1 of the *P2rx7* gene[13,19], which should prevent its expression. This mouse has been available for more than ten years and has been frequently used as a reference for *P2rx7* expression in the brain and as tool to monitor its expression in in vitro studies and disease models[20–23]. More recently, the Tg(RP24-114E20P2X7451P-StrepHis-EGFP)Ani reporter model was described. Here, the EGFP sequence was integrated in frame into the last exon of the *P2rx7* gene resulting in the expression of a P2X7-EGFP fusion protein[24].

Although in both P2X7 reporter models the EGFP constructs are expected to be expressed under the control of the *P2rx7* promoter, comparison of the available data indicated substantial differences in their cell type-specific expression[24]. Consequently, in the present study we carefully compared the RNA and protein expression of P2X7 and its neighbouring gene, the P2X4 receptor, in both mouse models. Furthermore, we performed a detailed comparison of the cell type-specific mRNA and protein expression in the CNS. Our results raise serious concerns regarding the reliability of the regional and cell type-specific reporter expression in the sEGFP reporter mouse model. Furthermore, initial functional experiments in a model of *status epilepticus* suggest that overexpression of P2X4 and/or P2X7 influence the pathophysiological response in this mouse.

Results

Comparison of BAC constructs. A critical point in generation of BAC transgenic mice is the selection of an optimal BAC clone: if the 5´and 3´ non-translated regions are too short, critical regulatory sequences might be missing. If these regions are too long (> 200,000 bp[13]), engineering becomes less efficient and neighbouring passenger genes could be included and cause unwanted effects. As shown in Table 1 and Fig. 1A, different BAC clones were used in the two reporter mouse models. In both, the gene encoding the intraflagellar transport protein (IFT)81 is present upstream of the *P2rx7* gene. IFT81 is part of the core of the IFT-B complex, which plays a crucial role in cilia formation and has been associated with ciliopathies[25,26]. In the sEGFP but not in the P2X7-EGFP reporter model, the *P2rx4* gene that lies downstream of the *P2rx7* gene is also present. Both passenger genes should theoretically result in the overexpression of their gene products. However, in the P2X7-EGFP model, the *Ift81* gene was cleaved prior to transformation using a singular *SacII* restriction site. Overexpression of the *Ift81* gene product in the sEGFP model remains to be determined.

Analysis of P2X4 and P2X7 expression levels. To test the possibility of P2X4 overexpression, quantitative RT-PCR and Western blot analysis were performed on brain and lung tissue, respectively, of both mouse models. As expected and shown in Fig. 1B,C, both P2X4 RNA and protein levels were about ten and eightfold higher, respectively, in the sEGFP mouse model. Surprisingly, also P2X7 RNA and protein levels were about threefold higher in this mouse. In contrast, both P2X4 and endogenous P2X7 protein levels were unaltered in the P2X7-EGFP mouse (see also[24]). Next, we performed immunofluorescence staining with a P2X4-specific antibody to investigate if the BAC transgenic P2X4 expression in the sEGFP model mirrors the endogenous P2X4 expression in wild type (wt) mice (Fig. 1D). In agreement with the above observations, a clearly stronger P2X4 signal is seen in cerebellar brain slices from the sEGFP reporter model, although this appears less evident in the hippocampus. The P2X4 expression pattern mirrors that of the endogenous P2X4 transcripts ([27,28], Allen brain atlas) as well as the fluorescent protein patterns described in a BAC transgenic P2X4 reporter mouse line that

	Begin	End	Length (bp)
RP23-181F3	122,505,388	122,736,196	230,809
RP24-114E20	122,541,108	122,701,415	160,308
Ifi81	122,550,204	122,614,518	64,314
P2rx7	122,643,911	122,691,432	47,521
P2rx4	122,707,544	122,729,738	22,194

Table 1. Comparison of BAC clones used for P2X7 reporter mouse lines and genes contained in one or both of the clones (data according to ensembl database).

expresses soluble tdTomato and a recently described conditional P2X4-mCherry knock-in mouse model[18,29]. In these studies, P2X4 transcripts or immunofluorescence were generally seen in Purkinje cells as well as the pyramidal and granular cell layers of the hippocampus and in cortical neurons. As shown in Supplementary Fig. 1, P2X4 staining in Purkinje cells of the sEGFP mice was even strong enough to reveal a pattern that supports its intracellular localisation[30–32].

Regarding the overexpression of P2X7, we wondered if this could be accounted for by the expression of the P2X7k variant[33]. This functional variant has the same length as the canonical P2X7a variant and is derived from the use of an alternative exon 1′ (compare Fig. 1A) that is present in the first intron of the *P2rx7* gene. To determine if the increased P2X7 transcript and protein levels in the sEGFP model represents P2X7a, maybe as a consequence of some "leakiness" of the introduced poly(A) signal, or if the additional P2X7 protein represents P2X7k that likely has its own regulatory sequences within intron 1, we also performed quantitative RT-PCR with specific primer pairs for both variants. However, in agreement with a lower expression of this variant in brain tissue[33] significant P2X7k levels could only be detected if PCR cycle numbers were increased. Under these conditions, the relative increase of transcript levels of the k and a variant were similar in the sEGFP (about twofold) and P2X7-EGFP mice (about sevenfold). This suggests that both variants underlie similar regulation mechanisms in both mice but that the k variant is expressed at much lower levels (Supplementary Fig. 2).

Expression pattern of sEGFP and P2X7-EGFP transcripts in the brain. To compare the expression pattern and region-specific expression levels of EGFP, *P2rx7*, and *P2rx4* transcripts in the two transgenic lines, we next carried out in situ hybridization (ISH) and quantitative RT-PCR in different brain areas (Fig. 2A). ISH revealed a clear EGFP signal and, in agreement with the quantitative PCR data described above, increased *P2rx7* mRNA levels throughout the brain of both mouse models. No differential pattern of P2X7 or EGFP expression was observed between wt and P2X7-EGFP overexpressing mice. In contrast, both the EGFP and P2X7 expression patterns in the sEGFP mouse line showed a clear signal in a region corresponding to the lateral septum, which was not seen in the wt mice. Similarly, a strong overexpression of *P2rx4* transcripts was detected in this same area as well as throughout the brain, which is not observed in P2X7-EGFP mice. A more detailed analysis of *P2rx7* and *P2rx4* expression levels in different brain regions by region-specific quantitative RT-PCR revealed a relatively even distribution of *P2rx4* and *P2rx7* transcripts in all investigated brain regions of the P2X7-EGFP mouse while both *P2rx4* and *P2rx7* levels in the sEGFP mouse varied considerably between regions (*P2rx7*: two to tenfold, *P2rx4*: five to 11-fold) with lowest expression of both transcripts in the thalamus and highest expression in the prefrontal cortex and cerebellum (Fig. 2B).

Expression pattern of sEGFP and P2X7-EGFP protein in the brain. To understand whether the *P2rx7* and EGFP expression patterns observed by ISH is translated into protein expression, we first performed immunofluorescence stainings with an anti-GFP antibody (Fig. 2C). While the EGFP staining pattern was homogenous in P2X7-EGFP transgenic mice, staining in slices of the sEGFP mouse showed again a clear signal in the lateral septum, as well as in cortical layers confirming the mRNA expression pattern observed by ISH (Fig. 2A). The same pattern was observed in both hemispheres and in several mice, indicating that it is region-dependent and does not represent an irregular expression.

To further compare the overall expression pattern of both reporter constructs, we next performed immunofluorescence stainings on sagittal brain sections. As seen in Fig. 3A, both reporter mouse models show a dominant EGFP staining in the molecular layer of the cerebellum. However, both the distribution and expression levels of EGFP clearly differed in the cerebrum. As shown before[24], P2X7-EGFP displays a relatively even distribution in all brain regions with more dominant staining in the cerebral cortex, olfactory bulb, thalamus, hypothalamus, substantia nigra, ventral pons, and a fine rim in the molecular layer that is adjacent to the granular layer of the dentate gyrus. In contrast, the soluble EGFP shows a much more localised expression in areas such as the caudate putamen, the superior colliculus and the granular and entire molecular layer of the dentate gyrus, while staining was very weak or even absent in the olfactory bulb and sparse in the pons. A diffuse expression is present in the hypothalamus.

To further confirm this and to allow comparison with the endogenous P2X7 distribution in wt mice, we next performed DAB stainings with an anti-GFP antibody (Fig. 3B) and a P2X7-specific nanobody (Fig. 3C). As seen in Fig. 3B, DAB staining of EGFP in the two reporter mouse models confirmed the overall expression pattern obtained by immunofluorescence staining and revealed further differences between both models. While P2X7-EGFP staining was enhanced in an approximately 50 µm wide rim surrounding the granular layer of the

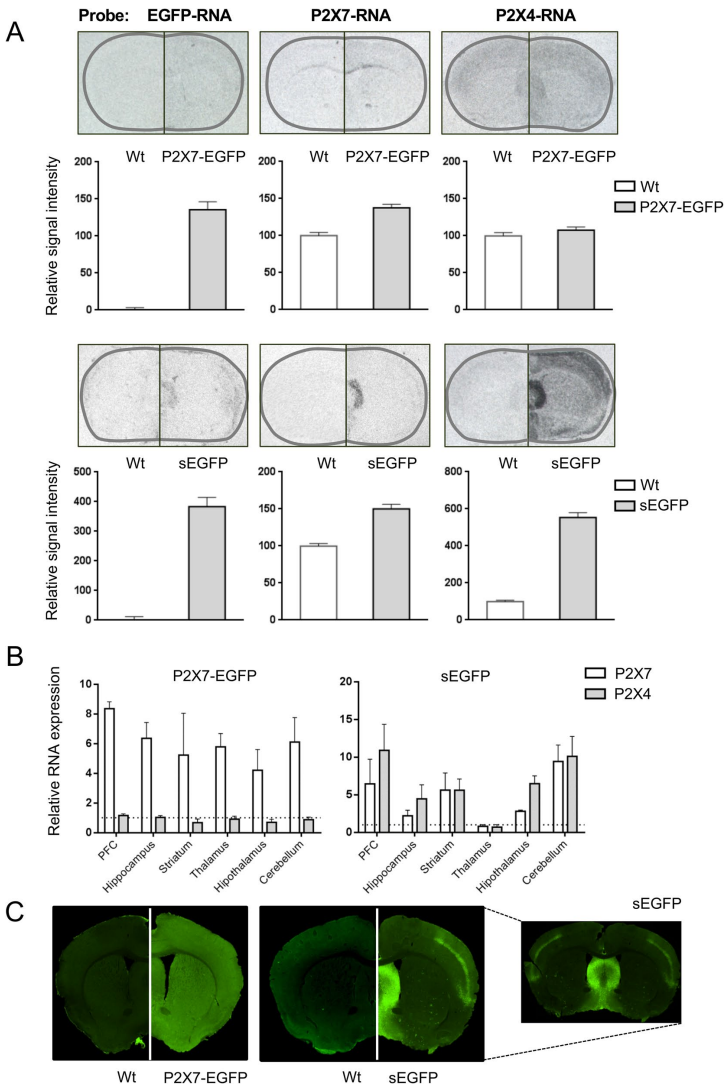

Figure 2. Comparison of EGFP, P2X7, and P2X4 transcript levels and expression patterns in sEGFP and P2X7-EGFP BAC transgenic P2X7 reporter mice. (**A**) In situ hybridization analysis of EGFP, P2X7, and P2X4 transcript levels in the two reporter mouse models in comparison to wt animals. Representative coronal sections (Bregma 0.62 approximately) are displayed. The signal intensities of 12 representative areas were measured on three different mice per group. The background noise was subtracted and the resulting values were normalized to values in wt animals. Bars represent mean ± SEM from three animals analysed in three independent experiments. (**B**) Region-specific quantitative PCR of P2X7 and P2X4 mRNA levels in the P2X7-EGFP and sEGFP mouse lines. RNA levels were normalized to levels in wt animals as well as a housekeeping gene (HPRT) which correspond to the dotted line. Bars represent mean ± SEM from three animals. (**C**) Immunofluorescence staining for EGFP in the P2X7-EGFP and sEGFP lines. Coronal sections from approximately Bregma 0.62 are shown.

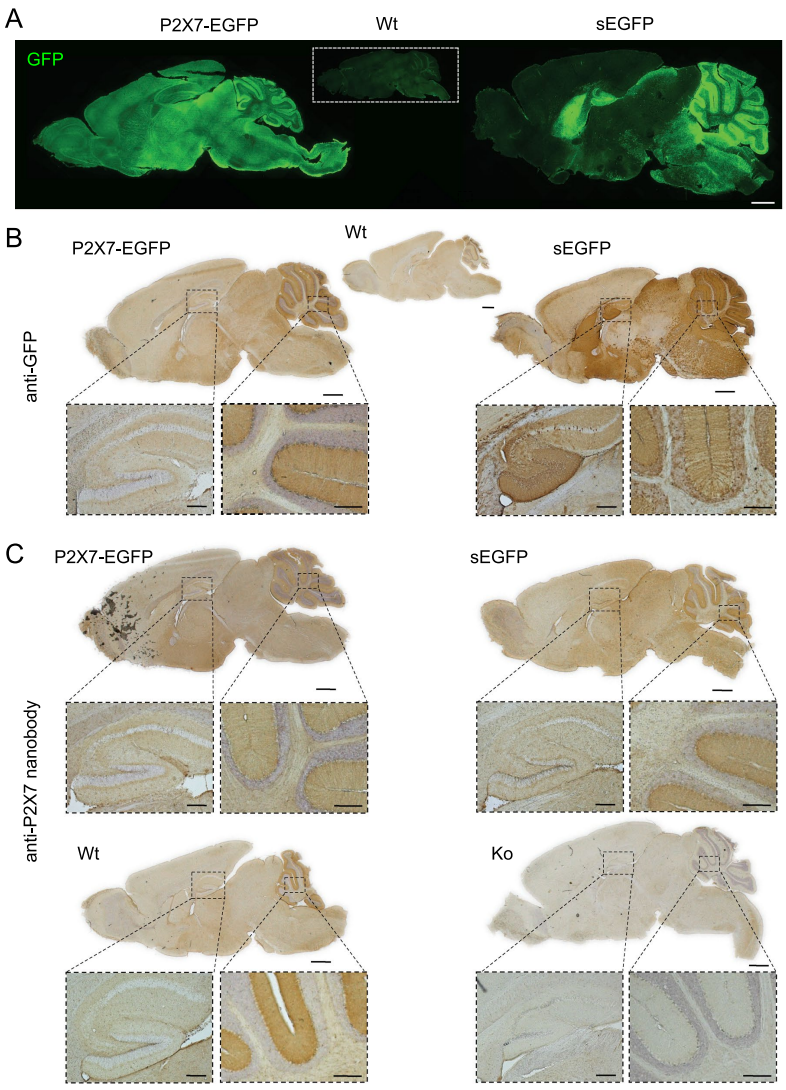

Figure 3. Comparison of EGFP and P2X7 protein expression patterns in sagittal brain sections of sEGFP and P2X7-EGFP BAC transgenic P2X7 reporter mice. (**A**) Immunofluorescence staining with an anti-GFP antibody. Note that signal intensities were individually adjusted to prevent saturation in the sEGFP mouse. Scale bars 1 mm. (**B**) DAB staining with an anti-GFP antibody. (**C**) DAB staining using a P2X7-specific nanobody. Scale bars: 1 mm in whole brain, 200 µm in insets. Representative stainings from 3 different animals per group are shown.

dentate gyrus and showed a more or less uniform distribution in the other hippocampal areas (as previously described[24]), sEGFP staining was dominant throughout the entire molecular layer of the dentate gyrus and, in addition, in the granular cell layer. In addition, a strong EGFP signal was found in large single cells with neuron-like morphology across the pyramidal cell layer of the CA region. In the cerebellum, a similar staining pattern of the molecular layer was obtained in both mouse models. However, again a clear staining of single cells within the granular layer was found in the sEGFP model and absent in the P2X7-EGFP mouse.

Since the colorimetric DAB staining gave a more intense signal with the P2X7-specific nanobody than immunofluorescence staining, this method also allowed comparison of the P2X7 expression in the reporter mouse models with that of endogenous P2X7 in wt animals. As seen in Fig. 3C, both BAC transgenic mouse models mirror the expression pattern seen in wt mice, although, as expected, with a higher intensity due to the P2X7 overexpression in both models. Specificity of the P2X7 staining was confirmed using P2X7 knockout mice. Importantly, the EGFP and P2X7 expression patterns were markedly different in the sEGFP mouse.

Cell type-specific expression of EGFP in the two reporter mouse models. To identify the respective EGFP-expressing cell types, we next performed double immunofluorescence stainings of EGFP together with cell type-specific marker proteins in the dentate gyrus, at the CA3-CA2 border, and in the cerebellum (Fig. 4). In agreement with previous findings, P2X7-EGFP was co-localised in all regions with the microglial marker protein Iba1 and the oligodendrocyte marker protein Olig2 but was absent in NeuN-positive neurons. In contrast, soluble EGFP was not detected in microglia and oligodendrocytes but co-localised with 16.33 ± 5.29% of the NeuN-positive neurons in the granular layer of the dentate gyrus (Fig. 4B) and sporadically with cells showing neuron-like morphology in the CA regions (arrowheads in Fig. 4A). The CA3-CA2 border was chosen because the sEGFP mouse revealed also a strong EGFP staining in the stratum lucidum, the suprapyramidal tract of unmyelinated inhibitory and excitatory mossy fibre projections. The EGFP signal in this region might originate from projections of the EGFP-positive granule cells in the DG. No clear co-localisation of soluble EGFP with the synaptic marker proteins calretinin or calbindin-1 (Calbindin D28k) for GABAergic interneurons or the vesicular Zinc transporter 3 (ZnT3) was found in this region (Fig. 5A).

In the cerebellum, both mice showed intense EGFP staining of Bergmann glia in the molecular layer (Figs. 4C, 5B, compare also[24]). In addition, sEGFP but not P2X7-EGFP[24] was sporadically (< 10% of the cells) found in Purkinje cells (white arrowheads in Fig. 5B) and an unidentified cell type, likely stellate cells or basket cells, in the molecular layer (arrows in Fig. 5B). This assumption is supported by the partial co-localisation of EGFP with the protein marker parvalbumin that has been shown to stain both cell types (Fig. 5C). Furthermore, some of the EGFP-positive cells in the molecular layer were NG2-positve (Fig. 5C), but the overlap was only sporadic and the majority of NG2-positive cells was EGFP-negative.

Finally, there was no co-localisation between the astroglial marker GFAP and EGFP in either mouse model (Supplementary Fig. 3). Thus, cell type-specific EGFP expression appears to be almost opposed in both reporter mouse models with at least partial neuronal expression in sEGFP mouse, and dominant microglial and oligodendrocytic expression in the P2X7-EGFP mouse.

Analysis of EGFP expression in immune cells in the two reporter mouse models. To confirm the unexpected absence of EGFP in microglia of the sEGFP model, we next performed FACS analysis of microglia. As seen in Fig. 6A, staining with an anti-P2X7 antibody revealed increased P2X7 levels in the two reporter mouse models, in agreement with the increased P2X7 levels observed in the sEGFP mouse and the expected P2X7-EGFP overexpression, respectively. Detection of the direct fluorescence of the EGFP reporter in flow cytometric analyses, however, indicated an almost complete absence of EGFP fluorescence in microglia from the sEGFP mouse, which was comparable to that of wt microglia. In contrast, the histogram of microglia from P2X7-EGFP mice showed a clear right shift, as expected for EGFP-expressing cells.

Since P2X7 is best known for its function in macrophages and co-immunostaining in the third ventricle of P2X7-EGFP mouse (Fig. 6B) suggested its presence in Iba1-positive cells with a macrophage-like morphology, we next analysed its presence in macrophages of the brain. Using an antibody against the plasma membrane mannose receptor CD206, a marker protein for perivascular macrophages, confirmed the presence of P2X7-EGFP in this cell type but no other vessel-associated cells (Fig. 6C). The only other cells that were stained had microglia-like morphology. In the sEGFP model, however, no co-staining of EGFP with CD206-positive cells was observed. Instead, EGFP staining was identified in two other cell types on the outer side of the collagen-stained basement membrane of the vessel. Based on their morphology, these cells most likely corresponded to pericytes (extended, spindle-shaped) and smooth muscle cells (surrounding the vessel with split edges).

These unexpected findings prompted us to also compare EGFP reporter expression in peripheral immune cells. In peritoneal macrophages and mast cells of wt mice, a uniform population of endogenous P2X7 was clearly detected by staining with an anti-P2X7 antibody and the right-shifted histograms confirmed again its overexpression in both reporter mouse models (Fig. 6D). A similar shift and shape of the histogram was obtained when cells of the P2X7-EGFP mouse were analysed for EGFP fluorescence, confirming the overlap between (endogenous) P2X7 and EGFP expression in these mice. In contrast, clearly different histograms were seen in sEGFP mice. In macrophages, a very broad histogram was obtained indicating a high variability in EGFP expression levels ranging from macrophages with very low EGFP expression (overlap with the EGFP signal in wt mice) to macrophages with an EGFP signal that was even higher than in P2X7-EGFP overexpressing mice. In mast cells, at least three populations could be differentiated: a small population that showed no EGFP expression at all and two populations with exceptionally high EGFP expression, which was higher than that observed in P2X7-EGFP mice. Finally, analysis of spleen-derived $CD4^+$ T cells (Fig. 6E) revealed an almost complete absence of EGFP in regulatory T cells/activated helper T cells ($CD4^+CD25^+$) and helper T cells ($CD4^+CD25^-$) from sEGFP mice,

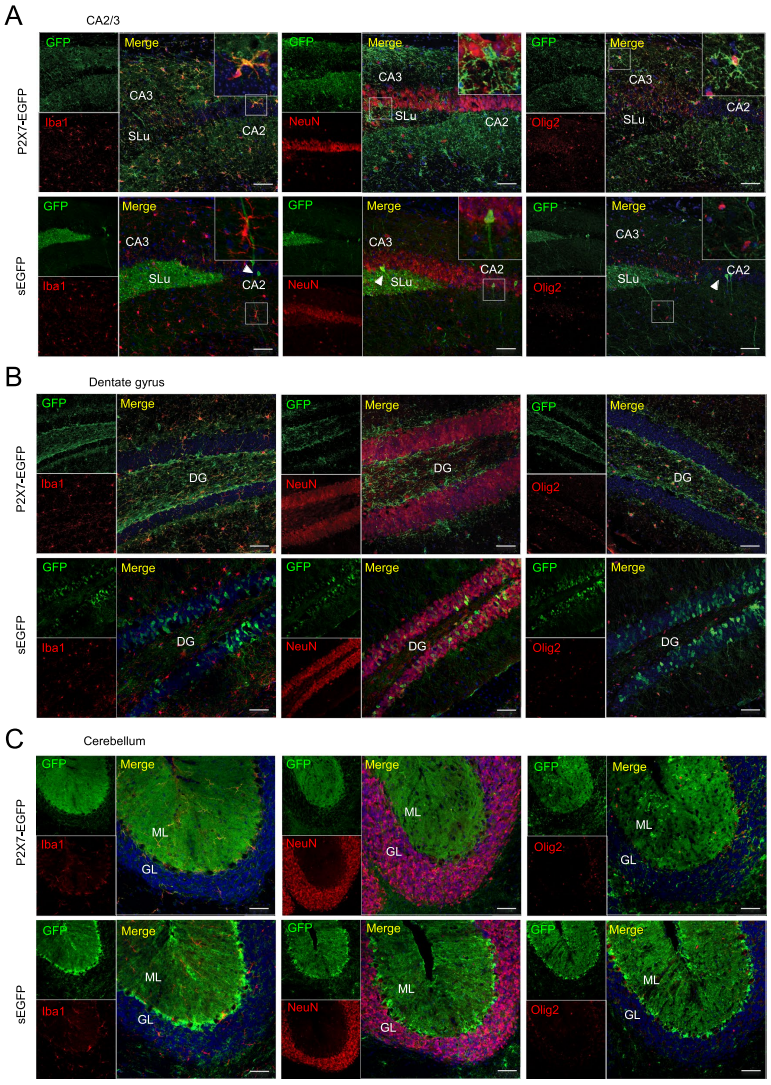

Figure 4. Cell type-specific EGFP protein expression in in sEGFP and P2X7-EGFP BAC transgenic P2X7 reporter mice. Brain slices from BAC transgenic mice were co-labelled with an anti-GFP antibody and antibodies against marker proteins for microglia (Iba1), neurons (NeuN), and oligodendrocytes (Olig2). Representative results are shown for the CA3-CA2 border (**A**), the dentate gyrus (**B**) and cerebellum (**C**). DAPI was used as nuclear counter stain (blue). Arrowheads indicate cells with neuron-like morphology in the CA regions. SLu, stratum lucidum; CA, cornu ammonis; DG, dentate gyrus; ML, molecular layer; GL, granular layer. Scale bar: 50 µm.

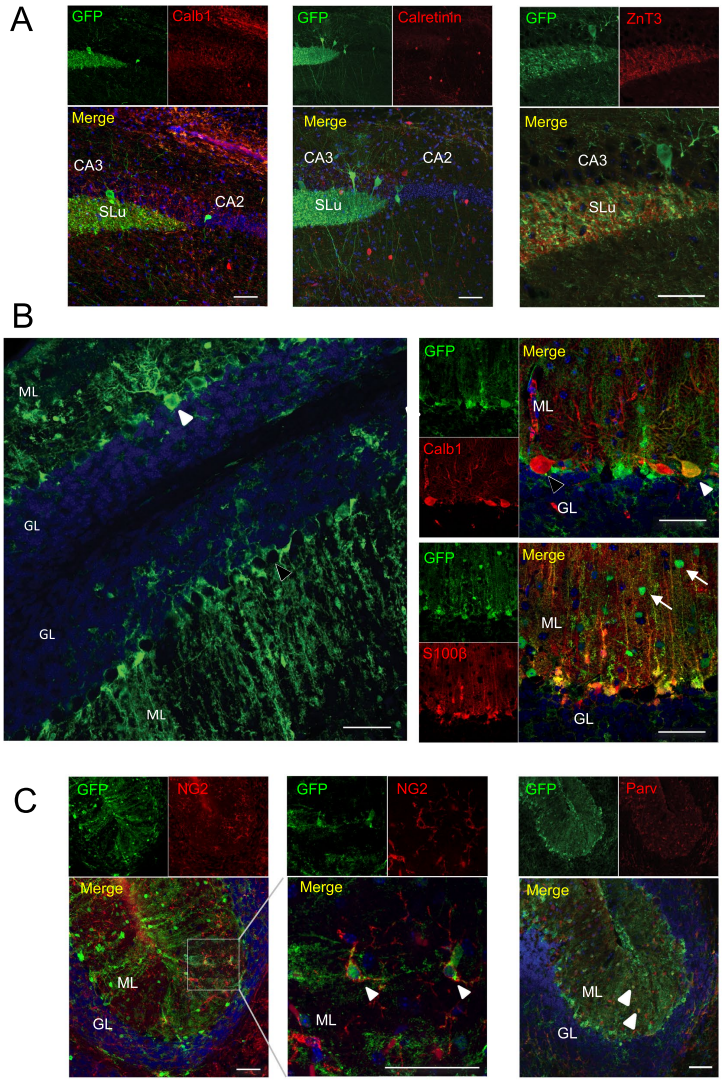

Figure 5. sEGFP-positive cells in the hippocampus and sporadic sEGFP expression in Purkinje cells. Brain slices from BAC transgenic sEGFP mice were co-labelled with an anti-GFP antibody and antibodies against marker proteins for neuronal and glial cell types. Representative immunofluorescence stainings are shown. (**A**) Immunofluorescence staining in the CA3-CA2 border with antibodies against calbindin-1 and calretinin (GABAergic interneurons) and in the CA3 region with an antibody against ZnT3 (synaptic vesicles). (**B**) Staining in the cerebellum with antibodies against Calbindin-1 (Purkinje cell) and S100β (Bergman Glia). Single EGFP-positive cells show Purkinje cell morphology (white arrowheads). Note that not all Purkinje cells are EGFP-positive (black arrowhead). White arrows indicate an unidentified cell type in the molecular layer. (**C**) Staining in the cerebellum with antibodies against NG2 (oligodendrocyte progenitor cells) and parvalbumin (Purkinje cells and molecular layer interneurons). Examples of double-positive cells are pointed out using white arrowheads in each case. DAPI staining is shown in blue. CA, cornu ammonis; ML, molecular layer; GR; granular layer. Scale bar: 50 µm.

www.nature.com/scientificreports/

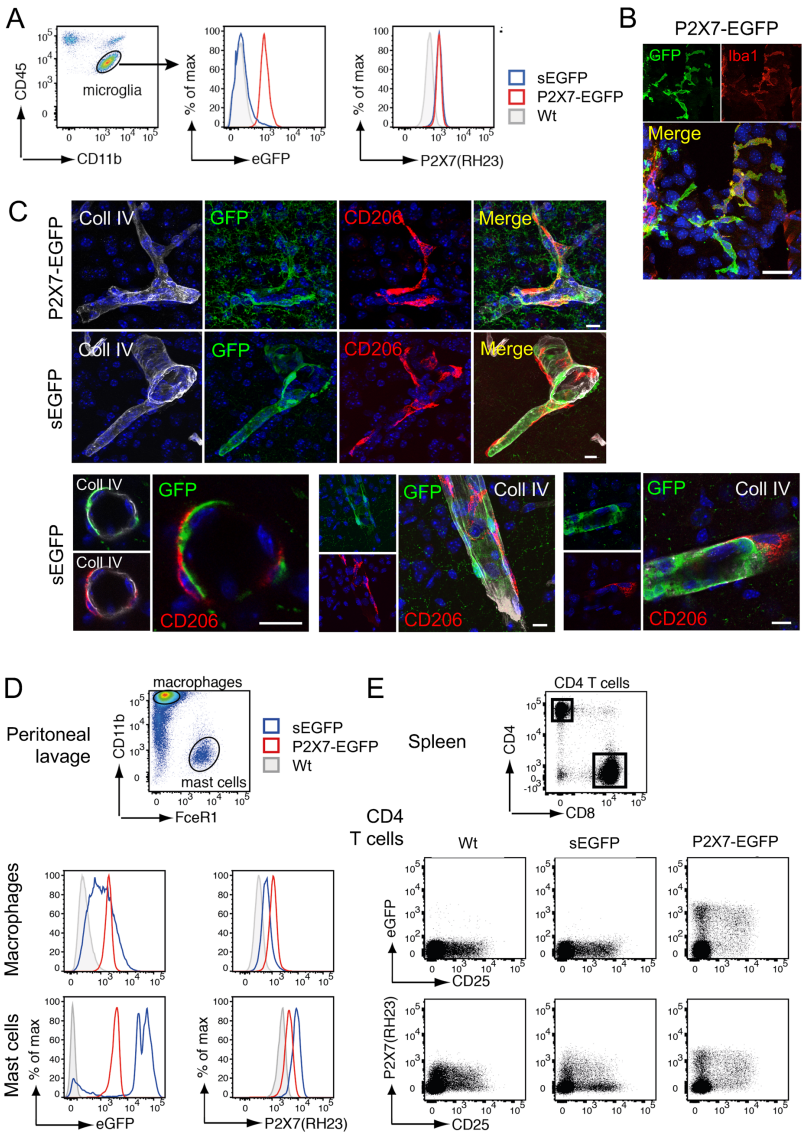

Figure 6. Comparison of EGFP expression in immune cells of the brain. (**A**) Brain microglia ($CD11b^{b}CD45^{low}$) from wt and BAC transgenic mice were analysed by flow cytometry for endogenous EGFP expression and cell surface P2X7 expression using a monoclonal antibody (clone RH23A44). (**B**) Immunofluorescence staining of Iba1 and EGFP in the third ventricle of the P2X7-EGFP mouse. Scale bar: 25 µm. (**C**) Comparison of perivascular macrophage staining in sEGFP and P2X7-EGFP mice. Anti-collagen IV antibody was used to stain blood vessels and CD206 was used as a marker for perivascular macrophages. Lower panel: detailed images from the sEGFP mouse showing a lack of overlap between EGFP and CD206 staining. Scale bar:10 µm, DAPI staining in blue. (**D**) Peritoneal macrophages ($CD11b^{+}FceR1^{-}$) and mast cells ($CD11b^{-}FceR1^{+}$) from wt and BAC transgenic mice were analysed by flow cytometry for endogenous EGFP expression and cell surface P2X7 expression. (**E**) $CD4^{+}$ T cells from the spleen wt and BAC transgenic mice were analysed by flow cytometry for endogenous EGFP expression and cell surface P2X7 expression. EGFP and P2X7 expression levels were compared on helper T cells ($CD4^{+}CD25^{-}$) and regulatory T cells ($CD4^{+}CD25^{+}$).

although cell surface P2X7 expression could be verified by using the anti-P2X7 antibody. In contrast, P2X7-EGFP $CD4^{+}$ T cells showed a similar staining pattern when comparing EGFP and cell surface P2X7 staining. In summary, the sEGFP mice show absence of the EGFP reporter in microglia and $CD4^{+}$ T cells, highly variable expression in macrophages and mast cells, with very strong expression in some mast cell populations. Overall, this pattern is strikingly different to that of the endogenous P2X7 receptor in wt mice, which is well reproduced in the P2X7-EGFP model.

Detection of a functional phenotype in the sEGFP reporter mouse model. Both P2X7 and P2X4 have previously been shown to be involved in seizure induction and seizure-induced cell death[20,34,35]. Therefore, we undertook a preliminary study to test whether the overexpression of P2X4 and/or P2X7 in the sEGFP mouse has functional consequences in these processes. sEGFP mice and wt littermates were subjected to *status epilepticus*[20] (Fig. 7A) via a microinjection of KA into the basolateral amygdala[36]. No difference was found in baseline EEG recordings between wt and sEGFP mice (total power: $4431 \pm 814.2\ \mu V^2$ wt vs. $5130 \pm 948.4\ \mu V^2$ sEGFP, $p = 0.6172$, n = 3 wt and 4 sEGFP) and both wt and sEGFP mice experienced similar seizure severity during a 40 min recording period starting at the time-point of KA injection until the administration of the anticonvulsant lorazepam (total power: $32{,}350 \pm 10{,}830\ \mu V^2$ wt vs $23{,}280 \pm 10{,}470\ \mu V^2$ sEGFP; $p = 0.581$, n = 3 wt and 4 sEGFP, Fig. 7B,C). Likewise, wt and sEGFP mice displayed similar behaviour changes during status epilepticus (Fig. 7D) and additional EEG recordings for 60 min post-lorazepam administration showed no difference between genotypes ($25{,}990 \pm 11{,}610\ \mu V^2$ wt vs $20{,}320 \pm 7196\ \mu V^2$; $p = 0.679$, n = 3 wt and 4 sEGFP). As intraamygdala KA-induced *status epilepticus* leads to characteristic lesions within the ipsilateral CA3 subfield comprising loss of selected neurons and gliosis, we also analysed hippocampal brain sections to compare the neuropathological outcomes. Here, sEGFP mice showed less neurodegeneration in the CA3 subfield of the ipsilateral hippocampus as evidenced by fewer FjB-positive cells (Fig. 7E). Thus, although showing no obvious differences in seizure threshold to intraamygdala KA-induced status epilepticus, neurodegeneration post-status epilepticus was reduced in sEGFP mice, suggesting that the increased expression of P2X4 and P2X7 has an impact on pathological processes.

Discussion

In this study, we analysed the P2X4 and P2X7 expression levels and the EGFP expression patterns in two BAC transgenic P2X7 reporter mouse models and compared it with the endogenous P2X7 distribution in wt mice. Our data show overexpression of a *P2rx4* passenger gene, and surprisingly also of the *P2rx7* gene, in the sEGFP model. We further demonstrate that the expression pattern of soluble EGFP can be reconciled with partial neuronal expression while the P2X7-EGFP fusion protein is dominantly expressed in microglia and oligodendrocytes but not detectable in neurons. Most surprisingly, sEGFP expression appeared to be largely absent in microglia and macrophages, at least under physiological conditions. It has to be noted though, that sEGFP expression was previously observed in microglia in models of *status epilepticus*[37] and Alzheimer´s disease[23], suggesting that it becomes upregulated under pathophysiological conditions. We conclude that the sEGFP reporter shows a partially aberrant expression pattern and preliminary functional data suggest that the observed P2X4 and/or P2X7 overexpression in the sEGFP mouse could influence outcomes during pathology.

BAC transgenic reporter mouse models have revolutionized the analysis of protein expression in vivo. They are widely used to study general or cell type-specific protein expression and to isolate and analyse specific target cells or proteins[14]. This methodology has been particularly useful to study complex cell systems such as the CNS[17,38] and more than 1000 BAC transgenic reporter, Cre-driver, and TRAP mouse lines have been generated and initially characterized within the GENSAT project[39], representing an invaluable resource for researchers. Considering the efficiency and large throughput with which these lines are generated[19], it is evident, that they can only be preliminary characterized and further in-depth analysis is required. In particular, limitations that are inherent to the BAC transgenic approach need to be considered, such as variability in the integrated BAC copy number, non-specific integration of the BAC in the genome and alterations in the gene structure and regulation of both the target gene on the BAC and genes that may be affected by the BAC integration. The need for careful validation of reporter mouse lines was shown, for example, in a comparative analysis of three transgenic mouse models for neuronal expression of the corticotropin-releasing hormone (CRH). Here, differences appeared to depend not only on the transgenic approach (IRES-CRE, BAC or Cre-loxP system targeting the *Crh* gene promoter) but also on the reporter used (GFP or tdTomato)[40]. In another example, leakiness of Cre-dependent reporter lines (resulting in unspecific EGFP distribution) and lack of specificity of BAC-derived Cre-driver

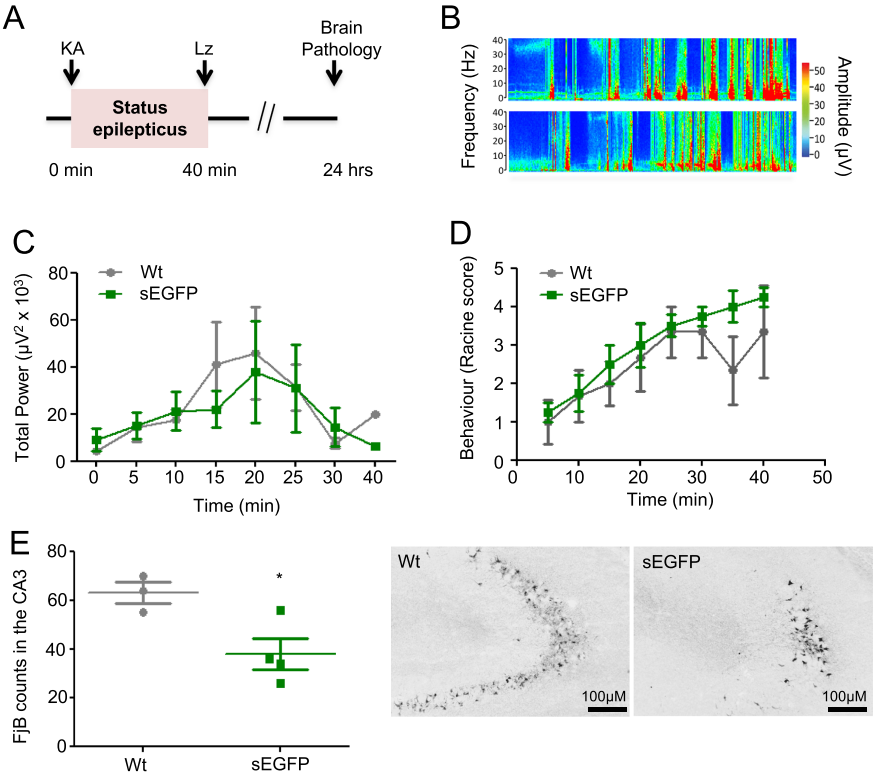

Figure 7. Functional phenotype of the sEGFP reporter mouse. (**A**) Experimental design of the intra-amygdala mouse model of status epilepticus. Status epilepticus is induced by an injection of 0.2 µg kainic acid (KA) into the basolateral nucleus of the ipsilateral amygdala. To reduce mortality and morbidity, the anti-convulsant lorazepam (Lz) is administered 40 min following KA injection. (**B**) Representative EEG recordings presented as heat maps of frequency and amplitude data during status epilepticus of wt and sEGFP mice. (**C**) Graphs showing similar seizure severity between wt and sEGFP mice during a 40 min recording period starting at the time of intraamygdala KA injection until administration of anticonvulsant lorazepam (wt, n = 3 and sEGFP, n = 4). (**D**) Graph showing similar changes in behaviour based on the Racine scale between genotypes (wt, n = 3 and sEGFP, n = 4). (**E**) Graph and photomicrographs (10 × lens) showing less FjB-positive cells in the ipsilateral CA3 subfield of the hippocampus 24 h after status epilepticus in sEGFP mice compared with wt mice (n = 3 (wt), 63.00 ± 4.359; n = 4 (sEGFP), 38.00 ± 6.377; t = 2.983 df = 5, unpaired t-test; p = 0.031). Scale bar, 100 µm.

lines for several microglia-specific Cx3cr1-Cre lines have recently been reported[41]. While knock-in approaches provide a more controlled way of gene modification[42], the BAC transgenic approach has the advantage of being fast and highly efficient. Furthermore, it allows the moderate overexpression of the target gene, which might help its efficient visualization and the analysis of overexpression effects.

While the P2X4 overexpression in the sEGFP mouse model is inherent to the BAC clone chosen for modification, the reason for the increased P2X7 expression level and divergent expression pattern in this model is not immediately clear. In the sEGFP construct, the *P2rx7* gene is practically interrupted by the EGFP encoding sequence followed by a pA signal and the targeting vector while in the P2X7-EGFP mouse, the *P2rx7* gene structure was largely unaltered, except for the EGFP sequence insertion. The pA signal following the sEGFP insertion should prevent formation of BAC-derived *P2rx7* transcripts in this model. Thus, sEGFP can be regarded as a read-out of *P2rx7* promoter activation while the P2X7-EGFP reporter mouse leads to the overexpression of the translated EGFP-tagged *P2rx7* gene product. Regarding the observed P2X7 overexpression, sequencing of the

integration sites of the EGFP cDNA revealed that the EGFP-encoding sequence plus an upstream 27 bp and the downstream targeting vector sequence were inserted directly after the A of the P2X7 start ATG (Supplementary Fig. 4). Due to the used recombination strategy, in which the BAC was not resolved[19], this resulted in duplication of the homology domain (ranging from -332 bp upstream of the transcription start site right to the start ATG (+ 163 bp downstream of the transcription start) and complementation of a second P2X7 start ATG at the 3´ integration site. According to a previous study[21], a fragment ranging from − 249 bp to + 220 bp was already sufficient for reporter gene expression and can therefore be assumed to contain essential promoter elements. Nevertheless, since the P2X7 overexpression is much lower than that of the P2X4 receptor, its expression might be partly prevented by the introduced pA signal. Finally, it cannot be excluded, that the P2X4 overexpression affects the P2X7 expression as mutual interactions between them have been described[43].

Regarding the different expression pattern in the sEGFP mouse, one explanation could be that the accessibility or structure of domains required for the regulation of P2X7 expression is affected by the described gene modification. Also, the posttranscriptional regulation of the sEGFP is likely different from that of the P2X7-EGFP as its expression should result in the generation of the much shorter EGFP transcript in which intronic *P2rx7* sequences and the 5`UTR are missing. For example, the first intron, which is not preserved in the sEGFP transcript, is particularly long in many genes and supposed to contain elements that are important for gene regulation. Intron 1 of *P2rx7*, for example, might contain elements that control expression of the P2X7k splice variant[33]. In addition, sequences encoding or binding regulatory RNAs might be eliminated and also other post-transcriptional mechanisms could affect protein expression such as RNA editing[44], changes in poly(A) tail length[45], mRNA capping, mRNA splicing, or protein turnover. For example, P2X7 has been shown to be targeted by several microRNAs, such as mir-22[46], and it cannot be excluded that this suppresses the expression of P2X7 or its EGFP-tagged version in neurons. Likewise, the strongly reduced or absent sEGFP expression in microglia, perivascular macrophages of the brain, and T cells indicates a lack of positive regulatory mechanisms.

It further needs to be considered that cytoplasmic sEGFP and the membrane bound P2X7-EGFP fusion construct have different cellular distribution. In cells like neurons with long and fine processes, this can result in apparent differences in the EGFP reporter localisation (e.g. in regions of the cell body like granular layers or the projection areas such as the mossy fiber area, Fig. 4A,B) and very different appearance of the respective staining (e.g. punctate and diffuse for membrane localised P2X7-EGFP as in the cerebellar Bergmann glia or filling the whole cell and representing the respective cell morphology as in the case of sEGFP in these cells, Fig. 4C). Thus, neuronal expression of membrane bound P2X7-EGFP might be difficult to detect in the complex cellular context of a brain slice if the protein is localised to discrete and tiny structures such as specific synapses or growth cones. In addition, the sEGFP mouse shows sparse, diffuse EGFP staining of cells with an irregular and variable shape throughout different brain areas (i.e. pons, superior colliculus, caudate putamen, compare Fig. 3). This is very similar to the staining described in the GENSAT database, which has been attributed to glial cells (www.gensat.org). However, this could not be confirmed using the glial markers Iba1, Olig2, and GFAP (data not shown). Likewise, no clear co-localisation with the neuronal marker NeuN was found in these regions, neither in sagittal nor coronal sections.

While BAC transgenic technology has greatly advanced neuroscience research, several caveats need to be considered and reporter lines need to be carefully planned and thoroughly examined. P2X7 reporter mice provide important tools for the elucidation of P2X7 receptor roles in CNS diseases. However, the presence of passenger genes and leaky or aberrant reporter expression may confound data interpretation and needs to be considered. Our data raise concerns about the reliability of the sEGFP mouse model and suggest that conclusions drawn from previous localisation studies need to be carefully re-evaluated.

Material and methods

Animals. Tg(P2rx7 EGFP)FY174Gsat (sEGFP) mice were generated by the Gene Expression Nervous System Atlas (GENSAT) project (https://www.gensat.org) and obtained from the Mutant Mouse Resource and Research Center (MMRRC). They were bred in FVB/N background or C57BL6 (only Fig. 2). P2rx7$^{tmid(EUCOMM)Wtsi}$ were in C57BL/6 background. Tg(RP24-114E20P2X7451P-StrepHis-EGFP)17Ani (P2X7-EGFP, line 17) mice[24] were in FVB/N (Fig. 1B) or C57BL/6 N (all other data) background. No differences in P2X7-EGFP or P2X7 expression were identified between both backgrounds (compare respective stainings from C57Bl/6 N (in this study) and FVB/N[24] and see supplementary Fig. 5). Male and female mice were used in all experiments. Mice were housed in standard conditions (22 °C, 12 h light–dark cycle, water/food ad libitum). All animal experiments were performed in accordance with the principles of the European Communities Council Directive (2010/63/EU). Procedures were reviewed and approved by the Research Ethics Committee of the Royal College of Surgeons in Ireland (REC 1322) and from the Health Products Regulatory Authority (HPRA, AE19127/P038) and the State of Upper Bavaria (55.2–1-54–2532-59–2016). All efforts were made to minimize suffering and number of animals.

Sequencings of sEGFP insertion site. The genotyping primers recommended for the sEGFP mouse (F: sequences Exon 1 of *P2rx7*, upstream of the Start ATG 5′-CGCTGCAGTCACTGGAGGAA-3′ R: EGFP 5′-TAG CGGCTGAAGCACTGCA-3′) and a primer pair consisting of a forward primer in the EGFP sequence (5′-TGCAGTGCTTCAGCCGCTA-3′) and a reverse primer in the coding sequence of exon 1 (5′-GTGGGTCTT GCACATGATCGTCT-3′) were used to amplify a 399 bp and a 3831 bp fragment, respectively from mouse tail DNA. From these fragments, the targeting vector sequence and the 5´ and 3´insertion sites were determined by sequencing (Eurofins, Munich, Germany).

RNA extraction and real-time PCR. RNA was extracted from one hippocampus using the QIAzol Lysis Reagent (Qiagen, Hilden, Germany) as described[47] and 500 ng of total RNA were reverse transcribed

with SuperScript II (Thermo-Fisher, MA, USA). Quantitative real-time PCR was performed using the Quanti-Tect SYBR Green PCR Kit (Qiagen, Hilden, Germany) and 1.25 µM of each primer pair in combination with a LightCycler 1.5 (Roche Diagnostics GmbH, Mannheim, Germany) according to the manufacturer's protocol. Data were analysed with the LightCycler 1.5 software and normalized to expression of β-actin. Primers were designed using Primer3 software (https://frodo.wi.mit.edu) and had the following sequences: *P2rx7* forward (F) 5′-ACTGGCAGGTGTGTGTTCCATA-3′ and reverse (R): 5′-TTGGCAAGATGTTTCTCGTG-3′; *P2rx4* F: 5′-TATGTGGTCCCAGCTCAGGA-3′ R: 5′-TCACAGACGCGTTGAATGGA-3′ EGFP F: 5′-ACGTAAACG GCCACAACTTC-3′ R: 5′-AAGTCGTGCTGCTTCATGTG-3′. To detect and differentiate alternatively spliced *P2rx7* transcripts we combined exon 1 and exon 1′ forward sequences (5′-CACATGATCGTCTTTTCCTAC-3′ and 5′-GCCCGTGAGCCACTTATGC-3, respectively) with reverse primers in exon 4 (5′-GGTCAGAAGAGC ACTGTGC-3′), exon 5 (5´-CCTTGTCTTGTCATATGGAAC-3′), and exon 7 (5′-TCTGTAAAGTTCTCTCCT GC-3′) and increased the number of amplification cycles from 40 to 55.

Tissue-specific real-time PCR Tissue punches of different brain areas were collected from frozen samples. Total RNA was extracted using the miRNeasy Mini Kit (QIAGEN). First-strand cDNA was produced by reverse transcription employing the Superscript III Reverse Transcriptase kit (ThermoFisher Scientific) with Oligo(dT)12–18 Primer (ThermoFisher Scientific). Relative levels of gene expression were obtained through quantitative real-time PCR carried out in a LightCycler 96 instrument (Roche) following the FastStart Essential DNA Green Master kit (Roche). The primer sequences employed for the testing were as follows: *P2rx7* F: 5-ACTGGCAGGTGT GTTCCATA-3′. R: 5′-TTGGCAAGATGTTTCTCGTG-3′, *P2rx4* F: 5′-TATGTGGTCCCAGCTCAGGA-3′, R: 5′-TCACAGACGCGTTGAATGGA-3′, HPRT (housekeeping) F: 5′-TGGGCTTACCTCACTGCTTTCC-3′, R: 5′-CCTGGTTCATCA TCGCTAATCACG-3′. Results were normalized to HPRT, as well as to wt animal values.

SDS-PAGE and Western Blot analysis. P2X protein was analysed as described[24]. 100–500 mg of lung tissue were cut into small pieces and homogenized in 600 µl of homogenization buffer (0.1 M sodium phosphate buffer, pH 8.0, 0.4 mM Pefabloc SC (Sigma) and Complete protease inhibitor (Roche Applied Science) using a Precellys homogenizer (Peqlab) and CK28 beads (15 s, 5.000 rpm). After centrifugation (10 min at 10,000×*g*, 4 °C), membranes were pelleted from the supernatant (30–60 min at 21,100×*g*, 4 °C), and extracted for 15 min with 100–300 µl of the above homogenization buffer containing 1% NP-40 (Sigma) as detergent. After centrifugation (10 min at 21,100×*g*, 4 °C) protein concentrations of the supernatants were determined by BCA Protein-Assay (ThermoFisher Scientific) and 30–75 µg of total protein per lane were separated on 8% SDS-PAGE gels using 20 mM DTT (Roth) as reducing agent. Proteins were wet-blotted onto Immobilon-FL PVDF membranes (Merck Millipore) for 16 h at 4 °C and the membranes blocked in Intercept (TBS) Blocking Buffer (LI-COR Biosciences) diluted 1:2 in TBS. Upon immunostaining, proteins were visualized with an Odyssey infrared imaging system (LI-COR Biosciences) and quantified using ImageStudio (LI-COR Biosciences). Statistical analysis was performed using GraphPad Prism.

In situ hybridization. In situ hybridization was carried out as previously described[48]. Fresh brains were frozen on dry ice and stored at -80 °C. For in situ hybridization, 20 µm cryosections were incubated overnight with gene-specific S^{35}-UTP- labelled riboprobes. The nucleotides targeted by the different probes were as follows: EGFP: 907–1698 of GenBank accession no. LC311024; P2*rx4*: 1004–1910 of GenBank accession no. NM_011026; *P2rx7*: 1199–1620 of GenBank accession no. NM_011027. Assessment of the signal intensity was carried out using ImageJ software. Results were normalized to values from wt animals.

Diaminobenzidine (DAB) immunohistochemistry. Stainings were performed as described[24]. Mice were anesthetized (Ketamine/Xylazine/Heparine) and transcardially perfused with 4% paraformaldehyde (PFA). Brains were dissected and post-fixed in 4% PFA for a minimum of 24 h, transferred to 30% sucrose for cryoprotection for at least 48 h, and embedded in 5% low melting point Agarose (Roth, Germany). 30 µm sagittal brain sections were prepared (VT1200s Leica Microsystems) and, after peroxidase block (1% H_2O_2 in PBS, 30 min RT), blocked with 10% Normal Goat Serum (Dako, Germany) and 0.1% Triton X-100 (Sigma, Germany)in PBS (1 h, RT), and incubated with primary antibody overnight at 4°C. After incubation with biotinylated secondary antibodies (1.5 h at RT), proteins were visualized using the ABC method with the Vectastain ABC kit (Vector Laboratories) and the DAB substrate Sigma Fast DAB Tablets (Sigma-Aldrich, Germany). Brain slices were mounted on glass slides and counter-stained with haematoxylin (Roth), followed by dehydration (70%, 80% and 100% ethanol, xylene) and embedding with phenol-free Kaiser's glycerol gelatine (Roth). Images were taken with a Zeiss AxioCam MR coupled to a Zeiss Axio Imager M2 using the Zeiss Axiovision software.

Immunofluorescence staining. Immunostaining was performed as described[49]. Adult mouse brains were fixed and cryoprotected as above and 40 µm cryostat sections were prepared. Tissue slices were washed (3×times 10 min, PBS), blocked (5% Normal Goat Serum (Dako Germany), 0.3% Triton X-100 (Sigma, Munich, Germany) in PBS, two hr at RT), and incubated with primary antibodies (16–24 h, 4°C) with gentle shaking. After washing as above, sections were incubated for 2 h with fluorescence conjugated secondary antibodies. DAPI staining was performed for 60–90 s and slices were mounted on object slides with Lab Vision PermaFluor Aqueous Mounting Medium (ThermoFisher Scientific). For perivascular macrophage staining, brains were cut on a vibratome and 50 µm floating sections were collected. Tissue slices were washed (3 times 10 min, TBS), blocked (1% BSA (Sigma, Munich, Germany), 0.5% Triton X-100 (Sigma, Munich, Germany), 0.1% Fish gelatine (Sigma, Munich, Germany) in TBS, 2–3 h at RT), and incubated with primary antibodies (24 h – 5 days, depending on the antibody, 4°C) with gentle shaking. After washing as above, sections were incubated for 2–3 h with fluorescence conjugated secondary antibodies and DAPI diluted in blocking buffer. Slices were mounted on glass

slides with Everbrite Mounting Medium (Biotium, Fremont CA, USA). Images were obtained by confocal laser scanning microscopy (Zeiss LSM 880). Quantitative analysis was performed with the StrataQuest automated cell counting software (TissueGnostics, Vienna, Austria).

Antibodies for Western blotting and immunohistochemistry. See Supplementary Table 1.

FACS analysis. *Isolation of primary cells.* Isolation of primary cells was described before[50]. For the isolation of brain microglia, mice were sacrificed under anesthesia by cervical dislocation. Single cell suspensions were prepared from brain by collagenase digestion at 37 °C for 30 min. Cells were passed through a 70 µm cell strainer (Greiner) and centrifuged for 5 min at 300 g. Microglia were separated from debris by percoll gradient centrifugation (33% percoll solution, GE Healthcare). The supernatant was removed and the pellet was resuspended in 1 ml ACK erythrocyte lysis buffer ice for 1 min to remove erythrocytes. Cells were washed with 10 ml FACS buffer (PBS + 0.2% BSA / 1 mM EDTA) and resuspended in FACS buffer.

For the isolation of peritoneal macrophages and mast cells, mice were sacrificed and 5 ml PBS + 1 mM EDTA were injected to lavage the peritoneal cavity. The peritoneal lavage was centrifuged for 5 min at 300 g and the pellet was resuspended in FACS buffer.

For the isolation of spleen T cells, mice were sacrificed, the spleen was collected and processed through a 70 µm cell strainer (Greiner) using a syringe piston. The cell suspension was centrifuged for 5 min at 300 g, erythrocytes were removed by ACK erythrocyte lysis as described above and the cells were resuspended in FACS buffer.

Antibodies and flow cytometry. Cells were stained with fluorochrome-conjugated mAbs for 30 min on ice in the presence of Fc block (anti-CD16/CD32; clone 2.4G2, BioXcell) and normal rat serum (Jackson). Staining and washing was performed in FACS buffer containing PBS, 0.1% BSA, and 1 mM EDTA. The following antibodies were used: anti-CD11b (clone M1/70; BioLegend), anti-P2X7 (clone RH23A44, UKE), anti-CD45 (30-F11, Biolegend), anti-CD4 (clone RM4-5; BioLegend), anti-CD8a (clone 53–6.7, Biolegend), anti-CD25 (clone PC61, Biolegend) and anti-FcεR1α (clone MAR1, Biolegend). Cells were analysed using a BD Celesta flow cytometer and data were analysed with FlowJo software (Treestar).

Intraamygdala kainic acid-induced status epilepticus mouse model. Intraamygdala kainic acid (KA)-induced status epilepticus was performed as described before[20]. Mice were anesthetized using isoflurane (5% induction, 1–2% maintenance) and maintained normothermic by means of a feedback-controlled heat blanket (Harvard Apparatus Ltd, Kent, UK). Under anesthetized conditions, mice were placed in a stereotaxic frame and a midline scalp incision was made to expose the skull. A guide cannula (coordinates from Bregma; AP = -0.94 mm, L = − 2.85 mm) and three electrodes, one on top of each hippocampus and the reference electrode on top of the frontal cortex, were fixed using dental cement to record surface electroencephalograms (EEG). Status epilepticus was induced by a microinjection of 0.2 µg kainic acid (KA) in 0.2 µl phosphate-buffered saline (PBS, Sigma-Aldrich, Dublin, Ireland) into the right basolateral amygdala. 40 min following intraamygdala KA injection, Lorazepam (6 mg/kg) (Wyeth, Taplow, UK) was delivered intraperitoneally to curtail seizures and reduce morbidity and mortality. EEG was recorded using a Xltek EEG system (Optima Medical Ltd., Guildford, UK) and recordings were commenced prior to intraamygdala KA injection and continued for 1 h post-lorazepam. EEG recordings were analysed by uploading EEG onto Labchart 8 reader software (ADInstruments) and total seizure power of EEG signals was calculated[20].

Fluoro-Jade B staining. To assess status epilepticus-induced neurodegeneration, Fluoro-Jade B (FjB) staining was carried out as before[51]. Briefly, 12 µm coronal sections at the medial level of the hippocampus (Bregma AP = − 1.94 mm) were cut on a cryostat. Tissue was fixed in 4% PFA, rehydrated in ethanol, and then transferred to a 0.006% potassium permanganate solution followed by incubation with 0.001% FjB (Chemicon Europe Ltd, Chandlers Ford, UK). Sections were mounted in Dibutylphthalate Polystyrene Xylene (DPX) mounting solution (Sigma Aldrich, Dublin, Ireland). Using an epifluorescence microscope, cells including all hippocampal subfields (dentate gyrus (DG), cornu amonis regions 1 and 3 (CA1 and CA3)) were counted under a 40 × lens in two adjacent sections and the average determined for each animal.

Statistical analysis. GraphPad Prism software was used to perform statistical analysis and data were presented as means ± standard error of the mean (SEM). Student's t-test was used to determine statistical differences between groups. Significance was accepted at $*p < 0.05$, $**p < 0.01$ $***s < 0.001$.

Received: 31 July 2020; Accepted: 23 October 2020
Published online: 16 November 2020

References

1. Di Virgilio, F., Sarti, A. C. & Grassi, F. Modulation of innate and adaptive immunity by P2X ion channels. *Curr. Opin. Immunol.* **52**, 51–59. https://doi.org/10.1016/j.coi.2018.03.026 (2018).
2. Kanellopoulos, J. M. & Delarasse, C. Pleiotropic roles of P2X7 in the central nervous system. *Front. Cell Neurosci.* **13**, 401. https://doi.org/10.3389/fncel.2019.00401 (2019).
3. Beamer, E., Fischer, W. & Engel, T. The ATP-gated P2X7 receptor as a target for the treatment of drug-resistant epilepsy. *Front. Neurosci.* **11**, 21. https://doi.org/10.3389/fnins.2017.00021 (2017).

4. Biber, K. *et al.* Microglial drug targets in ad: opportunities and challenges in drug discovery and development. *Front. Pharmacol.* **10**, 840. https://doi.org/10.3389/fphar.2019.00840 (2019).
5. Deussing, J. M. & Arzt, E. P2X7 receptor: a potential therapeutic target for depression?. *Trends Mol. Med.* **24**, 736–747. https://doi.org/10.1016/j.molmed.2018.07.005 (2018).
6. Domercq, M. & Matute, C. Targeting P2X4 and P2X7 receptors in multiple sclerosis. *Curr. Opin. Pharmacol.* **47**, 119–125. https://doi.org/10.1016/j.coph.2019.03.010 (2019).
7. Koch-Nolte, F. *et al.* Novel biologics targeting the P2X7 ion channel. *Curr. Opin. Pharmacol.* **47**, 110–118. https://doi.org/10.1016/j.coph.2019.03.001 (2019).
8. Diaz-Hernandez, M. *et al.* Altered P2X7-receptor level and function in mouse models of Huntington's disease and therapeutic efficacy of antagonist administration. *FASEB J.* **23**, 1893–1906. https://doi.org/10.1096/fj.08-122275 (2009).
9. Marin-Garcia, P., Sanchez-Nogueiro, J., Gomez-Villafuertes, R., Leon, D. & Miras-Portugal, M. T. Synaptic terminals from mice midbrain exhibit functional P2X7 receptor. *Neuroscience* **151**, 361–373. https://doi.org/10.1016/j.neuroscience.2007.10.038 (2008).
10. Ohishi, A. *et al.* Expression level of P2X7 receptor is a determinant of ATP-induced death of mouse cultured neurons. *Neuroscience* **319**, 35–45. https://doi.org/10.1016/j.neuroscience.2016.01.048 (2016).
11. Illes, P., Khan, T. M. & Rubini, P. Neuronal P2X7 receptors revisited: do they really exist?. *J. Neurosci.* **37**, 7049–7062. https://doi.org/10.1523/jneurosci.3103-16.2017 (2017).
12. Miras-Portugal, M. T., Sebastián-Serrano, Á., de Diego García, L. & Díaz-Hernández, M. Neuronal P2X7 receptor: involvement in neuronal physiology and pathology. *The Journal of Neuroscience* **37**, 7063–7072. https://doi.org/10.1523/jneurosci.3104-16.2017 (2017).
13. Gong, S. *et al.* A gene expression atlas of the central nervous system based on bacterial artificial chromosomes. *Nature* **425**, 917–925. https://doi.org/10.1038/nature02033 (2003).
14. Heintz, N. BAC to the future: the use of bac transgenic mice for neuroscience research. *Nat. Rev. Neurosci.* **2**, 861–870. https://doi.org/10.1038/35104049 (2001).
15. Yang, X. W. & Gong, S. An overview on the generation of BAC transgenic mice for neuroscience research. *Curr. Protocols Neurosci.* **Chapter 5**, Unit 5.20. https://doi.org/10.1002/0471142301.ns0520s31 (2005).
16. Gerfen, C. R., Paletzki, R. & Heintz, N. GENSAT BAC cre-recombinase driver lines to study the functional organization of cerebral cortical and basal ganglia circuits. *Neuron* **80**, 1368–1383. https://doi.org/10.1016/j.neuron.2013.10.016 (2013).
17. Srinivasan, R. *et al.* New transgenic mouse lines for selectively targeting astrocytes and studying calcium signals in astrocyte processes in situ and in vivo. *Neuron* **92**, 1181–1195. https://doi.org/10.1016/j.neuron.2016.11.030 (2016).
18. Xu, J. *et al.* P2X4 receptor reporter mice: sparse brain expression and feeding-related presynaptic facilitation in the arcuate nucleus. *J. Neurosci.* **36**, 8902–8920. https://doi.org/10.1523/JNEUROSCI.1496-16.2016 (2016).
19. Gong, S., Kus, L. & Heintz, N. Rapid bacterial artificial chromosome modification for large-scale mouse transgenesis. *Nat. Protoc.* **5**, 1678–1696. https://doi.org/10.1038/nprot.2010.131 (2010).
20. Engel, T. *et al.* Seizure suppression and neuroprotection by targeting the purinergic P2X7 receptor during status epilepticus in mice. *FASEB J.* **26**, 1616–1628. https://doi.org/10.1096/fj.11-196089 (2012).
21. Garcia-Huerta, P. *et al.* The specificity protein factor Sp1 mediates transcriptional regulation of P2X7 receptors in the nervous system. *J. Biol. Chem.* **287**, 44628–44644. https://doi.org/10.1074/jbc.M112.390971 (2012).
22. Hirayama, Y. *et al.* Astrocyte-mediated ischemic tolerance. *J. Neurosci.* **35**, 3794–3805. https://doi.org/10.1523/JNEUROSCI.4218-14.2015 (2015).
23. Martinez-Frailes, C. *et al.* Amyloid peptide induced neuroinflammation increases the P2X7 receptor expression in microglial cells, impacting on its functionality. *Front. Cell Neurosci.* **13**, 143. https://doi.org/10.3389/fncel.2019.00143 (2019).
24. Kaczmarek-Hajek, K. *et al.* Re-evaluation of neuronal P2X7 expression using novel mouse models and a P2X7-specific nanobody. *eLife 7, e36217*. https://doi.org/10.7554/elife.36217 (2018).
25. Perrault, I. *et al.* IFT81, encoding an IFT-B core protein, as a very rare cause of a ciliopathy phenotype. *J. Med. Genet.* **52**, 657–665. https://doi.org/10.1136/jmedgenet-2014-102838 (2015).
26. Wachter, S. *et al.* Binding of IFT22 to the intraflagellar transport complex is essential for flagellum assembly. *EMBO J.* **38**, e101251. https://doi.org/10.15252/embj.2018101251 (2019).
27. Collo, G. *et al.* Cloning OF P2X5 and P2X6 receptors and the distribution and properties of an extended family of ATP-gated ion channels. *J. Neurosci.* **16**, 2495–2507. https://doi.org/10.1523/JNEUROSCI.16-08-02495.1996 (1996).
28. Soto, F. *et al.* P2X4: an ATP-activated ionotropic receptor cloned from rat brain. *Proc. Natl. Acad. Sci. USA* **93**, 3684–3688. https://doi.org/10.1073/pnas.93.8.3684 (1996).
29. Bertin, E. *et al.* Increased surface P2X4 receptor regulates anxiety and memory in P2X4 internalization-defective knock-in mice. *Mol. Psychiatry* https://doi.org/10.1038/s41380-019-0641-8 (2020).
30. Murrell-Lagnado, R. D. & Frick, M. P2X4 and lysosome fusion. *Curr. Opin. Pharmacol.* **47**, 126–132. https://doi.org/10.1016/j.coph.2019.03.002 (2019).
31. Qureshi, O. S., Paramasivam, A., Yu, J. C. H. & Murrell-Lagnado, R. D. Regulation of P2X4 receptors by lysosomal targeting, glycan protection and exocytosis. *J. Cell Sci.* **120**, 3838–3849. https://doi.org/10.1242/jcs.010348 (2007).
32. Varga, R. E. *et al.* In vivo evidence for lysosome depletion and impaired autophagic clearance in hereditary spastic paraplegia type SPG11. *PLoS Genet.* **11**, e1005454. https://doi.org/10.1371/journal.pgen.1005454 (2015).
33. Nicke, A. *et al.* A functional P2X7 splice variant with an alternative transmembrane domain 1 escapes gene inactivation in P2X7 knock-out mice. *J. Biol. Chem.* **284**, 25813–25822. https://doi.org/10.1074/jbc.M109.033134 (2009).
34. Jimenez-Pacheco, A. *et al.* Increased neocortical expression of the P2X7 receptor after status epilepticus and anticonvulsant effect of P2X7 receptor antagonist A-438079. *Epilepsia* **54**, 1551–1561. https://doi.org/10.1111/epi.12257 (2013).
35. Ulmann, L. *et al.* Involvement of P2X4 receptors in hippocampal microglial activation after status epilepticus. *Glia* **61**, 1306–1319. https://doi.org/10.1002/glia.22516 (2013).
36. Mouri, G. *et al.* Unilateral hippocampal CA3-predominant damage and short latency epileptogenesis after intra-amygdala microinjection of kainic acid in mice. *Brain Res.* **1213**, 140–151. https://doi.org/10.1016/j.brainres.2008.03.061 (2008).
37. Jimenez-Pacheco, A. *et al.* Transient P2X7 receptor antagonism produces lasting reductions in spontaneous seizures and gliosis in experimental temporal lobe epilepsy. *J. Neurosci.* **36**, 5920–5932. https://doi.org/10.1523/JNEUROSCI.4009-15.2016 (2016).
38. Shuen, J. A., Chen, M., Gloss, B. & Calakos, N. Drd1a-tdTomato BAC transgenic mice for simultaneous visualization of medium spiny neurons in the direct and indirect pathways of the basal ganglia. *J. Neurosci.* **28**, 2681–2685. https://doi.org/10.1523/JNEUROSCI.5492-07.2008 (2008).
39. Schmidt, E. F., Kus, L., Gong, S. & Heintz, N. BAC transgenic mice and the GENSAT database of engineered mouse strains. *Cold Spring Harbor Protoc.* https://doi.org/10.1101/pdb.top073692 (2013).
40. Chen, Y., Molet, J., Gunn, B. G., Ressler, K. & Baram, T. Z. Diversity of reporter expression patterns in transgenic mouse lines targeting corticotropin-releasing hormone-expressing neurons. *Endocrinology* **156**, 4769–4780. https://doi.org/10.1210/en.2015-1673 (2015).
41. Zhao, X. F. *et al.* Targeting microglia using Cx3cr1-Cre lines: revisiting the specificity. *eNeuro* https://doi.org/10.1523/ENEURO.0114-19.2019 (2019).
42. Beil, J., Fairbairn, L., Pelczar, P. & Buch, T. Is BAC transgenesis obsolete? State of the art in the era of designer nucleases. *J. Biomed. Biotechnol.* **2012**, 308414. https://doi.org/10.1155/2012/308414 (2012).

43. Kopp, R., Krautloher, A., Ramirez-Fernandez, A. & Nicke, A. P2X7 interactions and signalling: making head or tail of it. *Front. Mol. Neurosci.* **12**, 183. https://doi.org/10.3389/fnmol.2019.00183 (2019).
44. Srivastava, P. K. *et al*. Genome-wide analysis of differential RNA editing in epilepsy. *Genome Res.* **27**, 440–450. https://doi.org/10.1101/gr.210740.116 (2017).
45. Weill, L., Belloc, E., Bava, F. A. & Mendez, R. Translational control by changes in poly(A) tail length: recycling mRNAs. *Nat. Struct. Mol. Biol.* **19**, 577–585. https://doi.org/10.1038/nsmb.2311 (2012).
46. Jimenez-Mateos, E. M. *et al.* microRNA targeting of the P2X7 purinoceptor opposes a contralateral epileptogenic focus in the hippocampus. *Sci. Rep.* **5**, 17486. https://doi.org/10.1038/srep17486 (2015).
47. Engel, T. *et al.* CHOP regulates the p53-MDM2 axis and is required for neuronal survival after seizures. *Brain* **136**(2), 577–592. https://doi.org/10.1093/brain/aws337 (2013).
48. Refojo, D. *et al.* Glutamatergic and dopaminergic neurons mediate anxiogenic and anxiolytic effects of CRHR1. *Science* **333**, 1903–1907. https://doi.org/10.1126/science.1202107 (2011).
49. Zhang, J. *et al.* Germ-line recombination activity of the widely used hGFAP-Cre and nestin-Cre transgenes. *PLoS ONE* **8**(12), e82818. https://doi.org/10.1371/journal.pone.0082818 (2013).
50. Rissiek, B. *et al.* Astrocytes and microglia are resistant to NAD(+)-mediated cell death along the ARTC2/P2X7 axis. *Front. Mol. Neurosci.* **12**, 330. https://doi.org/10.3389/fnmol.2019.00330 (2020).
51. Engel, T. *et al.* Bi-directional genetic modulation of GSK-3beta exacerbates hippocampal neuropathology in experimental status epilepticus. *Cell Death Dis.* **9**, 969. https://doi.org/10.1038/s41419-018-0963-5 (2018).

Acknowledgements
We thank Heinz Janser and Uta Mamrak for technical assistance.

Author contributions
Study design and manuscript preparation: A.N.. Experiments: A.R.F., R.K., T.E., M.A., G.C., L.U.T., B.R., J.Z., A.D. Data analysis: A.R.F., R.K., G.C., M.A., L.U.T., N.S., B.R., J.D., N.P., A.D. Contribution of essential material: F.K.N.. Funding acquisition: A.N., T.E., T.M., F.K.N., J.D. All authors contributed to, reviewed, and approved the manuscript.

Funding
This work was supported by funding from the Health Research Board HRA-POR-2015-1243; the Science Foundation Ireland (17/CDA/4708, and co-funded under the European Regional Development Fund and by FutureNeuro industry partners 16/RC/3948) the European Union's Horizon 2020 research and innovation programme under the Marie Skłodowska-Curie grant agreement (No 766124), and the Deutsche Forschungsgemeinschaft (DFG, German Research Foundation)—Project-ID: 335447717—SFB 1328. Open Access funding enabled and organized by Projekt DEAL.

Competing interests
The authors declare no competing interests.

Additional information
Supplementary information is available for this paper at https://doi.org/10.1038/s41598-020-76428-0.

Correspondence and requests for materials should be addressed to A.N.

Reprints and permissions information is available at www.nature.com/reprints.

Publisher's note Springer Nature remains neutral with regard to jurisdictional claims in published maps and institutional affiliations.

Deviant reporter expression and P2X4 passenger gene overexpression in the soluble EGFP BAC transgenic P2X7 reporter mouse model

Antonio Ramírez-Fernández[1], Lidia Urbina-Treviño[2], Giorgia Conte[3], Mariana Alves[3], Björn Rissiek[4], Anna Durner[1], Nicolas Scalbert[1], Jiong Zhang[1], Tim Magnus[4], Friedrich Koch-Nolte[5], Nikolaus Plesnila[6], Jan M. Deussing[2], Tobias Engel[3,7], Robin Kopp[1], Annette Nicke[1]*

[1] Walther Straub Institute of Pharmacology and Toxicology, Faculty of Medicine, LMU Munich, Munich, Germany
[2] Max Planck Institute of Psychiatry, Molecular Neurogenetics, Munich, Germany
[3] Department of Physiology & Medical Physics, Royal College of Surgeons in Ireland, Dublin D02 YN77, Ireland
[4] Department of Neurology, University Medical Center Hamburg-Eppendorf, Hamburg, Germany
[5] Institute of Immunology, University Medical Center Hamburg-Eppendorf, Hamburg, Germany
[6] Institute for Stroke and Dementia Research, Munich University Hospital, LMU Munich, Germany
[7] FutureNeuro, SFI Research Centre for Chronic and Rare Neurological Diseases. RCSI, Dublin D02 YN77, Ireland

Correspondence:
Annette Nicke
annette.nicke@lrz.uni-muenchen.de

Running title: BAC transgene comparison

Suppl. Fig. 1

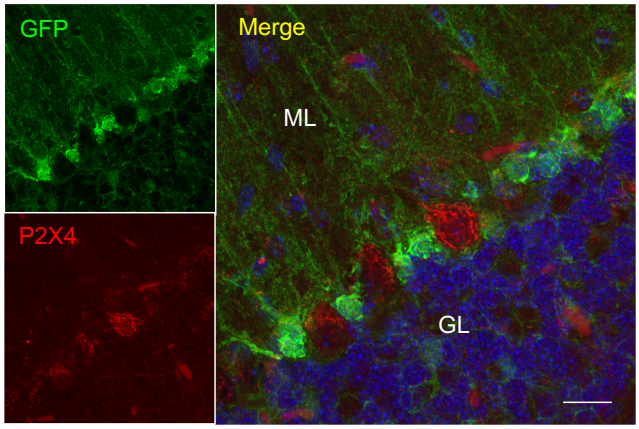

Supplementary Figure 1:
P2X4 Expression in Purkinje cells of the sEGFP mouse model.
Immunofluorescence staining of cerebellar slices of the sEGFP mouse with antibodies against P2X4 and GFP (Thermo Fischer CA10262). Nuclear staining with DAPI is shown in blue. A representative image out of the three individual animals is shown. GL, Granular cell layer; ML, molecular cell layer. Scale bar: 20 µm.

Suppl. Fig. 2

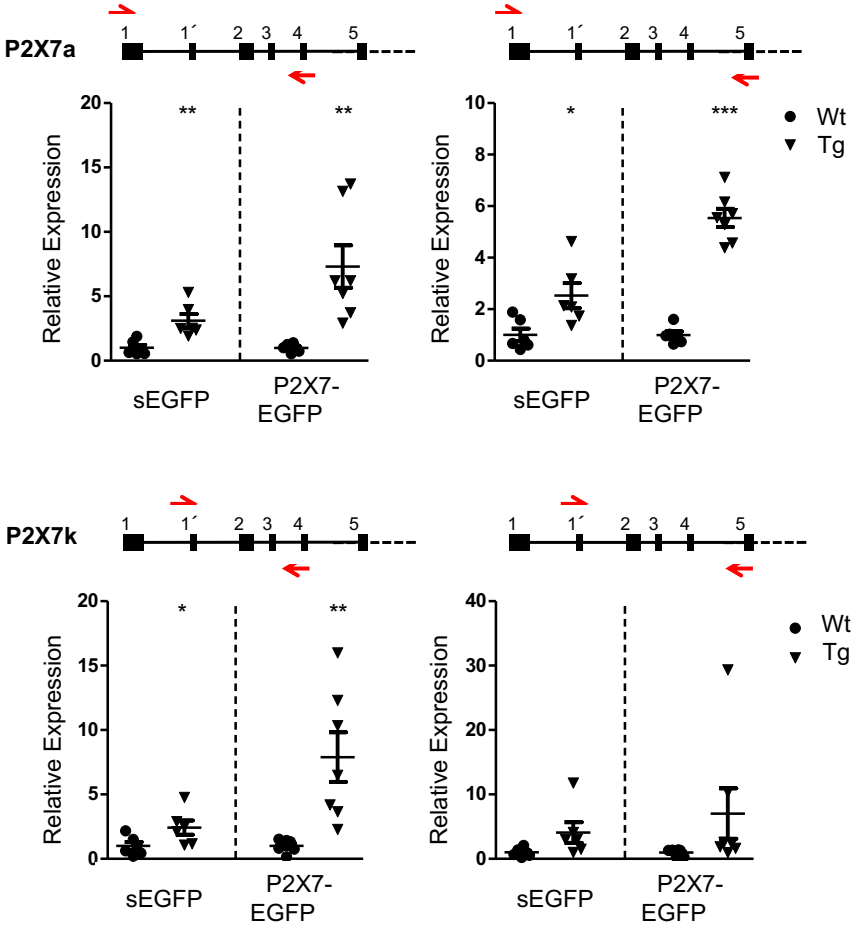

Supplementary Figure 2:
P2X7 Splice variant expression in sEGFP and P2X7-EGFP transgenic models. RNA was extracted from hippocampus and quantitative PCR was performed with primers directed against sequences in the indicated *P2rx7* exons. Data were normalized to expression of β-actin and the respective levels in wt controls. Bars represent mean ± SEM from 2 independent experiments and 6-7 mice. Significance was analysed using unpaired two-tailed Student's t-test and is indicated as *p<0.05, **p<0.01, ***p<0.001 (*P2rx7a* levels Ex1-Ex4: sEGFP 3.105 ± 0.5231, n=6; P2X7-EGFP 7.309 ± 1.649, n=7, Ex1-Ex5: sEGFP 2.525 ± 0.4881, n=6; P2X7-EGFP 5.541 ± 0.3531, n=7; *P2rx7k* levels Ex1'-Ex4 sEGFP 2.425 ± 0.5552, n=6, P2X7-EGFP 7.897 ± 1.926, n=7; Ex1'-Ex5 sEGFP 4.087 ± 1.606, n=6; P2X7-EGFP 7.024 ± 3.911, n=7).

Suppl. Fig. 3

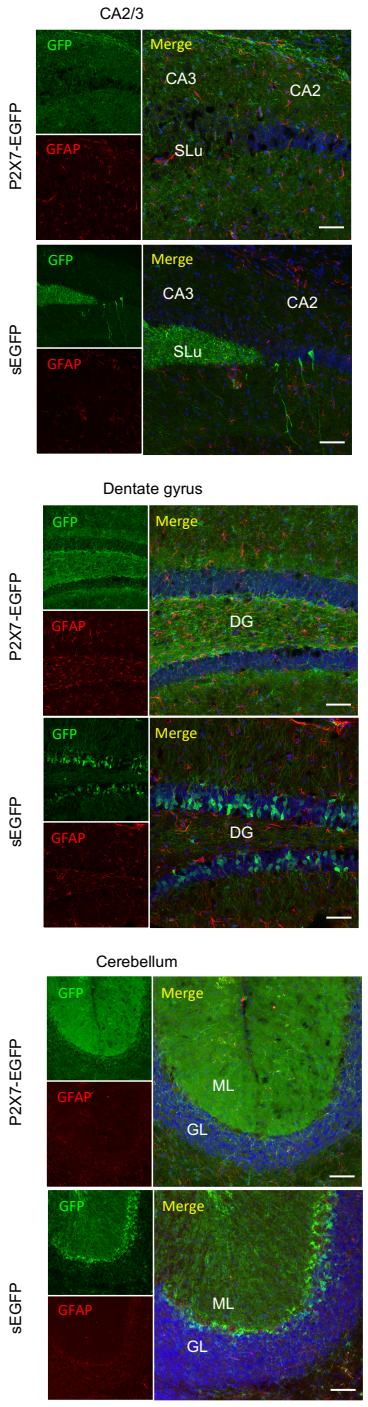

Supplementary Figure 3:
Analysis on the colocalization of EGFP with the astrocytic marker GFAP in sEGFP and P2X7-EGFP BAC transgenic P2X7 reporter mice.
Saggital brain slices (40 µm) were labelled with antibodies against GFAP and GFP (Abcam ab6556). Images show representative samples from at least three mice per group in the following regions: (**A**) CA3-CA2 border (**B**) Dentate gyrus (**C**) Cerebellum. DAPI staining is shown in blue. Scale bars: 50 µm.

Suppl. Fig. 4

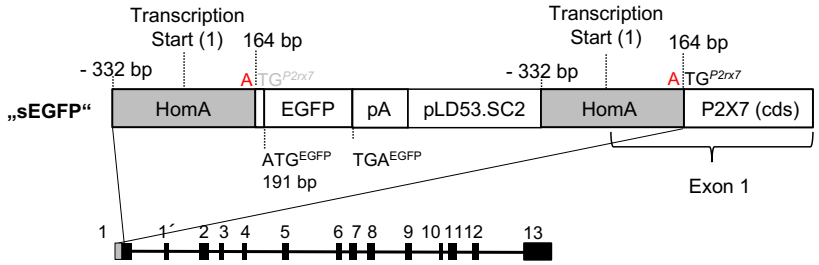

Supplementary Figure 4:
Scheme depicting the integration of the targeting vector encoding the soluble EGFP into the Start ATG of the *P2rx7* gene.
The A of the *P2rx7* Start ATG is the last residue in the Homology arm (Hom A) and shown in red. The bases TG (shown in grey) are replaced by 27 bp of targeting vector sequence followed by the EGFP coding sequence, poly adenylation signal and the targeting vector pLD53.SC2. Due to the non-resolving homologous recombination strategy, the homology region A is duplicated and therefore complements the *P2rx7* Start ATG.

Suppl. Fig. 5

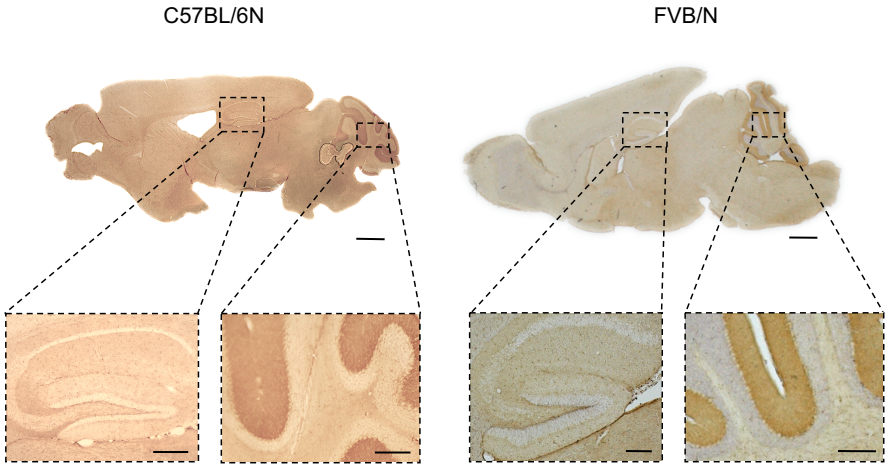

Supplementary Figure 5:
Direct comparison of P2X7 protein expression pattern in wildtype mice from C57BL/6N and FVB/N genetic backgrounds. DAB staining was performed with a P2X7-specific nanobody. Note that no counterstaining for haematoxylin was performed in the presented C57BL/6 sample and that images were taken on different microscopes. Scale bars: 200 µm.

Suppl. Fig. 6

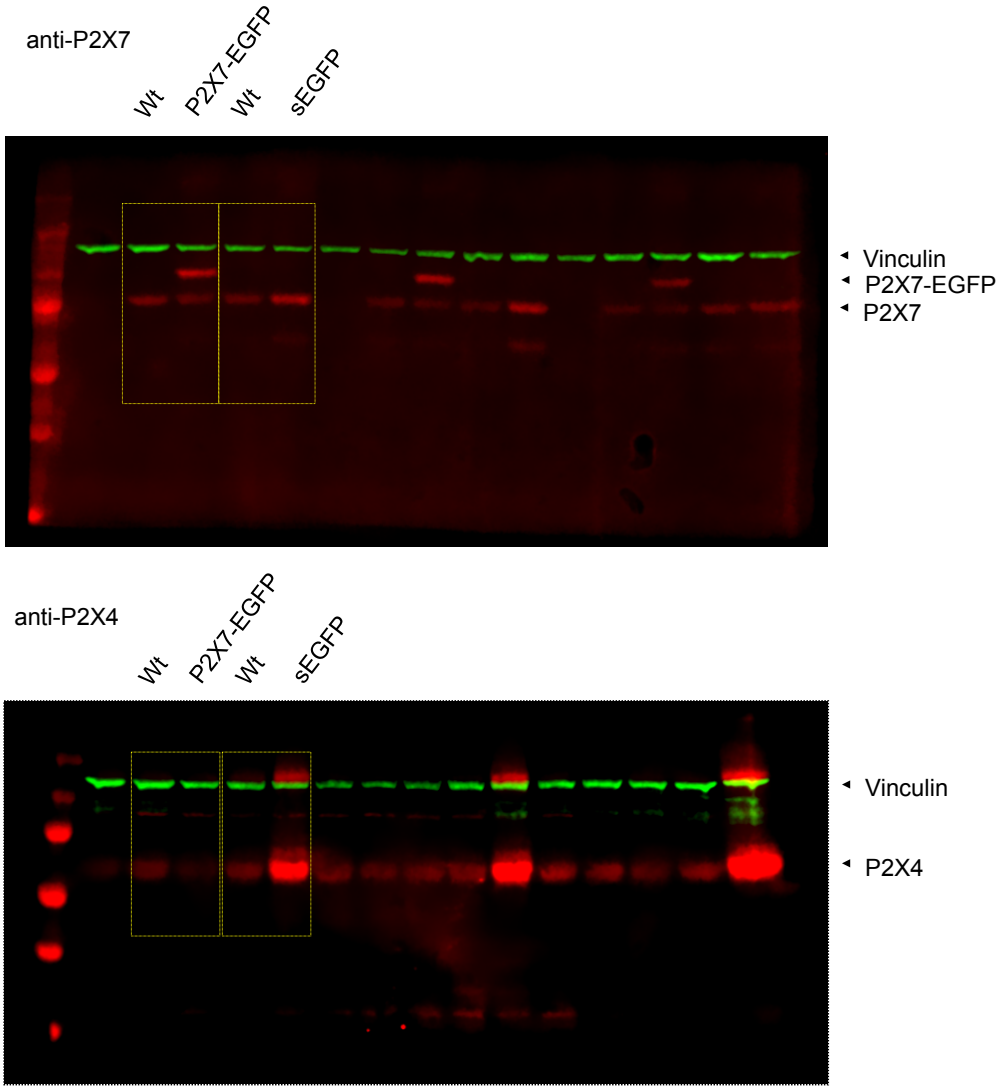

Supplementary Figure 6:
Full-length blots from Figure 1C.
The parts shown in Fig 1C are indicated by dashed lines. For details see Figure 1C.

Supplementary Table 1:
Antibodies used for Western blotting and immunohistochemistry

Antibody	Supplier	Cat# RRID:	Application and dilution
P2X7 C-term (rb pAb)	Synaptic Systems	177003, AB_887755	WB 1:1500
P2X4	Alomone	APR-002, AB_2040058	WB 1:1000 IHC 1:200
Vinculin (ms hVin-1)	Sigma-Aldrich	V9131, AB_477629	WB 1:10.000
800CW gt anti-ms	LI-COR	925–32210, AB_2687825	WB 1:15.000
680RD dk anti-rb	LI-COR	925–68073, AB_2716687	WB 1:15.000
P2X7 ECD, 7E2-rbIgG	Nolte lab	Nanobody rbIgG fusion construct	DAB 6.7 ng/mL
GFP (rb pAb)	Abcam	ab6556, AB_305564	IHC 1:2000 DAB 1:5000
GFP (chk pAb)	Thermo Fisher	CA10262, AB_2534023	IHC 1:400
GFP (gt pAb)	Abcam	AB_5450 AB_304897	IHC 1:100
NeuN (ms A60)	Millipore	MAB377, AB_2298772	IHC 1:500
GFAP (ms GA5)	Millipore/ Sigma-Aldrich	MAB360, AB_11212597	IHC 1:200
Iba1 (rb pAb)	WAKO	019–19741, AB_839504	IHC 1:100
Olig 2 (ms 211F1.1)	Millipore	MABN50, AB_10807410	IHC 1:200
Calbindin D28k (ms CB-955)	Sigma-Aldrich	C9848, AB_476894	IHC 1:1000
Calretinin (ms 37C9)	Synaptic Systems	214111, AB_2619904	IHC 1:200
Parvalbumin (ms 58E1)	Synaptic Systems	195011, AB_2619882	IHC 1:500
ZnT3 (ms 180C1)	Synaptic Systems	197011, AB_2189665	IHC 1:100
S100β (rb pAb)	Synaptic Systems	287003, AB_2620024	IHC 1:500
Collagen IV (rb pAb)	Abcam	AB_19808 AB_445160	IHC 1:100
CD 206 (rb mAb)	Biorad	MCA2235GA AB_322613	IHC 1:100
A594 gt anti-rb	Thermo Fisher	A11037, AB_2534095	IHC 1:400
A594 gt anti-ms	Thermo Fisher	A11032, AB_2534091	IHC 1:400
A594 gt anti-rat	Thermo Fisher	A11007, AB_10561522	IHC 1:400
A546 gt anti-ms	Thermo Fisher	A-11003, AB_2534071	IHC 1:400
A488 gt anti-rb	Thermo Fisher	A11008, AB_143165	IHC 1:400
A488 gt anti-chk	Thermo Fisher	A11039, AB_2534096	IHC 1:400

3.4 Backbone Cyclization Turns a Venom Peptide into a Stable and Equipotent Ligand at Both Muscle and Neuronal Nicotinic Receptors

In this article, three novel analogues of the paralytic, muscle-type α-conotoxin CIA from the venom of *Conus catus* were produced by backbone cyclization. In contrast to other blockers of muscle-type nicotinic receptors with a typical 3/5 α-conotoxin disulfide framework, CIA is also active at the $\alpha 3\beta 2$ neuronal nicotinic receptor, however, with reduced potency.
CIA cyclic analogues (cCIA-2, cCIA-3, cCIA-4) were synthesized using amino acid linkers of various length (10-19 Å) greater than the intertermini spacing (9.8 Å) to minimize structural distortions. The overall structure and native disulfide bond connectivity was preserved in all cCIAs as confirmed by nuclear magnetic resonance (NMR) spectroscopy, although the linker length seems to affect structural stability as NMR data also revealed possible alternative conformations for two of the three cyclic analogues (cCIA-2 and cCIA-4). The resistance toward enzymatic degradation was greatly improved by cyclization, as demonstrated with a serum stability assay by determining the amount of intact peptide after incubation in serum AB at periodic time intervals.
The potencies of the cyclic analogues were assessed by TEVC experiments using rat nAChR expressing *X. laevis* oocytes. In comparison to CIA, all of its cyclic analogues retained a low nanomolar potency at the fetal muscle-type nAChR $(\alpha 1)_2\beta 1\gamma\delta$ (IC_{50} 4-9 nM), but show significantly slower dissociation rates with up to 6-fold smaller dissociation constants (K_{off}). At the $\alpha 3\beta 2$ neuronal nAChR, the cyclic analogues were significantly more potent than CIA (IC_{50} 68.2 nM), with cCIA-3 being the most potent peptide (IC_{50} 1.3 nM). Although the fast dissociation rates observed for cCIAs from the $\alpha 3\beta 2$ receptor suggested allosteric modulation, functional competition binding experiments with the potent, competitive antagonist MII rather point towards competitive binding of cCIA-3 to the orthosteric $\alpha 3\beta 2$ binding site. In a mouse muscle contraction assay, 3,4-daminopyridine-evoked acetylcholine (ACh) release from nerve terminals reversed cCIA-3-induced blocking of nerve-evoked muscle contraction, probably by displacing the cyclic analogue from the muscle endplate nAChR. Together, the electrophysiology recordings and the mouse muscle contraction assay support our assumption that the peptide cCIA-3 acts as a competitive antagonist on both the muscle-type nAChR and the $\alpha 3\beta 2$ neuronal subtype. Surprisingly, neither CIA nor its cyclic analogues produced a train-of-four (TOF) fade, meaning a reduction of the fourth to the first twitch amplitude in a train under repetitive nerve stimulation, contradicting the hypothesis that blockade of presynaptic $\alpha 3\beta 2$ receptors at the neuromuscular junction attenuates autofacilitatory ACh release and subsequent stimulation of postsynaptic muscle nAChRs, finally leading to the fading of nerve-evoked muscle contraction. Nevertheless, because of their low nanomolar inhibitory potencies on both muscle and neuronal nAChRs, the novel cyclic CIA analogues represent potent pharmacological probes that can be used for further investigations of neuromuscular transmission.
I contributed to the electrophysiological experiments with characterization and validation of nAChR constructs, cRNA preparation, help with TEVC instrumentations, supervision of measurements, and manuscript editing.

Backbone Cyclization Turns a Venom Peptide into a Stable and Equipotent Ligand at Both Muscle and Neuronal Nicotinic Receptors

Julien Giribaldi[†], Yves Haufe[†], Edward R. J. Evans, Muriel Amar, Anna Durner, Casey Schmidt, Adèle Faucherre, Hamid Moha Ou Maati, Christine Enjalbal, Jordi Molgó, Denis Servent, David T. Wilson, Norelle L. Daly, Annette Nicke, and Sébastien Dutertre

[†]*these authors contributed equally to this publication*

published in

J. Med. Chem. 2020, 63, 12682-12692

Reprinted from [88]

Journal of Medicinal Chemistry

pubs.acs.org/jmc Article

Backbone Cyclization Turns a Venom Peptide into a Stable and Equipotent Ligand at Both Muscle and Neuronal Nicotinic Receptors

Julien Giribaldi, Yves Haufe, Edward R. J. Evans, Muriel Amar, Anna Durner, Casey Schmidt, Adèle Faucherre, Hamid Moha Ou Maati, Christine Enjalbal, Jordi Molgó, Denis Servent, David T. Wilson, Norelle L. Daly, Annette Nicke, and Sébastien Dutertre*

Cite This: J. Med. Chem. 2020, 63, 12682−12692 Read Online

ACCESS | Metrics & More | Article Recommendations | Supporting Information

ABSTRACT: Venom peptides are promising drug leads, but their therapeutic use is often limited by stability and bioavailability issues. In this study, we designed cyclic analogues of α-conotoxin CIA, a potent muscle nicotinic acetylcholine receptor (nAChR) blocker with a significantly lower affinity at the neuronal α3β2 subtype. Remarkably, all analogues retained the low nanomolar activity of native CIA toward muscle-type nAChRs but showed greatly improved resistance to degradation in human serum and, surprisingly, displayed up to 52-fold higher potency for the α3β2 neuronal nAChR subtype (IC_{50} 1.3 nM). Comparison of nuclear magnetic resonance-derived structures revealed some differences that might explain the gain of potency at α3β2 nAChRs. All peptides were highly paralytic when injected into adult zebrafish and bath-applied to zebrafish larvae, suggesting barrier-crossing capabilities and efficient uptake. Finally, these cyclic CIA analogues were shown to be unique pharmacological tools to investigate the contribution of the presynaptic α3β2 nAChR subtype to the train-of-four fade.

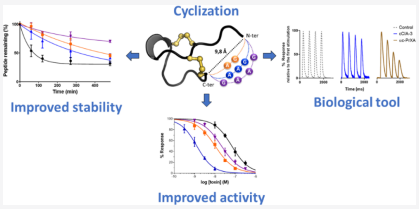

INTRODUCTION

Natural extracts from animals, plants, and bacteria provide one of the richest sources of bioactive peptides, some of which have entered clinical development for the treatment of human diseases such as diabetes, HIV, hepatitis, and cancer. Animal venom peptides are of particular interest, as they have been finely tuned by millions of years of prey-predator coevolution to potently and selectively target receptors involved in key physiological functions and, consequently, they are widely employed as potent pharmacological probes.[1] Cone snails are predatory marine mollusks that have evolved and radiated into more than 800 different species and nowhere is peptide diversity more apparent than within their venom.[2] They have developed extremely potent and fast acting neurotoxic venoms mainly composed of small peptides (10−40 residues) called conotoxins. These conotoxins are generally highly constrained by disulfide bridges (2−4 bridges), and target a wide range of receptors with key physiological functions for rapid prey immobilization and defense.[3,4] Disulfide bridges provide conotoxins with rigid conformations, enabling a tight and specific interaction with their molecular targets, which are mainly ion channels, but also transporters and G protein-coupled receptors.[5,6]

Members of the α-conotoxin subfamily specifically block the nicotinic acetylcholine receptors (nAChRs).[6,7] nAChRs are ligand-gated ion channels of primary importance in the peripheral and central nervous systems, where they intervene in a wide range of physiological and pathophysiological processes, including muscle contraction, pain sensation, nicotine addiction, and neurological disorders such as Parkinson's and Alzheimer's diseases.[6] These receptors exist as homopentamers or heteropentamers composed of a large variety of homologous subunits. Subunits α2−α10 and β2−β4 assemble into the diverse group of neuronal nicotinic receptors, while the muscle-type nicotinic receptor exists only as adult $(\alpha1)_2\beta1\varepsilon\delta$ and fetal $(\alpha1)_2\beta1\gamma\delta$ subunit combinations.[8] α-Conotoxins are classified according to the number of residues within the loops formed by two conserved disulfide bridges. Interestingly, in most cases, the size of the loops seems to determine their specificity for different nAChR subtypes. Thus, 3/4 α-conotoxins target homomeric neuronal nAChRs, 3/5 α-conotoxins target muscle-type nAChRs, and 4/4, 4/6 and 4/7 α-conotoxins target different heteromeric and/or homomeric neuronal nAChRs.[6]

Received: June 8, 2020
Published: October 16, 2020

https://dx.doi.org/10.1021/acs.jmedchem.0c00957
J. Med. Chem. 2020, 63, 12682−12692

Journal of Medicinal Chemistry pubs.acs.org/jmc Article

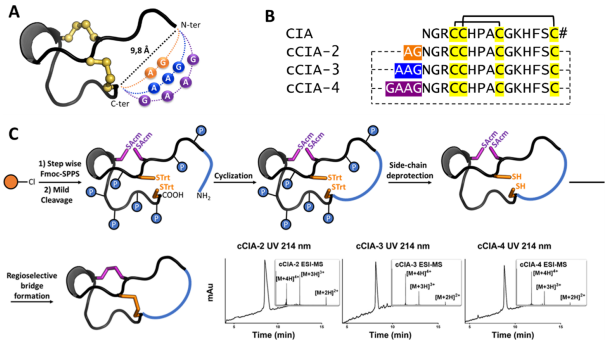

Figure 1. Sequences and chemical synthesis strategy for α-conotoxin CIA cyclic analogues (cCIAs). (A) NMR structure (backbone representation) of CIA. CIA exhibits a classical α-conotoxin fold with Cys I−Cys III and Cys II−Cys IV disulfide connectivity (represented in yellow). (B) Based on the intertermini spacing, amino acid linkers with a length between 10 and 19 Å were designed. Symbol # indicates an amidated C-terminal residue. (C) Strategy for the synthesis of three cyclic α-CIA peptides and the respective RP-HPLC/ESI-MS analysis to confirm purity >95%. The orange round circle represents a PS-chloro-(2′-chloro) trityl resin and P represents common side chain-protecting groups used in Fmoc-SPPS. RP-HPLC−UV (ACN gradient from 0 to 30% in 30 min) coupled to ESI-MS analyses revealed the presence of dominant peaks of the expected masses.

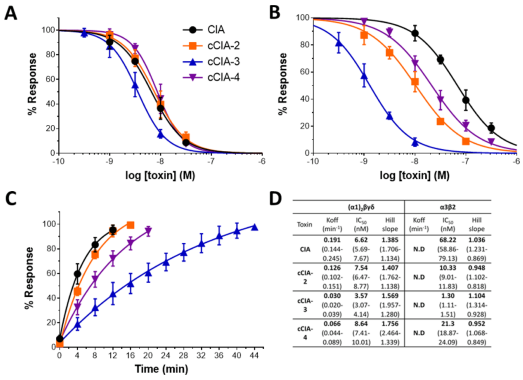

	(α1)2βγδ			α3β2		
Toxin	Koff (min⁻¹)	IC_{50} (nM)	Hill slope	Koff (min⁻¹)	IC_{50} (nM)	Hill slope
CIA	0.191 (0.144-0.245)	6.62 (5.69-7.67)	1.385 (1.706-1.134)	N.D	68.22 (58.86-79.13)	1.036 (1.231-0.869)
cCIA-2	0.126 (0.102-0.151)	7.54 (6.47-8.77)	1.407 (1.762-1.138)	N.D	10.33 (9.01-11.83)	0.948 (1.102-0.818)
cCIA-3	0.030 (0.020-0.039)	3.57 (3.07-4.14)	1.569 (1.957-1.280)	N.D	1.30 (1.11-1.51)	1.104 (1.314-0.928)
cCIA-4	0.066 (0.044-0.089)	8.64 (7.41-10.01)	1.756 (2.464-1.339)	N.D	21.3 (18.87-24.09)	0.952 (1.068-0.849)

Figure 2. CIA cyclic analogues retain potency at the muscle-type nAChR and show increased affinity at $\alpha3\beta2$ nAChRs. Dose−response curves of CIA and the three cyclic analogues (cCIA-2, cCIA-3, and cCIA-4) on (A) rat muscle-type and (B) neuronal $\alpha3\beta2$ nAChRs. *X. laevis* oocytes expressing the indicated receptors were analyzed by two-electrode voltage-clamp at −70 mV holding potential. Responses to 2 s pulses of 100 μM ACh were recorded after 3 min preincubation with the respective toxin. (C) Recovery of muscle-type nAChRs from toxin block measured in 4 min intervals. Each point represents the mean of measurements from at least three different oocytes. Error bars represent SD. (D) Summary of inhibition and dissociation constants of the toxins. Numbers in brackets are 95% confidence intervals. N.D. = not determined.

Despite great advances in peptide synthesis and drug development, the direct utilization of conotoxins as therapeutics is limited because of their poor bioavailability, mostly because of amide bond breakdown by digestive enzymes, as well as their high polarity and molecular weight, which restrict their intestinal absorption. Thus, alternative routes of application, such as intrathecal administration, have been developed.[9] However, head-to-tail cyclization, N-acetylation, and C-amidation are widely employed strategies to improve peptide stability through prevention of degradation by aminopeptidases and carboxypeptidases.[10] Although N-acetylation and C-amidation are relatively easy to implement via chemical techniques, the more challenging head-to-tail cyclization is often preferred because it results in an increased permeability through biological barriers.[11,12]

Whereas cyclization was previously shown to improve the stability of several α-conotoxins with specificity for neuronal nAChRs,[13−17] backbone cyclization of a paralytic, muscle-type 3/5 α-conotoxin has not been reported before. Here, we describe the synthesis, pharmacological characterization, and structure determination of three cyclic analogues of the muscle-type α-conotoxin α-CIA and demonstrate their

https://dx.doi.org/10.1021/acs.jmedchem.0c00957
J. Med. Chem. 2020, 63, 12682−12692

Journal of Medicinal Chemistry pubs.acs.org/jmc Article

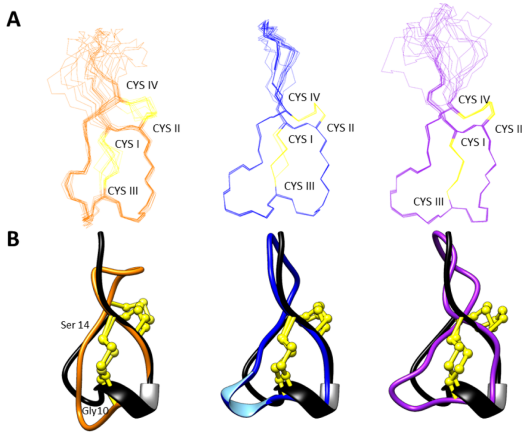

Figure 3. NMR-derived structures of the cyclic CIA analogues. (A) The 15 lowest energy structures are superimposed over the backbone atoms for residues 6−17 (cCIA-2; orange, left), 4−18 (cCIA-3, blue, middle) and 5−19 (cCIA-4, mauve, right), and the disulfide bonds are shown in yellow ball and stick representation. (B) cCIA-2 (left), cCIA-3 (middle), and cCIA-4 (right) superimposed over α-CIA backbone atoms (black) for residues 3−17 (cCIA-2), 4−18 (cCIA-3), and 5−19 (cCIA-4).

increased stability and altered subtype selectivity. In addition, we show how their unique selectivity profile can be used to study the weakening of the muscle during repetitive nerve stimulation (fading of muscle twitches during the "train-of-four" (TOF) repetitive stimulation pattern).

RESULTS

The previously described α-conotoxin CIA[18] from the predation-evoked venom of *Conus catus* is a highly potent blocker of muscle-type nicotinic receptors. It has a typical 3/5 α-conotoxin disulfide framework (Cys1−Cys3; Cys2−Cys4) and displays high sequence homology with other known muscle-type conotoxins. However, contrary to other 3/5 α-conotoxins, it also shows activity at the $\alpha3\beta2$ neuronal subtype. Interestingly, the nuclear magnetic resonance (NMR) structure of α-CIA revealed a relatively short intertermini distance of about 10 Å that favors head-to-tail cyclization (Figure 1A). Therefore, we investigated the effect of backbone cyclization of this peptide with amino acid linkers of different lengths (Figure 1B). The objective of this modification was to produce the first proteolysis-resistant and highly potent blocker of both neuronal and muscle-type nicotinic receptors, representing a unique pharmacological tool.

Chemical Synthesis of Cyclic α-Conotoxin CIA Analogues. After anchoring of the C-terminal residue on a chloro-(2′-chloro) trityl resin, elongation of the peptide chain was performed manually using fluorenylmethoxycarbonyl (Fmoc)-based solid-phase peptide synthesis (SPPS).[19,20] Mild cleavage conditions were used to allow the separation of the peptide from the resin without affecting the side-chain-protecting groups. The crude protected peptide was cyclized under coupling conditions.[21] Side-chain deprotection and subsequent purification produced the cyclic peptide. Next, a regioselective folding strategy using acetamidomethyl (Acm)-protecting groups (Cys I−Cys III) was employed to produce the disulfide bond connectivity of the native peptide.[18] After final purification, the homogeneity of folded cCIA peptides was assessed by analytical reversed-phase high performance liquid chromatography (RP-HPLC)−ultra-violet (UV) coupled to electrospray ionization mass spectrometry (ESI-MS) (Figures 1C and S1).

Electrophysiology and Binding Assays. The inhibitory potencies of the cCIA peptides were investigated using the two-electrode voltage-clamp method on rat $\alpha3\beta2$ neuronal nAChRs subtypes and fetal rat muscle-type nAChR ($(\alpha1)_2\beta\gamma\delta$) expressed in *Xenopus laevis* oocytes. All three cyclic analogues retained the low nanomolar (IC_{50} 4−9 nM) potency of the native toxin (IC_{50} 6.6 nM) at the fetal muscle-type nAChR (Figure 2A). Surprisingly, cyclization significantly improved the potency of CIA (IC_{50} 68.2 nM)[a] at the $\alpha3\beta2$ subtype with up to 52-fold increase in potency for the most active analogue cCIA-3 (IC_{50} 1.3 nM, Figure 2B). Thus, α-cCIA-3 is the first highly potent blocker that displays low nanomolar IC_{50} values for both the neuronal $\alpha3\beta2$ subtype and the muscle-type nAChRs.

As the potency increase at the $\alpha3\beta2$ receptor was accompanied by a slower recovery of the receptor from the block, we next measured the dissociation of the toxin from both muscle-type and $\alpha3\beta2$ nAChR subtypes. Despite the similar potency of CIA and cCIA analogues on the muscle-type nAChR, the cyclic analogues displayed significantly slower off-rates with cCIA-3 having the smallest dissociation constant (K_{off}) and a wash-out time of ≈30 min to reach 80% recovery of ACh-induced current responses (Figures 2C and S2) at the muscle-type nAChRs. In contrast, complete dissociation from neuronal $\alpha3\beta2$ subtypes occurred within seconds and could not be determined with the established protocol. Therefore, the real-time receptor reactivation during a 10 s agonist application (Figures S3 and S4) was analyzed and compared to

https://dx.doi.org/10.1021/acs.jmedchem.0c00957
J. Med. Chem. 2020, 63, 12682−12692

Journal of Medicinal Chemistry pubs.acs.org/jmc Article

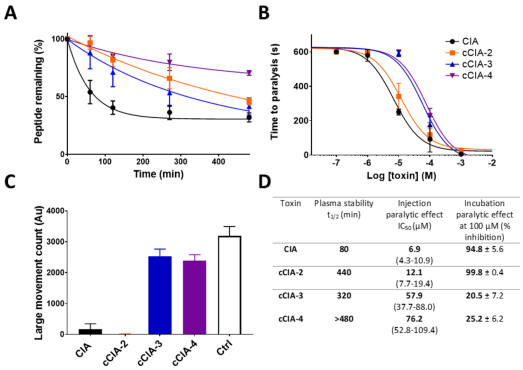

Toxin	Plasma stability $t_{1/2}$ (min)	Injection paralytic effect IC_{50} (μM)	Incubation paralytic effect at 100 μM (% inhibition)
CIA	80	6.9 (4.3-10.9)	94.8 ± 5.6
cCIA-2	440	12.1 (7.7-19.4)	99.8 ± 0.4
cCIA-3	320	57.9 (37.7-88.0)	20.5 ± 7.2
cCIA-4	>480	76.2 (52.8-109.4)	25.2 ± 6.2

Figure 4. Serum stability of CIA and cCIA analogues and the paralytic effect of the cCIA analogues on zebrafish (*D. rerio*). (A) Stability of CIA and cCIA analogues in human serum. Positive control: linear peptide, negative control: incubation in water. Points represent the mean of one measurement performed in triplicate. Error bars represent the SD. (B) Dose−response analysis of paralysis induced by intramuscular injection of conotoxins CIA and cCIA analogues in adult zebrafish. Experiment was performed in triplicate with a negative control (water injection). Points represent the mean of the triplicate. Error bars represent the SD. (C) Large movement count over 1 h of *D. rerio* larvae movement tracking after addition of the toxins into the water at a concentration of 100 μM. Each point represents the mean of measurements from six different larvae. Error bars represent the SD. (D) Summary of results, 95% confidence intervals are in brackets. Symbol ± indicates the SD.

provide an estimate of the dissociation of the cCIA analogues from this receptor. Again, this revealed that cCIA-3 has the slowest dissociation rate. As many $\alpha3\beta2$-selective α-conotoxins show a rather high affinity at the $\alpha3\beta2$-binding site and alternative α-conotoxin-binding sites have been suggested, we wondered whether cCIA-3 may bind to an allosteric binding site at the $\alpha3\beta2$ receptor. However, functional competition binding experiments with α-conotoxin MII, a potent competitive antagonist at the $\alpha3\beta2$ subtype, showed that preincubation with 100 nM cCIA-3 inhibited binding of MII, a result consistent with a competitive binding of cCIA-3 to the orthosteric $\alpha3\beta2$-binding site (Figure S5). The potency of α-cCIA-3 was further evaluated on several nAChR subtypes. Responses in the presence of 10 μM of cCIA-3 were 80% or higher for rat $\alpha2\beta2$, $\alpha2\beta4$, $\alpha3\beta4$, $\alpha4\beta2$, $\alpha4\beta4$, and human $\alpha9\alpha10$ neuronal nAChRs, demonstrating no significant inhibitory activity (Table S1). Only weak activity was detected at the human $\alpha7$ subtype at 10 μM (65% of response). Remarkably, however, cCIA-3 readily blocked the $\alpha6/\alpha3\beta2\beta3$ subtype and the adult muscle nAChR with IC_{50s} of 8.64 nM and 184 pM, respectively (Figure S6A,B). The recovery of block from cCIA appears more than twice as slow for the human adult nAChR (K_{off}: 0.013 vs 0.03 min^{-1}) compared to the fetal nAChR (Figure S7).

NMR Spectroscopy. High-resolution NMR spectroscopy allowed the determination of three-dimensional structures of the CIA cyclic analogues (Figure 3A). Two-dimensional TOCSY, NOESY, COSY, and HSQC spectra were collected for all three CIA cyclic analogues and the assignments were made using standard approaches[22] (Table S2). Structures were determined based on the NOE data, and angle restraints were predicted from TALOS.[23] Additional peaks are present in the cCIA-2 and cCIA-4 spectra, most likely representing alternative conformations, whereas cCIA-3 has primarily one set of peaks corresponding to a single conformation. Therefore, the linker length appears to impact the structural stability. The dominant conformations were assigned for the peptides and a superposition of the structures with native α-CIA is shown in Figure 3B, highlighting the similarity between the cyclic analogues and the native peptide. The most striking structural deviation is within residues 10−14 of CIA, where the root mean square deviation (rmsd) values of the backbone atoms with their corresponding atoms in the cyclic analogues equate to 1.67, 4.28, and 4.10 Å for cCIA-2, cCIA-3, and cCIA-4, respectively.

Serum Stability Assay. The stability of CIA and its cyclic analogues toward enzymatic degradation was determined by incubation with human serum AB. Peptides were incubated for 8 h at 37 °C and the amount of intact peptide remaining was determined by liquid chromatography/MS analysis of aliquots taken at 0, 1, 2, 4, and 8 h postincubation. As shown in Figure 4A, the degradation kinetics of the cyclic analogues were much slower than that of CIA, especially during the first 3 h. cCIA-4 showed the highest resistance to serum degradation, with up to 70% intact peptide remaining after 8 h of incubation. In comparison, cCIA-2 and cCIA-3 have half-life values of 440 and 320 min, respectively. Finally, degradation of native α-CIA was the fastest, with a half-life of 80 min. Thus, CIA cyclization greatly improved (≥4−6-fold) the resistance against enzymatic degradation, consistent with previously published data on conotoxin cyclization.[13−17]

Zebrafish In vivo Assays. Prior to investigating a potential oral/transcutaneous uptake of CIA and its three cyclic analogues, we first performed in vivo intramuscular injections into adult zebrafish (*Danio rerio*) to evaluate the potency in this species. Intramuscular injection of α-conotoxin CIA and its three cyclic analogues produced a rapid flaccid paralysis of skeletal muscle, as evidenced by a loss of an upright posture of the fish, and ultimately complete immobilization. Paralysis induced by CIA and cCIA analogues exhibited a dose-

https://dx.doi.org/10.1021/acs.jmedchem.0c00957
J. Med. Chem. 2020, 63, 12682−12692

Journal of Medicinal Chemistry pubs.acs.org/jmc Article

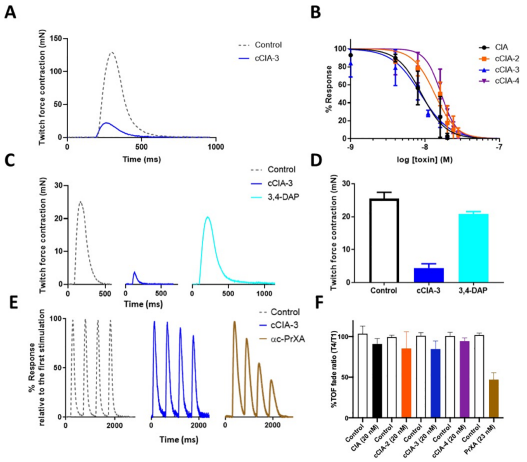

Figure 5. In vitro mouse hemidiaphragm muscle recordings and the TOF fade ratio of CIA and the cyclic analogues. (A) Typical twitch responses upon nerve stimulation (0.1 Hz) under control conditions and during the action of cCIA-3 (16 nM). (B) Concentration−response curves for CIA (IC_{50} = 8.98 nM), cCIA-2 (IC_{50} = 13.48 nM), cCIA-3 (IC_{50} = 8.70 nM), and cCIA-4 (IC_{50} = 16.47 nM). Data points represent the mean ± SD of twitch responses from 1−9 nerve-muscle preparations, after 20−25 min toxin exposure, relative to the respective controls. (C) Isometric twitch tension recordings evoked by nerve stimulation (0.1 Hz) on the same phrenic-nerve hemidiaphragm preparation under control conditions, following 30 min incubation with 16 nM cCIA-3, and after 27 min of 10 μM 3,4-DAP action. Note the different time course of twitch recordings between the control and after 3,4-DAP-treatment. (D) Data obtained in the same preparation and expressed as means ± SD (n = 14). (E) Isometric tension developed during TOF nerve stimulation (2 Hz) under control conditions, and in the presence of cCIA-3 and αC-PrXA. Note the TOF fade in the presence of αC-PrXA. Signal amplitude is relative to the maximum response of each compound (F) TOF fade ratio (T4/T1) in the presence of α-CIA, cCIA analogues, and αC-PrXA. Note that a significant fade is only seen for PrXA. Control experiments are represented in white.

dependent effect, with IC_{50} values for CIA, cCIA-2, cCIA-3, and cCIA-4 of 6.88, 12.1, 57.87, and 76.22 μM, respectively (Figure 4B). This evaluation of paralysis caused by muscle nAChR blockade led to investigation of the oral/transcutaneous toxin uptake by tracking the movement of zebrafish larvae in 100 μM toxin for 1 h using the ZebraBox tracking system (Figure 4C). Consistent with the intramuscular injection data, native CIA and cCIA-2 induced a strong paralysis, suggesting efficient uptake of these toxins, whereas cCIA-3 and cCIA-4 were less potent (Figure 4D).

Mouse Muscle Contraction Assays. *α-CIA and Analogues Block Nerve-Evoked Muscle Contraction.* When applied at nanomolar concentrations to isolated phrenic-nerve hemidiaphragm muscle preparation, CIA and cCIA analogues produced a concentration- and time-dependent reduction of the isometric twitch force evoked by nerve stimulation at 0.1 Hz (Figure 5A,B).

For the most active peptide (cCIA-3), the time required to block 50% of nerve-evoked muscle contraction was 19.0 ± 6.2 min (n = 4), and a 40% recovery was obtained in 32.6 ± 1.8 min (n = 3) (data not shown), in agreement with muscle-type nAChR blockade. The effect of all peptides was reversible upon washing the preparations with an extracellular medium free of α-conotoxins. These results indicate that CIA and analogues are effective neuromuscular blockers, and are 2−3 fold more potent than the previously studied αC-PrXA, a highly specific and potent inhibitor of muscle-type nAChR.[24]

In order to confirm that cCIA-3 acts as a competitive antagonist at the muscle-type nAChR, we determined if an increase of evoked ACh release from nerve terminals could displace cCIA-3 from its nAChR-binding site. Therefore, we used 3,4-diaminopyridine (3,4-DAP), which greatly increases quantal ACh release by reversibly blocking voltage-gated K^+ channels in motor nerve terminals,[25−27] which is used to treat certain forms of muscle weakness.

As shown in Figure 5C, cCIA-3 (16 nM) blocked the peak amplitude of nerve-evoked contraction by approximately 85%, and this effect was 80% reversed upon addition of 3,4-DAP (10 μM) to the medium (Figure 5C,D). Interestingly, when computing twitch tension-time integrals instead of peak amplitudes, the reversal was in the range of 96−98%. This difference in values is explained by the fact that nerve-evoked contractions exhibit a prolonged time course in the presence of 3,4-DAP (shown in a comparison of the control and 3,4-DAP traces in Figure 5C). In conclusion, these data can be explained by a mechanism in which 3,4-DAP increases acetylcholine release from nerve terminals and the increased ACh displaces the cCIA-3 analogue from the muscle endplate nAChR, and thus strongly supports our assumption that the peptide acts in a competitive manner on the muscle-type nAChR, in agreement with the described mode of action of α-conotoxins.

Train-of-Four Fade in the Presence of Conotoxins with Muscle and Dual Muscle/α3β2 Selectivity. TOF stimulation is commonly used to monitor neuromuscular transmission

https://dx.doi.org/10.1021/acs.jmedchem.0c00957
J. Med. Chem. 2020, 63, 12682−12692

when muscle relaxants are applied. A fade in muscle twitches (reduction of the twitch amplitude after repetitive nerve stimulation) is observed with nondepolarizing but not with depolarizing muscle relaxants.[28−30] Curare-like agents (competitive inhibitors of the muscle-type nAChR) that produce a nondepolarizing neuromuscular block at the neuromuscular junction are known to display a typical TOF fade, both in vitro and in vivo.[31−33] The TOF fade corresponds to the T4/T1 ratio, where T4 and T1 are the fourth and first twitch tensions in the same TOF stimulations. The inhibition of the presynaptic facilitatory $\alpha3\beta2$ nAChR autoreceptor at motor nerve terminals and the resulting inhibition of autofacilitatory ACh release have been suggested as an explanation for the TOF fade seen during a nondepolarizing neuromuscular block.[28,29] However, this hypothesis was recently challenged by using ligands with different selectivities for pre- and postsynaptic receptors.[34] Therefore, because of their original dual muscular/$\alpha3\beta2$ nAChRs antagonist property, it was of interest to determine whether α-CIA and the cCIA analogues were able to produce TOF fade.

Under control conditions (in the absence of peptides), no TOF fade is observed as shown by the typical recordings (Figure 5E). Remarkably, when nerve-evoked contraction was inhibited about 76% by cCIA-3, no significant TOF fade was observed either. In contrast, a marked TOF fade was observed with the highly muscle-selective αC-PrXA peptide (no inhibitory activity at $\alpha3\beta2$), already at approximately 45% neuromuscular block (Figure 5E). As shown in Figure 5F, TOF fadings were determined at different conotoxin concentrations. If a 50% decrease of TOF fade was measured with αC-PrXA (23 nM), no significant effect was observed at any concentrations of the α-CIA and cCIA analogues studied. Therefore, these data strongly argue against the common explanation of TOF fade, that is, the blockade of $\alpha3\beta2$ autoreceptors at the neuromuscular junction.

■ DISCUSSION AND CONCLUSIONS

Backbone cyclization has previously been reported to enhance stability and in some cases to improve the permeability of the cyclic analogue through biological membranes.[13−17] Considering the unusual dual activity of the 3/5 α-conotoxin CIA on muscle and neuronal nAChR $\alpha3\beta2$ subtypes, we investigated the effect of backbone cyclization on its pharmacology and stability. During the cyclization process, a linker minimizing perturbations of the three-dimensional structure of a bioactive native toxin is highly desirable. Indeed, Clark et al. showed that an inappropriate linker can distort the structure by introducing strain to the peptide leading to a loss of bioactivity.[13,14] Therefore, based on the intertermini spacing (9.8 Å), amino acid linkers with a length between 10 and 19 Å were chosen.

Overall conservation of the structure between CIA and its cyclic analogues was confirmed by NMR spectroscopy. Nevertheless, the linker length appeared to have a significant impact locally, particularly for residues 10−14 of CIA (Table S1). cCIA-3 displays the lowest rmsd value and, therefore, has the most well-defined structure, and shows only one predominant conformation in the NMR spectra in contrast to the other two cyclic analogues.

Consistent with the NMR data, structural conservation of the cCIA analogues compared to the native CIA led to the conservation of the bioactivity toward muscle-type nAChRs at low nanomolar concentrations. However, the significant decrease in K_{off} values suggests stronger interaction of the cyclic analogues within one, or both, of the two orthosteric muscle nAChR-binding sites. Considering the high sequence homology of α-CIA with α-MI and α-GI, α-CIA is most likely binding at the $\alpha-\delta$ interface.[35,36] It has been demonstrated that the ACh-binding pocket is mostly composed of hydrophobic residues that interact with residues of the two conotoxin loops formed by the disulfide bridges. Although, the linker is outside of these cysteine loops, the lower K_{off} values of cCIA-3 and cCIA-4 might be because of stronger hydrophobic interactions arising from the additional alanine residues in the linker compared to cCIA-2. Interestingly, and in contrast to our observations at the muscle nAChRs, dissociation rates from the neuronal $\alpha3\beta2$ subtype were so fast that dissociation constants could not be determined with established protocols despite a strong potency increase at these subtypes. This raised the question of how exactly the native α-CIA and the cyclic analogues bind to the $\alpha3\beta2$ subtype. Indeed, allosteric modulators usually display very fast dissociation rates, however, functional competition binding experiments suggested a competitive binding of cCIA-3 to the orthosteric $\alpha3\beta2$-binding site and we can reasonably extend this hypothesis to cCIA-2, -4 and native α-CIA toxin. Surprisingly, all of the cyclic analogues also displayed a significantly increased potency at the $\alpha3\beta2$ subtypes, with cCIA-3 being the most potent with a 52-fold decreased IC_{50} value compared to native α-CIA. The high rmsd value (4.28 Å) in the region of residues 13−17 of cCIA-3 (compared to the equivalent residues in CIA) might allow favorable structural changes further enhanced by the well-defined structures of cCIA-3 (0.29 Å over backbone atoms) compared to native α-CIA (0.95 Å over backbone atoms) possibly facilitating toxin binding to the receptor and explaining the higher potency of cCIA-3 at the $\alpha3\beta2$ nAChR subtype.

Cyclization of α-CIA leads to an improved stability toward enzymatic degradation, in agreement with the previously published data on α-conotoxin cyclization.[13−17] cCIA-4 was the most resistant to degradation in serum, exhibiting a serum half-life of more than 8 h (70% remaining peptide), followed by cCIA-2, cCIA-3, and native CIA, which is degraded at least four times faster. Nevertheless, CIA and the cCIA analogues appear to be more readily degraded in serum than cVc1.1 and cMII, as shown in the study by Clark et al.[13,14] Unlike Vc1.1 and MII conotoxins, CIA contains one arginine residue before the first cysteine residue, and one lysine residue in the second loop that can be cleaved by endopeptidases.

A visible paralyzing effect, resulting from the block of muscle-type nAChR, was observed when CIA or the cCIA analogues were injected intramuscularly into zebrafish. Paralysis activity of the conotoxins could also be monitored by movement tracking of zebrafish (*D. rerio*) larvae, after incubation with the toxins in the tank water. Based on the inhibition values obtained by intramuscular injection, we performed the assay at a concentration of 100 μM (higher doses would require large amounts of peptides). CIA and cCIAs showed a paralyzing effect when added into the swimming water of *D. rerio* larvae in comparison to the control, with CIA and cCIA-2 being the most potent. cCIA-3 and cCIA-4 exhibited a weaker activity, which is consistent with the intramuscular injection data. Zebrafish (*D. rerio*) might not have the required metabolic means to completely digest the native CIA and make it completely inactive.

Considering the unique capacity of α-CIA and cCIAs to block both muscle-type and neuronal $\alpha3\beta2$ subtype nAChRs,

https://dx.doi.org/10.1021/acs.jmedchem.0c00957
J. Med. Chem. 2020, 63, 12682−12692

they represent a novel pharmacological tool to study the contribution of the $\alpha3\beta2$ subtype neuromuscular transmission in the presence of neuromuscular blockers. Consistent with the electrophysiology data, CIA and its cyclic analogues block the phrenic nerve-evoked isometric twitch force in mouse hemidiaphragm muscles in the nanomolar range. The cCIA-3-induced block was reversed when increasing the quantal ACh release by 3,4-DAP, thus confirming the competitive binding evidenced by electrophysiological binding experiments.

A role of the presynaptic $\alpha3\beta2$ nicotinic receptor in the TOF fade phenomenon has been proposed previously.[34] One of the persevering theories is that presynaptic $\alpha3\beta2$ nicotinic receptors would increase the release of acetylcholine via a positive feedback mechanism to maintain the contraction at the same level following repeated nerve stimulation at the neuromuscular junction. Thus, the presynaptic $\alpha3\beta2$ inhibition could explain the attenuated release of acetylcholine leading to nerve-evoked muscle contraction fade.[37] This hypothesis was recently challenged by using ligands with different selectivities for pre- and postsynaptic receptors:[34] it was found that, in in vivo experiments, the TOF fade was clearly correlated with the administration of postsynaptic muscle-type antagonist such as α-bungarotoxin or α-conotoxin GI, while the $\alpha3\beta2$ blocker DHβE was shown to potentiate the TOF fade. Nevertheless, DHβE is a nonselective neuronal receptor blocker, thus justifying the re-examination of the precise role of the presynaptic $\alpha3\beta2$ subtype here. Considering their high potency and distinct selectivities to both muscle-type and neuronal $\alpha3\beta2$ nAChRs, CIA and its cyclic analogues represent unique pharmacological tools to address this question. Surprisingly, neither CIA nor its cyclic analogues induced a visible TOF fade, in contrast to the muscle-specific αC-PrXA conotoxin. Hence, in contradiction to the generally accepted hypothesis that TOF fade results from a dual block of presynaptic $\alpha3\beta2$ and postsynaptic muscle nAChRs, our data show that dual blockade of $\alpha3\beta2$ and muscle-type nAChRs is able to prevent this phenomenon. Thus, the role of the $\alpha3\beta2$ nAChR in neuromuscular transmission needs to be studied in more detail, and the cyclic CIA analogues could provide the necessary pharmacological tools.

EXPERIMENTAL SECTION

Chemical Synthesis. *N*,*N*′-Dimethylformamide (DMF), N,N-diisopropylethylamine (DIPEA), acetonitrile (ACN), triisopropylsilane (TIS), trifluoroacetic acid (TFA), piperidine, and all others reagents were obtained from Sigma-Aldrich (Saint-Louis, MI, USA) or Merck (Darmstadt, Germany) and were used as supplied. Fmoc (L) amino acid derivatives and HATU were purchased from Iris Biotech (Marktredwitz, Germany). PS-2-Chlorotrityl chloride resin (100−200 mesh, 1.6 mmol/g) was purchased from Iris Biotech (Marktredwitz, Germany). The following side-chain-protecting groups were used: Asn(Trt), Cys(Trt), His(Trt), Arg(Pbf), Cys(Acm), Lys(Boc), and Ser(*t*Bu). Peptides were manually synthesized using the Fmoc-based solid-phase peptide synthesis technique on a VWR (Radnor, PA, USA) microplate shaker. All Fmoc amino acids and HATU were dissolved in DMF to reach 0.5 M. The first amino acid was coupled onto the resin for 6 h in a 1/1 (v/v) mix of DMF and dichloromethane (DCM), with a 2.5-fold excess of amino acid and 5-fold excess of DIPEA followed by the addition of methanol and further mixing for 15 min to cap any remaining reactive functionalities on the resin. The resin was washed with DMF, DCM, MeOH, and DMF. Fmoc deprotection was carried out with piperidine in DMF (1/2 v/v) twice for 3 min. Subsequent amino acids were coupled onto 0.1 mmol of prepared resin (a determined loading value of 0.73 mmol/g) twice for 10 min using an amino acid/HATU/DIPEA ratio of 5:5:10 relative to resin loading. DMF was used for resin washing between deprotection and coupling steps. After chain assembly was complete, the terminal Fmoc group was removed and the resin was washed with DMF and DCM. Cleavage of the peptide from the resin without affecting the side-chain-protecting group was carried out in a reaction vessel and treated 10 times with 10 mL of 1% TFA in DCM (v/v) for 5 min. Eluates were collected and combined into a round-bottomed flask then DCM and TFA were removed under vacuum and cold diethyl ether was added to precipitate the peptide. The crude side-chain-protected peptide was dissolved in DMF at a concentration of 2 mM in a round-bottom flask. HATU was added to the solution to give a final concentration of 5 mM and mixed for 30 s. DIPEA was added to a final concentration of 10 mM, and the solution was stirred for 4 h at room temperature. DMF was removed under vacuum and residues were uptaken in ACN/H_2O (1/1 v/v) and freeze dried overnight. Side-chain (except acm) deprotection was carried out by adding 6.25 mL of TFA/TIS/H_2O (95/2.5/2.5 v/v/v) per 100 mg of the crude peptide and stirring the mixture for 2.5 h at room temperature. Crude peptides were purified by preparative RP-HPLC and pure fractions were combined and freeze dried. A two-step oxidation procedure was then carried out. The first disulfide bridge is formed between the free cysteine residues CysII−CysIV by dissolving the peptide at 0.2 mM in 50 mM Tris-HCl buffer adjusted to pH 8 and adding 7 equiv of 2,2′-dithiopyridine (DTP) at 10 mM in MeOH dropwise. When the reaction was complete, the reaction mixture was acidified to pH 3 and loaded onto preparative RP-HPLC and pure fractions were combined. The second disulfide bridge CysI−CysIII was formed by deprotection/oxidation of the Acm-protecting group directly on the combined pure fractions of the monobridged intermediates by treatment with 20 equiv of 10 mM iodine in H_2O/TFA/ACN (78/2/20 v/v/v). When the reaction was complete, the reaction mixture was quenched with 20 mM ascorbic acid until total discoloration of the solution, acidified, and purified by preparative RP-HPLC. The combined pure fractions were freeze dried and their purity were confirmed by LC/ESI-MS. cCIA-2,-3,-4 peptides have been obtained with 6.3, 7.5, and 5.4% yields, respectively (purity > 95%). The peptide content was estimated at 60% from dry weight.

Mass Spectrometry. Solvents used for liquid chromatography/mass spectrometry (LC/MS) were of HPLC grade. The LC/MS system consisted of a Waters (Milford, OH, USA) Alliance 2695 HPLC, coupled to a Waters Micromass ZQ spectrometer (electrospray ionization mode, ESI^+). All the analyses were carried out using a Chromolith (Fontenay sous Bois, France) HighResolution RP-18e (4.6 × 25 mm, 15 nm to 1.15 μm particle size, and a flow rate of 3.0 mL/min) column. A flow rate of 3 mL/min and a gradient of 0−100% B over 2.5 min for routine analyses and 0−30% B over 30 min for quality control of pure products were used. Solvent A: water/0.1% HCO_2H; solvent B: ACN/0.1% HCO_2H. UV detection was performed at 214 nm. Electrospray mass spectra were acquired at a solvent flow rate of 200 μL/min. Nitrogen was used for both the nebulizing and drying gases. The data were obtained in a scan mode ranging from 100 to 1000 m/z or 250 to 1500 m/z to in 0.7 s intervals.

Folded peptides were characterized using a Synapt G2-S high resolution MS system (Waters Corp., Milford, MA) equipped with an ESI source. Chromatographic separation was carried out at a flow rate of 0.4 mL/min on an Acquity H-Class ultrahigh performance liquid chromatography (UPLC) system (Waters Corp., Milford, MA), equipped with a Kinetex C18 100 Å column (100 × 2.1 mm, 2.6 μm particle size) from Phenomenex (France). The mobile phase consisted of water (solvent A) and ACN (solvent B) with both phases acidified by 0.1% (v/v) formic acid. Mass spectra were acquired in the positive ionization mode.

Preparative RP-HPLC. Preparative RP-HPLC was run on a Gilson PLC 2250 Purification system (Villiers le Bel, France) instrument using a preparative column (Waters DeltaPak C18 Radial-Pak Cartridge, 100 Å, 40 × 100 mm, 15 μm particle size, and a flow rate of 50.0 mL/min). Solvent A was 0.1% TFA in water, and solvent B was 0.1% TFA in ACN. A gradient of 0−50% B over 50 min was used.

https://dx.doi.org/10.1021/acs.jmedchem.0c00957
J. Med. Chem. 2020, 63, 12682−12692

Electrophysiological Recordings. cDNAs encoding rats $\alpha 2$, $\alpha 3$, $\alpha 4$, $\alpha 6$, $\beta 2$, and $\beta 4$ nAChRs were provided by Jim Patrick (Baylor College of Medicine, Houston, TX, USA) and subcloned into the oocyte expression vector pNKS2. The rat $\alpha 6/\alpha 3$ Chimera[38,39] was generated by Gibson assembly in the pNKS2 vector. Fetal rat muscle-type ($\alpha 1$, $\beta 1$, γ, and δ) subunit cDNAs in pSPOoD were provided by Veit Witzemann (MPI for Medical Research, Heidelberg, Germany). Plasmids for expression of $\alpha 7$, $\alpha 9$, $\alpha 10$, and adult muscle-type ($\alpha 1$, $\beta 1$, ε, and δ) nAChRs were a gift from David Adams (Illawara Health and Medical Research Institute, Wollongong University, Australia). Synthesized human muscle subunit cDNAs (Integrated DNA Technologies (IDT) (Coralville, IA, USA) and human $\alpha 9$ and $\alpha 10$ pCMV6-XL5 constructs (OriGene (Rockville, MD, USA) were cloned in pT7TS. Human $\alpha 7$ in pMXT was provided by Prof. Jon Lindstrom (Uni. Pennsylvania, PA, USA). cRNA was synthesized from linearized plasmids with SP6 or T7 RNA polymerase using the mMessageMachine kit (Invitrogen, Thermo Fisher Scientific, USA). *X. laevis* oocytes were kindly provided by Prof. Luis Pardo (MPI of Experimental Medicine, Göttingen), injected with 50 nL aliquots of cRNA (0.5 μg/μL), and kept at 16 °C in filtered ND96 (96 mM NaCl, 2 mM KCl, 1 mM $CaCl_2$, 1 mM $MgCl_2$, 5 mM HEPES, and pH 7.4) containing gentamicin (5 μg/mL).

Two-electrode voltage clamp recordings were performed 1−5 days after cRNA injection at a holding potential of −70 mV. Pipettes were pulled from borosilicate glass and filled with 3 M KCl. Resistances were below 1 MΩ. Membrane currents were recorded using a Turbo Tec 05X Amplifier (npi electronic, Tamm, Germany) filtered at 200 Hz and digitized at 400 Hz. CellWorks software was used for recording. The perfusion medium was automatically switched between ND96 with or without agonist (100 μM ACh) using a custom-made magnetic valve system. A fast and reproducible solution exchange (<300 ms) for agonist application was achieved using a 50 μL funnel-shaped oocyte chamber combined with a fast solution flow (150 μL/s) fed through a custom-made manifold mounted immediately above the oocyte. ACh pulses were applied for 2 s at 4 min intervals. After each application, the cell was superfused for 54 s with agonist-free solution, and the flow was then stopped for 3 min. Immediately at the beginning of this interval, peptide (prepared in filtered ND96 containing 0.1% BSA m/v) was mixed from a 10-fold stock into the static bath when responses of three consecutive agonist applications differed by less than 10%. The use of BSA showed no change in toxin potency but produced more stable measurements at low toxin concentrations. ACh-evoked current peaks following peptide incubation were normalized to the ACh current peak before peptide exposure.

The analysis of the electrophysiological data was performed using GraphPad Prism version 8.0. Dose−response curves were fit to the data using the Hill equation: % response = bottom + (top-bottom)/(1 + $10^{*}((\log IC_{50} - X) \times \text{HillSlope})$) and constraints of 100 and 0% for top and bottom, respectively. Dissociation curves were fit to the data with the equation % response = (response (time 0) − plateau) × exp(−K × time) + plateau.

The functional analysis of competitive binding was performed as previously described.[40] Briefly, 2 s ACh pulses were applied in 1 min intervals until stable responses were obtained. The perfusion was then stopped for 7 min for application of cCIA-3 (after 1 min) and/or MII (after 4 min) in the static bath. As a control, ND96 was applied instead of a peptide. All peak currents were normalized to the mean of the four stable ACh-evoked peak currents before the peptide incubation.

All experiments were performed with oocytes from at least two different frogs.

NMR Spectroscopy. Lyophilized synthetic peptides (∼1.5−2 mg) were resuspended in 90% H_2O:10% D_2O. 2D $^1H-^1H$ TOCSY, $^1H-^1H$ NOESY, $^1H-^1H$ DQF-COSY, $^1H-^{15}N$ HSQC, and $^1H-^{13}C$ HSQC spectra were acquired at 290 K using a 600 MHz AVANCE III NMR spectrometer (Bruker, Karlsruhe, Germany) equipped with a cryogenically cooled probe. All spectra were recorded with an interscan delay of 1 s. NOESY spectra were acquired with mixing times of 200−250 ms, and the TOCSY spectra were acquired with isotropic mixing periods of 80 ms. Two-dimensional spectra were collected over 4096 data points in the f2 dimension and 512 increments in the f1 dimension over a spectral width of 12 ppm. Standard Bruker pulse sequences were used with an excitation sculpting scheme for solvent suppression. The two-dimensional NOESY spectra of the cCIA analogues were automatically assigned and an ensemble of structures was calculated using the program CYANA.[41] Torsion-angle restraints from TALOS+ were used in the structure calculations. The final structures were visualized using Pymol (The PyMOL Molecular Graphics System, Version 2.0 Schrödinger, LLC.), MOLMOL,[42] and UCSF Chimera.[43]

Monitoring of the Paralysis Effect after Injection into Adult Zebrafish (*D. rerio*). Sixty three adult male and female (2−5 months) zebrafish wild-type AB were maintained under standardized conditions and experiments were conducted in accordance with the European Communities council directive 2010/63, procedures were approved by Ethical Committee for Animal Experiment of Languedoc Roussillon no 36 (reference number: 2018040911129080 #14665 v4). The AB wild-type zebrafish line has been obtained from ZIRC (Zebrafish International Resource Center, Oregon, USA; ID ZL1) and bred in-house. Toxins were diluted in Milli-Q water and 5 μL of incremental doses were injected intramuscularly into adult zebrafish with a 10 μL Neuros Syringe from Hamilton (Bonaduz, Switzerland). Each dose was repeated three times on three different fishes to determine error bars. The onset of paralysis was measured over a maximum observation time of 10 min. Paralysis was considered total when the fish went on its back. Negative control experiments were performed according to the same protocol by injecting water instead of toxins.

Monitoring of the Paralysis Effect after Incubation into Zebrafish (*D. rerio*) Larvae Swimming Water. Experiments were conducted on 5-day-old larvae of zebrafish wild-type AB. Six larvae per toxin were placed in a 96-well plate and a controlled volume of swimming water was added. Small volumes of toxin were added to reach the final desired concentration of 100 μM. Immediately after incubation, the plate was placed in the movement-tracking chamber. The movement of larvae was video captured and quantified using the ZebraBox infrared camera setup and tracking extension of the ZebraLab software system (Viewpoint Life Sciences, Canada). The integration period for movement data was set to 30 min. Each time the animal speed goes above the small/large movement threshold, the large movement counter is incremented. Negative control experiments were performed according to the same protocol by adding water instead of toxins.

In vitro Assays on Isolated Mouse Nerve-Muscle Preparations. *Animals.* Twenty eight adult (14 male and 14 female) Swiss mice (*Mus musculus*, 2−5 months of age and 23−28 g of body weight) were purchased from Janvier Elevage (Le Genest-Saint-Isle, France). Mice were acclimatized at the CEA animal facility for at least 48 h before experiments. Live animals were treated according to the European Community guidelines for laboratory animal handling and the guidelines established by the French Council on animal care "Guide for the Care and Use of Laboratory Animals" (EEC86/609 Council Directive—Decree 2001-131). Mice were housed four- to six-wise in cages with environmental enrichment, in a room with constant temperature and a standard light cycle of 12 h light/12 h darkness and had free access to water and food. All experimental procedures on mice were approved by the Animal Ethics Committee of the CEA and by the French General Directorate for Research and Innovation (project APAFIS#2671-2015110915123958v4 authorized to E. Benoit). Male and female mice were anesthetized by isoflurane (Aerrane, Baxter S.A., Lessines, Belgium) inhalation before being euthanized by dislocation of the cervical vertebrae.

Recordings on Isolated Nerve-Muscle Preparations. In vitro assays were performed on left phrenic-nerve hemidiaphragm muscle preparations quickly removed and mounted in a silicone-lined organ bath (4 mL capacity). Preparations were bathed in a Krebs−Ringer solution of the following composition: 150 mM NaCl, 5 mM KCl, 2 mM $CaCl_2$, 1 mM $MgCl_2$, 11 mM glucose, and 5 mM HEPES (pH 7.4), continuously superfused with pure O_2 throughout the experi-

https://dx.doi.org/10.1021/acs.jmedchem.0c00957
J. Med. Chem. 2020, 63, 12682−12692

ment at a constant temperature of 22 °C, unless otherwise indicated. For nerve-evoked isometric twitch tension measurements, the phrenic nerve was usually stimulated with a suction microelectrode (adapted to the diameter of the nerve) with supramaximal current pulses of 0.25 ms duration, at a frequency of 0.1 Hz delivered by the isolation unit of a stimulator (S-44 Grass Instruments, West Warwick, RI, USA). The hemidiaphragm tendons (at the rib side) were tightly anchored onto the silicone-coated bath with stainless pins, and the other tendon (central medial tendon) was attached via an adjustable stainless-steel hook to a FT03 isometric force transducer (Grass Instruments). The resting tension was monitored for each preparation tested and adjusted with a mobile micrometer stage allowing variations of muscle length in order to obtain maximal contraction amplitude in response to motor nerve stimulation. Once maximal contraction was obtained, the resting tension was fixed, and monitored during the whole duration of the experiment. Signals from the isometric transducer were amplified, collected, and digitized with the aid of a computer equipped with an Axon Digidata-1550B A/D (interface board low-noise acquisition systemplus hum silencer), using the PClamp/Axoscope 10.7 version software (Axon Instruments, Molecular Devices Inc., Sunnyvale, CA, USA).

In some experiments, a TOF stimuli was delivered to the phrenic nerve trunk at a frequency of 2 Hz for 2 s, at a train rate of 0.033 Hz. The ratio of muscle tension developed in the mouse hemidiaphragm by the fourth to the first stimulus was evaluated $[T(4)/T(1)]$ at different peptide concentrations.

Statistical Analysis. Data are presented as means ± standard deviations (SD) of n different experiments. Differences between values were tested using the parametric two-tailed Student's *t*-test (either paired samples for comparison within a single population or unpaired samples for comparison between two independent populations) or the Kolmogorov−Smirnov two-sample test. Differences were considered significant when $P < 0.05$.

Serum Stability Assay. Human AB serum (VWR, Fontenay-sous-Bois, France) was centrifuged at 12,000*g* for 10 min for the removal of the lipid component. Supernatant was taken out and incubated for 15 min at 37 °C before the assay. All peptides were tested at a final concentration of 30 μM after dilution in serum (water for negative control). The incubation time points were 1, 2, 4, and 8 h at 37 °C. Controls and test peptides were incubated in parallel at each time point. Serum proteins were denatured by quenching with 40 μL of 6 M urea (10 min, 4 °C), followed by the precipitation of proteins with an addition of 40 μL of 20% trichloroacetic acid (10 min, 4 °C). These solutions were then centrifuged at 12,000*g* for 10 min. A volume of 100 μL of the supernatant was taken out at each time point. Chromatographic separation was carried out at a flow rate of 0.4 mL/min on an Acquity H-Class UPLC system (Waters, Corp., Milford, MA, United States), equipped with a Kinetex C18 100A column (100 mm × 2.1 mm, 2.6 mm particle size) from Phenomenex (France). The mobile phase consisted of water (solvent A) and ACN (solvent B) with both phases acidified by 0.1% (v/v) formic acid and the gradient was 0−80% B in 10 min. Mass spectra were acquired in the positive ionization mode. The elution time for each peptide was determined by the zero-time point. The stability at each time point was calculated as the area of the serum-treated peptide peaks on RP-HPLC at 214 nm as percentage of the area of the 0 h serum-treated peptides. Controls were an eight-residue linear peptide incubated in serum for the positive control and incubated in water for the negative control. Each experiment was performed in triplicate.

■ ASSOCIATED CONTENT

Supporting Information

The Supporting Information is available free of charge at https://pubs.acs.org/doi/10.1021/acs.jmedchem.0c00957.

Additional figures illustrating binding assays and chemical synthesis as well as a structural statistics NMR table (PDF)

■ AUTHOR INFORMATION

Corresponding Author

Sébastien Dutertre − *Institut des Biomolécules Max Mousseron, Université de Montpellier, CNRS, ENSCM, 34095 Montpellier, France;* orcid.org/0000-0002-2945-1484; Email: sebastien.dutertre@umontpellier.fr

Authors

Julien Giribaldi − *Institut des Biomolécules Max Mousseron, Université de Montpellier, CNRS, ENSCM, 34095 Montpellier, France*

Yves Haufe − *Walther Straub Institute of Pharmacology and Toxicology, Faculty of Medicine, LMU Munich, 80336 Munich, Germany*

Edward R. J. Evans − *Centre for Molecular Therapeutics, Australian Institute of Tropical Health and Medicine, James Cook University, Cairns, Queensland 4878, Australia*

Muriel Amar − *Département Médicaments et Technologies pour la Santé (DMTS), Université Paris-Saclay, CEA, SIMoS, ERL CNRS 9004, F-91191 Gif sur Yvette, France*

Anna Durner − *Walther Straub Institute of Pharmacology and Toxicology, Faculty of Medicine, LMU Munich, 80336 Munich, Germany*

Casey Schmidt − *Centre for Molecular Therapeutics, Australian Institute of Tropical Health and Medicine, James Cook University, Cairns, Queensland 4878, Australia*

Adèle Faucherre − *Département de Physiologie, Institut de Génomique Fonctionnelle, CNRS/INSERM UMR 5203, Université de Montpellier, 34095 Montpellier, France*

Hamid Moha Ou Maati − *Département de Physiologie, Institut de Génomique Fonctionnelle, CNRS/INSERM UMR 5203, Université de Montpellier, 34095 Montpellier, France*

Christine Enjalbal − *Institut des Biomolécules Max Mousseron, Université de Montpellier, CNRS, ENSCM, 34095 Montpellier, France;* orcid.org/0000-0003-4646-4583

Jordi Molgó − *Département Médicaments et Technologies pour la Santé (DMTS), Université Paris-Saclay, CEA, SIMoS, ERL CNRS 9004, F-91191 Gif sur Yvette, France;* orcid.org/0000-0002-0693-8994

Denis Servent − *Département Médicaments et Technologies pour la Santé (DMTS), Université Paris-Saclay, CEA, SIMoS, ERL CNRS 9004, F-91191 Gif sur Yvette, France*

David T. Wilson − *Centre for Molecular Therapeutics, Australian Institute of Tropical Health and Medicine, James Cook University, Cairns, Queensland 4878, Australia*

Norelle L. Daly − *Centre for Molecular Therapeutics, Australian Institute of Tropical Health and Medicine, James Cook University, Cairns, Queensland 4878, Australia;* orcid.org/0000-0002-4697-6602

Annette Nicke − *Walther Straub Institute of Pharmacology and Toxicology, Faculty of Medicine, LMU Munich, 80336 Munich, Germany*

Complete contact information is available at: https://pubs.acs.org/10.1021/acs.jmedchem.0c00957

Author Contributions

J.G. and Y.H. contributed equally to this work. J.G. and S.D. conceived and led the study. J.G. performed peptide chemistry cyclization, stability assays, and zebrafish experiments, with input from S.D., C.E., A.F., H.M.O.M. Y.H., and A.D. carried out the electrophysiological recordings, with input from A.N. E.R.J.E., and C.S. performed the NMR experiments and analyses, with input from D.T.W. and N.L.D. M.A., and J.M.

https://dx.doi.org/10.1021/acs.jmedchem.0c00957
J. Med. Chem. 2020, 63, 12682−12692

performed in vitro assays and recordings on isolated mouse nerve-muscle preparations, with input from D.S. J.G. wrote the manuscript with input from all authors.

Notes

The authors declare no competing financial interest.

■ ACKNOWLEDGMENTS

This work was supported by the French Ministry of Higher Education, Research, and Innovation (PhD scholarship to J.G.), the French National Research Agency (ANR-16-CE34-0002 to S.D.), and a grant of the DFG (Research Training Group GRK2338, P01) to A.N. We thank Pranavkumar Shadamarshan for help with the oocyte recordings and Han Shen Tae and David Adams (Illawara Health and Medical Research Institute, Wollongong University, Australia) for subcloning and providing nAChR cDNAs.

■ ABBREVIATIONS

Acm, acetamidomethyl; ACN, acetonitrile; Boc, *tert*-butoxycarbonyl; DCM, dichloromethane; DIPEA, diisopropylethylamine; DMF, *N*,*N*′-dimethylformamide; DTP, 2,2′-dithiopyridine; ESI-MS, electrospray ionization mass spectrometry; Fmoc, fluorenylmethoxycarbonyl; HATU, 1[bis(dimethylamino)methylene]-1*H*-1,2,3-triazolo[4,5-*b*]pyridinium 3-oxide hexafluorophosphate; LC/MS, liquid chromatography/mass spectrometry; MeOH, methanol; nAChR, nicotinic acetylcholine receptor; NMR, nuclear magnetic resonance; Pbf, pentamethyl-dihydrobenzofuran-5-sulfonyl; RP-HPLC, reversed-phase high performance liquid chromatography; SPPS, solid-phase peptide synthesis; *t*-Bu, *tert*-butyl; TFA, trifluoroacetic acid; TIS, triisopropylsilane; Tris, 2-amino-2-(hydroxymethyl)propane-1,3-diol; Trt, trityl; UV, ultraviolet

■ ADDITIONAL NOTE

[a]Please note that different IC_{50} values of native CIA were found in a previous study.[18] We determined that the use of BSA in the conotoxin dilutions likely reduced the nonspecific binding and resulted in higher potencies.

■ REFERENCES

(1) Lewis, R. J.; Garcia, M. L. Therapeutic Potential of Venom Peptides. *Nat. Rev. Drug Discov.* **2003**, *2*, 790−802.
(2) Puillandre, N.; Duda, T. F.; Meyer, C.; Olivera, B. M.; Bouchet, P. One, Four or 100 Genera? A New Classification of the Cone Snails. *J. Molluscan Stud.* **2015**, *81*, 1−23.
(3) Davis, J.; Jones, A.; Lewis, R. J. Remarkable Inter- and Intra-Species Complexity of Conotoxins Revealed by LC/MS. *Peptides* **2009**, *30*, 1222−1227.
(4) Prashanth, J. R.; Brust, A.; Jin, A.-H.; Alewood, P. F.; Dutertre, S.; Lewis, R. J. Cone Snail Venomics: From Novel Biology to Novel Therapeutics. *Future Med. Chem.* **2014**, *6*, 1659−1675.
(5) Akondi, K. B.; Muttenthaler, M.; Dutertre, S.; Kaas, Q.; Craik, D. J.; Lewis, R. J.; Alewood, P. F. Discovery, Synthesis, and Structure-Activity Relationships of Conotoxins. *Chem. Rev.* **2014**, *114*, 5815−5847.
(6) Giribaldi, J.; Dutertre, S. α-Conotoxins to Explore the Molecular, Physiological and Pathophysiological Functions of Neuronal Nicotinic Acetylcholine Receptors. *Neurosci. Lett.* **2018**, *679*, 24−34.
(7) Lebbe, E.; Peigneur, S.; Wijesekara, I.; Tytgat, J. Conotoxins Targeting Nicotinic Acetylcholine Receptors: An Overview. *Mar. Drugs* **2014**, *12*, 2970−3004.
(8) Albuquerque, E. X.; Pereira, E. F. R.; Alkondon, M.; Rogers, S. W. Mammalian Nicotinic Acetylcholine Receptors: From Structure to Function. *Physiol. Rev.* **2009**, *89*, 73−120.
(9) Lau, J. L.; Dunn, M. K. Therapeutic Peptides: Historical Perspectives, Current Development Trends, and Future Directions. *Bioorg. Med. Chem.* **2018**, *26*, 2700−2707.
(10) Sato, A. K.; Viswanathan, M.; Kent, R. B.; Wood, C. R. Therapeutic Peptides: Technological Advances Driving Peptides into Development. *Curr. Opin. Biotechnol.* **2006**, *17*, 638−642.
(11) Ovadia, O.; Linde, Y.; Haskell-Luevano, C.; Dirain, M. L.; Sheynis, T.; Jelinek, R.; Gilon, C.; Hoffman, A. The Effect of Backbone Cyclization on PK/PD Properties of Bioactive Peptide-Peptoid Hybrids: The Melanocortin Agonist Paradigm. *Bioorg. Med. Chem.* **2010**, *18*, 580−589.
(12) Wang, C. K.; Craik, D. J. Designing Macrocyclic Disulfide-Rich Peptides for Biotechnological Applications. *Nat. Chem. Biol.* **2018**, *14*, 417−427.
(13) Clark, R. J.; Jensen, J.; Nevin, S. T.; Callaghan, B. P.; Adams, D. J.; Craik, D. J. The Engineering of an Orally Active Conotoxin for the Treatment of Neuropathic Pain. *Angew. Chem., Int. Ed.* **2010**, *49*, 6545−6548.
(14) Clark, R. J.; Fischer, H.; Dempster, L.; Daly, N. L.; Rosengren, K. J.; Nevin, S. T.; Meunier, F. A.; Adams, D. J.; Craik, D. J. Engineering Stable Peptide Toxins by Means of Backbone Cyclization: Stabilization of the α-Conotoxin MII. *Proc. Natl. Acad. Sci. U.S.A.* **2005**, *102*, 13767−13772.
(15) Halai, R.; Callaghan, B.; Daly, N. L.; Clark, R. J.; Adams, D. J.; Craik, D. J. Effects of Cyclization on Stability, Structure, and Activity of α-Conotoxin RgIA at the A9α10 Nicotinic Acetylcholine Receptor and GABA(B) Receptor. *J. Med. Chem.* **2011**, *54*, 6984−6992.
(16) Armishaw, C. J.; Jensen, A. A.; Balle, L. D.; Scott, K. C. M.; Sørensen, L.; Strømgaard, K. Improving the Stability of α-Conotoxin AuIB Through N-to-C Cyclization: The Effect of Linker Length on Stability and Activity at Nicotinic Acetylcholine Receptors. *Antioxid. Redox Signaling* **2011**, *14*, 65−76.
(17) Lovelace, E. S.; Armishaw, C. J.; Colgrave, M. L.; Wahlstrom, M. E.; Alewood, P. F.; Daly, N. L.; Craik, D. J. Cyclic MrIA: A Stable and Potent Cyclic Conotoxin with a Novel Topological Fold That Targets the Norepinephrine Transporter. *J. Med. Chem.* **2006**, *49*, 6561−6568.
(18) Giribaldi, J.; Wilson, D.; Nicke, A.; El Hamdaoui, Y.; Laconde, G.; Faucherre, A.; Moha Ou Maati, H.; Daly, N.; Enjalbal, C.; Dutertre, S. Synthesis, Structure and Biological Activity of CIA and CIB, Two α-Conotoxins from the Predation-Evoked Venom of *Conus catus*. *Toxins* **2018**, *10*, 222.
(19) Carpino, L. A.; Han, G. Y. 9-Fluorenylmethoxycarbonyl Function, a New Base-Sensitive Amino-Protecting Group. *J. Am. Chem. Soc.* **1970**, *92*, 5748−5749.
(20) Barlos, K.; Chatzi, O.; Gatos, D.; Stavropoulos, G. 2-Chlorotrityl Chloride Resin. Studies on Anchoring of Fmoc-Amino Acids and Peptide Cleavage. *Int. J. Pept. Protein Res.* **1991**, *37*, 513−520.
(21) Cheneval, O.; Schroeder, C. I.; Durek, T.; Walsh, P.; Huang, Y.-H.; Liras, S.; Price, D. A.; Craik, D. J. Fmoc-Based Synthesis of Disulfide-Rich Cyclic Peptides. *J. Org. Chem.* **2014**, *79*, 5538−5544.
(22) Wüthrich, K. *NMR of Proteins and Nucleic Acids*; The George Fisher Baker Non-Resident Lectureship in Chemistry at Cornell University; Wiley: New York, 1986.
(23) Shen, Y.; Delaglio, F.; Cornilescu, G.; Bax, A. TALOS+: A Hybrid Method for Predicting Protein Backbone Torsion Angles from NMR Chemical Shifts. *J. Biomol. NMR* **2009**, *44*, 213−223.
(24) Jimenez, E. C.; Olivera, B. M.; Teichert, R. W. αC-Conotoxin PrXA: A New Family of Nicotinic Acetylcholine Receptor Antagonists. *Biochemistry* **2007**, *46*, 8717−8724.
(25) Molgo, J. Effects of Aminopyridines on Neuromuscular Transmission. *Aminopyridines and Similarly Acting Drugs: Effects on Nerves, Muscles and Synapses*; Elsevier, 1982; pp 95−116.
(26) Molgó, J.; Lemeignan, M.; Guerrero, S. Facilitatory Effects of 4-Aminopyridine on Strontium-Mediated Evoked and Delayed Trans-

https://dx.doi.org/10.1021/acs.jmedchem.0c00957
J. Med. Chem. 2020, 63, 12682−12692

mitter Release from Motor Nerve Terminals. *Eur. J. Pharmacol.* **1982**, *84*, 1−7.
(27) Sanders, D. B.; Juel, V. C.; Harati, Y.; Smith, A. G.; Peltier, A. C.; Marburger, T.; Lou, J. S.; Pascuzzi, R. M.; Richman, D. P.; Xie, T.; Demmel, V.; Jacobus, L. R.; Aleš, K. L.; Jacobus, D. P. The Dapper Study Team. 3,4-diaminopyridine Base Effectively Treats the Weakness of Lambert-Eaton Myasthenia. *Muscle Nerve* **2018**, *57*, 561−568.
(28) Jonsson, M.; Gurley, D.; Dabrowski, M.; Larsson, O.; Johnson, E. C.; Eriksson, L. I. Distinct Pharmacologic Properties of Neuromuscular Blocking Agents on Human Neuronal Nicotinic Acetylcholine Receptors: A Possible Explanation for the Train-of-Four Fade. *Anesthesiology* **2006**, *105*, 521−533.
(29) Fagerlund, M. J.; Eriksson, L. I. Current Concepts in Neuromuscular Transmission. *Br. J. Anaesth.* **2009**, *103*, 108−114.
(30) Tajima, T.; Amaya, J.; Katayama, K.; Koizumi, T. Difference of Train-of-Four Fade Induced by Nondepolarizing Neuromuscular Blocking Drugs: A Theoretical Consideration on the Underlying Mechanisms. *J. Anesth.* **1995**, *9*, 333−337.
(31) Cheah, L. S.; Gwee, M. C. E. Train-Of-Four Fade During Neuromuscular Blockade Induced by Tubocurarine, Succinylcholine or α-Bungarotoxin in the Rat Isolated Hemidiaphragm. *Clin. Exp. Pharmacol. Physiol.* **1988**, *15*, 937−943.
(32) Robbins, R.; Donati, F.; Bevan, D. R.; Bevan, J. C. Differential Effects of Myoneural Blocking Drugs on Neuromuscular Transmission in Infants. *Br. J. Anaesth.* **1984**, *56*, 1095−1099.
(33) Baird, W. L. M.; Bowman, W. C.; Kerr, W. J. Some Actions of Org NC45 and of Edrophonum in the Anaesthetized Cat and in Man. *Br. J. Anaesth.* **1982**, *54*, 375−385.
(34) Nagashima, M.; Yasuhara, S.; Martyn, J. A. J. Train-of-Four and Tetanic Fade Are Not Always a Prejunctional Phenomenon as Evaluated by Toxins Having Highly Specific Pre- and Postjunctional Actions. *Anesth. Analg.* **2013**, *116*, 994−1000.
(35) Bren, N.; Sine, S. M. Hydrophobic Pairwise Interactions Stabilize α-Conotoxin MI in the Muscle Acetylcholine Receptor Binding Site. *J. Biol. Chem.* **2000**, *275*, 12692−12700.
(36) Ning, J.; Li, R.; Ren, J.; Zhangsun, D.; Zhu, X.; Wu, Y.; Luo, S. Alanine-Scanning Mutagenesis of α-Conotoxin GI Reveals the Residues Crucial for Activity at the Muscle Acetylcholine Receptor. *Mar. Drugs* **2018**, *16*, 507.
(37) Bowman, W. C.; Prior, C.; Marshall, I. G. Presynaptic Receptors in the Neuromuscular Junction. *Ann. N.Y. Acad. Sci.* **1990**, *604*, 69−81.
(38) Kuryatov, A.; Olale, F.; Cooper, J.; Choi, C.; Lindstrom, J. Human α6 AChR Subtypes: Subunit Composition, Assembly, and Pharmacological Responses. *Neuropharmacology* **2000**, *39*, 2570−2590.
(39) McIntosh, J. M.; Azam, L.; Staheli, S.; Dowell, C.; Lindstrom, J. M.; Kuryatov, A.; Garrett, J. E.; Marks, M. J.; Whiteaker, P. Analogs of α-Conotoxin MII Are Selective for α6-Containing Nicotinic Acetylcholine Receptors. *Mol. Pharmacol.* **2004**, *65*, 944−952.
(40) Ellison, M.; McIntosh, J. M.; Olivera, B. M. α-Conotoxins ImI and ImII: Similar A7 Nicotinic Receptor Antagonists Act at Different Sites. *J. Biol. Chem.* **2003**, *278*, 757−764.
(41) Güntert, P. Automated NMR Structure Calculation with CYANA. *Methods Mol. Biol.* **2004**, *278*, 353−378.
(42) Koradi, R.; Billeter, M.; Wüthrich, K. MOLMOL: A Program for Display and Analysis of Macromolecular Structures. *J. Mol. Graph.* **1996**, *14*, 51−55.
(43) Pettersen, E. F.; Goddard, T. D.; Huang, C. C.; Couch, G. S.; Greenblatt, D. M.; Meng, E. C.; Ferrin, T. E. UCSF Chimera?A Visualization System for Exploratory Research and Analysis. *J. Comput. Chem.* **2004**, *25*, 1605−1612.

https://dx.doi.org/10.1021/acs.jmedchem.0c00957
J. Med. Chem. 2020, 63, 12682−12692

Supporting information

Backbone cyclization turns a venom peptide into a stable and equipotent ligand at both muscle and neuronal nicotinic receptors

Julien Giribaldi†, Yves Haufe†, Edward Evans, Muriel Amar, Anna Durner, Casey Schmidt, Adèle Faucherre, Hamid Moha Ou Maati, Christine Enjalbal, Jordi Molgó, Denis Servent, David T. Wilson, Norelle L. Daly, Annette Nicke and Sébastien Dutertre*

Content

Figures

Tables

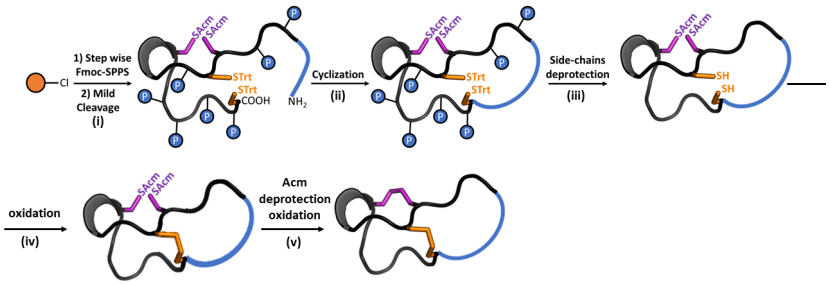
1) Step wise Fmoc-SPPS
2) Mild Cleavage
(i)
Cyclization
(ii)
Side-chains deprotection
(iii)
oxidation
(iv)
Acm deprotection oxidation
(v)
SAcm
SAcm
STrt
STrt
COOH
NH2
SH
SH

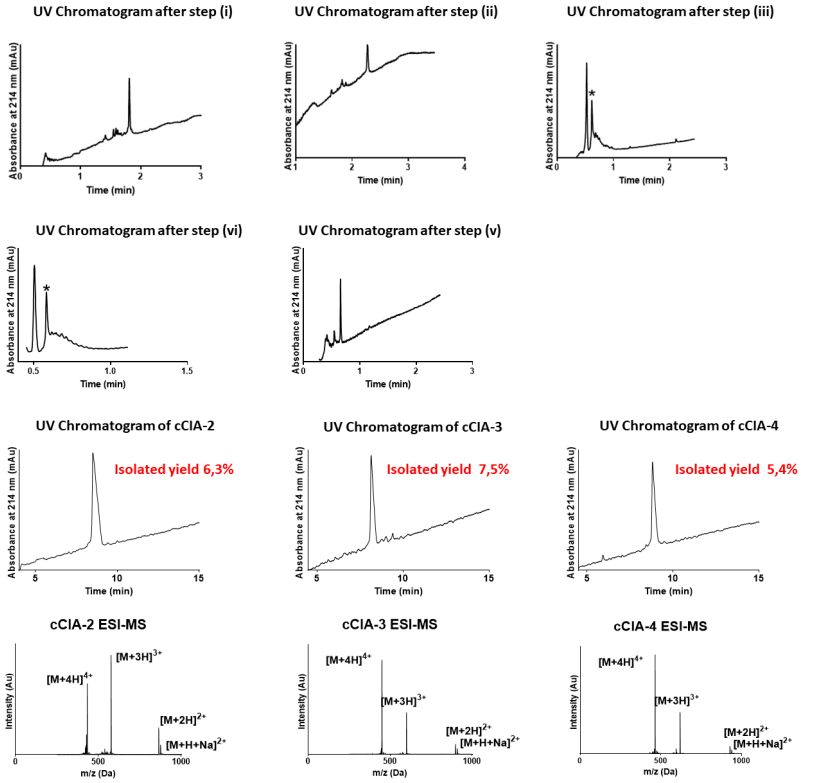
UV Chromatogram after step (i)
UV Chromatogram after step (ii)
UV Chromatogram after step (iii)
UV Chromatogram after step (vi)
UV Chromatogram after step (v)
UV Chromatogram of cCIA-2
Isolated yield 6,3%
UV Chromatogram of cCIA-3
Isolated yield 7,5%
UV Chromatogram of cCIA-4
Isolated yield 5,4%
cCIA-2 ESI-MS
cCIA-3 ESI-MS
cCIA-4 ESI-MS
Absorbance at 214 nm (mAu)
Time (min)
Intensity (Au)
m/z (Da)
[M+4H]4+
[M+3H]3+
[M+2H]2+
[M+H+Na]2+

S2

Figure S1: Synthesis strategy of the three cylic analogues of CIA and respective RP-HPLC-UV chromatograms and ESI/MS analyses. (i) 1% TFA in DCM (v/v) 10 x 5 min (ii) HATU (2,5eq)/DIEA (5eq) 4 h (iii) TFA/TIS/H_2O (95/2.5/2.5 v/v/v) 2,5 hr (iv) Tris-HCl 50 mM buffer pH 8, DTP (7eq), 10 min (v) I_2 10 mM (20eq) in H_20/TFA/ACN (78/2/20 v/v/v), 10 min. The orange round circle represents a chloro-(2'-chloro) trityl resin and P represents common side chains protective groups used in Fmoc-SPPS (Solid Phase Peptide Synthesis). The asterisk indicates the peak of interest. RP-HPLC-UV (ACN gradient from 0 to 30% in 30 min) coupled to ESI-MS analyses revealed the presence of dominant peaks of the expected masses.

S3

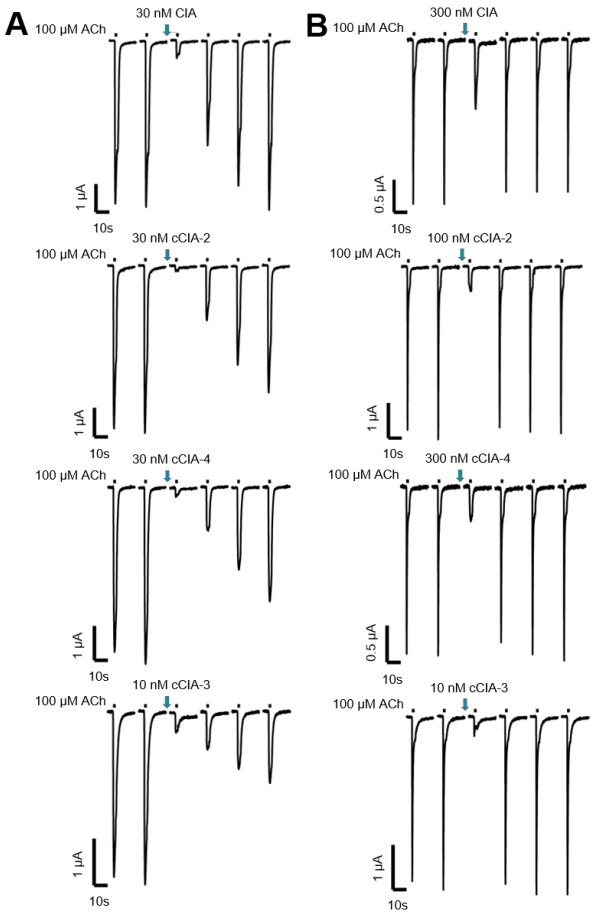

Figure S2: Recovery of ACh-induced muscle-type (A) and $\alpha 3\beta 2$ (B) nAChR currents after inhibition by CIA analogues (indicated by green arrow). 2s-pulses of ACh (100 µM, black bar) were applied in 4 min intervals (1 min under perfusion, 3 min in a static bath). Once stable current responses were obtained, toxins were applied for 3 min in the static bath in concentrations that produced at least 80% inhibition.

S4

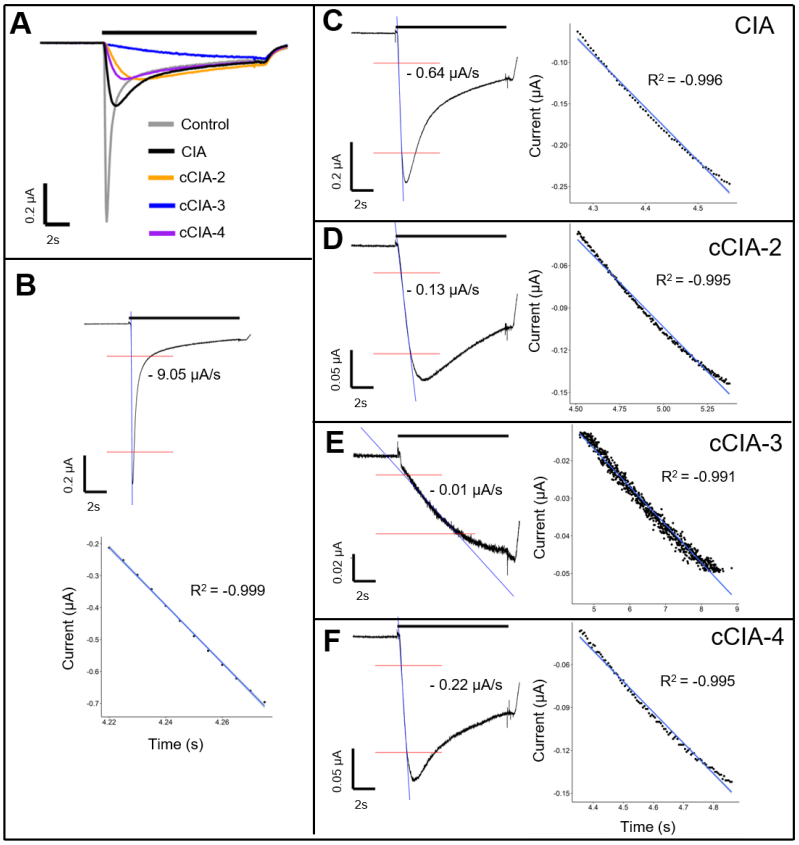

Figure S3: Real-time recovery of α3β2 currents after inhibition by CIA and its cyclic derivates. (A) Merged current responses during a 10s application of ACh (100 µM, black bar) evoked before (control) and after 3 min incubation with the indicated peptides. Note the delayed current peak due to dissociation of the peptide during the agonist application. The steepness of the rising phase of the current was used as a surrogate for the off rate. (B-F) Isolated peak traces are shown with red lines indicating the rising phases from 20% to 80% of the peak currents and a linear regression (blue line) within these borders was performed. (B) control (ND96), (C) 1 µM native CIA, (D) 1 µM cCIA-2, (E) 100 nM cCIA-3, and (F) 1 µM cCIA-4. The slope of each linear regression is written in the graph and the linear regression in the chosen borders is shown in detail with regression coefficient (R^2).

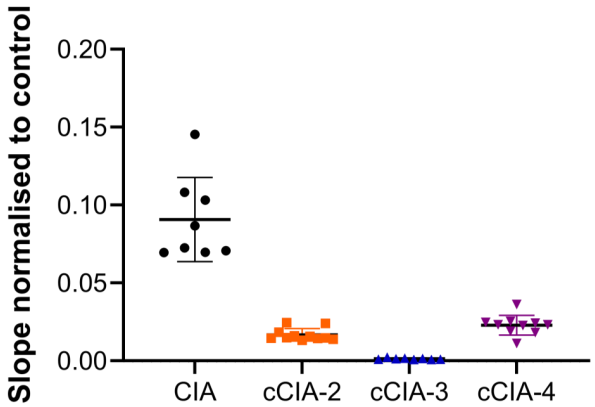

Figure S4: Comparison of the dissociation of CIA and its cyclic derivates from α3β2 using the slope of the rising phase of the ACh evoked current as surrogate. The slopes were determined as shown in Figure 2 and normalized to the slope of the control response before incubation with the peptide (antagonist slope / control slope). The single values are shown with the mean as straight bar and S.D., n = 8-11. Note that higher values indicate a faster dissociation.

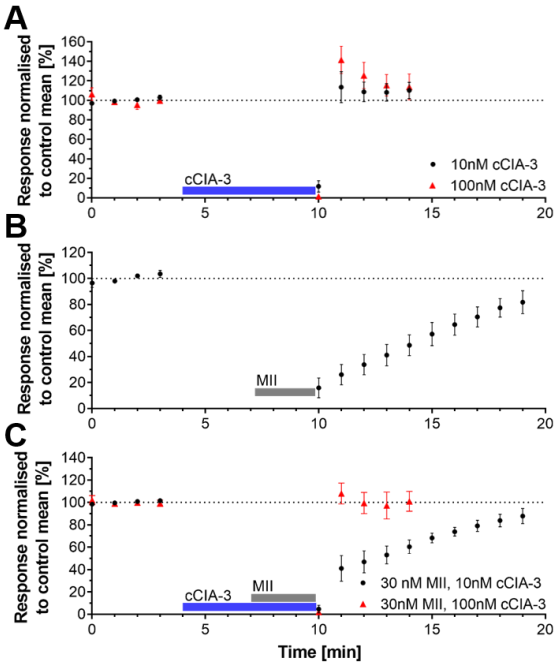

Figure S5: Functional competition between cCIA-3 and MII on the α3β2 receptor. Responses to 2s-ACh pulses were recorded at 1-min intervals and normalized to the mean of 4 current peaks recorded prior to peptide incubation in a static bath. Three different protocols were conducted: (A) 1 min after ACh wash-out, cCIA-3 (10 or 100nM) was added to the static bath for 6 min before ACh applications were continued, (B) 4 min after ACh wash-out, MII (30 nM) was added to the static bath for 3 min before ACh applications were continued (C) cCIA-3 (10 or 100 nM) was added after 1 min and MII (30nM) was added after 3 min. ACh applications were continued after 6 min. Data are represented as MEAN ± S.D. with $n \geq 5$.

S7

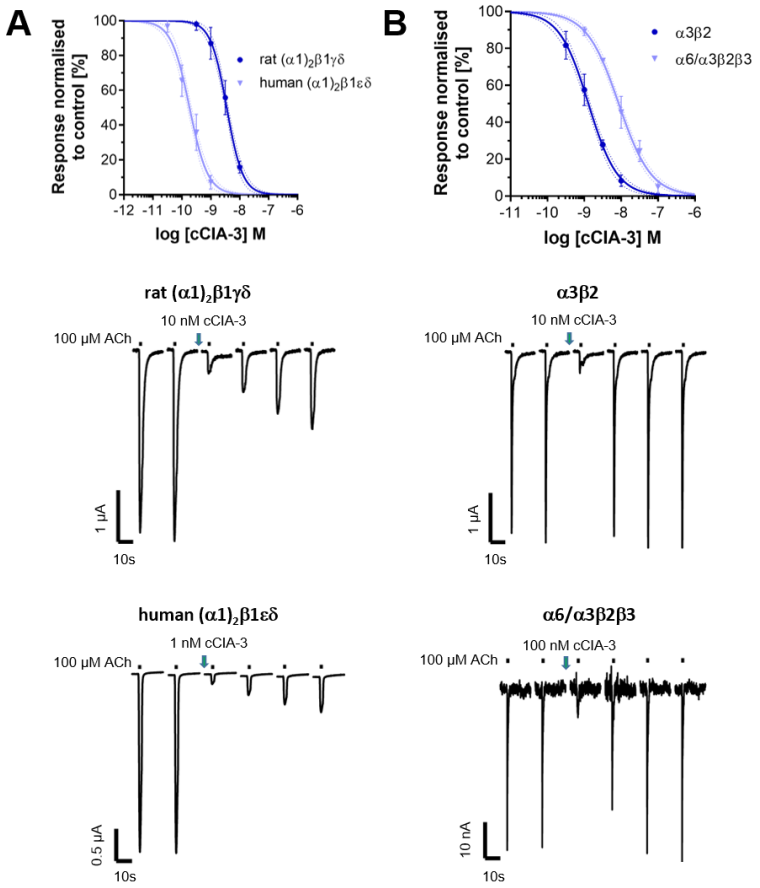

Figure S6: Dose response curves of α-cCIA-3 and recovery of ACh-evoked currents after α-cCIA-3 application. (A) Dose response curves at adult and fetal muscle type nAChRs and (B) α3β2 and α6/α3β2β3 neuronal nAChRs. 2s-pulses of ACh (100 µM, black bar) were applied in 4 min intervals (1 min under perfusion, 3 min in a static bath). Once stable current responses were obtained, toxins were applied for 3 min in the static bath. IC_{50} values and Hill-Slopes (in brackets) were 57 nM (-1.57) for rat $(\alpha1)_2\beta1\gamma\delta$, 184.5 pM (-1.38) for human $(\alpha1)_2\beta1\varepsilon\delta$, 1.30 nM (-1.10) for $\alpha3\beta2$ and 8.64 nM (-1.0) for $\alpha6/\alpha3\beta2\beta3$. Each point represents the mean of at least 3 different oocytes with S.D.

S8

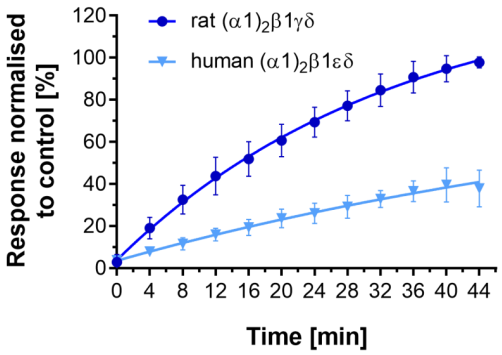

Figure S7: Recovery of fetal ($(\alpha1)_2\beta1\gamma\delta$) and adult($(\alpha1)_2\beta1\varepsilon\delta$) muscle-type nAChRs from toxin block. *X. laevis* oocytes expressing the indicated receptors were analyzed by TEVC at -70 mV. 1 nM for adult muscle type and 100 nM for fetal muscle type of α-cCIA-3 was preincubated for 3 min. Responses to 2-s pulses of 100 µM ACh were measured in 4 min intervals. Each point represents the mean of measurements from at least 3 different oocytes, error bars represent S.D. The koff values are 0.03 min^{-1} for the rat fetal muscle type and 0.013 min^{-1} for adult mucle type nAChR.

S9

Table S1: Normalized responses of additional nAChR subtypes to 10 µM α-cCIA-3. In order to save peptide, and given that responses were 80% or higher, only 2 recordings were performed on two different oocytes, except for human α7 that produced a response <80% (n=3). Unless otherwise stated, the subtypes were injected in a 1:1 subunit-ratio.

Subtype	Species	Ach [µM]	% Response as mean ± S.D.
$\alpha 2\beta 2$	rat	100	93 ± 14%
$\alpha 2\beta 4$	rat	100	96 ± 14%
$\alpha 3\beta 4$	rat	100	86 ± 15%
$\alpha 4\beta 2$ (Ratio 5:1)	rat	100	103 ± 16%
$\alpha 4\beta 4$	rat	30	92 ± 14%
$\alpha 7$	human	100	65 ± 13%
$\alpha 9\alpha 10$ (Ratioc5:1)	human	40	81 ± 14%

S10

Table S2: Structural statistics for the cCIA analogues.

Structural statistics for the cCIA ensembles			
Experimental restraints	cCIA-2	cCIA-3	cCIA-4
Interproton distance restraints	136	179	154
Intraresidue	36	53	49
Sequential	51	75	67
Medium range (i-j < 5)	23	33	19
Long range (i-j ≥5)	26	18	19
Dihedral-angle restraints	21	23	21
R.m.s. deviations from mean coordinate structure (Å)			
Backbone atoms (with linker)	0.91 ± 0.35	0.29 ± 0.17	1.05 ± 0.45
All heavy atoms (with linker)	1.78 ± 0.46	0.85 ± 0.24	1.59 ± 0.46
Backbone atoms (without linker)	0.72 ± 0.26	0.13 ± 0.06	0.27 ± 0.11
All heavy atoms (without linker)	1.73 ± 0.46	0.82 ± 0.22	1.17 ± 0.35
Ramachandran Statistics			
% in most favoured region	68.5%	61.10%	76.40%
% in additionally allowed region	31.5%	38.9%	23.6%

Part III

Appendix

4
Additional Publications and Contributions

4.1 P2X7 Interactions and Signaling - Making Head or Tail of It (Review)

This review provides a structured overview about the numerous downstream signaling effects, protein interactions, and interaction domains, that have been proposed for the P2X7R and mainly associated with its unique intracellular C-terminus. After a short introduction to the overall structure of P2XRs, the structural and functional features distinguishing the P2X7R from the other P2X familiy members as well as differences between different P2X7 isoforms are explained, and its expression pattern as well as its role in inflammation and immune signaling are described. Then, data providing evidence for and against an interaction of the P2X7R with the P2X4R are illuminated. Besides sequence similarity, overlapping expression patterns, and similar patho-/physiological functions, there is evidence for functional interaction and direct association between both receptors, however, data are not consistent.
The next part focuses on the function of the long P2X7R C-terminal tail and reviews identified sequence motifs, proposed interaction domains, and single nucleotide polymorphisms (SNPs) of the long P2X7-tail. In addition, the so-called "macropore" formation, which is a characteristic P2X7 property that involves the C-terminus, is discussed. We then present proteins found to be involved in P2X7 mediated signaling pathways, namely inflammatory processes such as cytokine release and production of reactive oxygen species (ROS), lipid interactions, activation of lipases, plasma membrane re-/organization, kinase activation, neurotransmitter release, activation of transcription factors, and different forms of cell death. Next, the hitherto more than 50 published P2X7 interaction partners are summarized in a table together with the method with which they were identified and evidence for physical and/or functional association of these candidates is visualized in an interaction network. Some interactors, for which functional evidence has been published, such as pannexin-1 and calmodulin (CaM), are then described in more detail. We conclude the review with the notion, that while numerous P2X7-mediated signaling pathways have been identified, the underlying, specific molecular mechanisms are still largely unknown. We remark on technical problems arising from possible bias from experimental methods, setups, and over-/expression systems in use, and the need for critical data interpretation.
Robin Kopp and I contributed equally to this review with extensive literature and database research and preparation of the first manuscript draft. In particular, I prepared the part *"The structure of the P2X7 C-terminus and its involvement in P2X7 signaling"* including figure 1 summarizing identified and proposed motifs and interaction domains within the P2X7 C-terminus.

P2X7 Interactions and Signaling - Making Head or Tail of It

Robin Kopp†, Anna Krautloher†, Antonio Ramírez-Fernández, Annette Nicke

†*these authors contributed equally to this publication*

published in

Front. Mol. Neurosci. 2019, 12:183

frontiers in Molecular Neuroscience

REVIEW
published: 07 August 2019
doi: 10.3389/fnmol.2019.00183

P2X7 Interactions and Signaling – Making Head or Tail of It

Robin Kopp†, Anna Krautloher*†, Antonio Ramírez-Fernández and Annette Nicke**

Walther Straub Institute of Pharmacology and Toxicology, Faculty of Medicine, LMU Munich, Munich, Germany

Extracellular adenine nucleotides play important roles in cell–cell communication and tissue homeostasis. High concentrations of extracellular ATP released by dying cells are sensed as a danger signal by the P2X7 receptor, a non-specific cation channel. Studies in P2X7 knockout mice and numerous disease models have demonstrated an important role of this receptor in inflammatory processes. P2X7 activation has been shown to induce a variety of cellular responses that are not usually associated with ion channel function, for example changes in the plasma membrane composition and morphology, ectodomain shedding, activation of lipases, kinases, and transcription factors, as well as cytokine release and apoptosis. In contrast to all other P2X family members, the P2X7 receptor contains a long intracellular C-terminus that constitutes 40% of the whole protein and is considered essential for most of these effects. So far, over 50 different proteins have been identified to physically interact with the P2X7 receptor. However, few of these interactions have been confirmed in independent studies and for the majority of these proteins, the interaction domains and the physiological consequences of the interactions are only poorly described. Also, while the structure of the P2X7 extracellular domain has recently been resolved, information about the organization and structure of its C-terminal tail remains elusive. After shortly describing the structure and assembly of the P2X7 receptor, this review gives an update of the identified or proposed interaction domains within the P2X7 C-terminus, describes signaling pathways in which this receptor has been involved, and provides an overlook of the identified interaction partners.

Keywords: C-terminus, protein-protein interaction (PPI), signaling/signaling pathways, P2X7 (purino) receptor, network

OPEN ACCESS

Edited by:
Eric Boué-Grabot,
Université de Bordeaux, France

Reviewed by:
Hana Zemkova,
Institute of Physiology (ASCR), Czechia
Toshi Kawate,
Cornell University, United States

****Correspondence:***
Robin Kopp
Robin.Stocklauser@lrz.uni-muenchen.de
Anna Krautloher
a.krautloher@lrz.uni-muenchen.de
Annette Nicke
annette.nicke@lrz.uni-muenchen.de

† These authors have contributed equally to this work

Received: *31 May 2019*
Accepted: *11 July 2019*
Published: *07 August 2019*

Citation:
Kopp R, Krautloher A, Ramírez-Fernández A and Nicke A (2019) P2X7 Interactions and Signaling – Making Head or Tail of It. Front. Mol. Neurosci. 12:183. doi: 10.3389/fnmol.2019.00183

INTRODUCTION

The ATP-gated P2X receptors are trimeric ion channels with inter-subunit ATP-binding sites (Kaczmarek-Hájek et al., 2012). In contrast to most other ion channel families, six of the seven cloned subunits can form functional homomeric receptors but heteromeric receptors have also been identified, for example P2X2/3 and P2X1/5 receptors (Saul et al., 2013). A single P2X subunit has been structurally compared to a dolphin (**Figure 1A**) and contains two α-helical transmembrane domains (fluke) that are linked by a large extracellular domain [269–288 amino acids (aa) long] that is mostly formed by β-sheets (body) and several loop domains (head, dorsal fin, and flippers) (Kawate et al., 2009). The intracellular N- and C- termini are less conserved than the rest of the protein. The N-termini are 20–45 aa long, while the intracellular C-termini are more variable

in length with 29–87 aa for most subunits. P2X2, and in particular P2X7 contain considerably longer C-termini of 113/125 (human/mouse) and 240 aa, respectively. Human P2X5 and P2X6 have C-terminal sequences of 82 and 87 aa, respectively. Only in case of the ATP-bound open state of the human P2X3 receptor, a structure of these intracellular domains has been obtained so far (Mansoor et al., 2016). In this ATP-bound structure, the N- and C-termini form a network of three β-sheets (each formed by the C-terminus of one subunit and the N-termini of the two neighboring subunits) that is capping the cytoplasmic side of the pore. The termini appear to be disordered and flexible in the apo state.

The P2X7 receptor differs not only structurally but also functionally from all other P2X subtypes. In comparison, it has 10 to 100-fold reduced ATP sensitivity, suggesting that it functions as a "danger signal" detector for high ATP concentrations that are released at sites of tissue damage (Linden et al., 2019). A P2X7 splice variant (P2X7k) has been identified in rodents but not in humans, that can also be activated by extracellular nicotinamide adenine dinucleotide (NAD) via covalent enzymatic modification (ADP ribosylation) (Schwarz et al., 2012; Xu et al., 2012). The P2X7k variant also shows a higher ATP sensitivity.

Also, unlike other ion channels, P2X7 activation does not only open a non-selective cation channel, but in addition mediates a membrane permeability increase by forming a so-called "macropore" that can reach a diameter of 8.5 Å and allows the passage of large molecules such as the fluorescent dyes ethidium and YO-PRO1 (Di Virgilio et al., 2018b). P2X7 activation furthermore initiates a variety of signaling cascades that trigger caspase activation and cytokine release, plasma membrane reorganization, ectodomain shedding, and cell death to only name a few. Some of these effects are likely consequences of P2X7-dependent Ca^{2+} influx and/or K^+ efflux, although a detailed description of the molecular interactions and signaling complexes involved is generally lacking. The C-terminus appears to be required for most of these effects and probably plays a role in positioning of the receptor in membrane microdomains (e.g., lipid rafts (Murrell-Lagnado, 2017) and/or signaling complexes (Kim et al., 2001)) that allow efficient signaling and/or direct interaction with signaling molecules.

It has to be mentioned, that considerable differences exist in the pharmacology of rat, mouse, and human P2X7 (Donnelly-Roberts et al., 2009). For example, at the rat isoform ATP and BzATP were 8 and 70 times more potent than at the mouse isoform and 10 and 25 times more potent than at the human isoform, respectively. While this could be attributed to single aa differences in the ligand-binding ectodomain of rat and mouse P2X7 (Young et al., 2007), a positive effect of the intracellular C-terminus on BzATP potency was shown in P2X7 chimeras, in which the human P2X7 C-terminus was replaced by the respective rat sequence (Rassendren et al., 1997). Likewise, sensitivity to divalent cations, dye-uptake efficiency and selectivity, and current kinetics largely differ between human and rodent isoforms and also between different cell types (Rassendren et al., 1997; Hibell et al., 2001; Janks et al., 2019) with the human and mouse isoforms being less efficient in dye uptake. However, despite these differences, the principal effects of P2X7 activation, such as dye uptake, interleukine-1β (IL-1β) release, phosphatidylserine-flip (PS)-flip, and blebbing appear to be present in all isoforms. Nevertheless, a systematic comparison is urgently needed.

P2X7 receptors are highly expressed in immune cells (in particular macrophages, T-cells, mast cells, and microglia), epithelial cells, oligodendrocytes of the CNS, and Schwann cells of the PNS (Di Virgilio et al., 2018a; Kaczmarek-Hájek et al., 2018). Their presence in neurons is more controversial (Illes et al., 2017; Miras-Portugal et al., 2017). Numerous studies describe P2X7 expression and function in astrocytes (Ballerini et al., 1996; Duan et al., 2003; Narcisse et al., 2005; Sperlagh et al., 2006; Norenberg et al., 2010; Oliveira et al., 2011; Sperlagh and Illes, 2014) while there is also contradictory evidence (Jabs et al., 2007). Thus, P2X7 detection in these cell types might depend on factors such as the species, tissue, model system, and activation state, or disease phase that is investigated. Furthermore, interpretation of findings depends on the sensitivity and/or specificity of the detection methods, as specificity of the most widely used antagonists (oxidized ATP and brilliant blue G) and the available P2X7 antibodies is questionable and proper control experiments (for example using P2X7 knockout animals) need to be performed (Sim et al., 2004; Anderson and Nedergaard, 2006).

The best-investigated and most widely accepted P2X7 functions are its roles in inflammation and immune signaling. Blockade or genetic ablation of the P2X7 receptor has early confirmed, that it is a major trigger of processing and release of pro-inflammatory IL-1β and resulted in amelioration of disease parameters in various experimental models ranging from inflammatory processes induced by infection, allograft rejection, and autoimmune diseases to numerous models of tissue or organ damage as well as various neurological diseases (Burnstock and Knight, 2018; Savio et al., 2018). In addition to its role in immune function and inflammation, which is often associated with the deleterious effects of its activation, P2X7 has also been shown to exert trophic roles, for example in microglia (Monif et al., 2009) or different cancer cells (Orioli et al., 2017). In humans, a truncated splice variant was identified that lacks the C-terminus and appears to serve mainly trophic functions (Adinolfi et al., 2010). In the following, we will provide an overview of the direct and indirect protein interactions and signaling pathways in which P2X7 has most commonly been involved.

INTERACTION OF THE P2X7 RECEPTOR WITH THE P2X4 RECEPTOR

Within the P2X receptor family, P2X4 shows the highest sequence similarity to P2X7 (47% amino acid identity of the human isoforms). The *P2rx4* gene is located just downstream of the *P2rx7* gene and they are thought to have originated from the same gene by gene duplication (Dubyak, 2007; Hou and Cao, 2016). Both subtypes show a widely overlapping expression pattern, in particular in immune cells and epithelial cells (Guo et al., 2007; Kaczmarek-Hájek et al., 2012), and have been linked to similar physiological and pathophysiological functions in inflammatory

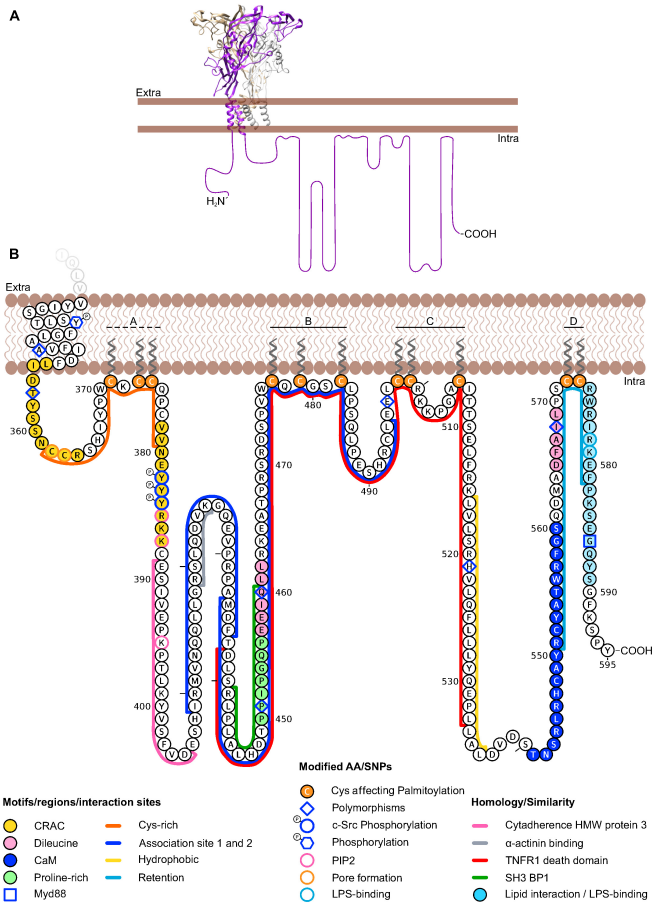

FIGURE 1 | Schematic representation of the human P2X7 receptor depicting details of its intracellular C-terminus. **(A)** Homology model (https://swissmodel.expasy.org/) based on the crystal structure of the panda P2X7 in the closed, apo state (PDB ID: 5U1L) is shown with the three P2X7 subunits represented in gray, brown, and purple. Note the dolphin-shaped structure of a single subunit with the transmembrane regions representing the fluke. The structure of the intracellular C-terminus has not been determined. The estimated length of one unfolded C-terminus is represented in scale to the crystallized domains. **(B)** Amino acid sequence of the human P2X7 intracellular C-terminus representing individual amino acid residues and domains discussed in the text. Note that some of the motifs/domains are putative and species variations are not considered. Groups of palmitoylated cysteines (A–D) according are shown. A dashed line indicates partial palmitoylation (Gonnord et al., 2008). The aa sequence was drawn with Protter and manually modified: http://wlab.ethz.ch/protter/ (Omasits et al., 2014).

processes, such as reactive oxygen species (ROS) production and the secretion of mature IL-1β and IL-18 through the activation of the NLRP3 inflammasome (Babelova et al., 2009; Kawano et al., 2012; Hung et al., 2013). For example, P2X4 was shown to affect the P2X7-mediated maturation and release of IL-1β, (Pérez-Flores et al., 2015) and a rapid initial P2X4-mediated Ca^{2+} influx was suggested to initiate this cascade (Sakaki et al., 2013). Both receptors have also been involved in phagosome

function (Qureshi et al., 2007; Kuehnel et al., 2009), autophagy, macrophage death (Kawano et al., 2012), as well as autocrine and paracrine activation of T cells via ATP-induced Ca^{2+} influx (Schenk et al., 2008; Yip et al., 2009; Woehrle et al., 2010; Manohar et al., 2012; Wang et al., 2014).

While heteromerisation of both subunits in trimeric complexes (Guo et al., 2007) was not confirmed (Torres et al., 1999; Nicke, 2008; Boumechache et al., 2009; Antonio et al., 2011), a number of studies provide evidence in favor of a direct physical association of both receptor types and/or a mutual functional interaction between both subtypes. Thus, both subunits could be co-immunoprecipitated from transfected cells, as well as various cell lines and primary cells (Guo et al., 2007; Boumechache et al., 2009; Weinhold et al., 2010; Hung et al., 2013; Pérez-Flores et al., 2015) and FRET studies on *Xenopus laevis* oocyte- and HEK293 cell-expressed subunits support a close association or heteromerisation (Pérez-Flores et al., 2015; Schneider et al., 2017). A close proximity within transfected HEK293 cells was also shown by *in situ* proximity ligation assays (Antonio et al., 2011). Functional evidence for an interaction was described in native and recombinant mammalian cells (Ma et al., 2006; Guo et al., 2007; Casas-Pruneda et al., 2009; Kawano et al., 2012; Pérez-Flores et al., 2015) but not in a more recent study (Schneider et al., 2017) in *Xenopus laevis* oocytes. Finally, a mutual interrelation between P2X4 and P2X7 mRNA and protein expression levels was described in kidney, E10 alveolar epithelial cells, and bone marrow derived dendritic cells (Weinhold et al., 2010; Craigie et al., 2013; Zech et al., 2016). To evaluate these results, it has to be considered, however, that the P2X4 subtype is mostly found intracellularly and co-localized with lysosomal markers (Bobanovic et al., 2002; Guo et al., 2007; Qureshi et al., 2007), whereas P2X7 is generally localized at the plasma membrane. Nonetheless, upon stimulation of the respective cells [e.g., via lipopolysacharide (LPS), CCL2/12 or ionomycin] an increased fraction of P2X4 receptors was found at the cell surface (Qureshi et al., 2007; Boumechache et al., 2009; Toulme et al., 2010; Toyomitsu et al., 2012).

STRUCTURE OF THE P2X7 C-TERMINUS AND ITS INVOLVEMENT IN P2X7 SIGNALING

The P2X7 C-terminus constitutes about 40% of the whole P2X7 protein (**Figure 1**) and amino acid sequence identity between rat, mouse, and human C-termini is 80%. Except for the domains described below, the so-called P2X7-tail shows no sequence homology to other proteins. It is supposed to be localized intracellularly, but contains a lipophilic stretch of 21 aa (residues 516–536 in human P2X7) that would be long enough to form another transmembrane domain or reentry loop. Deletion or truncation of the majority of this intracellular tail prevents P2X7-mediated effects such as dye uptake (Surprenant et al., 1996) and plasma membrane blebbing (Wilson et al., 2002), and alters channel kinetics (Becker et al., 2008), but does not impair cell surface expression or ion channel function (Smart et al., 2003; Becker et al., 2008). In the following, we will shortly explain the current understanding of P2X7 pore formation and then describe identified domains and motifs within the P2X7 tail, starting from the very terminus toward the second TM domain.

Pore Formation

A hallmark feature of P2X7 activation is the formation of a non-selective macropore. Both, naturally occurring splice variants of P2X7 and *in vitro* experiments with C-terminally truncated P2X7 receptors demonstrated that this property requires the C-terminus (Surprenant et al., 1996; Adinolfi et al., 2010). Basically two mechanisms of pore formation were discussed: According to the "pore dilation" hypothesis, pore formation is an intrinsic channel property and the consequence of a permeability increase from an initially cation selective channel to a non-selective pore. Alternatively, direct or indirect interaction with other pore forming proteins was suggested, with the large transmembrane channel Pannexin 1 (Panx1) representing the most prominent candidate (Pelegrin and Surprenant, 2006) (see below). Noteworthy, permeability to larger molecules like YO-PRO-1 or *N*-methyl-D-glucamine (NMDG) was also observed for P2X2 and P2X4 family members (Khakh et al., 1999; Virginio et al., 1999). However, at least for the P2X2 receptor this property appeared intrinsic to the receptor (Khakh and Egan, 2005; Chaumont and Khakh, 2008) and it was later shown that the time-dependent shift in the reversal potential of extracellular NMDG, that was generally interpreted as an increase in pore diameter, can also be the result of changes in intracellular ion concentration during whole-cell patch-clamp recordings (Li et al., 2015). While the mechanism of pore formation in P2X7 has been a long-standing debate (excellently reviewed in Di Virgilio et al., 2018b), more recent electrophysiological, photochemical, and biochemical experiments indicate that the pathway for larger molecules like NMDG or spermidine is also intrinsic to the P2X7 receptor and, similar to P2X2 (Li et al., 2015), the P2X7 channel is upon activation immediately permeable to both, small cations and large molecules (Riedel et al., 2007; Browne et al., 2013; Harkat et al., 2017; Karasawa et al., 2017; Pippel et al., 2017). Whether a P2X7-activated pathway for large anions that is observed in some cell types is also intrinsic to the P2X7 protein or mediated by a separate channel or pore, remains to be determined (Ugur and Ugur, 2019).

Trafficking and Lipid Interaction Domains (~Residues 540–595)

In the search for domains in the P2X7 C-terminus that control P2X7 channel function, pore forming properties, and plasma membrane expression, truncated P2X7 versions were investigated (Smart et al., 2003) and it was found that 95% (i.e., the sequence up to residue 581) of the rat P2X7 C-terminus are required to mediate ethidium uptake in HEK293 cells. Truncations between aa 551–581 as well as some single point mutations (C572G, R574G, or F581G) in this region resulted in a loss of surface expression. Upon further truncation (residues 380–550), the ion channel but not the pore activity was regained. Thus it was suggested, that amino acid residues 551–581 contain a *retention motif* that is generally masked but becomes exposed

by truncations or single point mutations in this region and then inhibits surface expression. In support of a role of this region in receptor trafficking, the loss-of-function polymorphism I568N in this region of the human P2X7 was also found to inhibit cell surface expression (Wiley et al., 2003).

The supposed retention/retrieval region overlaps with a *lipid interaction or putative LPS-binding motif* (residues 574–589) that is homologous to the LPS binding domains of LPS-binding protein (LBP 44% identity) and bactericidal permeability-increasing protein (BPI 31% identity) and was shown to bind LPS *in vitro* (Denlinger et al., 2001). Both surface expression and LPS binding were abolished when the basic residues R578 and K579 were mutated in human P2X7 (Denlinger et al., 2003). LBP and BPI are pattern recognition proteins that, upon LPS-binding, can stimulate a defensive host response to gram-negative bacteria, although in different ways: LBP is a plasma protein, that increases the host cell's sensitivity to endotoxins by disaggregating, transporting, and binding LPS to other LPS-binding proteins, such as the pattern recognition receptor CD14. CD14 is a glycosylphosphatidylinositol (GPI)-anchored receptor that acts as a co-receptor for the toll-like receptor (TLR) 4 complex (Ranoa et al., 2013). Upon LPS binding, TLR4 induces via the adaptor protein myeloid differentiation primary-response protein 88 (MyD88) and the transcription factor NF-κB cytokine production. Interestingly, the very C-terminus of mouse P2X7, in particular G586 was described to directly interact with MyD88 (Liu et al., 2011) (see also Section "Proteins Involved in P2X7-Mediated Interleukin Secretion").

The soluble BPI has anti-endotoxin and direct bactericidal properties against gram-negative bacteria and can neutralize LPS, thereby inhibiting LPS-triggered cytokine production and an overshooting immune response (Weiss, 2003). Cytosolic LPS, experimentally delivered by cholera toxin B or by transfection of mouse bone marrow-derived macrophages, was shown to decrease the threshold for ATP-induced P2X7-associated pore opening, supposedly by allosteric modulation via the putative LPS binding motif in the P2X7 C-terminus (Yang et al., 2015). Internalization of LPS is facilitated by CD14. Accordingly, the presence of CD14 resulted in an increased co-localization of LPS and P2X7 in transfected HEK293 cells. A direct interaction between P2X7 and CD14 was also reported (Dagvadorj et al., 2015) (see also Section "Proteins Involved in P2X7-Mediated Interleukin Secretion").

Signaling requires the spatial organization (co-localization or sequestration) of its components in subcellular environments for example by protein scaffolds or membrane domains. The lipid interaction motif in P2X7 was not only suggested to serve as a binding domain for LPS, but also for phospholipids and thereby modulating the receptor's localization (Denlinger et al., 2001), for example in lipid rafts. An association between P2X7 and lipid rafts was found in T-cells, where P2X7 is ADP-ribosylated by ART2.2 (Bannas et al., 2005), in mouse lung alveolar epithelial cells (Barth et al., 2007), and in rat submandibular gland cells. In the latter, a lipid-raft pool and a non-raft fraction of P2X7 receptors were described that couple to different signaling pathways (Garcia-Marcos et al., 2006a). This would be in accordance with studies, showing that P2X7 modulates phospholipase A2, C, and D (el-Moatassim and Dubyak, 1992; Hung and Sun, 2002; Garcia-Marcos et al., 2006b; El Ouaaliti et al., 2012) (see also Section "P2X7 – Mediated Lipase Activation and Lipid Interactions"). Also functional regulation of P2X7 by phosphatidylinositol 4,5-bisphosphate (PIP2) was shown in patch-clamp experiments with *Xenopus laevis* oocytes. Although no direct binding of the P2X7 C-terminus and PIP2 could be observed, residues R385, K387 and K395 of the human P2X7 receptor were shown to be important for the interaction with PIP2 (Zhao et al., 2007).

Just upstream of the LPS binding motif, Gonnord et al. (2008) identified two *palmitoylated cysteine residues* (C572, C573) in mouse P2X7 that were essential for P2X7 surface trafficking. Likewise, two more proximal groups of cysteine residues (C477, C479, C482 and C498, C499, C506) were palmitoylated and required for surface expression. Mutation of the juxtamembrane cysteine residues C371, C373, and C374, however, showed only a 50% decrease in palmitoylation and reduced surface localization (Gonnord et al., 2008). Palmitoylation is a reversible posttranslational modification that increases membrane association and can also affect function, stability, and subcellular trafficking of proteins into membrane compartments, as for example the cholesterol- and sphingolipid-enriched lipid rafts.

Interestingly, the permeability of the P2X7 appears to depend not solely on the C-terminus, but also on the lipid composition of the cell membrane (Karasawa et al., 2017). In *in vitro* experiments with purified truncated panda P2X7 in artificial liposomes, phosphatidylglycerol and sphingomyelin facilitated YO-PRO-1 permeation, whereas cholesterol had an inhibitory effect. It was concluded that the palmitoylated cysteine residues in full-length receptors prevent the inhibitory effect of cholesterol by shielding the TM domains, while in C-terminally truncated P2X7, cholesterol can interact with the transmembrane helices and thereby limits its permeability. Thus, the pore forming properties of the P2X7 could be influenced by modulation of the membrane composition and may be cell-type specific (Di Virgilio et al., 2018b).

An unusual Ca^{2+}-dependent *calmodulin (CaM) binding motif* was functionally and biochemically identified in HEK293 cell-expressed rat P2X7 [residues I541-S560, Roger et al., 2008). In this sequence ([I-x(3)-L-x(10)-W]), key bulky amino acid residues form a 1-5-16 motif. CaM is a calcium sensor that modulates the function of a wide variety of enzymes and ion channels, but can also act as an adaptor, interacting with other target proteins (Villalobo et al., 2018). CaM binding to P2X7 was found to facilitate currents and blebbing. In human P2X7, both the CaM binding motif and current facilitation were not detected, but could be reconstituted by replacement of critical residues (T541I, C552S, and G559V) (Roger et al., 2010). P2X7 signaling via Ca^{2+}calmodulin-dependent kinase II (CaMKII) was also shown (Diaz-Hernandez et al., 2008; Gomez-Villafuertes et al., 2009).

The Death Domain (~Residues 430–530)

Based on comparative sequence analysis, residues 438–533 of the human P2X7 were found to be similar (20% identity, 50% conservation) to the *death domain (DD)* of the human tumor

necrosis factor receptor 1 (TNFR1) (Denlinger et al., 2001). The DD is a subclass of protein motifs known as the death fold. It is a protein interaction domain that is contained in numerous proteins and enables them to oligomerize. Many DD-containing proteins are involved in apoptosis and inflammation.

Within the postulated P2X7 DD homology domain, a *proline-rich region* (residues 450–456) contains two overlapping PxxP motifs and may represent a canonical binding site for *cellular sarcoma tyrosine kinase (c-Src) homology 3 (SH3) domains* (Watters et al., 2001). An alignment (ClustalW) between the human SH3-domain binding protein 1 (Q9Y3L3) and residues 441–460 of the human P2X7 receptor shows a 40% sequence identity, in agreement with (Denlinger et al., 2001). SH3 domains are approximately 60 aa long modules that mediate protein interactions and are involved in various intracellular signaling pathways. They recognize *proline-rich regions* containing the PxxP motif (Kurochkina and Guha, 2013) and are present in phospholipases, tyrosine kinases and other signaling proteins (Kaneko et al., 2008). The interaction between the scaffolding protein MAGuK and the P2X7 receptor was suggested to be mediated via SH3 domains, but evidence is lacking (Kim et al., 2001).

There are also two sequences (457–462 and 565–569) with similarities to *a dileucine motif* ([D/E]xxxL[I/L]) (Wiley et al., 2011). This short signaling motif allows for interaction between cargo proteins and adaptor proteins for trafficking and controls endosomal sorting (Kozik et al., 2010).

C-terminal truncation of the human P2X7 at positions 408, 436, and 505 (Becker et al., 2008) lead to reduced ATP-induced inward currents and loss of its biphasic activation and deactivation kinetics when expressed in *Xenopus laevis* oocytes. In case of the 1–436 and 1–505 core receptors, the electrophysiological phenotype of the full-length receptor could be reconstituted by co-expression of a soluble tail construct (residues 434–595). Based on affinity purification, BN-PAGE, and cross-linking experiments a stable *association between the regions* 409–436 and 434–494 was identified, which provides the first information on molecular interactions within the P2X7 tail.

Between the sequence with homology to the death domain and the juxtamembrane region (see below) two regions with homology to *binding sites for cytoskeletal proteins* have been identified. Residues 389–405 of human P2X7 show 53% identity with the *cytadherence high molecular weight protein 3* from *Mycoplasma genitalium,* which binds actin filaments (Denlinger et al., 2001; Watters et al., 2001). Residues 419-425 in rat P2X7 (KSLQDVK) are homologous to the α-*actinin 2 binding sequence in the glutamate receptor NR1 subunit.* In support of a close interaction with the cytoskeleton, the cytoskeletal proteins α-actinin 4 and supervillin, which both interact directly with β-actin were identified in a search for possible interaction partners of rat P2X7 (Kim et al., 2001; Gu et al., 2009).

Juxtamembrane Region(s) (Residues 1–26 and 357–387)

Deletion of the juxtamembrane *cysteine-rich domain* (residues 362–379) was shown to affect the permeation and/or pore forming properties of rat and human P2X7 (Jiang et al., 2005; Robinson et al., 2014). Additionally, it was shown in a chimeric approach (Allsopp and Evans, 2015), that both the N- and the C-terminal juxtamembrane regions of the human P2X7 (including the cysteine-rich domain) are important for pore formation and regulation of channel kinetics. In the panda P2X7, serine-substitutions of C362 and C363 in this region resulted in complete inhibition of YO-PRO-1 uptake (Karasawa et al., 2017). Upstream (residues 354-364) and downstream (residues 378-387) of this cysteine-rich domain, there are at least two *cholesterol recognition amino acid consensus (CRAC) motifs* [(L/V)X1–5 YX1–5(K/R)] that are conserved in human and rodent P2X7. Further CRAC motifs have been identified in the N-terminus, the extracellular end of TM1, and the C-terminus of P2X7 (Robinson et al., 2014). Based on these findings, it was suggested that the juxtamembrane cysteine-rich domain framed by the CRAC motifs could alter the tilting angle of TM2 or act as a membrane anchor and thereby facilitate movements required for channel and/or pore opening (Allsopp and Evans, 2015; Karasawa et al., 2017). A similar anchor-like function that stabilizes the open state was ascribed to the cytoplasmic cap in the human P2X3, which is assumed to undergo profound reorganization upon channel activation (Mansoor et al., 2016).

Within the distal CRAC motif, three neighboring tyrosine residues (Y382-Y384) were identified that can be phosphorylated by the *c-Src tyrosine kinase* (Leduc-Pessah et al., 2017). In this study, it was found that Src kinase activation by morphine (via μ-opioid receptors) and subsequent P2X7 phosphorylation resulted in increased receptor expression and activity in rat spinal microglia. The resulting loss of morphine-induced analgesia linked P2X7 activity to the development of morphine tolerance.

Single Nucleotide Polymorphisms (SNPs) in the P2X7-Tail

The human P2X7 is highly polymorphic (Bartlett et al., 2014). The *T357S* polymorphism was found by ATP-induced influx measurements to cause a partial loss of function in human monocytes, lymphocytes, and macrophages, and was associated with impaired mycobacterial killing (Shemon et al., 2006; Miller et al., 2011). Interestingly, this SNP resulted in a complete loss of function when occurring in homozygote constellation or in combination with another loss-of-function SNP. A loss-of function phenotype was confirmed in *Xenopus laevis* oocytes and HEK293 cells overexpressing the mutant T357S P2X7 (Shemon et al., 2006).

Based on genetic studies, the *human Q460R* polymorphism has been associated with bipolar disorders and major depressive disorder (Barden et al., 2006; Lucae et al., 2006; McQuillin et al., 2009). ATP-induced ethidium uptake measurements in Q460R P2X7-transfected HEK293 cells revealed a slight reduction in pore formation (Fuller et al., 2009; Stokes et al., 2010). Interestingly, careful functional studies showed that this SNP is not *per se* compromised in its function, but shows impaired Ca^{2+} influx, channel currents, intracellular signaling, and also affected the sleep quality in a humanized Q460R P2X7 knock-in mouse model, if co-expressed with the respective non-polymorphic variant (Aprile-Garcia et al., 2016; Metzger et al., 2017).

The *E496A* SNP was found to prevent ATP-induced ethidium uptake, Ba^{2+} permeation, and induction of apoptosis in human B lymphocytes and was associated with cancer metastasis (Gu et al., 2001; Ghiringhelli et al., 2009). When expressed in *Xenopus laevis* oocytes or HEK293 cells and analyzed electrophysiologically, however, the E496A substitution had no effect on the ion channel functions of the receptor (Boldt et al., 2013).

The human loss-of-function SNP, *I568N*, was reported to prevent receptor trafficking and cell surface expression [see also Section "Trafficking and Lipid Interaction Domains (∼Residues 540–595)"] (Wiley et al., 2003), supposedly because of its localization within a sequence [DFAI(568)L] (Wiley et al., 2011) similar to a dileucine motif – [D/E]xxxL[I/L]– [(Kozik et al., 2010), compare Section "The Death Domain (∼Residues 430–530)"].

A gain of function in pore formation and IL- 1β secretion has been reported for the *human A348T* SNP (Stokes et al., 2010), whereas *H521Q* has been reported to represent a neutral SNP (Wiley et al., 2011).

The *murine P451L* loss-of-function SNP was identified by comparison of T-cells from different mouse strains (Adriouch et al., 2002). This SNP is found in the commonly used C57BL/6 strain, but not in BALB/c mice, rats, or humans. It impairs ATP-induced cation fluxes, pore formation, PS externalization, NAD-sensitivity as well as lysis and apoptosis of thymocytes (Schwarz et al., 2012; Rissiek et al., 2015), and has been associated with reduced pain sensitivity (Sorge et al., 2012). It lies within the SH3-binding domain [compare Section "The Death Domain (∼Residues 430–530)"].

P2X7 MEDIATED SIGNALING PATHWAYS

A multitude of downstream events have been identified upon P2X7 activation. In the following, we will focus on the proteins involved in the P2X7 activated signaling pathways rather than the physiological consequences or cell types in which these have been observed.

Release of IL-1β and Other Cytokines

The most investigated P2X7 function is probably its role in NLRP3 inflammasome assembly and subsequent maturation and release of IL-1β by macrophages and other immune cells. The pro-inflammatory IL-1β is a member of the interleukine-1 cytokine family, which comprises the IL-1 (IL-1α, IL-1β, IL-33, IL-1Ra), IL-18 (IL-18, IL-37), and IL-36 (IL-36Rα, IL-36α,β,γ, IL-38) subfamilies and includes pro- and anti-inflammatory cytokines (Dinarello, 2018). Due to its earlier identification and major role in host defense of the innate immune system and autoinflammatory diseases, IL-1β is so far best studied. Pro-IL-1β synthesis (and also that of NLRP3, see below) is induced by the transcription factor NF-κB, which in turn is activated upon binding of pathogen-associated molecular patterns (PAMPs), such as LPS, to the TLR4 (priming). Processing and release of mature IL-1β is then induced in a second step (activation) by inflammasome assembly and activation of caspase 1 by a diverse range of damage- or danger-associated molecular patterns (DAMPs), including ATP (Mariathasan et al., 2006).

Activation of caspase 1 by proteolytic conversion of pro-caspase 1 requires the NLRP3 inflammasome, a multiprotein complex that consists of the pattern recognition receptor NLRP3, the adaptor apoptosis-associated speck-like protein containing a caspase-recruitment domain (ASC), and the cysteine protease caspase 1 (Gross et al., 2011). In addition, never-in-mitosis A (NIMA)-related kinase 7 (NEK7) was recently identified as an essential component (He et al., 2016b; Shi et al., 2016).

K^+ efflux and depletion was early shown to constitute a critical step in ATP-induced IL-1β production (Perregaux and Gabel, 1998) and generation of the first P2X7 knockout mouse clearly demonstrated the involvement of the P2X7 in this process (Solle et al., 2001). More recently, K^+ depletion has been confirmed to represent an essential and sufficient requirement for inflammasome assembly induced by a diverse variety of DAMPs (Munoz-Planillo et al., 2013). However, while the P2X7 was generally assumed to represent the K^+ conduit, a recent study identified the two-pore domain K^+ channel TWIK2 as an ATP-responsive K^+ efflux channel (Di et al., 2018). According to this study, P2X7-induced cation influx generates the driving force for K^+ efflux. The molecular mechanisms of inflammasome assembly and caspase activation are little understood. Based on immunoprecipitation and co-localization studies in cell lines and primary mouse microglia, it has been suggested that the P2X7 is directly interacting with NLRP3 (Franceschini et al., 2015). Likewise, an interaction between P2X7 and the NLRP2 inflammasome was proposed in human astrocytes (Minkiewicz et al., 2013) (see also Section "Proteins Involved in P2X7-Mediated Interleukin Secretion").

In addition to K^+ depletion, cytosolic ROS production, either by NADPH oxidase or due to mitochondrial dysfunction, has been implicated in NLRP3 inflammasome activation and its exact role remains to be determined (He et al., 2016a). With the exception of the interleukine receptor antagonist (IL-1Ra), all IL-1 family members lack a signal peptide and are formed as precursor in the cytoplasm. Various mechanisms of non-classical IL-1β release mechanism including exocytosis via lysosomes, microvesicle shedding, exosome release, and release upon pyroptotic cell death have been proposed (for references and details see Dubyak, 2012; Giuliani et al., 2017). While PLC, PLA2 (Andrei et al., 2004), src kinase, p38, acid sphingomyelinase (Bianco et al., 2009), caspase 1 (Keller et al., 2008), and gasdermin (Evavold et al., 2018) have been involved, the exact mechanism(s) and P2X7 involvement remain(s) incompletely understood. In addition to IL-1β, numerous other cytokines, chemokines, and proteins have been shown to be released upon P2X7 activation (e.g., de Torre-Minguela et al., 2016).

ROS Formation/Mitochondrial Function

ROS are continuously generated by the mitochondrial electron transport chain or by activation of NADPH oxidases (NOXs). They represent important signaling molecules under physiological conditions. Under pathological conditions, increased ROS production contributes to immune signaling and killing of phagocytosed microorganisms, but also to deleterious effects such as protein, lipid, and DNA modification and damage. Seven NOX family members are known and the respective

NADPH oxidase complexes are subtype-specifically localized in internal and plasma membranes. They consist of the membrane integrated catalytic subunit with or without the p22phox protein and regulating cytosolic proteins including the Rho-GTPase Rac. NOX are activated by numerous receptors and NOX complex assembly and activity can be further regulated by Ca^{2+} signaling and subunit phosphorylation for example by protein kinase C isoforms, p38 and ERK1/2 MAP kinases, and phosphoinositide-3 kinase (PI3Ks) (Guerra et al., 2007; Spooner and Yilmaz, 2011; Haslund-Vinding et al., 2017; Belambri et al., 2018). P2X7-mediated NOX subunit phosphorylation and ROS production has been shown in microglia and macrophages (Parvathenani et al., 2003; Moore and MacKenzie, 2009; Lenertz et al., 2009) and few other cell types (Wang and Sluyter, 2013). The molecular mechanisms were suggested to involve kinase activation via Ca^{2+} influx (Guerra et al., 2007; Noguchi et al., 2008; Martel-Gallegos et al., 2013).

Interestingly, tonic stimulation by low levels of ATP was found to hyperpolarize the mitochondrial potential, increase mitochondrial Ca^{2+} content, and increase the cells' ATP content in transfected cells. This effect was dependent on the C-terminus and proposed to be due to a P2X7-mediated constant but low level Ca^{2+} transfer into the mitochondria that stimulates trophic effects whereas strong P2X7 stimulation causes mitochondrial Ca^{2+} overload and collapse and results in cell death (Adinolfi et al., 2005). P2X7-expressing cells also upregulated the glucose transporter and glycolytic enzymes, showed increased glycolysis, oxidative phosphorylation, and protein kinase B phosphorylation, and were able to proliferate even in the absence of serum and glucose (Amoroso et al., 2012) (see also Di Virgilio et al., 2017).

P2X7 – Mediated Lipase Activation and Lipid Interactions

Phospholipids, glycolipids, and cholesterol represent the major lipid components of animal plasma membranes. Cholesterol is an important constituent of lipid rafts and phospholipids can be broken down by phospholipases to produce different lipid second messengers or bioactive mediators of cellular signaling. Cholesterol as well as several phospholipases have been proposed to be involved in P2X7 signaling and function.

Phospholipase A2 (PLA2)

PLA2 phospholipases cleave phospholipids preferentially in the middle position of glycerol to release fatty acids and lysophospholipids.

Out of the six diverse groups of mammalian PLA2 enzyme families, the cytosolic PLA2α is the best-investigated enzyme. It belongs together with the β,γ,δ,ε, and ζ subtypes to the group IV family of cytosolic PLA2 (Leslie, 2015). cPLA2α preferentially catalyzes the hydrolysis of phospholipids to arachidonic acid and lysophospholipids, which are precursors for numerous bioactive lipids such as prostaglandins, leukotrienes, and epoxyeicosatrienoic acids (EETs). Ca^{2+}-independent PLA2 (iPLA2, group VI) are similar to cPLA2 but do not require Ca^{2+} for activation. Both types are also implicated in the regulation of intracellular membrane trafficking by the induction of changes in the membrane curvature that is required for membrane budding (Leslie, 2015).

cPLA2α is widely expressed in all tissues and regulated by its transcriptional level (e.g., induced by Ras and MAPK pathways and NF-κB, hypoxia-inducible factor, Sp1, and c-Jun), Ca^{2+}, and phosphorylation by MAPK. Ca^{2+} increase promotes its translocation to intracellular membranes, a requirement for arachidonic acid release. Phosphorylation by MAPKs can enhance its activity (Leslie, 2015). P2X7-mediated activation of cPLA2 and iPLA2 has been reported in immune and epithelial cells (Alzola et al., 1998; Chaib et al., 2000; Andrei et al., 2004; Kahlenberg and Dubyak, 2004; Garcia-Marcos et al., 2006b; Costa-Junior et al., 2011) and has been associated with various downstream effects such as PLD activation, kallikrein secretion, bioactive lipid generation, and pore formation as well as IL-1β processing, blebbing, and PS-flip (Garcia-Marcos et al., 2006b; Anrather et al., 2011; Costa-Junior et al., 2011; Norris et al., 2014; Wan et al., 2014; Alarcon-Vila et al., 2019; Janks et al., 2019). Janks et al. (2019) recently reported an involvement of undefined chloride channels downstream of PLA2 in some of these processes. The mechanism of PLA2 activation by P2X7 remains unclear but was suggested to involve MAP kinases, P-I4 kinase/PIP2 (Garcia-Marcos et al., 2006b; Wan et al., 2014) and/or n-SMase activation in lipid rafts (Garcia-Marcos et al., 2006a). In case of cPLA2, it might also be activated by Ca^{2+} influx through P2X7.

Phospholipase C (PLC)

In animals, PLC cleaves phosphatidylinositol-4,5-bisphosphate (PIP2) into the second messengers diacylglycerol and inositol-1,4,5,-triphosphate (Suh et al., 2008; Fukami et al., 2010). Besides PKC activation and mobilization of intracellular Ca^{2+} (via DAG and IP3, respectively) this process also influences the local concentration of PIP2 (an important membrane anchor and modulator of multiple processes and receptors) and the synthesis of the signaling molecule PIP3, which is generated by phosphatidylinositol 3-kinase (PI3K) from PIP2. Thirteen mammalian PLC isoforms that are organized in six groups are known and expressed in a tissue and/or cell-specific manner. In addition to the common catalytic and Ca^{2+}-binding domains all but the PLCζ isotype contain pleckstrin homology (PH) domains that can mediate interactions with phosphatidylinositol lipids, G protein βγ subunits, or other proteins. Furthermore, some isotypes have specific domains that contribute to their individual functions: thus the src homlogy (SH) domains in PLCγ allow its interaction with and activation by receptor and cytosolic tyrosine kinases. Ras-associating domains and Ras-GTPase exchange factor-like domains in PLCε mediate its interactions with members of the Ras family of small G proteins, and the long C-terminus of PLCβ contains determinants for Gq protein interactions, membrane binding, and nuclear localization (Suh et al., 2008; Fukami et al., 2010).

Several GPCRs, including some P2Y receptors, activate PLC. However, few reports exist on the activation of PLC by P2X7 (Carrasquero et al., 2010) and K^+ depletion has been suggested as a mechanism (Andrei et al., 2004; Clark et al., 2010). Also, modulation of PLC downstream effects by P2X7 has been

reported but appears to be indirect and not dependent on influx of extracellular Ca^{2+} (Garcia-Marcos et al., 2006b). In microglia, for example, it was found that P2X7-induced Ca^{2+} rise increases DAG lipase activity and thus favors production of the endocannabinoid 2-AG from DAG, which is generated by PLC (Witting et al., 2004). A negative modulation of P2X7 through the depletion of PIP2 (supposedly due to PLC) has also been reported (Zhao et al., 2007) and three residues in the C-terminus (R385, K387, K395) might be involved in this interaction. However, the mechanism could also be indirect as no direct PIP2-P2X7 interaction was identified (Bernier et al., 2013) [compare Section "Trafficking and Lipid Interaction Domains (~Residues 540–595)"].

Phospholipase D (PLD)

PLDs represent a family of phosphodiesterases that catalyze the removal of head groups from glycerophospholipids (typically phosphatidylcholine), thereby generating the regulatory molecule phosphatidic acid (PA). More generally, this process represents a headgroup exchange by water and in the presence of primary alcohols generates phosphatidylalcohol. PA, due to its small negatively charged headgroup, can induce negative curvature of membranes if sufficient concentrations are reached. In addition, PAs can act as lipid anchors for numerous PA binding proteins and can modulate/activate various proteins, such as the NOX complex, kinases, PLC and G-protein regulatory proteins, to only name a few (Bruntz et al., 2014). PA can also be converted to DAG and lysophosphatidic acid.

In mammals, the two isoforms PLD1 and PLD2 occur almost ubiquitously, associate with membranes, and participate in processes that involve membrane remodeling such as vesicular transport and endocytosis but also many others. PLDs are activated by a variety of receptors (GPCRs, receptor tyrosine kinases, and integrins) and signaling molecules. Direct interaction and activation has been shown for PKC and the small Ras GTPases RhoA and ARF (Selvy et al., 2011; Bruntz et al., 2014). In a macrophage cell line, P2X7 activation was found to induce rapid PLD activation that was only partially dependent on Ca^{2+} and PKC (Humphreys and Dubyak, 1996) and subsequent studies in human and mouse macrophages showed that P2X7-dependent killing of intracellular pathogens requires PLD activation (Kusner and Adams, 2000; Fairbairn et al., 2001; Coutinho-Silva et al., 2003). In thymocytes, Ca^{2+}-dependent activation of PLD by P2X7 was shown (Le Stunff et al., 2004). What links P2X7 to PLD activation is not known in detail but influx of bivalent cations (Gargett et al., 1996), kinases (Hung and Sun, 2002; Perez-Andres et al., 2002; Pochet et al., 2003), and small G-protein interactions via the putative SH3 domain (Denlinger et al., 2001) have been involved.

Sphingomyelinase

Sphingomyelin is a phospholipid based on the unsaturated aminoalcohol sphingosine instead of glycerol. It is the most abundant sphingolipid with particularly high levels in the CNS and constitutes a major component of the plasma membrane. Due to its ability to bind cholesterol, it plays an important role in the formation of lipid rafts. Its content in the cell is regulated by *de novo* synthesis in the ER/Golgi (a multistep process involving sphingomyelin synthases) and its degradation by sphingomyelinases (SMases). SMases hydrolize sphingomyelin to phosphocholine and ceramide (sphingosine coupled via an amide bound to a fatty acid), a bioactive molecule that is involved in apoptosis, cell cycle, organization of membrane domains ("ceramide platforms"), inflammation, and various diseases (Gomez-Munoz et al., 2016). In addition, ceramide can be metabolized to further bioactive sphingolipids, such as the mitogenic sphingosine-1-phosphate.

Six types of SMases have been identified and were grouped according to the optimal pH value for their activation into acidic, alkaline and four neutral SMases. Of these, the lysosomal acidic a-SMase and Mg^{2+}-dependent neutral n-SMase2 are best characterized and considered the major candidates for ceramide production. n-SMase is located in Golgi and plasma membrane domains and regulated by transcription, anionic phospholipids, phosphorylation, and in response to several cytokines, including TNF-α and IL-1β (Shamseddine et al., 2015).

In thymocytes and macrophages, P2X7 has been involved in the *de novo* synthesis of ceramide and subsequent apoptosis (Lepine et al., 2006; Raymond and Le Stunff, 2006) and it was speculated that the P2X7 death domain might be involved in ceramide production in macrophages. Similarly, this domain was suggested to be involved in P2X7-induced activation of n-SMase in lipid rafts and subsequent PLA2 activation in submandibular gland cells. In a more recent study on astrocytes it was concluded that P2X7, via src kinase (maybe by interacting with the SH2 domain) and p38MAPK activation, induces translocation of a-SMase to the outer plasma membrane leaflet where it induces blebbing and shedding of IL-1β-containing micro particles (Bianco et al., 2009). It was also suggested that P2X7, via a-SMase activation can induce the rapid release of HIV-1-containing compartments from HIV-infected macrophages (Graziano et al., 2015).

P2X7 Effects on Membrane Organization and Morphology

Phosphatidylserine Exposure (PS-Flip) and Shedding

In healthy cells, PS is distributed to the inner leaflet of the plasma membrane. So-called flippases, most likely P4-ATPase ATP11C and its chaperone CDC50A, are required to keep this asymmetry (Segawa et al., 2014). Under certain conditions, for example during apoptosis, PS is translocated to the cell surface by scramblases (Segawa and Nagata, 2015). Anoctamin-6/TMEM16F (Ano6) and Xk-related protein 8 (Xkr8) were identified as scramblases (Suzuki et al., 2010, 2013) and proposed to account for Ca^{2+}-induced PS scrambling and a caspase/apoptosis-induced scrambling respectively (Suzuki et al., 2013). For the latter, simultaneous inactivation of ATP11C and activation of Xkr8 by caspases is required (Suzuki et al., 2013; Segawa et al., 2014).

Brief activation of P2X7 was shown to result in a reversible PS translocation, while prolonged activation results in irreversible exposure of PS and subsequent cell death (Mackenzie et al., 2005). A functional and physical interaction between P2X7

and the Ca^{2+} activated Cl^- channel Ano6 was identified and suggested to mediate the translocation of PS (Ousingsawat et al., 2015). However, the molecular mechanisms of this interaction are unclear and interaction between Ano6 and P2X7 was not confirmed in another study (Stolz et al., 2015).

Reversible PS flip is also part of a signal transduction pathway in response to pathological conditions and P2X7-mediated PS flip can lead to shedding of L-selectin (CD62L) (Elliott et al., 2005), a cell adhesion molecule that initiates leukocyte tethering, the first step of the adherens and migration cascade (Ivetic, 2018). Shedding of CD62L from human monocytes occurs precisely during transmigration and is important for the invasion and direction of migration (Rzeniewicz et al., 2015) and PS exposure increased the adhesion of cells to the endothelial cell layer (Manodori et al., 2000). Thus PS translocation appears to be relevant for leukocyte migration and P2X7-mediated PS flip might increase the membrane fluidity and plasticity of the cell and thereby facilitate the transmigration processes (Elliott et al., 2005; Qu and Dubyak, 2009).

In addition to CD62L (Jamieson et al., 1996; Gu et al., 1998; Labasi et al., 2002; Elliott et al., 2005; Sengstake et al., 2006; Scheuplein et al., 2009; Schwarz et al., 2012), shedding of low affinity immunoglobulin epsilon Fc receptor (CD23) (Gu et al., 1998; Chen et al., 1999; Sluyter and Wiley, 2002; Pupovac et al., 2015), complement receptor type 2 (CD21) (Sengstake et al., 2006), tumor necrosis factor receptor superfamily member 7 (CD27) (Moon et al., 2006), IL-6R (Garbers et al., 2011), CXCL16 (Pupovac et al., 2013), and vascular cell adhesion molecule 1 (VCAM-1) (Mishra et al., 2016) was reported upon P2X7 activation and was mainly linked to activation of membrane-associated metalloproteases, in particular the a disintegrin and metalloprotease domain-containing proteins (ADAM) 10 and ADAM17. Out of the 21 ADAM family members, these two have been studied the most. They are widely expressed by immune cells and their activity is controlled by multiple regulatory mechanisms (Grötzinger et al., 2017; Lambrecht et al., 2018). Interestingly, it was shown that PS exposure is required for ADAM17 activity (Sommer et al., 2016) and phosphorylation by ERK and p38 is important for its activation (Diaz-Rodriguez et al., 2002) and membrane trafficking (Soond, 2005), thus providing a direct link between metalloprotease activity and these described P2X7 signaling pathways.

Plasma Membrane Blebbing

Blebbing is the formation of spherical protrusions of the plasma membrane. It requires the detachment and/or local rupture of the actomyosin cortex from the membrane (bleb nucleation or initiation) as well as increased myosin activity and intracellular pressure (bleb expansion) and is reversed by subsequent reformation of an actin cortex at the blebbed membrane and myosin-driven retraction. While generally considered as a hallmark of apoptosis, blebbing is also involved in cell migration and cytokinesis (Charras, 2008; Paluch and Raz, 2013). The molecular details of these events are little understood but activation of the small G protein Rho by extra- or intracellular signals, its subsequent activation of the effector kinase Rho-associated kinase (ROCK), and phosphorylation of myosin light chain by ROCK appear to be central processes. In addition, proteins and lipids (such as PIP2) influencing the cortex-membrane interaction and alterations in the cell adhesion properties appear to play a role (Fackler and Grosse, 2008). P2X7 receptor activation causes reversible blebbing in native and recombinant systems (MacKenzie et al., 2001; Mackenzie et al., 2005). This effect is dependent on the P2X7 tail (Wilson et al., 2002) and in a Y2H screen an interaction with the epithelial membrane protein (EMP)-2 was identified and biochemically confirmed for the related proteins EMP-1, EMP-3, and peripheral myelin protein (PMP)-22, which are all widely expressed (references in Wilson et al., 2002). Overexpression of these proteins in HEK293 cells resulted in an increase of caspase-dependent apoptotic-like behavior and blebbing, although a specific interaction domain or mechanism was not identified. In subsequent studies, RhoA, ROCKI, and p38 MAP kinase (Morelli et al., 2003; Verhoef et al., 2003; Pfeiffer et al., 2004) have been shown to be involved in P2X7-induced blebbing and it was demonstrated that the signaling pathway that leads to blebbing is caspase independent and different from that promoting IL-1β release (Verhoef et al., 2003). However, dependence of blebbing on extracellular Ca^{2+}- was inconsistent in different studies and both Ca^{2+}-dependent and independent pathways leading to blebbing have therefore been proposed (Mackenzie et al., 2005). According to this model, the faster Ca^{2+}-dependent zeiotic form of membrane blebbing is a consequence of local Ca^{2+} overload that via induction of PS-flip leads to the disruption of plasma membrane actin interaction. In favor of this model, deregulation of Ca^{2+} entry as a consequence of CaM binding to the P2X7 C-terminus was found to facilitate blebbing (Roger et al., 2008). How Rho is activated remains unresolved. Based on findings in osteoblasts, it was proposed that P2X7 activation leads via PLD and PLA2 activation to LPA, and LPA, by activation of the LPA receptor (a GPCR), activates Rho (Panupinthu et al., 2007). Involvement of PLA2 activation in addition to an undefined Cl^- channel in blebbing is supported by a recent study on macrophages (Janks et al., 2019).

Additional effects of P2X7 on cellular membrane trafficking and organization have been reported. These include microvesiculation (MacKenzie et al., 2001; Bianco et al., 2005; Pizzirani et al., 2007), exosome release (Qu et al., 2009; Barberà-Cremades et al., 2017), phagosome maturation (Fairbairn et al., 2001), and formation of multinucleated giant cells (Lemaire et al., 2006). For review see Qu and Dubyak (2009).

Kinase Activation

Protein Kinase C (PKC)

PKCs are a family of serine/threonine kinases and represent central mediators of cytoplasmic signaling cascades that regulate a variety of cellular functions.

Three PKC subfamilies (classical, novel, and atypical) have been determined: The classical (PKCα, PKCβ, PKCγ) and the novel (PKCδ, PKCε, PKCθ, and PKCη) PKCs both require the second messenger DAG for activation. The cPKCs require Ca^{2+} as a cofactor while the nPKCs are Ca^{2+}-independent. The aPKCs

are independent of Ca^{2+} and DAG. Most PKCs are ubiquitously expressed. Their activation is associated with translocation of the enzyme from the cytosolic fraction to the plasma membrane or cell organelles. Besides mediating signal transduction from the plasma membrane, PKCs have been identified within the nucleus, where their role is less well studied (Lim et al., 2015).

P2X7-dependent translocation of Ca^{2+}-dependent PKCs has been described in osteoclasts (Armstrong et al., 2009) and Ca^{2+}-independent PKCs have also been involved in P2X7 signaling (Bradford and Soltoff, 2002; Gendron et al., 2003) although the molecular interactions and the source of DAG remained unclear in these studies. P2X7 modulation by PKC and its physical interaction with PKCγ was also suggested (Hung et al., 2005).

Mitogen Activated Protein Kinases (MAPK)

MAPKs are serine/threonine-specific protein kinases that are activated by phosphorylation as a result of a multi-level signaling cascade. Three types of MAPKs have been found to be phosphorylated upon P2X7 activation, the closely related extracellular signal regulated kinases ERK1 and ERK2, the c-Jun N-terminal kinases (JNKs), and the p38 MAPK (Hu et al., 1998; Armstrong et al., 2002). The ERK1/2 pathway is best investigated and starts with an extracellular ligand binding to its receptor, which then couples to and activates the small GTPase Ras, which via RAF kinases and mitogen-activated protein kinase kinases (MEK1/2) activates ERK1/2. ERK1/2 can regulate RNA translation and several transcription factors and plays an important role in cell division and proliferation. Activation of P38 and JNK MAPKs is more complex and includes numerous kinases that are mostly shared between both MAPKs. Activating stimuli include inflammatory signals and stress and these kinases are involved in apoptosis, proliferation, and inflammation.

Many studies have shown phosphorylation of these kinases following P2X7 activation (Humphreys et al., 2000; Panenka et al., 2001; Gendron et al., 2003). Activation of ERK1 was suggested to be mediated via Ca^{2+}, PI3K, c-Src (Gendron et al., 2003; Auger et al., 2005), and EGF receptor transactivation (Stefano et al., 2007). ERK activation was shown to depend mainly on the N-terminus of P2X7 since it was affected by N- but not C-terminal truncations (Amstrup and Novak, 2003).

Cellular Sarcoma Tyrosine Kinase (c-Src)

c-Src is a member of the Src kinase family and a protooncogene. It is via myristoylation associated with the plasma membrane and contains src homology (SH) domains 1–4. Its activation causes dephosphorylation of a tyrosine residue and opening of the SH2, SH3, and kinase domains and autophosphorylation. It can be activated by several membrane proteins and can activate various proteins, including focal adhesion proteins, adaptor proteins, and transcription factors and thereby directly or indirectly activates numerous signaling molecules including MAPKs.

Besides activating downstream signaling pathways, the P2X7 receptor itself could serve as a substrate for kinases or phosphatases. For example, Y343 in TM2 was assumed to be dephosphorylated upon receptor activation, since phenylalanine-substitution of Y343 in rat P2X7-expressing HEK293 cells prevented run-down of agonist-evoked currents as well as the effect of phosphatase inhibitors on currents and onset of membrane blebbing (Kim et al., 2001). Additionally, tyrosine residues Y382, Y383, and Y384 in rat P2X7 were found to be phosphorylated by c-Src (Leduc-Pessah et al., 2017).

Phosphoinositide 3-Kinase (PI3Ks)/Protein Kinase B (PKB Also Known as Akt)

PI3Ks are a family of kinases that, upon activation by receptors phosphorylate the hydroxyl group in position 3 of phosphatidylinositol, thereby generating various phosphoinositides that are able to recruit signaling proteins with phosphoinositide binding PH domains to membranes. Thus, the PH domains of the serine/threonine kinase protein kinase B and the phosphoinositide-dependent kinase (PDK1) bind to PtdIns(3,4,5)P3 (PIP3) and PtdIns(3,4)P2 (PIP2) and thereby localize to the plasma membrane where they interact.

PKB is a serine/threonine kinase that contains a PH domain, which binds with high affinity to phosphatidylinositol (3,4,5)-trisphosphate (PIP3) and is activated by the phosphoinositide-dependent kinase (PDK) 1 and the mammalian target of rapamycin complex 2 (mTOR2). This results in the activation of multiple substrates including mTOR. PKB is involved in antiapoptotic pathways, glucose metabolism, protein synthesis, and cell proliferation and tightly regulated. Numerous and complex effects of P2X7 on Akt have been reported. For example, in neuroblastoma cells and astrocytes, stimulation of P2X7 lead to Akt activation (Jacques-Silva et al., 2004; Amoroso et al., 2015). In another study on neuroblastoma cells, P2X7 inhibition was associated with neuritogenesis and increased Akt phosphorylation (Gomez-Villafuertes et al., 2009) and in pancreatic cancer cells, P2X7 activation was involved in activation of protein and lipid phosphatases that lead to nuclear Akt depletion and inhibited proliferation (Mistafa et al., 2010). Extra- and intracellular calcium, a c-Src-related tyrosine kinase, PI3K, and CaMKII have been involved in Akt activation by P2X7 (Jacques-Silva et al., 2004; Gomez-Villafuertes et al., 2009).

Neurotransmitter Release

A wealth of literature describes P2X7 localization and function in neuronal cells and its involvement in the release of various neurotransmitters and gliotransmitters. This effect is generally supposed to be a consequence of P2X7-mediated Ca^{2+} increase and beyond the scope of this review. Excellent overviews are given in Sperlagh and Illes (2014) and Miras-Portugal et al. (2017).

Role in Gene Transcription

P2X7 has been involved in the activation of several transcription factors, most of which play a role in inflammation.

Nuclear Factor κ-Light Chain Enhancer of Activated B Cells (NF-κB)

NF-κB is an ubiquitously expressed protein complex that acts as a rapid primary transcription factor (Zhang et al., 2017) and binds to so-called κB-motifs that are present in

numerous regulatory DNA regions. It is activated by stressful and pro-inflammatory stimuli such as cytokines, bacterial and viral antigens via a variety of cell surface receptors and initiates the transcription of genes involved in inflammation, proliferation, or survival. In unstimulated cells, NF-κB is bound in the cytoplasm to the inhibitor of κB (IκB). Phosphorylation of IκB by IκB kinase (IKK) leads to its degradation in the proteasome and enables NF-κB to translocate into the nucleus where it binds to target gene promoter sequences. In addition, activity of NF-κB is modulated by phosphorylation (Christian et al., 2016). Activation of P2X7 has been shown to lead to IκB degradation, NF-κB phosphorylation, nuclear translocation, and induced transcription in NF-κB reporter assays (Ferrari et al., 1997b; Aga et al., 2002; Korcok et al., 2004; Genetos et al., 2011; Kim et al., 2013). The signaling mechanisms have not been conclusively resolved but were suggested to involve ROS generation and caspase activation (Ferrari et al., 1997b), ERK1/2 and Akt, (Tafani et al., 2011), MAP kinases (Aga et al., 2004), and MyD88 (Liu et al., 2011). While it is generally accepted that P2X7-induced caspase 1 activation and subsequent IL-1β maturation requires TLR-induced NF-κB signaling (Kahlenberg et al., 2005), a role for P2X7-induced NF-κB signaling and IL-1β transcription (together with NLRP3 components) has also been shown in sterile inflammation upon mechanical trauma (Albalawi et al., 2017).

Nuclear Factor of Activated T Cells (NFAT)

The NFAT family consists of five (NFAT1-NFAT5) members and is related to the REL-NF-κB family of transcription factors (Serfling et al., 2012). NFAT1-NFAT4 are activated via CaM and the phosphatase calcineurin, by cell surface receptors that couple to Ca^{2+} mobilization. NFAT5 is activated by osmotic stress and not further discussed here. In its inactivated state, NFAT is phosphorylated and upon dephosphorylation by calcineurin, translocates to the nucleus. Here, it cooperates with other transcription factors (including the AP-1 and Rel family) to regulate immune function and inflammation as well as cell proliferation, cell differentiation and cancer growth. NFAT phosphorylation and inactivation is regulated by multiple kinases in the nucleus (e.g., GSK3) and/or cytoplasm (e.g., CK1). In addition, several other mechanisms, such as caspase 3 cleavage, can regulate NFAT (Müller and Rao, 2010).

In T cells, where NFAT function is best investigated, ATP release and autocrine or paracrine feedback signaling via P2X7 activation has been shown to lead to NFAT induction and release of IL-2 (Yip et al., 2009). In stimulated B cells, however, NFAT internalization in the nucleus was decreased by P2X7-induced membrane depolarisation (Pippel et al., 2015). In microglia cell lines, P2X7 signaling has been shown to activate NFAT proteins (Ferrari et al., 1999) and more recently, the inflammatory CC-motif chemokine ligand 3 (CCL3) was found to be released as a result of this signaling pathway (Kataoka et al., 2009).

Adinolfi et al. (2009) observed an induction in the expression of NFATc1 by heterologous expression of P2X7 in HEK293 cells that lead to promotion of growth and prevention of apoptosis. This effect was confirmed by P2X7 transfection in cancer cell lines and caused an increase in the tumor size and growth rate (Adinolfi et al., 2012). Likewise, transfection of P2X7 into osteosarcoma cells led to an increase in NFATc1 translocation to the nucleus and its activation has been associated with cell growth and proliferation (Giuliani et al., 2014).

Hypoxia Inducible Factor (HIF)

Hypoxia inducible factor is a heterodimeric (HIF-α and HIF-β) transcription factor that is upregulated under conditions of low oxygen availability and is implicated in tumor growth. P2X7-mediated upregulation of HIF-1α and ischemic tolerance was reported after ischemic insult in astrocytes (Hirayama et al., 2015; Hirayama and Koizumi, 2017) and P2X7 downmodulation reduced HIF-1α (Amoroso et al., 2015). HIF-1α has also been proposed to regulate the expression of P2X7 in the hypoxic microenvironment, which via Akt and Erk phosphorylation promotes nuclear translocation of NF-κB and tumor cell invasion (Tafani et al., 2011).

Other Transcription Factors

Other transcription factors that were reported to be induced upon P2X7 activation include activator protein 1 (AP-1) (Gavala et al., 2010), the early growth response transcription factors (Egr) (Stefano et al., 2007; Friedle et al., 2011), Runt related factor-2 (Runx2) (Yang et al., 2018), and cyclic AMP response element binding protein (CREB) (Ortega et al., 2011). For additional information please refer to Lenertz et al. (2011).

Cell Death

P2X7 is involved in different forms of cell death. While it is generally reported to cause apoptosis and/or necrosis, multiple alternative cytotoxic routes like pyroptosis and autophagy have also been described (Dubyak, 2012; Yang et al., 2015; Young et al., 2015). Whereas cell swelling and cytolysis could be explained by the plasma membrane permeabilizing properties of the P2X7 receptor (Surprenant et al., 1996) the exact mechanisms of different other forms of necrosis or apoptosis are not known in detail (for a recent review see Di Virgilio et al., 2017). Nevertheless, typical markers of apoptosis such as cytochrome c release, PS-flip, blebbing, cleavage of caspase-3, caspase-8, and caspase-9 have been observed in various systems (Ferrari et al., 1997a; Humphreys et al., 2000; Mackenzie et al., 2005).

DIRECT PROTEIN P2X7 INTERACTIONS OR INTERACTIONS WITHIN PROTEIN COMPLEXES

More than 50 proteins have been identified to physically interact with the P2X7 receptor (**Table 1**). Analysis of their STRING interaction network (**Figure 2**, Szklarczyk et al., 2019) shows that 22 of these proteins are involved in the innate immune response, in agreement with the proposed pro-inflammatory functions of P2X7. For the majority of the identified proteins, the interaction domains and the physiological consequences of this

TABLE 1 | Published P2X7 interaction partners (adapted from http://www.p2x7.co.uk).

Gene	Protein name	Uniprot ID (human)	Method	Cell system	References
ABL1	Tyrosine-protein kinase ABL1	P00519	Peptide array	*In vitro*	Wu et al., 2007
ACTB*	Actin, cytoplasmic 1 (β-actin)	P60709	IP-MS/WB	HEK293	Kim et al., 2001
			IP-MS	THP-1	Gu et al., 2009
ACTN4*	α-actinin 4	O43707	IP-MS/WB	HEK293	Kim et al., 2001
ANO6	Anoctamin-6	Q4KMQ2	IP-WB	HEK293	Ousingsawat et al., 2015
ARRB2	β-arrestin 2	P32121	IP-WB	CaSKI / HEK293	Feng et al., 2005
Bgn	Biglycan	P21810	IP-WB	Peritoneal macrophages	Babelova et al., 2009
CALM1*	Calmodulin	P0DP23	IP-WB	HEK293	Roger et al., 2008
					Roger et al., 2010
CASK	Peripheral plasma membrane protein CASK	O14936	Y2H	Liver cDNA library	Wang et al., 2011
Cav1/3	Caveolin-1	Q03135	PD/IP-WB	Alveolar epithelial E10 cells	Barth et al., 2008
			nPAGE/IP-WB	Alveolar epithelial E10 cells	Weinhold et al., 2010
			nPAGE-WB	HL-1	Pfleger et al., 2012
	Caveolin-3	P56539	nPAGE-WB	HL-1	Pfleger et al., 2012
CD14	Monocyte differentiation antigen CD14	P08571	IP-WB	HEK293	Dagvadorj et al., 2015
CD44	CD44 antigen	P16070	IP-WB	CHO-K1	Moura et al., 2015
CLTA/B/C/D	Clathrin		IP-WB	CaSKI / HEK293	Feng et al., 2005
CYFIP1	Cytoplasmic FMR1-interacting protein 1	Q7L576	IP-WB	Mouse prefrontal cortex	Li et al., 2017
DEFA1	Neutrophil defensin 1	P59665	PD-WB	HEK293	Chen et al., 2014
DNM1	Dynamin-1	Q05193	IP-WB	CaSKI / HEK293	Feng et al., 2005
EFNB3	Ephrin-B3	Q15768	Y2H	Liver cDNA library	Wang et al., 2011
EMP1/2/3	Epithelial membrane protein 1/2/3	P54849, P54851, P54852	Y2H, PD/IP-WB	HEK293	Wilson et al., 2002
Fyn	Tyrosine-protein kinase Fyn	P06241	IP-WB	OPCs, HEK293	Feng et al., 2015
GRB2	Growth factor receptor-bound protein 2	P62993	Peptide array	*In vitro*	Wu et al., 2007
GRK3	β-adrenergic receptor kinase 2	P35626	IP-WB	CaSKI / HEK293	Feng et al., 2005
HSP90AB1*	Heat shock protein HSP 90-β	P08238	IP-MS/WB	HEK293	Kim et al., 2001
			IP-WB	HEK293, peritoneal macrophages	Adinolfi et al., 2003
			IP-MS	HEK293	Gu et al., 2009
			IP-WB	PC12	Franco et al., 2013
HSPA1A*	Heat shock 70 kDa protein 1A/1B	P0DMV8	IP-MS/WB	HEK293	Kim et al., 2001
			IP-MS	HEK293	Gu et al., 2009
HSPA8*	Heat shock cognate 71 kDa protein	P11142	IP-MS/WB	HEK293	Kim et al., 2001
ITGB2	Integrin β-2	P05107	IP-MS/WB	HEK293	Kim et al., 2001
LAMA3	Laminin subunit α-3	Q16787	IP-MS/WB	HEK293	Kim et al., 2001
MPP3	MAGUK p55 subfamily member 3	Q13368	IP-MS/WB	HEK293	Kim et al., 2001
MYH9*	Myosin-9 (Myosin heavy chain, non-muscle IIa)	P35579	IP-MS/WB	THP-1	Gu et al., 2009
MyD88	Myeloid differentiation primary response protein MyD88	Q99836	IP-WB	HEK293	Liu et al., 2011
MYL12A/B*	Myosin regulatory light chain 12A, Myosin regulatory light chain 12B	P19105 O14950	IP-MS	THP-1	Gu et al., 2009
MYO5A	Unconventional myosin-Va	Q9Y4I1	IP-MS/WB	HEK293	Gu et al., 2009
NCK1	Cytoplasmic protein NCK1	P16333	Peptide array	*In vitro*	Wu et al., 2007
NLRP2/3	NACHT, LRR and PYD domains-containing protein 2	Q9NX02	IP-WB	Astrocytes	Minkiewicz et al., 2013
	NACHT, LRR and PYD domains-containing protein 3	Q9NX02	IP-WB	N13 microglia	Franceschini et al., 2015
NME2	Nucleoside diphosphate kinase B	P22392	IP-MS	HEK293	Gu et al., 2009
NOS1	Nitric oxide synthase, brain	P29475	IP-WB	Mouse brain	Pereira et al., 2013

(Continued)

TABLE 1 | Continued

Gene	Protein name	Uniprot ID (human)	Method	Cell system	References
P2RX4	P2X4 Receptor	Q99571	IP-WB	HEK293, BMDM	Guo et al., 2007
			IP-WB	BMDM	Boumechache et al., 2009
			nPAGE/IP-WB	Alveolar epithelial E10 cells	Weinhold et al., 2010
			PD/IP-WB	tsA 201	Antonio et al., 2011
			IP-WB	Primary gingival epithelial cells	Hung et al., 2013
			IP-WB	HEK293	Pérez-Flores et al., 2015
PANX1	Pannexin-1	Q96RD7	IP-WB	HEK293	Pelegrin and Surprenant, 2006
			IP-WB	J774.2	Iglesias et al., 2008
			IP-WB	Primary neurons	Silverman et al., 2009
			IP-WB	HEK293	Li et al., 2011
			IP-WB	N2a	Poornima et al., 2012
			IP-WB	HPDL	Kanjanamekanant et al., 2014
			PD-WB	N2a	Boyce and Swayne, 2017
PI4KA	Phosphatidylinositol 4-kinase α	P42356	IP-MS/WB	HEK293	Kim et al., 2001
PPIP5K1	Inositol hexakisphosphate and diphosphoinositol-pentakisphosphate kinase 1	Q6PFW1	IP-MS	THP-1	Gu et al., 2009
PMP22	Peripheral myelin protein 22	Q01453	Y2H, PD-WB	HEK293	Wilson et al., 2002
PRKCG	Protein kinase C γ type	P05129	IP-WB	Astrocyte cell line (RBA-2)	Hung et al., 2005
PTPN6	Tyrosine-protein phosphatase non-receptor type 6	P29350	IP-MS	THP-1	Gu et al., 2009
PTPRB	Receptor-type tyrosine-protein phosphatase β	P23467	IP-MS	HEK293	Kim et al., 2001
PYCARD	Apoptosis-associated speck-like protein containing a CARD (ASC)	Q9ULZ3	IP-WB	Primary neurons	Silverman et al., 2009
			IP-WB	Astrocytes	Minkiewicz et al., 2013
Snca	α-synuclein	P37840	IP-WB	Microglia cell line BV2	Jiang et al., 2015
SVIL	Supervillin	O95425	IP-MS/WB	HEK293	Kim et al., 2001
Tlr2/4	Toll-like receptor 2/4	O60603 O00206	IP-WB	Peritoneal macrophages	Babelova et al., 2009
TM9SF1	Transmembrane 9 superfamily member 1	O15321	Y2H	Liver cDNA library	Wang et al., 2011
TPR	Nucleoprotein TPR	P12270	IP-MS	HEK293	Gu et al., 2009
TRIM21*	E3 ubiquitin-protein ligase TRIM21 (52 kDa Ro protein)	P19474	IP-MS	THP-1; HEK293	Gu et al., 2009
TUBB*	Tubulin β chain	P07437	IP-MS	HEK293	Gu et al., 2009

Asterisks indicate proteins that are frequently found as contaminants in MS-based approaches (Mellacheruvu et al., 2013). PD, pull down; IP, immunoprecipitation; WB, western blot; MS, mass spectrometry; nPAGE, native PAGE; Y2H, yeast two-hybrid.

interactions have not been described. Only interaction partners that were studied in more detail and selected proteins will be briefly described in the following sections.

Proteins Involved in P2X7-Mediated Interleukin Secretion

Pathogen-associated molecular patterns like LPS activate innate immune responses via binding to TLR4. CD14 serves as a co-receptor of TLR4 to facilitate the cellular responses to LPS (Zanoni and Granucci, 2013). As described [see Section "Trafficking and Lipid Interaction Domains (∼residues 540–595)"], P2X7 harbors a potential LPS binding motif in its C-terminal domain (Denlinger et al., 2001) and CD14 was identified as a potential co-receptor of P2X7 that enables LPS internalization and binding to P2X7. Their physical interaction was shown in immunoprecipitation experiments with transfected HEK293 cells. LPS stimulation increased their co-localization and the amount of co-precipitated CD14 or P2X7 proteins (Dagvadorj et al., 2015).

MyD88 is another protein that is tightly associated with TLR function. TLR4 can signal through MyD88 to induce the synthesis of pro-inflammatory cytokines via the activation of NF-κB. In transfected HEK293 cells, it was shown that MyD88 physically interacts with P2X7, suggesting that MyD88 is responsible for P2X7-mediated NF-κB activation. The C-terminus of P2X7 and, in particular, the amino acid G586 was shown to be important for this interaction. Alanine substitution of G586 lead to a loss of P2X7 function, decreased caspase 1 cleavage activity, altered cellular localization, and impaired interaction between P2X7 and MyD88 in mouse, P2X7-expressing HEK293 cells and RAW264.7 cells (Liu et al., 2011).

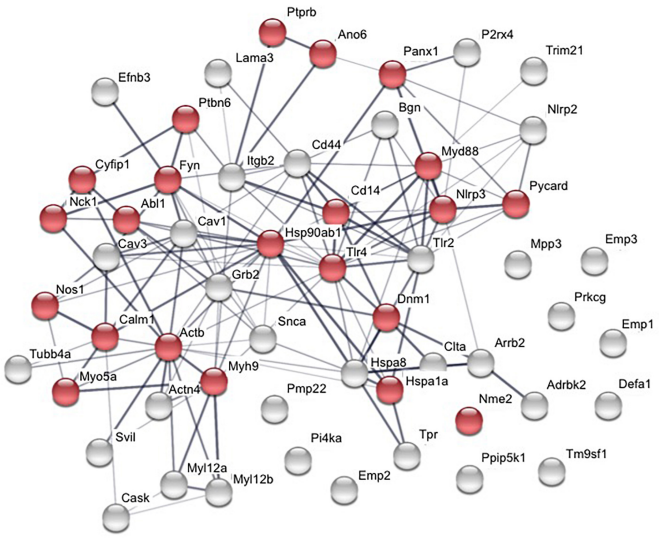

FIGURE 2 | Interaction network of published P2X7 interaction partners. Proteins were analyzed using STRING database (v11.0; Szklarczyk et al., 2019). Twenty-two proteins are involved in function of the innate immune system (shown in red). The thickness of the connecting lines indicates the strength of data support for physical and/or functional associations.

Inflammation is not only triggered by the binding of exogenous PAMPs to TLR4, but also mediated via endogenous structures. Soluble biglycan, a proteoglycan of the extracellular matrix, can activate TLR2 and 4 and stimulate inflammatory responses (Schaefer et al., 2005; Moreth et al., 2014). Co-precipitation experiments showed that biglycan can directly interact with P2X4 and P2X7 in peritoneal macrophages (Babelova et al., 2009). Interestingly, also TLR2 and 4 were co-precipitated with anti-P2X4 or anti-P2X7 antibodies in the presence of biglycan.

P2X7 was also found to directly interact with components of the inflammasome such as the adaptor protein ASC of the NLRP1 inflammasome in neurons (Silverman et al., 2009), ASC, and the NLR subunit of the NLRP2 inflammasome in astrocytes (Minkiewicz et al., 2013), and NLRP3 in N13 mouse microglial cells (Franceschini et al., 2015). For NLRP3 and P2X7 also a mutual relationship in mRNA and protein levels was detected and both proteins co-localize at discrete sites in the subplasmalemmal cytoplasm (Franceschini et al., 2015).

Pannexin-1

Pannexin-1 belongs to the pannexin family of channel-forming glycoproteins and has been reported to mediate the release of ATP (Chekeni et al., 2010). It can be activated by various stimuli (e.g., mechanical, caspase cleavage, cytoplasmic Ca^{2+}, membrane depolarization, extracellular ATP, and K^{+}; Penuela et al., 2013) and has been proposed to form the P2X7-associated macropore (Pelegrin and Surprenant, 2006). Indeed, several co-precipitation experiments revealed a physical interaction with the P2X7 receptor (Pelegrin and Surprenant, 2006; Iglesias et al., 2008; Silverman et al., 2009; Li et al., 2011; Poornima et al., 2012; Kanjanamekanant et al., 2014; Boyce and Swayne, 2017). However, negative pull-down experiments were also reported and more recent studies indicate that the macropore is an intrinsic property of P2X7 and opens immediately upon activation (Harkat et al., 2017; Karasawa et al., 2017; Pippel et al., 2017; Di Virgilio et al., 2018b). A functional interaction of P2X7 and pannexin in inflammasome activation was also described (Pelegrin and Surprenant, 2006; Locovei et al., 2007; Iglesias et al., 2008; Hung et al., 2013; Boyce et al., 2015; Boyce and Swayne, 2017) but is under discussion (Qu et al., 2011; Hanley et al., 2012; Alberto et al., 2013). As pannexin is considered to mediate the release of ATP, it might play a role upstream of P2X7 by controlling its activation (Chekeni et al., 2010; Isakson and Thompson, 2014).

Heat Shock Protein 90

Heat shock protein (HSP) 90 is a molecular chaperone and ATPase and one of the most abundant cytosolic proteins in eukaryotes. It is essential for protein folding and maturation and has been involved in many different pathologies, including

infections, cancer, and neurodegenerative diseases (Schopf et al., 2017). Two independent MS-based screening approaches in HEK293 cells identified HSP90 as potential interactor of P2X7 (Kim et al., 2001; Gu et al., 2009) and the cysteine-rich domain in the C-terminus was identified to be important for this interaction (Migita et al., 2016). Phosphorylation of HSP90 was shown to decrease P2X7 currents and membrane blebbing in HEK293 cells and rat peritoneal macrophages (Adinolfi et al., 2003). Nitration of the chaperone increased P2X7-dependent activation of the Fas pathway and subsequent apoptosis in PC12 cells (Franco et al., 2013). Fas (CD95) is a member of the tumor necrosis factor receptor (TNFR) superfamily and plays a central role in apoptosis. HSP90 was also found to be involved in P2X7 pore formation and P2X7-dependent autophagic death of dystrophic muscles (Young et al., 2015) as well as the activation of the P2X7/NLRP3 inflammasome pathway (Zuo et al., 2018). It was shown that HSP90 directly interacts with the LRR and NACHT domains of NLRP3 and is essential for inflammasome function and activity (Mayor et al., 2007).

Caveolin

Caveolins are the most abundant membrane proteins in caveolae and act as scaffolding and membrane curvature inducing proteins. Caveolae are invaginations of the plasma membrane and, similar to lipid rafts, enriched in cholesterol and glycosphingolipids (Patel and Insel, 2008). The caveolin family comprises three family members (caveolin-1, -2, -3). In E10 alveolar epithelial cells, P2X7 was found to be associated with caveolae and partially co-localized with caveolin-1 (Barth et al., 2007). A direct interaction of both proteins was shown via co-precipitation (Barth et al., 2008). This interaction was further verified via native PAGE, which indicated that both proteins are present in the same protein complex (Weinhold et al., 2010). Similar results were obtained in cardiomyocytes, where also caveolin-3 was detected (Pfleger et al., 2012). A mutual relation in expression and localization was shown (Barth et al., 2007; Weinhold et al., 2010).

Anoctamin Channels

Anoctamin channels (TMEM16 family) are calcium-activated Cl^- channels and are co-expressed with P2X7 in various cell types. Since a P2X7-mediated increase in anion conductance has been observed in several studies, a physical or functional interaction with anoctamin channels was investigated (Stolz et al., 2015). In *Xenopus laevis* and *Ambystoma mexicanum* oocytes [which lack endogenous anoctamin(s)], a functional interaction between heterologously expressed P2X7 and anoctamin-1 could be shown, but not for anoctamin-6 (Stolz et al., 2015). However, another study in the same year could show a P2X7-mediated activation of anoctamin-6 in *Xenopus laevis* oocytes, transfected HEK293 cells, and mouse macrophages and a physical interaction was also shown in co-immunoprecipitation experiments with transfected HEK293 cells (Ousingsawat et al., 2015).

Calmodulin

A novel CaM binding motif was identified in the C-terminus of rat P2X7 [compare Section "Trafficking and Lipid Interaction Domains (∼Residues 540–595)"]. The specific binding of CaM to this region was shown by co-immunoprecipitation and mutagenesis of the binding motif in HEK293 cells (Roger et al., 2008). Interestingly, this binding motif is absent in human and mouse P2X7 and indeed, an interaction of CaM with the human receptor could not be detected but reconstituted by mutagenesis (Roger et al., 2010). The binding of CaM facilitates and prolongs Ca^{2+} entry and was proposed to play a role in cytoskeletal rearrangements and membrane blebbing (Roger et al., 2008).

Myosin-9

The non-muscle myosin-9 was not only shown to co-precipitate with P2X7, but also to co-localize in the plasma membrane and membranes of intracellular organelles in a human monocytic cell line (THP-1 cells). A close association with P2X7 was confirmed by FRET experiments in HEK293 cells (Gu et al., 2009). It was proposed that P2X7 is anchored in the membrane by myosin-9 and activation of P2X7 via extracellular ATP leads to dissociation of the myosin-P2X7 complex and the formation of the large pore and membrane blebbing. It was further suggested that the integrity of this complex is required to regulate P2X7-mediated phagocytosis (Gu et al., 2010).

CONCLUSION

Blockade or genetic deletion of the P2X7 receptor has shown positive effects in numerous disease models and genetic association studies have linked SNPs of this receptor with various human diseases. While P2X7-induced cytokine secretion and/or cell death have been identified as important mechanisms that contribute to its pathophysiological role, the relevance and in particular, the molecular mechanism leading to the induction of many other identified P2X7-induced effects remain much less investigated. The extended P2X7 C-terminus has been involved in many P2X7-specific functions and is supposed to constitute a platform for intracellular interactions that initiate multiple signaling pathways. Although more than 50 interacting proteins have been identified (**Table 1**), their roles in receptor signaling, trafficking, regulation, or modification remain largely obscure and in most cases, the sites of interaction, the aa involved, and the molecular mechanisms are unknown. Many of the identified interactions are likely to depend on the type and/or state of the cell and might also be indirect or due to the association of proteins in larger domains or complexes (e.g., lipid rafts). However, the data need to be interpreted with caution as they include proteins that tend to interact with the solid-phase support or the used affinity tags and are frequently found as contaminants in affinity purification approaches followed by mass spectrometry (MS) (Mellacheruvu et al., 2013) (marked with asterisk in **Table 1**). It further has to be considered, that several proteins were identified in targeted rather than unbiased

screening approaches and most experiments were carried out in heterologous expression systems (in some of which P2X7 is not naturally occurring) and with overexpressed interaction partners, which might bear the risk of artificial aggregation.

In contrast to other receptor complexes, for which interaction partners have been defined (Schwenk et al., 2012, 2016; Hanack et al., 2015), few tight interactions that survived purification were identified for P2X7 and BN-PAGE analysis in mouse and rat tissues did not reveal bands that are reconcilable with complexes containing additional proteins besides the three P2X7 subunits (Nicke, 2008). Of the interaction partners identified in pull-down experiments, only few have been repeatedly identified or confirmed in independent studies. Thus, P2X7 interactions or complexes appear to be rather instable and the P2X7 tail might mainly have a structural role and/or serve as a scaffold for temporary and short-lived interactions in which Ca^{2+} signaling and interactions with membrane components are likely to play a major role. The specific molecular mechanisms involved are largely hypothetical and only few interaction sites have been determined by mutagenesis. Elucidation of these interactions and the downstream signaling pathways involved bears the potential to identify novel ways for therapeutic intervention.

AUTHOR CONTRIBUTIONS

AN conceived and supervised the project. All authors wrote, reviewed, and approved the manuscript. RK prepared the table. AK and RK designed the figures.

FUNDING

This work was supported by grants from the DFG (SFB 1328, A15) and the European Union's Horizon 2020 Research and Innovation Programme (Marie Skłowdowska-Curie Grant Agreement 766124) to AN.

ACKNOWLEDGMENTS

We would like to thank Isabel Müller for help with sequence comparisons.

REFERENCES

Adinolfi, E., Callegari, M. G., Cirillo, M., Pinton, P., Giorgio, C., Cavagna, D., et al. (2009). Expression of the P2X7 receptor increases the Ca2+ content of the endoplasmic reticulum, activates NFATc1, and protects from apoptosis. *J. Biol. Chem.* 284, 10120–10128. doi: 10.1074/jbc.M805805200

Adinolfi, E., Callegari, M. G., Ferrari, D., Bolognesi, C., Minelli, M., Wieckowski, M. R., et al. (2005). Basal activation of the P2X7 ATP receptor elevates mitochondrial calcium and potential, increases cellular ATP levels, and promotes serum-independent growth. *Mol. Biol. Cell* 16, 3260–3272. doi: 10.1091/mbc.e04-11-1025

Adinolfi, E., Cirillo, M., Woltersdorf, R., Falzoni, S., Chiozzi, P., Pellegatti, P., et al. (2010). Trophic activity of a naturally occurring truncated isoform of the P2X7 receptor. *FASEB J.* 24, 3393–3404. doi: 10.1096/fj.09-153601

Adinolfi, E., Kim, M., Young, M. T., Di Virgilio, F., and Surprenant, A. (2003). Tyrosine phosphorylation of HSP90 within the P2X7 receptor complex negatively regulates P2X7 receptors. *J. Biol. Chem.* 278, 37344–37351. doi: 10.1074/jbc.M301508200

Adinolfi, E., Raffaghello, L., Giuliani, A. L., Cavazzini, L., Capece, M., Chiozzi, P., et al. (2012). Expression of P2X7 receptor increases in vivo tumor growth. *Cancer Res.* 72, 2957–2969. doi: 10.1158/0008-5472.CAN-11-1947

Adriouch, S., Dox, C., Welge, V., Seman, M., Koch-Nolte, F., and Haag, F. (2002). Cutting edge: a natural P451L mutation in the cytoplasmic domain impairs the function of the mouse P2X7 receptor. *J. Immunol.* 169, 4108–4112. doi: 10.4049/jimmunol.169.8.4108

Aga, M., Johnson, C. J., Hart, A. P., Guadarrama, A. G., Suresh, M., Svaren, J., et al. (2002). Modulation of monocyte signaling and pore formation in response to agonists of the nucleotide receptor P2X(7). *J. Leukoc. Biol.* 72, 222–232.

Aga, M., Watters, J. J., Pfeiffer, Z. A., Wiepz, G. J., Sommer, J. A., and Bertics, P. J. (2004). Evidence for nucleotide receptor modulation of cross talk between MAP kinase and NF-κB signaling pathways in murine RAW 264.7 macrophages. *Am. J. Physiol. Cell Physiol.* 286, C923–C930. doi: 10.1152/ajpcell.00417.2003

Alarcon-Vila, C., Pizzuto, M., and Pelegrin, P. (2019). Purinergic receptors and the inflammatory response mediated by lipids. *Curr. Opin. Pharmacol.* 47, 90–96. doi: 10.1016/j.coph.2019.02.004

Albalawi, F., Lu, W., Beckel, J. M., Lim, J. C., McCaughey, S. A., and Mitchell, C. H. (2017). The P2X7 receptor primes IL-1β and the NLRP3 inflammasome in astrocytes exposed to mechanical strain. *Front. Cell. Neurosci.* 11:227. doi: 10.3389/fncel.2017.00227

Alberto, A. V. P., Faria, R. X., Couto, C. G. C., Ferreira, L. G. B., Souza, C. A. M., Teixeira, P. C. N., et al. (2013). Is pannexin the pore associated with the P2X7 receptor? *Naunyn Schmiedeberg's Arch. Pharmacol.* 386, 775–787. doi: 10.1007/s00210-013-0868-x

Allsopp, R. C., and Evans, R. J. (2015). Contribution of the juxtatransmembrane intracellular regions to the time course and permeation of ATP-gated P2X7 receptor ion channels. *J. Biol. Chem.* 290, 14556–14566. doi: 10.1074/jbc.M115.642033

Alzola, E., Perez-Etxebarria, A., Kabre, E., Fogarty, D. J., Metioui, M., Chaib, N., et al. (1998). Activation by P2X7 agonists of two phospholipases A2 (PLA2) in ductal cells of rat submandibular gland. Coupling of the calcium-independent PLA2 with kallikrein secretion. *J. Biol. Chem.* 273, 30208–30217. doi: 10.1074/jbc.273.46.30208

Amoroso, F., Capece, M., Rotondo, A., Cangelosi, D., Ferracin, M., Franceschini, A., et al. (2015). The P2X7 receptor is a key modulator of the PI3K/GSK3β/VEGF signaling network: evidence in experimental neuroblastoma. *Oncogene* 34, 5240–5251. doi: 10.1038/onc.2014.444

Amoroso, F., Falzoni, S., Adinolfi, E., Ferrari, D., and Di Virgilio, F. (2012). The P2X7 receptor is a key modulator of aerobic glycolysis. *Cell Death Dis.* 3:e370. doi: 10.1038/cddis.2012.105

Amstrup, J., and Novak, I. (2003). P2X7 receptor activates extracellular signal-regulated kinases ERK1 and ERK2 independently of Ca2+ influx. *Biochem. J.* 374(Pt 1), 51–61. doi: 10.1042/BJ20030585

Anderson, C. M., and Nedergaard, M. (2006). Emerging challenges of assigning P2X7 receptor function and immunoreactivity in neurons. *Trends Neurosci.* 29, 257–262. doi: 10.1016/j.tins.2006.03.003

Andrei, C., Margiocco, P., Poggi, A., Lotti, L. V., Torrisi, M. R., and Rubartelli, A. (2004). Phospholipases C and A2 control lysosome-mediated IL-1 β secretion: implications for inflammatory processes. *Proc. Natl. Acad. Sci. U.S.A.* 101, 9745–9750. doi: 10.1073/pnas.0308558101

Anrather, J., Gallo, E. F., Kawano, T., Orio, M., Abe, T., Gooden, C., et al. (2011). Purinergic signaling induces cyclooxygenase-1-dependent prostanoid synthesis in microglia: roles in the outcome of excitotoxic brain injury. *PLoS One* 6:e25916. doi: 10.1371/journal.pone.0025916

Antonio, L. S., Stewart, A. P., Xu, X. J., Varanda, W. A., Murrell-Lagnado, R. D., and Edwardson, J. M. (2011). P2X4 receptors interact with both P2X2 and P2X7 receptors in the form of homotrimers. *Br. J. Pharmacol.* 163, 1069–1077. doi: 10.1111/j.1476-5381.2011.01303.x

Aprile-Garcia, F., Metzger, M. W., Paez-Pereda, M., Stadler, H., Acuña, M., Liberman, A. C., et al. (2016). Co-Expression of wild-type P2X7R with Gln460Arg variant alters receptor function. *PLoS One* 11:e0151862. doi: 10.1371/journal.pone.0151862

Armstrong, J. N., Brust, T. B., Lewis, R. G., and MacVicar, B. A. (2002). Activation of presynaptic P2X7-like receptors depresses mossy fiber-CA3 synaptic transmission through p38 mitogen-activated protein kinase. *J. Neurosci.* 22, 5938–5945. doi: 10.1523/jneurosci.22-14-05938.2002

Armstrong, S., Pereverzev, A., Dixon, S. J., and Sims, S. M. (2009). Activation of P2X7 receptors causes isoform-specific translocation of protein kinase C in osteoclasts. *J. Cell Sci.* 122(Pt 1), 136–144. doi: 10.1242/jcs.031534

Auger, R., Motta, I., Benihoud, K., Ojcius, D. M., and Kanellopoulos, J. M. (2005). A role for mitogen-activated protein kinase(Erk1/2) activation and non-selective pore formation in P2X7 receptor-mediated thymocyte death. *J. Biol. Chem.* 280, 28142–28151. doi: 10.1074/jbc.M501290200

Babelova, A., Moreth, K., Tsalastra-Greul, W., Zeng-Brouwers, J., Eickelberg, O., Young, M. F., et al. (2009). Biglycan, a danger signal that activates the NLRP3 inflammasome via toll-like and P2X receptors. *J. Biol. Chem.* 284, 24035–24048. doi: 10.1074/jbc.M109.014266

Ballerini, P., Rathbone, M. P., Di Iorio, P., Renzetti, A., Giuliani, P., D'Alimonte, I., et al. (1996). Rat astroglial P2Z (P2X7) receptors regulate intracellular calcium and purine release. *Neuroreport* 7, 2533–2537.

Bannas, P., Adriouch, S., Kahl, S., Braasch, F., Haag, F., and Koch-Nolte, F. (2005). Activity and specificity of toxin-related mouse T cell ecto-ADP-ribosyltransferase ART2.2 depends on its association with lipid rafts. *Blood* 105, 3663–3670. doi: 10.1182/blood-2004-08-3325

Barberà-Cremades, M., Gómez, A. I., Baroja-Mazo, A., Martínez-Alarcón, L., Martínez, C. M., de Torre-Minguela, C., et al. (2017). P2X7 receptor induces tumor necrosis factor-α converting enzyme activation and release to boost TNF-α production. *Front. Immunol.* 8:862. doi: 10.3389/fimmu.2017.00862

Barden, N., Harvey, M., Gagné, B., Shink, E., Tremblay, M., Raymond, C., et al. (2006). Analysis of single nucleotide polymorphisms in genes in the chromosome 12Q24.31 region points to P2RX7 as a susceptibility gene to bipolar affective disorder. *Am. J. Med. Genet. Part B* 141, 374–382. doi: 10.1002/ajmg.b.30303

Barth, K., Weinhold, K., Guenther, A., Linge, A., Gereke, M., and Kasper, M. (2008). Characterization of the molecular interaction between caveolin-1 and the P2X receptors 4 and 7 in E10 mouse lung alveolar epithelial cells. *Int. J. Biochem. Cell Biol.* 40, 2230–2239. doi: 10.1016/j.biocel.2008.03.001

Barth, K., Weinhold, K., Guenther, A., Young, M. T., Schnittler, H., and Kasper, M. (2007). Caveolin-1 influences P2X7 receptor expression and localization in mouse lung alveolar epithelial cells. *FEBS J.* 274, 3021–3033. doi: 10.1111/j.1742-4658.2007.05830.x

Bartlett, R., Stokes, L., and Sluyter, R. (2014). The P2X7 receptor channel: recent developments and the use of P2X7 antagonists in models of disease. *Pharmacol. Rev.* 66, 638–675. doi: 10.1124/pr.113.008003

Becker, D., Woltersdorf, R., Boldt, W., Schmitz, S., Braam, U., Schmalzing, G., et al. (2008). The P2X7 carboxyl tail is a regulatory module of P2X7 receptor channel activity. *J. Biol. Chem.* 283, 25725–25734. doi: 10.1074/jbc.M803855200

Belambri, S. A., Rolas, L., Raad, H., Hurtado-Nedelec, M., Dang, P. M., and El-Benna, J. (2018). NADPH oxidase activation in neutrophils: role of the phosphorylation of its subunits. *Eur. J. Clin. Invest.* 48(Suppl. 2), e12951. doi: 10.1111/eci.12951

Bernier, L. P., Ase, A. R., and Seguela, P. (2013). Post-translational regulation of P2X receptor channels: modulation by phospholipids. *Front. Cell Neurosci.* 7:226. doi: 10.3389/fncel.2013.00226

Bianco, F., Perrotta, C., Novellino, L., Francolini, M., Riganti, L., Menna, E., et al. (2009). Acid sphingomyelinase activity triggers microparticle release from glial cells. *EMBO J.* 28, 1043–1054. doi:10.1038/emboj.2009.45

Bianco, F., Pravettoni, E., Colombo, A., Schenk, U., Möller, T., Matteoli, M., et al. (2005). Astrocyte-derived ATP induces vesicle shedding and IL-1 β release from microglia. *J. Immunol.* 174, 7268–7277. doi:10.4049/jimmunol.174.11.7268

Bobanovic, L. K., Royle, S. J., and Murrell-Lagnado, R. D. (2002). P2X receptor trafficking in neurons is subunit specific. *J. Neurosci.* 22, 4814–4824. doi: 10.1523/jneurosci.22-12-04814.2002

Boldt, W., Klapperstück, M., Büttner, C., Sadtler, S., Schmalzing, G., and Markwardt, F. (2013). Glu 496 Ala polymorphism of human P2X 7 receptor does not affect its electrophysiological phenotype. *Am. J. Physiol. Cell Physiol.* 284, C749–C756. doi: 10.1152/ajpcell.00042.2002

Boumechache, M., Masin, M., Edwardson, J. M., Górecki, D., and Murrell-Lagnado, R. (2009). Analysis of assembly and trafficking of native P2X4 and P2X7 receptor complexes in rodent immune cells. *J. Biol. Chem.* 284, 13446–13454. doi: 10.1074/jbc.M901255200

Boyce, A. K. J., Kim, M. S., Wicki-Stordeur, L. E., and Swayne, L. A. (2015). ATP stimulates pannexin 1 internalization to endosomal compartments. *Biochem. J.* 470, 319–330. doi: 10.1042/BJ20141551

Boyce, A. K. J., and Swayne, L. A. (2017). P2X7 receptor cross-talk regulates ATP-induced pannexin 1 internalization. *Biochem. J.* 474, 2133–2144. doi: 10.1042/BCJ20170257

Bradford, M. D., and Soltoff, S. P. (2002). P2X7 receptors activate protein kinase D and p42/p44 mitogen-activated protein kinase (MAPK) downstream of protein kinase C. *Biochem. J.* 366(Pt 3), 745–755. doi: 10.1042/BJ20020358

Browne, L. E., Compan, V., Bragg, L., and North, R. A. (2013). P2X7 receptor channels allow direct permeation of nanometer-sized dyes. *J. Neurosci.* 33, 3557–3566. doi: 10.1523/jneurosci.2235-12.2013

Bruntz, R. C., Lindsley, C. W., and Brown, H. A. (2014). Phospholipase D signaling pathways and phosphatidic acid as therapeutic targets in cancer. *Pharmacol. Rev.* 66, 1033–1079. doi: 10.1124/pr.114.009217

Burnstock, G., and Knight, G. E. (2018). The potential of P2X7 receptors as a therapeutic target, including inflammation and tumour progression. *Purinergic Signal.* 14, 1–18. doi: 10.1007/s11302-017-9593-0

Carrasquero, L. M., Delicado, E. G., Sanchez-Ruiloba, L., Iglesias, T., and Miras-Portugal, M. T. (2010). Mechanisms of protein kinase D activation in response to P2Y(2) and P2X7 receptors in primary astrocytes. *Glia* 58, 984–995. doi: 10.1002/glia.20980

Casas-Pruneda, G., Reyes, J. P., Pérez-Flores, G., Pérez-Cornejo, P., and Arreola, J. (2009). Functional interactions between P2X4 and P2X7 receptors from mouse salivary epithelia. *J. Physiol.* 587, 2887–2901. doi: 10.1113/jphysiol.2008.167395

Chaib, N., Kabre, E., Alzola, E., Pochet, S., and Dehaye, J. P. (2000). Bromoenol lactone enhances the permeabilization of rat submandibular acinar cells by P2X7 agonists. *Br. J. Pharmacol.* 129, 703–708. doi: 10.1038/sj.bjp.0703124

Charras, G. T. (2008). A short history of blebbing. *J. Microsc.* 231, 466–478. doi: 10.1111/j.1365-2818.2008.02059.x

Chaumont, S., and Khakh, B. S. (2008). Patch-clamp coordinated spectroscopy shows P2X2 receptor permeability dynamics require cytosolic domain rearrangements but not Panx-1 channels. *Proc. Natl. Acad. Sci. U.S.A.* 105, 12063–12068. doi: 10.1073/pnas.0803008105

Chekeni, F. B., Elliott, M. R., Sandilos, J. K., Walk, S. F., Kinchen, J. M., Lazarowski, E. R., et al. (2010). Pannexin 1 channels mediate 'find-me' signal release and membrane permeability during apoptosis. *Nature* 467, 863–867. doi: 10.1038/nature09413

Chen, J. R., Ben, J. G. U., Dao, L. P., Bradley, C. J., Mulligan, S. P., and Wiley, J. S. (1999). Transendothelial migration of lymphocytes in chronic lymphocytic leukaemia is impaired and involves down-regulation of both L-selectin and CD23. *Br. J. Haematol.* 105, 181–189. doi: 10.1111/j.1365-2141.1999.01278.x

Chen, Q., Jin, Y., Zhang, K., Li, H., Chen, W., Meng, G., et al. (2014). Alarmin HNP-1 promotes pyroptosis and IL-1β release through different roles of NLRP3 inflammasome via P2X7 in LPS-primed macrophages. *Innate Immun.* 20, 290–300. doi: 10.1177/1753425913490575

Christian, F., Smith, E., and Carmody, R. (2016). The Regulation of NF-κB subunits by phosphorylation. *Cells* 5, 12–12. doi: 10.3390/cells5010012

Clark, A. K., Wodarski, R., Guida, F., Sasso, O., and Malcangio, M. (2010). Cathepsin S release from primary cultured microglia is regulated by the P2X7 receptor. *Glia* 58, 1710–1726. doi: 10.1002/glia.21042

Costa-Junior, H. M., Marques-da-Silva, C., Vieira, F. S., Moncao-Ribeiro, L. C., and Coutinho-Silva, R. (2011). Lipid metabolism modulation by the P2X7 receptor in the immune system and during the course of infection: new insights into the old view. *Purinergic Signal.* 7, 381–392. doi: 10.1007/s11302-011-9255-6

Coutinho-Silva, R., Stahl, L., Raymond, M. N., Jungas, T., Verbeke, P., Burnstock, G., et al. (2003). Inhibition of chlamydial infectious activity due to P2X7R-dependent phospholipase D activation. *Immunity* 19, 403–412. doi: 10.1016/s1074-7613(03)00235-8

Craigie, E., Birch, R. E., Unwin, R. J., and Wildman, S. S. (2013). The relationship between P2X4 and P2X7: A physiologically important interaction? *Front. Physiol.* 4:216. doi: 10.3389/fphys.2013.00216

Dagvadorj, J., Shimada, K., Chen, S., Jones, H. D., Tumurkhuu, G., Zhang, W., et al. (2015). Lipopolysaccharide induces alveolar macrophage necrosis via CD14 and the P2X7 receptor leading to interleukin-1α release. *Immunity* 42, 640–653. doi: 10.1016/j.immuni.2015.03.007

de Torre-Minguela, C., Barbera-Cremades, M., Gomez, A. I., Martin-Sanchez, F., and Pelegrin, P. (2016). Macrophage activation and polarization modify P2X7 receptor secretome influencing the inflammatory process. *Sci. Rep.* 6:22586. doi: 10.1038/srep22586

Denlinger, L. C., Fisette, P. L., Sommer, J. A., Watters, J. J., Prabhu, U., Dubyak, G. R., et al. (2001). Cutting edge: the nucleotide receptor P2X7 contains multiple protein- and lipid-interaction motifs including a potential binding site for bacterial lipopolysaccharide. *J. Immunol.* 167, 1871–1876. doi: 10.4049/jimmunol.167.4.1871

Denlinger, L. C., Sommer, J. A., Parker, K., Gudipaty, L., Fisette, P. L., Watters, J. W., et al. (2003). Mutation of a dibasic amino acid motif within the C terminus of the P2X7 nucleotide receptor results in trafficking defects and impaired function. *J. Immunol.* 171, 1304–1311. doi: 10.4049/jimmunol.171.3.1304

Di, A., Xiong, S., Ye, Z., Malireddi, R. K. S., Kometani, S., Zhong, M., et al. (2018). The TWIK2 Potassium Efflux Channel in Macrophages Mediates NLRP3 Inflammasome-Induced Inflammation. *Immunity* 49, 56.e4–65.e4. doi: 10.1016/j.immuni.2018.04.032

Di Virgilio, F., Dal Ben, D., Sarti, A. C., Giuliani, A. L., and Falzoni, S. (2017). The P2X7 Receptor in Infection and Inflammation. *Immunity* 47, 15–31. doi: 10.1016/j.immuni.2017.06.020

Di Virgilio, F., Sarti, A. C., and Grassi, F. (2018a). Modulation of innate and adaptive immunity by P2X ion channels. *Curr. Opin. Immun.* 52, 51–59. doi: 10.1016/j.coi.2018.03.026

Di Virgilio, F., Schmalzing, G., and Markwardt, F. (2018b). The elusive P2X7 macropore. *Trends Cell Biol.* 28, 392–404. doi: 10.1016/j.tcb.2018.01.005

Diaz-Hernandez, M., del Puerto, A., Diaz-Hernandez, J. I., Diez-Zaera, M., Lucas, J. J., Garrido, J. J., et al. (2008). Inhibition of the ATP-gated P2X7 receptor promotes axonal growth and branching in cultured hippocampal neurons. *J. Cell Sci.* 121(Pt 22), 3717–3728. doi: 10.1242/jcs.034082

Diaz-Rodriguez, E., Montero, J. C., Esparis-Ogando, A., Yuste, L., and Pandiella, A. (2002). Extracellular signal-regulated kinase phosphorylates tumor necrosis factor α-converting enzyme at threonine 735: a potential role in regulated shedding. *Mol. Biol. Cell* 13, 2031–2044. doi: 10.1091/mbc.01-11-0561

Dinarello, C. A. (2018). Introduction to the interleukin-1 family of cytokines and receptors: drivers of innate inflammation and acquired immunity. *Immunol. Rev.* 281, 5–7. doi: 10.1111/imr.12624

Donnelly-Roberts, D. L., Namovic, M. T., Han, P., and Jarvis, M. F. (2009). Mammalian P2X7 receptor pharmacology: comparison of recombinant mouse, rat and human P2X7 receptors. *Br. J. Pharmacol.* 157, 1203–1214. doi: 10.1111/j.1476-5381.2009.00233.x

Duan, S., Anderson, C. M., Keung, E. C., Chen, Y., Chen, Y., and Swanson, R. A. (2003). P2X7 receptor-mediated release of excitatory amino acids from astrocytes. *J. Neurosci.* 23, 1320–1328. doi: 10.1523/jneurosci.23-04-01320.2003

Dubyak, G. R. (2007). Go it alone no more–P2X7 joins the society of heteromeric ATP-gated receptor channels. *Mol. Pharmacol.* 72, 1402–1405. doi: 10.1124/mol.107.042077

Dubyak, G. R. (2012). P2X7 receptor regulation of non-classical secretion from immune effector cells. *Cell Microbiol.* 14, 1697–1706. doi: 10.1111/cmi.12001

El Ouaaliti, M., Seil, M., and Dehaye, J. P. (2012). Activation of calcium-insensitive phospholipase A2 (iPLA 2) by P2X7 receptors in murine peritoneal macrophages. *Prostaglandins Other Lipid Mediat.* 99, 116–123. doi: 10.1016/j.prostaglandins.2012.09.005

Elliott, J. I., Surprenant, A., Marelli-Berg, F. M., Cooper, J. C., Cassady-Cain, R. L., Wooding, C., et al. (2005). Membrane phosphatidylserine distribution as a non-apoptotic signalling mechanism in lymphocytes. *Nature Cell Biol.* 7, 808–816. doi: 10.1038/ncb1279

el-Moatassim, C., and Dubyak, G. R. (1992). A novel pathway for the activation of phospholipase D by P2z purinergic receptors in BAC1.2F5 macrophages. *J. Biol. Chem.* 267, 23664–23673.

Evavold, C. L., Ruan, J., Tan, Y., Xia, S., Wu, H., and Kagan, J. C. (2018). The pore-forming protein gasdermin D regulates interleukin-1 secretion from living macrophages. *Immunity* 48 35.e6–44.e6. doi: 10.1016/j.immuni.2017.11.013

Fackler, O. T., and Grosse, R. (2008). Cell motility through plasma membrane blebbing. *J. Cell Biol.* 181, 879–884. doi: 10.1083/jcb.200802081

Fairbairn, I. P., Stober, C. B., Kumararatne, D. S., and Lammas, D. A. (2001). ATP-mediated killing of intracellular mycobacteria by macrophages is a P2X(7)-dependent process inducing bacterial death by phagosome-lysosome fusion. *J. Immunol.* 167, 3300–3307. doi: 10.4049/jimmunol.167.6.3300

Feng, J.-F., Gao, X.-F., Pu, Y.-y., Burnstock, G., Xiang, Z., and He, C. (2015). P2X7 receptors and Fyn kinase mediate ATP-induced oligodendrocyte progenitor cell migration. *Purinergic Signal.* 11, 361–369. doi: 10.1007/s11302-015-9458-3

Feng, Y.-H., Wang, L., Wang, Q., Li, X., Zeng, R., and Gorodeski, G. I. (2005). ATP stimulates GRK-3 phosphorylation and β-arrestin-2-dependent internalization of $P2X_7$ receptor. *Am. J. Physiol. Cell Physiol.* 288, C1342–C1356. doi: 10.1152/ajpcell.00315.2004

Ferrari, D., Chiozzi, P., Falzoni, S., Dal Susino, M., Collo, G., Buell, G., et al. (1997a). ATP-mediated cytotoxicity in microglial cells. *Neuropharmacology* 36, 1295–1301. doi: 10.1016/s0028-3908(97)00137-8

Ferrari, D., Wesselborg, S., Bauer, M. K., and Schulze-Osthoff, K. (1997b). Extracellular ATP activates transcription factor NF-kappaB through the P2Z purinoreceptor by selectively targeting NF-kappaB p65. *J. Cell Biol.* 139, 1635–1643. doi: 10.1083/jcb.139.7.1635

Ferrari, D., Stroh, C., and Schulze-Osthoff, K. (1999). P2X7/P2Z purinoreceptor-mediated activation of transcription factor NFAT in microglial cells. *J. Biol. Chem.* 274, 13205–13210. doi: 10.1074/jbc.274.19.13205

Franceschini, A., Capece, M., Chiozzi, P., Falzoni, S., Sanz, J. M., Sarti, A. C., et al. (2015). The P2X7 receptor directly interacts with the NLRP3 inflammasome scaffold protein. *FASEB J.* 29, 2450–2461. doi: 10.1096/fj.14-268714

Franco, M. C., Ye, Y., Refakis, C. A., Feldman, J. L., Stokes, A. L., Basso, M., et al. (2013). Nitration of Hsp90 induces cell death. *Proc. Natl. Acad. Sci.* 110, E1102–E1111. doi: 10.1073/pnas.1215177110

Friedle, S. A., Brautigam, V. M., Nikodemova, M., Wright, M. L., and Watters, J. J. (2011). The P2X7-Egr pathway regulates nucleotide-dependent inflammatory gene expression in microglia. *Glia* 59, 1–13. doi: 10.1002/glia.21071

Fukami, K., Inanobe, S., Kanemaru, K., and Nakamura, Y. (2010). Phospholipase C is a key enzyme regulating intracellular calcium and modulating the phosphoinositide balance. *Prog. Lipid Res.* 49, 429–437. doi: 10.1016/j.plipres.2010.06.001

Fuller, S. J., Stokes, L., Skarratt, K. K., Gu, B. J., and Wiley, J. S. (2009). Genetics of the P2X7 receptor and human disease. *Purinergic signal.* 5, 257–262. doi: 10.1007/s11302-009-9136-4

Garbers, C., Jänner, N., Chalaris, A., Moss, M. L., Floss, D. M., Meyer, D., et al. (2011). Species specificity of ADAM10 and ADAM17 proteins in interleukin-6 (IL-6) trans-signaling and novel role of ADAM10 in inducible IL-6 receptor shedding. *J. Biol. Chem.* 286, 14804–14811. doi: 10.1074/jbc.M111.229393

Garcia-Marcos, M., Pérez-Andrés, E., Tandel, S., Fontanils, U., Kumps, A., Kabré, E., et al. (2006a). Coupling of two pools of P2X7 receptors to distinct intracellular signaling pathways in rat submandibular gland. *J. Lipid Res.* 47, 705–714. doi: 10.1194/jlr.M500408-JLR200

Garcia-Marcos, M., Pochet, S., Marino, A., and Dehaye, J.-P. (2006b). P2X7 and phospholipid signalling: the search of the "missing link" in epithelial cells. *Cell. Signal.* 18, 2098–2104. doi: 10.1016/j.cellsig.2006.05.008

Gargett, C. E., Cornish, E. J., and Wiley, J. S. (1996). Phospholipase D activation by P2Z-purinoceptor agonists in human lymphocytes is dependent on bivalent cation influx. *Biochem. J.* 313(Pt 2), 529–535. doi: 10.1042/bj3130529

Gavala, M. L., Hill, L. M., Lenertz, L. Y., Karta, M. R., and Bertics, P. J. (2010). Activation of the transcription factor FosB/activating protein-1 (AP-1) is a prominent downstream signal of the extracellular nucleotide receptor P2RX7 in monocytic and osteoblastic cells. *J. Biol. Chem.* 285, 34288–34298. doi: 10.1074/jbc.M110.142091

Gendron, F. P., Neary, J. T., Theiss, P. M., Sun, G. Y., Gonzalez, F. A., and Weisman, G. A. (2003). Mechanisms of P2X7 receptor-mediated ERK1/2 phosphorylation

in human astrocytoma cells. *Am. J. Physiol. Cell Physiol.* 284, C571–C581. doi: 10.1152/ajpcell.00286.2002

Genetos, D. C., Karin, N. J., Geist, D. J., Donahue, H. J., and Duncan, R. L. (2011). Purinergic signaling is required for fluid shear stress-induced NF-κB translocation in osteoblasts. *Exp. Cell Res.* 317, 737–744. doi: 10.1016/j.yexcr.2011.01.007

Ghiringhelli, F., Apetoh, L., Tesniere, A., Aymeric, L., Ma, Y., Ortiz, C., et al. (2009). Activation of the NLRP3 inflammasome in dendritic cells induces IL-1B-dependent adaptive immunity against tumors. *Nat. Med.* 15, 1170–1178. doi: 10.1038/nm.2028

Giuliani, A. L., Colognesi, D., Ricco, T., Roncato, C., Capece, M., Amoroso, F., et al. (2014). Trophic activity of human P2X7 receptor isoforms A and B in osteosarcoma. *PLoS One* 9:e107224. doi: 10.1371/journal.pone.0107224

Giuliani, A. L., Sarti, A. C., Falzoni, S., and Di Virgilio, F. (2017). The P2X7 Receptor-Interleukin-1 liaison. *Front. Pharmacol.* 8:123. doi: 10.3389/fphar.2017.00123

Gomez-Munoz, A., Presa, N., Gomez-Larrauri, A., Rivera, I. G., Trueba, M., and Ordonez, M. (2016). Control of inflammatory responses by ceramide, sphingosine 1-phosphate and ceramide 1-phosphate. *Prog. Lipid Res.* 61, 51–62. doi: 10.1016/j.plipres.2015.09.002

Gomez-Villafuertes, R., del Puerto, A., Diaz-Hernandez, M., Bustillo, D., Diaz-Hernandez, J. I., Huerta, P. G., et al. (2009). Ca2+/calmodulin-dependent kinase II signalling cascade mediates P2X7 receptor-dependent inhibition of neuritogenesis in neuroblastoma cells. *FEBS J.* 276, 5307–5325. doi: 10.1111/j.1742-4658.2009.07228.x

Gonnord, P., Delarasse, C., Auger, R., Benihoud, K., Prigent, M., Cuif, M. H., et al. (2008). Palmitoylation of the P2X7 receptor, an ATP-gated channel, controls its expression and association with lipid rafts. *FASEB J.* 23, 795–805. doi: 10.1096/fj.08-114637

Graziano, F., Desdouits, M., Garzetti, L., Podini, P., Alfano, M., Rubartelli, A., et al. (2015). Extracellular ATP induces the rapid release of HIV-1 from virus containing compartments of human macrophages. *Proc. Natl. Acad. Sci. U.S.A.* 112, E3265–E3273. doi: 10.1073/pnas.1500656112

Gross, O., Thomas, C. J., Guarda, G., and Tschopp, J. (2011). The inflammasome: an integrated view. *Immunol. Rev.* 243, 136–151. doi: 10.1111/j.1600-065X.2011.01046.x

Grötzinger, J., Lorenzen, I., and Düsterhöft, S. (2017). Molecular insights into the multilayered regulation of ADAM17: the role of the extracellular region. *Biochim. Biophys. Acta Mol. Cell Res.* 1864, 2088–2095. doi: 10.1016/j.bbamcr.2017.05.024

Gu, B., Bendall, L. J., and Wiley, J. S. (1998). Adenosine triphosphate-induced shedding of CD23 and L-selectin (CD62L) from lymphocytes is mediated by the same receptor but different metalloproteases. *Blood* 92, 946–951.

Gu, B. J., Rathsam, C., Stokes, L., McGeachie, A. B., and Wiley, J. S. (2009). Extracellular ATP dissociates nonmuscle myosin from P2X(7) complex: this dissociation regulates P2X(7) pore formation. *Am. J. Physiol. Cell Physiol.* 297, C430–C439. doi: 10.1152/ajpcell.00079.2009

Gu, B. J., Saunders, B. M., Jursik, C., and Wiley, J. S. (2010). The P2X7-nonmuscle myosin membrane complex regulates phagocytosis of nonopsonized particles and bacteria by a pathway attenuated by extracellular ATP. *Blood* 115, 1621–1631. doi: 10.1182/blood-2009-11-251744

Gu, B. J., Zhang, W., Worthington, R. A., Sluyter, R., Dao-Ung, P., Petrou, S., et al. (2001). A Glu-496 to Ala polymorphism leads to loss of function of the human P2X7 receptor. *J. Biol. Chem.* 276, 11135–11142. doi: 10.1074/jbc.M010353200

Guerra, A. N., Gavala, M. L., Chung, H. S., and Bertics, P. J. (2007). Nucleotide receptor signalling and the generation of reactive oxygen species. *Purinergic Signal.* 3, 39–51. doi: 10.1007/s11302-006-9035-x

Guo, C., Masin, M., Qureshi, O. S., and Murrell-Lagnado, R. D. (2007). Evidence for functional P2X4/P2X7 heteromeric receptors. *Mol. Pharmacol.* 72, 1447–1456. doi: 10.1124/mol.107.035980

Hanack, C., Moroni, M., Lima, W. C., Wende, H., Kirchner, M., Adelfinger, L., et al. (2015). GABA blocks pathological but not acute TRPV1 pain signals. *Cell* 160, 759–770. doi: 10.1016/j.cell.2015.01.022

Hanley, P. J., Kronlage, M., Kirschning, C., Del Rey, A., Di Virgilio, F., Leipziger, J., et al. (2012). Transient P2X 7 receptor activation triggers macrophage death independent of toll-like receptors 2 and 4, caspase-1, and pannexin-1 proteins. *J. Biol. Chem.* 287, 10650–10663. doi: 10.1074/jbc.M111.332676

Harkat, M., Peverini, L., Cerdan, A. H., Dunning, K., Beudez, J., Martz, A., et al. (2017). On the permeation of large organic cations through the pore of ATP-gated P2X receptors. *Proc. Natl. Acad. Sci. U.S.A.* 114, E3786–E3795. doi: 10.1073/pnas.1701379114

Haslund-Vinding, J., McBean, G., Jaquet, V., and Vilhardt, F. (2017). NADPH oxidases in oxidant production by microglia: activating receptors, pharmacology and association with disease. *Br. J. Pharmacol.* 174, 1733–1749. doi: 10.1111/bph.13425

He, Y., Hara, H., and Nunez, G. (2016a). Mechanism and regulation of NLRP3 inflammasome activation. *Trends Biochem. Sci.* 41, 1012–1021. doi: 10.1016/j.tibs.2016.09.002

He, Y., Zeng, M. Y., Yang, D., Motro, B., and Nunez, G. (2016b). NEK7 is an essential mediator of NLRP3 activation downstream of potassium efflux. *Nature* 530, 354–357. doi: 10.1038/nature16959

Hibell, A. D., Thompson, K. M., Simon, J., Xing, M., Humphrey, P. P., and Michel, A. D. (2001). Species- and agonist-dependent differences in the deactivation-kinetics of P2X7 receptors. *Naunyn Schmiedebergs Arch. Pharmacol.* 363, 639–648. doi: 10.1007/s002100100412

Hirayama, Y., Ikeda-Matsuo, Y., Notomi, S., Enaida, H., Kinouchi, H., and Koizumi, S. (2015). Astrocyte-mediated ischemic tolerance. *J. Neurosci.* 35, 3794–3805. doi: 10.1523/JNEUROSCI.4218-14.2015

Hirayama, Y., and Koizumi, S. (2017). Hypoxia-independent mechanisms of HIF-1α expression in astrocytes after ischemic preconditioning. *Glia* 65, 523–530. doi: 10.1002/glia.23109

Hou, Z., and Cao, J. (2016). Comparative study of the P2X gene family in animals and plants. *Purinergic Signal.* 12, 269–281. doi: 10.1007/s11302-016-9501-z

Hu, Y., Fisette, P. L., Denlinger, L. C., Guadarrama, A. G., Sommer, J. A., Proctor, R. A., et al. (1998). Purinergic receptor modulation of lipopolysaccharide signaling and inducible nitric-oxide synthase expression in RAW 264.7 macrophages. *J. Biol. Chem.* 273, 27170–27175. doi: 10.1074/jbc.273.42.27170

Humphreys, B. D., and Dubyak, G. R. (1996). Induction of the P2z/P2X7 nucleotide receptor and associated phospholipase D activity by lipopolysaccharide and IFN-gamma in the human THP-1 monocytic cell line. *J. Immunol.* 157, 5627–5637.

Humphreys, B. D., Rice, J., Kertesy, S. B., and Dubyak, G. R. (2000). Stress-activated protein kinase/JNK activation and apoptotic induction by the macrophage P2X7 nucleotide receptor. *J. Biol. Chem.* 275, 26792–26798. doi: 10.1074/jbc.M002770200

Hung, A. C., Chu, Y. J., Lin, Y. H., Weng, J. Y., Chen, H. B., Au, Y. C., et al. (2005). Roles of protein kinase C in regulation of P2X7 receptor-mediated calcium signalling of cultured type-2 astrocyte cell line, RBA-2. *Cell. Signal.* 17, 1384–1396. doi: 10.1016/j.cellsig.2005.02.009

Hung, A. C., and Sun, S. H. (2002). The P2X(7) receptor-mediated phospholipase D activation is regulated by both PKC-dependent and PKC-independent pathways in a rat brain-derived Type-2 astrocyte cell line, RBA-2. *Cell. Signal.* 14, 83–92. doi: 10.1016/s0898-6568(01)00230-3

Hung, S. C., Choi, C. H., Said-Sadier, N., Johnson, L., Atanasova, K. R., Sellami, H., et al. (2013). P2X4 assembles with P2X7 and Pannexin-1 in gingival epithelial cells and modulates ATP-induced reactive oxygen species production and inflammasome activation. *PLoS One* 8:e70210. doi: 10.1371/journal.pone.0070210

Iglesias, R., Locovei, S., Roque, A., Alberto, A. P., Dahl, G., Spray, D. C., et al. (2008). P2X 7 receptor-Pannexin1 complex: pharmacology and signaling. *Am. J. Physiol. Cell Physiol.* 295, C752–C760. doi: 10.1152/ajpcell.00228.2008

Illes, P., Khan, T. M., and Rubini, P. (2017). Neuronal P2X7 receptors revisited: do they really exist? *J. Neurosci.* 37, 7049–7062. doi: 10.1523/jneurosci.3103-16.2017

Isakson, B. E., and Thompson, R. J. (2014). Pannexin-1 as a potentiator of ligand-gated receptor signaling. *Channels* 8, 118–123. doi: 10.4161/chan.27978

Ivetic, A. (2018). A head-to-tail view of L-selectin and its impact on neutrophil behaviour. *Cell Tissue Res.* 371, 437–453. doi: 10.1007/s00441-017-2774-x

Jabs, R., Matthias, K., Grote, A., Grauer, M., Seifert, G., and Steinhauser, C. (2007). Lack of P2X receptor mediated currents in astrocytes and GluR type glial cells of the hippocampal CA1 region. *Glia* 55, 1648–1655. doi: 10.1002/glia.20580

Jacques-Silva, M. C., Rodnight, R., Lenz, G., Liao, Z., Kong, Q., Tran, M., et al. (2004). P2X7 receptors stimulate AKT phosphorylation in astrocytes. *Br. J. Pharmacol.* 141, 1106–1117. doi: 10.1038/sj.bjp.0705685

Jamieson, G. P., Snook, M. B., Thurlow, P. J., and Wiley, J. S. (1996). Extracellular ATP causes loss of L-selectin from human lymphocytes via occupancy of P2Z purinoceptors. *J. Cell. Physiol.* 166, 637–642. doi: 10.1002/(sici)1097-4652(199603)166:3<637::aid-jcp19>3.3.co;2-1

Janks, L., Sprague, R. S., and Egan, T. M. (2019). ATP-gated P2X7 receptors require chloride channels to promote inflammation in human macrophages. *J. Immunol.* 202, 883–898. doi: 10.4049/jimmunol.1801101

Jiang, L.-H., Rassendren, F., Mackenzie, A., Zhang, Y.-H., Surprenant, A., and North, R. A. (2005). N-methyl-d-glucamine and propidium dyes utilize different permeation pathways at rat P2X7 receptors. *Am. J. Physiol. Cell Physiol.* 289, C1295–C1302. doi: 10.1152/ajpcell.00253.2005

Jiang, T., Hoekstra, J., Heng, X., Kang, W., Ding, J., Liu, J., et al. (2015). P2X7 receptor is critical in α-synuclein–mediated microglial NADPH oxidase activation. *Neurobiol. Aging* 36, 2304–2318. doi: 10.1016/j.neurobiolaging.2015.03.015

Kaczmarek-Hájek, K., Lörinczi, É, Hausmann, R., and Nicke, A. (2012). Molecular and functional properties of P2X receptors-recent progress and persisting challenges. *Purinergic Signal.* 8, 375–417. doi: 10.1007/s11302-012-9314-7

Kaczmarek-Hájek, K., Zhang, J., Kopp, R., Grosche, A., Rissiek, B., Saul, A., et al. (2018). Re-evaluation of neuronal P2X7 expression using novel mouse models and a P2X7-specific nanobody. *eLife* 7:e36217. doi: 10.7554/elife.36217

Kahlenberg, J. M., and Dubyak, G. R. (2004). Mechanisms of caspase-1 activation by P2X7 receptor-mediated K+ release. *Am. J. Physiol. Cell Physiol.* 286, C1100–C1108. doi: 10.1152/ajpcell.00494.2003

Kahlenberg, J. M., Lundberg, K. C., Kertesy, S. B., Qu, Y., and Dubyak, G. R. (2005). Potentiation of caspase-1 activation by the P2X7 receptor is dependent on TLR signals and requires NF-kappaB-driven protein synthesis. *J. Immunol.* 175, 7611–7622. doi: 10.4049/jimmunol.175.11.7611

Kaneko, T., Li, L., and Li, S. S. C. (2008). The SH3 domain–a family of versatile peptide- and protein-recognition module. *Front. Biosci.* 13, 4938–4952.

Kanjanamekanant, K., Luckprom, P., and Pavasant, P. (2014). P2X7 receptor-Pannexin1 interaction mediates stress-induced interleukin-1 β expression in human periodontal ligament cells. *J. Periodontal Res.* 49, 595–602. doi: 10.1111/jre.12139

Karasawa, A., Michalski, K., Mikhelzon, P., and Kawate, T. (2017). The P2X7 receptor forms a dye-permeable pore independent of its intracellular domain but dependent on membrane lipid composition. *eLife* 6, 1–22. doi: 10.7554/elife.31186

Kataoka, A., Tozaki-Saitoh, H., Koga, Y., Tsuda, M., and Inoue, K. (2009). Activation of P2X7 receptors induces CCL3 production in microglial cells through transcription factor NFAT. *J. Neurochem.* 108, 115–125. doi: 10.1111/j.1471-4159.2008.05744.x

Kawano, A., Tsukimoto, M., Noguchi, T., Hotta, N., Harada, H., Takenouchi, T., et al. (2012). Involvement of P2X4 receptor in P2X7 receptor-dependent cell death of mouse macrophages. *Biochem. Biophys. Res. Commun.* 419, 374–380. doi: 10.1016/j.bbrc.2012.01.156

Kawate, T., Michel, J. C., Birdsong, W. T., and Gouaux, E. (2009). Crystal structure of the ATP-gated P2X4 ion channel in the closed state. *Nature* 460, 592–598. doi: 10.1038/nature08198

Keller, M., Ruegg, A., Werner, S., and Beer, H. D. (2008). Active caspase-1 is a regulator of unconventional protein secretion. *Cell* 132, 818–831. doi: 10.1016/j.cell.2007.12.040

Khakh, B. S., Bao, X. R., Labarca, C., and Lester, H. A. (1999). Neuronal P2X transmitter-gated cation channels change their ion selectivity in seconds. *Nat. Neurosci.* 2, 322–330. doi: 10.1038/7233

Khakh, B. S., and Egan, T. M. (2005). Contribution of transmembrane regions to ATP-gated P2X2 channel permeability dynamics. *J. Biol. Chem.* 280, 6118–6129. doi: 10.1074/jbc.M411324200

Kim, J. E., Kim, D. S., Jin Ryu, H., Il Kim, W., Kim, M. J., Won Kim, D., et al. (2013). The effect of P2X7 receptor activation on nuclear factor-kappa B phosphorylation induced by status epilepticus in the rat hippocampus. *Hippocampus* 23, 500–514. doi: 10.1002/hipo.22109

Kim, M., Jiang, L. H., Wilson, H. L., North, R. A., and Surprenant, A. (2001). Proteomic and functional evidence for a P2X7 receptor signalling complex. *EMBO J.* 20, 6347–6358. doi: 10.1093/emboj/20.22.6347

Korcok, J., Raimundo, L. N., Ke, H. Z., Sims, S. M., and Dixon, S. J. (2004). Extracellular nucleotides act through P2X7 receptors to activate NF-κB in osteoclasts. *J. Bone Miner. Res.* 19, 642–651. doi: 10.1359/JBMR.040108

Kozik, P., Francis, R. W., Seaman, M. N. J., and Robinson, M. S. (2010). A screen for endocytic motifs. *Traffic* 11, 843–855. doi: 10.1111/j.1600-0854.2010.01056.x

Kuehnel, M. P., Rybin, V., Anand, P. K., Anes, E., and Griffiths, G. (2009). Lipids regulate P2X7-receptor-dependent actin assembly by phagosomes via ADP translocation and ATP synthesis in the phagosome lumen. *J. Cell Sci.* 122, 499–504. doi: 10.1242/jcs.034199

Kurochkina, N., and Guha, U. (2013). SH3 domains: modules of protein-protein interactions. *Biophys. Rev.* 5, 29–39. doi:10.1007/s12551-012-0081-z

Kusner, D. J., and Adams, J. (2000). ATP-induced killing of virulent Mycobacterium tuberculosis within human macrophages requires phospholipase D. *J. Immunol.* 164, 379–388. doi: 10.4049/jimmunol.164.1.379

Labasi, J. M., Petrushova, N., Donovan, C., McCurdy, S., Lira, P., Payette, M. M., et al. (2002). Absence of the P2X7 receptor alters leukocyte function and attenuates an inflammatory response. *J. Immunol.* 168, 6436–6445. doi: 10.4049/jimmunol.168.12.6436

Lambrecht, B. N., Vanderkerken, M., and Hammad, H. (2018). The emerging role of ADAM metalloproteinases in immunity. *Nat. Rev. Immunol.* 18, 745–758. doi: 10.1038/s41577-018-0068-5

Le Stunff, H., Auger, R., Kanellopoulos, J., and Raymond, M. N. (2004). The Pro-451 to Leu polymorphism within the C-terminal tail of P2X7 receptor impairs cell death but not phospholipase D activation in murine thymocytes. *J. Biol. Chem.* 279, 16918–16926. doi: 10.1074/jbc.M313064200

Leduc-Pessah, H., Weilinger, N. L., Fan, C. Y., Burma, N. E., Thompson, R. J., and Trang, T. (2017). Site-specific regulation of P2X7 receptor function in microglia gates morphine analgesic tolerance. *J. Neurosci.* 37, 10154–10172. doi: 10.1523/JNEUROSCI.0852-17.2017

Lemaire, I., Falzoni, S., Leduc, N., Zhang, B., Pellegatti, P., Adinolfi, E., et al. (2006). Involvement of the purinergic P2X7 receptor in the formation of multinucleated giant cells. *J. Immunol.* 177, 7257–7265. doi: 10.4049/jimmunol.177.10.7257

Lenertz, L. Y., Gavala, M. L., Hill, L. M., and Bertics, P. J. (2009). Cell signaling via the P2X(7) nucleotide receptor: linkage to ROS production, gene transcription, and receptor trafficking. *Purinergic Signal.* 5, 175–187. doi: 10.1007/s11302-009-9133-7

Lenertz, L. Y., Gavala, M. L., Zhu, Y., and Bertics, P. J. (2011). Transcriptional control mechanisms associated with the nucleotide receptor P2X7, a critical regulator of immunologic, osteogenic, and neurologic functions. *Immunol. Res.* 50, 22–38. doi: 10.1007/s12026-011-8203-4

Lepine, S., Le Stunff, H., Lakatos, B., Sulpice, J. C., and Giraud, F. (2006). ATP-induced apoptosis of thymocytes is mediated by activation of P2 X 7 receptor and involves de novo ceramide synthesis and mitochondria. *Biochim. Biophys. Acta* 1761, 73–82. doi: 10.1016/j.bbalip.2005.10.001

Leslie, C. C. (2015). Cytosolic phospholipase A(2): physiological function and role in disease. *J. Lipid Res.* 56, 1386–1402. doi: 10.1194/jlr.R057588

Li, J., Zhang, W., Yang, H., Howrigan, D. P., Wilkinson, B., Souaiaia, T., et al. (2017). Spatiotemporal profile of postsynaptic interactomes integrates components of complex brain disorders. *Nat. Neurosci.* 20, 1150–1161. doi: 10.1038/nn.4594

Li, M., Toombes, G. E. S., Silberberg, S. D., and Swartz, K. J. (2015). Physical basis of apparent pore dilation of ATP-activated P2X receptor channels. *Nat. Neurosci.* 18, 1577–1583. doi: 10.1038/nn.4120

Li, S., Tomić, M., and Stojilkovic, S. S. (2011). Characterization of novel Pannexin 1 isoforms from rat pituitary cells and their association with ATP-gated P2X channels. *Gen. Comp. Endocrinol.* 174, 202–210. doi: 10.1016/j.ygcen.2011.08.019

Lim, P. S., Sutton, C. R., and Rao, S. (2015). Protein kinase C in the immune system: from signalling to chromatin regulation. *Immunology* 146, 508–522. doi: 10.1111/imm.12510

Linden, J., Koch-Nolte, F., and Dahl, G. (2019). Purine release, metabolism, and signaling in the inflammatory response. *Ann. Rev. Immunol.* 37, 325–347. doi: 10.1146/annurev-immunol-051116-052406

Liu, Y., Xiao, Y., and Li, Z. (2011). P2X7 receptor positively regulates MyD88-dependent NF-κB activation. *Cytokine* 55, 229–236. doi: 10.1016/j.cyto.2011.05.003

Locovei, S., Scemes, E., Qiu, F., Spray, D. C., and Dahl, G. (2007). Pannexin1 is part of the pore forming unit of the P2X7 receptor death complex. *FEBS Lett.* 581, 483–488. doi: 10.1016/j.febslet.2006.12.056

Lucae, S., Salyakina, D., Barden, N., Harvey, M., Gagné, B., Labbé, M., et al. (2006). P2RX7, a gene coding for a purinergic ligand-gated ion channel, is associated with major depressive disorder. *Hum. Mol. Genet.* 15, 2438–2445. doi: 10.1093/hmg/ddl166

Ma, W., Korngreen, A., Weil, S., Cohen, E. B. T., Priel, A., Kuzin, L., et al. (2006). Pore properties and pharmacological features of the P2X receptor channel in airway ciliated cells. *J. Physiol.* 571, 503–517. doi: 10.1113/jphysiol.2005.103408

MacKenzie, A., Wilson, H. L., Kiss-Toth, E., Dower, S. K., North, R. A., and Surprenant, A. (2001). Rapid secretion of interleukin-1β by microvesicle shedding. *Immunity* 15, 825–835. doi: 10.1016/s1074-7613(01)00229-1

Mackenzie, A. B., Young, M. T., Adinolfi, E., and Surprenant, A. (2005). Pseudoapoptosis induced by brief activation of ATP-gated P2X7 receptors. *J. Biol. Chem.* 280, 33968–33976. doi: 10.1074/jbc.M502705200

Manodori, A. B., Barabino, G. A., Lubin, B. H., and Kuypers, F. A. (2000). Adherence of phosphatidylserine-exposing erythrocytes to endothelial matrix thrombospondin. *Blood* 95, 1293–1300.

Manohar, M., Hirsh, M. I., Chen, Y., Woehrle, T., Karande, A. A., and Junger, W. G. (2012). ATP release and autocrine signaling through P2X4 receptors regulate γδ T cell activation. *J. Leukoc. Biol.* 92, 787–794. doi: 10.1189/jlb.0312121

Mansoor, S. E., Lü, W., Oosterheert, W., Shekhar, M., Tajkhorshid, E., and Gouaux, E. (2016). X-ray structures define human P2X3 receptor gating cycle and antagonist action. *Nature* 538, 66–71. doi: 10.1038/nature19367

Mariathasan, S., Weiss, D. S., Newton, K., McBride, J., O'Rourke, K., Roose-Girma, M., et al. (2006). Cryopyrin activates the inflammasome in response to toxins and ATP. *Nature* 440, 228–232. doi: 10.1038/nature04515

Martel-Gallegos, G., Casas-Pruneda, G., Ortega-Ortega, F., Sanchez-Armass, S., Olivares-Reyes, J. A., Diebold, B., et al. (2013). Oxidative stress induced by P2X7 receptor stimulation in murine macrophages is mediated by c-Src/Pyk2 and ERK1/2. *Biochim. Biophys. Acta* 1830, 4650–4659. doi: 10.1016/j.bbagen.2013.05.023

Mayor, A., Martinon, F., De Smedt, T., Petrilli, V., and Tschopp, J. (2007). A crucial function of SGT1 and HSP90 in inflammasome activity links mammalian and plant innate immune responses. *Nat. Immunol.* 8, 497–503. doi: 10.1038/ni1459

McQuillin, A., Bass, N. J., Choudhury, K., Puri, V., Kosmin, M., Lawrence, J., et al. (2009). Case-control studies show that a non-conservative amino-acid change from a glutamine to arginine in the P2RX7 purinergic receptor protein is associated with both bipolar- and unipolar-affective disorders. *Mol. Psychiatry* 14, 614–620. doi: 10.1038/mp.2008.6

Mellacheruvu, D., Wright, Z., Couzens, A. L., Lambert, J. P., St-Denis, N. A., Li, T., et al. (2013). The CRAPome: a contaminant repository for affinity purification-mass spectrometry data. *Nat. Methods* 10, 730–736. doi: 10.1038/nmeth.2557

Metzger, M. W., Walser, S. M., Dedic, N., Aprile-Garcia, F., Jakubcakova, V., Adamczyk, M., et al. (2017). Heterozygosity for the mood disorder-associated variant Gln460Arg alters P2X7 receptor function and sleep quality. *J. Neurosci.* 37, 11688–11700. doi: 10.1523/JNEUROSCI.3487-16.2017

Migita, K., Ozaki, T., Shimoyama, S., Yamada, J., Nikaido, Y., Furukawa, T., et al. (2016). HSP90 regulation of P2X7 Receptor function requires an intact cytoplasmic C-terminus. *Mol. Pharmacol.* 90, 116–126. doi: 10.1124/mol.115.102988

Miller, C. M., Boulter, N. R., Fuller, S. J., Zakrzewski, A. M., Lees, M. P., Saunders, B. M., et al. (2011). The role of the P2X7 receptor in infectious diseases. *PLoS Pathog.* 7:e1002212. doi: 10.1371/journal.ppat.1002212

Minkiewicz, J., de Rivero Vaccari, J. P., and Keane, R. W. (2013). Human astrocytes express a novel NLRP2 inflammasome. *Glia* 61, 1113–1121. doi: 10.1002/glia.22499

Miras-Portugal, M. T., Sebastián-Serrano, Á, de Diego García, L., and Díaz-Hernández, M. (2017). Neuronal P2X7 receptor: involvement in neuronal physiology and pathology. *J. Neurosci.* 37, 7063–7072. doi: 10.1523/jneurosci.3104-16.2017

Mishra, A., Guo, Y., Zhang, L., More, S., Weng, T., Chintagari, N. R., et al. (2016). A Critical Role for P2X7 Receptor–Induced VCAM-1 shedding and neutrophil infiltration during acute lung injury. *J. Immunol.* 197, 2828–2837. doi: 10.4049/jimmunol.1501041

Mistafa, O., Ghalali, A., Kadekar, S., Hogberg, J., and Stenius, U. (2010). Purinergic receptor-mediated rapid depletion of nuclear phosphorylated Akt depends on pleckstrin homology domain leucine-rich repeat phosphatase, calcineurin, protein phosphatase 2A, and PTEN phosphatases. *J. Biol. Chem.* 285, 27900–27910. doi: 10.1074/jbc.M110.117093

Monif, M., Reid, C. A., Powell, K. L., Smart, M. L., and Williams, D. A. (2009). The P2X7 receptor drives microglial activation and proliferation: a trophic role for P2X7R pore. *J. Neurosci.* 29, 3781–3791. doi: 10.1523/jneurosci.5512-08.2009

Moon, H., Na, H. Y., Chong, K. H., and Kim, T. J. (2006). P2X 7 receptor-dependent ATP-induced shedding of CD27 in mouse lymphocytes. *Immunol. Lett.* 102, 98–105. doi: 10.1016/j.imlet.2005.08.004

Moore, S. F., and MacKenzie, A. B. (2009). NADPH oxidase NOX2 mediates rapid cellular oxidation following ATP stimulation of endotoxin-primed macrophages. *J. Immunol.* 183, 3302–3308. doi: 10.4049/jimmunol.0900394

Morelli, A., Chiozzi, P., Chiesa, A., Ferrari, D., Sanz, J. M., Falzoni, S., et al. (2003). Extracellular ATP causes ROCK I-dependent bleb formation in P2X7-transfected HEK293 cells. *Mol. Biol. Cell* 14, 2655–2664. doi: 10.1091/mbc.02-04-0061

Moreth, K., Frey, H., Hubo, M., Zeng-Brouwers, J., Nastase, M. V., Hsieh, L. T. H., et al. (2014). Biglycan-triggered TLR-2- and TLR-4-signaling exacerbates the pathophysiology of ischemic acute kidney injury. *Matrix Biol.* 35, 143–151. doi: 10.1016/j.matbio.2014.01.010

Moura, G., Lucena, S. V., Lima, M. A., Nascimento, F. D., Gesteira, T. F., Nader, H. B., et al. (2015). Post-translational allosteric activation of the P2X7 receptor through glycosaminoglycan chains of CD44 proteoglycans. *Cell Death Discov.* 1:15005. doi: 10.1038/cddiscovery.2015.5

Müller, M. R., and Rao, A. (2010). NFAT, immunity and cancer: a transcription factor comes of age. *Nat. Rev. Immunol.* 10, 645–656. doi: 10.1038/nri2818

Munoz-Planillo, R., Kuffa, P., Martinez-Colon, G., Smith, B. L., Rajendiran, T. M., and Nunez, G. (2013). K(+) efflux is the common trigger of NLRP3 inflammasome activation by bacterial toxins and particulate matter. *Immunity* 38, 1142–1153. doi: 10.1016/j.immuni.2013.05.016

Murrell-Lagnado, R. D. (2017). Regulation of P2X purinergic receptor signaling by cholesterol. *Curr. Top. Membr.* 80, 211–232. doi: 10.1016/bs.ctm.2017.05.004

Narcisse, L., Scemes, E., Zhao, Y., Lee, S. C., and Brosnan, C. F. (2005). The cytokine IL-1β transiently enhances P2X7 receptor expression and function in human astrocytes. *Glia* 49, 245–258. doi: 10.1002/glia.20110

Nicke, A. (2008). Homotrimeric complexes are the dominant assembly state of native P2X7 subunits. *Biochem. Biophys. Res. Commun.* 377, 803–808. doi: 10.1016/j.bbrc.2008.10.042

Noguchi, T., Ishii, K., Fukutomi, H., Naguro, I., Matsuzawa, A., Takeda, K., et al. (2008). Requirement of reactive oxygen species-dependent activation of ASK1-p38 MAPK pathway for extracellular ATP-induced apoptosis in macrophage. *J. Biol. Chem.* 283, 7657–7665. doi: 10.1074/jbc.M708402200

Norenberg, W., Schunk, J., Fischer, W., Sobottka, H., Riedel, T., Oliveira, J. F., et al. (2010). Electrophysiological classification of P2X7 receptors in rat cultured neocortical astroglia. *Br. J. Pharmacol.* 160, 1941–1952. doi: 10.1111/j.1476-5381.2010.00736.x

Norris, P. C., Gosselin, D., Reichart, D., Glass, C. K., and Dennis, E. A. (2014). Phospholipase A2 regulates eicosanoid class switching during inflammasome activation. *Proc. Natl. Acad. Sci. U.S.A.* 111, 12746–12751. doi: 10.1073/pnas.1404372111

Oliveira, J. F., Riedel, T., Leichsenring, A., Heine, C., Franke, H., Krugel, U., et al. (2011). Rodent cortical astroglia express in situ functional P2X7 receptors sensing pathologically high ATP concentrations. *Cereb. Cortex* 21, 806–820. doi: 10.1093/cercor/bhq154

Omasits, U., Ahrens, C. H., Müller, S., and Wollscheid, B. (2014). Protter: interactive protein feature visualization and integration with experimental proteomic data. *Bioinformatics* 30, 884–886. doi: 10.1093/bioinformatics/btt607

Orioli, E., De Marchi, E., Giuliani, A. L., and Adinolfi, E. (2017). P2X7 receptor orchestrates multiple signalling pathways triggering inflammation. autophagy and metabolic/trophic responses. *Curr. Med. Chem.* 24, 2261–2275. doi: 10.2174/0929867324666170303161659

Ortega, F., Pérez-Sen, R., Delicado, E. G., and Teresa Miras-Portugal, M. (2011). ERK1/2 activation is involved in the neuroprotective action of P2Y 13 and P2X7 receptors against glutamate excitotoxicity in cerebellar granule neurons. *Neuropharmacology* 61, 1210–1221. doi: 10.1016/j.neuropharm.2011.07.010

Ousingsawat, J., Wanitchakool, P., Kmit, A., Romao, A. M., Jantarajit, W., Schreiber, R., et al. (2015). Anoctamin 6 mediates effects essential for innate immunity downstream of P2X7 receptors in macrophages. *Nat. Commun.* 6, 6245–6245. doi: 10.1038/ncomms7245

Paluch, E. K., and Raz, E. (2013). The role and regulation of blebs in cell migration. *Curr. Opin. Cell Biol.* 25, 582–590. doi: 10.1016/j.ceb.2013.05.005

Panenka, W., Jijon, H., Herx, L. M., Armstrong, J. N., Feighan, D., Wei, T., et al. (2001). P2X7-like receptor activation in astrocytes increases chemokine monocyte chemoattractant protein-1 expression via mitogen-activated protein kinase. *J. Neurosci.* 21, 7135–7142. doi: 10.1523/jneurosci.21-18-07135.2001

Panupinthu, N., Zhao, L., Possmayer, F., Ke, H. Z., Sims, S. M., and Dixon, S. J. (2007). P2X7 nucleotide receptors mediate blebbing in osteoblasts through a pathway involving lysophosphatidic acid. *J. Biol. Chem.* 282, 3403–3412. doi: 10.1074/jbc.M605620200

Parvathenani, L. K., Tertyshnikova, S., Greco, C. R., Roberts, S. B., Robertson, B., and Posmantur, R. (2003). P2X7 mediates superoxide production in primary microglia and is up-regulated in a transgenic mouse model of Alzheimer's disease. *J. Biol. Chem.* 278, 13309–13317. doi: 10.1074/jbc.M209478200

Patel, H. H., and Insel, P. A. (2008). Lipid rafts and caveolae and their role in compartmentation of redox signaling. *Antioxid. Redox Signal.* 11, 1357–1372. doi: 10.1089/ars.2008.2365

Pelegrin, P., and Surprenant, A. (2006). Pannexin-1 mediates large pore formation and interleukin-1β release by the ATP-gated P2X7 receptor. *EMBO J.* 25, 5071–5082. doi: 10.1038/sj.emboj.7601378

Penuela, S., Gehi, R., and Laird, D. W. (2013). The biochemistry and function of pannexin channels. *Biochim. Biophys. Acta Biomembr.* 1828, 15–22. doi: 10.1016/j.bbamem.2012.01.017

Pereira, V. S., Casarotto, P. C., Hiroaki-Sato, V. A., Sartim, A. G., Guimaraes, F. S., and Joca, S. R. (2013). Antidepressant- and anticompulsive-like effects of purinergic receptor blockade: involvement of nitric oxide. *Eur. Neuropsychopharmacol.* 23, 1769–1778. doi: 10.1016/j.euroneuro.2013.01.008

Perez-Andres, E., Fernandez-Rodriguez, M., Gonzalez, M., Zubiaga, A., Vallejo, A., Garcia, I., et al. (2002). Activation of phospholipase D-2 by P2X(7) agonists in rat submandibular gland acini. *J. Lipid Res.* 43, 1244–1255.

Pérez-Flores, G., Lévesque, S. A., Pacheco, J., Vaca, L., Lacroix, S., Pérez-Cornejo, P., et al. (2015). The P2X7/P2X4 interaction shapes the purinergic response in murine macrophages. *Biochem. Biophys. Res. Commun.* 467, 484–490. doi: 10.1016/j.bbrc.2015.10.025

Perregaux, D. G., and Gabel, C. A. (1998). Human monocyte stimulus-coupled IL-1β posttranslational processing: modulation via monovalent cations. *Am. J. Physiol.* 275, C1538–C1547. doi: 10.1152/ajpcell.1998.275.6.C1538

Pfeiffer, Z. A., Aga, M., Prabhu, U., Watters, J. J., Hall, D. J., and Bertics, P. J. (2004). The nucleotide receptor P2X7 mediates actin reorganization and membrane blebbing in RAW 264.7 macrophages via p38 MAP kinase and Rho. *J. Leukoc. Biol.* 75, 1173–1182. doi: 10.1189/jlb.1203648

Pfleger, C., Ebeling, G., Blasche, R., Patton, M., Patel, H. H., Kasper, M., et al. (2012). Detection of caveolin-3/caveolin-1/P2X7R complexes in mice atrial cardiomyocytes in vivo and in vitro. *Histochem. Cell Biol.* 138, 231–241. doi: 10.1007/s00418-012-0961-0

Pippel, A., Beßler, B., Klapperstück, M., and Markwardt, F. (2015). Inhibition of antigen receptor-dependent Ca2+ signals and NF-AT activation by P2X7 receptors in human B lymphocytes. *Cell Calcium* 57, 275–289. doi: 10.1016/j.ceca.2015.01.010

Pippel, A., Stolz, M., Woltersdorf, R., Kless, A., Schmalzing, G., and Markwardt, F. (2017). Localization of the gate and selectivity filter of the full-length P2X7 receptor. *Proc. Natl. Acad. Sci.* 114, E2156–E2165. doi: 10.1073/pnas.1610414114

Pizzirani, C., Ferrari, D., Chiozzi, P., Adinolfi, E., Sandonà, D., Savaglio, E., et al. (2007). Stimulation of P2 receptors causes release of IL-1β-loaded microvesicles from human dendritic cells. *Blood* 109, 3856–3864. doi: 10.1182/blood-2005-06-031377

Pochet, S., Gomez-Munoz, A., Marino, A., and Dehaye, J. P. (2003). Regulation of phospholipase D by P2X7 receptors in submandibular ductal cells. *Cell. Signal.* 15, 927–935. doi: 10.1016/s0898-6568(03)00053-6

Poornima, V., Madhupriya, M., Kootar, S., Sujatha, G., Kumar, A., and Bera, A. K. (2012). P2X 7 receptor-pannexin 1 hemichannel association: effect of extracellular calcium on membrane permeabilization. *J. Mol. Neurosci.* 46, 585–594. doi: 10.1007/s12031-011-9646-8

Pupovac, A., Foster, C. M., and Sluyter, R. (2013). Human P2X7 receptor activation induces the rapid shedding of CXCL16. *Biochem. Biophys. Res. Commun.* 432, 626–631. doi: 10.1016/j.bbrc.2013.01.134

Pupovac, A., Geraghty, N. J., Watson, D., and Sluyter, R. (2015). Activation of the P2X7 receptor induces the rapid shedding of CD23 from human and murine B cells. *Immunol. Cell Biol.* 93, 77–85. doi: 10.1038/icb.2014.69

Qu, Y., and Dubyak, G. R. (2009). P2X7 receptors regulate multiple types of membrane trafficking responses and non-classical secretion pathways. *Purinergic Signal.* 5, 163–173. doi: 10.1007/s11302-009-9132-8

Qu, Y., Misaghi, S., Newton, K., Gilmour, L. L., Louie, S., Cupp, J. E., et al. (2011). Pannexin-1 Is required for ATP release during apoptosis but not for inflammasome activation. *J. Immunol.* 186, 6553–6561. doi: 10.4049/jimmunol.1100478

Qu, Y., Ramachandra, L., Mohr, S., Franchi, L., Harding, C. V., Nunez, G., et al. (2009). P2X7 receptor-stimulated secretion of MHC class II-containing exosomes requires the ASC/NLRP3 inflammasome but is independent of Caspase-1. *J. Immunol.* 182, 5052–5062. doi: 10.4049/jimmunol.0802968

Qureshi, O. S., Paramasivam, A., Yu, J. C. H., and Murrell-Lagnado, R. D. (2007). Regulation of P2X4 receptors by lysosomal targeting, glycan protection and exocytosis. *J. Cell Sci.* 120, 3838–3849. doi: 10.1242/jcs.010348

Ranoa, D. R. E., Kelley, S. L., and Tapping, R. I. (2013). Human lipopolysaccharide-binding protein (LBP) and CD14 independently deliver triacylated lipoproteins to Toll-like receptor 1 (TLR1) and TLR2 and enhance formation of the ternary signaling complex. *J. Biol. Chem.* 288, 9729–9741. doi: 10.1074/jbc.M113.453266

Rassendren, F., Buell, G. N., Virginio, C., Collo, G., North, R. A., and Surprenant, A. (1997). The permeabilizing ATP receptor, P2X7. Cloning and expression of a human cDNA. *J. Biol. Chem.* 272, 5482–5486. doi: 10.1074/jbc.272.9.5482

Raymond, M. N., and Le Stunff, H. (2006). Involvement of de novo ceramide biosynthesis in macrophage death induced by activation of ATP-sensitive P2X7 receptor. *FEBS Lett.* 580, 131–136. doi: 10.1016/j.febslet.2005.11.066

Riedel, T., Schmalzing, G., and Markwardt, F. (2007). Influence of extracellular monovalent cations on pore and gating properties of P2X7 receptor-operated single-channel currents. *Biophys. J.* 93, 846–858. doi: 10.1529/BIOPHYSJ.106.103614

Rissiek, B., Haag, F., Boyer, O., Koch-Nolte, F., and Adriouch, S. (2015). P2X7 on mouse T cells: one channel, many functions. *Front. Immunol.* 6:204. doi: 10.3389/fimmu.2015.00204

Robinson, L. E., Shridar, M., Smith, P., and Murrell-Lagnado, R. D. (2014). Plasma membrane cholesterol as a regulator of human and rodent P2X7 receptor activation and sensitization. *J. Biol. Chem.* 289, 31983–31994. doi: 10.1074/jbc.M114.574699

Roger, S., Gillet, L., Baroja-Mazo, A., Surprenant, A., and Pelegrin, P. (2010). C-terminal calmodulin-binding motif differentially controls human and rat P2X7 receptor current facilitation. *J. Biol. Chem.* 285, 17514–17524. doi: 10.1074/jbc.M109.053082

Roger, S., Pelegrin, P., and Surprenant, A. (2008). Facilitation of P2X7 receptor currents and membrane blebbing via constitutive and dynamic calmodulin binding. *J. Neurosci.* 28, 6393–6401. doi: 10.1523/jneurosci.0696-08.2008

Rzeniewicz, K., Newe, A., Rey Gallardo, A., Davies, J., Holt, M. R., Patel, A., et al. (2015). L-selectin shedding is activated specifically within transmigrating pseudopods of monocytes to regulate cell polarity in vitro. *Proc. Natl. Acad. Sci.* 112, E1461–E1470. doi: 10.1073/pnas.1417100112

Sakaki, H., Fujiwaki, T., Tsukimoto, M., Kawano, A., Harada, H., and Kojima, S. (2013). P2X4 receptor regulates P2X7 receptor-dependent IL-1β and IL-18 release in mouse bone marrow-derived dendritic cells. *Biochem. Biophys. Res. Commun.* 432, 406–411. doi: 10.1016/j.bbrc.2013.01.135

Saul, A., Hausmann, R., Kless, A., and Nicke, A. (2013). Heteromeric assembly of P2X subunits. *Front. Cell. Neurosci.* 7:250. doi: 10.3389/fncel.2013.00250

Savio, L. E. B., de Andrade Mello, P., da Silva, C. G., and Coutinho-Silva, R. (2018). The P2X7 receptor in inflammatory diseases: angel or demon? *Front. Pharmacol.* 9:52. doi: 10.3389/fphar.2018.00052

Schaefer, L., Babelova, A., Kiss, E., Hausser, H. J., Baliova, M., Krzyzankova, M., et al. (2005). The matrix component biglycan is proinflammatory and signals through Toll-like receptors 4 and 2 in macrophages. *J. Clin. Invest.* 115, 2223–2233. doi: 10.1172/JCI23755

Schenk, U., Westendorf, A. M., Radaelli, E., Casati, A., Ferro, M., Fumagalli, M., et al. (2008). Purinergic control of T cell activation by ATP released through pannexin-1 hemichannels. *Sci. Signal.* 1:ra6. doi: 10.1126/scisignal.1160583

Scheuplein, F., Schwarz, N., Adriouch, S., Krebs, C., Bannas, P., Rissiek, B., et al. (2009). NAD+ and ATP released from injured cells induce P2X7-dependent

shedding of CD62L and externalization of phosphatidylserine by murine T cells. *J. Immunol.* 182, 2898–2908. doi: 10.4049/jimmunol.0801711

Schneider, M., Prudic, K., Pippel, A., Klapperstück, M., Braam, U., Müller, C. E., et al. (2017). Interaction of purinergic P2X4 and P2X7 receptor subunits. *Front. Pharmacol.* 8:860. doi: 10.3389/fphar.2017.00860

Schopf, F. H., Biebl, M. M., and Buchner, J. (2017). The HSP90 chaperone machinery. *Nat. Rev. Mol. Cell Biol.* 18, 345–360. doi: 10.1038/nrm.2017.20

Schwarz, N., Drouot, L., Nicke, A., Fliegert, R., Boyer, O., Guse, A. H., et al. (2012). Alternative splicing of the N-terminal cytosolic and transmembrane domains of P2X7 controls gating of the ion channel by ADP-ribosylation. *PLoS One* 7:e41269. doi: 10.1371/journal.pone.0041269

Schwenk, J., Harmel, N., Brechet, A., Zolles, G., Berkefeld, H., Muller, C. S., et al. (2012). High-resolution proteomics unravel architecture and molecular diversity of native AMPA receptor complexes. *Neuron* 74, 621–633. doi: 10.1016/j.neuron.2012.03.034

Schwenk, J., Perez-Garci, E., Schneider, A., Kollewe, A., Gauthier-Kemper, A., Fritzius, T., et al. (2016). Modular composition and dynamics of native GABAB receptors identified by high-resolution proteomics. *Nat. Neurosci.* 19, 233–242. doi: 10.1038/nn.4198

Segawa, K., Kurata, S., Yanagihashi, Y., Brummelkamp, T. R., Matsuda, F., and Nagata, S. (2014). Caspase-mediated cleavage of phospholipid flippase for apoptotic phosphatidylserine exposure. *Science* 344, 1164–1168. doi: 10.1126/science.1252809

Segawa, K., and Nagata, S. (2015). An apoptotic 'Eat Me' signal: phosphatidylserine exposure. *Trends Cell Biol.* 25, 639–650. doi: 10.1016/j.tcb.2015.08.003

Selvy, P. E., Lavieri, R. R., Lindsley, C. W., and Brown, H. A. (2011). Phospholipase D: enzymology, functionality, and chemical modulation. *Chem. Rev.* 111, 6064–6119. doi: 10.1021/cr200296t

Sengstake, S., Boneberg, E. M., and Illges, H. (2006). CD21 and CD62L shedding are both inducible via P2X7Rs. *Int. Immunol.* 18, 1171–1178. doi: 10.1093/intimm/dxl051

Serfling, E., Avots, A., Klein-Hessling, S., Rudolf, R., Vaeth, M., and Berberich-Siebelt, F. (2012). NFATc1/A: the other face of NFAT factors in lymphocytes. *Cell Commun. Signal.* 10, 16–16. doi: 10.1186/1478-811X-10-16

Shamseddine, A. A., Airola, M. V., and Hannun, Y. A. (2015). Roles and regulation of neutral sphingomyelinase-2 in cellular and pathological processes. *Adv. Biol. Regul.* 57, 24–41. doi: 10.1016/j.jbior.2014.10.002

Shemon, A. N., Sluyter, R., Fernando, S. L., Clarke, A. L., Dao-Ung, L.-P., Skarratt, K. K., et al. (2006). A Thr357 to Ser polymorphism in homozygous and compound heterozygous subjects causes absent or reduced P2X7 function and impairs ATP-induced mycobacterial killing by macrophages. *J. Biol. Chem.* 281, 2079–2086. doi: 10.1074/jbc.M507816200

Shi, H., Wang, Y., Li, X., Zhan, X., Tang, M., Fina, M., et al. (2016). NLRP3 activation and mitosis are mutually exclusive events coordinated by NEK7, a new inflammasome component. *Nat. Immunol.* 17, 250–258. doi: 10.1038/ni.3333

Silverman, W. R., de Rivero Vaccari, J. P., Locovei, S., Qiu, F., Carlsson, S. K., Scemes, E., et al. (2009). The pannexin 1 channel activates the inflammasome in neurons and astrocytes. *J. Biol. Chem.* 284, 18143–18151. doi: 10.1074/jbc.M109.004804

Sim, J. A., Young, M. T., Sung, H. Y., North, R. A., and Surprenant, A. (2004). Reanalysis of P2X7 receptor expression in rodent brain. *J. Neurosci.* 24, 6307–6314. doi: 10.1523/JNEUROSCI.1469-04.2004

Sluyter, R., and Wiley, J. S. (2002). Extracellular adenosine 5'-triphosphate induces a loss of CD23 from human dendritic cells via activation of P2X 7 receptors. *Int. Immunol.* 14, 1415–1421. doi: 10.1093/intimm/dxf111

Smart, M. L., Gu, B., Panchal, R. G., Wiley, J., Cromer, B., Williams, D. A., et al. (2003). P2X7 receptor cell surface expression and cytolytic pore formation are regulated by a distal C-terminal region. *J. Biol. Chem.* 278, 8853–8860. doi: 10.1074/jbc.M211094200

Solle, M., Labasi, J., Perregaux, D. G., Stam, E., Petrushova, N., Koller, B. H., et al. (2001). Altered cytokine production in mice lacking P2X(7) receptors. *J. Biol. Chem.* 276, 125–132. doi: 10.1074/jbc.M006781200

Sommer, A., Kordowski, F., Büch, J., Maretzky, T., Evers, A., Andrä, J., et al. (2016). Phosphatidylserine exposure is required for ADAM17 sheddase function. *Nat. Commun.* 7, 11523–11523. doi: 10.1038/ncomms11523

Soond, S. M. (2005). ERK-mediated phosphorylation of Thr735 in TNF - converting enzyme and its potential role in TACE protein trafficking. *J. Cell Sci.* 118, 2371–2380. doi: 10.1242/jcs.02357

Sorge, R. E., Trang, T., Dorfman, R., Smith, S. B., Beggs, S., Ritchie, J., et al. (2012). Genetically determined P2X7 receptor pore formation regulates variability in chronic pain sensitivity. *Nat. Med.* 18, 595–599. doi: 10.1038/nm.2710

Sperlagh, B., and Illes, P. (2014). P2X7 receptor: an emerging target in central nervous system diseases. *Trends Pharmacol. Sci.* 35, 537–547. doi: 10.1016/j.tips.2014.08.002

Sperlagh, B., Vizi, E. S., Wirkner, K., and Illes, P. (2006). P2X7 receptors in the nervous system. *Prog. Neurobiol.* 78, 327–346. doi: 10.1016/j.pneurobio.2006.03.007

Spooner, R., and Yilmaz, O. (2011). The role of reactive-oxygen-species in microbial persistence and inflammation. *Int. J. Mol. Sci.* 12, 334–352. doi: 10.3390/ijms12010334

Stefano, L., Rössler, O. G., Griesemer, D., Hoth, M., and Thiel, G. (2007). P2X7 receptor stimulation upregulates Egr-1 biosynthesis involving a cytosolic Ca2+ rise, transactivation of the EGF receptor and phosphorylation of ERK and Elk-1. *J. Cell. Physiol.* 213, 36–44. doi: 10.1002/jcp.21085

Stokes, L., Fuller, S. J., Sluyter, R., Skarratt, K. K., Gu, B. J., and Wiley, J. S. (2010). Two haplotypes of the P2X 7 receptor containing the Ala-348 to Thr polymorphism exhibit a gain-of-function effect and enhanced interleukin-1β secretion. *FASEB J.* 24, 2916–2927. doi: 10.1096/fj.09-150862

Stolz, M., Klapperstück, M., Kendzierski, T., Detro-dassen, S., Panning, A., Schmalzing, G., et al. (2015). Homodimeric anoctamin-1, but not homodimeric anoctamin-6, is activated by calcium increases mediated by the P2Y1 and P2X7 receptors. *Pflugers Arch.* 467, 2121–2140. doi: 10.1007/s00424-015-1687-3

Suh, P. G., Park, J. I., Manzoli, L., Cocco, L., Peak, J. C., Katan, M., et al. (2008). Multiple roles of phosphoinositide-specific phospholipase C isozymes. *BMB Rep.* 41, 415–434. doi: 10.5483/bmbrep.2008.41.6.415

Surprenant, A., Rassendren, F., Kawashima, E., North, R. A., and Buell, G. (1996). The cytolytic P2Z receptor for extracellular ATP identified as a P2X receptor (P2X7). *Science* 272, 735–738. doi: 10.1126/SCIENCE.272.5262.735

Suzuki, J., Denning, D. P., Imanishi, E., Horvitz, H. R., and Nagata, S. (2013). Xk-related protein 8 and CED-8 promote phosphatidylserine exposure in apoptotic cells. *Science* 341, 403–406. doi: 10.1126/science.1236758

Suzuki, J., Umeda, M., Sims, P. J., and Nagata, S. (2010). Calcium-dependent phospholipid scrambling by TMEM16F. *Nature* 468, 834–840. doi: 10.1038/nature09583

Szklarczyk, D., Gable, A. L., Lyon, D., Junge, A., Wyder, S., Huerta-Cepas, J., et al. (2019). STRING v11: protein-protein association networks with increased coverage, supporting functional discovery in genome-wide experimental datasets. *Nucleic Acids Res.* 47, D607–D613. doi: 10.1093/nar/gky1131

Tafani, M., Schito, L., Pellegrini, L., Villanova, L., Marfe, G., Anwar, T., et al. (2011). Hypoxia-increased RAGE and P2X7R expression regulates tumor cell invasion through phosphorylation of Erk1/2 and Akt and nuclear translocation of NF-κB. *Carcinogenesis* 32, 1167–1175. doi: 10.1093/carcin/bgr101

Torres, G. E., Egan, T. M., and Voigt, M. M. (1999). Hetero-oligomeric assembly of P2X receptor subunits. Specificities exist with regard to possible partners. *J. Biol. Chem.* 274, 6653–6659. doi: 10.1074/jbc.274.10.6653

Toulme, E., Garcia, A., Samways, D., Egan, T. M., Carson, M. J., and Khakh, B. S. (2010). P2X4 receptors in activated C8-B4 cells of cerebellar microglial origin. *J. Gen. Physiol.* 135, 333–353. doi: 10.1085/jgp.200910336

Toyomitsu, E., Tsuda, M., Yamashita, T., Tozaki-Saitoh, H., Tanaka, Y., and Inoue, K. (2012). CCL2 promotes P2X4 receptor trafficking to the cell surface of microglia. *Purinergic Signal.* 8, 301–310. doi: 10.1007/s11302-011-9288-x

Ugur, M., and Ugur, O. (2019). A mechanism-based approach to P2X7 receptor action. *Mol. Pharmacol.* 95, 442–450. doi: 10.1124/mol.118.115022

Verhoef, P. A., Estacion, M., Schilling, W., and Dubyak, G. R. (2003). P2X7 receptor-dependent blebbing and the activation of Rho-effector kinases, caspases, and IL-1 β release. *J. Immunol.* 170, 5728–5738. doi: 10.4049/jimmunol.170.11.5728

Villalobo, A., Ishida, H., Vogel, H. J., and Berchtold, M. W. (2018). Calmodulin as a protein linker and a regulator of adaptor/scaffold proteins. *Biochim. Biophys. Acta Mol. Cell Res.* 1865, 507–521. doi: 10.1016/j.bbamcr.2017.12.004

Virginio, C., MacKenzie, A., Rassendren, F. A., North, R. A., and Surprenant, A. (1999). Pore dilation of neuronal P2X receptor channels. *Nat. Neurosci.* 2, 315–321. doi: 10.1038/7225

Wan, M., Soehnlein, O., Tang, X., van der Does, A. M., Smedler, E., Uhlen, P., et al. (2014). Cathelicidin LL-37 induces time-resolved release of LTB4 and TXA2 by human macrophages and triggers eicosanoid generation in vivo. *FASEB J.* 28, 3456–3467. doi: 10.1096/fj.14-251306

Wang, B., and Sluyter, R. (2013). P2X7 receptor activation induces reactive oxygen species formation in erythroid cells. *Purinergic Signal.* 9, 101–112. doi: 10.1007/s11302-012-9335-2

Wang, C. M., Ploia, C., Anselmi, F., Sarukhan, A., and Viola, A. (2014). Adenosine triphosphate acts as a paracrine signaling molecule to reduce the motility of T cells. *EMBO J.* 33, 1354–1364. doi: 10.15252/embj.201386666

Wang, J., Huo, K., Ma, L., Tang, L., Li, D., Huang, X., et al. (2011). Toward an understanding of the protein interaction network of the human liver. *Mol. Syst. Biol.* 7:536. doi: 10.1038/msb.2011.67

Watters, J. J., Sommer, J. A., Fisette, P. L., Pfeiffer, Z. A., Aga, M., Prabhu, U., et al. (2001). Macrophage signaling and mediator production. *Drug Dev. Res.* 104, 91–104. doi: 10.1002/ddr.1176

Weinhold, K., Krause-Buchholz, U., Rödel, G., Kasper, M., and Barth, K. (2010). Interaction and interrelation of P2X7 and P2X4 receptor complexes in mouse lung epithelial cells. *Cell. Mol. Life Sci.* 67, 2631–2642. doi: 10.1007/s00018-010-0355-1

Weiss, J. (2003). Bactericidal/permeability-increasing protein (BPI) and lipopolysaccharide-binding protein (LBP): structure, function and regulation in host defence against Gram-negative bacteria. *Biochem. Soc. Trans.* 31(Pt 4), 785–790.

Wiley, J. S., Dao-Ung, L.-P., Li, C., Shemon, A. N., Gu, B. J., Smart, M. L., et al. (2003). An Ile-568 to Asn polymorphism prevents normal trafficking and function of the human P2X7 receptor. *J. Biol. Chem.* 278, 17108–17113. doi: 10.1074/jbc.M212759200

Wiley, J. S., Sluyter, R., Gu, B. J., Stokes, L., and Fuller, S. J. (2011). The human P2X7 receptor and its role in innate immunity. *Tissue Antigens* 78, 321–332. doi: 10.1111/j.1399-0039.2011.01780.x

Wilson, H. L., Wilson, S. A., Surprenant, A., and Alan North, R. (2002). Epithelial membrane proteins induce membrane blebbing and interact with the P2X7 receptor C terminus. *J. Biol. Chem.* 277, 34017–34023. doi: 10.1074/jbc.M205120200

Witting, A., Walter, L., Wacker, J., Moller, T., and Stella, N. (2004). P2X7 receptors control 2-arachidonoylglycerol production by microglial cells. *Proc. Natl. Acad. Sci. U.S.A.* 101, 3214–3219. doi: 10.1073/pnas.0306707101

Woehrle, T., Yip, L., Elkhal, A., Sumi, Y., Chen, Y., Yao, Y., et al. (2010). Pannexin-1 hemichannel-mediated ATP release together with P2X1 and P2X4 receptors regulate T-cell activation at the immune synapse. *Blood* 116, 3475–3484. doi: 10.1182/blood-2010-04-277707

Wu, C., Ma, M. H., Brown, K. R., Geisler, M., Li, L., Tzeng, E., et al. (2007). Systematic identification of SH3 domain-mediated human protein-protein interactions by peptide array target screening. *Proteomics* 7, 1775–1785. doi: 10.1002/pmic.200601006

Xu, X. J., Boumechache, M., Robinson, L. E., Marschall, V., Gorecki, D. C., Masin, M., et al. (2012). Splice variants of the P2X7 receptor reveal differential agonist dependence and functional coupling with pannexin-1. *J. Cell Sci.* 125, 3776–3789. doi: 10.1242/jcs.099374

Yang, D., He, Y., Muñoz-Planillo, R., Liu, Q., and Núñez, G. (2015). Caspase-11 requires the Pannexin-1 channel and the purinergic P2X7 pore to mediate pyroptosis and endotoxic shock. *Immunity* 43, 923–932. doi: 10.1016/J.IMMUNI.2015.10.009

Yang, R., Yu, T., Kou, X., Gao, X., Chen, C., Liu, D., et al. (2018). Tet1 and Tet2 maintain mesenchymal stem cell homeostasis via demethylation of the P2rX7 promoter. *Nat. Commun.* 9:2143. doi: 10.1038/s41467-018-04464-6

Yip, L., Woehrle, T., Corriden, R., Hirsh, M., Chen, Y., Inoue, Y., et al. (2009). Autocrine regulation of T-cell activation by ATP release and P2X < *sub* > 7 < */sub* > receptors. *FASEB J.* 23, 1685–1693. doi: 10.1096/fj.08-126458

Young, C. N. J., Sinadinos, A., Lefebvre, A., Chan, P., Arkle, S., Vaudry, D., et al. (2015). A novel mechanism of autophagic cell death in dystrophic muscle regulated by P2RX7 receptor large-pore formation and HSP90. *Autophagy* 11, 113–130. doi: 10.4161/15548627.2014.994402

Young, M. T., Pelegrin, P., and Surprenant, A. (2007). Amino acid residues in the P2X7 receptor that mediate differential sensitivity to ATP and BzATP. *Mol. Pharmacol.* 71, 92–100. doi: 10.1124/mol.106.030163

Zanoni, I., and Granucci, F. (2013). Role of CD14 in host protection against infections and in metabolism regulation. *Front. Cell. Infect. Microb.* 3:32. doi: 10.3389/fcimb.2013.00032

Zech, A., Wiesler, B., Ayata, C. K., Schlaich, T., Dürk, T., Hoßfeld, M., et al. (2016). P2rx4 deficiency in mice alleviates allergen-induced airway inflammation. *Oncotarget* 7, 80288–80297. doi: 10.18632/oncotarget.13375

Zhang, Q., Lenardo, M. J., and Baltimore, D. (2017). 30 Years of NF-κB: a blossoming of relevance to human pathobiology. *Cell* 168, 37–57. doi: 10.1016/j.cell.2016.12.012

Zhao, Q., Yang, M., Ting, A. T., and Logothetis, D. E. (2007). PIP 2 regulates the ionic current of P2X receptors and P2X 7 receptor-mediated cell death. *Channels* 1, 46–55. doi: 10.4161/chan.3914

Zuo, Y., Wang, J., Liao, F., Yan, X., Li, J., Huang, L., et al. (2018). Inhibition of heat shock protein 90 by 17-AAG reduces inflammation via P2X7 receptor/NLRP3 inflammasome pathway and increases neurogenesis after subarachnoid hemorrhage in mice. *Front. Mol. Neurosci.* 11:401. doi: 10.3389/fnmol.2018.00401

Conflict of Interest Statement: The authors declare that the research was conducted in the absence of any commercial or financial relationships that could be construed as a potential conflict of interest.

4.2 A Simplified Protocol to Incorporate the Fluorescent Unnatural Amino Acid ANAP into *Xenopus laevis* Oocyte-Expressed P2X7 Receptors (Research Protocol)

This book chapter is part of a collection of molecular biology research methods and protocols that describe procedures to investigate the P2X7R and is published as part of the Methods in Molecular Biology book series. It details step-by-step instructions for the incorporation of the fUAA ANAP into *Xenopus laevis* oocyte expressed P2X7Rs using two different protocols. In addition, the procedures for analysis of P2X7 membrane expression by SDS-PAGE and its investigation by VCF are described.

A procedure for the expression of ANAP-containing receptors in *X. laevis* oocytes was previously published by Kalstrup and Blunck [78]: In this protocol, the plasmid encoding the tRNA/tRNA-synthetase pair (pANAP [1]) [75] is introduced into the oocyte via nuclear injection. One day later, ANAP and the receptor cRNA containing an *amber* stop codon are injected into the cytoplasm. In an effort to simplify this method and to avoid the intricate nuclear injection, I established a protocol, in which a chemically synthesized *amber* suppressor tRNA is directly injected into the cytosol together with *in vitro* synthesized cRNA encoding the respective aminoacyl-tRNA synthetase, ANAP, and the receptor cRNA containing an *amber* stop codon. In addition, I designed a modified pUC19 plasmid for protein expression in *X. laevis* oocytes. The book chapter also includes a protocol to validate surface expression of ANAP-containing receptors by labeling oocytes with membrane-impermeable Cy5 NHS-ester, subsequent purification of the His-tagged receptors with Ni-NTA beads, and SDS-PAGE analysis. It is shown, that both methods for ANAP incorporation yield comparable plasma membrane expression levels of ANAP-containing full-length P2X7Rs. In addition, the procedure for VCF recordings of *X. laevis* oocyte expressed ANAP-containing P2X7Rs is presented together with a short description of the VCF setup and helpful notes.

It has to be noted, that rebuilding and optimization of the VCF setup (including a technical drawing of the two-compartment recording chamber, evaluation and selection of all required optical parts, and careful adjustment and validation of the recording system) represent a major and essential part of my thesis work and required acquisition of expertise in optics and electronics.

For this publication, I established and optimized the described ANAP incorporation and VCF methods, performed all experiments, drafted the manuscript and prepared Fig.1 (B), Fig.2 (A-D), and Fig.3 (B-C).

[1] Addgene plasmid # 48696 ; http://n2t.net/addgene:48696 ; RRID:Addgene_48696

A Simplified Protocol to Incorporate the Fluorescent Unnatural Amino Acid ANAP into *Xenopus laevis* Oocyte-Expressed P2X7 Receptors

Anna Durner, Annette Nicke

published in

Methods Mol Biol, volume 2510, pp 193-216 [2022]

Reprinted from [89]

Chapter 10

A Simplified Protocol to Incorporate the Fluorescent Unnatural Amino Acid ANAP into *Xenopus laevis* Oocyte-Expressed P2X7 Receptors

Anna Durner and Annette Nicke

Abstract

The long intracellular P2X7 C-terminus accounts for diverse downstream effects of P2X7 activation. Although the recent determination of the cryo-EM structure of the full-length P2X7 receptor finally revealed the structure and several unexpected features of the large cytoplasmic domain, its molecular function remains enigmatic. Incorporation of unnatural amino acids (UAA) via an *amber* Stop codon has been a powerful tool for structure–function analysis of proteins. Voltage clamp fluorometry (VCF) with the fluorescent unnatural amino acid L-3-(6-acetylnaphthalen-2-ylamino)-2-aminopropanoic acid (ANAP) provides a means to study intracellular domain movements of ion channel receptors. In the *Xenopus laevis* oocyte expression system, site-specific introduction of this environment-sensitive fluorophore can be achieved by the nuclear injection of cDNA encoding an orthogonal *amber* suppressor tRNA/aminoacyl-tRNA synthetase pair and subsequent cytoplasmic injection of ANAP together with the respective cRNA containing the *amber* Stop codon. Here, we describe this protocol for expression of ANAP-labeled P2X7. In addition, we provide a simplified alternative protocol, in which we coinject cRNAs encoding the tRNA synthetase and mutant P2X7 together with the synthesized *amber* suppressor tRNA and ANAP in one step into the cytosol. We found that the new protocol yielded more reproducible results and was less harmful for the oocytes. By selective fluorescence labeling of the ANAP-labeled P2X7 protein in the oocyte plasma membrane and VCF recordings, we show that this method results in comparable levels of functional ANAP-labeled P2X7 protein.

Key words Fluorescent unnatural amino acid (fUAA), L-3-(6-acetylnaphthalen-2-ylamino)-2-aminopropanoic acid (ANAP), *Xenopus laevis* oocyte, *amber* stop codon, Nonsense suppression, Aminoacyl-tRNA synthetase, *amber* suppressor tRNA, His-tag purification, SDS-PAGE, Voltage clamp fluorometry (VCF)

1 Introduction

Activation of the P2X7 receptor has been shown to induce a variety of downstream effects ranging from macropore formation and plasma membrane reorganization, via activation of enzymes and transcription factors, to membrane protein shedding, cytokine

Annette Nicke (ed.), *The P2X7 Receptor: Methods and Protocols*, Methods in Molecular Biology, vol. 2510,
https://doi.org/10.1007/978-1-0716-2384-8_10,

release, and apoptosis. These functions have been associated with the long (240 aa) intracellular C-terminus of the P2X7 receptor, which is not found in other P2X family members. The recent determination of the full-length rat P2X7 cryo-EM structure confirmed not only a submembraneous cap and anchor domain that prevents desensitization but also an unexpected globular ballast domain containing a dinuclear zinc binding site and a guanosine nucleotide binding motif [1]. The functions of these novel structures are completely unknown.

Incorporation of unnatural or noncanonical amino acids (UAAs) represents a powerful method for structure function analysis of proteins, for example by introduction of fluorescent amino acids or amino acids with chemically reactive side chains that are able to cross-link proteins or can be modified by click chemistry. Protocols for the incorporation of such UAAs have been developed for prokaryotic and eukaryotic expression systems, including *E. coli*, *S. cerevisiae*, mammalian cell lines, and *Xenopus laevis* oocytes [2–6]. Shortly, in this method one of the stop codons (e.g., the *amber* stop codon TAG) is being repurposed to encode for a noncanonical amino acid which is introduced by a modified tRNA with the corresponding anticodon (CUA, Fig. 1a). To obtain the corresponding tRNA, coevolution and selection of an orthogonal *amber* suppressor tRNA/aminoacyl-tRNA synthetase pair for the specific UAA in bacteria is required [5].

For expression of UAA-labeled proteins in *Xenopus laevis* oocytes, a plasmid encoding the tRNA/aminoacyl-tRNA synthetase pair can be injected into the oocyte nucleus. The oocyte-transcribed tRNA is then loaded by the plasmid-encoded synthetase with the UAA, which is subsequently injected into the cytoplasm, together with the cRNA encoding the target protein [2]. Oocytes are amenable for an alternative procedure, where an orthogonal *amber* suppressor tRNA is chemically aminoacylated and directly injected [7]. This prevents the elaborate coevolution of the UAA-specific tRNA/aminoacyl-tRNA synthetase pair but requires appropriate chemical equipment and experience.

Here we provide two protocols for the introduction of the fluorescent amino acid L-3-(6-acetylnaphthalen-2-ylamino)-2-aminopropanoic acid (ANAP [6], Fig. 1b) into P2X7. According to the original 2-step protocol for ANAP introduction in oocyte-expressed proteins (Fig. 1c, [2]), a plasmid encoding several copies of *amber* suppressor tRNA and the corresponding aminoacyl-tRNA synthetase (AnapRS) is first injected into the nucleus of *Xenopus laevis* oocytes and on the following day, ANAP and the in vitro synthesized P2X7 cRNA containing an *amber* stop codon are injected together into the cytoplasm. In our simplified hybrid protocol (Fig. 1d), the uncharged chemically synthesized *amber* suppressor tRNA is directly injected into the cytosol together with the in vitro synthesized cRNAs encoding the aminoacyl-tRNA

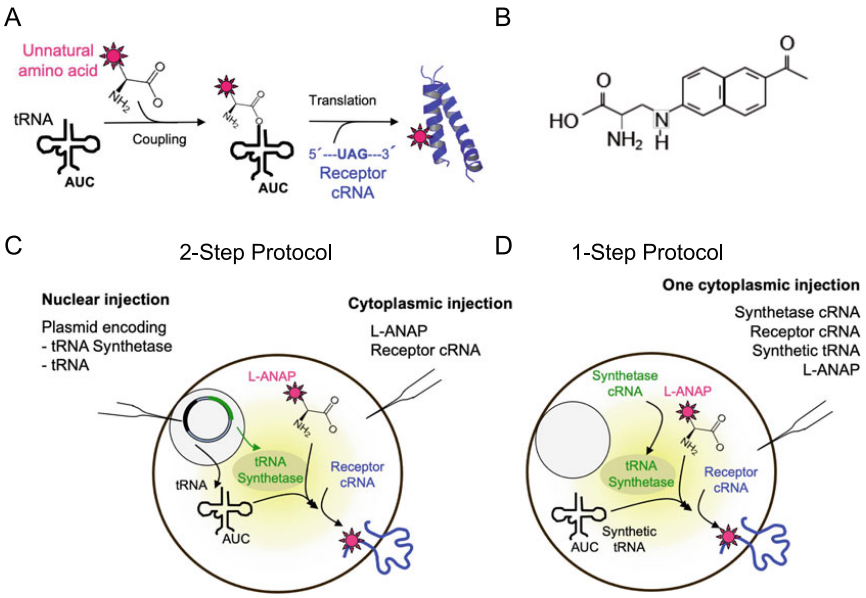

Fig. 1 Incorporation of unnatural amino acids (UAA) into *Xenopus laevis* oocyte-expressed P2X7 receptors. (**a**) Principle of UAA incorporation via an *amber* stop codon (TAG). The unnatural amino acid is coupled (chemically or by an oocyte-expressed synthetase) to the *amber* suppressor tRNA and during translation incorporated into the injected cRNA, which contains the respective codon (UAG at RNA level) in the desired position. (**b**) Structure of the fUAA L-3-(6-acetylnaphthalen-2-ylamino)-2-aminopropanoic acid (ANAP). (**c**, **d**) Schematic drawing of the reagents and injection steps required in the two protocols for UAA incorporation described in this chapter. In both protocols, the UAA is coupled by an oocyte-expressed aminoacyl-tRNA synthetase to the tRNA. In the 2-step protocol, both the tRNA and the synthetase are encoded by a plasmid that is injected into the nucleus. In the 1-step protocol, the tRNA is chemically synthesized and the synthetase is encoded by an in vitro synthesized cRNA

synthetase, a cRNA encoding the P2X7 receptor with a UAG codon at the site of interest, and ANAP. We find that this 1-step cytoplasmic injection is easier and faster to perform and less harmful for the oocytes. To show the efficiency of both protocols, we also provide descriptions for selective Cy5 labeling of His-tagged P2X7 receptors in the oocyte plasma membrane and their subsequent purification, and quantification by SDS-PAGE. Finally, we provide a protocol for voltage clamp fluorometry (VCF) recordings from the ANAP-labeled P2X7 receptor.

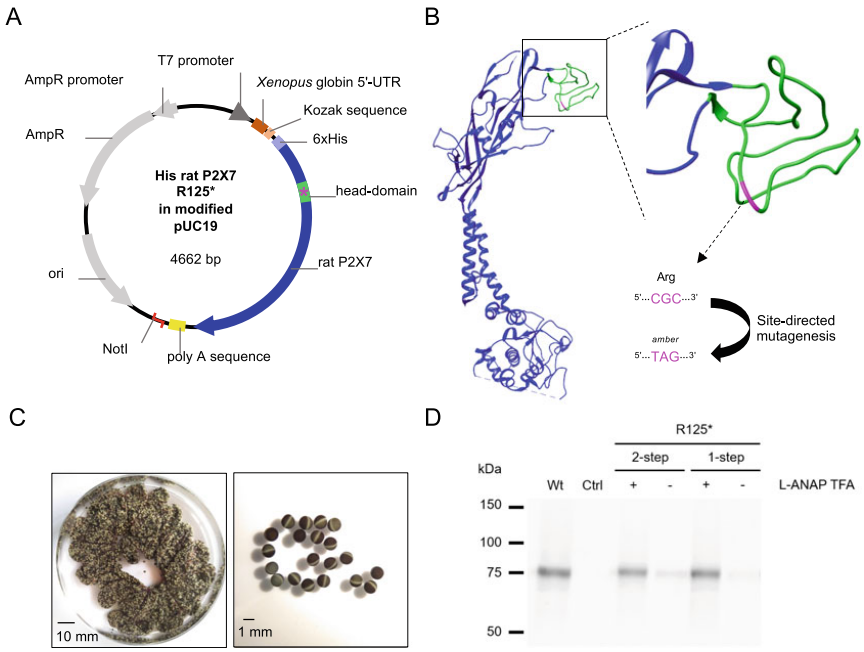

Fig. 2 Successful incorporation of ANAP into the head domain of His-tagged P2X7. (**a**) Plasmid map of the modified pUC19 vector containing the P2X7 coding sequence (blue). Elements that are required for in vitro synthesis of cRNA and support efficient protein expression in *Xenopus laevis* oocytes are colored: T7 promoter (dark gray), a *Xenopus* globin 5′-UTR (brown), Kozak sequence (orange), poly-A sequence (in this case 51 adenines, yellow), and singular restriction site after the poly-A (red). The N-terminal His-tag and the so-called head domain that reaches over the ATP binding site of the P2X7 receptor are shown in light blue and green, respectively. The mutated site is indicated by a pink asterisk. (**b**) Protein structure of one rat P2X7 subunit with the head-domain highlighted. The Arg125 encoding bases were replaced by an *amber* stop codon (colour coding as in (**a**)). (**c**) *Xenopus laevis* ovarian lobes before dissociation (left) and dissociated *Xenopus laevis* oocytes (right). Note the white ring that indicates stage VI oocytes. (**d**) SDS-PAGE gel to confirm successful ANAP incorporation. Oocytes were injected with cRNA and ANAP as indicated (Ctrl indicates noninjected oocytes). Intact oocytes were labeled with membrane impermeant Cy5-NHS ester and His-tagged wt and mutated P2X7 receptors were then purified from oocyte extracts and separated by SDS-PAGE. Note that all bands run at the same size, indicating efficient ANAP incorporation. A small amount of "read-through" product is detected in the absence of ANAP

2 Materials

2.1 Template Preparation and cRNA Synthesis

1. 10–50 µg plasmid for oocyte expression encoding N-terminally His-tagged rat P2X7 receptor containing an *amber* stop codon at the selected site (compare Fig. 2a, b, *see* **Notes 1** and **2**).

2. 10–50 µg oocyte expression plasmid containing a nonmutated His-P2X7 construct as negative control.
3. For 1-step-protocol only: 10–50 µg plasmid for oocyte expression encoding aminoacyl-tRNA synthetase (AnapRS, *see* **Note 3**).
4. Restriction enzymes for linearization of the above plasmids and appropriate 10× restriction enzyme buffer (*see* **Note 4**).
5. Alternatively, if no suitable restriction enzyme or insufficient amounts of plasmid are available: high-fidelity DNA polymerase and appropriate buffer containing 200 µM dNTPs, 2 mM Mg^{2+}, 10 µM forward and reverse primers to amplify template DNA (*see* **Note 5**).
6. DNA purification kit or, alternatively, PCR purification kit (*see* **Note 6**).
7. Agarose gel electrophoresis system with power supply, buffers, appropriate staining solution, and DNA ladder.
8. Photometer to determine cDNA and cRNA concentrations.
9. Ice.
10. RNase-free water (*see* **Note 7**).
11. RNase-free 10 µL filter tips, reaction tubes, and pipettors (*see* **Note 7**).
12. cRNA synthesis kit with the respective polymerase (SP6, T3, or T7, depending on plasmid, *see* **Note 8**).
13. LiCl solution: 7.5 M LiCl, 50 mM EDTA.
14. 70% Ethanol: add 3.333 mL of nuclease-free water to 7 mL of 99.5% EtOH.
15. −20 °C or −80 °C freezer.

2.2 Oocyte Preparation

1. *Xenopus laevis* ovarian lobes.
2. ND96 buffer: 96 mM NaCl, 2 mM KCl, 1 mM $MgCl_2$, 1 mM $CaCl_2$, 5 mM HEPES. For a 10× stock solution add 56.10 g NaCl, 1.49 g KCl, 0.95 g $MgCl_2$, 1.11 g $CaCl_2$, and 11.92 g HEPES to 800 mL of water. Adjust pH with NaOH to 7.5 and fill up to 1 L with water. The 1× working solution is prepared by dilution with water and the pH is adjusted to 7.4–7.5 with NaOH. For storage of oocytes, the buffer is filtered and supplemented with 5 µg/mL gentamicin.
3. Ca^{2+}-free ND96: 96 mM NaCl, 2 mM KCl, 1 mM $MgCl_2$, 5 mM HEPES, pH 7.4–7.5. Prepare a 10× stock solution and 1× working solution as described in **step 1**.
4. Collagenase solution: 1.5–2.5 mg/mL collagenase (origin: *Clostridium histolyticum*, activity: ≥0.18 U/mg) in ND 96. Prepare 15–25 mg aliquots of collagenase in 15 mL reaction tubes and store at 4 °C. Dissolve freshly when needed.

5. 0.22 µm syringe filters and 10 or 20 mL syringe.
6. Orbital shaker.
7. Two fine forceps (Drummond No. 5).
8. Glass pipettes for handling oocytes: break or cut with a glass cutter the tip of a Pasteur pipette at a diameter of around 1.5–2.0 mm. Shortly polish the sharp edges over a flame to avoid damage of oocytes.
9. Large and small cell culture dishes to sort and store oocytes.
10. Stereomicroscope.

2.3 Oocyte Injection

1. About 200 *Xenopus laevis* oocytes (commercially obtained or as described in Subheading 3.2).
2. Micropipette puller (e.g., Narishige PC-10 or similar).
3. Glass capillaries fitting the respective injector.
4. Microinjector (e.g., Drummond Nanoject II or similar) mounted on a manipulator.
5. Light mineral oil for molecular biology.
6. 1 mL Syringe with a long fine steel needle (about 5 cm long with outside diameter that fits into the glass capillaries).
7. Injection chamber: a petri dish with an immersed custom-made plate that contains grooves to line up the oocytes or alternatively, a piece of nylon web (about 0.5 mm meshes) suitable to keep oocytes in place.
8. Parafilm.
9. 2 µL Pipettor with nuclease-free tips.
10. RNase-free water.
11. Red-light illumination (*see* **Note 9**).
12. 1 mM ANAP trifluoroacetic salt (TFA) stock solution: Dissolve 5 mg ANAP TFA in a 10 mL of RNase-free water. If needed, add NaOH to dissolve completely. Adjust the pH to ~7.5 using pH test stripes and add RNase-free water to a final volume of 18.36 mL. Prepare 20 µL aliquots and store protected from light at −20 °C.
13. 1.0 µg/µL mutated and nonmutated P2X7 cRNA (prepared as described in Subheading 3.1).
14. Two-step protocol only: 0.1 µg/µL plasmid pANAP (Addgene #48696, [6]), encoding several copies of *amber* suppressor tRNA and the corresponding aminoacyl-tRNA synthetase (AnapRS).
15. One-step protocol only: 0.8 µg/µL AnapRS cRNA (*see* **Note 3**).

16. One-step protocol only: 1.6 μg/μL chemically synthetized *amber* suppressor tRNA purified via HPLC and PAGE (*see* **Note 10**): Dissolve the lyophilized tRNA in RNase-free water and dilute to a final concentration of 1.6 μg/μL. Prepare 5 μL aliquots and store at −20 °C (short-term storage) or at −80 °C (long-term storage). Avoid freeze–thaw cycles.
17. Small cell culture dishes (about 3–5 cm) to store oocytes.
18. Laboratory incubator, wine cooler, or incubator for reptile eggs to keep oocytes at 16–18 °C.
19. Stereomicroscope.

2.4 NHS-Ester Labeling

1. Cy5- (or other dye) NHS ester stock solution: Dissolve 1 mg Cy5-NHS ester in 100 μL water-free DMSO. If possible, prepare aliquots under argon atmosphere to prevent hydrolysis of the esters and store protected from light at −80 °C.
2. Labeling buffer: ND96 with pH adjusted to pH 8.4 (with NaOH).
3. Stereomicroscope.

2.5 Protein Purification

1. 0.1 M Sodium phosphate buffer (pH 8.0): 5.3 mM NaH_2PO_4, 94.7 mM Na_2HPO_4. Combine 5.3 mL of 0.2 M NaH_2PO_4 solution, 94.7 mL of 0.2 M Na_2HPO_4 solution, and 100 mL of water.
2. 0.4 M Pefabloc stock solution (1000 ×): Dissolve 100 mg of Pefabloc in 1 mL ultrapure water.
3. Homogenization buffer: 0.4 mM Pefabloc, 0.5% *n*-dodecyl-β-D-maltoside in 0.1 M sodium phosphate buffer (pH 8.0). Prepare freshly by dissolving 70 mg of *n*-dodecyl-β-D-maltoside in 14 mL of 0.1 M sodium phosphate buffer (pH 8.0) and add 14 μL of Pefabloc stock solution.
4. 1 M Imidazole solution (pH 8.0): Dissolve 3.4 g of imidazole in ~30 mL ultrapure water. Adjust pH to 8.0 and fill to 50 mL with ultrapure water. Store at 4 °C.
5. Wash buffer: 0.08 mM Pefabloc, 0.1% *n*-dodecyl-β-D-maltoside, 25 mM imidazole in 0.1 M sodium phosphate buffer (pH 8.0). Dilute homogenization buffer 1:5 with 0.1 M sodium phosphate buffer (pH 8.0) and add 25 μL 1 M imidazole/mL.
6. Elution buffer: 300 mM imidazole, 10 mM EDTA, and 0.5% *n*-dodecyl-β-D-maltoside in 20 mM Tris–HCl. Prepare freshly by mixing 50 mg *n*-dodecyl-β-D-maltoside, 200 μL of 1 M Tris–HCl (pH 7.4), 200 μL of 0.5 M EDTA, 3 mL of 1 M imidazole, and adjust with ultrapure water to a final volume of 10 mL.
7. Ni^{2+}-NTA agarose beads.

8. Ice.
9. Desktop cooling centrifuge for 1.5 mL reaction tubes.
10. Overhead shaker (placed at 4 °C).

2.6 SDS-PAGE

1. SDS gel apparatus with power supply.
2. 5× LiDS sample buffer: 5% (w/v) lithium dodecyl sulfate (LiDS), 0.1% bromophenol blue, 100 mM dithiothreitol (DTT), 40% (v/v) glycerol in 0.3 M Tris–HCl (pH 6.8).
3. SDS-PAGE running buffer: 25 mM Tris (base), 192 mM glycine, 0.1% SDS.
4. 4× Stacking gel buffer: 0.5 M Tris–HCl, 0.4% SDS, pH 6.8.
5. 4× Separation gel buffer: 1.5 M Tris–HCl, 0.4% SDS, pH 8.8.
6. 40% acrylamide–bisacrylamide solution (29:1).
7. *N*,*N*,*N*′,*N*′-Tetramethylethane-1,2-diamine (TEMED).
8. 10% ammonium peroxydisulfate (APS) solution. Prepare aliquots of 10–40 mg APS in 1.5 mL reaction tubes. Dissolve in ultrapure water (10 µL/1 mg) freshly when needed.
9. Fluorescence scanner or imager.

2.7 Voltage Clamp Fluorometry

1. Inverted fluorescence microscope with appropriate objective (*see* **Note 11**), light source, and optical filters for UV excitation and detection of emission wavelengths in the low visible spectrum (*see* **Note 12**).
2. Light sensor with signal amplifier (*see* **Note 13**).
3. Custom made recording chamber (see also Fig. 3a) and adapted microscope stage to insert the chamber.
4. Stereomicroscope with swing-arm positioned above the recording chamber.
5. Two-electrode voltage-clamp (TEVC) recording system.
6. Faraday cage (optional).
7. Two microelectrodes (potential and current): electrode holders, silver wire, bleach for chloriding (*see* **Note 14**), borosilicate glass capillaries with filament.
8. Micropipette puller.
9. 3 M KCl solution in ultrapure water.
10. Syringe equipped with 0.22 µm filter and flexible microfilament for backfilling glass capillaries (*see* **Note 15**).
11. Two bath electrodes (reference and ground) with silver chloride pellets.
12. Computer with data acquisition hardware and software (recording program).

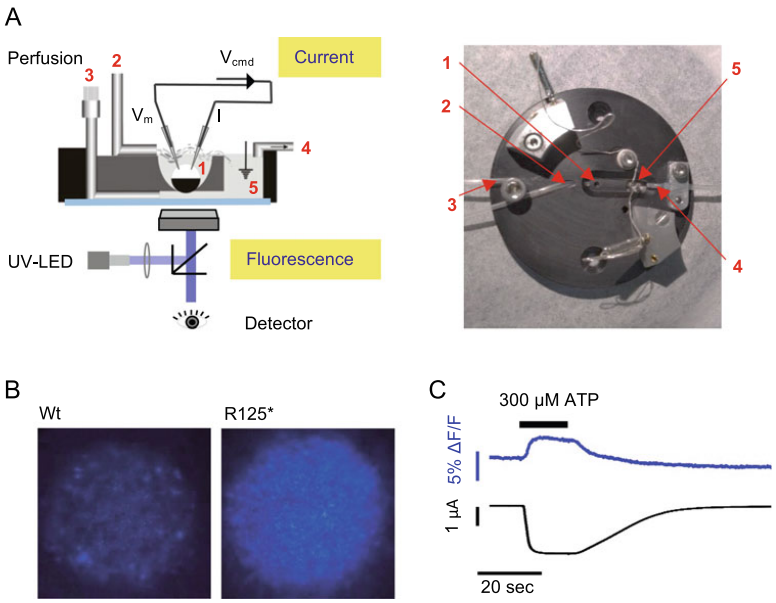

Fig. 3 Voltage clamp fluorometry (VCF) recording of ANAP-labeled P2X7. (**a**) Left: schematic side-view of VCF-setup indicating the two-compartment recording chamber with the oocyte sitting on a hole between both compartments (1), tubing to deliver recording solution into the upper compartment (2) and for delivery of agonist and recording solutions to the lower compartment (3), tubing connected to the pump (4), the two bath electrodes (5), and the optical path. Right: photograph (top-view) of the recording chamber (numbering as in left panel). Perfusion in both compartments is regulated separately via a gravity-based perfusion system. Recording solution and agonist solution are applied via a manifold and switching between solutions is computer-controlled through magnetic valves. A coverslip (light blue in left panel) serves as transparent bottom of the lower compartment. (**b**) View through the fluorescence microscope (630× magnification) focused on the membrane of oocytes co-injected with tRNA, AnapRS cRNA, ANAP and either cRNA encoding His-tagged wt rat P2X7 (left) or cRNA encoding P2X7 with and *amber* stop codon in position 125 (R125*). Images were taken four days after injection. (**c**) VCF-recording from an oocyte expressing P2X7 (R125*). The oocyte was voltage-clamped at −30 mV. The opening state of the channel and the domain movements and/or ligand interactions are recorded in parallel by electrophysiological and optical measurements, respectively

13. Computer-controlled magnetic valve system and gravity-based perfusion system for at least three solutions and manifold.
14. Membrane pump, vacuum flask with rubber stopper, and tubing.
15. Recording solution: 90 mM NaCl, 1 mM KCl, 5 mM HEPES, 100 µM EGTA, 100 µM flufenamic acid, pH 7.4–7.5. For a 10× stock solution add 52.6 g NaCl, 0.75 g KCl, and 11.92 g

HEPES to 800 mL of water, adjust pH to 7.5 with NaOH and fill up to 1 L with water. The 1× working solution is prepared by dilution with water. Add EGTA and flufenamic acid from 0.5 M (in water, pH 7.5) and 100 mM (in DMSO) stock solutions, respectively and adjust pH to 7.4–7.5.

16. 100 mM ATP stock solution in water (pH 7.4): add 551.14 mg of adenosine-5′-triphosphate disodium salt hydrate (Grade I, ≥99%) to 7 mL of filtered water, adjust pH with 1 M NaOH to 7.4, and the total volume to 10 mL. Prepare 1 mL aliquots and store at −20 °C.
17. 70% EtOH: add 3.333 mL of ultrapure water to 7 mL of ethanol (99.5% purity).
18. Red-light illumination.
19. Glass pipette for oocyte handling (*see* Subheading 2.2).
20. UV-protection goggles.
21. 3% H_2O_2.
22. Ultrapure water.
23. Software for data visualization and statistical analysis (*see* **Note 16**).

3 Methods

3.1 Template Preparation and cRNA Synthesis

For the in vitro synthesis of capped cRNA either the enzymatically linearized plasmid DNA (**steps 1–3**) or PCR products containing an RNA polymerase promoter site (**steps 4–6**) can be used as template DNA.

1. Digest 10 µg of plasmid DNA with 10–20 units of restriction enzyme in a total reaction volume of 50 µL (*see* **Note 17**). To prepare the reaction mix, combine DNA and nuclease-free water to reach a volume of 44 µL, add 5 µL 10× restriction enzyme buffer and the enzyme. If the volume of the enzyme is more than 1 µL, adjust the amount of water accordingly.
2. Incubate for 1–2 h at 37 °C or according to the protocol provided with the restriction enzyme (*see* **Note 18**). Heat inactivation of the enzyme is not required because of the following purification step.
3. Confirm complete linearization of the plasmid DNA by agarose gel electrophoresis. Analyze 1 µL of the digestion mix on a 1% agarose gel according to standard protocols. Use undigested plasmid DNA as control. Only one clear band of the expected size must be visible in the digested sample. If linearization is incomplete, extend incubation time (*see* **Note 19**).

4. Assemble PCR reaction on ice according to the manufacturer's protocol. Combine plasmid DNA with DNA polymerase buffer containing dNTPs, Mg^{2+}, and primers. Add nuclease-free water to reach a final volume of 25 µL and add the DNA polymerase last.
5. Amplify according to standard PCR protocols and depending on the polymerase, for example, initialization for 0.5–10 min at 94–98 °C; 20–40 amplification cycles (denaturation: 5–30 s at 94–98 °C; annealing: 10–40 s at primer-specific temperature; elongation: primer-specific time at 72 °C), and a final elongation step of 1–10 min.
6. Check the PCR product for the correct size via agarose gel electrophoresis (*see* **step 3** above).
7. Purify the linear template DNA with a column-based DNA or PCR purification kit, elute in the smallest possible volume (depending on the kit) and determine the concentration using 1 µL of the eluate. Ideally, the concentration of linearized plasmid DNA should be at least 330 ng/µL. Amplified template DNA should be at least 70 ng/µL (*see* **Note 20**).
8. Prepare cRNA synthesis kit: Shortly spin down the enzyme mix and keep on ice. Thaw and vortex the 10× reaction buffer and the 2× NTP/CAP solution, place the NTP/CAP solution on ice. Make sure, the 10× reaction buffer is completely dissolved and keep at room temperature to avoid spermine precipitation.
9. Assemble the transcription reaction in the following order: 5 µL 2× NTP/CAP, 0.2–1.0 µg linear template DNA in 3 µL of RNase-free water, 1 µL 10× reaction buffer, and 1 µL enzyme (*see* **Note 21**).
10. Mix gently by flicking the tube with your fingers or carefully pipetting up and down. Spin down briefly.
11. Incubate at 37 °C for 2 h (*see* **Notes 18** and **22**).
12. Stop the transcription reaction by incubation with 1 µL of TURBO DNase for 15 min at 37 °C.
13. Add 15 µL of RNase-free water and 15 µL of LiCl solution and place at −20 °C or −80 °C for at least 2 h (*see* **Note 23**).
14. Pellet the cRNA by centrifugation (min. 21,000 × *g*, 4 °C, 20 min).
15. Carefully remove supernatant, add 0.5–1.0 mL cold 70% EtOH, and repeat centrifugation (*see* **Note 24**).
16. Completely remove the ethanol from the cRNA, shortly dry the pellet (a few minutes at RT or 10–20 min on ice), and dissolve in 10 µL of RNase-free water.
17. Determine the cRNA concentration and adjust concentration with nuclease-free water. We adjust to 1 µg/µL (P2X7) and 0.8 µg/µL (AnapRS). To reduce the risk of contamination, prepare 5 µL aliquots and store at −80 °C (*see* **Note 25**).

3.2 Oocyte Preparation

Oocytes can either be obtained commercially or prepared from ovarian lobes that are surgically extracted from adult female frogs. In the latter case, a permit for housing and partial ovarectomy of *Xenopus laevis* must be obtained. The ovaries are organized in lobes containing thousands of oocytes in varying stages, follicular cells, and connective tissue interspersed with blood vessels (Fig. 2c).

1. Wash the surgically obtained lobes in a 50 mL reaction tube with cold (4 °C) ND96 until the buffer is clear (*see* **Note 26**). If the oocytes are not immediately used, add gentamicin in the buffer (5 µg/mL) and store the lobes at 4 °C. Change the buffer daily (*see* **Note 27**).
2. Place the lobes into a petri dish with cold ND96 (4 °C). Use fine forceps to tear the lobes into pieces of about 0.5 cm.
3. Dissolve the collagenase in 10 mL of ND96, filter (0.22 µM), and transfer into a fresh 15 mL reaction tube (*see* **Note 28**).
4. Transfer the small oocyte lumps into the collagenase solution and place horizontally on an orbital shaker. Shake carefully at about 100 rpm at room temperature for 1–3 h until the majority of oocytes is isolated.
5. Discard the collagenase, refill the tube with Ca^{2+}-free ND96 solution, and discard the buffer again. Repeatedly wash the oocytes this way until the buffer is clear.
6. Transfer oocytes into a petri dish with Ca^{2+}-free buffer and shake for max. 15 min on an orbital shaker (about 100 rpm) to remove follicular cells.
7. Wash again with cold ND96 until the buffer is clear. Transfer the cells into a petri dish.
8. Using a stereomicroscope and a modified glass pipette, select evenly sized and colored stage V–VI oocytes (Fig. 2c) and put them into a small cell culture dish with fresh ND96 containing gentamicin (5 µg/mL). Store at 4 °C until injection.

3.3 Oocyte Injection: Two-Step Method

To estimate a possible read-through (formation of full-length receptors without ANAP incorporation), nuclease-free water is injected instead of ANAP ("read-through" control). As positive and negative controls, oocytes injected with nonmutated wt P2X7 receptor cRNA alone and noninjected oocytes are used, respectively.

1. Prepare glass pipettes for oocyte injection with a micropipette puller (*see* **Note 29**).
2. Use the syringe with steel needle to backfill the glass pipette with mineral oil. Make sure to avoid any air bubbles (except in the very tip of the pipette).

3. Loosen the collet of the nanoinjector, move out the wire plunger (about 2 cm), carefully slide the pipette over the plunger through the O-rings until it hits the spacer, and tighten the collet. Make sure the pipette is tightly fixed, but do not screw the collet too strong as it will damage the thread or can break the glass pipette.
4. Under a stereomicroscope, open the glass pipette by breaking off its tip with forceps. Using the controller, eject mineral oil until there are no more air bubbles in the tip. The speed with which the oil drops are ejected provides a good measure of the tip diameter. The tip should be as fine as possible (estimated diameter of about 10–30 μm) and oil drops should form very slowly upon pressing the "inject" button.
5. Place 1 μL of the pANAP plasmid on a piece of Parafilm (*see* **Note 30**). Using the manipulator and stereomicroscope, insert the micropipette tip into the plasmid solution and slowly load the glass pipette using the microinjector controller. It is important to avoid formation of air bubbles.
6. Arrange about 70–100 oocytes into the injection chamber or a small petri dish with a nylon mesh covered with ND96. Impale oocytes at the animal pole (about one third of an oocyte's diameter deep) and, using the controller, inject 9.6 nL of pANAP into the nucleus (*see* **Note 31**). Wait a few seconds before removing the pipette tip.
7. Keep injected oocytes for 1 day at 18 °C in ND96 supplemented with gentamicin.
8. On the next day, remove damaged oocytes.
9. For all following steps, use RNase-free equipment and water and a clean working space (*see* **Note 7**). Keep ANAP TFA, and cRNA on ice. Work in the dark to avoid bleaching of ANAP TFA (*see* **Note 9**).
10. Prepare a working solution of 0.25 mM ANAP TFA and place on ice.
11. Prepare an injection mix of 1.2 μL ANAP TFA and 0.4 μL mutated P2X7 cRNA.
12. For the "read-through" control, mix 1.2 μL of nuclease-free water with mutated P2X7 cRNA. For the positive control use only nonmutated P2X7 cRNA.
13. Prepare the injector as in **steps 1–4**. Adjust the injection volume to 46 nL. The tip of the glass pipette can be a bit wider than for nuclear injection. When pushing the "inject" button of the controller, a clearly visible oil drop should form within 1–2 s.

14. Place 1 µL injection mix on a piece of Parafilm and load the glass pipette as described in **step 5**.
15. Inject about 20 oocytes (from **step 7**) by impaling them at the border between the animal (black) and vegetal (white) pole. Place the tip just below the membrane. Successful injection is recognized by a slight swelling of the oocyte. For each injection group (ANAP-labeled receptor, "read-through" and positive control), use a fresh capillary and inject about 20 oocytes.
16. Place oocytes in ND96 supplemented with gentamicin and keep at 18 °C in the dark for at least 2 days. Label dishes at the bottom, to avoid mix-up.
17. Check daily and remove damaged oocytes. Exchange medium if cloudy.

3.4 Oocyte Injection: One-Step Method

1. Work at a clean place using RNase-free equipment (*see* **Note 7**) in the dark (*see* **Note 9**).
2. Thaw aliquots of P2X7 receptor cRNA, AnapRS cRNA, ANAP TFA, and *amber* suppressor tRNA on ice.
3. Mix equal parts of the four solutions to obtain the required amount of injection mix. Usually, 1 µL is sufficient for about 20 oocytes. For a "read-through" control, replace ANAP TFA with nuclease-free water.
4. Prepare the injector and inject into the cytoplasm of oocytes as described under Subheading 3.3, **steps 1–4**, **13**, and **14**.
5. Place oocytes in ND96 supplemented with gentamicin and keep in the dark at 18 °C for at least 2 days. Label dishes at the bottom, to avoid mix-up.
6. Check daily and remove damaged oocytes. Exchange medium if cloudy.

3.5 NHS-Ester Labeling of Surface Protein

To validate the surface expression of His-tagged P2X7 proteins, we label intact oocytes with the membrane-impermeant amino-reactive fluorescent dye Cy5-NHS ester (*see* **Note 32**).

1. After 2–5 days (depending on the position of ANAP-introduction), transfer injected oocytes into a small cell culture dish with cold ND96 labeling buffer and remove damaged or spotted oocytes.
2. Transfer 10–20 oocytes into a 1.5 mL reaction tube, and carefully remove the buffer.
3. Prepare the labeling solution immediately before use by adding 3 µL Cy5 NHS-ester stock solution to 1 mL of ND96 labeling buffer and add 200 µL per group of oocytes. Gently flick the tube with your finger to make sure that the oocytes are evenly covered by the solution and do not stick to the tube wall.

4. Incubate for 30 min under slow inversion (overhead shaker) at 4 °C in the dark.
5. Wash the oocytes in ND96 buffer, check under a stereomicroscope and remove damaged (bright blue) oocytes (*see* **Notes 33** and **34**).

3.6 Protein Purification Via His-Tag

1. The following steps should be performed on ice, using ice-cold buffers.
2. Select 10–20 oocytes of each group into a 1.5 mL reaction tube and place on ice. Remove buffer and add 10 µL homogenization buffer per oocyte. Homogenize by pipetting 10–20 times up and down with a 200 µL pipette tip and incubate on ice for 10 min.
3. Centrifuge for 10 min at 14,000 × *g* and 4 °C. Transfer supernatant into a fresh tube and repeat centrifugation step (*see* **Note 35**).
4. In the meantime, resuspend the Ni^{2+}-NTA agarose beads and transfer 50 µL of the slurry per experimental group into a fresh 1.5 mL reaction tube (*see* **Note 36**). Precondition the beads by washing them 2–3× with 0.5 mL wash buffer (*see* **Note 37**).
5. Add 100 µL of oocyte extract (supernatant from **step 3**), 400 µL of homogenization buffer, and 5 µL imidazole to the Ni^{2+}-NTA agarose beads and incubate for 1 h at 4 °C under slow inversion (overhead shaker) and protected from light.
6. Spin down the beads, remove supernatant, and wash the beads 3× with 0.5 mL wash buffer (*see* **Note 37**).
7. Remove supernatant, add 50 µL elution buffer, and incubate for 10 min at room temperature with occasional tube flicking. Spin down and transfer the supernatant into a new 1.5 mL reaction tube and place on ice. Repeat elution with another 50 µL and combine eluates. Keep on ice until used.

3.7 SDS-PAGE

1. Use a precast polyacrylamide SDS gel (8%) or prepare a gel as described in **steps 2** and **3**. We use a system with about 10 mL volume; for smaller gels adjust the volume accordingly.
2. For the 8% separation gel, mix 4.96 mL ultrapure water, 2.25 mL 4× separation gel buffer, 1.8 mL of 40% acrylamide, 4.5 µL TEMED, and 45 µL of 10% APS and immediately cast a gel with 1 mm spacers. Carefully cover with ultrapure water. After polymerization, remove the water, add the 4% stacking gel (3.18 mL ultrapure water, 1.26 mL 4× stacking gel buffer, 0.5 mL of 40% acrylamide, 5 µL TEMED, and 25 µL of 10% APS), and insert the comb. Make sure to avoid air bubbles.
3. After polymerization, remove the comb, assemble the electrophoresis system, and flush the wells with running buffer.

4. Add 8 µL of 5× LiDS sample buffer to 32 µL of eluate.
5. Load the SDS-gel and run at 100 V until the colored front has entered the separation gel, then continue at 120 V.
6. Analyze the SDS-gel at the appropriate wavelengths using a fluorescence scanner or imager. ANAP fluorescence cannot be detected with conventional imaging systems and successful ANAP-incorporation is recognized by the presence of the full-length protein. For comparison, the nonmutated full-length P2X7 is recommended as a positive control (Fig. 2d).

3.8 VCF-Measurement

1. Turn on the amplifiers (*see* **Note 38**) and the computer and start the recording program. Avoid direct light on the light sensor.
2. Install the two-compartment recording chamber on top of the inverted fluorescence microscope. Using the 10× or 20× objective, make sure, the hole in which the oocyte will be placed, is centered above the objective.
3. Prepare 100 mL of 300 µM ATP in recording solution.
4. Fill the perfusion system with recording solution and ATP solution. Flush the tubing and remove all air bubbles (*see* **Note 39**).
5. Connect the recording solution to the upper compartment of the recording chamber. Connect the manifold to the lower compartment of the recording chamber and to the recording solutions with and without ATP.
6. Connect the bath electrodes (reference and ground) and place them into the recording chamber (Fig. 3a).
7. Chloride the silver wires of the recording electrodes (*see* **Note 14**) and place into electrode holders.
8. Pull microelectrodes (resistance below 1 MΩ) from glass capillaries with filament using a micropipette puller (*see* **Note 40**).
9. Using a syringe with a microfilament, backfill the microelectrodes about one third with filtered KCl solution and carefully place them in the electrode holders. Make sure that the coated silver wire is in contact with the KCl solution. Place the microelectrode holders in the respective connectors of the potential and current electrode headstages.
10. Connect vacuum pump to recording chamber and turn it on (Fig. 3a).
11. Fill both compartments of the recording chamber with recording solution and insert the microelectrodes.
12. Confirm that the resistance is below 1 MΩ (*see* **Note 41**). Adjust the electrode offsets to 0 mV.

13. Turn on the light source of the fluorescence microscope, keep the shutter of the microscope closed, and choose the correct optical filters (*see* **Note 12**).
14. Choose the appropriate objective (*see* **Note 11**) and apply oil or ultrapure water, if necessary.
15. Place the stereomicroscope above the recording chamber and switch to red-light illumination.
16. Start the solution flow in the lower compartment of the recording chamber and place an oocyte with the animal pole facing down into the hole (compare Fig. 3a, *see* **Note 43**).
17. Insert the electrodes into the oocyte (*see* **Note 44**) and start the solution flow in the upper compartment at a slow speed (approximately 200 mL/h) so that the oocyte is always submersed but not flushed away.
18. Turn on the voltage clamp to the desired potential (we measure at −30 mV to keep the current amplitudes reproducible) and check the leak current over the oocyte membrane. Ideally, it should be less than 0.2 μA.
19. Turn off the red-light and put on UV-protection goggles. Switch the light path of the fluorescence microscope to the visual port, open the shutter, and focus on the oocyte membrane (Fig. 3b, *see* **Note 45**). Close the shutter again to minimize exposure of the oocyte to the UV-light before recording.
20. Switch the light path to the detection system.
21. Choose your prepared recording protocol in the recording software. We do repeated 15 s applications of ATP in 90–150 s intervals (*see* **Note 46**).
22. Open the shutter and start parallel recording of current and fluorescence signals.
23. After the measurement, turn off the voltage clamp, close the shutter and switch the light path to the visual port. Turn on the red light and remove the electrodes from the oocyte. Discard the oocyte and control the filling level of the recording and ligand solutions and the solution flow. Stop the upper solution flow before placing a new oocyte into the chamber and starting the next measurement.
24. When finished with all measurements, discard the oocyte, and stop the solution flow in both compartments of the chamber. Disconnect the recording chamber from the perfusion system and rinse with 70% EtOH and with ultrapure water several times (*see* **Note 47**). Turn off the vacuum pump.
25. Clean the tubing system by flushing it with ultrapure water or, if necessary, 3% H_2O_2 (*see* **Note 48**).

26. Export the recording data from the data acquisition software and use appropriate programs for visualization and analysis. A typical recording is seen in Fig. 3c.

4 Notes

1. We cloned the cDNA of the N-terminally His-tagged rat P2X7 receptor via Gibson assembly [8] into a modified pUC19 vector (Fig. 2a) containing a T7 promoter sequence, a *Xenopus* globin 5′-UTR, a Kozak sequence [9], and a poly-A tail. The T7 promoter sequence, the *Xenopus* globin 5′-UTR, and the Kozak sequence were chemically synthesized and the poly-A tail (51 adenines) was obtained from the pNKS2 vector [10].
2. To replace Arg125 in the so called "head-domain" of rat P2X7 with ANAP, the CGC codon was substituted with the *amber* stop codon (TAG, Fig. 2b). In addition, the stop codon of the P2X7 cDNA must be replaced by the ochre (TAA) or opal (TGA) stop codon. For site-directed mutagenesis, we used a kit based on PCR amplification with specifically designed primers and blunt-end ligation according to the manufacturer's protocol.
3. The cDNA sequence necessary for the in vitro cRNA synthesis of the aminoacyl-tRNA synthetase (AnapRS) was obtained from the plasmid pANAP [6] that encodes the coevolved suppressor tRNA/aminoacyl-tRNA synthetase pair and was cloned via Gibson Assembly [8] into the modified pUC19 vector (*see* **Note 1**).
4. Use a unique restriction site downstream of the cDNA of interest and of the poly-A tail. Unique sites for linearization in the His-P2X7/pUC19 vector are *XbaI* or *NotI* (Fig. 2a).
5. Design primers that amplify a promoter site (T7 or SP6), followed by the cDNA encoding the protein of interest (e.g., the aminoacyl-tRNA synthetase or the receptor construct with the introduced *amber* stop codon) and a poly-A tail. While the promoter site can be encoded by the primer, the poly-A tail should be encoded by the plasmid. We keep a distance of about ~50–60 nucleotides between the promoter and the Start ATG and use a molecular biology software to design primers and to calculate their melting temperature.
6. Use a purification kit that allows elution in small volumes (ideally about 10 μL) to obtain highly concentrated DNA.
7. An RNase-free working space is crucial. We work with gloves, use commercial cleaning solutions to destroy RNases on surfaces and equipment, use pipettors and equipment that are exclusively assigned for working with RNA, and use RNase-free solutions, filter tips and plastic ware.

8. We use the mMESSAGE mMACHINE™ T7/SP6 Transcription Kits with slight modifications as described in Subheading 3.1, **steps 8–16**.
9. The excitation maximum of ANAP (365 nm) is outside the visible range of light (~380–750 nm) but its absorption spectrum still overlaps with the emission spectra of most indoor light sources (its absorption intensity at 400 nm is less than 20% [6]). To minimize photobleaching, we work with red light using a simple bicycle rear light as a light source.
10. The sequence for the *amber* suppressor tRNA was translated from the plasmid pANAP that encodes the coevolved suppressor tRNA/aminoacyl-tRNA synthetase pair [6] and augmented with an universal 3′CCA sequence.
11. We use a 63× water immersion objective with a high numerical aperture (NA = 0.9) and free working distance (FWD) of 2.4 mm. The water on the objective lens must be regularly checked between measurements and reapplied if necessary.
12. As a light source, we use a UV LED with a nominal wavelength of 365 nm and optical filters for selecting excitation wavelengths of 355–375 nm and emission wavelengths of 430–490 nm.
13. We use a thermoelectrically cooled multipixel photon counter (MPPC) connected to an external power supply (±5 V) and installed via a custom-made adapter at the fluorescence microscope. To have a straight light path from the object to the detector and avoid a loss of light intensity, optical mirrors were avoided and the detection system was attached to the bottom port of the fluorescence microscope.
14. Silver wires can be chlorided either chemically by inserting them into bleach for at least 15 min or electrically. In the latter case, the wire is connected to the positive pole of a current source (a battery or the analog output of the amplifier (set to 1 V) can be used) and placed into a 1 M KCl solution. Another silver wire in the solution is connected to the negative pole. The coated silver wire should be of dark gray or brown color.
15. To avoid clogging of the microfilament with KCl crystals, flush it after use with ultrapure water.
16. We use a self-written Python-based program for analysis and visualization, but common software programs for statistical analysis and graphing such as Origin or GraphPad Prism can also be used.
17. To compensate for loss of material during the purification, we recommend to digest at least 10 μg of plasmid DNA.
18. When using a heating block for longer incubation times, some of the water can condensate at the lids resulting in a more

concentrated buffer and potential star activity of the enzyme. For a more controlled enzymatic reaction, use an incubator or incubate in a thermocycler at 37 °C chamber temperature and a slightly higher (45 °C) lid temperature.

19. If the enzymatic digestion of the plasmid DNA was incomplete, try to melt supercoiled DNA conformations by heating the plasmid DNA for a few minutes to 95 °C and then let it slowly cool down. This can be done in a beaker or water bath or using a thermocycler (lowering the temperature by 5 °C every 5 min over a period of 1 h). Then add fresh enzyme and start the digestion again.
20. We use a PCR cleanup kit and elute in two steps. Heating the elution buffer (or nuclease-free water) to 70 °C before applying to the column and incubating for 5 min before centrifugation can result in higher yields (check manufacturer's protocol). However, this can potentially also increase the amount of chaotropic salts in the sample. However, we did not notice any effects on downstream enzymatic applications (e.g., cRNA synthesis) with any of the kits we used.
21. To avoid precipitation of the spermine-containing 10× reaction buffer, assemble the transcription reaction at room temperature. We use 0.2 μg of PCR product or 1.0 μg of linearized plasmid DNA as DNA template per 10 μL reaction.
22. The mMESSAGE mMACHINE® protocol suggests an incubation time of 1–2 h for the transcription reaction. However, we recommend an incubation time of 3.5 h for better yields.
23. The mMESSAGE mMACHINE® protocol suggests cRNA precipitation for ≥30 min at −20 °C. In our experience, a longer uninterrupted incubation for 2 h or even over night at either −20 °C or −80 °C leads to better visible cRNA pellets.
24. After the first centrifugation, the transparent cRNA pellet is sometimes difficult to visualize. Always place the reaction tubes in the same orientation in the centrifuge to find the pellet more easily. After addition of EtOH, the pellet may float and is usually easier to detect. Make sure it is not discarded.
25. To check the quality of the cRNA sample, run a 1.2% agarose gel at low voltage with a standard 1 kb DNA ladder. Although the mobility of the single stranded cRNA is different to that of the marker DNA, this will give you some information about the successful synthesis and possible degradation. You should see a distinct single band without any smear.
26. Washing of the oocyte lobe works best in a 50 mL reaction tube. Gently invert the reaction tube, then decant the old buffer. For more complete buffer removal, use a glass pipette.

27. According to our experience, oocytes are more stable if stored as a lobe. If the buffer is exchanged daily, it can be stored up to 1 week. However, we recommend dissociation of the lobe not later than 3 days post-OP, since the quality of the oocytes decreases with longer storage and subsequent incubation times for protein expression might be more limited than with "fresh" oocytes.
28. The collagenase activity can vary between suppliers and from batch to batch. Therefore, the concentration and incubation time should be experimentally determined for every new batch of collagenase.
29. The form and shape of the glass pipette are determined by the temperature and pulling force. For details refer to the manual of the microelectrode puller.
30. When loading the micropipette, the tip of the glass pipette might repel the droplet of cDNA or cRNA due to electrostatic forces. To make the Parafilm more adhesive, stretch it over a microscope slide.
31. The nucleus is located just below the animal pole. In order to inject into the nucleus, make sure to insert the injection pipette through the center of the animal pole perpendicularly to the oocyte surface at an estimated depth of one third of the oocyte's diameter. The thin tip of the injection pipette used for nuclear injection is more likely to clog and solution flow should be checked regularly, for example, by injecting into the air.
32. NHS-esters react with nucleophiles like primary amines and covalently react with lysine residues. The reaction is pH-dependent and works best at pH 8.3–8.5 since the amino group is protonated at lower pH. To a lower extend, NHS-esters also react with serine, threonine, and tyrosine [11].
33. After labeling, intact oocytes show a hardly visible faint bluish color. If oocytes are damaged, the charged Cy5 NHS ester can enter, which is then recognized by dark blue color of the oocyte. Removing these damaged oocytes is crucial to avoid background fluorescence from dye-labeled intracellular proteins on the SDS-gel.
34. Labeled intact oocytes can be stored for about a week. Remove the buffer and store in 1.5 mL reaction tubes on ice protected from light.
35. After centrifugation of homogenized oocytes, there will be three phases: cell debris at the bottom, a fatty layer on top, and a clear phase in between. Transfer the clear phase into a new 1.5 mL reaction tube.

36. To avoid pipetting errors, make sure that the beads are properly suspended and gently swirl the suspension during pipetting. Cut off the tip of a 200 µL pipette tip to avoid clogging.
37. A vacuum pump connected to a vacuum flask and tubing with a fine pipette tip speeds up the process. Be careful to avoid aspiration of the beads.
38. The amplifier from the TEVC recording system contains analog circuits and is temperature-sensitive. It must be turned on at least 30 min before recordings in order for its internal temperature to reach steady-state values. This is also the case for thermoelectrically cooled light sensors.
39. To remove all air bubbles in the recording chamber (especially in the lower compartment, where air bubbles are often not visible), flush the chamber with 100–200 µL 70% EtOH pipetted into the hole between both compartments (Fig. 3a).
40. The opening and shape of the glass pipette determines the microelectrode resistance. Adjust the settings on the micropipette puller to obtain reproducible values.
41. If the electrode resistance is too high, check for air bubbles within the glass micropipette tip. Also check the electrical connection between the silver wire and the screw that provides the electrical connection to the headstage. In case the resistance is too low, the opening of the micropipette is generally too big. In this case, KCl leakage can often be observed around the tip and oocytes depolarize quickly if impaled.
42. Make sure that the bottles containing the recording and ligand solutions are filled to the same level and refill regularly or adjust the position of the flasks between measurements since differences in their filling level influence the solution speed and can create mechanical artefacts.
43. There should be a constant and laminar solution flow in the lower compartment that causes a Venturi effect and sucks the oocyte into the hole. If that is not the case, carefully readjust the position of the tube feeding into the lower compartment of the recording chamber.
44. Under red-light illumination, the microelectrode tips are difficult to visualize against the bright vegetal pole of the oocyte. It might be helpful to adjust the position of the microelectrodes using a dummy oocyte in normal white-light conditions prior to recordings. The general position of the electrodes should remain the same for each new oocyte and needs only slight adjustments. The successful impalement of the oocyte membrane with the microelectrodes is indicated by the potential changes.

45. For every new oocyte and after every renewal of immersion oil/water on the objective, the focus must be checked and, if necessary, readjusted. It might be helpful to use a dummy oocyte for rough focus adjustment so that only slight adjustments are necessary before each recording. It also helps to start with the objective in a low position and carefully moving it upward. However, check the distance of the objective from the coverslip/bottom of the recording chamber to avoid breaking it. If possible, use a different light source for the focusing procedure to avoid exciting the fluorophore before recordings.
46. VCF is sensitive to artefacts caused by oocyte movements upon solution switching. To test for this, begin and end the measurement protocol by switching between ATP-free recording solutions. Carefully readjust solution speed, if this causes a signal.
47. Clean the recording chamber with ultrapure water to remove salt bridges that potentially could cause artefacts.
48. Once a week, the tubing system should be rinsed with 3% H_2O_2 and depending on usage, the tubing system should be replaced to avoid contamination.

Acknowledgments

This work was supported by the Deutsche Forschungsgemeinschaft (DFG, German Research Foundation)—Project-ID: 335447717-SFB 1328. We thank Luis Pardo, MPI for Experimental Medicine in Göttingen and Monika Haberland, Biomedical Center Munich, LMU Munich for providing and preparing oocytes, and Ellis Durner for helpful discussion and technical advice.

References

1. McCarthy AE, Yoshioka C, Mansoor SE (2019) Full-length P2X7 structures reveal how palmitoylation prevents channel desensitization. Cell 179(3):659–670.e613. https://doi.org/10.1016/j.cell.2019.09.017
2. Kalstrup T, Blunck R (2013) Dynamics of internal pore opening in K(V) channels probed by a fluorescent unnatural amino acid. Proc Natl Acad Sci U S A 110(20):8272–8277. https://doi.org/10.1073/pnas.1220398110
3. Santoro SW, Anderson JC, Lakshman V, Schultz PG (2003) An archaebacteria-derived glutamyl-tRNA synthetase and tRNA pair for unnatural amino acid mutagenesis of proteins in Escherichia coli. Nucleic Acids Res 31(23):6700–6709. https://doi.org/10.1093/nar/gkg903
4. Wulf M, Pless SA (2018) High-sensitivity fluorometry to resolve ion channel conformational dynamics. Cell Rep 22(6):1615–1626. https://doi.org/10.1016/j.celrep.2018.01.029
5. Lee HS, Guo J, Lemke EA, Dimla RD, Schultz PG (2009) Genetic incorporation of a small, environmentally sensitive, fluorescent probe into proteins in Saccharomyces cerevisiae. J Am Chem Soc 131(36):12921–12923. https://doi.org/10.1021/ja904896s
6. Chatterjee A, Guo J, Lee HS, Schultz PG (2013) A genetically encoded fluorescent probe in mammalian cells. J Am Chem Soc 135(34):12540–12543. https://doi.org/10.1021/ja4059553

7. Dougherty DA, Van Arnam EB (2014) In vivo incorporation of non-canonical amino acids by using the chemical aminoacylation strategy: a broadly applicable mechanistic tool. ChemBioChem 15(12):1710–1720. https://doi.org/10.1002/cbic.201402080
8. Gibson DG, Young L, Chuang RY, Venter JC, Hutchison CA III, Smith HO (2009) Enzymatic assembly of DNA molecules up to several hundred kilobases. Nat Methods 6(5):343–345. https://doi.org/10.1038/nmeth.1318
9. Kozak M (1987) An analysis of 5′-noncoding sequences from 699 vertebrate messenger RNAs. Nucleic Acids Res 15(20):8125–8148. https://doi.org/10.1093/nar/15.20.8125
10. Gloor S, Pongs O, Schmalzing G (1995) A vector for the synthesis of cRNAs encoding Myc epitope-tagged proteins in Xenopus laevis oocytes. Gene 160(2):213–217. https://doi.org/10.1016/0378-1119(95)00226-v
11. Kalkhof S, Sinz A (2008) Chances and pitfalls of chemical cross-linking with amine-reactive N-hydroxysuccinimide esters. Anal Bioanal Chem 392(1–2):305–312. https://doi.org/10.1007/s00216-008-2231-5

4.3 Evaluation of Binding Kinetics and Inhibitory Potency of Novel P2X7 Antagonists (Manuscript in Preparation)

This project is part of a currently ongoing multidisciplinary collaboration aiming to develop new P2X7R inhibitors with drug-like properties. Besides chemical synthesis, this study involves MD simulations, drug metabolism and pharmacokinetics (DMPK) selection as well as electrophysiological experiments and *in vivo* studies with a murine disease model. The publication of this work is currently in preparation.
In these novel compounds, the adamantane ring structure is replaced by another slightly larger polycyclic scaffold, which resulted in a significant potency increase. Some of these compounds exhibit practically irreversible binding to the receptor, which results in very low nanomolar potencies. A first lead compound has already been shown to improve symptoms in a murine disease model and is currently modified to improve the pharmacokinetic properties (data not shown).

In this study, I performed the following electrophysiological experiments. I first evaluated antagonist potencies of four compounds by TEVC analysis on human P2X7R expressed in *X. laevis* oocytes. These experiments revealed ALT-P2HCl to be the most potent substance, which was then analyzed in more detail. Based on modelling experiments and the structural similarity of the compound to the reported allosteric inhibitor AZ10606120 [21], we expected ALT-P2HCl to bind to the allosteric P2X7 binding pocket, which is formed by neighboring subunits and juxtaposed to the ATP-binding site. To test this hypothesis, I generated two mutants via alanine-substitution in this binding site (F88A and K110A) and compared the potencies at wt and mutant receptors by TEVC. However, IC_{50} values obtained from the respective antagonist DRCs were overestimated, as the apparent binding kinetics did not result in a binding equilibrium within the application phase of the recording protocol. To obtain a more accurate estimate of the compound's potency, I applied a recording protocol to determine the association kinetic at different antagonist concentrations and calculated the theoretical on- and off-rate constants and K_i value from the observed association rate constants (k_{obs}). In addition, I analyzed the time course of antagonist dissociation from wt and mutant P2X7R mutants. Finally, to functionally characterize the compound's binding mode, DRCs for ATP on wt P2X7 and on the F88A mutant in the presence and in the absence of ALT-P2HCl were generated and compared: The compound shifted the DRC to higher concentrations while simultaneously reducing the maximum response.
Together, these data confirmed that the compound acts as a NAM and that F88 in the allosteric binding site is important for its high affinity binding.
I summarized my contribution to this work in the following short report that includes material and methods, results with figures, and a short discussion.

Material and Methods

Cloning and cRNA synthesis

A modified pUC19 vector with an N-terminally His-tagged human P2X7 receptor was generated via Gibson assembly according to the protocol of the manufacturer (Gibson Assembly® Master Mix, New England Biolabs, Frankfurt am Main, Germany). The His-P2X7 sequence together with the T7 promoter sequence, a *Xenopus* globin 5'-UTR, and a Kozak sequence (Kozak, 1987) were synthesized (GeneArt String DNA fragment, Life Technologies/Thermo Fisher Scientific Inc.) and a poly A tail was obtained from the pNKS2 vector (Gloor et al., 1995). F88A and K110A substitutions were introduced using the Q5® Site-Directed Mutagenesis Kit (New England Biolabs, Ipswich, MA, USA). Plasmids were linearized with NotI-HF (NEB) and purified with the MinElute Reaction Cleanup Kit (Qiagen, Hilden, Germany). Capped cRNA was synthesized using the mMESSAGE mMACHINE™ T7 Transcription Kit (ThermoFisher Scientific, Schwerte, Germany) and dissolved in nuclease-free water (500 ng/µl).

***Xenopus laevis* oocytes**

Xenopus laevis frogs were from Nasco International (Fort Atkinson, WI) and ovaries were kindly provided by Prof. Dr. Luis Pardo (Max Planck Institute for Experimental Medicine, Göttingen, Germany). Oocytes were isolated and defolliculated by treatment with collagenase (1.0-1.5 mg/ml, ≥2 hours shaking (110 rpm) at RT) and a 15-min treatment in Ca^{2+}-free oocyte Ringer (90 mM Nacl, 1 mM KCl, 2 mM $MgCl_2$, 5 mM HEPES), respectively. 50 nl of cRNA (0.5 µg/µl) were injected using a Nanoject II injector (Science Products, Drummond) and oocytes were kept in ND96 (96 mM NaCl, 2 mM KCl, 1 mM $MgCl_2$, 1 mM $CaCl_2$, 5 mM HEPES, pH 7.4-7.5) supplemented with Gentamicin (50 µg/ml) at 16°C for 2 days and then at 4°C to control expression levels.

Biochemical analysis of P2X7 surface expression

To analyze the surface expression of the His-tagged hP2X7 receptor constructs, oocytes were labeled with the membrane-impermeant amino-reactive fluorescent dye Cy5 (Cy5 Mono NHS Ester, Fisher Scientific, 0.001% in ND96, pH 8.5) for 1 hour under rotation in the dark. After labeling of the surface protein, oocytes were washed in ND 96 and 10 oocytes were supplemented with 10 µl homogenization buffer per oocyte (0.1 M sodium phosphate buffer (pH 8.0) containing 0.4 mM Pefabloc and 0.5% dodecylmaltoside (both Merck KGaA, Darmstadt, Germany)). Oocytes were homogenized by pipetting up and down and extracted for 10 min on ice. His-P2X7 complexes were purified by Ni^{2+}-NTA agarose as described (Nicke et al., 1998). Briefly, extracts were centrifuged (twice for ≥ 15 min at 15000 rpm and 4°C) and 100 µl of the supernatant were diluted with 400 µl of homogenization buffer and supplemented with 50 µl preconditioned (in washing buffer, see below) Ni^{2+}-NTA agarose beads and 10 mM imidazole. After 1 hours of inverting at 4°C in the dark, beads were washed 3-4 times with 500 µl washing buffer (0.1 M sodium phosphate buffer (pH 8.0) containing 0.08 mM Pefabloc, 0.1% dodecylmaltoside, and 25 mM imidazole). His-tagged protein was eluted at room temperature with 2 x 50 µl elution buffer (20 mM Tris-HCl, 300 mM imidazole, 10 mM EDTA, and 0.5% dodecylmaltoside) and 40 µl sample were separated by reducing SDS-PAGE (8%). Protein was dedected with a Typhoon trio fluorescence scanner (GE Healthcare).

Two-electrode voltage clamp (TEVC) electrophysiology

At least 36 hours after cRNA injection, two-electrode voltage clamp recordings were performed at RT and a holding potential of -70 mV using a Turbo Tec-05X Amplifier (npi electronic, Tamm, Germany), a magnetic valve system, and CellWorks E 5.5.1 software. Currents were filtered at 1 kHz and digitized at 200 Hz. Electrodes resistances were below 1.2 MΩ. A fast and reproducible solution exchange (<300 ms) was achieved with a 50-µl funnel-shaped oocyte chamber combined with a fast vertical solution flow fed through a custom-made manifold mounted immediately above the oocyte.

Recordings were performed in ND96. A standard concentration of 300 µM ATP in low divalent buffer (no $MgCl_2$, 0.5 mM $CaCl_2$) was applied for 2 sec in 4-min intervals, followed by a 1-min perfusion with buffer. To compare antagonist potencies, stable agonist responses were obtained and then 10 nM (final concentration) of compound were applied from a stock solution into the static bath and incubated for 3 min.

To estimate association and dissociation rates, ATP was applied in 2-min intervals. After stabilization of agonist-evoked responses, solutions were switched to antagonist-containing solutions and continuously superfused (association rates) or a sufficient block was established by a 1 min incubation with agonist in a static bath (dissociation rate) before perfusion proceeded. Responses following antagonist application were normalized to the preceding, stabilized agonist responses.
Association curves were fit to the data by the equation *% response = (100-Plateau)*exp(-k_{obs}*time)+Plateau*.
To create antagonist dose-response curves, ATP-evoked responses after 2-min antagonist perfusion were obtained from the association studies. IC_{50} values were calculated from a nonlinear fit of the Hill equation to these data : *% response =Bottom + (Top-Bottom)/(1+10^((LogIC_{50}-X)*n_H))*, where *Top* and *Bottom* are constrained to 100% and 0%, respectively, *X* corresponds to the log of concentration of the agonist, and n_H corresponds to the Hill coefficient . All data were analyzed using Prism software (Graphpad Software, Inc., Version 8.3.0, San Diego, CA) and are presented as means ± S.D. from at least three oocytes.

To determine agonist dose-response curves, a setup optimized for automatic application of small solution volumes and lateral perfusion was used and ATP was applied for 5 sec in 2-min intervals. A reference concentration of 1 mM ATP (ATP_{Ref}) was used to stabilize responses and was alternatively applied with test responses to different ATP concentrations (ATP_{test}). After each agonist application the cell was washed with buffer for 105 sec and antagonist was then pre-incubated for 15 sec before co-application together with the agonist. EC_{50} values were calculated from fitting to the four-parameter Hill equation *% response =Bottom + (Top-Bottom)/(1+10^((LogEC_{50}-X)*n_H))*, where all responses are normalized to the response of ATP_{Ref} *Bottom* was constrained to zero, *Top* corresponds to the maximum response, *X* corresponds to the log of concentration of the agonist, and n_H corresponds to the Hill coefficient. Note that due to the slow recovery from agonist block, DR data in the presence of antagonist were obtained from multiple oocytes.

Antagonist dilutions were made in ND96 or DMSO in a way that the final concentration of DMSO in the measuring chamber did not exceed 1%. Note that the potency of the compounds was influenced by the dilution procedure. If dilutions from a 1 mM stock were made in DMSO instead of ND96, the MBX-compounds were more potent and *vice versa*.

Results

The inhibitory potency of ALT-P2HCl, ALT-P2OHCl, MBX-46, and MBX-47 was evaluated by two-electrode voltage-clamp (TEVC) analysis using the human P2X7 receptor expressed in *Xenopus laevis* oocytes. Upon 3 min pre-incubation with 10 nM antagonist, ALT-P2HCl and ALT-P2OHCl produced an 80% and 60% reduction of ATP (300 μM)-induced current responses, respectively, while MBX-46 and MBX-47 produced less than 20% inhibition under these conditions (Fig. 1A).

Because of its structural similarities to the allosteric inhibitor AZ10606120, ALT-P2HCl is supposed to inhibit the P2X7 receptor by a negative allosteric mechanism. The binding site of AZ10606120 was shown to bind different structurally unrelated compounds. It is formed by neighboring subunits and juxtaposed to the ATP-binding pocket. The F88A mutation has previously been shown to reduce the potency of P2X7-specific inhibitors (A740003, A804598, AZ10606120, JNJ47965567) in a YO-PRO-1 uptake assay in HEK293 cells (Karasawa & Kawate, 2016). To confirm that ALT-P2HCl acts via a similar mechanism and to investigate its binding mode, we next generated two mutations, F88A and K110A, in the allosteric binding pocket. As shown by SDS-PAGE analysis in Fig. 1B, both mutants showed expression levels in the *Xenopus laevis* oocyte membrane comparable to the wt receptor.

In order to estimate the IC_{50} value of ALT-P2HCl for the P2X7 receptor constructs, we first investigated its binding kinetics in order to choose suitable pre-incubation times. Application of 300 μM ATP in 2-min intervals in the continuous presence of 10 nM ALT-P2HCl revealed that maximum antagonist binding was reached only after about 30 min. As such long pre-incubation times are not practical, we first determined the IC_{50} values based on the values obtained after a 2-min pre-incubation time (Table 1, Fig. 1C). We found an IC_{50} value of 54.99 nM for wt hP2X7, an about 10-fold lower IC_{50} value for hP2X7 K110A (4.90 nM) and an about 2-fold higher IC_{50} value for hP2X7 F88A (0.13 μM). As these values were measured before antagonist binding was completed and therefore are overestimated and much higher than the ones obtained above, we next set out to analyze the association and dissociation kinetics of ALT-P2HCl to obtain a more accurate estimate of its potency. As seen in Fig. 1D the different P2X7 constructs revealed marked differences in ALT-P2HCl binding kinetics and affinity. When ATP (300 μM) was applied in 2-min intervals under continuous superfusion with 3 nM antagonist, an about 50% block was obtained for the wt receptor but an equilibrium was still not reached after about 40 min. For the K110A mutant, however, an equilibrium and an about 80% block was reached after only 15 min, whereas the F88A mutant was completely unaffected at this concentration (Fig. 1D). Likewise, ALT-P2HCl showed minimal dissociation within 20 min from both wt hP2X7 and hP2X7 K110A receptors (Fig 1E). In contrast, hP2X7 F88A recovered fully after a 90-100% block by ALT-P2HCl (Fig. 1C, Supplement Fig. 2).

These data confirmed that the F88 is required for high affinity antagonist binding. In contrast, the association rate observed for hP2X7 K110A (about 9-fold higher than for the wt receptor) suggests, that the K110A substitution facilitates ALT-P2HCl binding.

Finally, to confirm that ALT-P2HCl acts as a negative allosteric modulator (NAM) on the P2X7 receptor, DRCs for ATP on P2X7 with and without 3 μM of the compound were generated (Table 2). As shown in Fig. 1F, ALT-P2HCl shifts the curve to higher concentrations and additionally decreases the maximum response, indicating a negative allosteric mechanism of ALT-P2HCl.

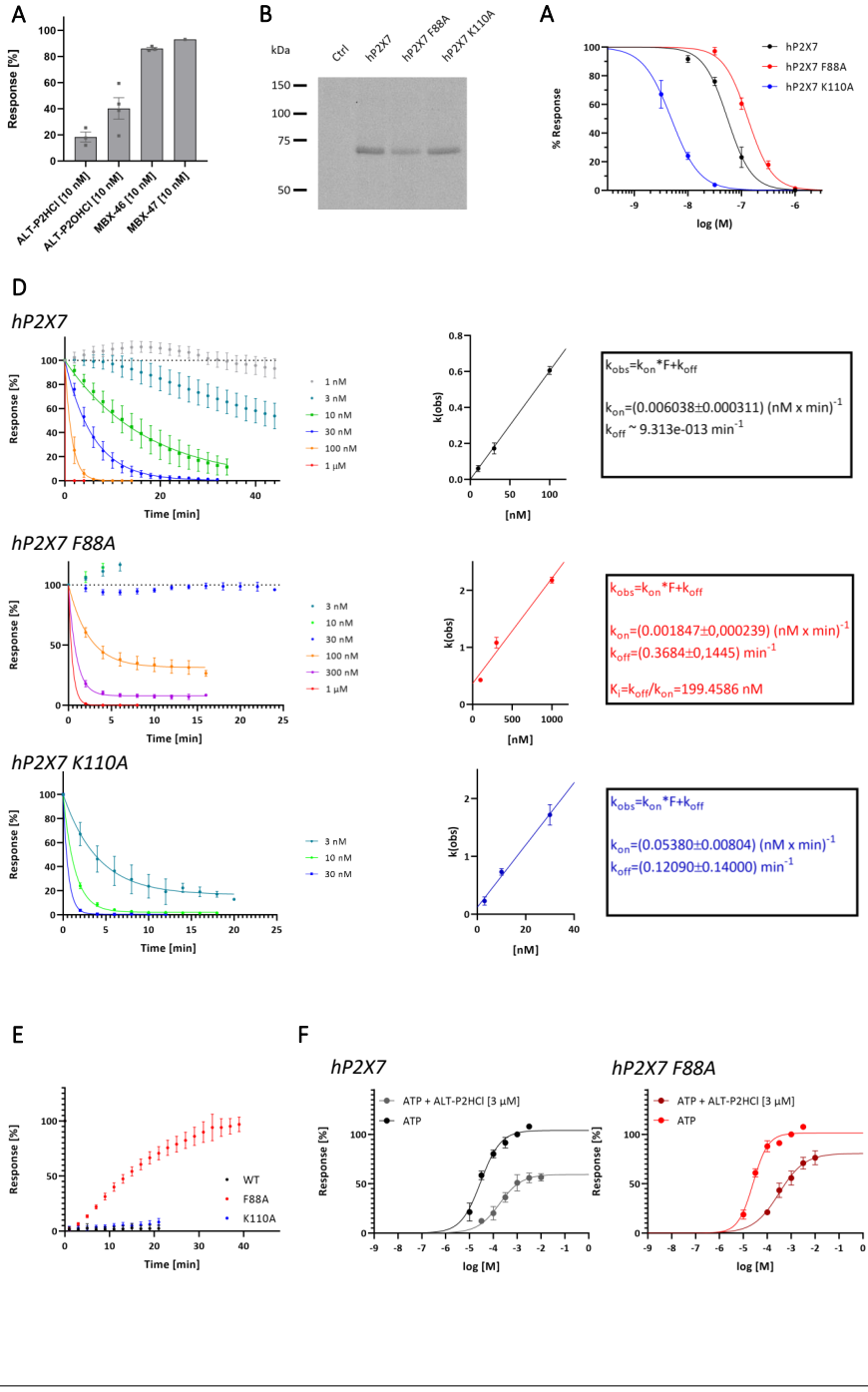
A
Response [%]
ALT-P2HCl [10 nM]
ALT-P2OHCl [10 nM]
MBX-46 [10 nM]
MBX-47 [10 nM]
B
kDa
Ctrl
hP2X7
hP2X7 F88A
hP2X7 K110A
150
100
75
50
A
% Response
log (M)
hP2X7
hP2X7 F88A
hP2X7 K110A
D
hP2X7
Response [%]
Time [min]
1 nM
3 nM
10 nM
30 nM
100 nM
1 µM
k(obs)
[nM]
kobs=kon*F+koff
kon=(0.006038±0.000311) (nM x min)-1
koff ~ 9.313e-013 min-1
hP2X7 F88A
300 nM
kon=(0.001847±0,000239) (nM x min)-1
koff=(0.3684±0,1445) min-1
Ki=koff/kon=199.4586 nM
hP2X7 K110A
kon=(0.05380±0.00804) (nM x min)-1
koff=(0.12090±0.14000) min-1
E
WT
F88A
K110A
F
ATP + ALT-P2HCl [3 µM]
ATP
log [M]

Figure 1: **Comparison of antagonist potency at *Xenopus* oocyte-expressed hP2X7 receptor mutants.** The indicated human P2X7 constructs were expressed in *Xenopus laevis* oocytes and analyzed by TEVC at -70 mV. **A** Comparison of the different antagonists at wt human P2X7 . Reduction of ATP (300 µM) responses after 3 min incubation with 10 nM of the indicated antagonists. Responses are normalized to ATP responses in the absence of antagonist. Error bars represent SEM **B** Plasma membrane expression of wt and mutant P2X7 receptors**.** The indicated His-tagged human P2X7 constructs were expressed in *Xenopus laevis* oocytes, labeled with membrane impermeant Cy5, purified by Ni^{2+}-NTA agarose and separated by SDS-PAGE. Gels were directly scanned with a fluorescence scanner. A representative result is shown. **C** Concentration-response analysis of ALT-P2HCl on wt and mutant hP2X7 receptors. Responses to 2-sec pulses of 300 µM ATP were recorded after a 2-min antagonist perfusion. IC_{50} values are given in Table 1. **D** Time course of ALT-P2HCl binding to wt and mutant P2X7 receptors. P2X7-expressing oocytes were continuously superfused with the indicated concentrations of ALT-P2HCl and ATP was applied in 2-min intervals. Experimentally determined on-rates (k_{obs}) were plotted against antagonist concentrations to obtain an estimate for the off-rate constant and the K_I value. *F* in the formula indicates the free antagonist concentration. **E** Time course of ALT-P2HCl dissociation from wt and mutant P2X7 receptors. Normalized responses to 2-sec pulses of ATP (300 µM) after a 90-100% block by ALT-P2HCl. **F** For binding mode analysis, the agonist dose-response relationship for ATP on hP2X7 (left) and on hP2X7 F88A (right) were compared in the presence and absence of 3 µM ALT-P2HCl. **All** data are represented as mean +/- S.D. from 3-9 measurements, if not otherwise stated.

Table 1: IC_{50}-values, theoretical on- and off-rate constants and K_I values according the equations $k_{obs}=k_{on}*F+k_{off}$ and $K_I=k_{off}/k_{on}$, for wt hP2X7, hP2X7 F88A, and hP2X7 K110A. Number in brackets are 95% Confidence Intervals, N.D. means not determined. Note that calculations based upon k_{obs} were oversimplified and represent only estimates (for details see discussion).

	hP2X7	**hP2X7 F88A**	**hP2X7 K110A**
IC_{50}	5.499e-008 M [4.812e-008 - 6.288e-008]	1.321e-007 M [1.199e-007 - 1.457e-007]	4.904e-009 M [4.239e-009 - 5.649e-009]
K_I calculated from k_{obs}	1.542398e-010 nM	199.4586 nM	2.24721 nM
k_{on} calculated from k_{obs}	0.006038 (nM x min)$^{-1}$ [0.005623 - 0.006338]	0.001847 (nM x min)$^{-1}$ [0.001609 - 0.002086]	0.05380 (nM x min)$^{-1}$ [0.04576 - 0.06181]
k_{off} calculated from k_{obs}	~ 9.313e-013 min^{-1} [N.D.]	0.3684 min^{-1} [0.2239 - 0.5128]	0.12090 min^{-1} [0.0000 - 0.2800]

Table 2: EC_{50} values for ATP with or without ALT-P2HCl on hP2X7 and hP2X7 F88A. Number in brackets are 95% Confidence Intervals.

	ATP	**ATP + ALT-P2HCl**
hP2X7	2.970e-005 M [2.421e-005 - 3.745e-005]	1.812e-004 M [1.202e-004 - 3.079e-004]
hP2X7 F88A	2.566e-005 M [2.156e-005 - 3.080e-005]	3.109e-004 M [1.995e-004 - 7.864e-004]

Discussion

Observed on-rates k_{obs} were determined by fitting the data to the function *% response = (100-Plateau)*exp(-k_{obs}*time)+Plateau* and the obtained constants were then plotted against the respective antagonist concentration. Assuming the most simple case of receptor-ligand kinetics, a 1:1 binding model, this formula was used to obtain an estimate of the theoretical off-rate constant k_{off} and the theoretical K_i value. It has to be considered, however, that the P2X7 receptor has three orthosteric ATP-binding sites and three allosteric drug-binding pockets with unknown single molecule binding kinetics. Thus, the binding model is most likely much more complex and this calculation can only be regarded as a rough estimation.

Supplemental Information

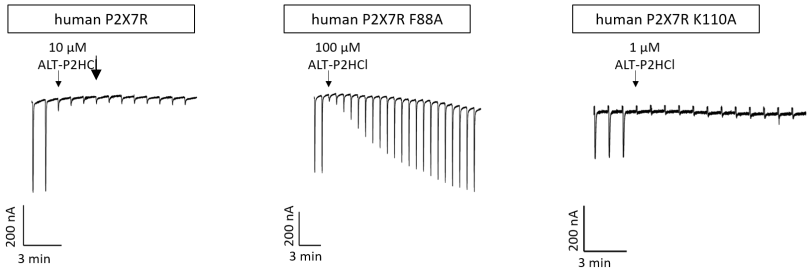

Figure 2: ***Antagonist dissociation from the indicated receptor constructs via the recovery of receptor function over time.*** *Representative current responses to 2-sec pulses of ATP (300 µM) after a 90-100% block by ALT-P2HCl. After stabilization of current responses, the antagonist was applied into the static bath at an appropriate concentration (wt: 10 µM, F88A: 100 µM, K110A: 1 µM) once and incubated for 1 min (indicated by arrow, incubation time not shown).Only hP2X7 F88A recovers fully after a 90-100% block by ALT-P2HCl. However, the recovery time is about 40 min.*

Additional Information

Diluting the compounds from a 1 mM stock with either DMSO or ND96 had an impact on the compounds' efficiency. Specifically, the ALT-compounds were more effective when diluted in buffer (10 nM), whereas the MBX-compunds were only effective when diluted in DMSO and a 100-fold higher concentrated (1 µM) (Fig. 4). The DMSO concentration in the recording chamber did not exceed 1%.

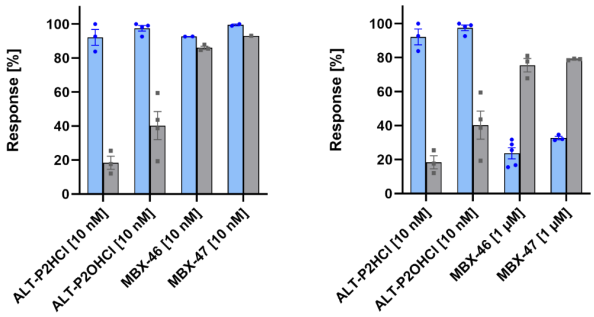

Figure 2: Dilution with either DMSO or buffer affects the activity of the compound.

Gloor, S., Pongs, O., & Schmalzing, G. (1995). A vector for the synthesis of cRNAs encoding Myc epitope-tagged proteins in xenopus laevis oocytes. *Gene*, *160*(2), 213–217. https://doi.org/10.1016/0378-1119(95)00226-V

Karasawa, A., & Kawate, T. (2016). Structural basis for subtype-specific inhibition of the P2X7 receptor. *ELife*, *5*. https://doi.org/10.7554/eLife.22153

Kozak, M. (1987). An analysis of 5'-noncoding sequences from 699 vertebrate messenger rNAS. *Nucleic Acids Research*, *15*(20), 8125–8148. https://doi.org/10.1093/nar/15.20.8125

Nicke, A., Bäumert, H. G., Rettinger, J., Eichele, A., Lambrecht, G., Mutschler, E., & Schmalzing, G. (1998). P2X1 and P2X3 receptors form stable trimers: A novel structural motif of ligand-gated ion channels. *EMBO Journal*, *17*(11), 3016–3028. https://doi.org/10.1093/emboj/17.11.3016

4.4 Re-evaluation of Neuronal P2X7 Expression Using Novel Mouse Models and a P2X7-specific Nanobody

This comprehensive publication addresses a potential neuronal expression of the P2X7R. Novel BAC transgenic mouse lines overexpressing a P2X7-EGFP fusion protein were generated, characterized, and used to investigate cell-type specific P2X7 protein expression in complex tissues, specifically in the central nervous system (CNS). In addition, functional consequences of P2X7 overexpression were investigated. The expression of the P2X7-EGFP fusion protein is expected to be under the control of the BAC-derived regulatory sequence, the mouse *P2rx7* promoter. A BAC transgenic approach was used, aiming to ensure reliable reproduction of the endogenous P2X7 expression pattern in transgenic mice and to analyze poteintial overexpression effects. It is shown, that P2X7-EGFP overexpression did not affect endogenous receptor synthesis, and that P2X7-EGFP subunits could be co-purified with endogenous P2X7 subunits, confirming efficient co-assembly of both. The functionality of the fusion protein was demonstrated via ATP-induced DAPI uptake in so-called 'rescue' mice, that were generated by crossing the P2X7-EGFP BAC transgenic mice with P2X7 knockout mice (*P2rx7*$^{-/-}$) and only expressed the transgenic P2X7-EGFP. To confirm the correct cell type-specific expression, the expression patterns of P2X7-EGFP and endogenous P2X7 were compared by immunostaining in brain slices, including DAB stainings with EGFP-specific antibodies and a novel mouse P2X7-specific nanobody-rbIgG fusion construct (7E2-rbIgG). Co-staining of brain sections from wt, *P2rx7*$^{-/-}$, and P2X7-EGFP overexpressing transgenic mice, with 7E2-rbIgG and commercially available P2X7-specific antibodies revealed that the nanobody-rbIgG fusion construct has superior specificity. Co-labeling with cell type-specific markers and quantitative analysis revealed P2X7-EGFP protein expression mainly in microglial cells, Bergmann glia, and oligodendrocytes, however, not in neurons. The dominant expression in microglia and oligodendrocytes was further confirmed by quantification of P2X7 protein (by Western blot) from brain tissue of the respective cell type-specific knockout mice. In addition, neuronal localization of P2X7 was investigated in the spinal cord, dorsal root ganglia, retina, and neuromuscular synapse, but could not be detected. Upregulation of P2X7 in neurons was also not found following *status epilepticus* or after neural tissue damage. Finally, the overexpression of P2X7 did not cause any obvious behavioral or morphological effects under physiological conditions but a trend towards increased microglia numbers/activation in disease models (stab wound, *status epilepticus*, ischemic retina).

It was concluded that P2X7 is either not present or not detectable in neurons and that reported P2X7-dependent neurodegeneration is more likely due to indirect effects caused by P2X7 activation in microglia or oligodendrocytes rather than by direct activation of neuronal P2X7Rs. This contrasts with findings in other P2X7 (reporter) mouse models (Tg(P2rx7 EGFP)FY174Gsat and P2rx7^{hP2RX7}), which might be explained by alterations in gene structure, possibly affecting transcriptional and/or translational regulatory mechanisms.

My contribution to this work was the validation of immunofluorescence staining experiments by DAB staining using the Avidin-Biotin Complex (ABC) method. This colorimetric technique has the advantage that the signal from the primary antibody is amplified and can be enhanced by a prolonged exposure. In this study, colorimetric

DAB stainings yielded more intense signals than immunofluorescence stainings using the same primary antibody (in this case 7E2-rbIgG) and thus allowed a comparison of P2X7 expression in the P2X7-EGFP overexpressing transgenic mice with that of endogenous P2X7 in wt animals. Finally, I also contributed with text editing to the manuscript.

Re-evaluation of Neuronal P2X7 Expression Using Novel Mouse Models and a P2X7-specific Nanobody

Karina Kaczmarek-Hajek†, Jiong Zhang†, Robin Kopp†, Antje Grosche, Björn Rissiek, Anika Saul, Santina Bruzzone, Tobias Engel, Tina Jooss, Anna Krautloher, Stefanie Schuster, Tim Magnus, Christine Stadelmann, Swetlana Sirko, Friedrich Koch-Nolte, Volker Eulenburg, Annette Nicke

†*these authors contributed equally to this publication*

published in

eLife 2018, 7:e36217

eLIFE elifesciences.org

RESEARCH ARTICLE

Re-evaluation of neuronal P2X7 expression using novel mouse models and a P2X7-specific nanobody

Karina Kaczmarek-Hajek[1†], Jiong Zhang[1,2†‡], Robin Kopp[2†], Antje Grosche[3,4], Björn Rissiek[5], Anika Saul[1§], Santina Bruzzone[6], Tobias Engel[7], Tina Jooss[2], Anna Krautloher[2], Stefanie Schuster[8], Tim Magnus[5], Christine Stadelmann[9], Swetlana Sirko[4,10], Friedrich Koch-Nolte[11], Volker Eulenburg[8,12], Annette Nicke[1,2*]

[1]Department of Molecular Biology of Neuronal Signals, Max Planck Institute for Experimental Medicine, Göttingen, Germany; [2]Walther Straub Institute for Pharmacology and Toxicology, Ludwig-Maximilians-Universität München, Munich, Germany; [3]Institute for Human Genetics, University of Regensburg, Regensburg, Germany; [4]Department of Physiological Genomics, Ludwig-Maximilians-Universität München, München, Germany; [5]Department of Neurology, University Hospital Hamburg-Eppendorf, Hamburg, Germany; [6]Department of Experimental Medicine and CEBR, University of Genova, Genova, Italy; [7]Department of Physiology and Medical Physics, Royal College of Surgeons in Ireland, Dublin, Ireland; [8]Institute of Biochemistry, University Erlangen-Nürnberg, Erlangen, Germany; [9]Institute of Neuropathology, University Medical Center, Göttingen, Germany; [10]Institute of Stem Cell Research, Helmholtz Center Munich, German Research Center for Environmental Health (GmbH), Neuherberg, Germany; [11]Department of Immunology, University Hospital Hamburg-Eppendorf, Hamburg, Germany; [12]Department of Anaesthesiology and Intensive Care Therapy, University of Leipzig, Leipzig, Germany

***For correspondence:** annette.nicke@lrz.uni-muenchen.de

[†]These authors contributed equally to this work

Present address: [‡]Department of Neurology, University Medical Center, Göttingen, Germany; [§]Synaptic Systems GmbH, Göttingen, Germany

Competing interest: See page 24

Funding: See page 24

Received: 05 March 2018
Accepted: 31 July 2018
Published: 03 August 2018

Reviewing editor: Kenton Jon Swartz, National Institute of Neurological Disorders and Stroke, National Institutes of Health, United States

Abstract The P2X7 channel is involved in the pathogenesis of various CNS diseases. An increasing number of studies suggest its presence in neurons where its putative functions remain controversial for more than a decade. To resolve this issue and to provide a model for analysis of P2X7 functions, we generated P2X7 BAC transgenic mice that allow visualization of functional EGFP-tagged P2X7 receptors *in vivo*. Extensive characterization of these mice revealed dominant P2X7-EGFP protein expression in microglia, Bergmann glia, and oligodendrocytes, but not in neurons. These findings were further validated by microglia- and oligodendrocyte-specific P2X7 deletion and a novel P2X7-specific nanobody. In addition to the first quantitative analysis of P2X7 protein expression in the CNS, we show potential consequences of its overexpression in ischemic retina and post-traumatic cerebral cortex grey matter. This novel mouse model overcomes previous limitations in P2X7 research and will help to determine its physiological roles and contribution to diseases.
DOI: https://doi.org/10.7554/eLife.36217.001

Introduction

The P2X7 receptor differs from all other P2X family members by its low sensitivity to ATP, a particularly long intracellular C-terminus, and its ability to trigger various short and long-term cellular events

eLife digest The human body relies on a molecule called ATP as an energy source and as a messenger. When cells die, for example if they are damaged or because of inflammation, they release large amounts of ATP into their environment. Their neighbors can detect the outpouring of ATP through specific receptors, the proteins that sit at the cell's surface and can bind external agents.

Scientists believe that one of these ATP-binding receptors, P2X7, responds to high levels of ATP by triggering a cascade of reactions that results in inflammation and cell death. P2X7 also seems to play a role in several brain diseases such as epilepsia and Alzheimer's, but the exact mechanisms are not known. In particular, how this receptor is involved in the death of neurons is unclear, and researchers still debate whether P2X7 is present in neurons and in other types of brain cells.

To answer this, Kaczmarek-Hájek, Zhang, Kopp et al. created genetically modified mice in which the P2X7 receptors carry a fluorescent dye. Powerful microscopes can pick up the light signal from the dye and help to reveal which cells have the receptors. These experiments show that neurons do not carry the protein; instead, P2X7 is present in certain brain cells that keep the neurons healthy. For example, it is found in the immune cells that 'clean up' the organ, and the cells that support and insulate neurons. Kaczmarek-Hájek et al. further provide preliminary data suggesting that, under certain conditions, if too many P2X7 receptors are present in these cells neuronal damage might be increased. It is therefore possible that the brain cells that carry P2X7 indirectly contribute to the death of neurons when large amounts of ATP are released.

The genetically engineered mouse designed for the experiments could be used in further studies to dissect the role that P2X7 plays in diseases of the nervous system. In particular, this mouse model might help to understand whether the receptor could become a drug target for neurodegenerative conditions.

DOI: https://doi.org/10.7554/eLife.36217.002

like the induction of dye uptake and cell death (***Saul et al., 2013***; ***Surprenant et al., 1996***; ***Li et al., 2015***; ***Harkat et al., 2017***; ***Di Virgilio et al., 2018***), which are incompletely understood and have mostly been described in cell culture systems. Probably best studied is its central role in NLRP3 (NOD-like receptor family, pyrin domain containing 3) inflammasome activation, cytokine maturation, and inflammation that was originally established in P2X7 knockout (*P2rx7*$^{-/-}$) mouse models (***Chessell et al., 2005***; ***Solle et al., 2001***; ***Di Virgilio et al., 2017***). A growing body of evidence suggests that an increased P2X7 receptor function plays a role in various diseases of the central nervous system (CNS) and peripheral nervous system (PNS) and further supports its importance as a drug target (***Bhattacharya and Biber, 2016***; ***Rassendren and Audinat, 2016***; ***Sperlágh and Illes, 2014***; ***Sociali et al., 2016***).

P2X7 receptors are expressed in cells of hematopoietic origin as well as different types of glial, epithelial, and endothelial cells. The presence and function of P2X7 receptors in neurons, however, remains a matter of debate (***Illes et al., 2017***; ***Miras-Portugal et al., 2017***), although an increasing amount of literature describing neuronal P2X7 functions imply a wide acceptance of this view (e.g. in [***Sperlágh and Illes, 2014***; ***Brown et al., 2016***; ***Engel et al., 2012***; ***Gulbransen et al., 2012***; ***Jimenez-Pacheco et al., 2013***]). In support of a neuronal expression, *P2rx7* mRNA was detected in neurons (***Yu et al., 2008***), P2X7 protein was identified in neuronal cell culture (***Ohishi et al., 2016***), and P2X7 receptors were pharmacologically shown to facilitate postsynaptic efficacy and affect neurotransmitter release (reviewed in [***Sperlágh and Illes, 2014***]). However, mRNA expression might not necessarily correlate with synthesis of the respective protein (***Carpenter et al., 2014***), selectivity of the available P2X7-specific antibodies has been questioned (***Anderson and Nedergaard, 2006***; ***Sim et al., 2004***), and pharmacology of purinergic receptors is rather complex (***Anderson and Nedergaard, 2006***; ***Compan et al., 2012***; ***Nörenberg et al., 2016***). Also, it has been difficult to differentiate between direct effects of neuronal P2X7 activation and indirect effects of ATP-activated neurotransmitter release from glia cells (***Sperlágh and Illes, 2014***; ***Illes et al., 2017***; ***Miras-Portugal et al., 2017***).

Taken together, the scarcity of information regarding the localization and the molecular and physiological functions of P2X7 receptors in the nervous system stands in sharp contrast to its proposed role as a drug target. To conclusively resolve these important questions, we generated transgenic mouse lines that overexpress EGFP-tagged P2X7 under the control of a BAC-derived mouse P2X7 gene (*P2rx7*) promoter. These mice allow the direct and indirect visualization of P2X7, its purification, and determination of functional consequences of its overexpression. Using this model, we provide the first comprehensive and quantitative analysis of the distribution of P2X7 protein within the CNS.

Results

Generation of P2X7-EGFP BAC transgenic mice

The *P2rx7* cDNA was obtained from C57BL/6 mouse brain and C-terminally fused to the EGFP-sequence via a Strep-tagII-Gly-7xHis-Gly linker sequence (***Figure 1—figure supplement 1A***) to provide additional labeling/purification options and minimize interference with the receptor function. As two allelic P2X7 variants, 451P ('wt') and 451L (SNP, present in C57BL/6), with different functionality have been described (***Adriouch et al., 2002***; ***Sorge et al., 2012***), the 'wt' L451P-variant was also generated by site directed mutagenesis. Efficient expression and functionality of the full-length proteins were confirmed by SDS-PAGE, patch-clamp analysis, and ATP-induced ethidium uptake in HEK cells (***Figure 1—figure supplement 1B–E***). Both variants and the non-tagged receptors revealed similar EC_{50} values, indicating that the dye uptake properties of the P2X7 receptor were not influenced by the EGFP-tag. Also, current kinetics were virtually identical. Next, BAC clone RP24-114E20, containing the full length *P2rx7* and more than 100 kb of the 5´region was modified accordingly by insertion of the Strep-His-EGFP sequence in exon 13 to preserve the exon-intron structure of the gene (***Figure 1A***). Upon verification by Southern blotting (***Figure 1B***, ***Figure 1—figure supplement 1F***) and sequencing, the linearized BAC was injected into pronuclei of FVB/N mouse oocytes (451L background). In total, 4 (451L) and 10 (451P) germline transmitters were obtained and five lines (451L: lines 46, 59 and 61; 451P: lines 15 and 17) were selected for initial characterization as described below (***Figure 1C*** and ***Figure 2—figure supplement 1***). Subsequent experiments were performed with the highest expressing line 17.

Expression, membrane targeting, and function of P2X7-EGFP in transgenic mice

Southern blot analysis revealed integration of 4–15 BAC copies in the different lines. The copy numbers correlated well with the respective P2X7-EGFP protein expression levels (***Figure 1C***), suggesting the functionality of most if not all integrated *P2rx7* BAC transgenes. Endogenous P2X7 protein synthesis was unaffected by the P2X7-EGFP overexpression (***Figure 1—figure supplement 1G***). Purification of P2X7-EGFP protein via Ni-NTA agarose demonstrated co-purification of endogenous P2X7 subunits confirming efficient co-assembly of tagged and non-tagged subunits (***Figure 1D***). In agreement with correct plasma membrane targeting, deglycosylation with endoglycosidase H and PNGase F revealed efficient complex glycosylation, indicating that the EGFP-tag did not disturb folding and ER-exit of the transgenic P2X7-EGFP protein (***Figure 1E***). To demonstrate functionality of the overexpressed P2X7-EGFP protein, the transgenic mice were, upon backcrossing into C57BL/6 for 8–10 generations, mated to *P2rx7*$^{-/-}$ mice (in C57BL/6) to obtain 'rescue' mice (***Table 1***) that express only the transgenic but not the endogenous P2X7 (***Figure 1F***). FACS analysis of microglia from these mice confirmed that the transgene is able to fully rescue the ATP-induced DAPI uptake, which is absent in these cells from *P2rx7*$^{-/-}$ mice (***Figure 1G***). Comparison of the kinetic and efficiency of DAPI uptake by simultaneous analysis of pooled and differentially labeled microglia revealed a stronger increase in the rescue mice compared to wt mice, most likely due to a higher number of functional P2X7 receptors at the cell surface. The specificity of the DAPI uptake was demonstrated using the P2X7 antagonist A438079 (***Figure 1—figure supplement 2***).

Analysis of P2X7-EGFP localization in the brain

To determine the overall pattern of P2X7 localization in the brain, 3, 3'-Diaminobenzidine (DAB) staining with EGFP-specific antibodies was performed on brain slices from all mouse lines. As shown

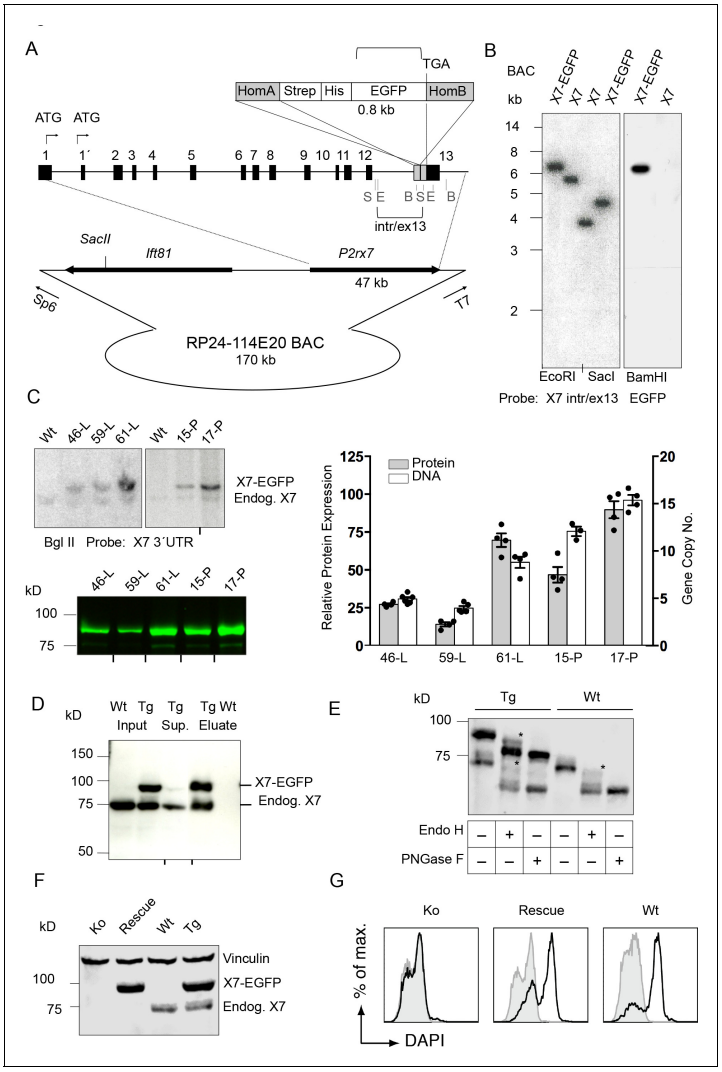

Figure 1. Generation and validation of BAC transgenic P2X7-EGFP mice. (**A**) Scheme of the BAC clone containing the full-length *P2rx7* plus about 103 kb (5') and 10 kb (3') flanking sequences. A Strep-His-EGFP cassette (0.8 kb) flanked by two homology arms (grey boxes) was inserted directly upstream of the stop codon into exon 13 of the *P2rx7*. Before pronuclear microinjection, the BAC-P2X7-EGFP construct was linearized at a unique SacII site. B, E, and S indicate BamHI, EcoRI, and SacI restriction sites, respectively. The probes used for Southern blot analysis are indicated as brackets. (**B**) Southern

Figure 1 continued on next page

Figure 1 continued

blot analysis of BAC DNA using these probes (X7 intr/ex13, EGFP) confirmed homologous recombination and correct integration of the Strep-His-EGFP cassette into the BAC. (**C**) Comparison of copy number and protein expression in different BAC transgenic P2X7-EGFP lines. Representative SDS-PAGE (direct EGFP fluorescence, 60 µg total protein/lane) and Southern blot data are shown (transgenic *P2rx7*, 5277 bp; endogenous *P2rx7*, 4561 bp). Black marks at the bottom indicate where replicates were excised from the figures. Data from 3–6 individual mice are represented. (**D**) Co-purification of endogenous P2X7 subunits with transgenic receptors. Protein complexes were purified under non-denaturing conditions via Ni-NTA agarose from dodecylmaltoside (0.5%) brain extracts (line 59). A representative result of n > 5 experiments with different lines is shown. P2X7-specific antibody: Synaptic Systems (**E**) Deglycosylation analysis of endogenous and transgenic P2X7. Protein extracts from spinal cord of wt and line 17 transgenic mice were treated with endoglycosidases as indicated and P2X7 protein was detected by immunoblotting (P2X7-specific antibody, Synaptic Systems). Asterisks indicate Endo H-resistant complex glycosylated protein. A representative result of n > 5 experiments with different organs is shown. (**F**) P2X7-EGFP (line 17) was crossed into *P2rx7*$^{-/-}$ background. Western blot analysis with an P2X7-specific antibody (Synaptic Systems) confirmed successful deletion of the endogenous P2X7 in this rescue mouse. (**G**) FACS analysis of microglia showing rescue of ATP-induced (1 mM) DAPI uptake by the P2X7 rescue (line 59) microglia in comparison to wt and *P2rx7*$^{-/-}$ microglia. A representative result from n = 3 animals is shown.

DOI: https://doi.org/10.7554/eLife.36217.003

The following figure supplements are available for figure 1:

Figure supplement 1. Expression and functionality of the P2X7-EGFP constructs in HEK cells and expression of the transgene in mice.

DOI: https://doi.org/10.7554/eLife.36217.004

Figure supplement 2. Efficiency and specificity of ATP-induced DAPI uptake in primary brain microglia from wt and P2X7-EGFP transgenic mice.

DOI: https://doi.org/10.7554/eLife.36217.005

for five selected lines (***Figure 2A***, ***Figure 2—figure supplement 1***), specific labeling with identical patterns (***Table 2***) was obtained. A particularly high P2X7-EGFP density was found in the molecular layers of the cerebellar cortex. In addition, strong labeling was detected in the molecular layer of the dentate gyrus (DG), the cerebral cortex and olfactory bulb as well as the thalamus, hypothalamus, substantia nigra, and ventral pons. Comparison of endogenous and transgenic P2X7 levels in different brain regions (***Figure 2B***) showed similar protein ratios and tissue-specific intensities, demonstrating that expression of the transgene mirrored both the expression pattern and expression level of endogenous P2X7 and thus implying that important regulatory elements governing P2X7 expression are preserved and functional in the chosen BAC construct. Due to the dense but diffuse signal and a higher background fluorescence (probably due to structural organization and/or a high content of endogenous fluorophores) in the cerebellar cortex, identification of cellular structures and P2X7-EGFP-expressing cell types proved difficult in adult cerebellum (***Figure 2—figure supplement 2A–C***): Using confocal microscopy, no conclusive co-localization was seen with Purkinje cell

Table 1. Mice

Strain	Official name	Origin
P2X7-EGFP	FVB/N-Tg(RP24-114E20P2X7-StrepHis-EGFP)Ani Lines 46, 59 (also in BL/6N), 61	This study
P2X7^{451P}-EGFP	FVB/N-Tg(RP24-114E20P2X7^{451P}-StrepHis-EGFP)Ani Lines 15, 17 (also in BL/6N) Transgenes were backcrossed into C57BL/6 for at least eight generations	This study
P2rx7$^{fl/fl}$	B6-P2rx7$^{tm1c(EUCOMM)Wtsi}$	This study (B6-P2rx7$^{tm1a(EUCOMM)Wtsi}$ x FLPe deleter mouse Gt(ROSA) 26Sor$^{tm1(FLP1)Dym}$ [***Farley et al., 2000***])
P2rx7$^{-/-}$	B6-P2rx7$^{tm1d(EUCOMM)Wtsi}$	This study (P2rx7$^{fl/fl}$ x Ella-Cre mouse Tg(Ella-cre)C5379Lmgd [***Lakso et al., 1996***])
P2X7 rescue	B6-P2rx7$^{tm1d(EUCOMM)Wtsi}$//B6.Cg-Tg(RP24-114E20P2X7-StrepHis-EGFP)Ani	This study (P2rx7$^{-/-}$ x P2X7-EGFP line 59 and 17 in C57BL/6)
Microglia-specific P2X7 knock-out	B6-P2rx7$^{tm1c(EUCOMM)Wtsi}$//B6-Cx3cr1$^{tm1.1(cre)Jung}$	This study (P2rx7$^{fl/fl}$ x Cx3cr1$^{tm1.1(cre)Jung}$ [***Yona et al., 2013***])
Oligodendrocyte-specific P2X7 knock-out	B6-P2rx7$^{tm1c(EUCOMM)Wtsi}$//B6- Cnp$^{tm1(cre)Kan}$	This study (P2rx7$^{fl/fl}$ x CNP-Cre mouse Cnp$^{tm1(cre)Kan}$ [***Lappe-Siefke et al., 2003***])

If not otherwise noted, mice of both genders (9–14 weeks) in FVB/N background were used. Given that FVB/NJ mice are homozygous for the retinal degeneration 1 allele of Pde6b^{rd1}, retinal stainings were performed in C57b/6 or FVB/N/C57b/6 hybrid mice.

DOI: https://doi.org/10.7554/eLife.36217.006

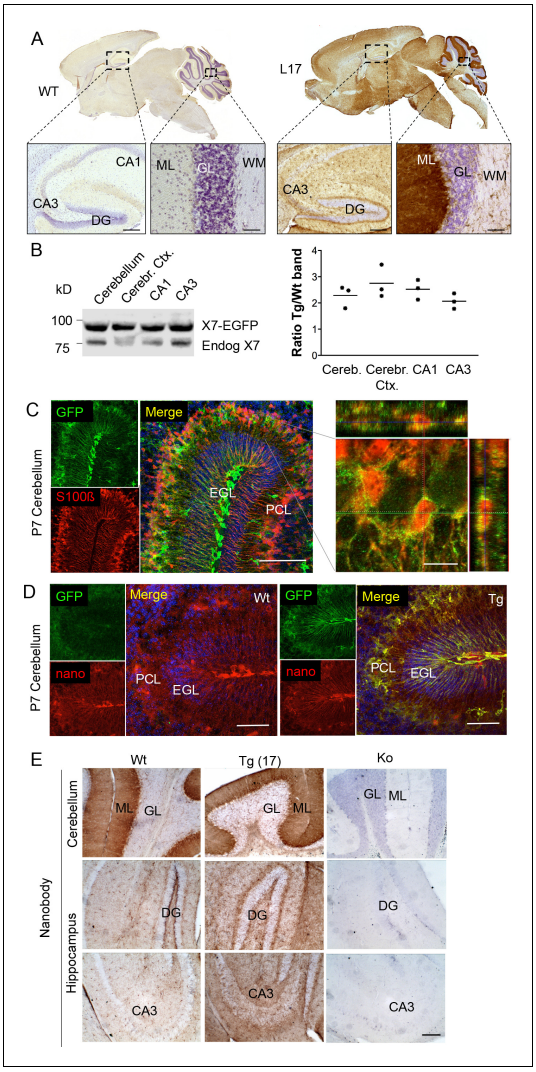

Figure 2. Distribution pattern of transgenic P2X7-EGFP. (**A**) DAB staining with an antibody against GFP (A11122, Thermo Fisher Scientific). Scale bars: 200 µm and 50 µm in hippocampus and cerebellum, respectively. A representative result from at least three animals is shown (**B**) Ratios of transgenic (line 17) and endogenous P2X7 protein in different brain regions. Protein extracts (1% NP40) were prepared and 75 µg per lane separated by SDS-

Figure 2 continued on next page

Figure 2 continued

PAGE. Bands were quantified upon western blotting by infrared imaging with antibodies against P2X7 (Synaptic Systems) and fluorescent secondary antibodies (LI-COR 680RD dk anti rb). Data are presented as means from three animals. (**C**) Co-labeling of line 17 P7 cerebellum with antibodies against GFP (A10262, Thermo Fisher Scientific) and S100β (S2532, Sigma Aldrich). A typical staining pattern for radial glia is seen. The close up of a representative area in the Purkinje cell layer (right) shows punctate P2X7 staining on cells with Bergmann glia morphology. Cell nuclei were counterstained with DAPI (blue). Scale bars represent 100 µm and 10 µm, respectively. CA1/3, cornu ammonis regions 1/3; DG, dentate gyrus; ML, molecular layer; GL, granular layer; WM, white matter; EGL, external granular layer; PCL, Purkinje cell layer. (**D**) Co-labeling of wt and tg line 17 cerebellar slices from P7 pubs with an anti-GFP antibody (A10262, Thermo Fischer Sci.) and the novel P2X7-specific nanobody-rbIgG fusion construct 7E2-rbIgG (***Danquah et al., 2016***) confirms the endogenous expression pattern and the specificity of the P2X7-EGFP signal. Representative results from n = 3 (Tg) and n = 2 (Wt) pubs are shown. Scale bar: 50 µm, DAPI staining in blue. PCL, Purkinje cell layer; GL, granular layer; ML, molecular layer; DG, dentate gyrus; CA3, cornu ammonis region 3; EGL, external granular layer. (**E**) Comparison of DAB staining in transgenic P2X7-EGFP mice, wt, and $P2X7^{-/-}$ mice with 7E2-rbIgG (***Danquah et al., 2016***). Scale bar: 100 µm. Representative results from three animals per line (line 17 and wt) are shown. For antibodies not specified in the legend see Key resources table.

DOI: https://doi.org/10.7554/eLife.36217.007

The following figure supplements are available for figure 2:

Figure supplement 1. Identical expression patterns in five transgenic lines and wt animals.

DOI: https://doi.org/10.7554/eLife.36217.008

Figure supplement 2. P2X7-EGFP immunofluorescence in the cerebellum.

DOI: https://doi.org/10.7554/eLife.36217.009

(calbindin D28k) and synaptic (vGlut2) marker proteins nor with astrocytes/Bergmann glia (GFAP or S100β). However, analysis of the cerebellum from animals at postnatal day 7 (P7), before Bergmann glia microdomains are formed (***Grosche et al., 2002***), revealed a more structured and clearer GFP signal that aligned with the cell bodies and radial extensions of S100β-immunopositive cells with typical Bergman glia morphology (***Figure 2C***). Thus, we conclude that P2X7 is expressed in Bergmann glia, in agreement with previous findings (***Habbas et al., 2011***). However, due to the localization in microdomains that give a very diffuse pattern, co-localization with the intracellular Bergmann glia marker GFAP, which visualizes mainly their radial extensions, could not be detected and co-

Table 2. P2X7-EGFP protein expression in comparison with other P2X7 (reporter) mouse models (Tg (P2rx7 EGFP)FY174Gsat, www.gensat.org, $P2rx7^{hP2RX7}$ (***Metzger et al., 2017***)

	Transgenic P2X7-EGFP	P2X7 reporter (Gensat)	Humanized P2X7
Brain region	Fusion protein	Soluble EGFP	RNA
Hippocampus	$M_{(ML+)}$, O, A	N, G	N (CA3+), O, A
Cerebral Cort.	M, O, A	N, G	M, O, A
Midbrain	M, O	N, G	nd
Thalamus	M, O	G	nd
Hypothalamus	M, O	N, G	nd
Cerebellum	M, O, A, BG (ML+)	N, G, BG (ML+)	O, A
Olfactory bulb	M	G	nd
Ventricle	EC	nd	nd
Corpus callosum	M, O	nd	nd

A high density of positive cells in a specific area is indicated by +whereas the presence in specific cells or structures is indicated by letters (N, neuron; PC, Purkinje cell; A, astrocyte; M, microglia; O, oligodendrocyte; BG, Bergmann glia; G, glia-like; EC, ependymal cells, ML, molecular layer; GCL, granular cell layer; nd, not determined). Data from the Gensat mouse are according to information given on the gensat web site (www.gensat.org) for fluorescence images listed under confirmed expression veracity.

DOI: https://doi.org/10.7554/eLife.36217.010

localization with S100β was only dissolved during postnatal development. In addition to Bergman glia, P2X7 is present in microglia of the cerebellum, which was confirmed in acutely dissociated cells from adult tissue (***Figure 2-figure supplement 2D***). Based on our data (***Figure 2E***, ***Figure 2—figure supplement 2B***), we exclude the expression in Purkinje cells in both adult and P7 mice. Specificity of the GFP labeling and congruency with the endogenous P2X7 expression pattern was further confirmed using a novel mouse P2X7-specific heavy chain antibody (nanobody 7E2 fused to the hinge, CH2 and CH3 domains of rabbit-IgG (7E2-rbIgG), see (***Danquah et al., 2016***) and Materials and methods) (***Figure 2D and E***).

Co-immunolabeling with cell type-specific markers (***Figure 3A–F***) and quantification of GFP-positive cells in the CA1 region of the hippocampus (***Figure 3G***) demonstrated that P2X7-EGFP is predominantly (57 ± 14%) expressed in microglial cells (93% of all Iba1-positive cells), while the majority, if not all, of the remaining GFP-positive cells (47 ± 10%) belong to the oligodendroglial lineage and co-express Olig2 (87% of Olig2-positive and 95% of NG2-positive oligodendrocyte precursor cells). In addition, 7 ± 4% of P2X7-EGFP-expressing cells represent S100β-positive but GFAP-negative cells. These cells comprised 8% of all S100β-positive cells and may represent either GFAP-negative astroglial cells or oligodendrocyte precursor cells. This distribution is in agreement with functional findings (***Jabs et al., 2007***) and cell type-specific RNA sequencing data (*P2rx7* mRNA in microglia/oligodendrocytes/astrocytes ≈ 28/26/5 fragments per kilobase of transcript sequence per million mapped fragments) obtained from cerebral cortex (***Zhang et al., 2014***) (http://web.stanford.edu/group/barres_lab/brain_rnaseq.html). Likewise, co-staining with Sox9 (for astrocytes) or neuronal (NeuN, MAP2) and synaptic (VGlut1, PSD95, synaptophysin, VGAT) markers did not reveal any overlap in the CA1, CA3, and dentate gyrus (***Figure 3A***, ***Figure 3—figure supplements 1***, ***2*** and ***3B***). A clear band of more intense GFP signal is regularly detected in the molecular layer of the dentate gyrus (e.g. ***Figure 2A***, ***Figure 3—figure supplement 1B***, bottom-right panel) and was attributed to a higher number and/or more ramified morphology of microglia that align at the border of the granular layer. In support of this explanation, the thickness of the band in this region equals the radius of microglia with their extensions (***Figure 3—figure supplement 3A***). As P2X7 protein expression has been described in nestin-positive neuronal/glia precursor cells in the subgranular zone (***Rozmer et al., 2017***), we also performed co-labeling of EGFP with nestin in this region but did not detect any co-localization (***Figure 3—figure supplement 4***). Likewise, no co-staining of EGFP with neurons was seen in other regions with a strong EGFP signal like basal ganglia, hypothalamus, and pons (***Figure 3—figure supplement 5***).

In addition, we performed co-stainings of brain sections with the commercially available P2X7-specific antibodies and the nanobody-rbIgG fusion construct 7E2-rbIgG (***Danquah et al., 2016***). However, the commercially available antibodies yielded unspecific or insufficient staining (either in comparison to *P2rx7*$^{-/-}$ mice or in the P2X7-EGFP overexpressing line 17) (***Figure 3—figure supplement 6***). In contrast, 7E2-rbIgG showed specific staining of endogenous P2X7 protein in wild-type (wt) but not *P2rx7*$^{-/-}$ mice (***Figure 2E***) and clear overlap with the transgenic P2X7-EGFP (***Figure 2E***, ***Figure 3—figure supplement 6***). To further verify that the observed transgene expression pattern correlates with the endogenous P2X7 expression, mice deficient in microglial or oligodendroglial P2X7 were generated by mating *P2rx7*$^{fl/fl}$ mice with Cx3cr1$^{tm1.1(cre)Jung}$ (***Yona et al., 2013***) and Cnp$^{tm1(cre)Kan}$ lines (***Lappe-Siefke et al., 2003***), respectively (specificity of Cre expression is shown in ***Figure 3—figure supplement 7***). In comparison to *P2rx7*$^{fl/fl}$ mice, Cx3cr1-Cre-positive mice showed 51.5% (±4.5%) and Cnp-Cre-positive mice showed 60.4% (±2.9%) reduction of P2X7 protein in the brain, which correlates well with the percentage of P2X7 expressing cells determined in the brains of our transgenic mice (***Figure 3H***).

Analysis of P2X7-EGFP localization in other neuronal preparations

Since neuronal P2X7 expression and function has been described in amacrine cells (interneurons) as well as in ganglion cells, photoreceptors, and pigment epithelial cells of the retina (***Sanderson et al., 2014***), we further probed if neuronal P2X7 expression was detectable in this tissue with histologically clear architecture. In contrast to previous reports, however, P2X7-EGFP was exclusively expressed in microglia (***Figure 4A***). Likewise, P2X7-EGFP expression was not found in neurons of the spinal cord, DRG, or of teased sciatic nerve fibers (***Figure 4B–D***, ***Figure 4—figure supplement 1***). In Schwann cells of the sciatic nerve fibers, however, P2X7-EGFP was localized to nodes of Ranvier and Schmidt-Lantermann incisures, in perfect agreement with the subcellular distribution pattern of endogenous

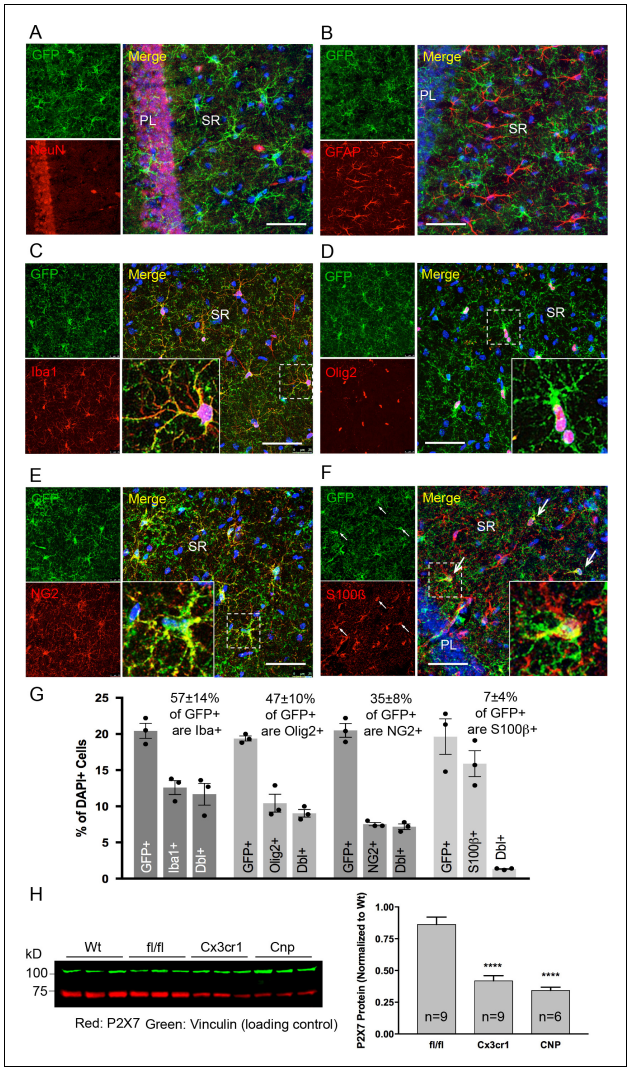

Figure 3. Identity and quantity of P2X7-EGFP expressing cell types in the CA1 region and comparison with P2X7 expression in wt mice. (**A–F**) Co-labeling of tg line 17 brain slices with anti-GFP antibody (ab6556, Abcam; A10262, Thermo Fisher Scientific) and antibodies for the indicated marker proteins (GFAP (MAB360, Millipore), S100β (S2532, Sigma Aldrich)). Hippocampal CA1 regions are shown. Arrows indicate co-staining for S100β and GFP. Cell

Figure 3 continued on next page

Figure 3 continued

nuclei were counterstained with DAPI (blue). PL, pyramidal cell layer; SR, stratum radiatum. Scale bar: 50 μm (**G**) Quantitative analysis of 10 'counting boxes' (as shown in **C–F**) from five sections/mouse in each experiment. Bars represent mean ±SEM of three independent experiments/animals (total cell numbers in transgenic versus wt animals were: 14.4% vs. 12.2% Iba1 +cells, 10.4% vs. 11.0% Olig2 +cells, 7.3% vs. 8.4% NG2 +cells, 16.1 vs. 14.1% S100β + cells). (**H**) Quantitative analysis of P2X7 protein reduction in conditional $P2X7^{-/-}$ mice (CNP-cre, Cx3cr1-cre). 75 μg cerebrum extracts (1% NP40) were analyzed by western blotting and infrared imaging with antibodies against P2X7 (Synaptic Systems) and fluorescent secondary antibodies (LI-COR 680RD dk anti-rb; LI-COR 800CW gt anti-ms). Data were normalized to P2X7 protein in wt animals. Bars represent mean ± SEM from 6 to 9 animals analyzed in three independent experiments. Significance between means was analyzed using two-tailed unpaired Student's *t*-test and indicated as ****p<0.0001 compared to $P2rx7^{fl/fl}$. For antibodies not specified in the legend see Key resources table.

DOI: https://doi.org/10.7554/eLife.36217.011

The following figure supplements are available for figure 3:

Figure supplement 1. No co-localization of P2X7-EGFP with neuronal/synaptic markers in the CA1 region

DOI: https://doi.org/10.7554/eLife.36217.012

Figure supplement 2. No co-localization of P2X7-EGFP with neuronal/synaptic markers in the CA3 region.

DOI: https://doi.org/10.7554/eLife.36217.013

Figure supplement 3. Further analysis of P2X7-EGFP expressing cells in the dentate gyrus and CA1 region.

DOI: https://doi.org/10.7554/eLife.36217.014

Figure supplement 4. Co-stainings of EGFP (ab6556, Abcam) and the neuronal/astroglial precursor marker nestin in the subgranular zone of the dentate gyrus.

DOI: https://doi.org/10.7554/eLife.36217.015

Figure supplement 5. Co-stainings of EGFP (A10262, Thermo Fischer Scientific; ab6556, Abcam) and neuronal markers tyrosine hydroxylase (dopaminergic neurons, (**B**) and NeuN (**C**) in the substantia nigra (SN), hypothalamus (Hy) and pons (P).

DOI: https://doi.org/10.7554/eLife.36217.016

Figure supplement 6. Comparison of the specificity of commercially available anti-P2X7 antibodies and an anti-P2X7 nanobody-rbIgG heavy chain antibody (7E2-rbIgG) in CA1 (**A**) and cerebellar (**B**) slices of adult line 17 mice and $P2X7^{-/-}$ mice.

DOI: https://doi.org/10.7554/eLife.36217.017

Figure supplement 7. Cell type-specific Cre-expression in the hippocampal CA1 region and cerebral cortex (Ctx) of Cx3cr1- and CNP-Cre mice.

DOI: https://doi.org/10.7554/eLife.36217.018

P2X7 (***Figure 4C***). At the neuromuscular junction, P2X7-EGFP was found in close association with terminal Schwann cells (S100β-positive), but did not co-localize with them or with the post- (α-bungarotoxin-positive) or presynaptic (synaptophysin-positive) membrane, in contrast to previous findings (***Deuchars et al., 2001***). Based on the localization and morphology, we suggest its presence on kranocytes, a fibroblast-like cell type (***Court et al., 2008***). In agreement with previous reports on P2X7 localization in DRGs (***Zhang et al., 2005***; ***Jager and Vaegter, 2016***), we identified P2X7-EGFP in cells that show the localization and typical morphology of satellite glia cells which ensheath large sensory neurons. This was confirmed by co-labeling experiments using the satellite cell marker glutamine synthetase. Unlike in sciatic nerves, however, it was not found in myelin protein zero (MPZ)-positive Schwann cells of the DRG (***Figure 4—figure supplement 1A***). Finally, P2X7-EGFP localization was investigated in the myenteric plexus of the colon, a part of the enteric nervous system, but was also not detected in neurons or GFAP-positive glia (***Figure 4—figure supplement 1B***).

Consequences of P2X7 overexpression under physiological and pathological conditions

Detailed analyses of brain parenchyma and other types of nervous tissues indicates that the BAC transgenic P2X7-EGFP is correctly regulated in our mouse model and that P2X7 protein is either below detection limit or not synthesized in neurons, at least under physiological conditions in adult mice.

Despite the well-documented role of P2X7 in inflammation and cell death, P2X7 overexpression did not result in an obvious pathology or behavioral changes under physiological conditions

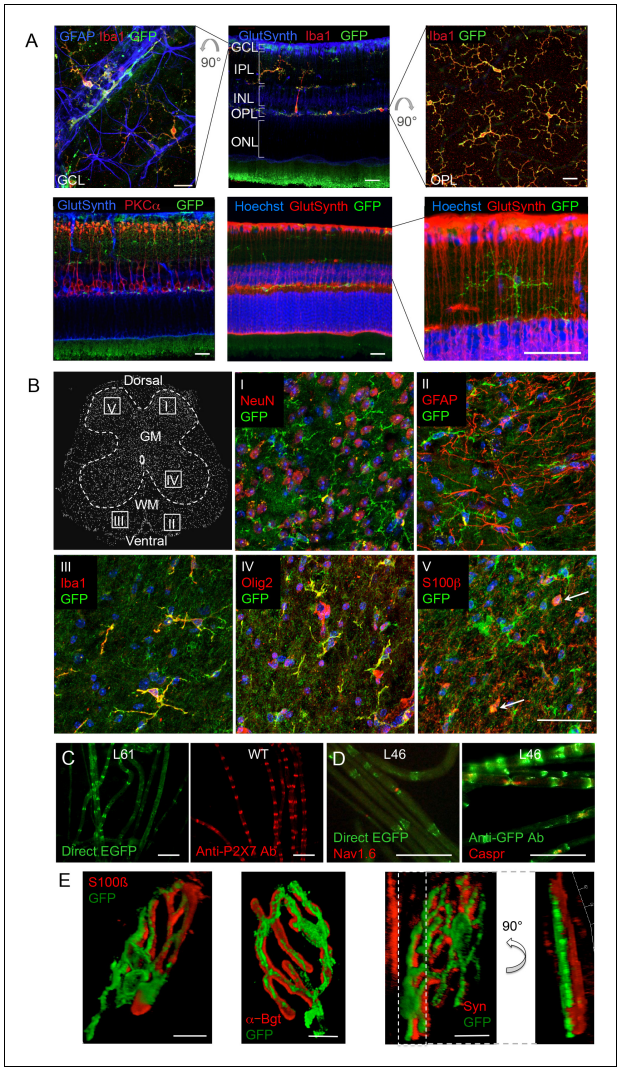

Figure 4. P2X7-EGFP expression in retina, sciatic nerves, spinal cord, and at the neuromuscular synapse. (**A**) EGFP exclusively co-localizes with microglia and endothelial cells in the adult mouse retina. Upper panel: *Middle*, retinal slice labeled for GFP (600 101 215, Rockland), Iba1 (marker for microglia/macrophages) and glutamine synthetase (marker for Müller glia). *Left and right*, retinal flat mounts scanned at the plane of the ganlion cell layer (GCL) and

Figure 4 continued on next page

Figure 4 continued

outer plexiform layer (OPL), respectively, to delineate microglia residing in these retinal layers. Astrocytes in the GCL were labeled with GFAP (G6171, Sigma-Aldrich). IPL, inner plexiform layer; INL, inner nuclear layer; ONL, outer nuclear layer. Lower panel: Co-staining of EGFP with neuronal marker PKCα (*left*) and glutamine synthetase (two right panels) at higher contrast and resolution to show absence of neuronal P2X7-EGFP. Cell nuclei were counterstained with Hoechst 33342 (blue) Scale bars: 20 μm. n = 2 individual line 61 in FVB/C57b/6 hybrid mice (**B**) Confocal images of GFP (ab6556, Abcam; A10262 or Thermo Fisher Scientific) co-immunostaining with antibodies against the indicated marker proteins in transgenic mice line 17 spinal cord slices (GFAP (MAB360, Millipore), S100β (S2532, Sigma Aldrich)). Representative images were taken from the areas shown in the schematic overview. Arrows indicate co-staining for S100ß and GFP. Scale bar: 40 μm. Cell nuclei were counterstained with DAPI (blue). Representative images from n = 3 animals are shown. (**C**) Comparison of transgenic P2X7-EGFP fluorescence and endogenous P2X7 immunofluorescence (P2X7 antibody, Synaptic Systems) in teased sciatic nerve fibers of line 61 and wt mice, respectively. Representative images from at least 3 animals are shown. (**D**) Co-staining of P2X7-EGFP (A11122, Thermo Fischer Scientific, dilution 1:1000) in teased sciatic nerve fibers of line 46 with antibodies against axonal marker proteins demonstrates localization of the transgene at perinodal regions of Schwann cells. Scale bars: 50 μm. (**E**) Reconstructed 3-D images of the neuromuscular junction showing co-staining of P2X7-EGFP (ab6556, Abcam; or A10262, Thermo Fisher Scientific) with perisynaptic Schwann cells (S100β (S2532, Sigma Aldrich)) as well as postsynaptic (α-Bungarotoxin, α-Bgt) and presynaptic (synaptophysin, Syn) marker proteins. The side view in the right panel shows no overlap between GFP and synaptophysin staining. Scale bars: 10 μm and 20 μm, respectively. Representative images from n = 3 animals are shown. For antibodies not specified in the legend see Key resources table.

DOI: https://doi.org/10.7554/eLife.36217.019

The following figure supplement is available for figure 4:

Figure supplement 1. P2X7-EGFP localization in DRG and myenteric plexus preparations.

DOI: https://doi.org/10.7554/eLife.36217.020

(***Figure 5—figure supplement 3A–D***). To test if tissue damage, that is a condition that is associated with neuroinflammation, could induce neuronal P2X7-EGFP synthesis, we proceeded our analysis with three experimental models of acute and/or invasive CNS injury: ischemic retina, stab wound, and kainic acid-induced status epilepticus. In preliminary experiments with a small number of animals (n = 3–4), an increased microglia reaction (***Figure 5A***) and microglia number (***Figure 5B***) as well as other Iba1/P2X7-positive cells (possibly invading macrophages, ***Figure 5—figure supplement 1***) were observed upon transient retinal ischemia in wt animals. Interestingly, this effect appeared to be enhanced in P2X7-EGFP transgenic mice (***Figure 5A,B***). Importantly, however, P2X7 was not upregulated in other cell types than microglia, at least 3 days post injury (***Figure 5—figure supplement 1***). In this context, it should be emphasized, that a similar trend was observed in mice subjected to the stab wound injury of the somatosensory grey matter (GM). Compared to the situation in wt mice (n = 2) at 5 days after injury, post-traumatic GM of P2X7-EGFP transgenic mice (n = 3) showed a trend toward increased reactivity of microglial cells at the injury site and increased lesion area (***Figure 5C***). These data support the functionality and correct transcriptional regulation of the construct and suggest a deleterious effect of P2X7 overactivation on neurons (***Sperlágh and Illes, 2014***). The low number of animals, however, requires confirmation in future studies. Nevertheless, no induction of neuronal or astroglial P2X7-EGFP synthesis was found in the affected lesion area (***Figure 5D***), although we cannot exclude a potential obfuscation of the EGFP signal due to autofluorescence in the direct vicinity to the injury. Finally, no induction of P2X7 protein expression was observed in neurons of the dentate gyrus, CA1, and CA3 regions 24 hr after induction of status epilepticus by a unilateral intra-amygdala kainic acid injection, although a change of microglia morphology clearly indicated their activation (***Figure 5—figure supplement 2***). In conclusion, we suggest that P2X7-dependent neurodegeneration that has been observed in various studies is caused by an indirect mechanism, most likely involving P2X7 activation in microglia or oligodendrocytes.

Discussion

P2X7 research has suffered from a lack of specific and sensitive antibodies. While some antibodies detect P2X7 in western blots and upon overexpression in cultured cells, they fail to localize it reliably in complex preparations such as brain sections. In addition, an intricate pharmacology and

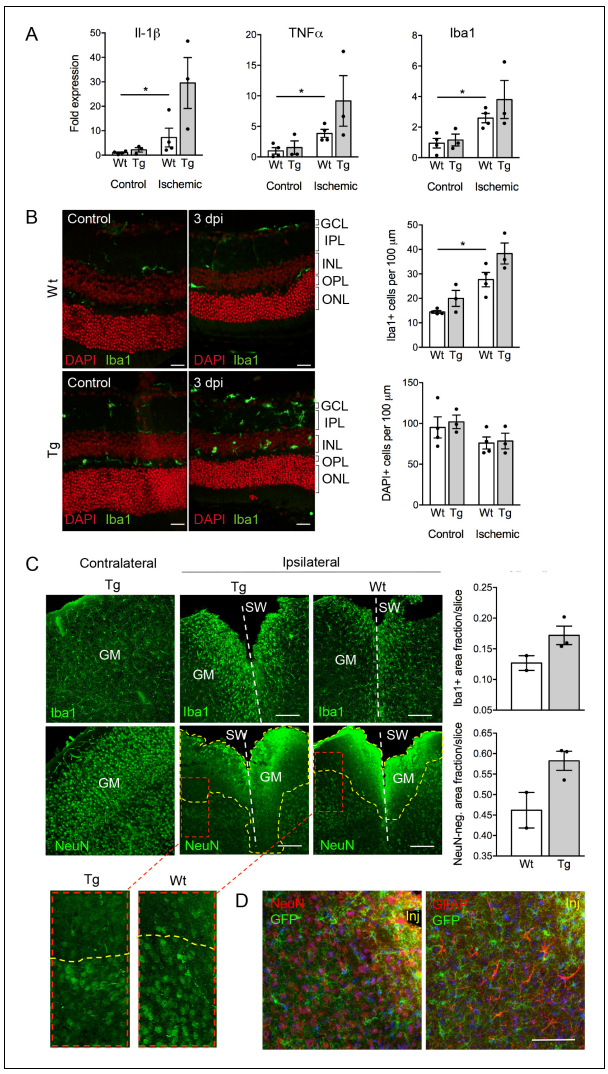

Figure 5. Consequences of P2X7 overexpression under physiological and pathophysiological conditions. (**A**) Quantitative real-time PCR was performed in duplicates on samples from microglia isolated by immunomagnetic separation from control and postischemic (3 days post injury, 3 dpi) retinae. Bars represent mean ±SEM and include data from 3-4 animals/each genotype/condition. Significance between expression level in the untreated

Figure 5 continued on next page

Figure 5 continued

control eye of the respective genotype was analyzed using unpaired two-tailed Mann-Whitney-U-test and indicated as: *p<0.05. (**B**) Retinal slices labeled for the microglia/macrophage marker Iba1. Cell nuclei were counterstained with DAPI (red). Retinae were isolated from mice of which one eye had been subjected to transient ischemia. The untreated contralateral eye served as internal control. Dpi, days post-injury. Scale bars: 20 μm. Cell numbers of the inner retinal layers and microglia specifically were quantified in 2–5 central retinal slices per animal on basis of DAPI and Iba1 staining, respectively. Bars represent mean ±SEM and include data from 3 to 4 animals/genotype/condition. Note that data from transgenic mice were not significantly different in A and B. (**C**) Representative confocal images of coronal sections from posttraumatic GM at 5 dpi. Slices of the somatosensory grey matter (GM) from wt and transgenic animals stained for NeuN- (neurons) and Iba1- (microglia) positive cells are shown. White dotted lines indicate stab wounds; yellow dotted lines indicate NeuN-negative lesion areas. Insets show chosen borders between NeuN-positive and negative areas. Bar diagrams depict fractions of Iba1-positive and NeuN-negative areas in relation to DAPI-positive areas. Means of N = 2–3 animals (n = 6–7 sections per animal)±SEM are shown. Scale bar: 200 μm. One wt tissue broke and could not be analyzed. (**D**) Double immunostaining with GFP (ab6556, Abcam) and NeuN or GFAP (for astroglia (MAB360, Millipore)) shows no upregulation of P2X7-EGFP in these cell types within the penumbra of P2X7-EGFP and wt mice at 5 dpi. Note that immunofluorescence in the area immediately adjacent to the lesion core (–0–75 μm) is non-specific due to autofluorescence of cells within damaged tissue (inj), and this might obfuscate a potential P2X7-EGFP signal. Cell nuclei were counterstained with DAPI (blue). Scale bar: 100 μm. For antibodies not specified in the legend see Key resources table.

DOI: https://doi.org/10.7554/eLife.36217.021

The following figure supplements are available for figure 5:

Figure supplement 1. Upregulation of P2X7 expression in postischemic retinae 3 days post injury (dpi) of wt and P2X7-EGFP transgenic animals.

DOI: https://doi.org/10.7554/eLife.36217.022

Figure supplement 2. Cell type-specific P2X7-EGFP expression in the three hippocampal subfields (DG, CA1, and CA3) upon induction of status epilepticus.

DOI: https://doi.org/10.7554/eLife.36217.023

Figure supplement 3. Effects of P2X7 overexpression under physiological conditions.

DOI: https://doi.org/10.7554/eLife.36217.024

compromised *P2rx7*$^{-/-}$ models (***Masin et al., 2012***; ***Nicke et al., 2009***) complicate the analysis of its localization and function *in vivo*. Here, we present a novel P2X7-EGFP BAC transgenic mouse model that overexpresses functional fluorescence-tagged P2X7 and is able to specifically report P2X7 expression at the protein level. Moreover, this model permits studies of the functional consequences of P2X7 overexpression. Detailed analyses of these mice under physiological conditions show that in the CNS, P2X7 is predominantly located in microglia and oligodendrocytes and to a minor extent in a fraction of S100β-positive cells in the cerebrum as well as Bergmann glia in the cerebellum. Given this distribution in physiology and the fact that no upregulation of P2X7 protein in neurons was observed after neural tissue damage or following status epilepticus, it is conceivable that the reported P2X7-dependent neuronal damage is the consequence of the pronounced manifestation of microglia activation rather than direct activation of neuronal P2X7 receptors.

The BAC transgenic approach

Numerous examples demonstrate that BAC transgenics are valuable tools to investigate endogenous protein expression patterns (***Gerfen et al., 2013***; ***Yang and Gong, 2005***). In comparison to knock-in approaches, they provide the advantages of a stronger signal due to the moderate overexpression which might boost physiological functions and thus make them accessible for an in depth analysis. Together with classical and/or conditional knock-out strategies, this provides a powerful combination for the *in vivo* analysis of protein functions. In contrast to small transgenes, in which the expression patterns are often affected by the integration site, BAC transgenes show in most cases an expression pattern that reflects the endogenous promoter within the BAC. However, position effects such as gene deletion or aberrant expression due to integration of (truncated) BAC transgenes in other genes or regulatory elements cannot be excluded. Thus, five transgenic lines were analyzed in detail in this study, and all showed identical expression patterns. A correct expression pattern was further corroborated by 1) a comparative analysis of P2X7-EGFP transgene expression

and endogenous P2X7 expression in wt mice using a novel P2X7-specific nanobody-rbIgG fusion construct and 2) cell type-specific P2X7 deletion in oligodendrocytes and microglia using conditional P2X7 knock-out mouse models. Together, these findings all argue against an ectopic P2X7-EGFP expression pattern and indicate a predominant expression of P2X7 in non-neuronal cells within the brain parenchyma.

P2X7 protein localization in neurons?

The absence of a neuronal localization of P2X7-EGFP contrasts with findings in a BAC transgenic reporter mouse line (Tg(P2rx7 EGFP)FY174Gsat; GenSat) in which soluble EGFP is expressed under the control of a BAC transgenic P2X7 promoter and a recently described humanized P2X7 knock-in mouse model (**Metzger et al., 2017**). Both models show neuronal P2X7 expression but differ remarkably in the observed expression patterns (**Engel et al., 2012**; **Jimenez-Pacheco et al., 2013**; **Metzger et al., 2017**). Neuronal expression of the soluble EGFP reporter in the GenSat mouse is seen in multiple brain regions whereas P2X7 transcripts in the humanized P2X7 mouse model seem to predominate in CA3 neurons (**Metzger et al., 2017**) (**Table 2**). In contrast to our findings at the protein level, the knock-in model showed only a minor reduction in P2X7 expression in microglia-specific knock-out animals. A possible explanation for these discrepancies could be that alterations in gene structure introduced into the GenSat P2X7 BAC EGFP mice influence post-transcriptional and translational regulatory mechanisms. For example, intron 1, the importance of which is evidenced by the P2X7 k splice variant (**Nicke et al., 2009**), is not fully preserved in the EGFP reporter mouse and soluble EGFP is translated from a truncated mRNA which might lack regulatory elements. In case of the humanized P2X7 model, only RNA transcripts were analyzed which might not correlate with protein synthesis. Moreover, different sensitivities of the detection methods (*in situ* hybridization versus immunohistochemistry) could also account for some of the observed differences. As even minor gene modifications, such as the flanking of the exons with the comparatively small loxP sequences, are able to influence gene expression (**Requardt et al., 2009**; **Zhang et al., 2013**) (**Figure 3H**), we kept the *P2rx7* gene structure almost untouched and retained as much of the UTRs as possible to avoid such unpredictable influences. Although we cannot completely rule out an effect of the introduced gene modification within the BAC or a loss of possible modulatory elements that lie outside of the chosen BAC, comparison of the BAC transgenic P2X7-EGFP with endogenous P2X7 expression as analyzed with the novel nanobody-based heavy chain antibody, provide strong evidence that the expression pattern observed in our mouse line matches that of the endogenous protein. This, however, does not preclude species differences. For example, in human but not in murine Müller cells, functional and immunohistological evidence for P2X7 expression has been shown (**Franke et al., 2005**; **Innocenti et al., 2004**; **Pannicke et al., 2000**).

Finally, we cannot exclude neuronal expression that is below the detection limit. As the P2X7 receptor is known to be a highly regulated protein and has been shown to be deleterious to cultured neuronal cells (**Ohishi et al., 2016**), its expression and localization should be tightly regulated in post-mitotic cells like neurons. If present in neurons, its presence would likely be limited to subcellular regions were synapse formation and selection takes place and/or to areas where damaged cells need to be removed by apoptosis. Possible extrasynaptic or growth cones localizations (**Díaz-Hernandez et al., 2008**) would be difficult or impossible to resolve *in situ* using the described antibodies and conventional microscopy. However, even upon induction of tissue damage, virtually no P2X7 expression in cerebral cell types other than microglia or oligodendrocytes was observed. Based on our data, we therefore suggest that P2X7-induced neurodegeneration is due to an indirect effect (i.e. extended glial reaction within the acute post-traumatic period), which requires further investigation.

Can P2X7 splice variants account for neuronal P2X7 expression?

Five murine P2X7 splice variants (**Masin et al., 2012**; **Nicke et al., 2009**) have been identified. Two of these (variants a and k) contain the C-terminal sequence that was fused to EGFP and should be detectable in our mouse model. The other three variants (b, c, and d) are C-terminally truncated or altered and could therefore escape the detection by both our EGFP-tag and the most commonly used antibodies against the P2X7 C-terminus. However, the nanobody used in our study was selected on intact P2X7 expressing cells and therefore binds at the extracellular P2X7 domain which

is present in splice variants b and c. Together with the fact that in the original study (***Masin et al., 2012***), protein of the deleted variants was not detected in the brain, this strongly argues against the presence of the mouse P2X7 variants b and c in neurons. Splice variant d contains only one TM domain and cannot be expected to form functional receptors. We therefore consider it highly unlikely that one of the known mouse variants of P2X7 accounts for neuronal P2X7 function or detection. A 65 kD protein band is frequently detected by us and others with antibodies against the P2X7 C-terminus but, unlike the P2X7 protein (variant a, about 75 kD), does not show a size shift upon glycosidase treatment and therefore, most likely does not represent a P2X7 variant.

In summary, we generated and thoroughly characterized a novel transgenic P2X7-EGFP mouse model that should help to overcome previous limitations in P2X7 research. Using functional assays, we could show that transgenic expressed P2X7-EGFP rescues the phenotype of P2X7 deficiency thus confirming the functionality of the transgene. Our initial characterization, however, indicates that P2X7 overexpression does not per se induce any overt pathologies, but rather represents a natural response observed after tissue damage. This is in line with observations in Schwann cells, where overexpression of P2X7 alone does not alter the basal Ca^{2+} concentration: overexpression of the peripheral myelin protein 22 (as it occurs in Schwann cells from patients suffering from Charcot Marie Tooth type 1A), causes instead a secondary overexpression of P2X7 and consequent Schwann cells functional derangement (***Nobbio et al., 2009***), suggesting that in addition to P2X7 overexpression, other factors are required to induce P2X7-associated pathologies. Most importantly for our study, neuronal P2X7 protein expression was not induced under pathological conditions. An unresolved question is, whether the high ATP concentrations required to activate the receptor occur physiologically or if the receptor is silent under physiological conditions and mainly expressed and/or activated under pathophysiological conditions. The presented mouse model provides a new tool for addressing this question.

Materials and methods

Key resources table

Type	Designation	Source or reference	Identifiers	Additional information
BAC clone	BAC clone, RP24-114E20	Children's Hospital Oakland Research Institute, Oakland, CA		Strep-tagII-Gly-7xHis-Gly-EGFP-sequence was inserted into the *P2r* × 7 BAC clone RP24-114E20
Strain (*Mus musculus*)	P2X7 EGFP (FVB/N-Tg(RP24-114E20P2X 7 StrepHis-EGFP)Ani)	this paper		Lines: 46, 59 (also in BL/6N), 61
Strain (*Mus musculus*)	P2X7^{451P}-EGFP (FVB/N-Tg(RP24-114E20P2 X7451P-StrepHis-EGFP)Ani)	this paper		Lines: 15, 17 (also in BL/6N) Transgenes were backcrossed into C57BL/6 for at least eight generations
Strain (*Mus musculus*)	B6-P2rx7$^{tm1a(EUCOMM)Wtsi}$	European Mutant Mouse Archive	MGI:4432150	
Strain (*Mus musculus*)	Gt(ROSA)26Sor$^{tm1(FLP1)Dym}$	Farley FW, et al., Genesis. 2000	MGI:2429412	FLPe deleter
Strain (*Mus musculus*)	Tg(EIIa-cre)C5379Lmgd	Lakso M, et al., Proc Natl Acad Sci U S A. 1996	MGI:2137691	EIIa-Cre mouse
Strain (*Mus musculus*)	*B6-Cx3cr1*$^{tm1.1(cre)Jung}$	Yona S, et al., Immunity. 2013	MGI:5467983	Cx3cr-1-Cre
Strain (*Mus musculus*)	B6- Cnp$^{tm1(cre)Kan}$	Lappe-Siefke C, et al., Nat Genet. 2003	MGI:3051635	CNP-Cre
Antibody	P2X7 C-term (rb pAb)	Synaptic Systems	Cat# 177003, RRID: AB_887755	WB 1:1500 IHC 1:500
Antibody	P2X7 ECD (rb pAb)	Alomone	Cat# APR-008 RRID:AB_2040065	WB 1:500 IHC 1:500
Antibody	ß-Actin (ms AC-15)	Sigma-Aldrich	Cat# A3854 RRID:AB_262011	WB 1:15.000

Continued on next page

Continued

Type	Designation	Source or reference	Identifiers	Additional information
Antibody	Vinculin (ms hVin-1)	Sigma-Aldrich	Cat# V9131 RRID:AB_477629	WB 1:10.000
Antibody	800CW gt anti-ms	LI-COR	Cat# 925–32210 RRID:AB_2687825	WB 1:15.000
Antibody	680RD dk anti-rb	LI-COR	Cat# 925–68073 RRID:AB_2716687	WB 1:15.000
Antibody	680RD gt anti-rb	LI-COR	Cat# 925–68071 RRID:AB_2721181	WB 1:15.000
Antibody	CD11b-perCP (rat M1/70)	BioLegend	Cat# 101230, RRID:AB_2129374	FACS 1:100
Antibody	CD45-PE-Cy7 (rat 30-F11)	BioLegend	Cat# 103114, RRID:AB_312979	FACS 1:100
Antibody	CD16/32 (Fc-Block, rat 2.4G2)	BioXcell	Cat# BE0307 RRID:AB_2736987	FACS 1:100
Antibody	P2X7 C-term. (rb pAb)	Alomone	Cat# APR-004 RRID:AB_2040068	IHC 1:500
Antibody	P2X7 ECD, 7E2-rbIgG	Nolte lab	Nanobody rbIgG fusion construct	(0.1 ug/ml)
Antibody	GFP (rb pAb)	Abcam	Cat# ab6556 RRID:AB_305564	IHC 1:2000
Antibody	GFP (chk pAb)	Thermo Fisher	Cat# A10262, RRID:AB_2534023	IHC 1:400
Antibody	GFP (rb pAb)	Thermo Fisher	Cat# A6455, RRID:AB_221570	IHC 1:250
Antibody	GFP (rb pAb)	Thermo Fisher	Cat# A11122, RRID:AB_221569	IHC 1:400
Antibody	GFP (gt pAb)	Rockland	Cat# 600-101-215 RRID:AB_218182	IHC 1:200
Antibody	MAP2 (ms 198A5)	Synaptic Systems	Cat# 188011, RRID: AB_2147096	IHC 1:500
Antibody	NeuN (ms A60)	Millipore	Cat# MAB377 RRID:AB_2298772	IHC 1:500
Antibody	GFAP (ms GA5)	Millipore/Sigma-Aldrich	Cat# MAB360/G6171 RRID:AB_11212597/ AB_1840893	IHC 1:200/500
Antibody	GFAP (rb pAb)	Dako	Cat# Z0334, RRID:AB_10013382	IHC 1:1000
Antibody	S100ß (rb pAb)	Synaptic Systems	Cat# 287003, RRID: AB_2620024	IHC 1:500
Antibody	S100ß (rb pAb)	Abcam	ab7853 (not longer available)	IHC 1:1000
Antibody	S100ß (ms SHB1)	Sigma-Aldrich	Cat# S2532, RRID:AB_477499	IHC 1:400
Antibody	Iba1 (rb pAb)	WAKO	Cat# 019–19741 RRID:AB_839504	IHC 1:100
Antibody	Olig 2 (ms 211F1.1)	Millipore	Cat# MABN50 RRID:AB_10807410	IHC 1:200
Antibody	NG2 (rb pAb)	Millipore	Cat# AB5320 RRID:AB_91789	IHC 1:500
Antibody	VGAT (ms CL2793)	Molecular Probes	Cat# MA5-24643 RRID:AB_2637258	IHC 1:200
Antibody	vGlut1 (ms 317G6)	Synaptic Systems	Cat# 135511, RRID: AB_887879	IHC 1:100

Continued on next page

Continued

Type	Designation	Source or reference	Identifiers	Additional information
Antibody	vGlut2 (rb pAb)	Synaptic Systems	Cat# 135 403, RRID:AB_887883	IHC 1:100
Antibody	PSD95 (ms 108E10)	Synaptic Systems	Cat# 124011, RRID:AB_10804286	IHC 1:100/500
Antibody	Calretinin (ms 37C9)	Synaptic Systems	Cat# 214111, RRID: AB_2619904	IHC 1:1000
Antibody	Calbindin D28k (ms 351C10)	Synaptic Systems	Cat# 214011, RRID:AB_2068201	IHC 1:200
Antibody	Calbindin D28k (gp pAb)	Synaptic Systems	Cat# 214 005, RRID:AB_2619902	IHC 1:100 (only used for data confirmation, not in manuscript)
Antibody	Synaptophysin (ms pAb)	Synaptic Systems	Cat# 101011, RRID:AB_887824	IHC 1:500
Antibody	Nav 1.6 (rb pAb)	Alomone	Cat# ASC009 RRID:AB_2040202	IHC 1:100/500
Antibody	Caspr (ms K65/35)	Neuromab	Cat# 75–001 RRID:AB_2083496	IHC 1:1000
Antibody	Cre (ms 2D8)	Millipore	Cat# MAB3120 RRID:AB_2085748	IHC 1:200
Antibody	ß3-Turbulin (gp pAb)	Synaptic Systems	Cat# 302304 RRID:AB_10805138	IHC 1:200
Antibody	GlutSynth (ms GS-6)	Millipore	Cat# MAB302 RRID:AB_2110656	IHC 1:500
Antibody	PKCα (rb Y124)	Abcam	Cat# ab32376, RRID:AB_777294	IHC 1:200
Antibody	TH (rb pAb)	Millipore	Cat# AB152 RRID:AB_390204	IHC 1:200
Antibody	Nestin (ms rat-401)	Millipore	Cat# MAB353 RRID:AB_94911	IHC 1:100
Antibody	Sox9 (rb pAb)	Novus bio	Cat# NBP1-85551-25 RRID:AB_11002706	IHC 1:100
Antibody	MPZ (rb pAb)	Abcam	Cat# ab31851, RRID:AB_2144668	IHC 1:200
Antibody	Hu C/D (ms 16A11)	Thermo Fisher	Cat# A-21271, RRID:AB_221448	IHC 1:200
Antibody	A594 gt anti-ms	Thermo Fisher	Cat# A11032 RRID:AB_2534091	IHC 1:400
Antibody	A594 gt anti-rat	Thermo Fisher	Cat# A11007, RRID:AB_10561522	IHC 1:400
Antibody	A546 gt anti-ms	Thermo Fisher	Cat# A-11003, RRID:AB_2534071	IHC 1:400
Antibody	A488 gt anti-rb	Thermo Fisher	Cat# A11008, RRID:AB_143165	IHC 1:400
Antibody	A488 gt anti-chk	Thermo Fisher	Cat# A11039, RRID:AB_2534096	IHC 1:400
Antibody	A633 gt anti-rb	Thermo Fisher	Cat# A21070, RRID:AB_2535731	IHC 1:400
Antibody	A633 gt anti-gp	Thermo Fisher	Cat# A21105, RRID:AB_1500611	IHC 1:400
Antibody	Cy3 gt anti-rb	Jachkson Res.	Cat# 111-165-003, RRID:AB_2338000	IHC 1:300
Antibody	Cy3 gt anti-ms	Jachkson Res.	Cat# 115-165-146, RRID:AB_2338690	IHC 1:300

Analysis of the mP2X7-EGFP constructs upon expression in HEK cells

HEK293 cells were cultured and transiently transfected with 1.5-2 mg DNA/well of a 6-well-plate (Lipofectamin, Thermo Fisher Scientific). After 48 h, cells were washed and collected in PBSs (2 wells/experiment), pelleted in a desktop centrifuge (2'at 13,000 rpm) and extracted as described (Nicke et al., 2008) for 15 minutes on ice in 100 ml 0.1% sodium phosphate buffer (pH 8.0) containing 1% digitonin (Fluka, Buchs, Switzerland) and 0.4 mM Pefabloc SC (Fluka). 10ml of extract were separated by SDS-PAGE with with or without endoglycosidase treatment (30 min at 37 °C in the presence of reducing loading buffer (1x) and 5 IUB miliunits EndoH or 10 IUB miliunits PNGaseF (New England Biolabs)). For ethidium uptake measurements, cells were seeded after 27 h in 96-well plates ($5x10^4$ cells/well) and incubated in the presence of 20 mM ethidium bromide in PBS for 15 min. Dye influx was evaluated with a fluorescence plate reader (Fluostar Galaxy, BMG) upon addition of the indicated ATP concentrations, as described (***Bruzzone et al., 2010***). Patch-clamp recordings were performed as described (***Nicke et al., 2009***) in normal (147 mM NaCl, 2 mM KCl, 2 mM $CaCl_2$, 1 mM $MgCl_2$, 10 mM HEPES, and 13 mM glucose) or low divalent cation (0 $MgCl_2$, 0.1 mM $CaCl_2$) containing extracellular solution.

Generation of mP2X7-EGFP BAC transgenic mice (FVB/N-Tg(RP24-114E20-P2X7/StrepHisEGFP))

The Strep-tagII-Gly-7xHis-Gly-EGFP-sequence was inserted into the *P2rx7* BAC clone RP24-114E20 (Children's Hospital Oakland Research Institute, Oakland, CA), immediately upstream of the *P2rx7* stop codon by homologous recombination (***Warming et al., 2005***) using locus-specific homology arms of 50–60 bp length (Expand High Fidelity PCR, Roche Applied Science). The 451P variant was generated from the obtained BAC by the same strategy. BAC DNAs were verified after each recombination step by PCR, Southern blot and DNA fingerprinting. Upon sequencing of the coding regions (Eurofins Genomics, Germany), final BAC constructs were linearized with SacII (thereby destroying the unwanted Ift81 gene), purified (Sepharose CL-4B chromatography, Sigma-Aldrich), analyzed by pulsed field gel electrophoresis, and microinjected into pronuclei of FVB/N mouse zygotes (451L background) (for primers and probes see ***Supplementary files 1*** and ***2***).

Southern blot analysis

Genomic DNA was isolated from tail biopsies, digested with BglII, separated on an 0.8% agarose gel, and blotted onto Nylon membrane (Hybond N+, GE Healthcare) by capilliary transfer. After immobilization by UV irradiation (1500 µJ/cm^2), DNA was hybridized to a ^{32}P labeled probe (Random primed labeling Kit, Roche) corresponding to a 645 bp fragment 2.6 kb downstream of the *P2rx7* stop codon. Autoradiographic analysis (Phosphoimager plates, Molecular Dynamics) specifically detected the expected hybridization signals at 5277 bp (BAC transgene) and 4561 bp (endogenous *P2rx7*). The intensity ratios were used to determine the number of inserted BAC copies (for probes see ***Supplementary file 1***).

Biochemistry

Protein extracts were prepared as described (***Nicke, 2008***) using a Precellys homogenizer (Peqlab) with CK28 beads (15 s, 5.000 rpm) and NP40 (Sigma) as detergent. Protein concentrations were determined by BCA assay (Pierce). 30–75 µg of total protein per lane were loaded on 8% SDS-PAGE gels. Protein was either directly visualized by EGFP fluorescence scanning (Typhoon, GE Healthcare) or blotted onto Immobilon-FL PVDF membranes (Merck Millipore) and detected with an Odyssey infrared imaging system (LI-COR Biosciences) using the indicated antibodies (S1 Material and methods). Endoglycosidase (New England Biolabs) treatment was performed for 30 min at 37°C in 20 µl sample aliquots with loading buffer (IUB miliunits: EndoH 10, PNGaseF 20).

FACS analysis of microglia dye uptake

Mice (8–12 weeks, male and female) were sacrificed and single-cell suspensions prepared from brains by 30 min collagenase digestion at 37°C in a shaking water bath. Cell suspensions were filtered through a 70 µm cell strainer and centrifuged for 5 min at 300x g. Microglia were separated from debris by resuspending the pellet in 5 ml of a 33% Percoll solution (GE Healthcare) and centrifugation (20 min, 300x g). The pellet was resuspended in 1 ml ammonium-chloride-potassium

erythrocyte lysis buffer and incubated for 1 min on ice to remove erythrocytes. Cells were subsequently washed with 10 ml FACS buffer (PBS + 0.2% BSA/1 mM EDTA) and resuspended in 100 µl FACS buffer. Microglia were stained (30 min on ice) with anti-CD11b-perCP (Biolegend) and anti-CD45-PE-Cy7 (Biolegend) in the presence of Fc-blocking anti-CD16/CD32 (BioXcell) and normal rat serum. After washing 2x with FACS buffer cells were resuspended in 200 µl RPMI medium (Gibco). DAPI was added to a final concentration of 1.5 µM and cells were incubated in the presence or absence of 1 mM ATP at 37°C for 15 min. The DAPI uptake into $CD11b^{+}CD45^{low}$ microglia was subsequently measured using a BectonDickinson Celesta flow cytometer.

For monitoring of time-dependent DAPI uptake by real time flow cytometry, isolated microglia were differentiated by transgenic P2X7-EGFP expression and exogenous $eFluor^{670}$-labeling (WT or P2X7 knockout) and pooled in one FACS tube in 500 µl RPMI medium (Gibco) in the presence of DAPI (1.5 µM) in order to have identical stimulation conditions. The baseline DAPI signal was measured for 2 min at 37°C, then 1 mM ATP was added and measuring continued for 4 to 5 min. DAPI uptake over time was compared among the differentially labeled microglia.

Generation of P2X7-specific nanobody-based heavy chain antibody 7E2-rbIgG

The coding region for the P2X7-specific nanobody 7E2 was cloned into the pCSE2.5 vector (provided by T. Schirrmann, Technical University Braunschweig, Germany) (***Schirrmann and Büssow, 2010***) upstream of coding regions for the hinge, CH2 and CH3 domains of rabbit IgG (***Danquah et al., 2016***). Six days after transfection of this construct into HEK-6E cells (***Zhang et al., 2009***), 7E2-rbIgG was purified from the cell supernatant by affinity chromatography on a protein-G sepharose column. Buffer was exchanged by gel filtration on a PD-10 column. A panel of nanobody-rbIgG heavy chain antibodies was originally screened for binding to P2X7 transfected HEK cells before and after fixation with 4% PFA. 7E2-rbIgG was chosen because it retained the strongest staining after fixation in both immunofluorescence staining and a FACS-based dissociation assay analogous to that described in (***Fumey et al., 2017***). It only weakly antagonizes gating of P2X7 by ATP and by ADP-ribosylation but its potency was not further determined (***Danquah et al., 2016***).

Diaminobenzidine (DAB) immunohistochemistry

Mice were sacrificed by CO_2/cervical dislocation or anesthetized (Ketamin/Xylazin) and transcardially perfused with 4% PFA. Brains were fixed in 4% PFA for 72 hr or 24 hr, respectively, cryoprotected in 30% sucrose, and embedded in 5% LM Agarose (Roth, Germany). 30 µm sagittal brain sections were prepared (VT1200s Leica Microsystems) and either blocked with 4% skim milk and 10% FCS in PBS (1–1.5 hr, RT) or, after peroxidase block (3% H_2O_2 in 0.01 M PBS, 30 min RT), with 10% Normal Goat Serum and 0.1% Triton X-100 in PBS (1 hr, RT), prior to primary antibody incubation overnight at 4°C. Incubation with biotinylated secondary antibodies was at 37°C for 1 hr, or at RT for 1.5 hr. Staining was visualized using the ABC method with the Vectastain abc kit and the DAB substrate kit for peroxidase (Vectorlabs, USA) or SIGMA_FAST_ DAB Tablets (Sigma-Aldrich, Germany). Counterstaining was carried out with hematoxylin (Sigma-Aldrich), followed by dehydration and embedding. Images were taken with an Axio Observer 7 (Zeiss).

Immunofluorescence staining

Immunostaining was performed as described (***Zhang et al., 2013***). In brief, mice (P60-P90) were transcardially perfused with PBS and then 4% PFA in PBS. Brains or spinal cords were post-fixed over night in 4% PFA/PBS. P7 pups were decapitated and brains post-fixed in 4% PFA. After cryoprotection (30% sucrose in PBS (pH 7.4), 40 µm cryostat sections (Microm HM560, Walldorf, Germany) were washed (3 × 10 min, PBS), blocked (5% Normal Goat Serum (Dako Germany), 0.3% Triton X-100 (Sigma, Munich, Germany) in PBS, 2 hr at RT) and incubated with primary antibodies (16–24 hr, 4°C) with gentle shaking. After washing as above, sections were incubated for 2 hr with fluorescence conjugated secondary antibodies. Slices were mounted on object slides with Perma-Fluor Mounting Medium (Thermo Scientific).

Rectus femoris muscle was incubated in 30% sucrose (48 hr), embedded in OTC (Tissue TEK), and frozen in liquid nitrogen. 20 µm cryostat sections were collected on object slides, fixed with 4% PFA (10 min), blocked and permeabilized (30 min, 1% BSA, 0.2% Triton X-100 in PBS). Incubation with

Alexa 594 Fluor-conjugated α-bungarotoxin (1:1000, Thermo Fisher Scientific) and primary antibodies was overnight at 4˚C, and with secondary antibodies for 1 hr at RT.

Thoracic and lumbar DRGs were embedded in Tissue-Tek, sectioned in 10 µm slices, mounted on slides and frozen at −80˚. Before staining as described above, sections were post-fixed for 10 min in 4% PFA in PBS, incubated for 30 min in 0.1 M Glycine in PBS, and blocked for 1 hr (5% normal goat serum, 0.1% Triton X-100 in PBS). In case of glutamine synthetase and MPZ staining, tissue was treated with 10 mM sodium citrate (pH 6.0,>95˚ C) for 1 min just before blocking. Images were obtained by confocal laser scanning microscopy (Leica SP5 or Zeiss LSM 880).

Quantification and statistical analysis

EGFP-positive cells were quantified in every fifth slice in a series of 25–30 sections throughout the whole rostrocaudal extension of the hippocampus. DAPI-positive cells, EGFP-positive cells, and marker protein-positive cells in the hippocampus CA1 region were counted in z-stacks. To define the counting box (250 × 250 × 25 μm^3), confocal laser micrographs of the CA1 region were obtained (63 x/0,75 NA objective) at 1 µm intervals to a final depth of 25 µm. Cell nuclei located completely inside the counting frame and at the upper and right borders were counted. Data analysis was performed using Excel and Graphpad Prism 7 software. Data are given as mean ±SEM from N = 3 mice per group.

Dissociation of adult cerebellar tissue

Mice were killed by cervical dislocation and brains were rapidly removed, washed with ice cold PBS, and kept on ice. Cerebelli were homogenized using the GentleMacs neuronal tissue dissociation kit (T) (Miltenyi Biotech) according to the manufactures instruction. Dissociated cells were centrifuged (1000 g/ 15 min/4˚C), and washed twice with PBS (followed by centrifugation as above) to remove residual trypsin. Supernatant was carefully removed and cells fixed (4% PFA in PBS, 10 min, 4˚C) under gentle agitation, washed three times with PBS as described above, permeabilized with blocking solution (2% BSA, 2% normal goat serum, 0.2% Triton X-100 in PBS), and incubated with the indicated antibodies diluted in blocking solution overnight at 4˚C. After washing, cells were incubated with secondary antibodies for 1 hr, washed, incubated with DAPI (200 nM in PBS, 10 min), washed, and embedded in Aquamount (Polyscience). Imaging was performed using a Zeiss Confocal microscope (LSM 800) and the ZEN imaging software. In co-processed wild-type animals, no GFP (immuno)-fluorescence was detected.

Teased fiber preparation and staining

Sciatic nerves of adult mice were dissected and transferred into cold PBS. Under a stereomicroscope, the epineurium was carefully removed, nerves separated longitudinally into individual or small bundles of fascicles, transferred to a droplet of cold PBS on a superfrost slide, and gently teased apart. Samples were air-dried and stored at −20˚C if not processed immediately for immunocytochemistry. Preparations were post-fixed (5 min) in 4% PFA, permeabilized with ice-cold methanol (5 min), washed with PBS (3 × 5 min), and blocked (10% horse serum, 0.1% Tween 20 in PBS, 2 hr at RT). Slides were incubated overnight at 4˚C with the primary antibodies and after washing with PBS (3 × 5 min), secondary antibodies were applied (2 hr at RT). After final washing, fibers were mounted with Vectashield Mounting Medium containing DAPI (Vector Laboratories).

Histological and immunohistochemical staining of retinae

Retinae were immersion-fixed (4% PFA for 2 hr), washed with PBS, sucrose cryoprotected and cut in 20 µm thick sections. Retinal sections were permeabilized (0.3% Triton X-100 plus 1.0% DMSO in PBS) and blocked (5% normal goat serum with 0.3% Triton X-100 and 1.0% DMSO in PBS, 2 hr at RT). Primary antibodies were incubated overnight at 4˚C. Sections were washed (1% BSA in PBS) and incubated with secondary antibodies (2 hr at RT). Cell nuclei were labeled with DAPI (1:1000; Life Technologies). Control experiments without primary antibodies showed no unspecific labeling. Images were acquired using confocal microscopy (Visiscope, Visitron Systems).

For quantification of cell numbers or microglia only central retinal slices were used. Cells were quantified in a defined area of 100 µm in width (DAPI staining) or the whole scan field (~460 µm in

width; microglia) approximately 200–300 µm in distance from the optic nerve head. For each animal, 2–3 central slices were analyzed.

Myenteric plexus preparation and staining

For whole mount myenteric plexus preparation, mice were sacrificed by cervical dislocation and 1 cm segments were taken 1 cm distal from the proximal colon and transferred to ice-cold Krebs solution (containing in mM: 117 NaCl, 4.7 KCl, 1.2 $MgCl_2$, 1.2 NaH_2PO_4, 25 $NaHCO_3$, 2.5 $CaCl_2$, 11 glucose and aerated with carbogen to pH 7.4) in Sylgard (Dow Corning)-filled dissecting dishes. After flushing with Krebs buffer, segments were opened along the mesenteric border, pinned out, and fixed for 4 hr at 4˚C (4% PFA and 0.2% picric acid in 0.1 M phosphate buffer (pH 7.4). Tissue was rinsed (3 × 10 min) with phosphate buffer and dissected in PBS (pH 7.4). After carefully removing mucosa, submucosa and circular musculature using forceps and a binocular, myenteric plexus preparations were blocked (0.5%, Triton X-100, 0.1% NaN_3, 4% goat serum (Sigma-Aldrich) in PBS, 1 hr, RT), incubated with primary antibodies in the above solution (12 hr at RT), rinsed 3 × 10 min with PBS, and incubated with secondary antibodies (2 hr at RT). After washing (3x in PBS) preparations were mounted in PermaFluor (Thermo Fisher Scientific) on slides and images were acquired with a Zeiss 880 Airyscan confocal microscope and processed with ImageJ.

Magnetic-activated cell sorting (MACS) of retinal cells

For enrichment of distinct retinal cell types a previously described protocol was used with minor modifications (***Grosche et al., 2016***). Briefly, retinae were treated with papain (0.2 mg/ml; Roche Molecular Biochemicals) for 30 min at 37˚C in the dark in Ca^{2+}- and Mg^{2+}-free extracellular solution (140 mM NaCl, 3 mM KCl, 10 mM HEPES, 11 mM glucose, pH 7.4), washed several times in extracellular solution and incubated with DNase I (200 U/ml). Afterwards the tissue was triturated in extracellular solution containing (mM) 135 NaCl, 3 KCl, 2 $CaCl_2$, 1 $MgCl_2$, 1 Na_2HPO_4, 10 HEPES, and 11 glucose adjusted to pH 7.4 with Tris. After centrifugation, cells were resuspended and incubated in extracellular solution containing biotinylated hamster anti-CD29 (clone Ha2/5, 0.1 mg/ml, BD Biosciences, Heidelberg, Germany) for 15 min at 4˚C. Cells were washed in extracellular solution, spun down, resuspended in the presence of anti-biotin MicroBeads (1:5; Miltenyi Biotec, Bergisch Gladbach, Germany) and incubated for 10 min at 4˚C. After washing, CD29 +Müller cells were separated using large cell (LS) columns according to the manufacturer's instructions (Miltenyi Biotec). To purify microglial and vascular cells in addition to Müller cells, the retinal cell suspension was subsequently incubated with CD11b- and CD31 microbeads (Miltenyi Biotec) and depleted from the retinal suspension using LS-columns prior to Müller cell enrichment.

qRT-PCR

Total RNA was isolated from whole brain tissue using the PureLink RNA Micro Scale Kit (Thermo Fisher Scientific, Germany). Upon DNase-treatment to remove genomic DNA, first-strand cDNAs were synthesized from 50 ng of total RNA (RevertAid H Minus First-Strand cDNA Synthesis Kit, Fermentas by Thermo Fisher Scientific, Germany). Primers (see ***Supplementary file 2***) were designed using the Universal Probe Library Assay Design Center (Roche). Transcript levels of candidate genes were measured by qRT-PCR using the QuantStudio 5 Real-Time PCR system (384 well, Life Technologies) according to the company's guidelines. All data are expressed as mean ± standard error (SEM) unless stated otherwise. Statistical analyses were performed using Graphpad Prism 7 Software (San Diego, CA). Unless stated otherwise, the significance was determined by the non-parametric Mann-Whitney U test.

Retinal ischemia

Transient retinal ischemia was induced in one eye by the HIOP (high intraocular pressure) method as previously described (***Pannicke et al., 2014***). The other eye remained untreated as internal control. Anesthesia was induced with ketamine (100 mg/kg body weight, intraperitoneal (ip); Ratiopharm, Ulm, Germany), xylazine (5 mg/kg, ip; Bayer Vital, Leverkusen, Germany), and atropine sulfate (100 mg/kg, ip; Braun, Melsungen, Germany). The anterior chamber of the test eye was cannulated from the pars plana with a 30-gauge infusion needle, connected to a saline bottle. The intraocular pressure was increased to 160 mmHg for 60 min by elevating the bottle. After removing the needle, the

animals survived for 3 days and, subsequently, were sacrificed with carbon dioxide. Mice were in the C57BL/6N background.

Stab wound injury

Stab wound injury was performed in the somatosensory cortex, as previously described (***Heinrich et al., 2014***; ***Heimann et al., 2017***). Briefly, anesthetized animals received a stab wound of the somatosensory cortical GM with a lancet-shaped knife (Alcon) Coordinates from bregma: AP −0.8 to −2.0, ML 1.6 to 2.0 mm and DV −0.6. Animals were allocated to experimental groups regarding their genotype and kept under standard conditions with access to water and food *ad libitum*. Five days post injury (dpi), animals were transcardially perfused and brains processed for immunohistochemistry as described above.

For analysis, seven corresponding slices were prepared from each animal and triple staining of GFAP, NeuN, and Iba1 were performed sequentially (starting with NeuN and over night fixation, and followed by GFAP and Iba1 labeling). Confocal images were taken at identical exposure settings with single channel maximum intensity projections set to automatic threshold. Iba1- Neu-, and DAPI-positive areas were measured using NIH ImageJ software (Image > adjust > threshold; Analyse > measure). Iba1-positive areas and NeuN-negative/lesioned areas were normalized to DAPI-positive areas. Data were analyzed using Graphpad Prism 7.

Intra-amygdala kainic acid-induced status epilepticus mouse model

Procedures were undertaken as described previously (***Jimenez-Pacheco et al., 2013***) in 8–12 week-old mice (line 17/FVB/N) bred at the Biomedical Research Facility at RCSI. Mice were anesthetized with isoflurane (5% induction, 1–2% maintenance) and maintained normothermic by means of a feed-back-controlled heat blanket (Harvard Apparatus Ltd, Kent, UK). Fully anesthetized, mice were placed in a stereotaxic frame and a midline scalp incision was performed to expose the skull. A guide cannula (coordinates from Bregma; AP = −0.94 mm, L = −2.85 mm) for intra-amygdala kainic acid (Sigma Aldrich, Dublin, Ireland) injection was fixed in place with dental cement and status epilepticus induced in fully awake mice via microinjection of 0.3 µg KA (in 0.2 µl phosphate-buffered saline) into the basolateral amygdala. Control animals received 0.2 µl PBS. 40 min after injections, the anticonvulsive lorazepam (6 mg/kg, Wyetch, Taplow, UK) was delivered i.p. to curtail seizures and reduce morbidity and mortality. Mice were killed 24 hr after lorazepam injection and perfused (4% PFA in PBS). Brains were post-fixed overnight in 4% PFA, embedded in 2% agarose, and cut by vibratome in 30 µm sections. Sections were stored in glycol at −20˚ C until use.

Behavioral experiments

Experiments were performed with 10–13 weeks old mice on 3 consecutive days in the following order.

Balance beam

Mice were positioned in the middle of a 50 cm long and round (1 cm diameter) wooden bar, which was fixed 44 cm above a padded surface between two 14 × 10 cm wooden escape platforms. The time for which animals stayed on the beam was measured and if a platform was reached, 60 s were counted. Each test was performed three times for a duration of 60 s.

String suspension

A 3-mm-thick rope was loosely attached to the balance beam platforms in 35 cm height. Mice were hold in front of the middle of the string so that they could grab it with their fore-paws. The following scoring was used during a 60 s test duration: 0 = unable to stay on rope; 1 = hanging on rope with one pair of paws; 2 = like 1, but with attempt to climb; 3 = sitting on rope, keeping balance; 4 = rope grabbed with all paws and tail together with a laterally movement of the mouse; 5 = escape on platform.

Hot plate

The plate was set to 50˚C and surface temperature continuously monitored with a digital thermometer. Time measurement started when the animal was gently placed on the hot plate and stopped

when the animal licked its hind paw for the first time or jumped off. Animals that failed to react within 60 s were removed from the plate to avoid thermal injury, and were assigned the value of 60 s. Each test was performed three times with at least 15 min intervals between measurements.

Animals

Mice were housed in standard conditions (22°C, 12 hr light–dark cycle, water/food *ad libitum*). Animal handling and experimental procedures were performed in accordance with German and European Union guidelines and were approved by the State of Upper Bavaria (stab wound injury (55.2.1.54-2532-171-11), retinal ischemia (TVV 54/12; 55.2 DMS-2532-2-182), transcardial perfusion (55.2-1-54-2532-59-2016)) and Lower Saxony (generation of BAC transgenic mice, transcardial perfusion (33.9-42502-04-12/0863), behavioral experiments (3392 42502-04-13/1123)). Status epilepticus was induced in accordance with the principles of the European Communities Council Directive (86/609/EEC) and procedures reviewed and approved by the Research Ethics Committee of the Royal College of Surgeons in Ireland (REC 205 and 1322) and performed under license from the Department of Health and Children, Ireland. All efforts were made to minimize suffering and number of animals used.

Acknowledgements

We thank Conny Neblung, Sarah Schlagowski, Annett Sporning, Irina Zamolo, and Heinz Janser for technical assistance, Heinrich Betz and Walter Stühmer for generously providing support and facilities, Stephan Kröger for help with NMJ preparation, Ursula Fünfschilling for advice in animal breeding, Ablynx for permission to use mouse P2×7 specific nanobody 7E2, Klaus Armin Nave for FLIR, Ella-Cre, and cnp1-Cre mice, and Steffen Jung for Cx3cr1-Cre mice. We are also grateful to Susanne Koch, Nundehui Diaz Lezama, and Ali Rifat for their commitment during the revision. This work was financed by the DFG (Ni 592/4–5 and 7 (AN), No 310/11–1 (FK-N), and SFB 1328 (AN, FK-N, TM), the European Union's Horizon 2020 research and innovation programme under the Marie Sklodowska-Curie grant agreement (No 766124 (TE, AN), and the Science Foundation Ireland (13/SIRG/2098 and 17/CDA/4708 (TE)). SB was granted a Faculty Research Visit Grant from the DAAD (German Academic Exchange Service).

Additional information

Competing interests

Friedrich Koch-Nolte: FKN receives a share of antibody sales via MediGate GmbH, a wholly owned subsidiary of the University Medical Center Hamburg-Eppendorf. FKN is a co-inventor on patent applications on P2X7-specific nanobodies (WO2010070145, WO2013178783). The other authors declare that no competing interests exist.

Funding

Funder	Grant reference number	Author
Deutsche Forschungsgemeinschaft	Ni 592/4-5	Annette Nicke
Deutscher Akademischer Austauschdienst		Santina Bruzzone
Deutsche Forschungsgemeinschaft	No 310/11-1	Friedrich Koch-Nolte
Science Foundation Ireland	13/SIRG/2098	Tobias Engel
Horizon 2020 Framework Programme	766124	Tobias Engel Annette Nicke
Deutsche Forschungsgemeinschaft	SFB 1328	Tim Magnus Friedrich Koch-Nolte Annette Nicke
Science Foundation Ireland	17/CDA/4708	Tobias Engel

Deutsche Forschungsgemeinschaft	Ni 592/4-7	Annette Nicke

The funders had no role in study design, data collection and interpretation, or the decision to submit the work for publication.

Author contributions

Karina Kaczmarek-Hajek, Conceptualization, Formal analysis, Investigation, Visualization, Methodology, Writing—review and editing; Jiong Zhang, Formal analysis, Validation, Investigation, Visualization, Methodology, Writing—review and editing; Robin Kopp, Formal analysis, Validation, Investigation, Visualization, Writing—review and editing; Antje Grosche, Formal analysis, Investigation, Visualization, Methodology, Writing—review and editing; Björn Rissiek, Santina Bruzzone, Swetlana Sirko, Formal analysis, Investigation, Methodology, Writing—review and editing; Anika Saul, Investigation, Visualization, Writing—review and editing; Tobias Engel, Christine Stadelmann, Friedrich Koch-Nolte, Resources, Methodology, Writing—review and editing; Tina Jooss, Investigation, Visualization; Anna Krautloher, Validation, Investigation, Writing—review and editing; Stefanie Schuster, Formal analysis, Investigation; Tim Magnus, Resources, Funding acquisition; Volker Eulenburg, Conceptualization, Formal analysis, Investigation, Methodology, Writing—review and editing; Annette Nicke, Conceptualization, Resources, Formal analysis, Supervision, Funding acquisition, Investigation, Visualization, Methodology, Writing—original draft, Project administration

Author ORCIDs

Robin Kopp http://orcid.org/0000-0002-1639-2868
Björn Rissiek http://orcid.org/0000-0001-5327-5479
Swetlana Sirko http://orcid.org/0000-0001-5950-616X
Volker Eulenburg http://orcid.org/0000-0002-4878-5746
Annette Nicke http://orcid.org/0000-0001-6798-505X

Ethics

Animal experimentation: Animal handling and experimental procedures were performed in accordance with German and European Union guidelines and were approved by the State of Upper Bavaria (stab wound injury (55.2.1.54-2532-171-11), retinal ischemia (TVV 54/12; 55.2 DMS-2532-2-182), transcardial perfusion (55.2-1-54-2532-59-2016)) and Lower Saxony (generation of BAC transgenic mice, transcardial perfusion (33.9-42502-04-12/0863), behavioral experiments (3392 42502-04-13/1123)). Status epilepticus was induced in accordance with the principles of the European Communities Council Directive (86/609/EEC) and procedures reviewed and approved by the Research Ethics Committee of the Royal College of Surgeons in Ireland (REC 205 and 1322) and performed under license from the Department of Health and Children, Ireland. All efforts were made to minimize suffering and number of animals used.

Decision letter and Author response

Decision letter https://doi.org/10.7554/eLife.36217.029
Author response https://doi.org/10.7554/eLife.36217.030

Additional files

Supplementary files

- Supplementary file 1. List of probes.
DOI: https://doi.org/10.7554/eLife.36217.025
- Supplementary file 2. List of primers.
DOI: https://doi.org/10.7554/eLife.36217.026
- Transparent reporting form
DOI: https://doi.org/10.7554/eLife.36217.027

Data availability

All data generated or analysed during this study are included in the manuscript and supporting files.

References

Adriouch S, Dox C, Welge V, Seman M, Koch-Nolte F, Haag F. 2002. Cutting edge: a natural P451L mutation in the cytoplasmic domain impairs the function of the mouse P2X7 receptor. *The Journal of Immunology* **169**: 4108–4112. DOI: https://doi.org/10.4049/jimmunol.169.8.4108, PMID: 12370338

Anderson CM, Nedergaard M. 2006. Emerging challenges of assigning P2X7 receptor function and immunoreactivity in neurons. *Trends in Neurosciences* **29**:257–262. DOI: https://doi.org/10.1016/j.tins.2006.03.003, PMID: 16564580

Bhattacharya A, Biber K. 2016. The microglial ATP-gated ion channel P2X7 as a CNS drug target. *Glia* **64**:1772–1787. DOI: https://doi.org/10.1002/glia.23001, PMID: 27219534

Brown IA, McClain JL, Watson RE, Patel BA, Gulbransen BD. 2016. Enteric Glia mediate neuron death in colitis through purinergic pathways that require connexin-43 and nitric oxide. *Cellular and Molecular Gastroenterology and Hepatology* **2**:77–91. DOI: https://doi.org/10.1016/j.jcmgh.2015.08.007, PMID: 26771001

Bruzzone S, Basile G, Chothi MP, Nobbio L, Usai C, Jacchetti E, Schenone A, Guse AH, Di Virgilio F, De Flora A, Zocchi E. 2010. Diadenosine homodinucleotide products of ADP-ribosyl cyclases behave as modulators of the purinergic receptor P2X7. *Journal of Biological Chemistry* **285**:21165–21174. DOI: https://doi.org/10.1074/jbc.M109.097964, PMID: 20439466

Carpenter S, Ricci EP, Mercier BC, Moore MJ, Fitzgerald KA. 2014. Post-transcriptional regulation of gene expression in innate immunity. *Nature Reviews Immunology* **14**:361–376. DOI: https://doi.org/10.1038/nri3682, PMID: 24854588

Chessell IP, Hatcher JP, Bountra C, Michel AD, Hughes JP, Green P, Egerton J, Murfin M, Richardson J, Peck WL, Grahames CB, Casula MA, Yiangou Y, Birch R, Anand P, Buell GN. 2005. Disruption of the P2X7 purinoceptor gene abolishes chronic inflammatory and neuropathic pain. *Pain* **114**:386–396. DOI: https://doi.org/10.1016/j.pain.2005.01.002, PMID: 15777864

Compan V, Ulmann L, Stelmashenko O, Chemin J, Chaumont S, Rassendren F. 2012. P2X2 and P2X5 subunits define a new heteromeric receptor with P2X7-like properties. *Journal of Neuroscience* **32**:4284–4296. DOI: https://doi.org/10.1523/JNEUROSCI.6332-11.2012, PMID: 22442090

Court FA, Gillingwater TH, Melrose S, Sherman DL, Greenshields KN, Morton AJ, Harris JB, Willison HJ, Ribchester RR. 2008. Identity, developmental restriction and reactivity of extralaminar cells capping mammalian neuromuscular junctions. *Journal of Cell Science* **121**:3901–3911. DOI: https://doi.org/10.1242/jcs.031047, PMID: 19001504

Danquah W, Meyer-Schwesinger C, Rissiek B, Pinto C, Serracant-Prat A, Amadi M, Iacenda D, Knop JH, Hammel A, Bergmann P, Schwarz N, Assunção J, Rotthier W, Haag F, Tolosa E, Bannas P, Boué-Grabot E, Magnus T, Laeremans T, Stortelers C, et al. 2016. Nanobodies that block gating of the P2X7 ion channel ameliorate inflammation. *Science Translational Medicine* **8**:366ra162. DOI: https://doi.org/10.1126/scitranslmed.aaf8463, PMID: 27881823

Deuchars SA, Atkinson L, Brooke RE, Musa H, Milligan CJ, Batten TF, Buckley NJ, Parson SH, Deuchars J. 2001. Neuronal P2X7 receptors are targeted to presynaptic terminals in the central and peripheral nervous systems. *The Journal of Neuroscience* **21**:7143–7152. DOI: https://doi.org/10.1523/JNEUROSCI.21-18-07143.2001, PMID: 11549725

Di Virgilio F, Dal Ben D, Sarti AC, Giuliani AL, Falzoni S. 2017. The P2X7 receptor in infection and inflammation. *Immunity* **47**:15–31. DOI: https://doi.org/10.1016/j.immuni.2017.06.020, PMID: 28723547

Di Virgilio F, Schmalzing G, Markwardt F. 2018. The elusive P2X7 macropore. *Trends in Cell Biology* **28**:392–404. DOI: https://doi.org/10.1016/j.tcb.2018.01.005, PMID: 29439897

Díaz-Hernandez M, del Puerto A, Díaz-Hernandez JI, Diez-Zaera M, Lucas JJ, Garrido JJ, Miras-Portugal MT. 2008. Inhibition of the ATP-gated P2X7 receptor promotes axonal growth and branching in cultured hippocampal neurons. *Journal of Cell Science* **121**:3717–3728. DOI: https://doi.org/10.1242/jcs.034082, PMID: 18987356

Engel T, Gomez-Villafuertes R, Tanaka K, Mesuret G, Sanz-Rodriguez A, Garcia-Huerta P, Miras-Portugal MT, Henshall DC, Diaz-Hernandez M. 2012. Seizure suppression and neuroprotection by targeting the purinergic P2X7 receptor during status epilepticus in mice. *The FASEB Journal* **26**:1616–1628. DOI: https://doi.org/10.1096/fj.11-196089, PMID: 22198387

Farley FW, Soriano P, Steffen LS, Dymecki SM. 2000. Widespread recombinase expression using FLPeR (flipper) mice. *Genesis* **28**:106–110. DOI: https://doi.org/10.1002/1526-968X(200011/12)28:3/4<106::AID-GENE30>3.0.CO;2-T, PMID: 11105051

Franke H, Klimke K, Brinckmann U, Grosche J, Francke M, Sperlagh B, Reichenbach A, Liebert UG, Illes P. 2005. P2X(7) receptor-mRNA and -protein in the mouse retina; changes during retinal degeneration in BALBCrds mice. *Neurochemistry International* **47**:235–242. DOI: https://doi.org/10.1016/j.neuint.2005.04.022, PMID: 15964665

Fumey W, Koenigsdorf J, Kunick V, Menzel S, Schütze K, Unger M, Schriewer L, Haag F, Adam G, Oberle A, Binder M, Fliegert R, Guse A, Zhao YJ, Cheung Lee H, Malavasi F, Goldbaum F, van Hegelsom R, Stortelers C,

Bannas P, et al. 2017. Nanobodies effectively modulate the enzymatic activity of CD38 and allow specific imaging of CD38$^+$ tumors in mouse models in vivo. *Scientific Reports* **7**:14289. DOI: https://doi.org/10.1038/s41598-017-14112-6, PMID: 29084989

Gerfen CR, Paletzki R, Heintz N. 2013. GENSAT BAC cre-recombinase driver lines to study the functional organization of cerebral cortical and basal ganglia circuits. *Neuron* **80**:1368–1383. DOI: https://doi.org/10.1016/j.neuron.2013.10.016, PMID: 24360541

Grosche J, Kettenmann H, Reichenbach A. 2002. Bergmann glial cells form distinct morphological structures to interact with cerebellar neurons. *Journal of Neuroscience Research* **68**:138–149. DOI: https://doi.org/10.1002/jnr.10197, PMID: 11948659

Grosche A, Hauser A, Lepper MF, Mayo R, von Toerne C, Merl-Pham J, Hauck SM. 2016. The proteome of native adult müller glial cells from murine retina. *Molecular & Cellular Proteomics* **15**:462–480. DOI: https://doi.org/10.1074/mcp.M115.052183, PMID: 26324419

Gulbransen BD, Bashashati M, Hirota SA, Gui X, Roberts JA, MacDonald JA, Muruve DA, McKay DM, Beck PL, Mawe GM, Thompson RJ, Sharkey KA. 2012. Activation of neuronal P2X7 receptor-pannexin-1 mediates death of enteric neurons during colitis. *Nature Medicine* **18**:600–604. DOI: https://doi.org/10.1038/nm.2679, PMID: 22426419

Habbas S, Ango F, Daniel H, Galante M. 2011. Purinergic signaling in the cerebellum: bergmann glial cells express functional ionotropic P2X7 receptors. *Glia* **59**:1800–1812. DOI: https://doi.org/10.1002/glia.21224, PMID: 21830236

Harkat M, Peverini L, Cerdan AH, Dunning K, Beudez J, Martz A, Calimet N, Specht A, Cecchini M, Chataigneau T, Grutter T. 2017. On the permeation of large organic cations through the pore of ATP-gated P2X receptors. *PNAS* **114**:E3786–E3795. DOI: https://doi.org/10.1073/pnas.1701379114, PMID: 28442564

Heimann G, Canhos LL, Frik J, Jäger G, Lepko T, Ninkovic J, Götz M, Sirko S. 2017. Changes in the proliferative program limit astrocyte homeostasis in the aged Post-Traumatic murine cerebral cortex. *Cerebral Cortex* **27**:4213–4228. DOI: https://doi.org/10.1093/cercor/bhx112, PMID: 28472290

Heinrich C, Bergami M, Gascón S, Lepier A, Viganò F, Dimou L, Sutor B, Berninger B, Götz M. 2014. Sox2-mediated conversion of NG2 Glia into induced neurons in the injured adult cerebral cortex. *Stem Cell Reports* **3**:1000–1014. DOI: https://doi.org/10.1016/j.stemcr.2014.10.007, PMID: 25458895

Illes P, Khan TM, Rubini P. 2017. Neuronal P2X7 receptors revisited: do they really exist? *The Journal of Neuroscience* **37**:7049–7062. DOI: https://doi.org/10.1523/JNEUROSCI.3103-16.2017, PMID: 28747388

Innocenti B, Pfeiffer S, Zrenner E, Kohler K, Guenther E. 2004. ATP-induced non-neuronal cell permeabilization in the rat inner retina. *Journal of Neuroscience* **24**:8577–8583. DOI: https://doi.org/10.1523/JNEUROSCI.2812-04.2004, PMID: 15456831

Jabs R, Matthias K, Grote A, Grauer M, Seifert G, Steinhäuser C. 2007. Lack of P2X receptor mediated currents in astrocytes and GluR type glial cells of the hippocampal CA1 region. *Glia* **55**:1648–1655. DOI: https://doi.org/10.1002/glia.20580, PMID: 17849469

Jager SB, Vaegter CB. 2016. Avoiding experimental bias by systematic antibody validation. *Neural Regeneration Research* **11**:1079–1080. DOI: https://doi.org/10.4103/1673-5374.187037, PMID: 27630688

Jimenez-Pacheco A, Mesuret G, Sanz-Rodriguez A, Tanaka K, Mooney C, Conroy R, Miras-Portugal MT, Diaz-Hernandez M, Henshall DC, Engel T. 2013. Increased neocortical expression of the P2X7 receptor after status epilepticus and anticonvulsant effect of P2X7 receptor antagonist A-438079. *Epilepsia* **54**:1551–1561. DOI: https://doi.org/10.1111/epi.12257, PMID: 23808395

Lakso M, Pichel JG, Gorman JR, Sauer B, Okamoto Y, Lee E, Alt FW, Westphal H. 1996. Efficient in vivo manipulation of mouse genomic sequences at the zygote stage. *PNAS* **93**:5860–5865. DOI: https://doi.org/10.1073/pnas.93.12.5860, PMID: 8650183

Lappe-Siefke C, Goebbels S, Gravel M, Nicksch E, Lee J, Braun PE, Griffiths IR, Nave KA. 2003. Disruption of Cnp1 uncouples oligodendroglial functions in axonal support and myelination. *Nature Genetics* **33**:366–374. DOI: https://doi.org/10.1038/ng1095, PMID: 12590258

Li M, Toombes GE, Silberberg SD, Swartz KJ. 2015. Physical basis of apparent pore dilation of ATP-activated P2X receptor channels. *Nature Neuroscience* **18**:1577–1583. DOI: https://doi.org/10.1038/nn.4120, PMID: 26389841

Masin M, Young C, Lim K, Barnes SJ, Xu XJ, Marschall V, Brutkowski W, Mooney ER, Gorecki DC, Murrell-Lagnado R. 2012. Expression, assembly and function of novel C-terminal truncated variants of the mouse P2X7 receptor: re-evaluation of P2X7 knockouts. *British Journal of Pharmacology* **165**:978–993. DOI: https://doi.org/10.1111/j.1476-5381.2011.01624.x, PMID: 21838754

Metzger MW, Walser SM, Aprile-Garcia F, Dedic N, Chen A, Holsboer F, Arzt E, Wurst W, Deussing JM. 2017. Genetically dissecting P2rx7 expression within the central nervous system using conditional humanized mice. *Purinergic Signalling* **13**:153–170. DOI: https://doi.org/10.1007/s11302-016-9546-z, PMID: 27858314

Miras-Portugal MT, Sebastián-Serrano Á, de Diego García L, Díaz-Hernández M. 2017. Neuronal P2X7 receptor: involvement in neuronal physiology and pathology. *The Journal of Neuroscience* **37**:7063–7072. DOI: https://doi.org/10.1523/JNEUROSCI.3104-16.2017, PMID: 28747389

Nicke A. 2008. Homotrimeric complexes are the dominant assembly state of native P2X7 subunits. *Biochemical and Biophysical Research Communications* **377**:803–808. DOI: https://doi.org/10.1016/j.bbrc.2008.10.042, PMID: 18938136

Nicke A, Kuan YH, Masin M, Rettinger J, Marquez-Klaka B, Bender O, Górecki DC, Murrell-Lagnado RD, Soto F. 2009. A functional P2X7 splice variant with an alternative transmembrane domain 1 escapes gene inactivation

in P2X7 knock-out mice. *Journal of Biological Chemistry* **284**:25813–25822. DOI: https://doi.org/10.1074/jbc.M109.033134, PMID: 19546214

Nobbio L, Sturla L, Fiorese F, Usai C, Basile G, Moreschi I, Benvenuto F, Zocchi E, De Flora A, Schenone A, Bruzzone S. 2009. P2X7-mediated increased intracellular calcium causes functional derangement in schwann cells from rats with CMT1A neuropathy. *Journal of Biological Chemistry* **284**:23146–23158. DOI: https://doi.org/10.1074/jbc.M109.027128, PMID: 19546221

Nörenberg W, Plötz T, Sobottka H, Chubanov V, Mittermeier L, Kalwa H, Aigner A, Schaefer M. 2016. TRPM7 is a molecular substrate of ATP-evoked P2X7-like currents in tumor cells. *The Journal of General Physiology* **147**:467–483. DOI: https://doi.org/10.1085/jgp.201611595, PMID: 27185858

Ohishi A, Keno Y, Marumiya A, Sudo Y, Uda Y, Matsuda K, Morita Y, Furuta T, Nishida K, Nagasawa K. 2016. Expression level of P2X7 receptor is a determinant of ATP-induced death of mouse cultured neurons. *Neuroscience* **319**:35–45. DOI: https://doi.org/10.1016/j.neuroscience.2016.01.048, PMID: 26812038

Pannicke T, Fischer W, Biedermann B, Schädlich H, Grosche J, Faude F, Wiedemann P, Allgaier C, Illes P, Burnstock G, Reichenbach A. 2000. P2X7 receptors in müller glial cells from the human retina. *The Journal of Neuroscience* **20**:5965–5972 . DOI: https://doi.org/10.1523/JNEUROSCI.20-16-05965.2000, PMID: 10934244

Pannicke T, Frommherz I, Biedermann B, Wagner L, Sauer K, Ulbricht E, Härtig W, Krügel U, Ueberham U, Arendt T, Illes P, Bringmann A, Reichenbach A, Grosche A. 2014. Differential effects of P2Y1 deletion on glial activation and survival of photoreceptors and amacrine cells in the ischemic mouse retina. *Cell Death & Disease* **5**:e1353. DOI: https://doi.org/10.1038/cddis.2014.317, PMID: 25077539

Rassendren F, Audinat E. 2016. Purinergic signaling in epilepsy. *Journal of Neuroscience Research* **94**:781–793. DOI: https://doi.org/10.1002/jnr.23770, PMID: 27302739

Requardt RP, Kaczmarczyk L, Dublin P, Wallraff-Beck A, Mikeska T, Degen J, Waha A, Steinhäuser C, Willecke K, Theis M. 2009. Quality control of astrocyte-directed cre transgenic mice: the benefits of a direct link between loss of gene expression and reporter activation. *Glia* **57**:680–692. DOI: https://doi.org/10.1002/glia.20796, PMID: 18942753

Rozmer K, Gao P, Araújo MGL, Khan MT, Liu J, Rong W, Tang Y, Franke H, Krügel U, Fernandes MJS, Illes P. 2017. Pilocarpine-Induced status epilepticus increases the sensitivity of P2X7 and P2Y1 receptors to nucleotides at neural progenitor cells of the juvenile rodent Hippocampus. *Cerebral Cortex* **27**:3568–3585. DOI: https://doi.org/10.1093/cercor/bhw178, PMID: 27341850

Sanderson J, Dartt DA, Trinkaus-Randall V, Pintor J, Civan MM, Delamere NA, Fletcher EL, Salt TE, Grosche A, Mitchell CH. 2014. Purines in the eye: recent evidence for the physiological and pathological role of purines in the RPE, retinal neurons, astrocytes, müller cells, lens, trabecular meshwork, cornea and lacrimal gland. *Experimental Eye Research* **127**:270–279. DOI: https://doi.org/10.1016/j.exer.2014.08.009, PMID: 25151301

Saul A, Hausmann R, Kless A, Nicke A. 2013. Heteromeric assembly of P2X subunits. *Frontiers in Cellular Neuroscience* **7**:250. DOI: https://doi.org/10.3389/fncel.2013.00250, PMID: 24391538

Schirrmann T, Büssow K. 2010. Transient production of scFv-Fc fusion proteins in mammalian cells. *Antibody Engineering*:387–398.

Sim JA, Young MT, Sung HY, North RA, Surprenant A. 2004. Reanalysis of P2X7 receptor expression in rodent brain. *Journal of Neuroscience* **24**:6307–6314. DOI: https://doi.org/10.1523/JNEUROSCI.1469-04.2004, PMID: 15254086

Sociali G, Visigalli D, Prukop T, Cervellini I, Mannino E, Venturi C, Bruzzone S, Sereda MW, Schenone A. 2016. Tolerability and efficacy study of P2X7 inhibition in experimental Charcot-Marie-Tooth type 1A (CMT1A) neuropathy. *Neurobiology of Disease* **95**:145–157. DOI: https://doi.org/10.1016/j.nbd.2016.07.017, PMID: 27431093

Solle M, Labasi J, Perregaux DG, Stam E, Petrushova N, Koller BH, Griffiths RJ, Gabel CA. 2001. Altered cytokine production in mice lacking P2X(7) receptors. *The Journal of Biological Chemistry* **276**:125–132. DOI: https://doi.org/10.1074/jbc.M006781200, PMID: 11016935

Sorge RE, Trang T, Dorfman R, Smith SB, Beggs S, Ritchie J, Austin JS, Zaykin DV, Vander Meulen H, Costigan M, Herbert TA, Yarkoni-Abitbul M, Tichauer D, Livneh J, Gershon E, Zheng M, Tan K, John SL, Slade GD, Jordan J, et al. 2012. Genetically determined P2X7 receptor pore formation regulates variability in chronic pain sensitivity. *Nature Medicine* **18**:595–599. DOI: https://doi.org/10.1038/nm.2710, PMID: 22447075

Sperlágh B, Illes P. 2014. P2X7 receptor: an emerging target in central nervous system diseases. *Trends in Pharmacological Sciences* **35**:537–547. DOI: https://doi.org/10.1016/j.tips.2014.08.002, PMID: 25223574

Surprenant A, Rassendren F, Kawashima E, North RA, Buell G. 1996. The cytolytic P2Z receptor for extracellular ATP identified as a P2X receptor (P2X7). *Science* **272**:735–738. DOI: https://doi.org/10.1126/science.272.5262.735, PMID: 8614837

Warming S, Costantino N, Court DL, Jenkins NA, Copeland NG. 2005. Simple and highly efficient BAC recombineering using galK selection. *Nucleic Acids Research* **33**:e36. DOI: https://doi.org/10.1093/nar/gni035, PMID: 15731329

Yang XW, Gong S. 2005. An overview on the generation of BAC transgenic mice for neuroscience research. *Current Protocols in Neuroscience* **Chapter 5**:5.20.1–5.20.5. DOI: https://doi.org/10.1002/0471142301.ns0520s31

Yona S, Kim KW, Wolf Y, Mildner A, Varol D, Breker M, Strauss-Ayali D, Viukov S, Guilliams M, Misharin A, Hume DA, Perlman H, Malissen B, Zelzer E, Jung S. 2013. Fate mapping reveals origins and dynamics of monocytes and tissue macrophages under homeostasis. *Immunity* **38**:79–91. DOI: https://doi.org/10.1016/j.immuni.2012.12.001, PMID: 23273845

Yu Y, Ugawa S, Ueda T, Ishida Y, Inoue K, Kyaw Nyunt A, Umemura A, Mase M, Yamada K, Shimada S. 2008. Cellular localization of P2X7 receptor mRNA in the rat brain. *Brain Research* **1194**:45–55. DOI: https://doi.org/10.1016/j.brainres.2007.11.064, PMID: 18177631

Zhang XF, Han P, Faltynek CR, Jarvis MF, Shieh CC. 2005. Functional expression of P2X7 receptors in non-neuronal cells of rat dorsal root ganglia. *Brain Research* **1052**:63–70. DOI: https://doi.org/10.1016/j.brainres.2005.06.022, PMID: 16005856

Zhang J, Liu X, Bell A, To R, Baral TN, Azizi A, Li J, Cass B, Durocher Y. 2009. Transient expression and purification of chimeric heavy chain antibodies. *Protein Expression and Purification* **65**:77–82. DOI: https://doi.org/10.1016/j.pep.2008.10.011, PMID: 19007889

Zhang J, Dublin P, Griemsmann S, Klein A, Brehm R, Bedner P, Fleischmann BK, Steinhäuser C, Theis M. 2013. Germ-line recombination activity of the widely used hGFAP-Cre and nestin-Cre transgenes. *PLoS ONE* **8**: e82818. DOI: https://doi.org/10.1371/journal.pone.0082818, PMID: 24349371

Zhang Y, Chen K, Sloan SA, Bennett ML, Scholze AR, O'Keeffe S, Phatnani HP, Guarnieri P, Caneda C, Ruderisch N, Deng S, Liddelow SA, Zhang C, Daneman R, Maniatis T, Barres BA, Wu JQ. 2014. An RNA-sequencing transcriptome and splicing database of Glia, neurons, and vascular cells of the cerebral cortex. *Journal of Neuroscience* **34**:11929–11947. DOI: https://doi.org/10.1523/JNEUROSCI.1860-14.2014, PMID: 25186741

Supplementary file 1–Probes

Probe	Name	Sequence
StrepHisEGFP insertion Hom. recomb. 1 (GalK insertion)	X7Ex13GalKfw	GAAGGAGTTCCCCAAGACCGAGGGGCAGTATAG TGGCTTCAAGTATCCCTACCCTGTTGACAATTAAT CATCGGCA
	X7Ex13GalKrev	CTAGGTCTTTCCAAGGGAAGCTGTATTGTGAGCC ACCATGATGTGGCAGCCGTACCATCATCAGCACT GTCCTGCTCCTT
Hom. recomb. 2 StrepHisEGFP insertion	HomAEx13X7GFP	GAAGGAGTTCCCCAAGACCGAGGGGCAGTATAG TGGCTTCAAGTATCCCTACAGCGCCTGGAGCCAC CCGCAGTTC
	HomBEx13X7GFP	CTAGGTCTTTCCAAGGGAAGCTGTATTGTGAGCC ACCATGATGTGGCAGCCGTACCATCATTACTTGT ACAGCTCGTCCATG
L451P exchange Hom. recomb. 1 (GalK insertion)	X7L451PgalK_F	GGACTTCTCCGACCTGTCTAGGCTGTCCCTATCTC TCCACGACTCACCCCCCTGTTGACAATTAATCAT CGGCA
	X7L451PgalK_R	GGGCCACCTCTTCATGGAGCAGCTGAATTTCCTC AGATTGTCCAGGAGTCTCAGCACTGTCCTGCTCC TT
Hom. recomb. 2 L451P exchange	X7L451P_S	GGACTTCTCCGACCTGTCTAGGCTGTCCCTATCTC TCCACGACTCACCCCCGACTCCTGGACAATCTGA GGAAATTCAGCTGCTCCATGAAGAGGTGGCC
	X7L451P_AS	GGCCACCTCTTCATGGAGCAGCTGAATTTCCTCA GATTGTCCAGGAGTCGGGGGTGAGTCGTGGAGA GATAGGGACAGCCTAGACAGGTCGGAGAAGTCC
X7intr/ex13	Forward primer	GTGCTGGGATTAAAGGTGTGC
probe (606 bp)	Backward primer	AGCTTATGGAAGAGCTTGGAGGT
EGFP probe	Forward primer	GTAAACGGCCACAAGTTCAGC
(604 bp)	Backward primer	ACTCCAGCAGGACCATGTGAT
Southern blot	Forward primer	GCTTGTGATAAGGACGCC
probes	Backward primer	TTTTTGGTCTACTGCGTG

1

Supplementary file 2–Primers

Primer for	Name	Sequence
Genotyping	seqX7Ex13_F (in intron 12)	GGTTCTTAGCAGGCTTAACAGCA
	X7BAC5_R (in EGFP) or	ATGGGGGTGTTCTGCTGGTAGT
	seqX73UTR_R (in 3´UTR)	GCCATTGGTCTAATCAGCTCTC
Real time PCR	TM_Pdhb_for TM_Pdhb_rev (House keeper, Roche probe #4)	TTAAATCGGCCATTCGTGAT CAGGAAATCTTTTGACTGAGCTT
	TM_P2X7_for TM_P2X7_rev (Roche probe #42)	CTGGTTTTCGGCACTGGA CCAAAGTAGGACAGGGTGGA
	TM_Iba1_for TM_Iba1_rev (Roche probe #67)	ATCTGCCGTCCAAACTTGA CTAGGTGGGTCTTGGGAACC
	TM_ Tnfa_for TM_ Tnfa_rev (Roche probe #68)	CTGTAGCCCACGTCGTAGC TTTGAGATCCATGCCGTTG
	TM_ Il1b_for TM_ Il1b_rev (Roche probe #38)	AGTTGACGGACCCCAAAAG AGCTGGATGCTCTCATCAGG

1

List of Figures

Bibliography

[1] I. COUILLIN, A. GOMBAULT, and L. Baron, "ATP release and purinergic signaling in NLRP3 inflammasome activation", *Frontiers in Immunology*, vol. 3, 2013, ISSN: 1664-3224 (cit. on p. 3).

[2] G. Burnstock, "Purine and purinergic receptors", *Brain and Neuroscience Advances*, vol. 2, p. 2 398 212 818 817 494, Dec. 2018, ISSN: 2398-2128. DOI: 10.1177/2398212818817494 (cit. on p. 3).

[3] J. Dunn and M. H. Grider, "Physiology, Adenosine Triphosphate", eng, in *StatPearls*, Treasure Island (FL): StatPearls Publishing, 2022 (cit. on p. 3).

[4] D. Purves, G. J. Augustine, D. Fitzpatrick, L. C. Katz, A.-S. LaMantia, J. O. McNamara, and S. M. Williams, "Neurotransmitter Receptors and Their Effects", en, *Neuroscience. 2nd edition*, 2001, Publisher: Sinauer Associates (cit. on p. 3).

[5] S. Alexander, A. Mathie, and J. Peters, "ION CHANNELS: Ion Channels", en, *British Journal of Pharmacology*, vol. 164, S137–S174, Nov. 2011, ISSN: 00071188. DOI: 10.1111/j.1476-5381.2011.01649_5.x (cit. on p. 3).

[6] E. Faccenda, S. Maxwell, and J. L. Szarek, "The IUPHAR Pharmacology Education Project", en, *Clinical Pharmacology & Therapeutics*, vol. 105, no. 1, pp. 45–48, Jan. 2019, ISSN: 0009-9236, 1532-6535. DOI: 10.1002/cpt.1278 (cit. on p. 3).

[7] C. E. Müller and V. Namasivayam, "Agonists, Antagonists, and Modulators of P2X7 Receptors", en, in *The P2X7 Receptor: Methods and Protocols*, ser. Methods in Molecular Biology, A. Nicke, Ed., New York, NY: Springer US, 2022, pp. 31–52, ISBN: 978-1-07-162384-8. DOI: 10.1007/978-1-0716-2384-8_2 (cit. on pp. 3, 6).

[8] P. Illes, C. E. Müller, K. A. Jacobson, T. Grutter, A. Nicke, S. J. Fountain, C. Kennedy, G. Schmalzing, M. F. Jarvis, S. S. Stojilkovic, B. F. King, and F. Di Virgilio, "Update of P2X receptor properties and their pharmacology: IUPHAR Review 30", en, *British Journal of Pharmacology*, vol. 178, no. 3, pp. 489–514, 2021, _eprint: https://onlinelibrary.wiley.com/doi/pdf/10.1111/bph.15299, ISSN: 1476-5381. DOI: 10.1111/bph.15299 (cit. on pp. 4–6, 14).

[9] T. Kawate, J. C. Michel, W. T. Birdsong, and E. Gouaux, "Crystal structure of the ATP-gated P2X 4 ion channel in the closed state", *Nature*, vol. 460, no. 7255, pp. 592–598, 2009, Publisher: Nature Publishing Group, ISSN: 0028-0836. DOI: 10.1038/nature08198 (cit. on pp. 4, 10).

[10] K. Kaczmarek-Hájek, É. Lörinczi, R. Hausmann, and A. Nicke, "Molecular and functional properties of P2X receptors-recent progress and persisting challenges", *Purinergic Signalling*, vol. 8, no. 3, pp. 375–417, 2012, ISBN: 1573-9538, ISSN: 15739538. DOI: 10.1007/s11302-012-9314-7 (cit. on pp. 4, 5).

[11] B. Marquez-Klaka, J. Rettinger, Y. Bhargava, T. Eisele, and A. Nicke, "Identification of an intersubunit cross-link between substituted cysteine residues located in the putative ATP binding site of the P2X1 receptor.", *The Journal of neuroscience : the official journal of the Society for Neuroscience*, vol. 27, no. 6, pp. 1456–1466, 2007, ISSN: 0270-6474. DOI: 10.1523/JNEUROSCI.3105-06.2007 (cit. on p. 4).

[12] A. Saul, R. Hausmann, A. Kless, and A. Nicke, "Heteromeric assembly of P2X subunits", *Frontiers in Cellular Neuroscience*, vol. 7, no. December, p. 250, 2013, ISSN: 1662-5102. DOI: 10.3389/fncel.2013.00250 (cit. on p. 4).

[13] a. Nicke, H. G. Baumert, J. Rettinger, a. Eichele, G. Lambrecht, E. Mutschler, and G. Schmalzing, "P2X 1 and P2X 3 receptors form stable trimers: A novel structural motif of ligand-gated ion channels", *Embo J.*, vol. 17, no. 11, pp. 3016–3028, 1998 (cit. on p. 4).

[14] S. Ding and F. Sachs, "Single Channel Properties of P2X2 Purinoceptors", *Journal of General Physiology*, vol. 113, no. 5, pp. 695–720, May 1999, ISSN: 0022-1295. DOI: 10.1085/jgp.113.5.695 (cit. on p. 4).

[15] R. Stoop, S. Thomas, F. Rassendren, E. Kawashima, G. Buell, A. Surprenant, and R. A. North, "Contribution of Individual Subunits to the Multimeric P2X2 Receptor: Estimates based on Methanethiosulfonate Block at T336C", en, *Molecular Pharmacology*, vol. 56, no. 5, pp. 973–981, Nov. 1999, Publisher: American Society for Pharmacology and Experimental Therapeutics Section: Article, ISSN: 0026-895X, 1521-0111. DOI: 10.1124/mol.56.5.973 (cit. on p. 4).

[16] L.-H. Jiang, M. Kim, V. Spelta, X. Bo, A. Surprenant, and R. A. North, "Subunit Arrangement in P2X Receptors", en, *Journal of Neuroscience*, vol. 23, no. 26, pp. 8903–8910, Oct. 2003, Publisher: Society for Neuroscience Section: Cellular/Molecular, ISSN: 0270-6474, 1529-2401. DOI: 10.1523/JNEUROSCI.23-26-08903.2003 (cit. on p. 4).

[17] N. P. Barrera, S. J. Ormond, R. M. Henderson, R. D. Murrell-Lagnado, and J. M. Edwardson, "Atomic force microscopy imaging demonstrates that P2X2 receptors are trimers but that P2X6 receptor subunits do not oligomerize", eng, *The Journal of Biological Chemistry*, vol. 280, no. 11, pp. 10 759–10 765, Mar. 2005, ISSN: 0021-9258. DOI: 10.1074/jbc.M412265200 (cit. on p. 4).

[18] M. Hattori and E. Gouaux, "Molecular mechanism of ATP binding and ion channel activation in P2X receptors", *Nature*, vol. 485, no. 7397, pp. 207–212, May 2012, ISSN: 0028-0836. DOI: 10.1038/nature11010 (cit. on p. 4).

[19] G. Kasuya, Y. Fujiwara, M. Takemoto, N. Dohmae, Y. Nakada-Nakura, R. Ishitani, M. Hattori, and O. Nureki, "Structural Insights into Divalent Cation Modulations of ATP-Gated P2X Receptor Channels", English, *Cell Reports*, vol. 14, no. 4, pp. 932–944, Feb. 2016, Publisher: Elsevier, ISSN: 2211-1247. DOI: 10.1016/j.celrep.2015.12.087 (cit. on p. 4).

[20] G. Kasuya, T. Yamaura, X. B. Ma, R. Nakamura, M. Takemoto, H. Nagumo, E. Tanaka, N. Dohmae, T. Nakane, Y. Yu, R. Ishitani, O. Matsuzaki, M. Hattori, and O. Nureki, "Structural insights into the competitive inhibition of the ATP-gated P2X receptor channel", *Nature Communications*, vol. 8, no. 1, 2017, ISSN: 20411723. DOI: 10.1038/s41467-017-00887-9 (cit. on p. 4).

[21] A. Karasawa and T. Kawate, "Structural basis for subtype-specific inhibition of the P2X7 receptor", *eLife*, vol. 5, Dec. 2016, ISSN: 2050-084X. DOI: 10.7554/eLife.22153 (cit. on pp. 4, 6, 263).

[22] S. E. Mansoor, W. Lü, W. Oosterheert, M. Shekhar, E. Tajkhorshid, and E. Gouaux, "X-ray structures define human P2X3 receptor gating cycle and antagonist action", *Nature*, vol. 538, no. 7623, pp. 66–71, Sep. 2016, Publisher: Nature Publishing Group ISBN: 1476-4687 (Electronic) 0028-0836 (Linking), ISSN: 0028-0836. DOI: 10.1038/nature19367 (cit. on pp. 4, 10).

[23] D. Sheng and M. Hattori, "Recent progress in the structural biology of P2X receptors", en, *Proteins: Structure, Function, and Bioinformatics*, vol. n/a, no. n/a, _eprint: https://onlinelibrary.wiley.com/doi/pdf/10.1002/prot.26302, ISSN: 1097-0134. DOI: 10.1002/prot.26302 (cit. on p. 4).

[24] A. E. McCarthy, C. Yoshioka, and S. E. Mansoor, "Full-length P2X7 structures reveal how palmitoylation prevents channel desensitization", *Cell*, vol. 179, no. 3, 659–670.e13, Oct. 2019, ISSN: 0092-8674. DOI: 10.1016/j.cell.2019.09.017 (cit. on pp. 5, 10, 11, 14, 15).

[25] M. F. Jarvis and B. S. Khakh, "ATP-gated P2X cation-channels", en, *Neuropharmacology*, Ligand-Gated Ion Channels, vol. 56, no. 1, pp. 208–215, Jan. 2009, ISSN: 0028-3908. DOI: 10.1016/j.neuropharm.2008.06.067 (cit. on p. 5).

[26] S. Roger, P. Pelegrin, and A. Surprenant, "Facilitation of P2X7 Receptor Currents and Membrane Blebbing via Constitutive and Dynamic Calmodulin Binding", *Journal of Neuroscience*, vol. 28, no. 25, pp. 6393–6401, Jun. 2008, arXiv: 1011.1669v3 ISBN: 1529-2401 (Electronic)\n0270-6474 (Linking), ISSN: 0270-6474. DOI: 10.1523/JNEUROSCI.0696-08.2008 (cit. on p. 5).

[27] R. C. Allsopp and R. J. Evans, "Contribution of the Juxtatransmembrane Intracellular Regions to the Time Course and Permeation of ATP-gated P2X7 Receptor Ion Channels.", *The Journal of biological chemistry*, vol. 290, no. 23, pp. 14 556–66, Jun. 2015, Publisher: American Society for Biochemistry and Molecular Biology, ISSN: 1083-351X. DOI: 10.1074/jbc.M115.642033 (cit. on p. 5).

[28] L. Janks, R. S. Sprague, and T. M. Egan, "ATP-Gated P2X7 Receptors Require Chloride Channels To Promote Inflammation in Human Macrophages", en, *The Journal of Immunology*, vol. 202, no. 3, pp. 883–898, Feb. 2019, ISSN: 0022-1767, 1550-6606. DOI: 10.4049/jimmunol.1801101 (cit. on p. 5).

[29] R. Kopp, A. Krautloher, A. Ramírez-Fernández, and A. Nicke, "P2X7 Interactions and Signaling – Making Head or Tail of It", *Frontiers in Molecular Neuroscience*, vol. 12, 2019, ISSN: 1662-5099. DOI: https://doi.org/10.3389/fnmol.2019.00183 (cit. on pp. 5, 209).

[30] X.-J. Zhang, G.-G. Zheng, X.-T. Ma, Y.-H. Yang, G. Li, Q. Rao, K. Nie, and K.-F. Wu, "Expression of P2X7 in human hematopoietic cell lines and leukemia patients", eng, *Leukemia Research*, vol. 28, no. 12, pp. 1313–1322, Dec. 2004, ISSN: 0145-2126. DOI: 10.1016/j.leukres.2004.04.001 (cit. on p. 5).

[31] M. Garcia-Marcos, S. Pochet, A. Marino, and J.-P. Dehaye, "P2X7 and phospholipid signalling: The search of the "missing link" in epithelial cells", eng, *Cellular Signalling*, vol. 18, no. 12, pp. 2098–2104, Dec. 2006, ISSN: 0898-6568. DOI: 10.1016/j.cellsig.2006.05.008 (cit. on p. 5).

[32] B. G. Shokoples, P. Paradis, and E. L. Schiffrin, "P2X7 Receptors", *Arteriosclerosis, Thrombosis, and Vascular Biology*, vol. 41, no. 1, pp. 186–199, Jan. 2021, ISSN: 1079-5642. DOI: 10.1161/ATVBAHA.120.315116 (cit. on p. 5).

[33] J. Zhou, Z. Zhou, X. Liu, H.-Y. Yin, Y. Tang, and X. Cao, "P2X7 Receptor–Mediated Inflammation in Cardiovascular Disease", *Frontiers in Pharmacology*, vol. 12, 2021, ISSN: 1663-9812 (cit. on p. 5).

[34] F. Di Virgilio, A. C. Sarti, and F. Grassi, "Modulation of innate and adaptive immunity by P2X ion channels", en, *Current Opinion in Immunology*, vol. 52, pp. 51–59, Jun. 2018, ISSN: 0952-7915. DOI: 10.1016/j.coi.2018.03.026 (cit. on p. 5).

[35] K. Kaczmarek-Hajek, J. Zhang, R. Kopp, A. Grosche, B. Rissiek, A. Saul, S. Bruzzone, T. Engel, T. Jooss, A. Krautloher, S. Schuster, T. Magnus, C. Stadelmann, S. Sirko, F. Koch-Nolte, V. Eulenburg, and A. Nicke, "Re-evaluation of neuronal P2X7 expression using novel mouse models and a P2X7-specific nanobody", eng, *eLife*, vol. 7, e36217, Aug. 2018, ISSN: 2050-084X. DOI: 10.7554/eLife.36217 (cit. on pp. 5, 12, 273).

[36] M. T. Miras-Portugal, Á. Sebastián-Serrano, L. d. D. García, and M. Díaz-Hernández, "Neuronal P2X7 Receptor: Involvement in Neuronal Physiology and Pathology", en, *Journal of Neuroscience*, vol. 37, no. 30, pp. 7063–7072, Jul. 2017, Publisher: Society for Neuroscience Section: Dual Perspectives, ISSN: 0270-6474, 1529-2401. DOI: 10.1523/JNEUROSCI.3104-16.2017 (cit. on pp. 5, 14).

[37] P. Illes, T. M. Khan, and P. Rubini, "Neuronal P2X7 Receptors Revisited: Do They Really Exist?", en, *Journal of Neuroscience*, vol. 37, no. 30, pp. 7049–7062, Jul. 2017, Publisher: Society for Neuroscience Section: Dual Perspectives, ISSN: 0270-6474, 1529-2401. DOI: 10.1523/JNEUROSCI.3103-16.2017 (cit. on pp. 5, 14).

[38] J. M. Kanellopoulos and C. Delarasse, "Pleiotropic Roles of P2X7 in the Central Nervous System", *Frontiers in Cellular Neuroscience*, vol. 13, 2019, ISSN: 1662-5102 (cit. on pp. 5, 6, 14).

[39] G. Burnstock and G. E. Knight, "The potential of P2X7 receptors as a therapeutic target, including inflammation and tumour progression", en, *Purinergic Signalling*, vol. 14, no. 1, pp. 1–18, Mar. 2018, ISSN: 1573-9546. DOI: 10.1007/s11302-017-9593-0 (cit. on p. 5).

[40] F. Di Virgilio, G. Schmalzing, and F. Markwardt, "The Elusive P2X7 Macropore", *Trends in Cell Biology*, vol. 28, no. 5, pp. 392–404, May 2018, Publisher: Elsevier Ltd ISBN: 1879-3088 (Electronic) 0962-8924 (Linking), ISSN: 09628924. DOI: 10.1016/j.tcb.2018.01.005 (cit. on p. 5).

[41] J. S. Wiley, R. Sluyter, B. J. Gu, L. Stokes, and S. J. Fuller, "The human P2X7 receptor and its role in innate immunity", *Tissue Antigens*, vol. 78, no. 5, pp. 321–332, Nov. 2011, Publisher: John Wiley & Sons, Ltd (10.1111), ISSN: 00012815. DOI: 10.1111/j.1399-0039.2011.01780.x (cit. on p. 5).

[42] F. Di Virgilio, D. Dal Ben, A. C. Sarti, A. L. Giuliani, and S. Falzoni, "The P2X7 Receptor in Infection and Inflammation", *Immunity*, vol. 47, no. 1, pp. 15–31, Jul. 2017, Publisher: Elsevier ISBN: 1097-4180 (Electronic) 1074-7613 (Linking), ISSN: 10974180. DOI: 10.1016/j.immuni.2017.06.020 (cit. on pp. 5, 11, 14).

[43] A. L. Giuliani, A. C. Sarti, S. Falzoni, and F. Di Virgilio, "The P2X7 Receptor-Interleukin-1 Liaison.", *Frontiers in pharmacology*, vol. 8, p. 123, 2017, Publisher: Frontiers Media SA, ISSN: 1663-9812. DOI: 10.3389/fphar.2017.00123 (cit. on p. 5).

[44] L. E. B. Savio, P. de Andrade Mello, C. G. da Silva, and R. Coutinho-Silva, "The P2X7 Receptor in Inflammatory Diseases: Angel or Demon?", *Frontiers in Pharmacology*, vol. 9, 2018, ISSN: 1663-9812 (cit. on pp. 5, 6).

[45] E. Adinolfi, A. L. Giuliani, E. De Marchi, A. Pegoraro, E. Orioli, and F. Di Virgilio, "The P2X7 receptor: A main player in inflammation", en, *Biochemical Pharmacology*, vol. 151, pp. 234–244, May 2018, ISSN: 0006-2952. DOI: 10.1016/j.bcp.2017.12.021 (cit. on p. 5).

[46] E. Adinolfi, E. D. Marchi, E. Orioli, A. Pegoraro, and F. D. Virgilio, "Role of the P2X7 receptor in tumor-associated inflammation", en-GB, *Current Opinion in Pharmacology*, vol. 47, pp. 59–64, 2019, ISSN: 14714973. DOI: 10.1016/j.coph.2019.02.012 (cit. on p. 6).

[47] E. M. Jimenez-Mateos, J. Smith, A. Nicke, and T. Engel, "Regulation of P2X7 receptor expression and function in the brain", *Brain Research Bulletin*, 2019, ISSN: 18732747. DOI: 10.1016/j.brainresbull.2018.12.008 (cit. on p. 6).

[48] F. Cao, L.-Q. Hu, S.-R. Yao, Y. Hu, D.-G. Wang, Y.-G. Fan, G.-X. Pan, S.-S. Tao, Q. Zhang, H.-F. Pan, and G.-C. Wu, "P2X7 receptor: A potential therapeutic target for autoimmune diseases", en, *Autoimmunity Reviews*, vol. 18, no. 8, pp. 767–777, Aug. 2019, ISSN: 1568-9972. DOI: 10.1016/j.autrev.2019.06.009 (cit. on p. 6).

[49] R. Andrejew, Á. Oliveira-Giacomelli, D. E. Ribeiro, T. Glaser, V. F. Arnaud-Sampaio, C. Lameu, and H. Ulrich, "The P2X7 Receptor: Central Hub of Brain Diseases.", *Frontiers in molecular neuroscience*, vol. 13, p. 124, Jul. 2020, Publisher: Frontiers Media S.A., ISSN: 1662-5099. DOI: 10.3389/fnmol.2020.00124 (cit. on p. 6).

[50] F. Di Virgilio, V. Vultaggio-Poma, and A. C. Sarti, "P2X receptors in cancer growth and progression", en, *Biochemical Pharmacology*, Geoffrey Burnstock - an Accidental Pharmacologist, vol. 187, p. 114 350, May 2021, ISSN: 0006-2952. DOI: 10.1016/j.bcp.2020.114350 (cit. on p. 6).

[51] F. Grassi and B. De Ponte Conti, "The P2X7 Receptor in Tumor Immunity", *Frontiers in Cell and Developmental Biology*, vol. 9, 2021, ISSN: 2296-634X (cit. on p. 6).

[52] J. C. Rotondo, C. Mazziotta, C. Lanzillotti, C. Stefani, G. Badiale, G. Campione, F. Martini, and M. Tognon, "The Role of Purinergic P2X7 Receptor in Inflammation and Cancer: Novel Molecular Insights and Clinical Applications", en, *Cancers*, vol. 14, no. 5, p. 1116, Jan. 2022, Number: 5 Publisher: Multidisciplinary Digital Publishing Institute, ISSN: 2072-6694. DOI: 10.3390/cancers14051116 (cit. on p. 6).

[53] A. C. Sarti, V. Vultaggio-Poma, and F. Di Virgilio, "P2X7: A receptor with a split personality that raises new hopes for anti-cancer therapy", en, *Purinergic Signalling*, vol. 17, no. 2, pp. 175–178, Jun. 2021, ISSN: 1573-9546. DOI: 10.1007/s11302-021-09783-w (cit. on p. 6).

[54] C. C. Chrovian, J. C. Rech, A. Bhattacharya, and M. A. Letavic, "P2X7 antagonists as potential therapeutic agents for the treatment of CNS disorders", eng, *Progress in Medicinal Chemistry*, vol. 53, pp. 65–100, 2014, ISSN: 0079-6468. DOI: 10.1016/B978-0-444-63380-4.00002-0 (cit. on p. 6).

[55] C. F. Gelin, A. Bhattacharya, and M. A. Letavic, "P2X7 receptor antagonists for the treatment of systemic inflammatory disorders", eng, *Progress in Medicinal Chemistry*, vol. 59, pp. 63–99, 2020, ISSN: 0079-6468. DOI: 10.1016/bs.pmch.2019.11.002 (cit. on p. 6).

[56] J. H. Park and Y. C. Kim, "P2X7 receptor antagonists: A patent review (2010–2015)", *Expert Opinion on Therapeutic Patents*, vol. 27, no. 3, pp. 257–267, Mar. 2017, Publisher: Taylor and Francis Ltd, ISSN: 17447674. DOI: 10.1080/13543776.2017.1246538 (cit. on p. 6).

[57] M. Barniol-Xicota, S.-H. Kwak, S.-D. Lee, E. Caseley, E. Valverde, L.-H. Jiang, Y.-C. Kim, and S. Vázquez, "Escape from adamantane: Scaffold optimization of novel P2X7 antagonists featuring complex polycycles", en, *Bioorganic & Medicinal Chemistry Letters*, vol. 27, no. 4, pp. 759–763, Feb. 2017, ISSN: 0960-894X. DOI: 10.1016/j.bmcl.2017.01.039 (cit. on p. 6).

[58] R. C. Allsopp, S. Dayl, R. Schmid, and R. J. Evans, "Unique residues in the ATP gated human P2X7 receptor define a novel allosteric binding pocket for the selective antagonist AZ10606120", *Scientific Reports*, vol. 7, no. 1, p. 725, Dec. 2017, Publisher: Nature Publishing Group, ISSN: 20452322. DOI: 10.1038/s41598-017-00732-5 (cit. on p. 6).

[59] R. C. Allsopp, S. Dayl, A. B. Dayel, R. Schmid, and R. J. Evans, "Mapping the allosteric action of antagonists A740003 and A438079 reveals a role for the left flipper in ligand sensitivity at P2X7 receptorss", *Molecular Pharmacology*, vol. 93, no. 5, pp. 553–562, May 2018, Publisher: American Society for Pharmacology and Experimental Therapy, ISSN: 15210111. DOI: 10.1124/mol.117.111021 (cit. on p. 6).

[60] A. B. Dayel, R. J. Evans, and R. Schmid, "Mapping the site of action of human P2X7 receptor antagonists AZ11645373, Brilliant Blue G, KN-62, calmidazolium, and Zinc58368839 to the intersubunit allosteric pocket", *Molecular Pharmacology*, vol. 96, no. 3, pp. 355–363, Sep. 2019, Publisher: American Society for Pharmacology and Experimental Therapy, ISSN: 15210111. DOI: 10.1124/mol.119.116715 (cit. on p. 6).

[61] L.-H. Jiang, E. A. Caseley, S. P. Muench, and S. Roger, "Structural basis for the functional properties of the P2X7 receptor for extracellular ATP", en, *Purinergic Signalling*, vol. 17, no. 3, pp. 331–344, Sep. 2021, ISSN: 1573-9546. DOI: 10.1007/s11302-021-09790-x (cit. on p. 6).

[62] C. E. Müller and V. Namasivayam, "Recommended tool compounds and drugs for blocking P2X and P2Y receptors", *Purinergic Signalling*, vol. 17, no. 4, pp. 633–648, Dec. 2021, ISSN: 1573-9538. DOI: 10.1007/s11302-021-09813-7 (cit. on p. 6).

[63] C. S. Gandhi and R. Olcese, "The voltage-clamp fluorometry technique", eng, *Methods in Molecular Biology (Clifton, N.J.)*, vol. 491, pp. 213–231, 2008, ISSN: 1064-3745. DOI: 10.1007/978-1-59745-526-8_17 (cit. on p. 7).

[64] S. A. Pless and J. W. Lynch, "Illuminating the Structure and Function of Cys-Loop Receptors", en, *Clinical and Experimental Pharmacology and Physiology*, vol. 35, no. 10, pp. 1137–1142, 2008, _eprint: https://onlinelibrary.wiley.com/doi/pdf/10.1111/j.1440-1681.2008.04954.x, ISSN: 1440-1681. DOI: 10.1111/j.1440-1681.2008.04954.x (cit. on p. 7).

[65] E. Lorinczi, Y. Bhargava, S. F. Marino, a. Taly, K. Kaczmarek-Hajek, a. Barrantes-Freer, S. Dutertre, T. Grutter, J. Rettinger, and a. Nicke, "Involvement of the cysteine-rich head domain in activation and desensitization of the P2X1 receptor", *Proceedings of the National Academy of Sciences*, vol. 109, no. 28, pp. 11 396–11 401, 2012, ISBN: 1091-6490 (Electronic)\r0027-8424 (Linking), ISSN: 0027-8424. DOI: 10.1073/pnas.1118759109 (cit. on pp. 7, 10).

[66] M. H. Akabas, "Cysteine Modification: Probing Channel Structure, Function and Conformational Change", eng, *Advances in Experimental Medicine and Biology*, vol. 869, pp. 25–54, 2015, ISSN: 0065-2598. DOI: 10.1007/978-1-4939-2845-3_3 (cit. on p. 7).

[67] N. Braun, Z. P. Sheikh, and S. A. Pless, "The current chemical biology tool box for studying ion channels", en, *The Journal of Physiology*, vol. 598, no. 20, pp. 4455–4471, 2020, _eprint: https://onlinelibrary.wiley.com/doi/pdf/10.1113/JP276695, ISSN: 1469-7793. DOI: 10.1113/JP276695 (cit. on p. 7).

[68] L. Leisle, F. Valiyaveetil, R. A. Mehl, and C. A. Ahern, "Incorporation of Non-Canonical Amino Acids", en, in *Novel Chemical Tools to Study Ion Channel Biology*, C. Ahern and S. Pless, Eds., vol. 869, Series Title: Advances in Experimental Medicine and Biology, New York, NY: Springer New York, 2015, pp. 119–151, ISBN: 978-1-4939-2844-6 978-1-4939-2845-3. DOI: 10.1007/978-1-4939-2845-3_7 (cit. on p. 7).

[69] V. Klippenstein, L. Mony, and P. Paoletti, "Probing Ion Channel Structure and Function Using Light-Sensitive Amino Acids", *Trends in Biochemical Sciences*, vol. 43, no. 6, pp. 436–451, 2018, Publisher: Elsevier Ltd, ISSN: 13624326. DOI: 10.1016/j.tibs.2018.02.012 (cit. on p. 7).

[70] D. A. Dougherty and E. B. V. Arnam, "In Vivo Incorporation of Unnatural Amino Acids Using the Chemical Aminoacylation Strategy. A Broadly Applicable Mechanistic Tool", *Chembiochem : a European journal of chemical biology*, vol. 15, no. 12, p. 1710, Aug. 2014, Publisher: NIH Public Access. DOI: 10.1002/CBIC.201402080 (cit. on p. 7).

[71] L. Davis and J. W. Chin, "Designer proteins: Applications of genetic code expansion in cell biology", en, *Nature Reviews Molecular Cell Biology*, vol. 13, no. 3, pp. 168–182, Mar. 2012, ISSN: 1471-0072, 1471-0080. DOI: 10.1038/nrm3286 (cit. on p. 7).

[72] S. W. Santoro, J. C. Anderson, V. Lakshman, and P. G. Schultz, "An archaebacteria-derived glutamyl-tRNA synthetase and tRNA pair for unnatural amino acid mutagenesis of proteins in Escherichia coli", *Nucleic Acids Research*, vol. 31, no. 23, pp. 6700–6709, Dec. 2003, ISSN: 0305-1048. DOI: 10.1093/nar/gkg903 (cit. on p. 7).

[73] H. S. Lee, J. Guo, E. A. Lemke, R. D. Dimla, and P. G. Schultz, "The Genetic Incorporation of a Small, Environmentally Sensitive, Fluorescent Probe into Proteins in S. Cerevisiae", *Journal of the American Chemical Society*, vol. 131, no. 36, p. 12 921, Sep. 2009, Publisher: NIH Public Access. DOI: 10.1021/JA904896S (cit. on pp. 7, 10, 14).

[74] S. Ye, M. Riou, S. Carvalho, and P. Paoletti, "Expanding the genetic code in Xenopus laevis oocytes", eng, *Chembiochem: A European Journal of Chemical Biology*, vol. 14, no. 2, pp. 230–235, Jan. 2013, ISSN: 1439-7633. DOI: 10.1002/cbic.201200515 (cit. on p. 7).

[75] A. Chatterjee and J. Guo, "A genetically encoded fluorescent probe in mammalian cells", *Journal of the American . . .*, vol. 135, no. 34, pp. 12 540–12 543, 2013. DOI: 10.1021/ja4059553.A (cit. on pp. 7, 236).

[76] M. Wulf and S. A. Pless, "High-Sensitivity Fluorometry to Resolve Ion Channel Conformational Dynamics", *Cell Reports*, vol. 22, no. 6, pp. 1615–1626, 2018, Publisher: ElsevierCompany., ISSN: 22111247. DOI: 10.1016/j.celrep.2018.01.029 (cit. on p. 7).

[77] T. Kalstrup and R. Blunck, "Dynamics of internal pore opening in K V channels probed by a fl uorescent unnatural amino acid", *Proceedings of the National Academy of Sciences of the United States of America*, vol. 110, no. 20, pp. 8272–8277, 2013. DOI: 10.1073/pnas.1220398110/-/DCSupplemental.www.pnas.org/cgi/doi/10.1073/pnas.1220398110 (cit. on p. 7).

[78] T. Kalstrup and R. Blunck, "Voltage-clamp Fluorometry in Xenopus Oocytes Using Fluorescent Unnatural Amino Acids", *JoVE (Journal of Visualized Experiments)*, vol. 2017, no. 123, e55598, May 2017, Publisher: Journal of Visualized Experiments, ISSN: 1940-087X. DOI: 10.3791/55598 (cit. on pp. 7, 11, 14, 236).

[79] T. Kalstrup and R. Blunck, "S4–S5 linker movement during activation and inactivation in voltage-gated K+ channels", *Proceedings of the National Academy of Sciences*, vol. 115, no. 29, E6751–E6759, Jul. 2018, Publisher: Proceedings of the National Academy of Sciences. DOI: 10.1073/pnas.1719105115 (cit. on p. 7).

[80] A. Pippel, M. Stolz, R. Woltersdorf, A. Kless, G. Schmalzing, and F. Markwardt, "Localization of the gate and selectivity filter of the full-length P2X7 receptor", *Proceedings of the National Academy of Sciences*, vol. 114, no. 11, E2156–E2165, Mar. 2017, ISBN: 1091-6490 (Electronic) 0027-8424 (Linking), ISSN: 0027-8424. DOI: 10.1073/pnas.1610414114 (cit. on p. 10).

[81] M. Hattori and E. Gouaux, "Molecular mechanism of ATP binding and ion channel activation in P2X receptors", en, *Nature*, vol. 485, no. 7397, pp. 207–212, May 2012, Bandiera_abtest: a Cg_type: Nature Research Journals Number: 7397 Primary_atype: Research Publisher: Nature Publishing Group Subject_term: Ion channels in the nervous system;Molecular neuroscience;Neurophysiology;Structural

biology Subject_term_id: ion-channels-in-the-nervous-system;molecular-neuroscience;neurophysiology biology, ISSN: 1476-4687. DOI: 10.1038/nature11010 (cit. on p. 10).

[82] M. Furber, L. Alcaraz, J. E. Bent, A. Beyerbach, K. Bowers, M. Braddock, M. V. Caffrey, D. Cladingboel, J. Collington, D. K. Donald, M. Fagura, F. Ince, E. C. Kinchin, C. Laurent, M. Lawson, T. J. Luker, M. M. P. Mortimore, A. D. Pimm, R. J. Riley, N. Roberts, M. Robertson, J. Theaker, P. V. Thorne, R. Weaver, P. Webborn, and P. Willis, "Discovery of Potent and Selective Receptor Antagonists / Interleukin-1β Inhibitors", *Journal of Medicinal Chemistry*, vol. 50, no. 24, pp. 5882–5885, 2007, ISSN: 00222623. DOI: 10.1021/jm700949w (cit. on pp. 10, 12, 72).

[83] A. D. Michel, L. J. Chambers, W. C. Clay, J. P. Condreay, D. S. Walter, and I. P. Chessell, "Direct labelling of the human P2X7 receptor and identification of positive and negative cooperativity of binding", en, *British Journal of Pharmacology*, vol. 151, no. 1, pp. 84–95, 2007, _eprint: https://onlinelibrary.wiley.com/doi/pdf/10.1038/sj.bjp.0707196 ISSN: 1476-5381. DOI: 10.1038/sj.bjp.0707196 (cit. on p. 10).

[84] N. Heintz, "Gene Expression Nervous System Atlas (GENSAT)", en, *Nature Neuroscience*, vol. 7, no. 5, pp. 483–483, May 2004, Number: 5 Publisher: Nature Publishing Group, ISSN: 1546-1726. DOI: 10.1038/nn0504-483 (cit. on pp. 12, 151).

[85] A. Durner, E. Durner, and A. Nicke, "Improved ANAP incorporation and VCF analysis reveal details of P2X7 current facilitation and a limited conformational interplay between ATP binding and the intracellular ballast domain", *eLife*, vol. 12, S. A. Pless, R. W. Aldrich, and G. Dai, Eds., e82479, Jan. 2023, Publisher: eLife Sciences Publications, Ltd, ISSN: 2050-084X. DOI: 10.7554/eLife.82479 (cit. on p. 23).

[86] D. T. Pournara, A. Durner, E. Kritsi, A. Papakostas, P. Zoumpoulakis, A. Nicke, and M. Koufaki, "Design, Synthesis, and in vitro Evaluation of P2X7 Antagonists", en, *ChemMedChem*, vol. 15, no. 24, pp. 2530–2543, 2020, ISSN: 1860-7187. DOI: 10.1002/cmdc.202000303 (cit. on p. 73).

[87] A. Ramírez-Fernández, L. Urbina-Treviño, G. Conte, M. Alves, B. Rissiek, A. Durner, N. Scalbert, J. Zhang, T. Magnus, F. Koch-Nolte, N. Plesnila, J. M. Deussing, T. Engel, R. Kopp, and A. Nicke, "Deviant reporter expression and P2X4 passenger gene overexpression in the soluble EGFP BAC transgenic P2X7 reporter mouse model", en, *Scientific Reports*, vol. 10, no. 1, p. 19 876, Nov. 2020, Number: 1 Publisher: Nature Publishing Group, ISSN: 2045-2322. DOI: 10.1038/s41598-020-76428-0 (cit. on p. 153).

[88] J. Giribaldi, Y. Haufe, E. R. J. Evans, M. Amar, A. Durner, C. Schmidt, A. Faucherre, H. Moha Ou Maati, C. Enjalbal, J. Molgó, D. Servent, D. T. Wilson, N. L. Daly, A. Nicke, and S. Dutertre, "Backbone Cyclization Turns a Venom Peptide into a Stable and Equipotent Ligand at Both Muscle and Neuronal Nicotinic Receptors", *Journal of Medicinal Chemistry*, vol. 63, no. 21, pp. 12 682–12 692, Nov. 2020, Publisher: American Chemical Society, ISSN: 0022-2623. DOI: 10.1021/acs.jmedchem.0c00957 (cit. on p. 181).

[89] A. Durner and A. Nicke, "A Simplified Protocol to Incorporate the Fluorescent Unnatural Amino Acid ANAP into Xenopus laevis Oocyte-Expressed P2X7 Receptors", eng, *Methods in Molecular Biology (Clifton, N.J.)*, vol. 2510, pp. 193–216, 2022, ISSN: 1940-6029. DOI: 10.1007/978-1-0716-2384-8_10 (cit. on p. 237).

Acknowledgements

The work summarized in this doctoral thesis was made possible by the support and help of many dedicated people, to whom I would like to express my gratitude to.

Thanks to **Annette Nicke** for the opportunity to do my doctoral studies in her group and for continuously promoting my scientific education and advancements. I am especially thankful for the fact, that you would always listen to my ideas and gave me the freedom to try new things.

Special thanks to all my colleagues and lab mates, alumni and current members alike, with whom I shared more than lab space and experimental data. The solidarity and team spirit amongst the students at the WSI is amazing and I am happy I was part of it! Thanks for all the support! It came in every imaginable form and saved my day countless times!
Robin Kopp, for your expertise in protein biochemistry, for exploring Hamburg and Rome with me, and for the speakers in the lab (I still hate Helene Fischer's "Atemlos", though). **Antonio Ramírez-Fernández** for helpful discussions and sharing projects in science, for introducing me to your Spanish music I pretended to dislike (also for enduring me making fun of it). We shared a lot of highs and lows in the lab and I always appreciated your opinion. Thanks for being a great guy - and for the coffee, of course. **Yves Haufe** for spreading good mood and being supportive, for always being able to talk science, for helpful feedback, for delicious tea, and for setting up the second TEVC station with all its instruments. Also for listening - to all of it, my cursing and swearing, as well as my singing and whistling and in addition for disburdening me by taking over big parts of administrative and other tasks in the lab. This also goes for **Gonxhe Lokaj**, **Lukas Sassenbach**, and **PranavKumar Shadamarshan Rengasayee**. Thanks for keeping me sane, especially during these last couple of months. **Anna Heizmann** for exploring and establishing procedures and protocols together with me at the very beginning of our lab time together, for your optimistic and cheerful attitude, for memorable late-night measuring sessions accompanied by a lot of singing and/or cursing (both very loudly!), and for being a friend. **Carla Abrahamian** for your unique humour, your empathy, and your extensive knowledge not only in science, but also in history, politics, how-to-WhatsApp,... For feeding me in between experiments, for our friday-night sessions, and most importantly for being you (and for whistling in the most ear-piercing way - love it)! Thanks to all the practical and master students, medical doctoral candidates, and guests on whom I could train my teaching skills (sorry for my hideous drawings...) and from whom I learned new methods and gained different perspectives and feedback for my own work (and other things in life). You brought life to the lab and it would not have been the same without you! **Heinz Janser** for being a multi-talent and a great help in the lab, for administrative support, for countless trips to and from the animal facilities in Großhadern, for the emergency Muh-Muhs, and your general good nature. **Christine Hopfer** for sharing your experiences with me from my first day on at the institute, for your dedication to your work, and for your cute little notes. **Annett Sporning** and **Kerstin Dümke**

for always friendly and helpful support from afar and for providing our lab with countless *Xenopus laevis* oocytes over the years. **Monika Haberland** and her team from the animal facilities of the Biomedical Center Munich for taking care of our frogs and also for providing oocytes. **Dimitra Pournara and Maria Koufaki** as well as **Santiago Vázquez, Andreea Larisa Turcu, and David Soto** for great collaborations! This thesis was set using LaTeXand is based on a template from Jordan Suchow, although heavily altered by Markus Weiss-Brummer and Ellis Durner.

Outside the institute I would like to thank **Wolfgang Ott**, **Ellis Durner**, **Tobias Verdorfer**, **Markus Weiss-Brummer**, **Thomas Nicolaus**, and **Lukas Milles** for advice, encouragement, lab equipment (borrowed - of course), and for sharing your experiences. I benefitted immensely from your scientific backgrounds and learned a lot about good scientific practice from you guys - also how to party. I am very fortunate to have such great friends! **Markus and Stephanie Weiss-Brummer** for listening, understanding, and so much more. I value your opinions and our time together!

I want to thank my whole family for their continuous, great, and unconditional support! Despite the distance, they are always here for me. I could call them at any time and they would listen to all my highs and lows, no matter if I was talking about events, friends, or about my experiments. They were always interested in what I do, which made me feel good about my work. You gave me hold throughout the years. Thanks for always believing in me!
My parents **Yvonne and Peter Krautloher** found exceptional ways to continuously support and motivate me, whether it be coffee breaks via phone call during long lab days or snack boxes and survival packages sent directly to the institute. By letting me explain my projects and by asking questions, they helped me sort things out, clear my head, and get a fresh perspective. They even helped me to stay focused during seemingly not-ending periods of super unexciting desk work. Thanks for keeping me on track! My brother **Maximilian Krautloher** who has always been there for me, whether it be with valuable life advice, encouragement, or a piece of delicious cake during a 10 min change of trains just to say 'hi'. **Tatjana Krautloher**, without whom I would have never even made it through the first semesters of zoology and botany. I am still amazed by your contagious motivation, your ambition, and your humor!
Most of all, I want to thank **Ellis Durner**. The time and effort you put into optimizing and designing measurement setups and protocols with me went far beyond general interest in what I do. You spent nights and weekends building and programming components from scratch and, on top of it all, very patiently answered all my questions. I benefitted immensely from your scientific expertise and your sense of integrity. You shared your vast experiences and knowledge about optics, electronics, and laboratory procedures with me and in addition, taught me programming, wet-lab skills, critical thinking and so much more. We discussed, troubleshooted, joked, puzzled, and sometimes fought over various methods and experiments. You came up with ideas that had fundamental impact on my projects. Your feedback, advice, and encouragement were essential for me and fueled my motivation.
You gave me hold and kept me going through all of it.
... There is just no satisfying way I can express this in words...
Thank you.